Australian Government
Geoscience Australia

Metamorphic Evolution and Integrated Terrane Analysis of the Eastern Yilgarn Craton: Rationale, Methods, Outcomes and Interpretation

B. Goscombe, R.S. Blewett, K. Czarnota, P.B. Groenewald and R. Maas

Record
2009/23

GeoCat # 68806

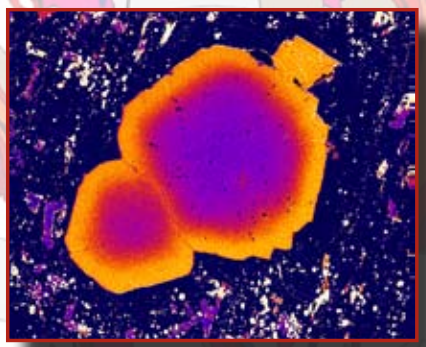

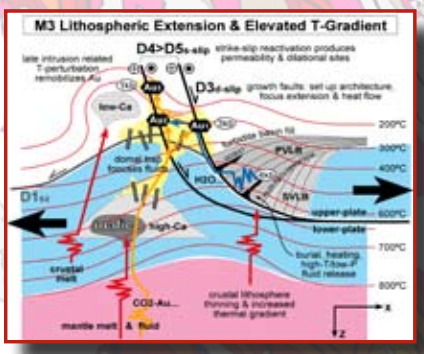

Metamorphic Evolution and Integrated Terrane Analysis of the Eastern Yilgarn Craton: Rationale, Methods, Outcomes and Interpretation

GEOSCIENCE AUSTRALIA
RECORD 2009/23

by

B. Goscombe[1], R.S. Blewett[2], K. Czarnota[2], P.B. Groenewald[3] and R. Maas[4].

Australian Government
Geoscience Australia

GEOLOGICAL SURVEY
WESTERN AUSTRALIA

1. Integrated Terrane Analysis Research (ITAR), 18 Cambridge Road Aldgate SA 5154
ben.goscombe@adelaide.edu.au
http://www.terraneanalysis.com.au
2. Predictive Mineral Discovery Cooperative Research Centre, c/- Geoscience Australia GPO Box 378 Canberra ACT 2601
3. Mincor Resources NL, PO Box 1810 West Perth WA 6872
4. School of Earth Sciences, University of Melbourne Parkville VIC 3010

Department of Resources, Energy and Tourism
Minister for Resources, Energy and Tourism: The Hon. Martin Ferguson, AM, MP
Secretary: Mr John Pierce

Geoscience Australia

Chief Executive Officer: Dr Neil Williams, PSM

ISSN 1448-2177

ISBN 978-1-921498-93-0 Web

ISBN 978-1-921498-94-7 DVD

ISBN 978-1-921498-95-4 Hardcopy

GeoCat # 68806

Bibliographic reference: Goscombe, B., Blewett, R.S., Czarnota, K., Groenewald, P.B. and Maas, R., 2009. Metamorphic evolution and integrated terrane analysis of the eastern Yilgarn Craton: rationale, methods, outcomes and interpretation. Geoscience Australia, Record 2009/23. 270pp.

Contents

Abbreviations

EYCMP	Eastern Yilgarn Craton Metamorphic Project, Module 3 of pmd*CRC Y4.
EYC	Eastern Yilgarn Craton (Cassidy, 2006; Cassidy et al., 2006).
EGST	Eastern Goldfields Superterrane (Cassidy, 2006; Cassidy et al., 2006).
SMG	Sequence of mineral growth.
CFPS	Coupled facies and pressure-series metamorphic map.
P	Pressure in kilobars (kb).
T	Temperature in degrees celsius (ºC).
G	Temperature/depth ratio, or average thermal regime in ºC/km.
PT	Pressure-temperature locus, as in a PT estimate.
P-T	Pressure-temperature space, as in the tracking of P-T paths.
R	Strain ratio.
γ	Shear strain.
QFII	Qualitative foliation intensity index.
MDB	Metamorphic database.
GIS	Geographical information system.
X, Y, Z	Axes of the finite strain ellipsoid.
β	Acute angle of obliquity between stretching lineation direction and foliation trace.
Minerals	All mineral abbreviations are lower-case after Kretz (1983); a few additional minerals have 4 character abbreviations and are listed in Appendix (1).
M…	Metamorphic period.
D…	Deformation event.
XRF	X-ray fluorescence.
XRD	X-ray diffraction.
GA	Geoscience Australia.
GSWA	Geological Survey of Western Australia.
pmd*CRC*	Predictive Mineral Discovery Cooperative Research Centre.
ITAR	Integrated Terrane Analysis Research.
N, S, E, W	North, south, east and west.
Pressure	The pressure categories used are relative and for the EYCMP only: high = >6.5 kb, medium = 4.6-6.5 kb, low = 4.5-3.0 kb and very low = <3.0 kb.
PVTB	Post-volcanic turbiditic basin.
PVFB	Post-volcanic fluvial basin.
SVB	Syn-volcanic clastic basin.

Executive Summary

METAMORPHIC EVOLUTION AND INTEGRATED TERRANE ANALYSIS OF THE EASTERN YILGARN CRATON

A metamorphic database covering the entire eastern Yilgarn Craton has been compiled from pre-existing mapping, 14,500 sites with qualitative metamorphic information, and 470 new key sites with detailed quantitative metamorphic data including P, T, temperature/depth ratio and P-T paths. The derived temporal and spatial patterns contrast with previous tectonic models and invariant crustal depth with the single prograde metamorphic event of the long-standing metamorphic paradigm. In particular, there are large variations in peak metamorphic crustal depths (12 to 31 km), and five metamorphic periods can now be recognised.

- M*a*: Very localised, low-P granulite of high temperature/depth ratio (>50ºC/km).
- M1: High-P (8.7kb), low temperature/depth ratio (≤20ºC/km) assemblages localised to major shear zones with clockwise isothermal decompression P-T paths.
- M2: Regional matrix parageneses with T ranging 300-550ºC across greenstone belts and elevated temperature/depth ratio of 30-40ºC/km throughout. Tight clockwise paths evolved through maximum prograde pressures of 6 kb and peak metamorphic pressures of 3.5-5.0 kb.
- M3a: An extension related thermal pulse localised on the Ockerburry Fault and post-volcanic late basins. Anticlockwise paths to peak conditions of 500-580ºC and 4.0 kb, define moderately high temperature/depth ratio of 40-50ºC/km.
- M3b: Multiple localised hydrothermal alteration events during a period of exhumation from 4 kb to 1 kb.

Metamorphic patterns during each event have been temporally and spatially integrated with the new deformation framework (Blewett and Czarnota, 2007c) by a process of metamorphic domain analysis and using metamorphic field gradients. The continual evolution with time of fundamental metamorphic parameters throughout the entire history have been constructed as evolution curves and integrated with the deformation, magmatic, stratigraphic and mineralization history. The evolution in metamorphic response can be related to the tectonic evolution of the East Yilgarn Craton. From crustal growth phase (M*a* and M1), to thermal priming of the crust at termination of volcanism and massive granite influx (M2), leading to runaway lithospheric extension (M3a) and finally a phase of inversion and reactivation (M3b).

Introduction

The EYCMP is a world-class gold and nickel mineral province that is reaching exploration maturity with a diminishing number of significant new finds. Effective mineral exploration is contingent on robust tectonic frameworks and knowledge of palaeo-tectonic settings (Goldfarb et al., 2001, 2005; Bierlein et al., 2002). The ***pmd****CRC* Y1, Y2, Y3 and the current Y4 programs on the Eastern Yilgarn Craton (EYC) were established to drive geological research in the region with the aim of original new insights and models that will both aid and stimulate new approaches to mineral exploration in the region.

Module 3 of the Y4 project was established to document the metamorphic patterns and metamorphic evolutions experienced in the region, as the East Yilgarn Craton Metamorphic Project (EYCMP). The history of the EYC spans the crucial temporal window in Earth history for the transition (continuum or globally episodic) from plume tectonics with symmetric downward advection to plate tectonics with asymmetric subduction. Metamorphic expressions of these two tectonic paradigms are fundamentally different, leading to metamorphic studies being one of the best ways to way to recognise this transition (Brown, 2006, 2007a, b, c). Consequently, the EYCMP also contributes to the ongoing debate on the establishment of ongoing globally dominant plate tectonics.

Metamorphic rocks preserve a record of transient first-order variables that are otherwise not available. Datasets such as temperature, crustal depth, thermal regime and rates of cooling/heating and exhumation/burial are generated by back engineering metamorphic rocks. These datasets are fundamental geological variables that crucially constrain first-order patterns and gradients, crustal evolution, crustal processes, tectonic setting and at second-order scales are inter-related with deformation, fluid flow and mineralization. Metamorphic rocks are crucial for three reasons: [1] they preserve a long and near continuous record of orogenic history; [2] are the only source of information on crustal depths and paths of individual particles through the crustal column, recognising lithospheric thinning and thickening events; and [3] are the only source of information that tracks the long thermal evolution of the crust. The study of metamorphic rocks results in quantitative datasets of fundamental geological variables such as temperature (T), crustal depth or pressure (P), thermal regime (T/depth), P-T evolution paths and age of crystallization events (t). The spatial distribution patterns of these variables are crucial datasets. Furthermore, the temporal integration of these datasets constrains the P-T evolutions tracked by different parts of the crust at different times and can constrain rates of crustal processes. The spatial and temporal patterns documented from metamorphic rocks constrain the evolution of orogenic systems in robust fundamental ways that not only contribute insights into tectonic settings and history but also the fluid history of the crust and mineralization events.

The rationale behind the EYCMP has been an integrated approach to generating new metamorphic datasets and also their interpretation by spatial and temporal integration with pre-existing datasets for deformation, deposition and magmatic history. The EYC is characterized by a heterogeneous strain distribution, which is a crucial indicator of well-endowed gold terranes (Bierlein pers. comm. 2007). Another crucial indicator of gold mineralization is steep metamorphic gradients as drivers of fluid formation and circulation (Hall, 1997; Sheldon et al., 2007). Consequently, there is a *prima facie* need to spatially link metamorphic and structural patterns and to temporally integrate these datasets to document crustal evolutions. Geological datasets are typically only integrated for a specific event at specific sites. The approach taken has been to integrate data over the full history of the EYC using evolution curves, and to spatially integrate data across the entire orogenic system using field gradients. The integration of structural, metamorphic and chronology datasets has been shown to be crucial to documenting dynamic crustal architectures (Goscombe et al., 2005a, 2006; Goscombe and Gray, 2007). The aims of the EYCMP are: [1] to compile a comprehensive GIS dataset of all currently available structural, metamorphic and chronologic data from the EYC; [2] produce new generation metamorphic maps that encapsulate crustal depth and age data as well as temperature; [3] document comprehensive P-T-t-deformation histories at key localities; [4] produce quantitative field gradients across the region to document structural and metamorphic variation.

The EYCMP has benefited greatly by following earlier Y1, Y3 and Y4 projects (www.pmdcrc.com.au) that delivered substantive findings that have established robust frameworks for the structural evolution (e.g., Blewett et al., 2004a; Blewett and Czarnota, 2005, 2007b, 2007c), extrusive stratigraphy (e.g., Groenewald et al., 2006), clastic stratigraphy (e.g., Krapez et al., 2000; Squire, 2006, 2007) and magmatic and geochemical evolution of the crust (e.g., Cassidy et al., 2002, 2006; Champion and Sheraton, 1997) as well as countless studies documenting mineralization systems (e.g., Dugdale and Hagemann, 2001; Salier et al., 2005; Miller and Rasmussen, 2006). During the course of these earlier modules, the influence of thermal and barometric evolution of the crust leading to Au-mineralization, and the paucity of robust metamorphic datasets became increasingly apparent. This recent neglect of metamorphic studies in the EYC contrasts strongly with a growing number of recent high quality and detailed metamorphic studies in Archaean terranes elsewhere: South Africa (e.g., Diener et al., 2005; Dziggle et al., 2006), Canada (e.g., Valli et al., 2004; Thompson, 2005) and Southern Cross Terrane (e.g., Dalstra et al., 1999).

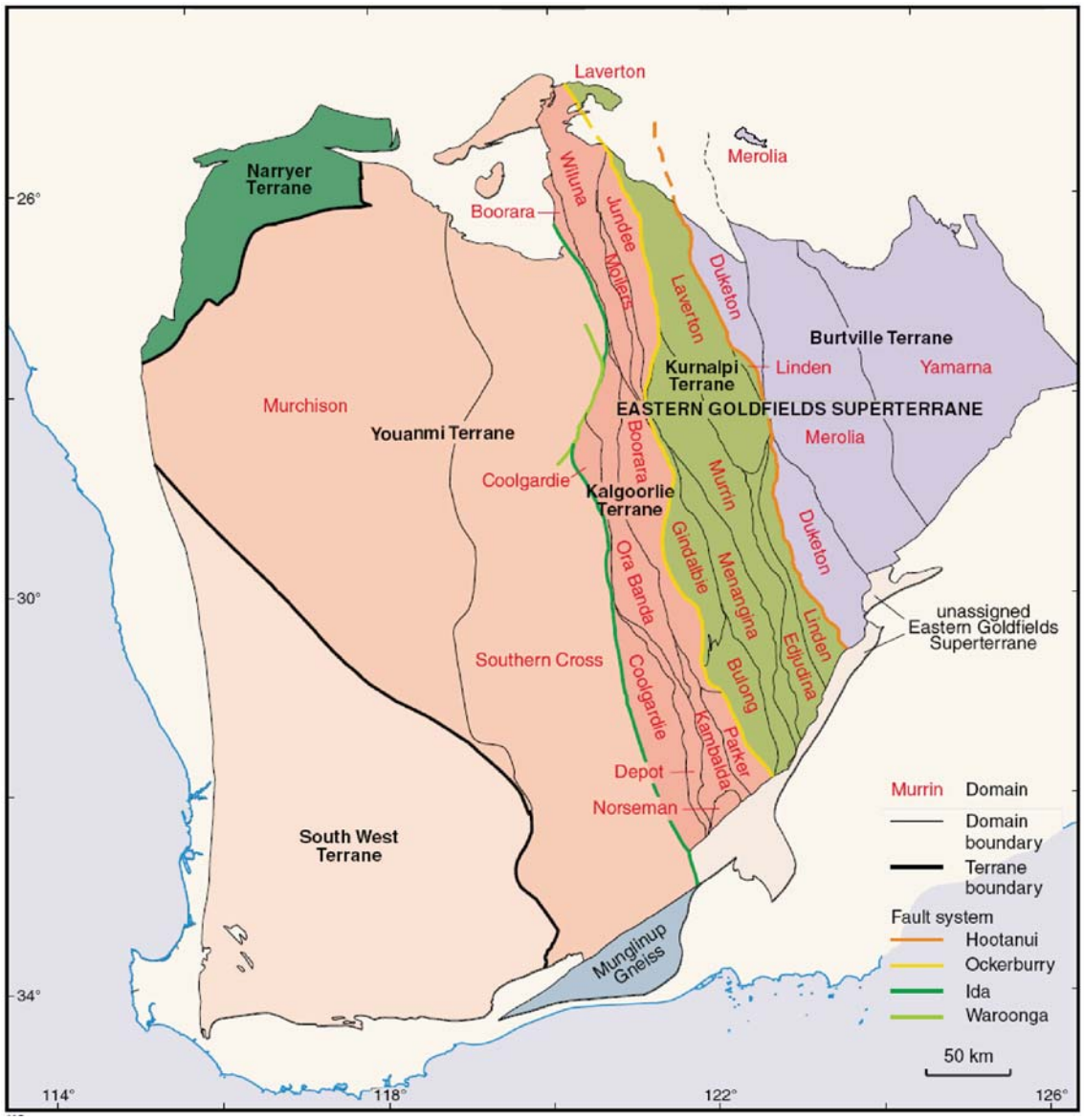

Figure 1: *Map outlining the broad tectonic units of the Yilgarn Craton and surrounding provinces (Geological Survey of Western Australia).*

SCOPE AND HISTORY OF EYCMP

The EYCMP was formally initiated in mid-2006 and funded by the ***pmd****CRC* and Geocience Australia (GA) with in kind support of the Geological Survey of Western Australia (GSWA). The current EYCMP program was built on two pre-existing foundations: [1] an integrated methodology that has been in development since 2000 by Goscombe (ITAR - http://www.terraneanalysis.com.au), and [2] preliminary metamorphic datasets that had been in development since 2003 by Goscombe with the support of GSWA. The EYCMP is primarily focused on a comprehensive documentation of metamorphism in the Kalgoorlie and Kurnalpi Terranes to the east of the Ida Fault System, with preliminary findings from the remaining terranes presented for comparison (Figure 1). The metamorphic and geological background, rationale, methodology, results and interpretation from the EYCMP (2003-2008) are presented in total in this GA Record 2009/23. This constitutes the first-phase of a larger Yilgarn Craton metamorphic program, the second-phase of which will be the analysis of terranes to the west of the Ida Fault System (WYCMP) to be funded by the GSWA in collaboration with GA.

Regional Geology Context

STRUCTURAL FRAMEWORK

The most recent framework for structural evolution and tectono-stratigraphy of the East Yilgarn Craton has been documented by Blewett and Czarnota (2005, 2007a, 2007b, 2007c), and is summarized here as context for the metamorphic study (Table 1).

Table 1: *Summary of structural events recognised in the EYC after Blewett and Czarnota (2007c) and correlation with metamorphic periods defined by the EYCMP.*

Deformation Style	Deformation	Metamorphism	Timing	Dominant Granite Type
Mesoproterozoic overprint in south		M4b		
Palaeo-Mesoproterozoic dykes		M4a		
Minor vertical shortening	D6	M3b	<2630 Ma	Low-Ca rare
N-S dextral strike-slip transtension	D5	M3b	2650-2635 Ma	Low-Ca (younger in west)
NNW sinistral transpression and thrusting	D4b	M3b	2655-2650 Ma	Waning High-Y TTG some syenite
NNW upright folding and reverse faulting	D4a	M3b	2655 Ma	High-Y TTG some syenite
NE-directed extension. Stage 2 late basins	D3b	M3a	2660-2655 Ma	Mafic granite, Syenite
Extensional doming. Stage 1 late basins	D3a	M3a	2665-2660 Ma	Mafic granite, Syenite
NNW upright folding and thrust. Volcanism terminated	D2	M2	2670-2665 Ma	Low-Y TTG
ENE extension and compression events. Bimodal volcanics	D1	M1, Mα	2800-2670 Ma	HHFSE passing into Low-Y TTG

Large-Scale Architecture

The East Yilgarn Craton (EYC) is characterized by a large-scale architecture in the horizontal plane of a network of inter-connected curvi-planar shear zones separating lenticular lower-strain domains (Figure 2). These shear zones are of 100 m to 5 km widths and of crustal scale, some penetrating through the crust and into the lithospheric mantle. Discrete shear zone sectors inter-connect to form laterally extensive curviplanar shear zone systems that are up to 800 km long. Three crustal-scale major shear zone systems divide the central part of the EYC, or Eastern Goldfields Superterrane (EGST) into the N-S elongate Kalgoorlie and Kurnalpi Terranes between the Southern Cross Terrane to the west and Burtville Terrane to the east. The Kalgoorlie and Kurnalpi Terranes have stratigraphies with similar general histories and partial connections but do show minor stratigraphic differences. The Burtville Terrane has Mesoarchaean to earliest Neoarchaean stratigraphy of similar age to the Southern Cross Terrane and basement stratigraphy within the EGST, and otherwise with Neoarchaean stratigraphy that is older than in the EGST (Barley et al., 2002, 2003). There are no differences in the structural evolution experienced by all EYC terranes including the Burtville Terrane. Other major shear zone systems further divide these Terranes into elongate lenticular shaped Domains (Figure 2), defined by Cassidy et al. (2006).

Deep seismic profiling shows a 3D geometry of easterly inclined listric shear zones that are typically steeper (40-70º) at the current exposure level, through 20º dips in the mid-crust to shallower in the lower crust (Goleby et al., 1993, 2002a, 2002b; Drummond et al., 2000). Large-scale crustal architecture geometries are the result of a combination of lithospheric extensional events and cannot be explained by thin-skinned or thick-skinned thrust architectures (Goleby et al., 2002a; Blewett and Czarnota, 2007a). Early-formed D1 extensional structures developed during attenuation of EGST crust and were later reactivated by D3 lithospheric extension (Blewett and Czarnota, 2007c). Early crustal attenuation and formation of juvenile Neoarchaean crust in the EGST is inferred from the distribution of Nd-model ages, which outline a NNW-trending rifted province between the Southern Cross and Burtville Terranes (Cassidy and Champion, 2004). Consequently, the Ida and Hootanui shear zone systems that bound the EGST and other internal structures, may have very early extensional pre-histories. Both Ida and Hootanui shear zone systems may also have convergent terrane accretion histories bringing the Southern Cross, EGST and Burtville Terranes together during D2 and establishing an early N-trending grain in the EGST (Blewett and Czarnota, 2007c). The Ockerburry shear zone system that divides the EGST has a D3 extensional history and is associated with late basins in the hanging wall (Blewett and Czarnota, 2007c). Other major extensional shear zones active during D3 and with associated late basins include Laverton, Hootanui, Ida, Bardoc,

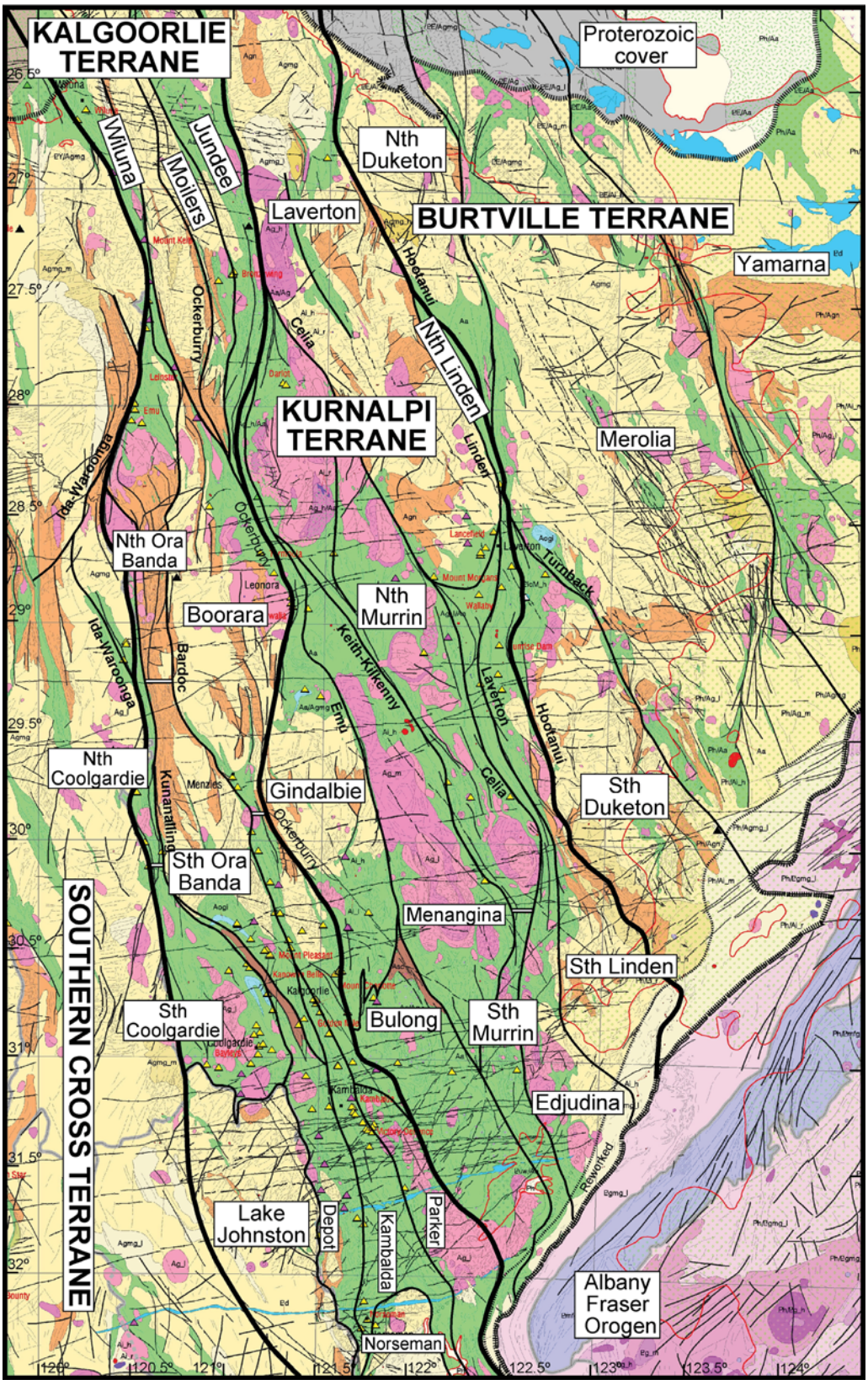

Figure 2: *Simplified geological map with the nomenclature and boundaries of domains and terranes after Cassidy et al. (2006).*

Celia, Kunanalling and Keith-Kilkenny shear zones (Figure 2; Blewett and Czarnota, 2005). Proterozoic dyke swarms may have exploited pre-existing crustal weaknesses corresponding to transfer zones that accommodated different dip directions in D3 extensional shear zones (Figure 3). D3 lithospheric extension established the dominant NNW-trending grain in the EGST. This grain was subsequently over-printed by N-trending D5 dextral transpressive shear zones that reactivated the pre-existing D2 N-trending grain (Blewett and Czarnota, 2007c).

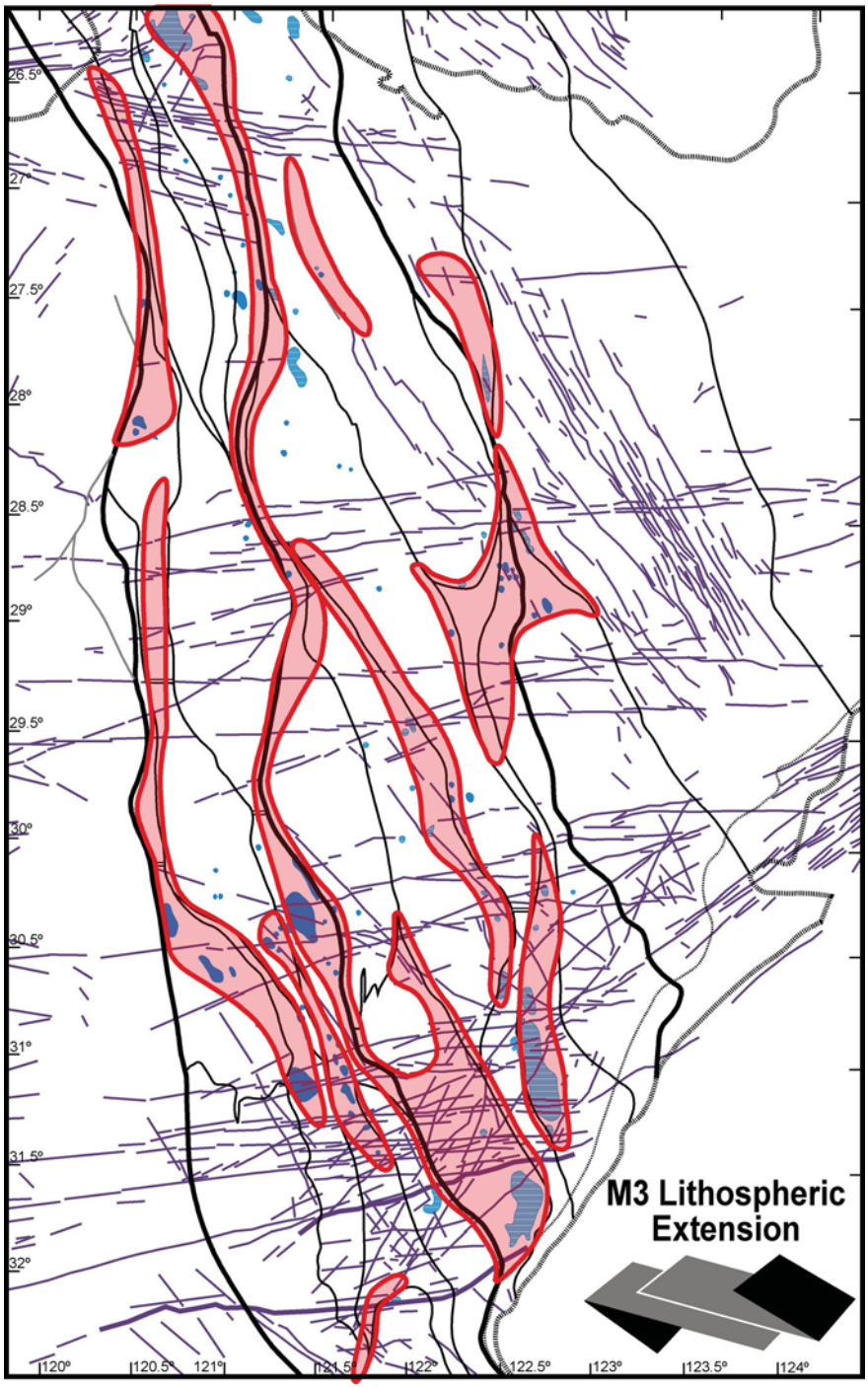

Figure 3: *Simplified map of Proterozoic mafic and ultramafic dyke swarms. These may be outlining fundamental crustal weaknesses established during Neoarchaean deformational events. Possible zones of high M3a extension (red) and syenitic magmas (blue) of the same age are indicated for comparison.*

D1: Early Extensional Rifting and Volcanic Period

The D1 period is a protracted period of back arc ENE-directed extension in the EGST, possibly related to retreating subduction in the east (Blewett et al., 2004a). The Kalgoorlie and Kurnalpi Terranes are rifted and attenuated pre-existing crust with an eastern margin at the Burtville Terrane and west margin at the Southern Cross Terrane (Cassidy and Champion, 2004). Youngest crust in this rifted system is in the western Kurnalpi Terrane, which is devoid of gold and relatively rich in VHMS deposits. The geological record of volcanism and clastic sedimentation was extensional throughout formation of the EGST, up to the termination of volcanism at approximately 2670 Ma. Extension of the EGST back arc produced the basinal architecture for volcanic sequences, crustal-scale extensional listric shear zones and established the N-trending orogenic architecture (Blewett et al., 2004a). Early extensional growth faults are documented by differential stratigraphic thicknesses in dolerite at Golden Mile (Gauthier et al., 2007) and in komatiites at St Ives (Squire et al., 2007). Early, flat lying shear zones invariably record extensional histories (Passchier, 1994; Blewett and Czarnota, 2005: McIntyre and Martyn, 2005) and the recumbent isoclinal folds are interpreted to have formed in an extensional environment as modelled by Harris et al. (2002). The punctuated compressional events early in the evolution of the EGST that were proposed by Swager (1989) and Swager and Griffins (1990) have not been substantiated.

D2: Contraction and Arc Termination

The first major contraction event (D2) juxtaposed disparate rock associations at approximately 2665 Ma, coinciding with termination of volcanism and active subduction. Shortening in the EGST back arc was possibly related to an advancing subduction system or catastrophic jamming of the subduction zone by an oceanic plateau or accretion of a magmatic arc for examples (Blewett and Czarnota, 2007b). Large-scale folds formed during D2 (Blewett et al., 2004a) and pre-date deposition of the fluvial late basins indicating folding was prior to 2660 Ma (Blewett et al., 2004a). D2 structures are tighter than both granite-gneiss domes (e.g., Mt Margaret Anticline) and folding of post-volcanic turbiditic basins (e.g., Wallaby Basin), indicating that D2 shortening was initiated prior to deposition in these basins at 2665 Ma. D2 structuring formed by ENE-WSW shortening, which was directed at a high angle to the early D1 grain of the EGST and resulted in some active thrusts such as the Foster Thrust at Kambalda (Blewett et al. 2004b). Across the whole EGST, D2 shortening was a low strain event, which did not produce pervasive foliation development and mesoscopic folds were uncommon (Blewett et al., 2004a). D2 deformation is characteristically heterogeneously distributed and the domains that did partitioned D2 strain typically saw little reworking during D3 (Blewett and Czarnota, 2005).

D3a: Early Extensional Basins and Deformation

The earlier generation of post-volcanic clastic basins with turbidite fill, formed by NW-SE extension, which is at a high angle to, and consistent with the ENE-WSW D2 shortening direction. These basins wrap around the granite batholith domes (e.g., Wallaby Basin), were deposited between 2670 and 2663 Ma age and overlap with the latest stages of D2 shortening, which also folded these turbiditic sequences (Blewett et al., 2004a; Blewett and Czarnota, 2005). Detritus sources are both local and distal, a portion being derived from deeply eroded granite domes. These extensional basins are sited in the hanging wall above a broad zone of splays and extensional shears that link with major extensional detachments that wrap around the margin of granite batholith domes (Figure 4). The overlap in age of deposition and upright D2 folding of turbiditic basins, as well as the consistent stress fields, suggest D2 shortening and D3a extension may be occurring together in a related event. NE-SW directed D2 contraction imposed across the pre-existing N-S grain may have resulted in a larger dextral transpressional system containing partitioned shortening and shearing domains, as well as up doming and extensional basins controlled by extension in the SE-NW direction. Consequently, this oblique shortening with coeval extensional escape to the NW and SE resulted in an orogenic system that didn't experience significant crustal thickening. NW-SE trending crustal-scale shear zones such as Celia, Zuleika and Keith-Kilkenny possibly developed as transfer structures that linked the arcuate extensional detachments wrapping the granite-gneiss domes (Blewett and Czarnota, 2005).

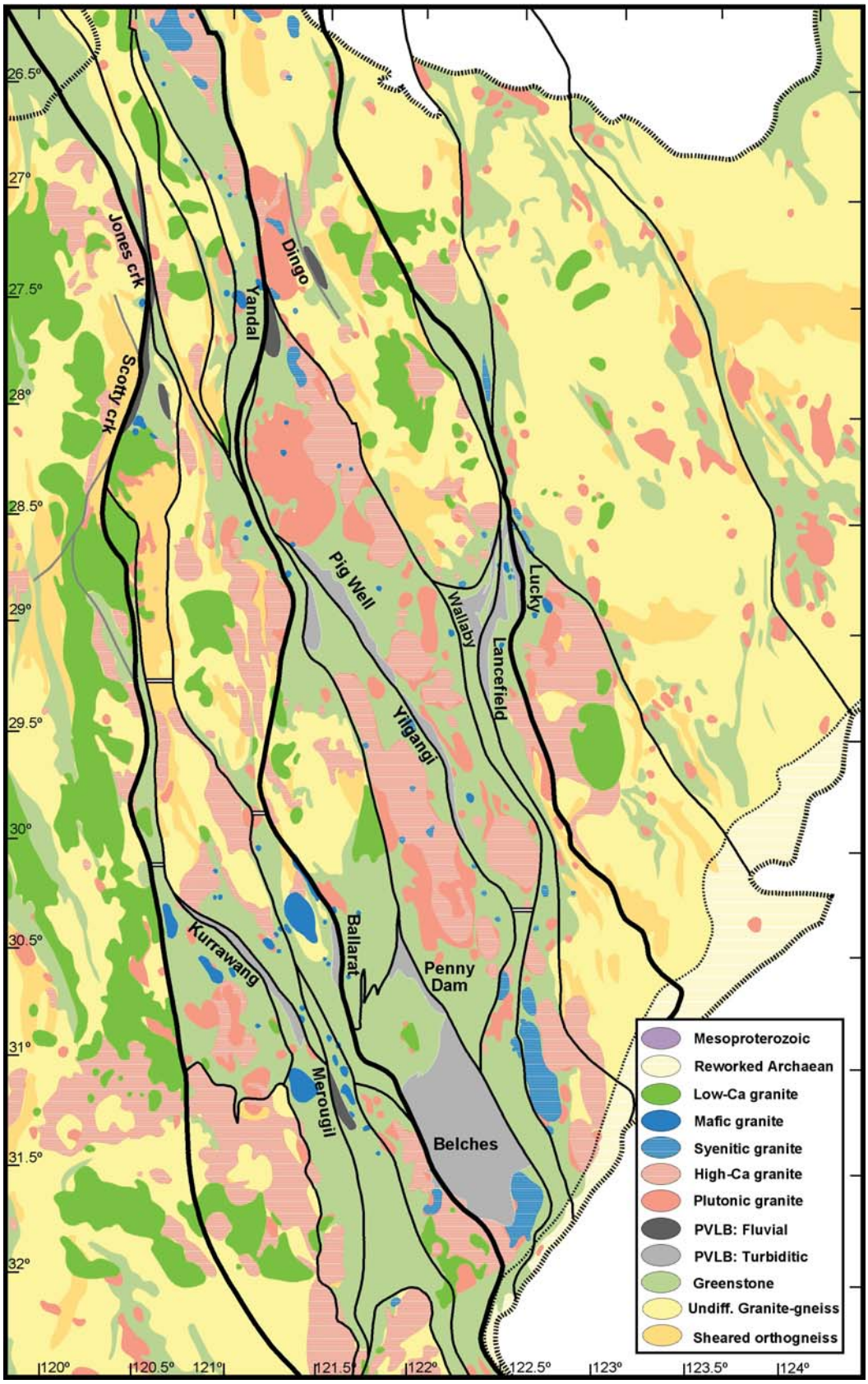

Figure 4: *Map of major geological units.*

D3b-D4a: Late Basin Formation and Deformation

A second generation of post-volcanic clastic basins contain fluviatile fill and formed in elongate and linear NNW-trending rifts associated with dominantly ENE-extension. Examples are the Pig Well and Kurrawang Grabens deposited after 2657 Ma (Krapez et al., 2000). These basins formed in a major lithospheric extension event that resulted in significant structural incision of the crust by crustal-scale extensional shear zones (D3b) as well as later deformation of the basinal fill (D4a). The extensional detachments define significant metamorphic grade jumps from amphibolite facies in the footwall to greenschist in the hanging wall consistent with extensional detachments (Williams and Whitaker, 1993). A deep seismic profile across the extensional detachment at Sons of Gwalia with a fluviatile late basin in the upper-plate shows a 4 km wide high-strain listric shear zone with variable dip that at depth rolls over a coeval granite domal structure akin to a core complex (Blewett and Czarnota, 2007c).

A seismic reflection profile across the Kilkenny shear zone and Pig Well basin in the upper-plate shows a similar low-angle extensional shear zone and half graben geometry (Blewett et al., 2004a). This extensional detachment is the major crustal-scale Ockerburry shear zone that defines the boundary between the Kalgoorlie and Kurnalpi Terranes. This structure has extensional kinematics along its entire length, and is the locus for all documented M3a anticlockwise P-T paths (see P-T Evolution Paths section). Extreme extension along these growth faults resulted in up to 12-16 km burial of late basin sequences in the hanging wall. Burial and rotation of grabens by listric faulting resulted in D4a shortening and folding of late basin sequences and reverse movements on N-S faults (Blewett and Czarnota, 2007c). Prior to D3a-D3b extension, the crustal section was not over-thickened during D2, with no more than 6-9 km of burial recorded by M2 metamorphic parageneses. Consequently, the D3a-D3b extensional period cannot be the result of gravitational collapse of an over-thickened orogen. This period is best understood in terms of horizontal unidirectional lithospheric extension (and crustal thinning) due to far field stresses, such as those resulting from cessation of subduction, sag of the subducted plate and retreat of the hinge (i.e., slab roll back). The D3 extensional events occurred during a period accompanying a major switch in palaeostress from D2 ENE–WSW contraction to D4b NNW–SSE contraction.

D4b: Sinistral Transpression

Low strain NW–SE to N-S contraction was caused by a stress switch of approximately 50-80º and is of unknown origin. Contraction resulted in sinistral transpressive reactivation of NNW- and N-trending faults and reverse movements on ENE-trending structures. This event was responsible for the main gold event in many localities, such as Kalgoorlie, St Ives, Wallaby and Sunrise Dam. Metamorphic growth continued after sinistral shearing as post-kinematic amphibole laths, indicating that the diminishing M3a thermal anomaly continued to at least 2645 Ma (Ross et al., 2004; Salier et al., 2004).

D5: Dextral Transtension

Another major stress switch of approximately 90º occurred approximately 15 Ma later (McNaughton et al., 2005). NE- to ENE-shortening reactivated N- to NNE-trending faults by strike-slip, dextral transtensional movements (Blewett and Czarnota, 2005). Dextral shearing events are locally very significant and the highest strain internal parts of shear zones host late-stage Au-mineralization events. Crustal-scale terrane boundaries such as the Hootanui and the Ida-Waroonga shear zone systems were reactivated by dextral transtension. Dextral reactivation of the Hootanui shear zone at Laverton involved high flattening strains that were indicated by multiple extension directions within the shear plane. Syn-kinematic Low-Ca granites indicate dextral transtensional reactivation occurred over a protracted period of time from 2650 to at least 2630 Ma (Blewett and Czarnota, 2007c). All dextral shear zones are of greenschist to sub-greenschist facies grade, significantly lower than all older shearing events.

D6: Vertical Shortening

D6 deformation produced spaced, sub-horizontal crenulations, kinkbands and dm-scale open folds in widely scattered localities throughout the EGST (Swager, 1997; Davis and Maidens, 2003). These structures indicate very minor vertical shortening (<<10%) late in EGST evolution, at shallow upper-crust levels (~3km depth). Little tectonic significance can be ascribed to this vertical shortening in the shallow crust. This shortening does not necessarily indicate lithospheric extension, as the EGST was already essentially exhumed before this stage. Formation in the shallow crust also precludes vertical shortening by an over-thickened crustal column. The localised distribution may indicate formation by shortening above Low-Ca granite plutons.

Rock Flow Regime

Rock Flow Regime Methods

To enable the large-scale tectonic interpretation of geological terranes, structural geology attempts to characterise the different parts utilising micro-, meso- and macro-scale structures preserved in the rock mass (Passchier and Trouw, 2005). The fundamental parameters needed for this characterization are; structure geometries, flow direction or kinematics, bulk-strain, strain rate and rock flow regime. Apart from rock flow regime, most of these parameters are well documented in the EYC (Blewett and Czarnota, 2005, 2007a, 2007b, 2007c). Rock flow regime is described by the rotational component of flow, which is quantified as the kinematic vorticity number (Wk) and the dilationary component is quantified as the kinematic dilationary number (Ak). General flow is a combination of two main end-members: coaxial flow or pure shear (Wk=0) and non-coaxial flow or simple shear (Wk=1). Because of the many variables, accurately quantifying rock flow regime from developed structures is universally accepted as impractical (Passchier and Trouw, 2005). Nevertheless, a qualitative assessment of the rock flow regime is crucial to the interpretation of deformation belts and ultimately palaeo-tectonic interpretations. Furthermore, rock flow regime has significant economic implications because rock flow regime greatly influences fluid flow circulation and thus the geometry of mineral deposits within shear systems (i.e., down-dip versus along-strike shoots).

A summary of possible field-based qualitative indicators of the dominant rock flow regime has been constructed as a field card (FieldCard_FlowRegime(07).pdf). The geometry of boudin blocks developed in both foliation-parallel and foliation-oblique boudin trains are influenced in part by rock flow regime, assuming the inter-boudin plane was self-generated and not controlled by pre-existing anisotropies (Goscombe and Passchier, 2003). Domino boudin geometries are the overwhelming dominant asymmetric boudin type in foliation-parallel and foliation-oblique boudin trains in coaxial flow regimes. Conversely, in non-coaxial regimes; domino and shear band boudins are equally developed in foliation-parallel boudin trains and shear band boudins are the overwhelming dominant asymmetric boudin type in foliation oblique boudin trains. Layers that were first shortened and subsequently boudinaged in the same progressive deformation can only have developed in non-coaxial flow (Passchier and Trow, 2005). Foliation-parallel boudin trains can develop multiple boudin geometry types within a single layer under coaxial flow, but typically only one boudin type in non-coaxial flow.

Shear zones with high coaxial flow can result in partitioning of vertical and horizontal stretch (Tikoff and Greene, 1997). Multiple stretch directions will be evident as multiple direction of stretching lineations, sheath long axes and boudinage directions (i.e., chocolate boudinage). Conversely, non-coaxial flow typically develops a uni-directional maximum extension direction.

Populations of shear sense based on asymmetric kinematic indicators can also vary in different flow regimes. In non-coaxial flow, the vast majority (>85%) of determinations show the same shear sense and typically less than 12% are antithetic to the dominant shear sense. Conversely, in coaxial flow both possible shear sense directions are more equally developed and the dominant direction makes up ~50-65% of the determinations. Mantled porphyroclasts are dominantly symmetric (>80%) in coaxial flow and dominantly asymmetric (>60%) in non-coaxial flow.

Coaxial flow more typically generates upright and symmetric folds, conjugate kinkband sets and flat cats-eye sections through sheath folds (Alsop and Holdsworth, 2006). Whereas non-coaxial flow will more typically produce asymmetric folds with shear band-like axial-planar crenulations, a single dominant kinkband set and elliptical cats-eye sections through sheaths. High coaxial flow will produce conjugate shear zone sets and the high-strain zones will be dominated by shortening or dissolution and show minimal lateral displacements with respect to the width of the zone.

Other deformation structures that involve dilation (Ak>0), such as dykes and veins are also very good qualitative indicators of rock flow regime (Daczko et al., 2001). Coaxial flow regimes can produce radial, planar-parallel and conjugate vein or dyke sets and vein opening more typically involves dilation only without lateral displacement (Ak=1). In contrast, non-coaxial flow will more typically produce a single dominant *en-échelon* or sigmoidal vein set and vein dilation may involve lateral slip as in the case of vein-faults (0<Ak<1).

Quantitative mean kinematic vorticity (Wm) gauges that utilise the aspect ratio of different porphyroclast types and the angle the long axis makes with the main foliation are available in the literature (Passchier, 1987; Wallis, 1995; Simpson and de Paor, 1993; Jessop et al., 2007). Other quantitative gauges in the literature that utilise a range of different structures are: fibre fringes (Passchier and Urai, 1988), sigmoidal tension gash arrays (Passchier and Trouw, 2005), foliation deflection in shear zones (Wallis, 1992, 1995; Passchier and Trouw, 2005), c-axis lattice orientation (Wallis, 1992, 1995) and angle between foliation and fabric attractor (Passchier and Trouw, 2005).

Rock Flow Regime in East Yilgarn Shear Zones

Rock flow regime seems to be a crucial difference between the sinistral D4b shear zones such as Yunndaga Pit and dextral D5 shear zones such as King of Creation and Lancefield pits (pit locations are represented in Figure 156 in the Integration chapter of this Record). The D4b shear zone at Yunndaga Pit has only shear band-type asymmetric boudins developed suggesting a high non-coaxial flow regime. Similarly, the D3b extensional shear zone exposed at Sons of Gwalia has only one vergence of asymmetry developed in the shear band population (Blewett and Czarnota, 2007c), indicating non-coaxial flow and confirming asymmetric lithospheric extension and not fabric development by simple vertical flattening. In contrast, the low-grade D5 shear zone at King of Creation has structures suggesting high coaxial flow regimes. Coaxial flow is suggested by; multiple boudin geometries within single layers, horizontal and vertical maximum stretching directions indicated by multiple sheathing directions and orthogonal stretching lineations, and kinkband vergence opposite to shear sense on the main foliation (Blewett and Czarnota, 2007c). Similarly Lancefield has two directions of shear bands of the same metamorphic grade developed in the main foliation (Blewett and Czarnota, 2007c), suggesting a possible interpretation of formation at the same time in a high coaxial flow regime. At larger scale, D5 shear zones are developed after the peak of all metamorphic events that contribute to peak metamorphic map pattern (M2-M3a), but nevertheless do not induce significant lateral displacement of isograds (Mikucki and Roberts, 2003). An absence of large-scale lateral movement in the horizontal plane during D5 can be accommodated by coaxial flow regimes and shortening and dissolution across these zones. Coaxial rock flow may have been initiated in part by an influx of fluid at these sites, producing a retrograde schist zone as well as accommodating deformation.

A change in rock flow regime from non-coaxial in D3b and D4b zones to coaxial in D5 shear zones is possibly crucial to the geometry of Au-mineralization bodies developed within these zones. Rock flow regime influences fluid circulation and thus the geometry of resulting ore bodies. Modelling by Potma et al. (2007) has shown down-dip ore shoots are preferentially developed over strike-oriented shoots, in shear zones with high pure shear. Furthermore, modelling by Sheldon et al. (2007) has shown extension on low-angle shear zones akin to D3b non-coaxial shear, drove horizontal fluid flow circulation, and pure shortening regimes generated largely vertical fluid flow. Consequently, there will be a preference for horizontal ore shoots in non-coaxial flow regimes, such as those developed in D3b zones at Sunrise Birthday (Gibson, 1907), Wallaby (Davis and Maidens, 2003) and Sons of Gwalia and in the D4b zone at Yunndaga Pit (Blewett and Czarnota, 2005). Vertical or

down-dip ore shoots will be preferentially developed in coaxial flow regimes, such as those developed in D5 zones at King of Creation and Lancefield (Hronsky, 1993; Blewett and Czarnota, 2005).

Qualitative Estimates of Strain Intensity

Qualitative Foliation Intensity Method

A major indicator of gold endowed provinces is heterogeneous strain patterns characterized by low-strain belts separated by a network of high strain shear zones (Bierlein et al., 2002). The EYC is indeed characterized by this strain pattern and is one of its distinguishing features. Consequently, a dataset that documents broad-scale strain variation in the EYC will be an important fundamental dataset. Most sites of Au-mineralization are in some way spatially related to zones of high-strain, or zones of high fluid flow associated with shear zones. To this end, a method for mapping the distribution of strain on a regional scale was developed (Goscombe and Gray, 2008). The NE Minerie 100K sheet (Figure 5) was selected as a test region to illustrate the utility of the developed method. The test region was contoured for qualitative foliation intensity utilising the QFII scheme outlined below, and this pattern was calibrated and tested against semi-quantitative strain calculations (Figure 5). A qualitative scheme provides a fast and practical field based tool for mapping the distribution of strain. Furthermore, qualitative estimates can be made retrospectively from outcrop descriptions in legacy databases and photographs etc. As a result, this method allows for the documentation of strain variation on an orogenic scale, as illustrated in Figure 6. The qualitative QFII method and semi-quantitative strain calculation methods are presented below and the assumptions and limitations of both field-based methods are discussed.

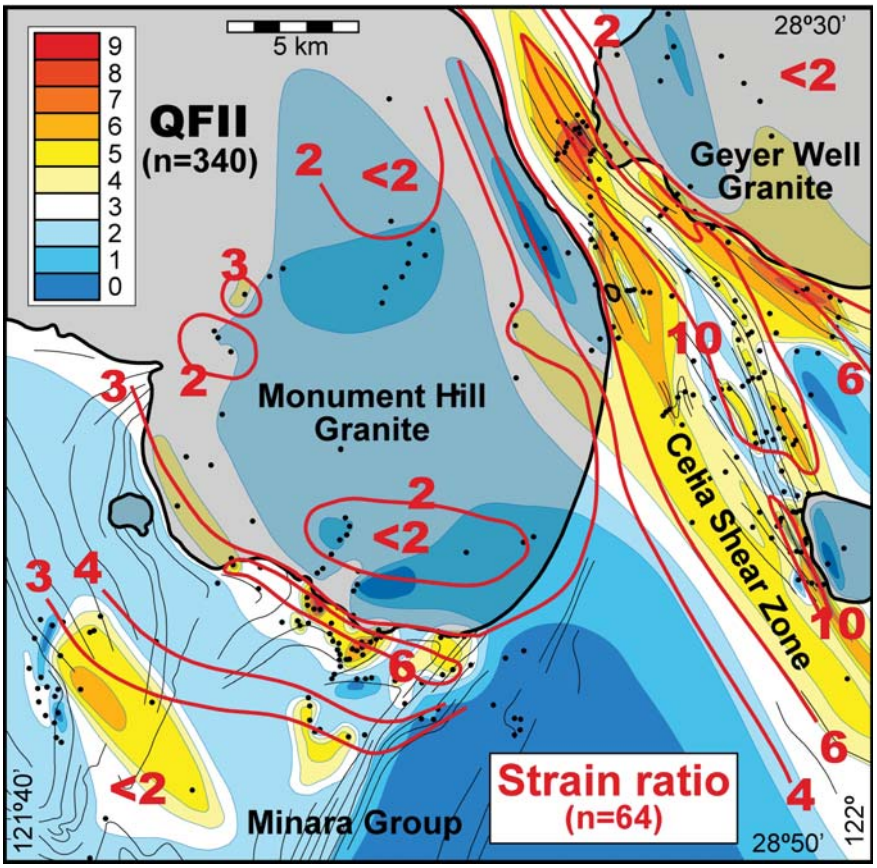

Figure 5: *Qualitative foliation intensity index map of a portion of the EYC straddling the Celia high-strain and relatively high-grade shear zone in the NE part of the Minerie 100K map sheet. Note the heterogeneity of the shear zone. This variation is dependent on rock-type and progressive evolution of the zone leading to a potential for different aged fabrics. Dots show data points (Table 2; Appendix 3).*

A qualitative scale (0 to 10) of bulk strain based on foliation intensity (FieldCard_QFII(07).pdf) has been developed as a simple field-based system for mapping stain and enabling a more continuous pattern of strain distribution. This qualitative foliation intensity index (QFII) has been modified after the method of Goscombe et al., (2006) and Goscombe and Gray (2008). High strain (QFII $\geq$ 7) is defined by the proportion of grain refinement, moderate strain (3 $\leq$ QFII $\leq$ 7) by the foliation intensity and at low strains (QFII $\leq$ 3) by the spacing of cleavage planes. Foliation intensity is simply a qualitative assessment of the ratio: grain shape (or aspect ratio) over spacing, of the planar (or linear) elements in the rock such as mica, amphibole and flattened mineral grains. Grain refinement is the proportion (%) of the rock that has been recrystallised to sub-grains and new mineral grains: >50% refinement in protomylonite, >70% in mylonite and >90% in ultramylonite (Passchier and Trouw, 2005). Grain refinement typically also involves grainsize reduction, which has not been quantified in this study.

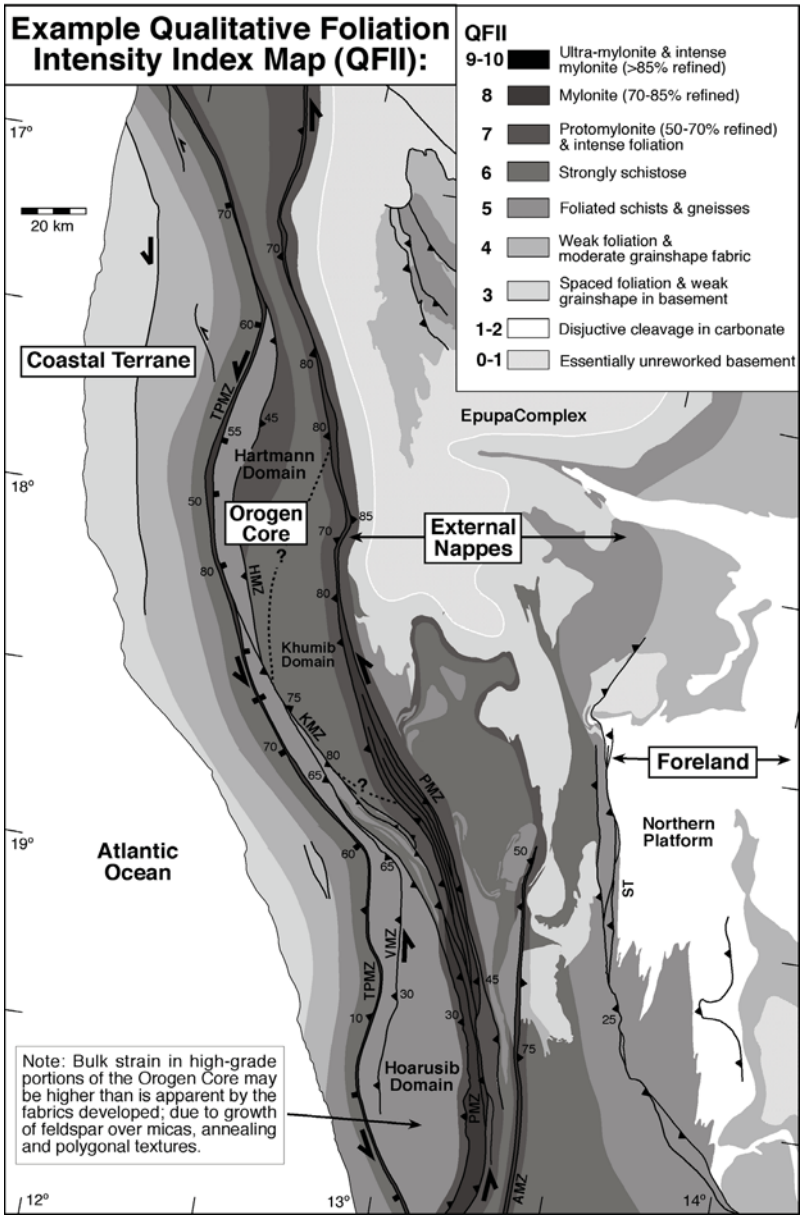

Figure 6: *Example of a qualitative foliation intensity index (QFII) map on orogenic scale, from a simple system that experienced a single transpressional orogeny in the Kaoko belt, Namibia (Goscombe and Gray, 2008).*

Because the QFII index is subjectively assigned, the method can only document relative strain intensity. Furthermore, fabric development is dependent on a multitude of variables, such as metamorphic grade, rock-type, deformation mechanism, strain rate, grainsize, mica proportion, fluid flux and rheology. An attempt has been made to account for metamorphic grade and different rock-types, making the scheme more widely applicable. Fabric intensity typically under-estimates bulk strain because; [1] rock fabrics do not record the full accumulative strain history, and [2] fabrics can be lost due to post-deformation annealing. Nevertheless, the QFII method is useful in documenting and illustrating relative strain distribution and strain gradients with a level of internal consistency (Goscombe et al., 2006; Goscombe and Gray 2008).

Qualitative Foliation Intensity in the East Yilgarn

The QFII method was tested by a detailed analysis of the NE Minerie 100K map sheet (Figure 5). The test area spans a typical high-strain, high-grade crustal-scale shear zone (Celia shear zone) and illustrates the heterogeneity of distributed strain between granites, deformed greenstones and shear zone that is typical of the EYC. This heterogeneity reflects both the differential partitioning of strain in different rock types and the complex history of the EYC having experienced multiple non-congruent deformational events (D2, D3, D4a, D4b and D5). The strain pattern at Minerie shows that the crustal shear zone is a wide (8 km) zone of moderate strain above background, and containing multiple splays and traces of very high strains (Figure 5). High strains of the Celia shear zone are strongly partitioned into the volcanic and volcanoclastic sequences between granite plutons. Background strain in these sequences outside of the Celia shear zone, shows extreme heterogeneity ranging from no strain to mylonitic. There are distributed patches of moderate strain and the highest strains are recorded immediately SW of the Monument Hill Granite body (Figure 5). Universally low strains are recoded in all of the granite bodies, which generally do not develop appreciable deformation fabrics, ranging to moderate grain shape fabrics that are typically at the margins of the plutons. The distribution of semi-quantitative strain calculations correlate very well with the QFII map pattern (Figure 5) and generally confirm the applicability of the QFII method to represent strain variation.

The QFII method has been applied across the entire EYC to generate a general strain intensity map that represents a composite of all accumulated strain across all deformation events. This has been achieved by assigning a QFII value to all localities in the MDB with sufficient outcrop description (approximately 27,000 data points). The criteria used to make assignments from legacy datasets is discussed later. The density and distribution of this QFII data (Appendix 2; eycmp1_QFII.pdf) is sufficient to generate a contoured strain intensity map that highlights high stain zones and static domains (Goscombe and Blewett, 2009). This method is limited to mapping the distribution of total accumulated strain experienced at a locality that may have experienced a complex history (Blewett and Czarnota, 2005). Nevertheless, this first-order strain distribution can be calibrated to some degree for the age of the dominant deformation fabric, when read in conjunction with the detailed analysis of Blewett and Czarnota (2005), which documented strain intensity at different times in key localities (i.e., Figure 65 in Blewett and Czarnota, 2005).

Semi-Quantitative Bulk Strain Calculations

Semi-Quantitative Strain Methods

Absolute strain determinations are notoriously difficult because all strain gauges have assumptions and rheology aspects that result in either or both, under- or over-estimation. Further limitations are the numerous geological constraints and the typically incomplete record of accumulative strain in rocks. Because of these limitations we have treated all bulk strain calculations as semi-quantitative estimates that are typically minimum estimates. The highly simplified field based methods for semi-quantitative estimation of bulk strain that have been used are summarized in a field card (FieldCard_Strain(07).pdf).

Semi-quantitative strain gauge methods that utilise a wide variety of deformation structures are outlined here. A simplified minimum estimate of strain ratio (R=X/Z) and Flynn ratio indicating strain type (k), are calculated from the aspect ratio of stretched conglomerate clasts and augen,

assuming an initial sphere (Ramsay, 1967). Shear strain is calculated from the inter-marginal hinge angle and aspect ratio of the cross sectional ellipse in sheath folds, assuming simple shear (Lacassin and Mattauer, 1985). A maximum estimate of shear strain is calculated from the degree of rotation of planar elements, such as tensional veins producing flanking folds, and assuming an original orientation orthogonal to layering (Ramsay and Graham, 1970). Accurate strain ratios are calculated from matrix extension indicated by pressure fringes, such as quartz fibres or partial melt around pyrite or garnet porphyroblasts that are assumed to be undeformed (Hobbs et al., 1983). Layer extension in drawn- and shear band-boudin trains is used as a simple minimum estimate of strain assuming no deformation of the boudin blocks (Ramsay, 1967; Goscombe et al., 2004a). Accurate strain ratios are calculated from the acute angle between schistosity and C-plane in composite S-C foliations, assuming simple shear (Ramsay and Graham, 1970).

Crucial simplifications and assumptions about rheology and flow regime have been compared and their potential effect on results has been evaluated. All methods assume plane strain and end-member flow regimes such as simple or pure shear that do not necessarily reflect natural systems. Sheath folds, rotated planes and C-S fabrics are moderately reliable methods that cannot under-estimate strain, but later flattening of these structures or initial obliquity of the rotated plane, can result in over-estimation. Pressure fringe methods are considered the most accurate because fringes record true extension of the matrix, inaccuracies arise only if the clasts are resorbed (over-estimate) or stretched (under-estimate). Boudin train extension typically under-estimates bulk strain because the assumption that all strain is partitioned into the matrix is rarely realised; most boudins are deformed to some degree, especially in high-grade ductile conditions (Goscombe et al., 2004a; Mandal et al., 2007). In most scenarios, the simplified methods that have been used to calculate strain from stretched clasts and augen, both under- and over-estimate strain. Clasts and augen are typically more competent than the matrix and do not partition strain giving an under-estimate and augen can further under-estimate strain due to recrystallization and mortar development (Schmid and Podladchikov, 2004). Trends towards over-estimation occur because the original clast shape and orientation have not been accounted for in this very simplified field method.

Semi-Quantitative Strain in the East Yilgarn

Bulk strain calculations from the Celia shear zone and adjacent low strain granites and volcanics in the NE Minerie 100K sheet have been plotted (Figure 5). When contoured, these semi-quantitative strain estimates define a pattern that is identical to the QFII pattern. Consequently, these calculations offer a bulk strain calibration of the QFII map, which has been applied across the entire EYC region (Appendix 2; eycmp1_QFII.pdf). The aspect ratios of flattened quartz grains within the granite bodies have very low strain ratios of 1.5 to 3.4 and one of 5.5 (Table 2), averaging 2.3. Strain type indicated by Flynn ratios range between 0.43 and 1.33 (averaging 0.7; n=17), indicating deformation in the flattening field. Volcanic and volcanclastic stratigraphy away from the Celia shear zone has very heterogeneous background strains, with strain ratios calculated from sheath folds, boudinage, C-S fabrics and stretched clasts ranging between 2.2 and 18.8 (averaging 7.1). Three stretched clast localities record Flynn ratios between 1.2 and 5.8, indicating constrictional strain.

Strain was calculated from splays of the Celia shear zone and the broader 8 km wide deformation zone using C-S fabrics, sheath folds, boudin trains, aspect ratios, pressure fringes and rotated fracture planes with flanking folds. Strain ratios range from 2.8 to 9.6 in the broad deformation zone (averaging 7.8) and up to 42.0 in the ultramylonite splays (averaging 18.6), matching the heterogeneous strain pattern documented for this crustal-scale shear zone by the QFII (Figure 5). A single stretched clast locality records a Flynn ratio of 3.3, indicating constrictional strain. C-S fabrics in other major shear zones also record high strain ratios: 8.6-14.0 in the Hootanui shear zone, 12.2-50.7 in the Laverton shear zone, 5.7-18.8 in the Ockerburry shear zone, 24 in the Ida shear zone and 16 in the Keith-Kilkenny shear zone (Table 2). Maximum background strain from outside of the major shear zones can be estimated from a few moderately deformed localities with structures allowing calculations. These calculated strains are generally low with strain ratios between 3.6 and 7.7.

Table 2: *Data table of semi-quantitative bulk strain calculations from across EYC.*

Structure sub-domain	Locality	Method	R	k	Stratigraphy	Domain
Celia Shear Zone on Minerie 100K:						
Celia SZ	Y64	C-S angle	9.6		meta-volcanics	Laverton
Celia SZ	Y65	C-S angle	9.6		meta-volcanics	Laverton
Celia SZ	Y67	C-S angle	9.6		porphyry dyke	Laverton
Celia SZ	Y67	C-S angle	10.2		porphyry dyke	Laverton
Celia SZ	Y72	C-S angle	8.6		porphyry dyke	Laverton
Celia SZ	Y83	C-S angle	8.6		porphyry dyke	Laverton
Celia SZ	Y83	C-S angle	9.6		porphyry dyke	Laverton
Celia SZ	Y85	C-S angle	4.8		porphyry dyke	Laverton
Celia SZ	Y90	C-S angle	9.6		porphyry dyke	Laverton
Celia SZ	Y145	C-S angle	7.7		meta-volcanics	Laverton
Celia SZ	Y159	C-S angle	12.2		porphyry dyke	Laverton
Celia SZ	Y164	Boudinage	2.8		porphyry dyke	Laverton
Celia SZ	Y169	C-S angle	12.2		porphyry dyke	Laverton
Celia SZ	Y180	Rotated plane	41.9		meta-chert	Laverton
Celia SZ	Y180	Sheath fold	34.4		meta-chert	Laverton
Celia SZ	Y180	Rotated line	40.9		meta-chert	Laverton
Celia SZ	Y181	C-S angle	8.6		porphyry dyke	Laverton
Celia SZ	Y181	C-S angle	7.7		porphyry dyke	Laverton
Celia SZ	Y185	C-S angle	12.2		porphyry dyke	Laverton
Celia SZ	Y192	C-S angle	10.8		meta-volcanics	Laverton
Celia SZ	Y193	C-S angle	16.1		meta-volcanics	Laverton
Celia SZ	Y208	C-S angle	9.6		porphyry dyke	Laverton
Celia SZ	Y218	Aspect ratio	8.5	3.25	granite pluton	Murrin Nth
Celia SZ	Y229	C-S angle	4.4		meta-volcanics	Laverton
Celia SZ	Y231	C-S angle	12.2		meta-volcanics	Laverton
Celia SZ	Y233	C-S angle	12.2		porphyry dyke	Laverton
Celia SZ	Y234	C-S angle	12.2		meta-volcanics	Laverton
Celia SZ	Y235	C-S angle	8.6		meta-volcanics	Laverton
Celia SZ	Y238	Rotated plane	3.4		meta-volcanics	Laverton
Celia SZ	Y239	Rotated line	8.5		meta-volcanics	Laverton
Celia SZ	Y239	Rotated plane	18.1		meta-volcanics	Laverton
Celia SZ	Y259	C-S angle	14.0		meta-volcanics	Laverton
Celia SZ	Y260	C-S angle	14.0		meta-volcanics	Laverton
Celia SZ	Y263	C-S angle	5.7		meta-volcanics	Laverton
Celia SZ	Y275	C-S angle	7.7		meta-volcanics	Laverton
Celia SZ	Y275	Sheath fold	13.1		meta-volcanics	Laverton
Celia SZ	Y276	C-S angle	29.1		meta-volcanics	Laverton
Celia SZ	Y285	C-S angle	9.6		porphyry dyke	Murrin Nth
Stratigraphy on Minerie 100K:						
Minara Group	Y54	Aspect ratio	2.2	1.20	meta-volcanics	Murrin Nth
Minara Group	Y116	C-S angle	18.8		granite pluton	Murrin Nth
Minara Group	Y116	C-S angle	6.9		granite pluton	Murrin Nth
Minara Group	Y129	Aspect ratio	5.5	2.42	meta-volcanics	Murrin Nth
Minara Group	Y130	C-S angle	9.6		porphyry dyke	Murrin Nth
Minara Group	Y354	Boudinage	4.6		meta-volcanics	Murrin Nth
Minara Group	Y354	Boudinage	6.0		meta-volcanics	Murrin Nth
Minara Group	Y369	Sheath fold	18.7		meta-volcanics	Murrin Nth
Minara Group	Y369	Boudinage	5.0		meta-volcanics	Murrin Nth
Minara Group	Y377	Aspect ratio	5.0	5.83	meta-volcanics	Murrin Nth
Minara Group	Y388	Aspect ratio	2.4		meta-volcanics	Murrin Nth
Granite on Minerie 100K:						
Monument Hill Granite	Y100	Aspect ratio	1.5	0.74	granite pluton	Murrin Nth
Monument Hill Granite	Y108	Aspect ratio	1.7	0.55	granite pluton	Murrin Nth
Monument Hill Granite	Y133	Aspect ratio	2.3	0.53	granite pluton	Murrin Nth
Monument Hill Granite	Y137	Aspect ratio	2.2	1.05	granite pluton	Murrin Nth
Monument Hill Granite	Y220	Aspect ratio	3.1		granite pluton	Murrin Nth
Monument Hill Granite	Y220	Aspect ratio	3.1		granite pluton	Murrin Nth
Monument Hill Granite	Y221	Aspect ratio	2.3	1.33	granite pluton	Murrin Nth
Monument Hill Granite	Y221	Aspect ratio	2.5	0.43	granite pluton	Murrin Nth
Monument Hill Granite	Y297	Aspect ratio	2.5	0.35	granite pluton	Murrin Nth
Monument Hill Granite	Y299	Aspect ratio	2.2	1.10	granite pluton	Murrin Nth
Monument Hill Granite	Y301	Aspect ratio	2.1	0.68	granite pluton	Murrin Nth
Monument Hill Granite	Y302	Aspect ratio	5.5		granite pluton	Murrin Nth
Monument Hill Granite	Y307	Aspect ratio	1.7	0.67	granite pluton	Murrin Nth
Monument Hill Granite	Y314	Aspect ratio	3.4		granite pluton	Murrin Nth
Monument Hill Granite	Y314	Aspect ratio	1.9		granite pluton	Murrin Nth
Monument Hill Granite	Y314	Aspect ratio	2.4	0.43	granite pluton	Murrin Nth
Monument Hill Granite	Y314	Aspect ratio	1.8	0.68	granite pluton	Murrin Nth
Monument Hill Granite	Y314	Aspect ratio	1.9	0.77	granite pluton	Murrin Nth
Monument Hill Granite	Y319	Aspect ratio	2.2	0.47	granite pluton	Murrin Nth
Monument Hill Granite	Y396	Aspect ratio	1.8	0.59	granite pluton	Murrin Nth
Monument Hill Granite	Y397	Aspect ratio	1.6	0.90	granite pluton	Murrin Nth
Monument Hill Granite	Y398	Aspect ratio	1.5	0.80	granite pluton	Murrin Nth
Other Shear Zones:						
Keith-Kilkenny SZ	BG6-125	C-S angle	16.1		meta-volcanics	Murrin Nth
Ida SZ	BG6-187	Aspect ratio	24.0	0.95	granite pluton	Coolgardie Nth
Ockerburry SZ	Y305	Pressure fringe	9.5		meta-volcanics	Gindalbie
Ockerburry SZ	2002964003	C-S angle	5.7		unknown	Gindalbie
Ockerburry SZ	98965695	C-S angle	6.9		unknown	Gindalbie
Ockerburry SZ	99965916	C-S angle	18.8		unknown	Gindalbie
Ockerburry SZ	98965573.4	C-S angle	10.8		unknown	Gindalbie
Hootanui East SZ	99965942	C-S angle	8.6		unknown	Linden Sth
Hootanui East SZ	98965694	C-S angle	14.0		unknown	Linden Sth
Hootanui West SZ	98965648	C-S angle	12.2		unknown	Edjudina
Hootanui West SZ	98965693.1	C-S angle	50.7		unknown	Edjudina
Hootanui West SZ	BG6-116	Aspect ratio	14.0	6.00	meta-volcanics	Linden Sth
Hootanui West SZ	BG6-116	Aspect ratio	16.5	2.25	meta-volcanics	Linden Sth
Hootanui West SZ	BG6-116	Aspect ratio	13.6	5.80	meta-volcanics	Linden Sth
Other Structural Domains:						
Menangina Domain	Y303	Aspect ratio	6.5	1.17	granite pluton	Menangina
Laverton Dome	24184	C-S angle	3.6		unknown	Laverton
Laverton Dome	21736	C-S angle	2.8		unknown	Laverton
Merolia Domain	24183	C-S angle	5.7		unknown	Merolia
Moilers Domain	94962232	C-S angle	7.7		unknown	Moilers

Large-Scale Patterns of Structural Elements

Orogen Geometry

Patterns of orogenic geometry across the whole EYC are indicated by a foliation trace array based on all main foliation orientation data in the MDB (Appendix 2; eycmp1_Stike.pdf). The foliation trace array illustrates the time integrated structural grain throughout the EYC. In particular the foliation traces demarcates a swing into parallelism towards the crustal shear zone systems. The domal shapes of the granite-gneiss batholiths are also well outlined by foliations sub-parallel their margins. The vertical dimension of an orogen's architecture is illustrated by the dip of the main foliations (Appendix 2; eycmp1_Dip.pdf). Patterns of foliation dip indicate that shallow dipping domains are uncommon and typically found at the lateral terminations of granite-gneiss domes. The steepest domains are in the crustal-scale shear zones and steep foliation dips are otherwise generally widespread.

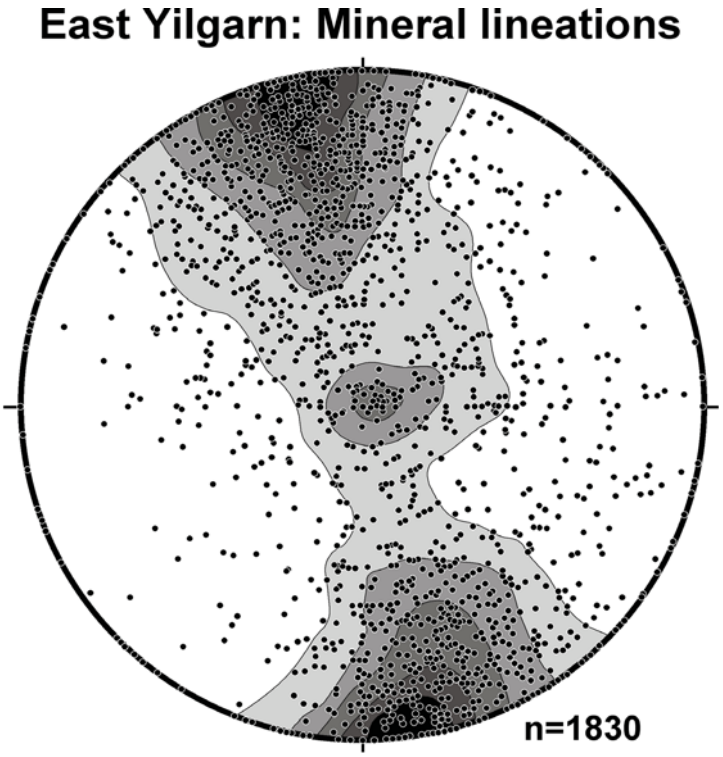

Figure 7: *All stretching lineations (aligned mineral and mineral aggregate lineations) from the East Yilgarn Craton sourced from the GSWA database. Contouring of the same data is superimposed. Note most stretching lineations are strike-slip to shallow plunging indicating a dominantly transpressional to strike-slip system. There is also a distinct smaller sub-set of steep lineations due to dip-slip movements and indicating a complex evolution of multiple deformation events with contrasting kinematics (Blewett and Czarnota, 2005, 2007c).*

Kinematic Array

The distribution of stretching lineations in the GSWA database for the EYC is overwhelmingly shallow plunging to sub-horizontal (Figure 7). These lineations indicate a predominance of strike-slip movements in deformation events (D4a, D4b, D5) spanning the history of the EYC (Blewett and Czarnota, 2007c). Stretching lineations with plunges less than 30º predominantly occur within major shear zones and are present in all EYC shear zone systems (Figure 8). The minor population of steeper and dip-slip stretching lineations are also concentrated in shear zones but are more heterogeneously distributed and are not evident in all shear zones (Figure 9). These dip-slip lineations indicate maximum extension or transport during M2 convergence and during M3a lithospheric extension.

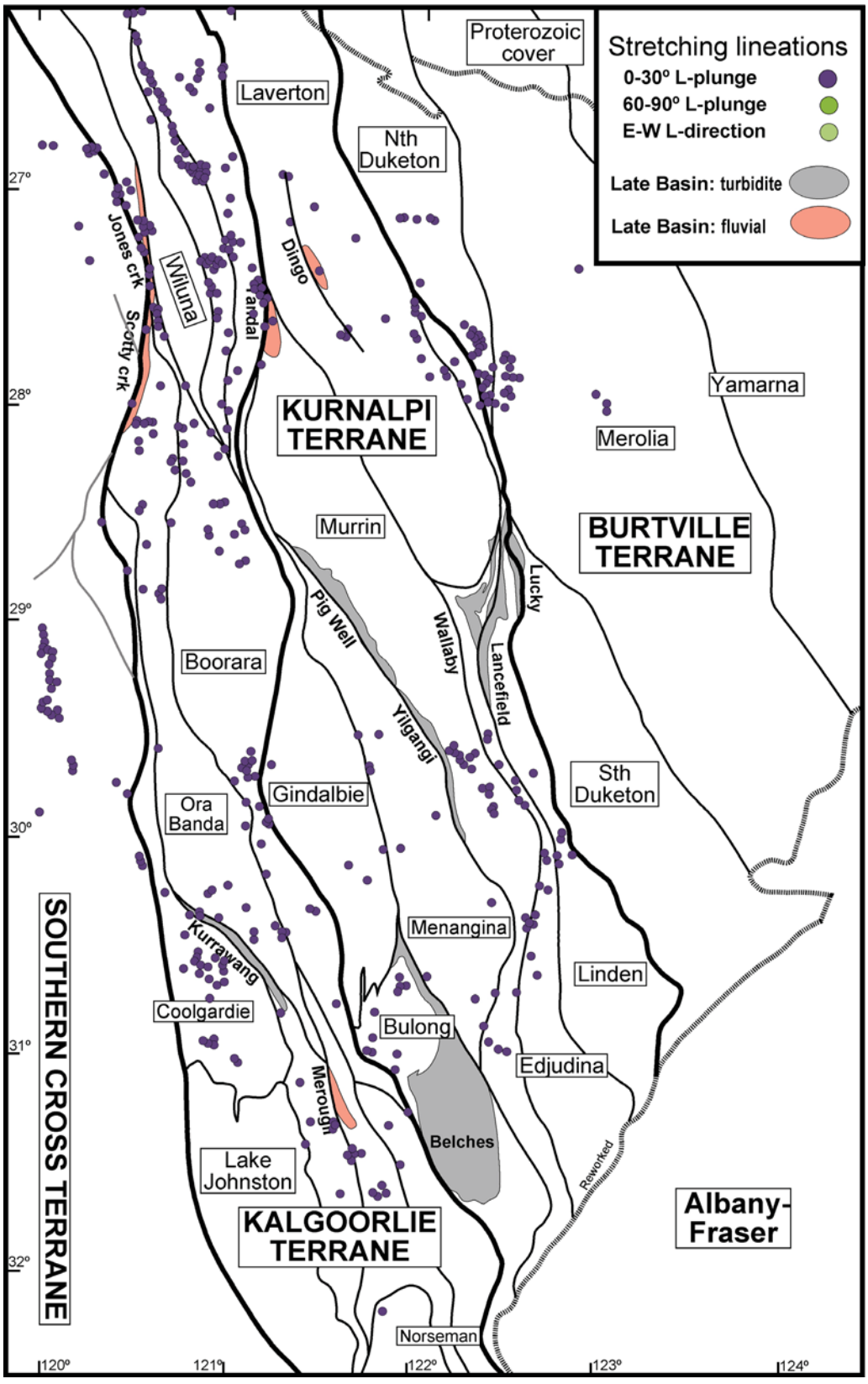

Figure 8: *Strike-slip localities indicated by lineation plunges <30°. Stretching lineation data sourced from GSWA database.*

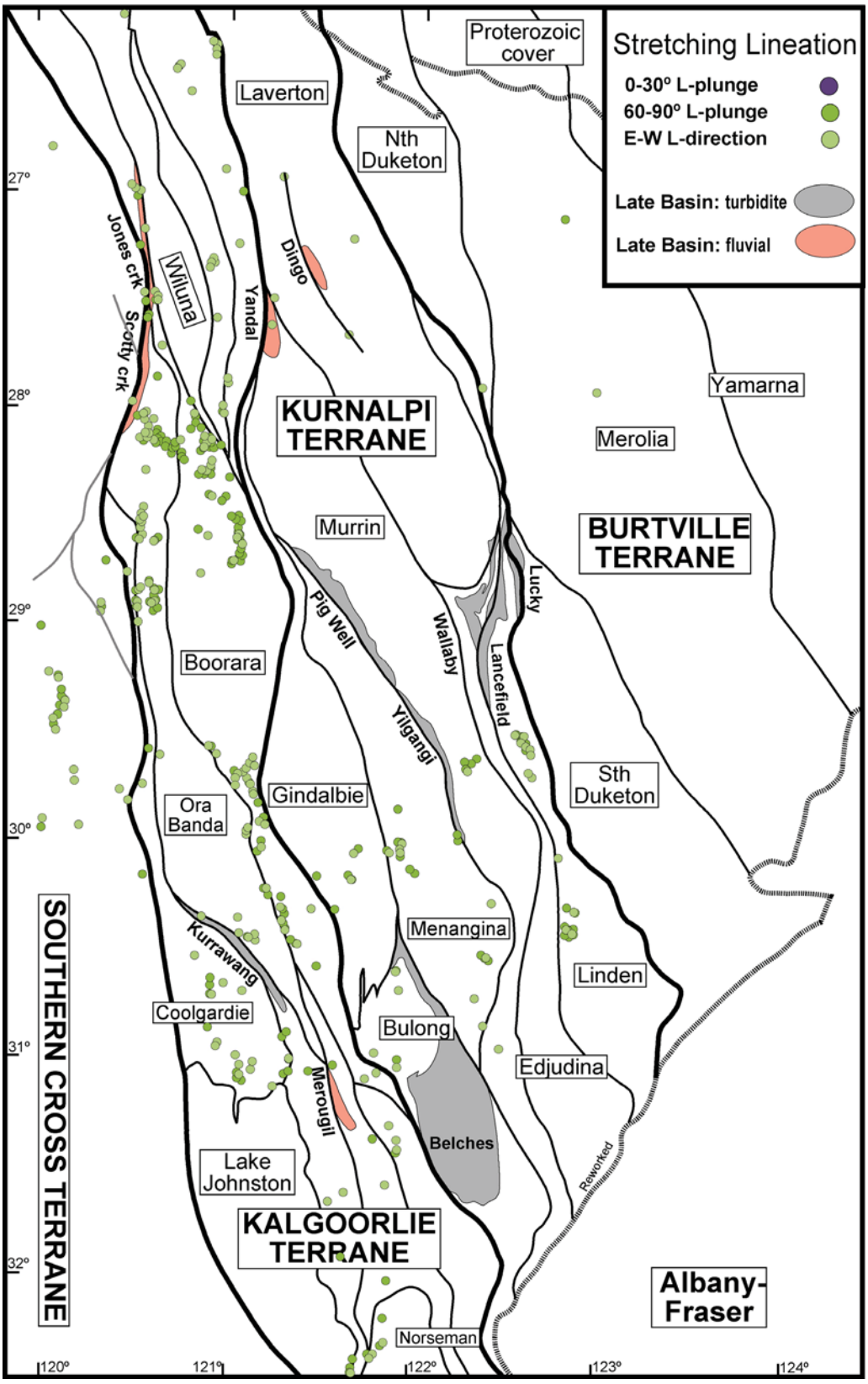

Figure 9: *Dip-slip localities indicated by lineation plunges >60° or ENE-WSW directed plunge directions. Stretching lineation data sourced from GSWA database.*

A kinematic array for the EYC is defined by the maximum extension direction indicated by the trace of stretching lineations (Appendix 2; eycmp1_PlungeDirection.pdf). The patterns of stretching lineations document clear domains of strike-slip and dip-slip maximum extension. Strike-parallel stretch is illustrated by a dominantly parallel pattern of stretching lineations in the vicinity of shear zones indicating generally NNW sub-horizontal extension (Davis and Maidens, 2003). Conversely, there are also small, clustered domains of stretching lineations at high-angle to the more typical strike-parallel trend. Radial stretching lineation patterns are documented around the terminations of granite-gneiss domes (Blewett and Czarnota, 2005). The pattern of obliquity that the stretching lineation trace makes with the dominant foliation (β) has been contoured across the EYC (App 2. eycmp1_Obliquity.pdf). This map can give an indication of the pattern of obliquity of transport within the EYC. Stretching lineations at mid-crustal levels are generally sub-parallel to the plate tectonic convergence vector where it can be documented, such in the Himalayan Orogen (Shackleton and Ries, 1984). This general correlation is not always the case at shallow crustal levels and in transpressional systems, where the maximum extension direction may be developed orthogonal to the transport vector (Tikoff and Greene, 1997). The pattern of obliquity variation across the EYC shows a general low angle of obliquity both in the major shear zones and in lower strain domains between them. Mixed domains with both high-obliquity and low-obliquity sites in close proximity are uncommon.

Where shear sense information is available, it has been combined with the stretching lineation array to document patterns of kinematics, or relative movement, in different parts of the EYC (Appendix 2; eycmp1_ShearSense.pdf). The shear sense data in the MDB is far from complete and based on GA and GSWA datasets and fieldwork undertaken for the EYCMP. Shear sense has been determined at outcrop by a range of asymmetric structures as summarized in a field card (FieldCard_ShearSense(07).pdf). The kinematic dataset for the Yilgarn Craton that is contained in the MDB can be improved substantially in two ways. Firstly, there is a body of shear sense data available in literature that has not been compiled (e.g., Swager, 1994c; Chen *et. al*., 2001a, 2001b, 2003; Bloem et al., 1997; Passchier, 1994; Stewart, 1992; Libby, 1992; Nguyen, et al., 1998; Davis and Maidens, 2003). Secondly, correlations between kinematics at different times with different stretching lineation directions need to be made. The dataset of Blewett and Czarnota (2005) constitutes the only broad-scale age-correlated kinematic data, and could form the basis for calibrating the kinematic array for different deformation events.

GRANITOIDS

HFSE Granitoids

High field-strength element granites and minor granodiorites form a minor (5-10%) component of the juvenile EYC crust and are almost absent from the remainder of the Yilgarn Craton (Champion and Cassidy, 2007). These HFSE granitoids are high-level intrusive rocks associated with early magmatic arcs, volcanic complexes and volcanism. They occur in juvenile crust on a rifted margin, forming in the absence of old crust and so are particularly prominent in the Kurnalpi Terrane (Champion and Cassidy, 2007). These granitoids give the first magmatic peak in the EYC with most being emplaced between 2700 and 2680 Ma and young in age westward across the Kurnalpi Terrane (Champion et al., 2001). These magmatic arc granitoids indicate a west-dipping subduction zone to the east of the Kurnalpi Terrane (Champion and Cassidy, 2007). At the same time, plume-related processes were generating ultramafic volcanic rocks in the Kalgoorlie Terrane to the west (Barley et al., 2003).

High-Ca Granitoids

High-Ca granitoids constitute the greatest volume (60-70%) of all granite types. They are widely distributed and form the bulk of the exposed portions of the large-scale granite-gneiss domes in the EYC (Figure 10). All granite types together make up 70% of the current exposure level and thus High-Ca granites 50%. The early phase of High-Ca granite magma chemistry requires melting of mafic rocks at high pressure, leaving garnet-bearing mafic rocks or eclogite restite, or form through a two-stage process involving remelting of the initial high-pressure melts. Melting of mafics in the

eclogite field result in low-Y granite melts that can form from subducting oceanic crust or at the base of crustal lithosphere with accreted mafic material (Champion and Sheraton, 1997; Champion and Cassidy, 2007). The tectonic setting for early phase High-Ca melts is interpreted to be subduction related at a continental margin with a component of crustal recycling, probably as the crust thickened or subduction dip changed (Cassidy et al., 2002). The large volume of High-Ca granitoids was responsible for thermally stratifying the crust during M2 by both the advection of large volumes of melt into the upper crust and by radiogenic heat production from these Th-enriched granites (Beakhouse, 2007).

High-Ca granite magmatism in the EYC spans a long period from 2700 to 2640 Ma, most between 2680 and 2660 Ma, and with multiple peaks and diachronaity across different terranes. Two peaks are recognised in the Kalgoorlie Terrane with High-Ca magmatism starting with felsic volcanism at ~2700 Ma and increasing to a peak at ~2675 Ma, immediately before the termination of all volcanism at ~2670 Ma (Champion et al., 2001). A second peak in the Kalgoorlie Terrane at ~2660 Ma coincides with the major peak in the Burtville Terrane. High-Ca magmatism in the Kurnalpi peaks immediately before termination of volcanism and together all terranes document a general decrease in age towards the east. The second phase of High-Ca granite has higher Y-contents indicating no garnet in the restite and shallower melting. This is interpreted to indicate cessation of subducted slab melting and the shallower melting zone may have involved a higher crustal melt component. The two peaks in the High-Ca granite bloom, immediately before and immediately after termination of volcanism, probably signify a major switch in tectonic setting. For example, the cessation of subduction processes and crustal thickening, followed by lithospheric extension processes leading to shallower melting at crustal levels during the second peak. The start of High-Ca granite bloom in the EYC coincides with the termination of High-Ca magmatism in the Southern Cross and Murchison Terranes to the west.

Mafic and Syenitic Granitoids

Mafic and syenitic granitoids make up a small component of the EYC, 5% and <1% respectively and are almost absent from the Southern Cross Terrane to the west. The syenitic melts are derived by partial melting of a metasomatized mantle source and are consequently related to magmatic arcs (Champion and Cassidy, 2007). These mantle derived syenitic melts are associated with dry CO_2-rich mantle fluids and magmatic carbonate veins (Blewett and Czarnota, 2007c). Mafic granitoids are dark, amphibole-bearing diorites, granites, granodiorites and tonalite of ~2680-2650 Ma age, with a peak at 2665 Ma in both Kalgoorlie and Kurnalpi Terranes (Champion et al., 2001). Syenites also peak at 2665 Ma in the Kalgoorlie and Burtville Terranes and span a longer period and are younger in the Kurnalpi Terrane, peaking at ~2650 Ma. Both mafic granites and syenites are closely associated with gold deposits and possibly related to the transfer of gold from a mantle source into the upper crust. Other late-stage mantle-derived magmas recognised in the EYC are lamprophyres and carbonatite (Groenewald et al., 2006).

Low-Ca Granitoids

Low-Ca biotite granite and granodiorite constitute 30% of EYC granitoids. These range in size from dykes to large sheet-like bodies and most typically post-date pervasive deformation events (i.e., D1, D2 and D3). These post-date crustal growth processes such as volcanism and arc magmatism and range in age from 2660 to 2610 Ma, with most of 2655-2630 Ma age (Champion et al., 2001). Low-Ca melts were generated by partial melting of a middle to lower crust that was dominated by High-Ca granites with mafic and meta-sedimentary rocks (Champion and Sheraton, 1997). These partial melts do not contain a mantle component, did not involve subduction processes and are interpreted to be associated with lithospheric extension (Champion et al., 2001; Champion and Cassidy, 2007). Low-Ca granites of the same age are widespread across the entire Yilgarn Craton and show a slight diachronaity, younging westward across the EYC. The greatest concentration is at the east margin of the Southern Cross Terrane and may be related to decompression induced melting in the footwall during extensional reactivation of the Ida Shear Zone. In the EYC Low-Ca granites are preferentially emplaced into High-Ca granite-gneiss domes (Figure 10) and this spatial association may also be related to decompression melting at depth below these domes as they developed. Or alternatively,

the current distribution is an artifact of the slightly different crustal levels exposed. The process of transferring Low-Ca crustal melts from the lower-crust to shallow crustal levels also transfers heat out of the lower crust and aids cratonization.

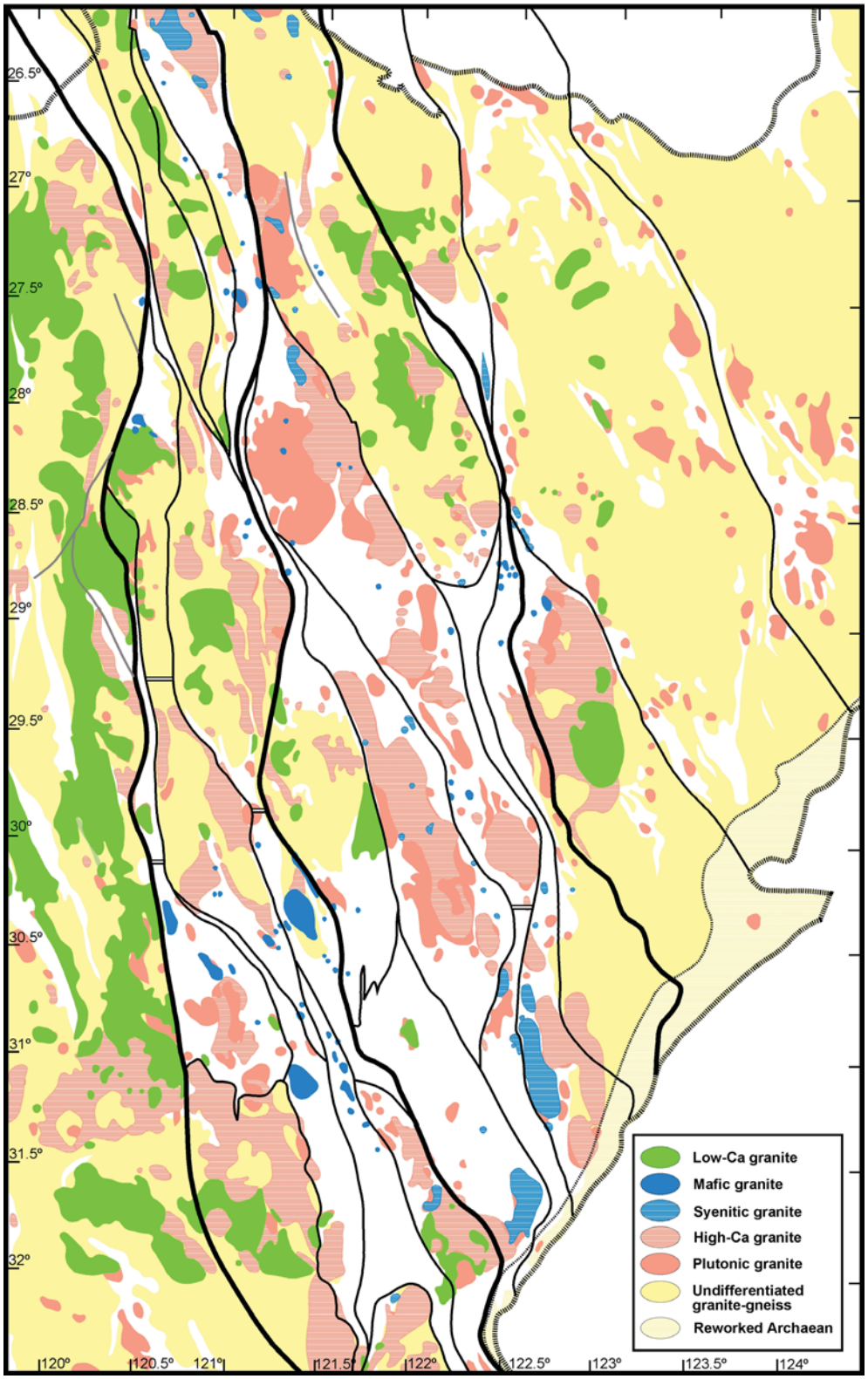

Figure 10: *Map of plutonic granite types.*

AGE CONSTRAINTS

All robust high-resolution geochronology available for the Yilgarn Craton has been collated and is contained within the MDB (Appendix 3). These data are also presented in a specific table of geochronology (Appendix 4), this contains a near comprehensive listing of published age data from the Yilgarn Craton (Pidgeon, 1986; Compston et al., 1986; Clark et al., 1988; Cloue-Long et al., 1988; Hill et al., 1989; McNaughton and Cassidy, 1990; Pidgeon and Wilde, 1990; Hill et al., 1992; Hill and Campbell, 1993; Wiedenbeck and Watkins. 1993; Kerrich and Cassidy, 1994; Nemchin et al., 1994; Witt, 1994; Bloem et al., 1995; Kent and McDougall, 1995; Ahmat, 1995; Nelson, 1995; Schiotte and Campbell, 1996; Kent et al., 1996; Kent and Hagemann, 1996; Nelson, 1996; Swager and Nelson, 1997; Swager, 1997; Hall, 1997; Campbell et al., 1998; Napier et al., 1998; Nelson, 1998; Lambert et al., 1998; Barley et al., 1998; Qiu et al., 1998; Ren and Heithersay, 1998; Nemchin and Pidgeon, 1999; Qiu and Groves, 1999; Nelson, 1999; Krapez et al., 2000; Mueller and McNaughton, 2000; Nelson, 2000; Fletcher et al., 2001; Cassidy et al., 2002; Barley et al., 2002; Brown, et al., 2002; Black et al., 2002; Mueller and Nemchin, 2003; Barley et al., 2003; Bucci et al., 2004; Griffin et al., 2004; Mueller et al., 2004; Ross et al., 2004; Roberts, 2004; McNaughton et al., 2005; Baggott et al., 2005; Salier, et al., 2005; Phillips and Miller, 2006; Miller and Rasmussen, 2006; Squire, 2006; Groenewald et al., 2006; Neumayr et al., 2007; Squire, 2007).

The data collated in Appendix (4) is restricted to robust age constraints from the mid-1980's and Rb-Sr and Ar-Ar data are generally ignored. All data are sorted by tectonic domain. The best available summary of all EYC geochronology (Figure 11) from granitoids, volcanic stratigraphy, maximum deposition ages, deformation ages and gold mineralization events is in the time-space diagram of Blewett and Czarnota (2007c). Significant other high resolution age dating has been undertaken by the Centre for Exploration Targeting but is otherwise generally unavailable. Crucially, dating programs at the Centre for Exploration Targeting have focused on direct dating of metamorphic minerals, which has generally not been undertaken to date in the Yilgarn Craton. For example, programs include U-Pb and Pb-Pb dating of titanite (Tc=500-600 ºC) and Pb-Pb dating of monazite, xenotime and zircon. Dating of monazite and titanite is particularly useful because these avoid xenocrystic problems, both grow over a large temperature range, both form metamorphic overgrowths on detrital grains and both igneous and hydrothermal monazite are easily recognised by high-Th and low-Th values respectively.

Age determinations by Lu-Hf dating of different episodes of metamorphic garnet was undertaken for the EYCMP by Roland Maas at the University of Melbourne (see Geochronology section). The resulting ages are consistently older (by ~20-25 Ma) than the stratigraphic and structural constraints on the dated sample. Nevertheless, these ages define a systematic pattern that is geologically reasonable, indicating a geochronological error that apparently equally applies to all samples (see Geochronology section). Consequently, these age determinations give relative age constraints that confirm four significant aspects of the metamorphic evolution of the EYC. [1] At least three distinct prograde metamorphic events are confirmed by the garnet chronology. [2] The distinct high-P, low-G metamorphic parageneses (M1) are unrelated to and significantly older (by ~14 and ~30 Ma) than the other metamorphic parageneses. [3] The widespread regional metamorphic parageneses (M2) formed after the high-P M1 parageneses and before metamorphism of the late basins. [4] Metamorphism of the Mount Belches post-volcanic turbiditic basin was during a distinct over-printing thermal event (M3a) that occurred approximately 17-23 Ma after regional metamorphic parageneses.

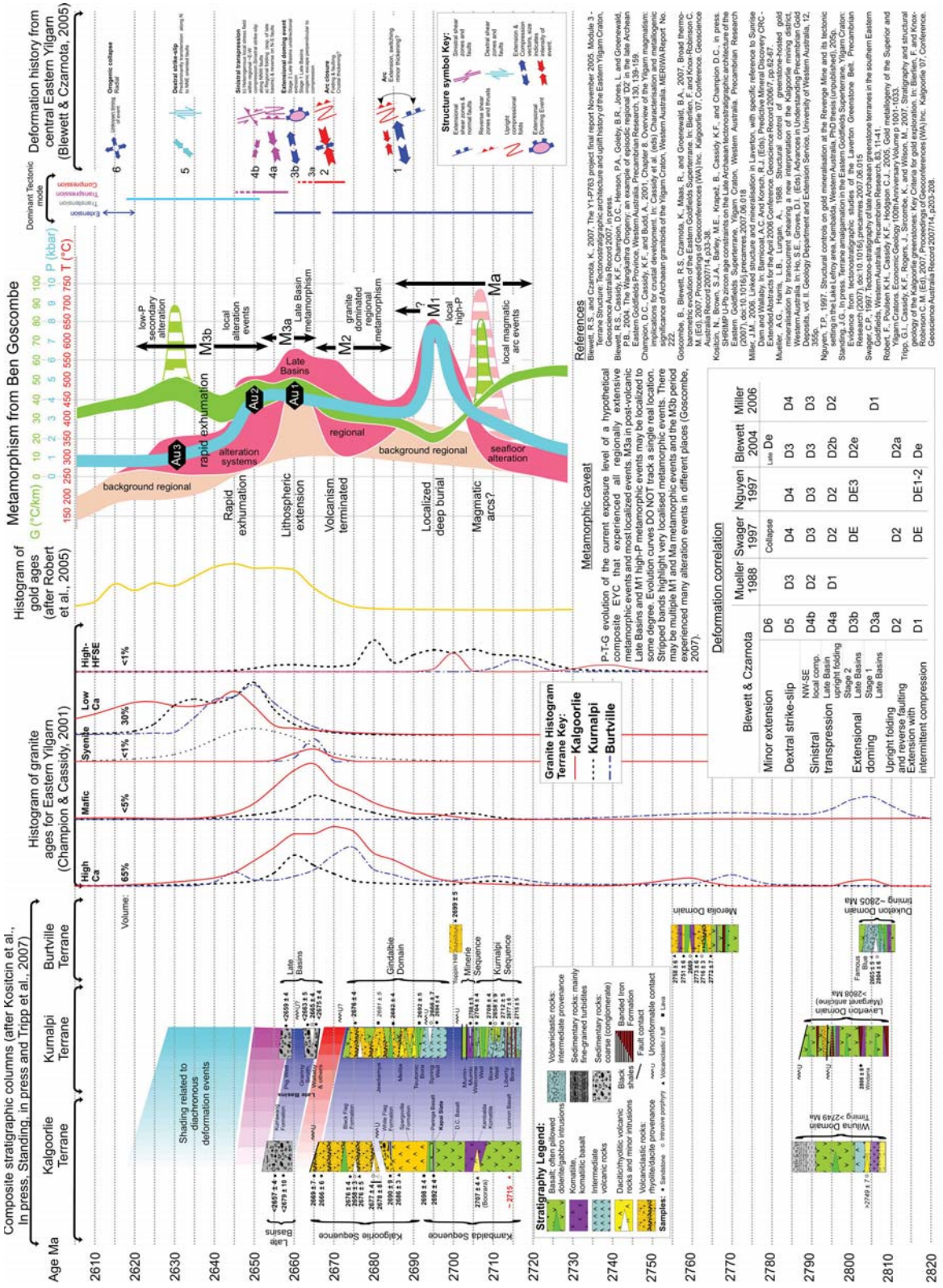

Figure 11: *Currently accepted time-space diagram for the fundamental geological events and processes in the EYC (Blewett and Czarnota, 2007c), including deformation, stratigraphy, volcanism, intrusions, metamorphism and gold mineralization.*

D1 Events

The best geochronological dataset available for constraining deformation and metamorphic ages has come from the granites (Blewett et al., 2004b). Most temporal constraints on deformation events have been made by correlation with the large body of magmatic chronology available in the literature. The granite geochronology framework (e.g., Nelson, 1996, 1997; Fletcher et al., 2001; Champion et al., 2001; Cassidy et al., 2002; Dunphy et al., 2003) indicate that the EYC was deformed by long-lived extensional stages with granite emplacement, interspersed with short-lived contractional stages (Figure 11). D1 is interpreted as a long-lived extensional period recorded by the volcanic, volcanoclastic and clastic stratigraphic rock record. It is unknown to what extent this extensional record was episodic or continuous. The Kambalda Komatiite is dated around 2705 Ma (Nelson, 1997), and the Upper Basalt is younger than the Kapai Slate, which is dated around 2692±4 Ma (Claoue-Long et al., 1989). The Kalgoorlie Sequence (Black Flag Formation) has age ranges from 2690 to 2665 Ma (Krapez et al., 2000). The Kalgoorlie Sequence has a number of unconformities. The major unconformity is at ~2673 Ma at the top of the Black Flag Formation followed by the onset of coarse clastic sedimentation (White Flag Formation). This unconformity coincides with the termination of volcanism in the EYC, first major exhumation and erosion period and also a peak in the major High-Ca granitic magmatism. High volumes of High-Ca magmatism also occurred before and after termination of volcanism (Champion et al., 2001). High-Ca granite magmatism was diachronous, with the first major peak in the Kurnalpi Terrane (~2675 Ma) and the last in the Burtville Terrane (~2660 Ma), and the Kalgoorlie Terrane recording both of these peaks (Figure 1). The age of the gneissic fabrics are in the range of: 2672±2 (Two Lids Soak); 2675±2 (Barrett Well); 2670±10 (Ivor Rocks); 2681±4 Ma (Isolated Hill), and 2674±3 Ma (Wilbah). This regional consistency suggest a minimum limiting age or ~2672 Ma for D1 extension and a maximum age for regional metamorphism (M2) at this time.

D2 Events

The maximum age constraint for the first contractional event (D2) is the age of deformed granites and the minimum age is established by cross cutting granites (Blewett et al., 2004a). In the Burtville Terrane, D2 occurred in the range <2668±4 Ma (Ironstone Point) and is inferred to be >2664±2 (Hanns Camp Syenite) based on a relative timing correlation. In the Kurnalpi Terrane D2 occurred at <2667±4 Ma (Pindinnis), <2665±4 Ma (Granny Smith Granodiorite), <2667±5 Ma (Porphyry), <2657±8 Ma (Porphyry), and is inferred to be >2660±5 Ma (Bulla Rocks) based on a relative timing correlation.

D3 Events

The D3a and D3b extensional events are associated with both the development of post-volcanic clastic basins and emplacement of the mantle-derived syenitic and mafic granites (Champion and Sheraton, 1997). A maximum age for the major D3b event can be inferred from the overprint of extensional fabrics on granites such as the 2664±2 Ma Hanns Camp Syenite and 2660±5 Ma Bulla Rocks Monzogranite. Mineralization at Sunrise Dam is interpreted to be associated with D3b extension and the 2658±4 Ma age of Au-mineralization constrains D3 to this time (Brown et al., 2002). This age is consistent with the maximum deposition ages for fluviatile late rift basins, being 2662±5 Ma for the Scotty Creek and 2657±7 Ma for the Kurrawang late basins (Krapez et al., 2000).

D4, D5 and Mineralization Events

The D4a contractional stage occurred prior to almost all Low-Ca granite magmatism, which is present across all terranes of the Yilgarn Craton. Initiation of Low-Ca granite emplacement coincides with a stress switch back to NE-SW contraction experienced during the protracted D5 event. These granites constrain the maximum age for D5 as <2652±5 Ma (Pink Well), <2650±8 Ma (Mount Denis), and <2645±6 Ma (Surprise Rocks). At Mars Bore a Low-Ca granite dyke of 2647±3 Ma age, both over-prints and is over-printed by D5 dextral shear zones. A minimum age for D5 is obtained from Low-Ca granite dykes of 2638±2 Ma age that overprint D5 fabrics at Ironstone Point in the Burtville Terrane.

Inaccurate age constraints indicate old Au-mineralization events between 2675 and 2658 Ma, at Golden Mile (Gauthier et al., 2004), Kanowna (Ross et al., 2004) and Jundee (Yeats et al., 2001). Direct dating of the major gold deposits of Wallaby (Salier et al., 2004; Miller, 2005), Sunrise Dam (Brown et al., 2002) and Chalice (Bucci et al., 2004) give ages centred on ~2650 Ma. Au-mineralization is interpreted to also be of ~2650 Ma age at Lancefield (Blewett and Czarnota, 2007c), Mount Morgans (Vielreicher et al., 2003) and Granny Smith (Ojala et al., 1997). This age coincides with the switch from High-Ca to Low-Ca granite magmatism and the stress switch from ENE- and ESE-directed D4 contraction to NE-directed D5 contraction (Blewett and Czarnota, 2005, 2007c). Younger Au-mineralization events dated between ~2640 and 2610 Ma are widespread, such as at Golden Mile, Revenge, Chalice and Victory-Defiance (Bucci et al., 2004; Clark et al., 1989; McNaughton et al., 2005; Vielreicher et al., 2003; Tripp et al., 2007). Unpublished dating from the Centre for Exploration Targeting and dating at the Golden Mile (Tripp et al., 2007), report lamprophyres of ~2640 and <2636 Ma age, indicating a mantle component brought into the upper crust at a late-stage in EYC evolution.

D6 Events

The same Ironstone Point dykes are overprinted by later ENE-WSW contraction and are considered the maximum age limit on D6 vertical shortening. At Moon Rocks, 2637±7 Ma Low–Ca granite dykes are syn-deformational with dextral faulting during post-D6 NW-SE contraction. Consequently, the D6 vertical shortening event is interpreted to be of approximately 2635 Ma age (Blewett and Czarnota, 2007c). Vertical shortening is common late in orogenic cycles, as a mechanism for final stage tectonic unloading in response to diminishing tectonic driving forces (Duclaux et al., 2007).

Metamorphic Background

PREVIOUS METAMORPHIC PARADIGM AND PRELIMINARY DATA

The previous metamorphic paradigm for the Yilgarn Craton is overly simplistic and three inherent assumptions and interpretations are incorrect. [1] Metamorphic response has been modelled on craton-wide continental collision tectonics involving crustal over-thickening, possibly with plume effects (Groves and Phillips, 1987; Rey et al., 2003). [2] Current exposure level is assumed to represent a near uniform crustal level corresponding to 4 kb (Figure 12; Binns et al., 1976; Ahmat, 1986; Wilkins, 1997). [3] Main matrix assemblages are generally assumed to have formed in a single prograde metamorphic cycle with post-kinematic peak, and are over-printed only by retrograde and hydrothermal alteration events and not by multiple prograde thermal pulses (Binns et al., 1976; Swager et al., 1990; Wilkins, 1997; Dalstra, et al., 1999). Aspects of this simplistic picture have previously been shown to be incorrect by metamorphic investigations that have recognised baric and temporal complexities (e.g., Witt, 1994, 1998; Bickle and Archibald, 1984; Williams and Whitaker, 1993; Williams and Currie, 1993; Ridley, 1992, 1993; Mikucki and Roberts, 2003). Nevertheless, an overly simplistic picture of Yilgarn metamorphism has become generally established. This has come about by both a neglect of detailed metamorphic studies aimed at documenting thermal and barometric evolutions and a general under-appreciation of the importance of crustal thermal evolution to this world-class mineral province. This oversight, particularly during a recent period where new Au-mineralization models were being sought by the exploration industry, has delayed understanding of one of the fundamental drivers leading to Au-mineralization - the thermal evolution of the crust (e.g., Hall, 1997). Recognition of this connection has recently reinvigorated the ongoing endeavour to document metamorphic patterns and evolutions in the Yilgarn Craton (e.g., Mikucki and Roberts, 2003; Goscombe et al., 2007) and thermo-mechanical modelling of the relationships between metamorphism and mineralization (e.g., Sheldon et al., 2007, 2008).

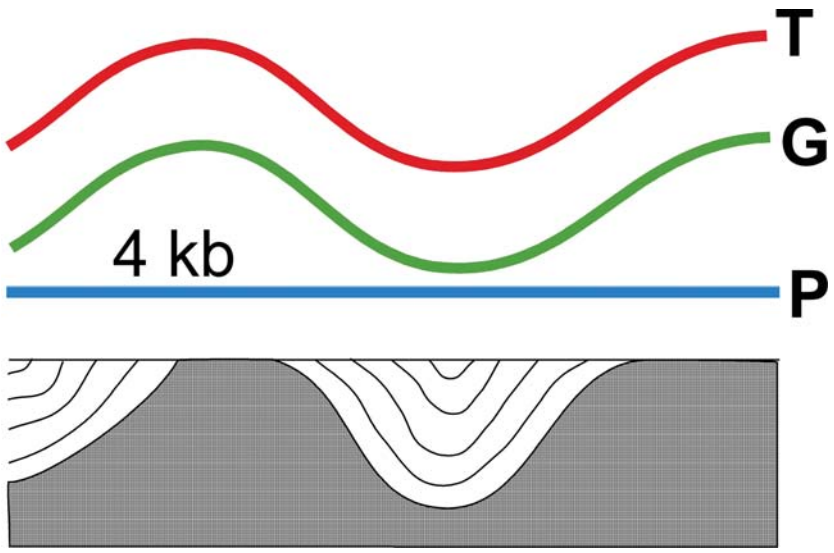

Figure 12: *Diagrammatic representation of the metamorphic field gradients implicit in the original paradigm for Yilgarn Craton metamorphism that assumed a uniform crustal level throughout. The findings of the EYCMP have shown these assumed field gradients across greenstone synforms to granitoid domes (shaded) are incorrect.*

Metamorphic conditions recorded by rocks in the EYC can be simplified into three groups based on pre-existing datasets in the literature and preliminary calculations (i.e., pre-2006). Results of preliminary metamorphic calculations and data from literature (Figure 13), show a broad P-T array with clusters based on different P, T and temperature/depth ratio, which also correlate with different metamorphic style and structural and stratigraphic settings. The three groups are:

[1] High-P and low thermal gradient: Parageneses with high pressures and low temperature/depth ratio are restricted to high-grade, high-strain shear zones of 1-5 km width that are commonly adjacent to granite-gneiss domes. The low temperature/depth ratios indicate that these rocks are cooler than all other parts of the EYC at similar crustal levels. Peak parageneses are generally foliated, indicating syn-kinematic peak metamorphism. Peak parageneses are often reworked and down graded by later low-grade events. These parageneses show clockwise P-T loops with steep to isothermal decompression paths defined by plagioclase coronas after high-P garnet parageneses in mafic rocks.

[2] Medium to low-P and moderate thermal gradient: Parageneses with intermediate pressures and moderately elevated temperature/depth ratio are regionally developed outside the high-strain, high-grade zones. Strain is variable, ranging from static to dynamic and metamorphism is of "regional-contact" type. These parageneses show tight clockwise P-T paths defined by early chloritoid and staurolite over-printed by later formed garnet and andalusite in metapelite.

[3] Low-P and high thermal gradient: Low-P and high temperature/depth ratio parageneses are characterized by mid-amphibolite facies metapelites with garnet, staurolite, cordierite and andalusite-bearing assemblages typically developed in post-volcanic turbiditic basins. Significantly, these parageneses show uniquely anticlockwise P-T paths defined by early cordierite and andalusite and post-kinematic garnet and staurolite in metapelite.

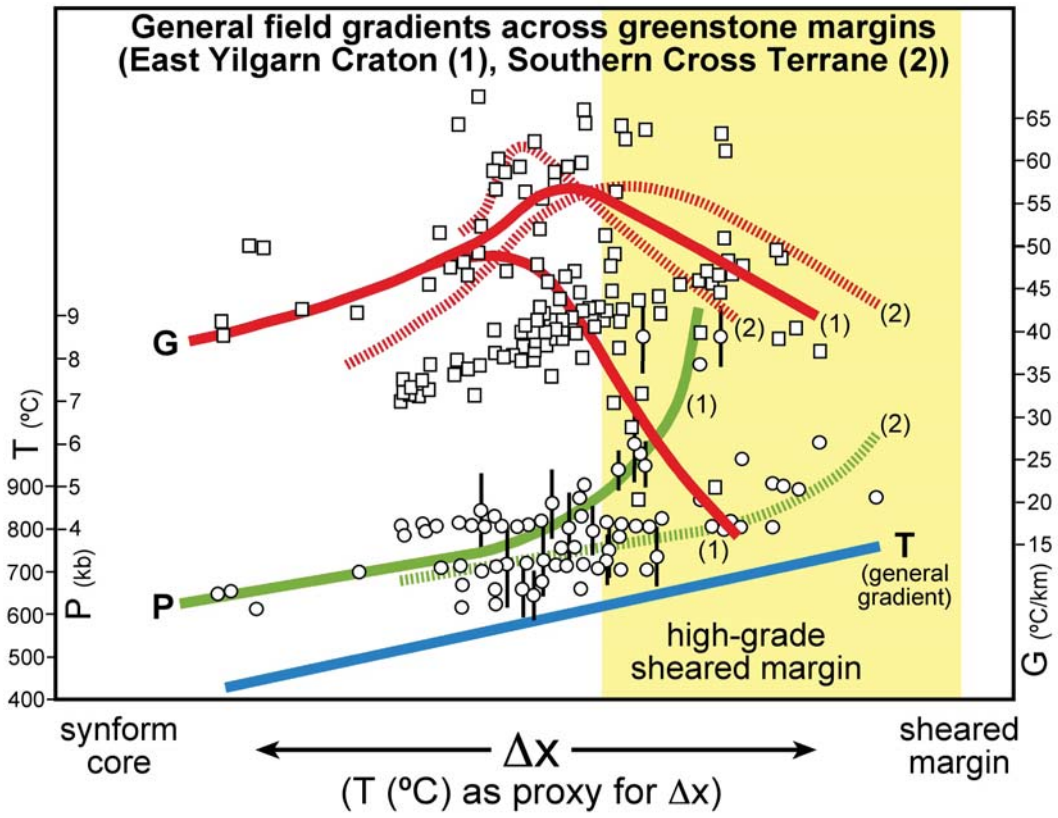

Figure 13: *Generalized metamorphic P-T arrays based on preliminary (at 2003) P-T calculations from the East Yilgarn Craton and Southern Cross Province. Ellipses are average P-T calculations using THERMOCALC v3.1 (Powell and Holland, 1998). Dots are P-T estimates by conventional geothermobarometry from the literature. Note that most P-T estimates from literature assume a value of 4.0 or 3.0 kb and very few legacy data attempted to calculate pressures. These P-T arrays represent generalized metamorphic field gradients across a generalized greenstone belt from low-grade synform to high-grade margins near gneiss-granitoid domes, with the temperature axis being a proxy for the Δx length scale.*

These groupings facilitate a discussion on the fundamental problems and critical issues that need to be addressed by metamorphic studies of the EYC. Hypothetical metamorphic field gradients between the high-P and low-P parageneses (Figure 14) illustrates the salient differences between generalized, end-member tectono-metamorphic domains. There is insufficient information to extrapolate these generalized field gradients into the granite-gneiss domes (Figure 15). The crucial issues are: what is the relative timing between these different metamorphic parageneses, how did they come to be juxtaposed at the same crustal level, and what plausible tectonic settings could generate these different metamorphic responses in close proximity? Linking all of these is the fundamental question; are the different parageneses making up EYC P-T array (Figure 13) of similar or different ages? Because of an apparent correlation with different stratigraphic settings, the different parageneses are not anticipated to be time equivalent. On completion of the EYCMP, both the absence of accurate direct dating of metamorphic parageneses and barometric constraints from within granite-gneiss domes, still remain the two crucial outstanding datasets required to fully constrain tectonic models. For example testing for convective overturn and vertical tectonics can be readily assessed with robust P constraints from granite-gneiss domes (Figure 15).

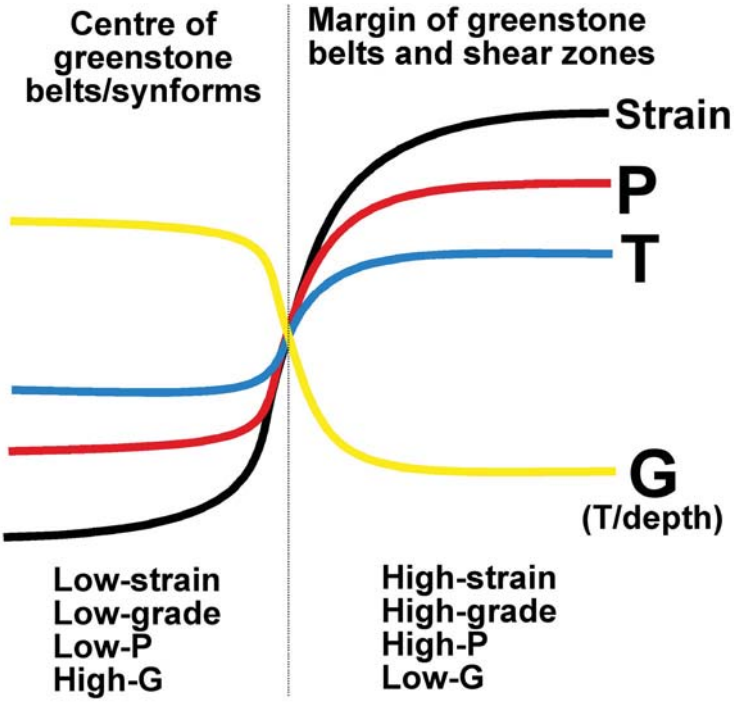

Figure 14: *The observed generalized metamorphic field gradients across greenstone belts, from low-grade synform to high-grade margins near gneiss-granitoid domes.*

MODELS FOR JUXTAPOSED THERMAL REGIMES

The EYC is distinctively characterized by a marked metamorphic duality and highly partitioned strain distribution. The high-P and low-P parageneses of the EYC (Figure 14) indicate entirely distinct thermal regimes of metamorphism. Similarly strain is heterogeneously distributed into low-strain granite-gneiss domes, high-strain crustal shear zones that often coincide with dome margins and highly variable greenstone synformal regions (e.g., Figure 5). What distinguishes the EYC from other simpler orogenic systems, such as the Himalayan Orogen (Goscombe et al., 2006), is that metamorphic and kinematic partitioning is non-systematic. Steep gradients in both strain and metamorphic conditions are a defining aspect of the character of the EYC. Unlike most orogenic belts, there is no systematic pattern to deformation and metamorphic variation; the complexity is possibly an artefact of either over-printing multiple tectono-thermal events or a mosaic of over-lapping orogenic sub-systems making up the larger cratonic-scale orogenic system.

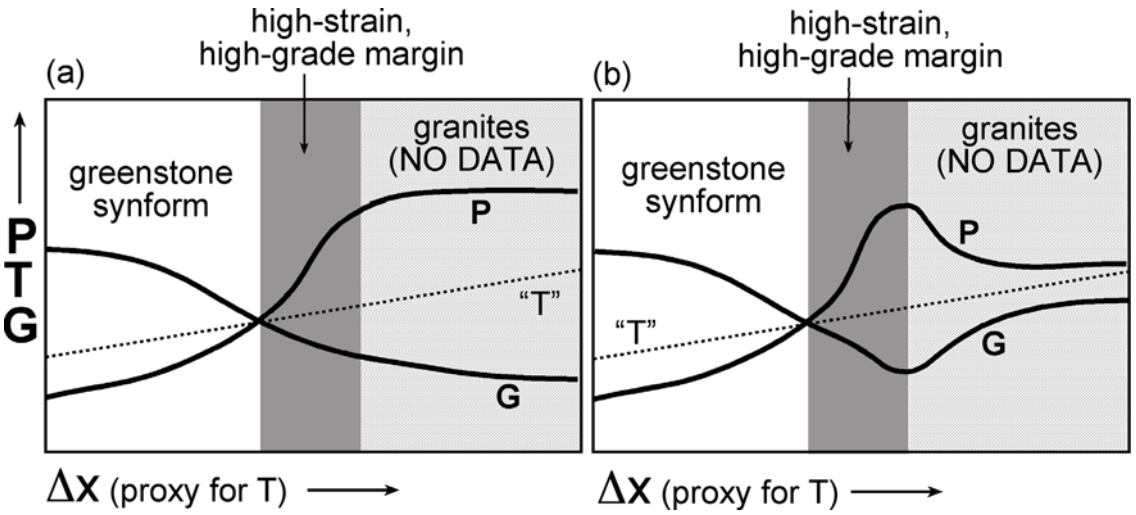

Figure 15: *Alternative models for hypothetical extension of the metamorphic field gradient into the gneiss-granitoid domes where almost no P-T constraints exist. In model (a) the granitoids representing deeper crustal levels than the adjacent greenstones. Though early higher-P parageneses are not preserved or evident in these domes, this is the preferred model. In model (b) the granitoid domes represent crustal levels not significantly different to the adjacent greenstones and the highest-pressure rocks are localized only to shear zones at the margins of these granitoid domes.*

Heterogeneous strain distribution is possibly an artefact of deformation at upper crustal levels, leading to strong partitioning. In contrast, the cause for heterogeneous distribution of metamorphic variables such as T, P, and temperature/depth ratio (G) is not so immediately obvious. Differential pressures potentially indicate differential exhumation, exposing different crustal levels, in which case the post-metamorphic history controls the final metamorphic pattern. However, because both T and G also vary, this indicates that truly different metamorphic thermal regimes were developed across the EYC. Crucially, the high-P and low-P groupings do not share the same thermal regimes (G) and so cannot simply be different crustal levels of the same metamorphic event. Consequently, the currently exposed metamorphic patterns must be explained by one of the following mutually exclusive end-member processes (Figure 16).

[1] Retrograde Metamorphic Patterns: Metamorphic patterns developed during retrograde evolution, or an unrelated reworking event, result from late-stage differential uplift and juxtaposition of metamorphically contrasted domains (Figure 16a). Late-stage differential exhumation will result in pressure differences without necessarily variation in the temperature/depth ratio. This will be evident if parageneses recording different pressures are of the same age, indicating a metamorphic pattern that merely represents different crustal levels of the same thermal regime. Alternatively, contrasting metamorphic parageneses of different age can be juxtaposed by differential uplift after they were metamorphosed or during the latest metamorphic event. This latter scenario can result from late-stage lithospheric extension, juxtaposing assemblages of different age and different crustal levels, as interpreted for M3a metamorphism in the EYC, and represented in a schematic crustal section (Figure 17). In this hypothetical scenario, older high-P and low-G rocks are exhumed and juxtaposed against shallower rocks of different metamorphic age and thermal regime, by extensional telescoping of the crust (Figure 17).

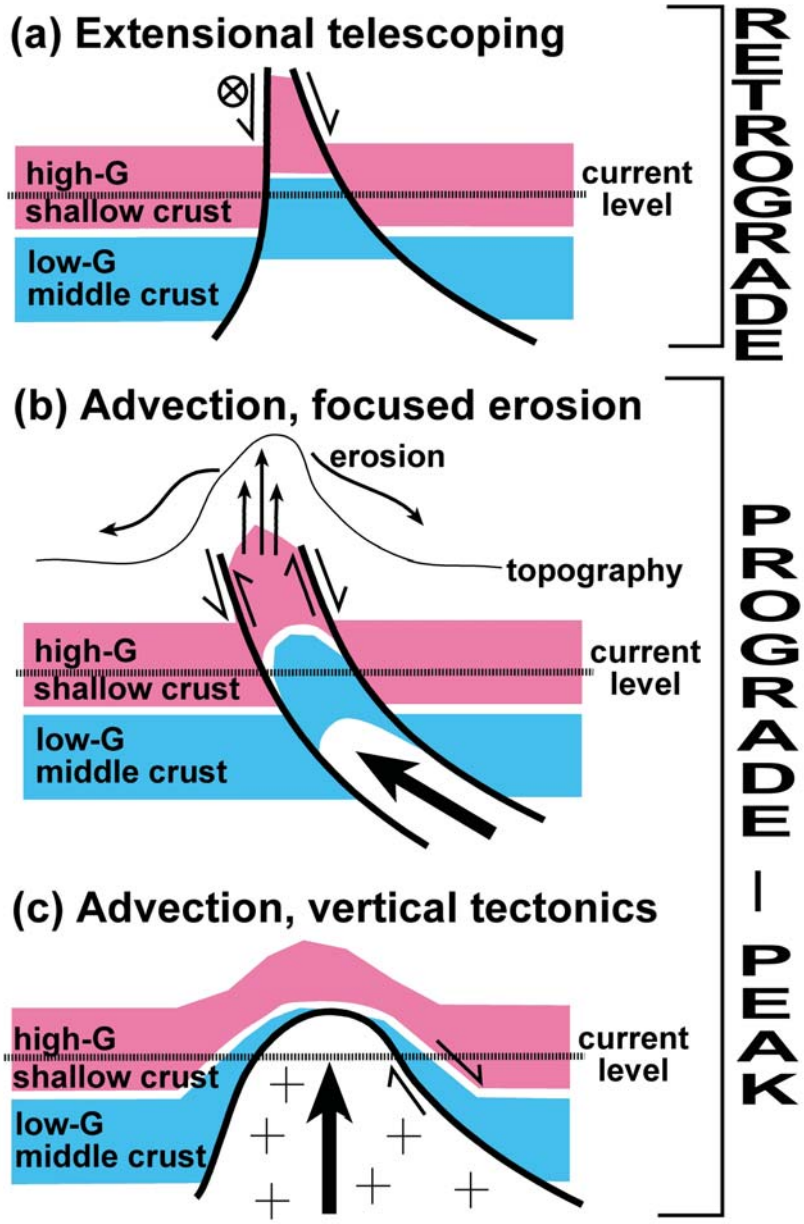

Figure 16: *Three end-member models for the juxtaposition of domains of different thermal regime, in the case of the EYC a upper-crust with relatively high temperature/depth ratio resulting from the pooling of granitoid magmas. Juxtaposition models break into two classes; (a) those that involve juxtaposition after peak metamorphism during the retrograde evolution of the terrane, and (b, c) those that involve juxtaposition by the advection of material accompanying metamorphism in the same orogenic cycle.*

[2] Peak Metamorphic Patterns: Alternatively, metamorphic patterns may be primary and were developed during prograde or the peak of metamorphism. Peak metamorphic patterns may be preserved where orogens have been exhumed without significant dissection or modification during the retrograde history. Counter-intuitively, peak metamorphic patterns may also display a marked primary variation in both pressure and thermal regime, developed at essentially the same time in the one metamorphic cycle. A primary pattern showing different thermal regimes of essentially the same age juxtaposed together is a common feature of metamorphic belts (e.g., Armstrong et al., 1992; Goscombe and Hand, 2000; Brown 2006). Primary metamorphic partitioning commonly correlates with kinematic partitioning (Thompson et al., 1997) and results from scenarios where the advection

of heat (and material) out competes the conduction of heat during prograde and peak metamorphism (Sandiford, 2002). A familiar example is in subduction settings, where fast downward advection of relatively cold material juxtaposed domains of different thermal regime, generating a paired metamorphic belt. Similarly, extrusion or channel flow of hot material from deep to shallow crustal levels also results in a primary paired metamorphic pattern (e.g., Beaumont et al., 2001; Jamieson et al., 2002; Goscombe et al. 2005a, 2006). A hypothetical compressional scenario with partitioned advection of material, resulting in the juxtaposition of coeval but contrasting metamorphic conditions similar to those experienced in the EYC, is represented in a schematic crustal section (Figure 18). In this hypothetical scenario the high-P, low-G rocks are advected upwards at higher rates than adjacent domains. This is within a high strain channel at the margin of granite-gneiss domes, accommodated by reverse movement at the lower-plate margin and extensional movement at the upper-plate margin (Figure 18).

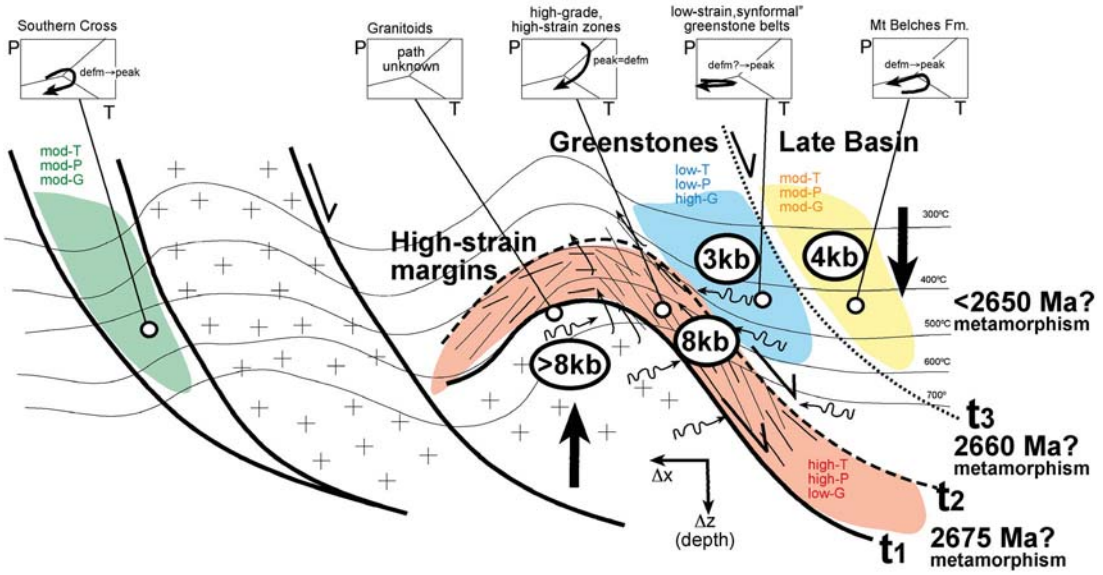

Figure 17: *Diagrammatic cross-section of the preferred model for the metamorphic consequences of lithospheric extension during the M3a period accompanying granitoid domes and late-basin development. Note this model also explains the juxtaposition of M1, M2 and M3a metamorphic parageneses at the same crustal level by extensional telescoping of the upper crust.*

To test between the two end-member processes for generating metamorphic patterns containing juxtaposed contrasting thermal regimes such as the EYC, an integrated terrane analysis approach has been taken. Structural and metamorphic datasets have been integrated spatially using mapped patterns and field gradients (e.g., Figures 157 to 162 in the Integration chapter of this Record) and have been integrated temporally using the available geochronology to construct evolution curves for fundamental structural and metamorphic parameters. Relative chronology of the different metamorphic domains is crucial to this interpretation. This approach allows insights into both the lateral and vertical translation of rock units at different crustal levels and the flow of heat, magma and fluids. Generally the horizontal components of translation can be deduced from structural data (Blewett and Czarnota, 2007c) and the vertical components are largely deduced from metamorphic data documenting barometric variations (Goscombe et al., 2005a). The paths tracked by individual rocks in an evolving orogenic system are very complex because of the progressive nature of orogenesis, multiple shortening and extensional episodes and superimposed processes such as variations in crustal thickness and isostatic response. Nevertheless, relative transports between distinct tectono-metamorphic domains and generalized paths at key sites can be documented with robust metamorphic constraints (e.g., Figures 159 to 161 in the Integration chapter of this Record).

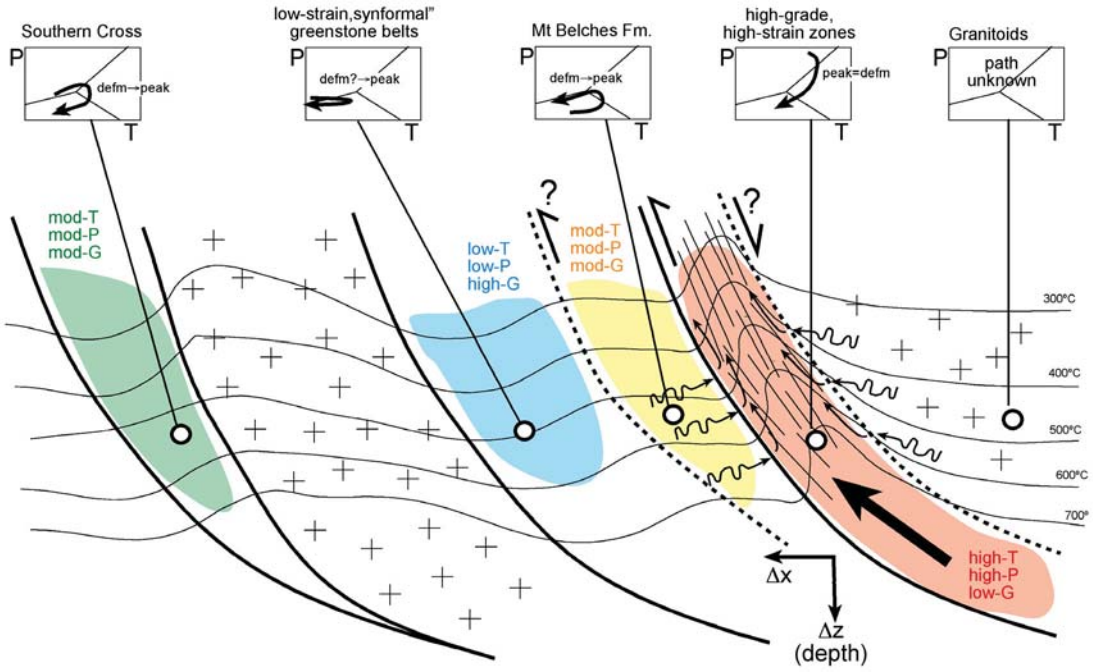

Figure 18: *Diagrammatic cross-section model attempting to explain the juxtaposition of the different EYC metamorphic domains by advection of middle-crustal rocks during compressional orogenesis. This advection model does not predict the documented metamorphic field gradients and P-T paths, and is inconsistent with crustal architectures and structural evolution (Blewett and Czarnota, 2005, 2007c).*

METAMORPHIC GRADIENTS AS A TECTONIC TOOL

Classification of Metamorphic Gradients

Metamorphic gradients are first order variables that are dependent upon the tectonic setting and crustal architecture of orogens. Consequently, metamorphic gradients offer a unique way to encompass a whole orogenic system and have the potential to act as discriminatory tools to determine palaeo-tectonic setting in metamorphic belts. Metamorphic gradients are simply the variation in metamorphic variables (pressure – P, temperature – T and temperature/depth ratio – G) of approximately the same age from a common metamorphic cycle, with respect to a length scale. **Metamorphic gradients** can be divided into two broad types. [1] **Temperature/depth ratio** (G - ºC/km) or average thermal gradient. Not to be confused with the instantaneous thermal gradient (Figure 19). [2] **Metamorphic field gradients** (Figure 20) are the variation in metamorphic parameters (ΔT, ΔP and ΔG) with respect to a horizontal length scale (Figure 21), such as along an orogen (Δy) or across an orogen (Δx).

Temperature/Depth Ratio or Average Thermal Gradient

Temperature/depth ratio is a single variable that can be determined at a site, but nevertheless encapsulates the vertical distribution of temperature through the crust and offers critical constraints to plausible tectonic settings of metamorphism (Figure 19; Spear, 1993). Temperature/depth ratio characterizes thermal regime, which is an outcome of the competition between the advection of heat and the conduction of heat in a metamorphic belt. For example; systems with G<15 ºC/km are dominated by the advection of heat and material over conduction of heat and can only occur in a subduction zone setting. Systems with G between 15 and 30 ºC/km occur where there is a balance between heat conduction and heat advection such as in typical collisional orogenic belts. Systems with G>30 ºC/km are dominated by heat conduction in settings that may be pervaded by magma, involve crustal extension, thermal blanketing and/or mantle under-plating.

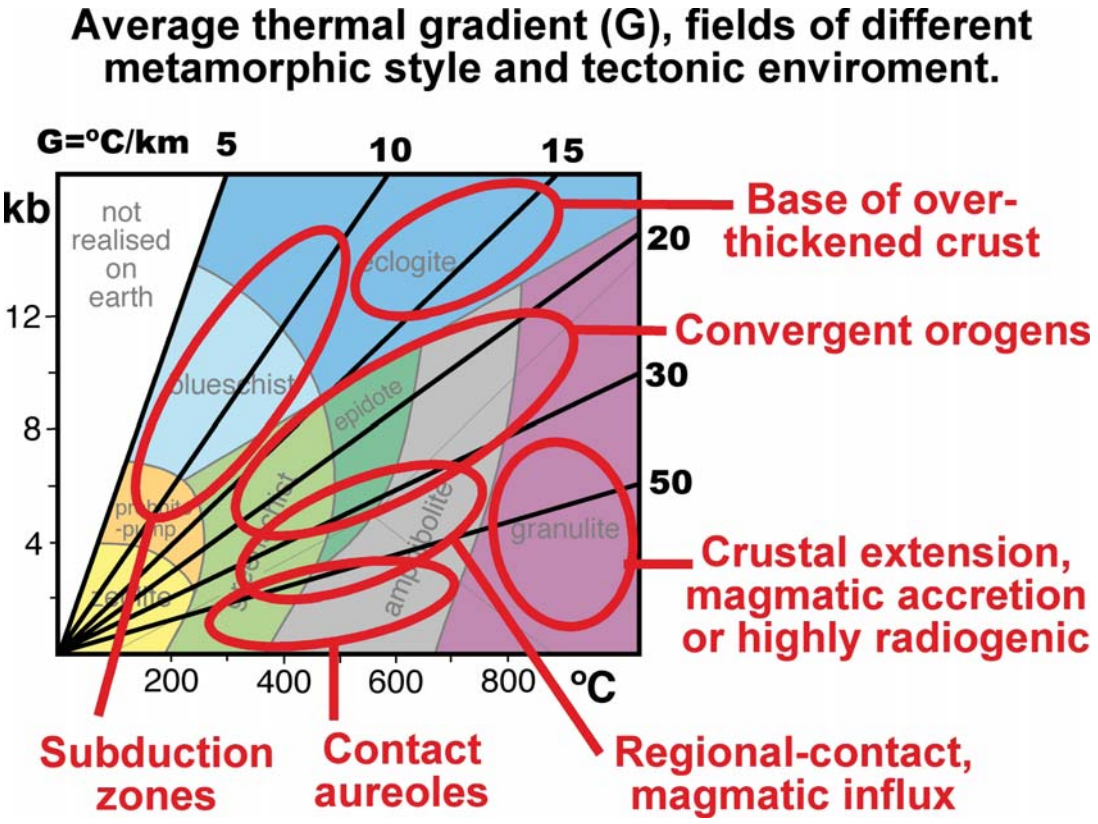

Figure 19: *Field of possible metamorphic conditions with lines of constant temperature/depth ratio (G) overlayed (5, 10, 15, 20, 30, 50 ºC/km). The red ellipses outline approximate regions with distinct metamorphic conditions (T, P and G) and typical tectonic regime associated with this style of metamorphism (Spear, 1993).*

Metamorphic Field Gradients

Metamorphic field gradients (Figure 20), in contrast, document spatial patterns and illustrate the metamorphic variation in a horizontal plane throughout the metamorphic belt. As a consequence, metamorphic field gradients are dependent on first-order orogenic variables such as degree of convergence obliquity, as well as second-order, orogen specific, variables such as magma history, orogen architecture, distribution of radiogenic elements and basin thickness among many others. Metamorphic field gradients across and along orogens therefore offer a way to pool these many and varied second-order variables and uniquely characterise an orogenic system. To illustrate their utility we have determined metamorphic gradients from metamorphic belts across a large range of inferred palaeo-tectonic settings, such as the transpressional Kaoko Belt, convergent Damara Orogen and collisional Himalayas. Crucially, metamorphic gradients offer a simple way to spatially integrate structural and metamorphic quantitative variables

Utilization of Metamorphic Gradients

Many old metamorphic terranes are typically dismembered and isolated domains without boundary conditions and tectonic context preserved. Where metamorphic conditions can be constrained, temperature over depth (G) can be utilised to characterize tectonic regime and thus plausible tectonic settings that would be otherwise unknown. Temperature over depth can also be used to show when crustal blocks were juxtaposed: either during the prograde-peak period (i.e., different G in different blocks) or during the retrograde-uplift evolution (i.e., same G in different blocks) where the different conditions merely reflect different crustal levels with the same thermal regimes.

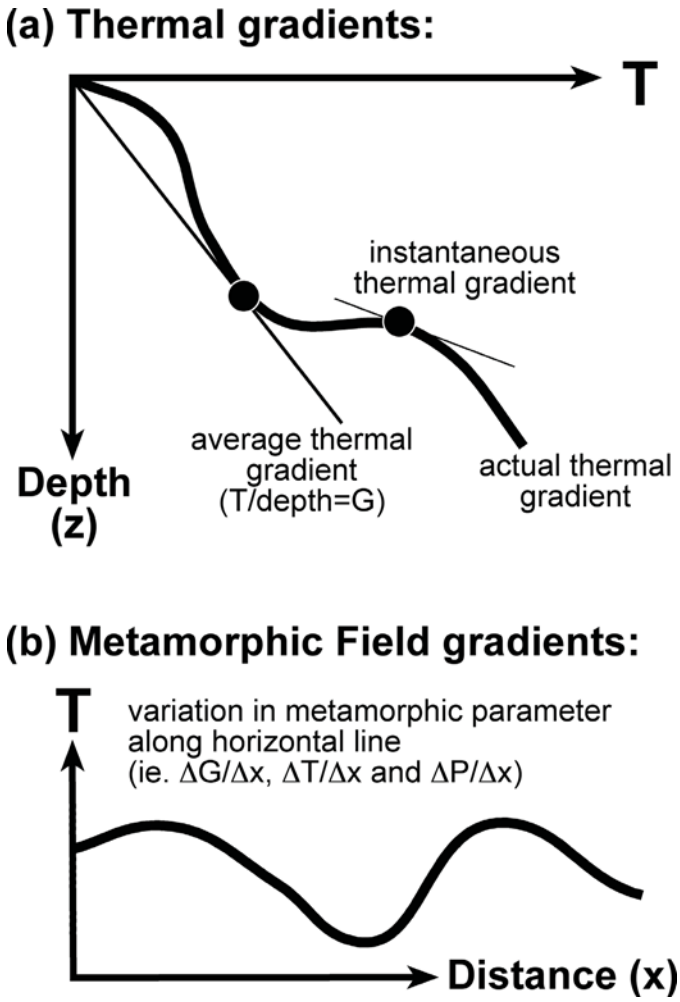

Figure 20: *Definition of different metamorphic gradients. (a) Instantaneous thermal gradient at a point, the actual thermal gradient through the crustal profile at a given instant in time and the temperature/depth ratio (G - ºC/km). (b) Metamorphic field gradients.*

Where there is spatial variation in metamorphic conditions, metamorphic field gradients can be used to extract further tectonic information that is otherwise not available (Goscombe and Gray, 2009). By documenting the metamorphic heterogeneity of an orogenic system, field gradients are indicators of different crustal levels and metamorphic partitioning, which is typically also related to structural patterns. For example, the developed metamorphic patterns will mirror the crustal-scale architecture of the orogen and distribution of radiogenic elements or other heat sources such as mantle lithosphere thickness and magma accretion. Co-temporal composite metamorphic belts, which are composed of contrasting tectono-metamorphic domains formed in the same orogenic cycle, contain much information on fundamental orogenic processes. In such orogens, the developed metamorphic field gradients can be used to indicate degree of convergence obliquity; the relative rate of transport of material through the crustal column and field gradient polarity will indicate the direction of tectonic vergence (Goscombe and Gray, 2009).

Of the many variables governing crustal processes during orogenesis (Dewey et al., 1998; Lin et al., 1998; Goscombe et al., 2004, 2005a), possibly the four most fundamental and significant are; [1] width scale of the orogen, [2] rate of convergence or divergence, [3] gross inclination geometry of the orogen and [4] degree of obliquity of tectonic convergence or divergence ($\beta\sigma$). The simplified tectono-metamorphic variables defining orogenic systems at a gross scale are illustrated in Figure 21.

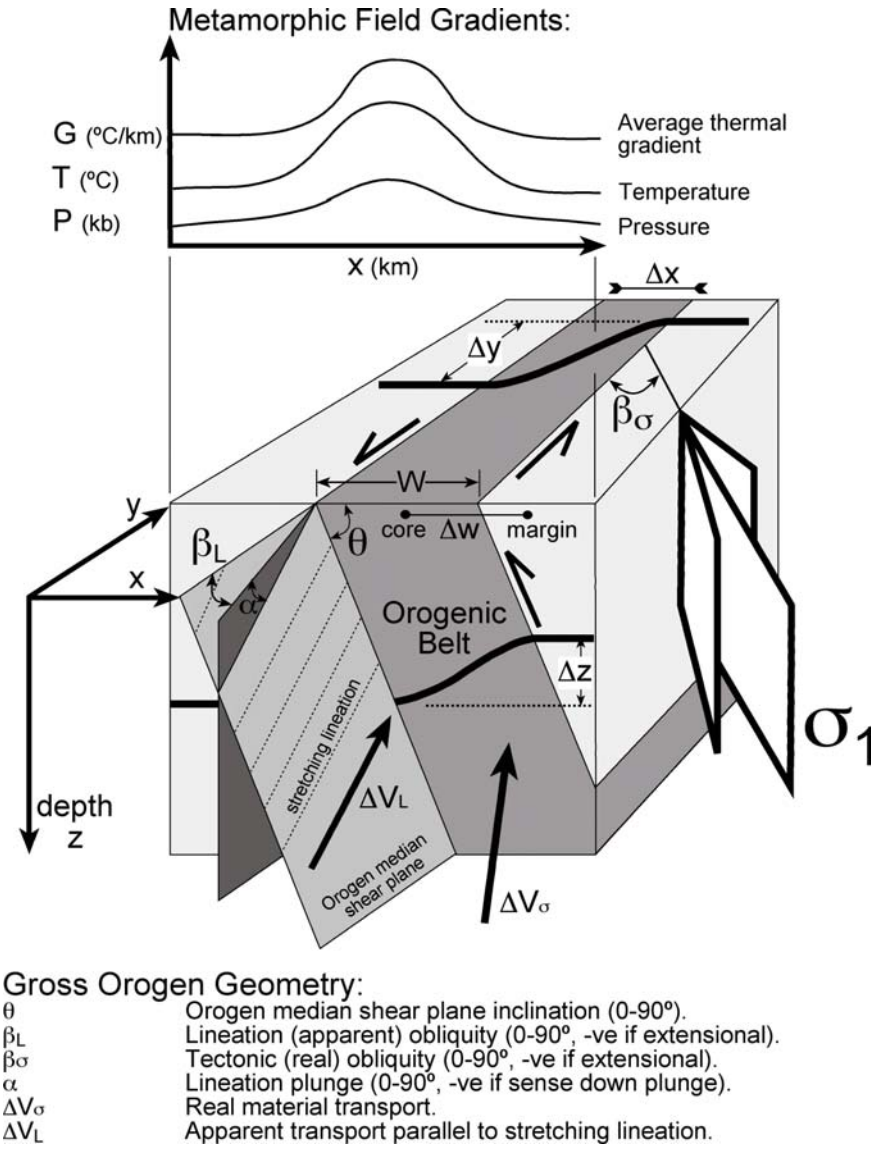

Figure 21: *Definition of variables that describe the gross geometry of orogenic systems, peak metamorphic field gradient response to orogenesis and the components of relative material transport experienced (Goscombe and Gray, 2009).*

Obliquity

Tectonic obliquity (βσ) can only be determined for recent orogens that preserve a seafloor record, and is otherwise notoriously difficult to determine in older orogens eroded to middle-crustal levels. A *prima facie* approximation of obliquity can be determined from an average of the regional pattern of stretching lineation directions, defining a stretching lineation obliquity (βL) for the orogen (Goscombe and Gray, 2009). The recent Himalayan orogen validates this gross approximation, where βσ approximates βL (Shackleton and Ries, 1984). Thompson et al., (1997) used thermal modelling to look at the relationships between convergence obliquity and metamorphic response, and showed that metamorphic field gradients have the potential to indicate obliquity in old orogenic belts. It was found that higher angles of convergence are dominated by advection giving lower temperature/depth ratio in the high-grade core of orogens, resulting in negative ΔG field gradients across the orogen from margin to the core. In contrast, low-angle convergent (transpressional) orogens are dominated by conduction giving higher temperature/depth ratio in the high-grade orogen core, resulting in positive ΔG field gradients across the orogen.

A range of different transpressional orogens show field gradients similar to that predicted by Thompson et al. (1997), of higher pressures and lower temperature/depth ratio within the core of different orogens across a range of increasing stretching lineation obliquity (Figure 22). This trend only holds for low angles of convergence (βL <60º) such as the Kaoko Belt (Figure 23) and Kalinjala Shear Zone (Figure 24). Higher angles of convergence such as in the Himalayan and Damara Orogens, give a distinctly different and tightly constrained pattern of metamorphic response that is separate to the transpressional trend. High temperature equilibration of the orogen core at upper crustal levels gives rise to higher temperature/depth ratio and results in a positive ΔG field gradient between Barrovian external nappes and the high-grade internal core (Figures 22, 25). The Himalayan example involved equilibration at high-T/moderate-P conditions when the orogen core extruded up into upper crustal levels (Figure 26). The Damara Orogen in contrast did not involve extrusion of the high-grade orogen core and was equilibrated at high-T/low-P conditions as a result of magmatic influx and high radiogenic heat production (Figure 27).

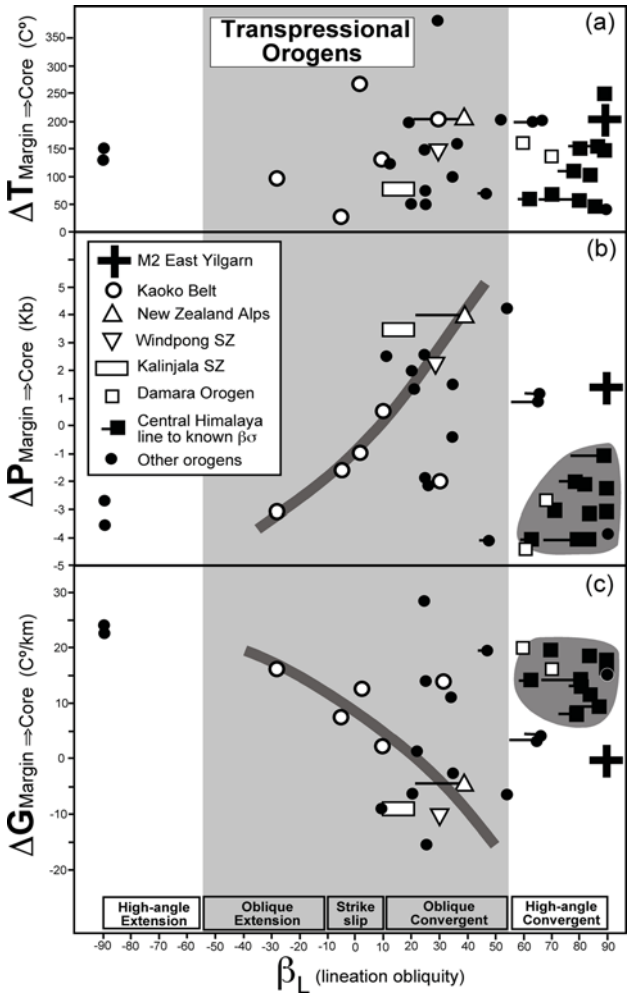

Figure 22: *Field gradients in peak metamorphic parameters (T - temperature, P - pressure and G – temperature/depth) between the lower-grade external margin and high-grade orogen core of co-temporal composite metamorphic belts (Goscombe and Gray, 2009). The metamorphic field gradients are plotted against stretching lineation obliquity (β_L) as a proxy for different orogen types. For Himalayan and New Zealand examples the real tectonic obliquity of transport($\beta\sigma$) is known from recent plate motion, and indicated by lines emanating from data points based on lineation obliquity (βL). Note a large range in the metamorphic field gradients in transpressional systems compared to both convergent and extensional orogens with high-angle lineation obliquity (i.e. β_L > 60º). Regional-contact metamorphism (M2) phase in the Eastern Yilgarn, is indicated by a thick cross.*

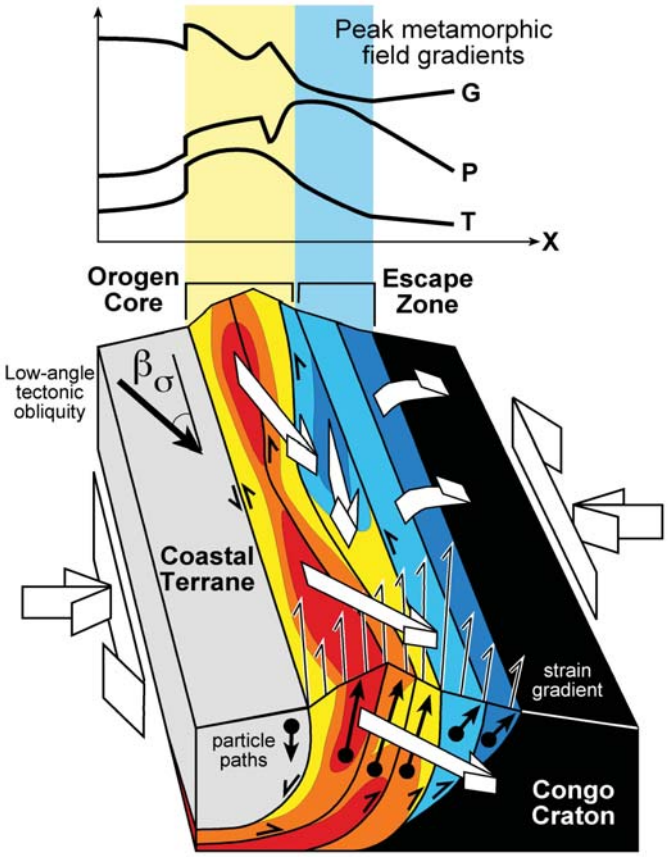

Figure 23: *Model of the Kaoko Belt, an example of a co-temporal composite transpressional orogen centred on a wide high-grade orogen core. Material transport in the orogen core is governed by lower-crust extrusion into middle-crust levels along oblique, up-plunging particle paths (Goscombe et al., 2005a). In this steeply inclined transpressional system, extrusion is along the length of the orogen, in contrast to the Himalayas (Figure 26).*

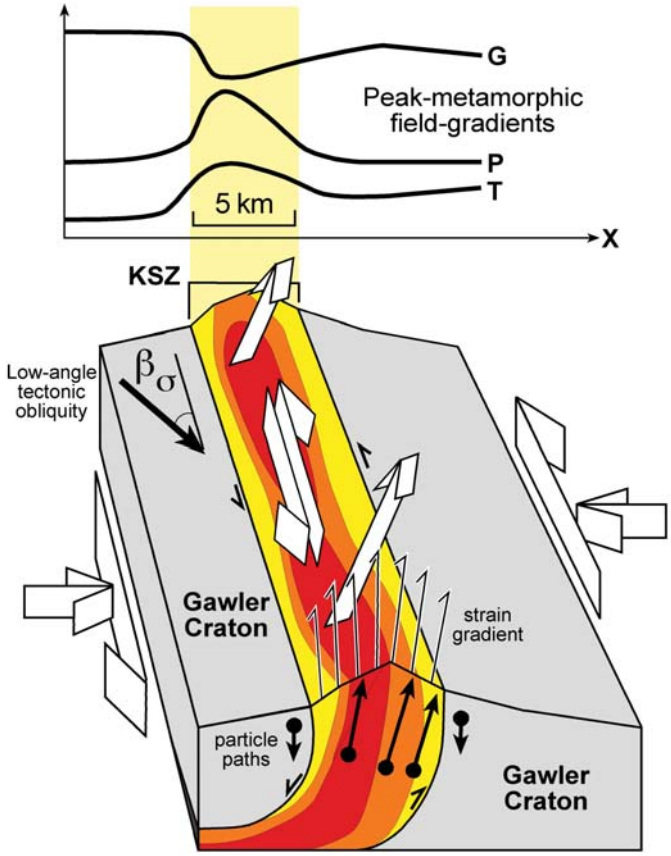

Figure 24: *Diagrammatic model and documented metamorphic field gradients in a small-scale transpressional system. This is based on the Kalinjala Shear Zone (Hand et al., 1995, 1996), which developed a metamorphic response that contrasts strongly with the larger Kaoko Belt (Figure 23). High pressures in the orogen core indicate vertical extrusional paths, which are not reflected by the sub-horizontal stretching lineations.*

Orogen Geometry

The gross geometry, or architecture, of orogens strongly controls both kinematic partitioning and metamorphic response. The effect of variation in orogen architecture on metamorphic response has been documented by field gradients that vary at different sites along the length of individual orogens (Goscombe et al., 2004, 2005a, 2006). Orogens with high-angle obliquity (convergence or extension) and shallow inclination (θ), have high ΔG and low ΔP metamorphic field gradients from orogen margin to core (Figure 22). In contrast, steeply inclined transpressional orogens generally have lower ΔG and higher ΔP metamorphic field gradients from margin to core (Figure 22). Variation in orogen inclination has greatest influence on the ΔP metamorphic field gradient, with ΔP decreasing with increasing inclination in moderate to steep orogens and all shallow (θ<35º) orogens have negative ΔP field gradients. These broad trends are largely independent of the scale of the orogenic system (Goscombe and Gray, 2009).

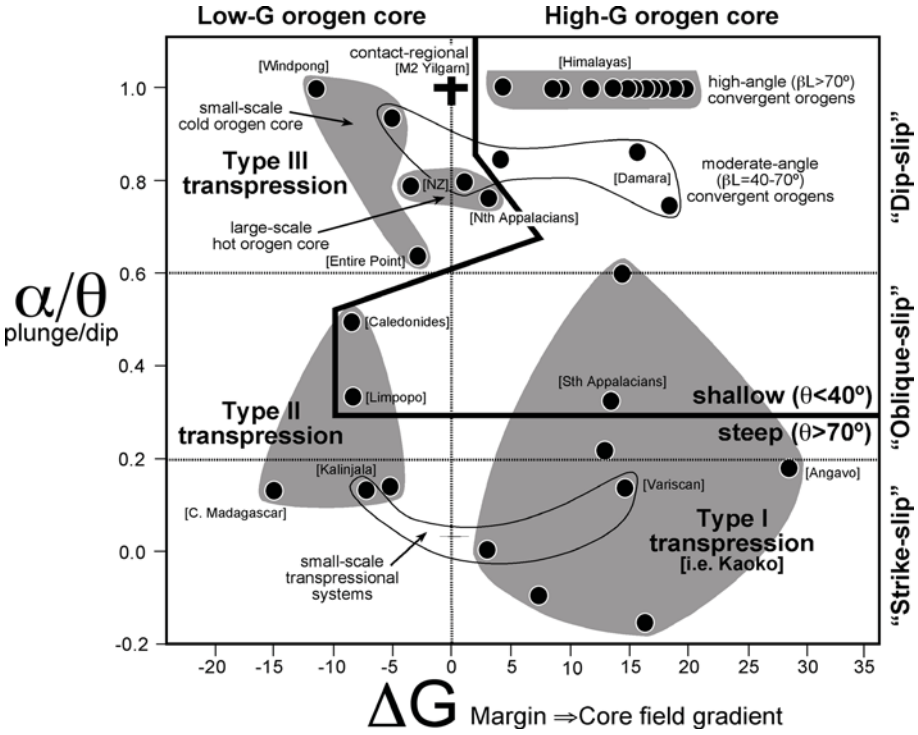

Figure 25: *A broad classification of metamorphic response in orogens of different gross geometry, with distinct groupings shaded (Goscombe and Gray, 2009). Different transpressional orogen types are compared to high-angle convergent orogens such as the Himalayan Orogen (white dots in black field). Regional-contact metamorphism (M2) phase in the Eastern Yilgarn, is indicated by a thick cross. Orogen geometry is summarized by the α/θ ratio between general plunge of stretching lineation within the orogen core (α) and the general inclination of the orogen architecture (θ). Metamorphic response is summarized simply by the field gradient in temperature/depth (ΔG) between the external margin and the high-grade orogen core.*

Variation in temperature/depth ratio across transpressional orogens (ΔG) is influenced by kinematic geometry indicated by a combination of stretching lineation plunge with respect to inclination of the grain of the orogen (α/θ; Figure 25). Steep orogens with strike-slip to oblique-slip kinematic geometries fall into two metamorphic responses: Type-I with positive ΔG and; Type-II with negative ΔG in large-scale and small-scale transpressional systems respectively (Figure 25). Moderately to steeply inclined transpressional systems with down-dip stretching lineations are uncommon (Kirkwood et al., 1995; Tikoff and Greene, 1996; Johnson and Kattan, 2001) and constitute Type-III transpression (Figure 25). Small-scale (Δw<20 km) Type-III transpressional systems such as the Wing Pond Shear Zone in Newfoundland (Jones et al., 2006), the Entire Point Shear Zone in the

Arunta Block (Scrimgeour and Raith, 2001) and Coast Mountains Orogen in British Columbia (Stowell and Crawford, 2000) have negative ΔG field gradients from margin to core. In contrast, large-scale Type-II transpressional systems such as New Zealand Alps and Northern Appalachians have neutral ΔG field gradients from margin to core. Shallowly inclined orogens with down-dip lineation arrays such as the Himalayas have positive ΔG field gradients (Figure 25).

Orogen Scale and Orogenic Rate

Metamorphic response to transpression (i.e., βL<60º) in steeply inclined to listric orogens is also dependent on the width of the orogen (Δw), which may also correlate with the rate of orogenesis (Goscombe and Gray, 2009). Relatively narrow transpressional systems (Δw<20 km) such as the Kalinjala Shear Zone (Hand et al., 1995, 1996) and Wing Pond Shear Zone (Jones et al., 2006) have relatively high pressures and low temperature/depth ratio in the orogen core, resulting in negative ΔG field gradients from margin to core of the orogen (Figures 22, 25). These field gradients imply rapid exhumation of material within these shear zones, possibly due to higher rates of orogenesis in these smaller systems. In contrast, larger orogen-scale transpressional systems such as the Kaoko Belt have relatively high temperature/depth ratio in the orogen cores giving positive ΔG field gradients (Figures 22, 25). A sub-set of large transpressional orogens are recognised such as the New Zealand Alps (Grapes and Watanabe, 1992; Little et al., 2002; Koons et al., 2003) and Acadian Orogeny in the Northern Appalachians (Brown and Solar, 1999), that developed neutral ΔG field gradients (Figure 25). These have similar ΔP field gradients to the small-scale transpressional systems but differ by having hot orogen cores reflecting either the larger scale of the systems or slower rates of orogenesis.

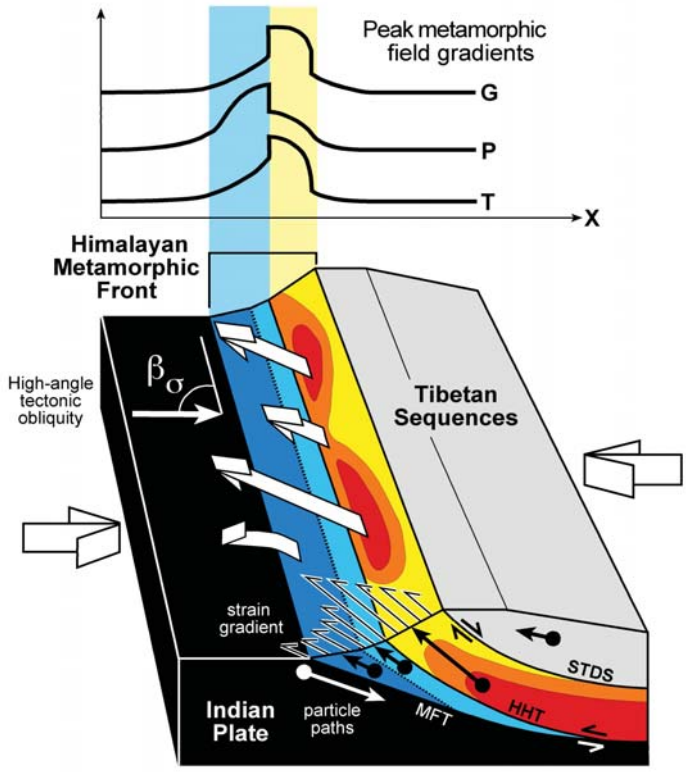

Figure 26: *Diagrammatic model of extrusional tectonics in the high-angle convergent scenario of the central Himalayas (Goscombe et al., 2006). Extrusion of high temperature/depth ratio rocks in the orogen core (reds-oranges) occurs between two crustal-scale shear zones with contrasting shear sense. The orogenic core is juxtaposed against the low temperature/depth ratio Barrovian (blues) external nappes by shallowly inclined extrusion at a high-angle to the orogenic front. STDS – South Tibet Detachment System, HHT – High Himal Thrust, MFT – Main Frontal Thrust.*

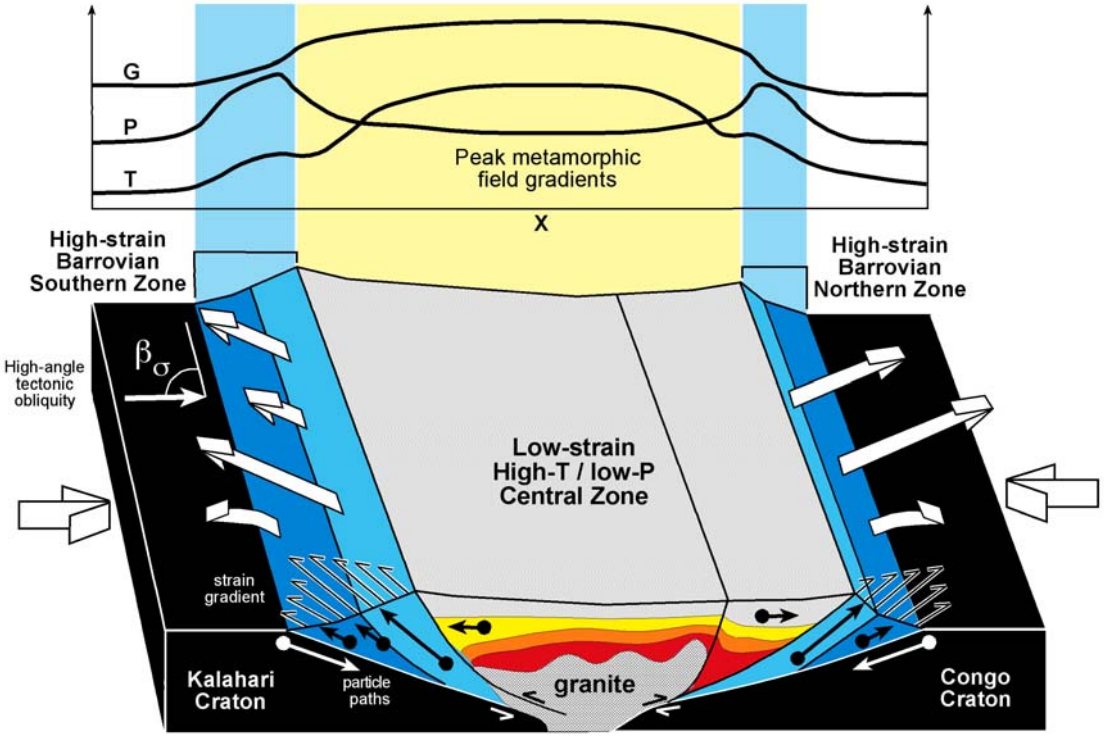

Figure 27: *Model of the Damara Orogen, a symmetric high-angle convergent orogen (Goscombe and Hand, 2001). The central upper-plate region experienced high-T/low-P metamorphism and is pervaded by numerous granites. Both north and south margins of the orogen are highly strained zones of pervasive shear and external nappes that experienced high-P/moderate-T Barrovian metamorphism. Note that peak metamorphic gradients are not necessarily time equivalent across the model orogens (Figures 24 to 26).*

METAMORPHIC MAPS

Metamorphic Mapping Background

Until recently the current paradigm for metamorphism in the Yilgarn Craton assumed that current exposure represents an invariant crustal level of ~14 km and that matrix parageneses formed in a single collisional metamorphic cycle. Metamorphic field gradients documented in this study show peak metamorphic pressure variation of 3.5-8.7 kb, indicating palaeo-crustal depths between 12 and 31 km are exposed and juxtaposed against each other. This over-simplification lead to a perception that thermal regime, or rate of temperature increase with depth, did not vary across the Yilgarn Craton. Similarly, at least five distinct metamorphic periods are recognised with different pressures, temperature range and thermal regime (temperature/depth ratio). Consequently, previous collisional tectonic interpretations and aligned models for Au-mineralization (Groves and Phillips, 1987) were not supported by legacy and new metamorphic datasets. It follows, that a new generation of tectonic and mineralization models will require robust and detailed metamorphic datasets that accurately map the variations in T, P and thermal regime (T/depth). Crucially, new generation metamorphic maps must be able to represent variations in crustal depth and thus also thermal regime, to avoid misinterpretation of the preserved metamorphic patterns (see Plate 1).

There is a large body of published partial metamorphic maps for different parts of the EYC (Binns et al., 1976; Archibald and Bettenay, 1977; Archibald et al., 1978; Hallberg, 1985; Clark et al., 1986; Ahmat 1986; Swager et al., 1990; Witt, 1991; Ridley, 1992; Swager et al., 1992; Williams and Whitaker, 1993; Witt, 1993; Ridley, 1993; McNaughton et al., 1993; Williams and Whitaker, 1993; Williams and Currie, 1993; Swager, 1994a; Swager, 1994b; Swager, 1994c; Witt, 1994a,b; Smithies, 1994; Swager, 1995; Swager and Nelson, 1997; Bloem et al., 1997; Witt, 1997; Wilkins, 1997; Swager, 1997; Witt and Davy, 1997; Witt et al., 1997b; Langford and Farrell, 1998; Libby and

DeLaeter, 1998; Dalstra, 1999; Groenewald et al., 2000; Painter and Groenewald, 2001; Stewart, 2001; Wyche et al., 2001; Mikucki and Roberts, 2003; Stewart, 2004; Jones, 2006; Stewart, 2007). The most recent and best-constrained metamorphic map is that of Mikucki and Roberts (2003). This map (Figure 28) is constrained by detailed petrological descriptions from ~1300 thin sections and define a metamorphic pattern in the Kalgoorlie region that is similar to other parts of the EYC such as the Leonora-Laverton region (Hallberg, 1985). In particular, this map pattern illustrates metamorphic isograds that both mimic the granite greenstone boundary indicating the genetic correlation between pervasive granite influx and regional metamorphism. Secondly, the isograds cut across major crustal structures and shear zones, indicating a late-stage thermal peak of metamorphism, the early pre-existence of the crustal scale structures and that late-stage reactivation of these structures did not give appreciable displacements. This metamorphic pattern is inconsistent with the documented deformation in these shear zones subsequent to the peak of metamorphism. Furthermore, this "shear zone independent" metamorphic pattern has not been replicated by the EYCMP database and final metamorphic map as discussed later.

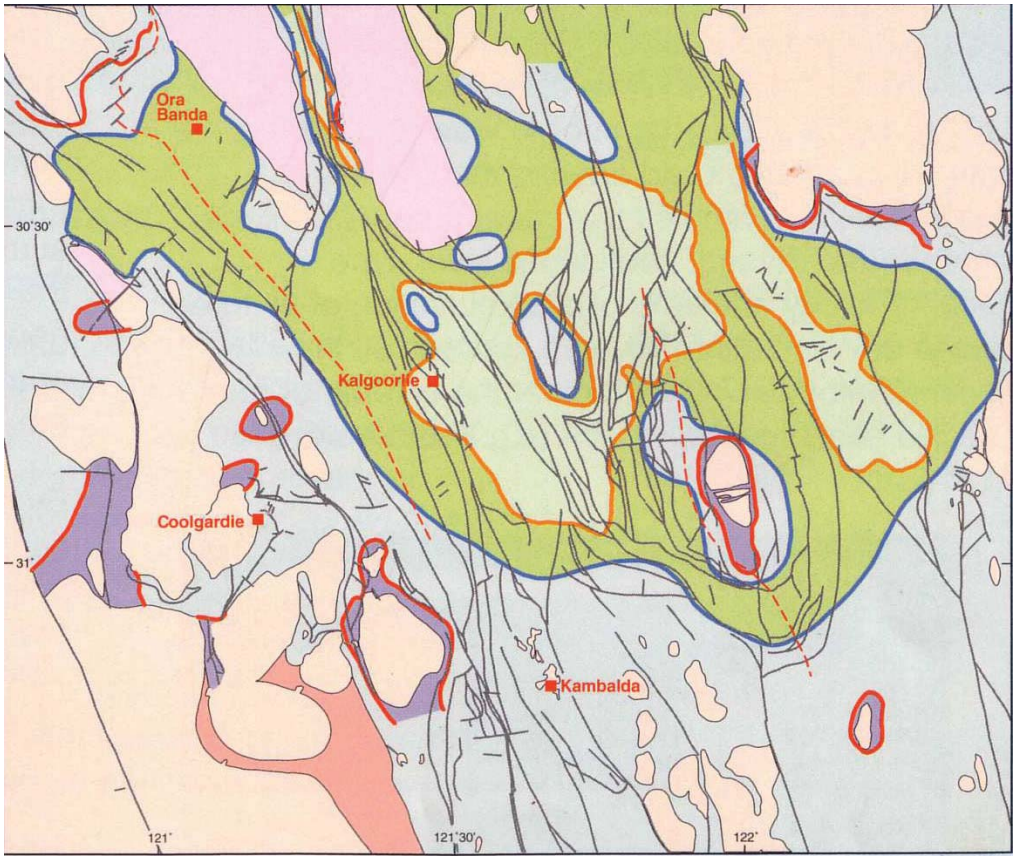

Figure 28: *Metamorphic facies map for the central EYC region centred on Kalgoorlie and based on detailed description of ~1200 thin sections (Mikucki and Roberts, 2003).*

The traditional metamorphic map suffers from being based on metamorphic facies (Figure 29), which document temperature variation and typically contain little pressure information (Figure 30). Without pressure information encoded, traditional metamorphic map patterns can lead to deceptive interpretations. For example, in the EYC the progressive increase in metamorphic facies grade (i.e., T) towards granite/gneiss domes gives a superficial impression of simple contact metamorphism. However, the highest-grade rocks at the dome margins also experienced disproportionally higher pressures and were counter-intuitively formed in much cooler thermal regimes (i.e., T/depth). Consequently, the high-grade margins are incompatible with both contact metamorphism and could not have formed at the same time as the lower grade, but higher thermal regime rocks, distant from the domes.

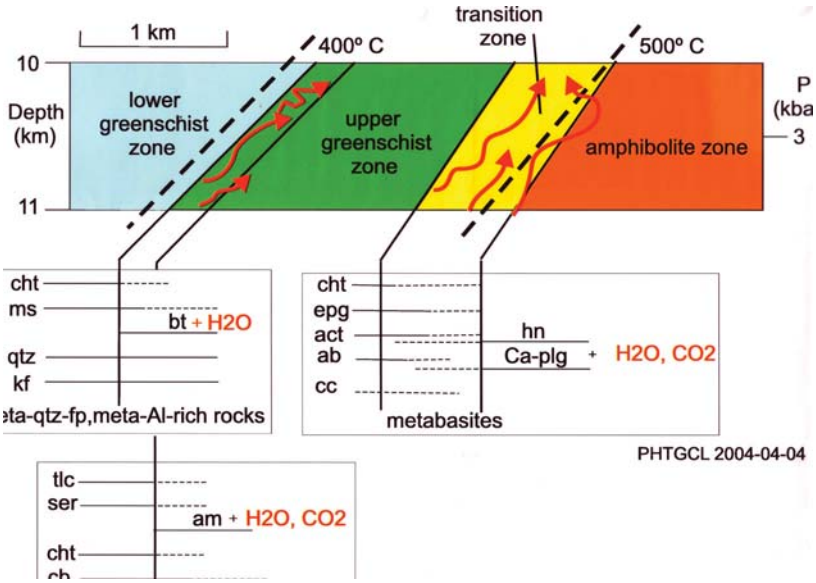

Figure 29: *Definition of metamorphic facies for different bulk compositions (Thompson, 2005).*

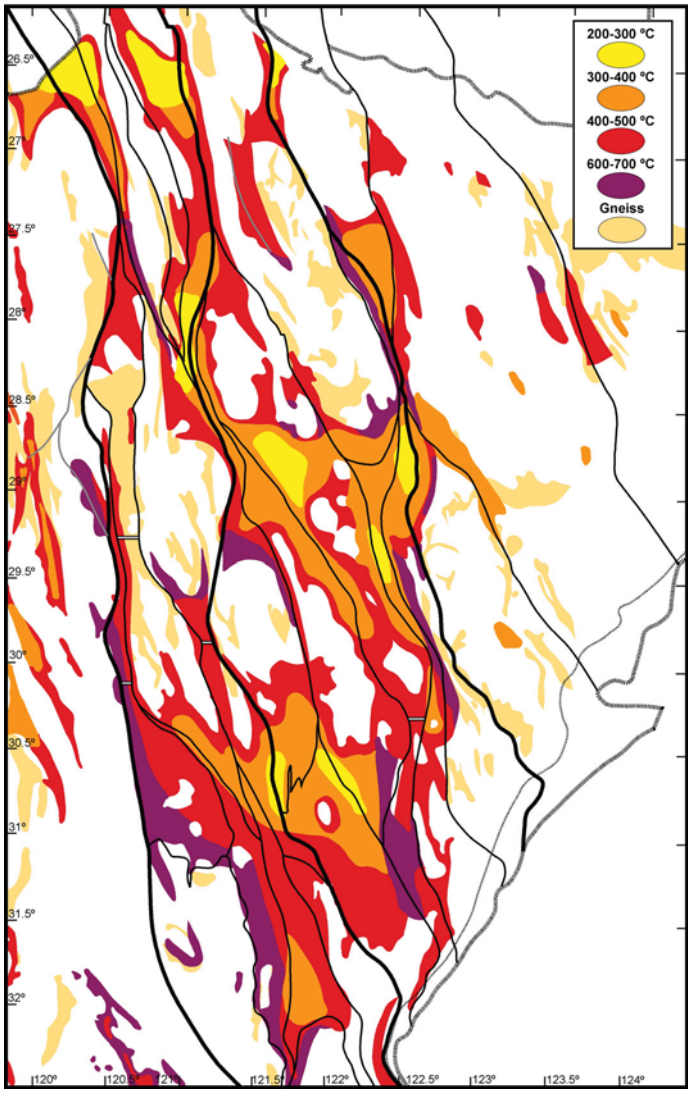

Figure 30: *Simplified map of metamorphic temperatures based on assignment of metamorphic facies to assemblages. Map pattern is a composite of all metamorphic parageneses. At least four peak metamorphic events are recognised which in some cases cannot always be separated. Compiled from numerous papers in the literature (e.g. Binns et al., 1976; Swager, 1997 etc).*

Diagnostic Mineral Fields

A scheme has been developed for a new generation of metamorphic maps that visually represent pressure and thermal regime (T/depth) data as well as temperature (see below). This scheme is based on a legend for metamorphic polygons that are based on dividing P-T space into diagnostic mineral fields (DMF). Unlike metamorphic facies, which largely only represent variation in temperature, diagnostic mineral fields have been defined for finite ranges in pressure as well as temperature, for a range of common bulk compositions (Figures 31 to 34). The diagnostic mineral fields are defined by unique phase stability fields within composite P-T pseudosections that have been constructed from a range of calculated P-T pseudosections available in the literature. Composite P-T pseudosections have been constructed in MnNCKFMASH for average metapelite (Figure 31) and in NCFMASH for average tholeiite (Figure 33) bulk compositions. The details of the individual pseudosections used, including the chemical system, excess phases and fluid and melt relations are presented in the captions (Figures 31, 33). The composite pseudosections form the basis of petrogenetic grids with diagnostic mineral fields covering the P-T space of interest (0-800 ºC, 0-12 kb) for pelite and tholeiite bulk compositions (Figures 32, 34). Diagnostic mineral fields are best-fit P-T fields with key mineral assemblages and are not true pseudosection fields. The diagnostic mineral field grids form the legend for metamorphic maps and are not intended to replace specific P-T pseudosections for the interpretation of individual rock samples (i.e., Appendix 5). Bands of diagnostic mineral fields sharing similar thermal regimes (G=T/depth), otherwise called pressure-series, are represented on metamorphic maps by a colour theme that ranges in intensity with increasing temperature. Simplified diagnostic mineral field grids are available as a field card to aid assessment of metamorphic conditions in the field (FieldCard_DMF(07).pdf). Simple summaries of experimental and calculated mineral reactions have been constructed for aluminous altered ultramafic (Figure 35) and calcsilicate bulk compositions (Figure 36), to aid in the interpretation of these rocks.

Figure 31: *Figure on next page. Composite quantitative PT petrogenetic grid with diagnostic mineral fields (DMF) for average metapelite bulk composition. Additional diagnostic minerals from slightly different bulk compositions are included in square brackets. The different colour series indicate different temperature/depth ratio or thermal regimes. Grid based on published PT pseudosections as listed below.*

<450ºC, <12kb:	*KCFASHC, excess qtz (Cartwright and Buick, 1995).*
<550ºC, <12kb:	*KFMASH, excess qtz, average pelite (Spear and Cheney, 1989).*
<550ºC, <12kb:	*MnNCKFMASH, excess qtz+pl, average pelite (Tinkham et al., 2001).*
550-760ºC, <12kb:	*MnNCKFMASH, excess qtz+pl, average pelite (Johnson et al., 2003).*
760-900ºC, <12kb:	*NCKFMASH, excess qtz and pl, average pelite (White et al., 2001).*
Fluid / Melt:	*Water is in excess throughout except at high-T above melting reactions.*
Quartz:	*Quartz is in excess throughout and not represented for clarity.*
Plagioclase:	*Na-Ca feldspar may be present throughout.*
Al2SiO5:	*(Powell and Holland, 1990).*

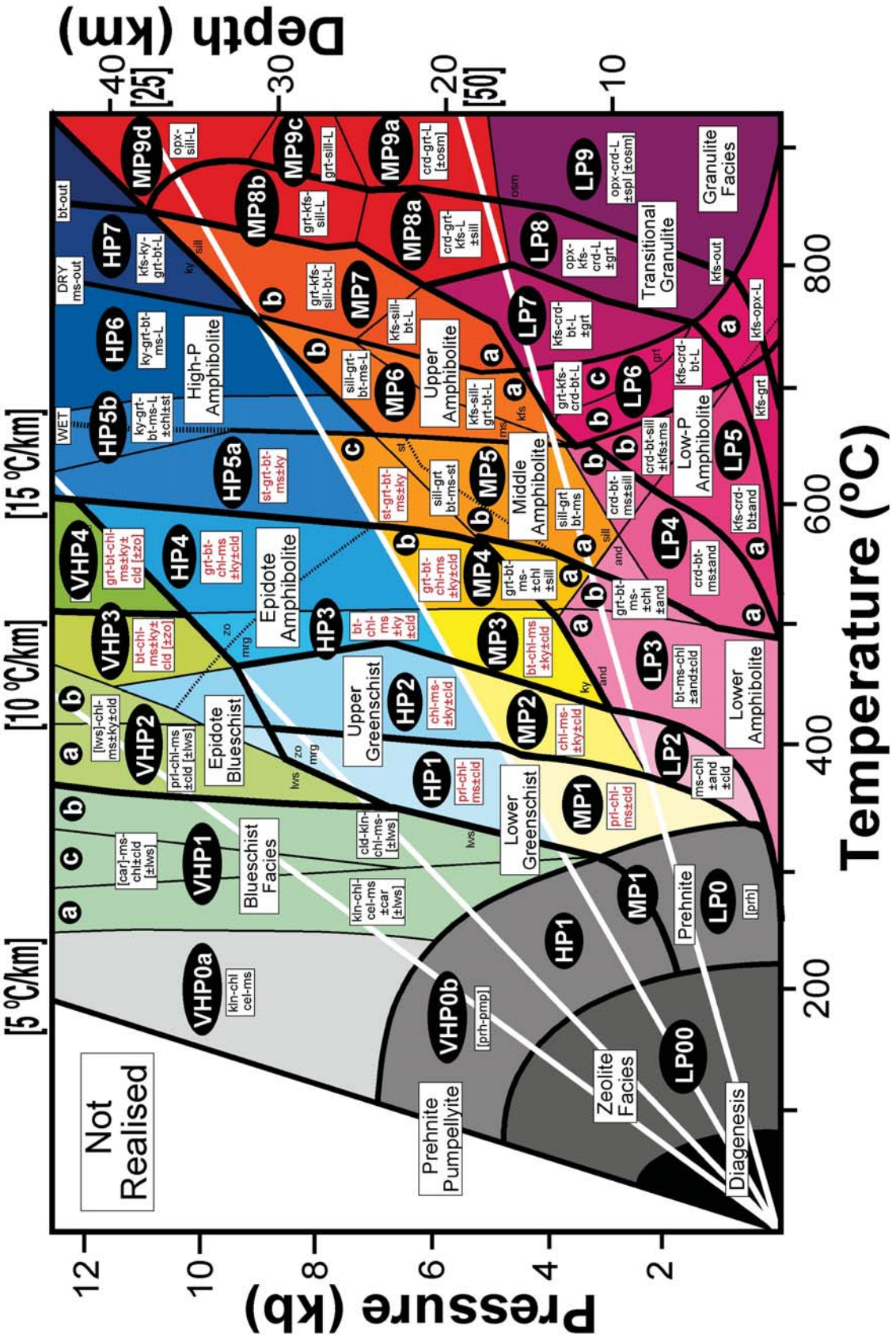
Pressure (kb)
Temperature (°C)
Depth (km)
[5 °C/km]
[10 °C/km]
[15 °C/km]
[25]
[50]
Not Realised
Zeolite Facies
Prehnite Pumpellyite
Diagenesis
Blueschist Facies
Epidote Blueschist
Greenschist Facies
Lower Greenschist
Upper Greenschist
Epidote Amphibolite
Amphibolite Facies
Lower Amphibolite
Middle Amphibolite
Upper Amphibolite
High-P Amphibolite
Granulite Facies
Transitional Granulite
Low-P Amphibolite
Prehnite
WET
DRY
VHP0a
VHP0b
VHP1
VHP2
VHP3
VHP4
HP1
HP2
HP3
HP4
HP5a
HP5b
HP6
HP7
MP1
MP2
MP3
MP4
MP5
MP6
MP7
MP8a
MP8b
MP9a
MP9c
MP9d
LP00
LP0
LP2
LP3
LP4
LP5
LP6
LP7
LP8
LP9

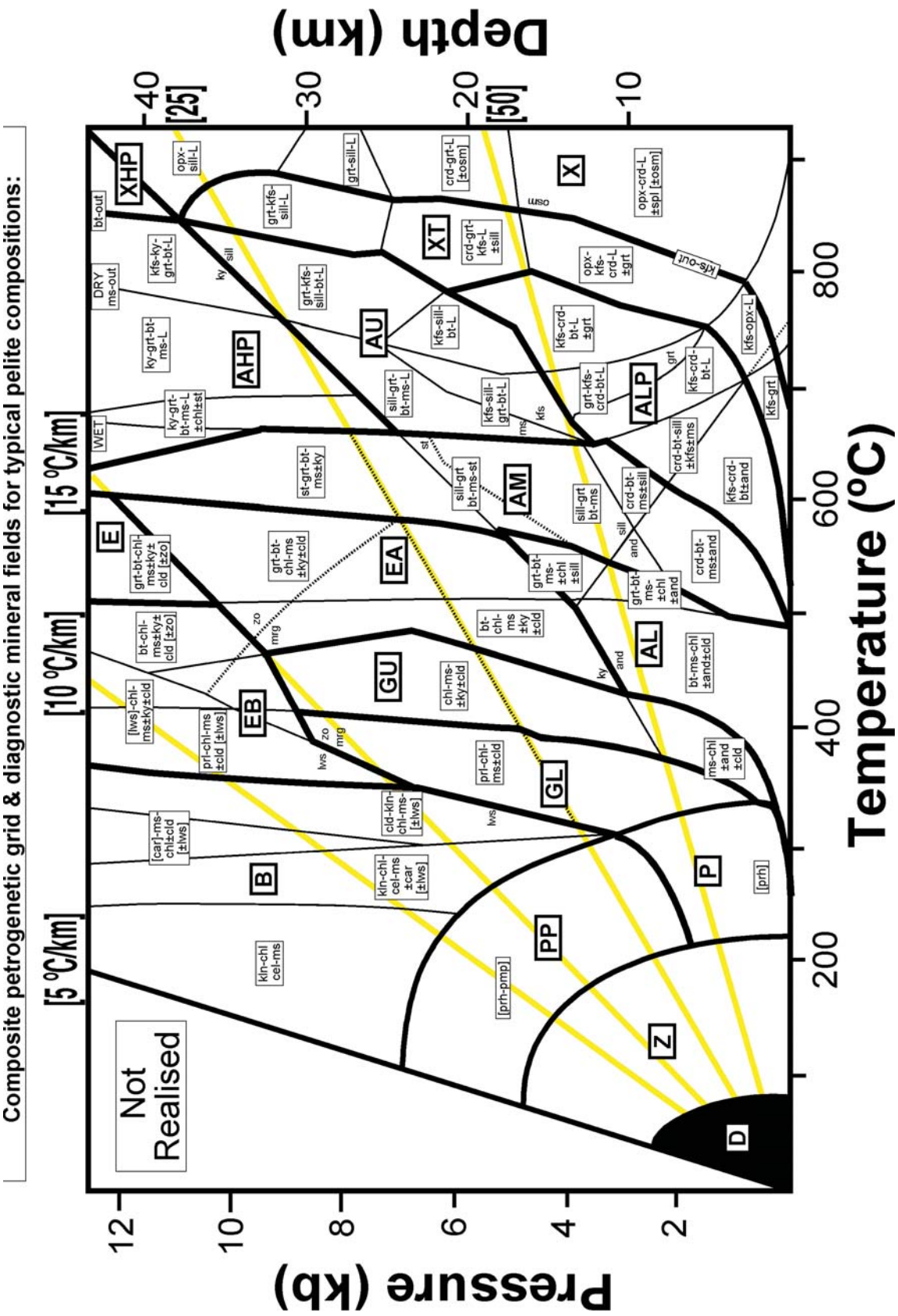

Figure 32: *Simple metapelite petrogenetic grid based on Figure 31.*

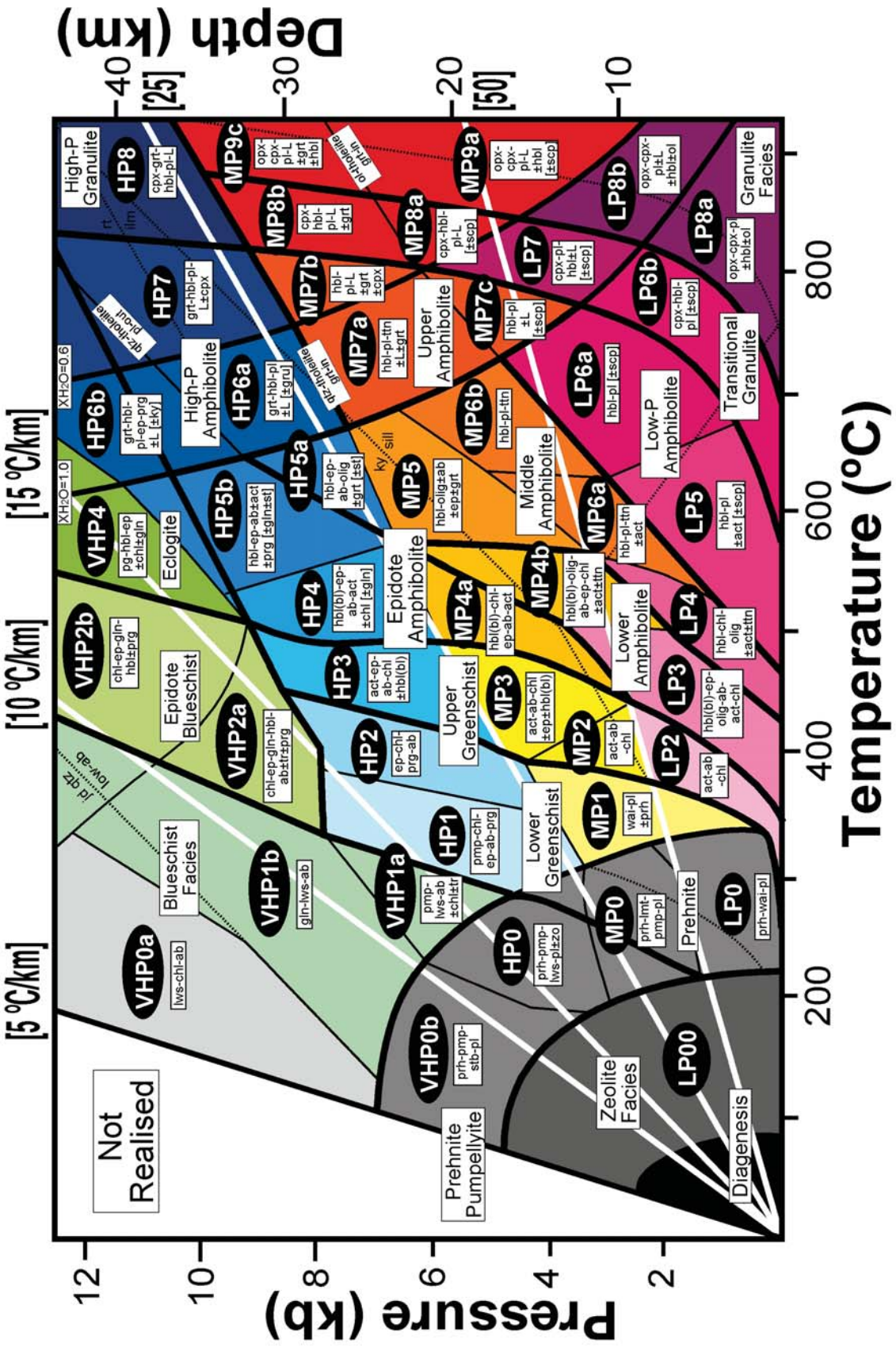
Depth (km)
[25]
[50]
Temperature (°C)
Pressure (kb)
[5 °C/km]
[10 °C/km]
[15 °C/km]
XH2O=1.0
XH2O=0.6
Not Realised
Prehnite Pumpellyite
Zeolite Facies
Diagenesis
Blueschist Facies
Epidote Blueschist
Eclogite
Lower Greenschist
Upper Greenschist
Epidote Amphibolite
High-P Amphibolite
Middle Amphibolite
Upper Amphibolite
Lower Amphibolite
Low-P Amphibolite
High-P Granulite
Transitional Granulite
Granulite Facies
VHP0a
VHP0b
VHP1a
VHP1b
VHP2a
VHP2b
VHP4
HP0
HP1
HP2
HP3
HP4
HP5a
HP5b
HP6a
HP6b
HP7
HP8
MP0
MP1
MP2
MP3
MP4a
MP4b
MP5
MP6a
MP6b
MP7a
MP7b
MP7c
MP8a
MP8b
MP9a
MP9c
LP00
LP0
LP2
LP3
LP4
LP5
LP6a
LP6b
LP7
LP8a
LP8b
lws-chl-ab
prh-pmp-stb-pl
pmp-lws-ab ±chl±tr
gln-lws-ab
prh-pmp-lws-pl±zo
pmp-chl-ep-ab-prg
wai-pl ±prh
prh-lmt-pmp-pl
prh-wai-pl
chl-ep-gln-hbl-ab±tr±prg
chl-ep-gln-hbl±prg
pg-hbl-ep ±chl±gln
ep-chl-prg-ab
act-ep-ab-chl ±hbl(bl)
hbl(bl)-ep-ab-act ±chl [±gln]
hbl-ep-ab±act ±prg [±gln±si]
act-ab-chl ±ep±hbl(bl)
hbl(bl)-chl-ep-ab-act
act-ab -chl
hbl-ep-ab-olig ±grt [±si]
hbl-olig±ab ±ep±grt
hbl-pl-ttn
hbl(bl)-olig-ab-ep-chl ±act±ttn
hbl-pl-ttn ±act
hbl-pl ±act [±scp]
hbl-chl-olig ±act±ttn
hbl(bl)-ep-olig-ab-act-chl
act-ab -chl
grt-hbl-pl-L ±cpx
grt-hbl-pl ±L [±gru]
hbl-pl-ttn ±L±grt
hbl-pl-L ±grt ±cpx
hbl-pl ±L [±scp]
cpx-hbl-pl-L [±scp]
cpx-hbl-pl-L ±grt
cpx-grt-hbl-pl-L
grt-hbl-pl-prg ±L [±ky]
hbl-ep-ab±act ±prg [±gln±si]
cpx-hbl-pl [±scp]
cpx-pl-hbl±L [±scp]
hbl-pl [±scp]
opx-cpx-pl±L ±hbl±ol
opx-cpx-pl±L ±hbl [±scp]
opx-cpx-pl ±hbl±ol
cpx-grt-hbl-pl-L
qtz-hbl-plag
qtz-hbl-grt-rn
grt-hbl-pl-L±cpx
ol-hbl-grt-rn
opx-cpx-pl±L ±grt ±hbl
ky
sill
rt
ilm
jd qtz low-ab

Figure 33: *Figure on previous page. Composite quantitative PT petrogenetic grid with diagnostic mineral fields for average tholeiite bulk composition. Grid based on published PT pseudosections as listed below.*

<400ºC, <4kb:	*CASH, CNASH, excess H_2O (Thompson, 1971; Liou, 1971a,b,c; Perkins et al., 1980; Spear, 1993).*
<400ºC, <10kb:	*CNMASH, excess H_2O (El-Shazly, 1994).*
400-650ºC, <7kb:	*CNASH, CFMASH, excess qtz and H_2O (Liou, 1973; Liou et al., 1974; Apted and Liou, 1983; Spear, 1993; Zeh et al., 2005).*
400-550ºC, >8kb:	*NCFMASHO, excess qtz+H_2O, mafic eclogites (Ballevre et al., 2003).*
480-640ºC, 8-21kb:	*NCFMASH, excess qtz and H_2O, mafic eclogite, meta-basite (Carson et al., 1999; Marmo et al., 2002; Wei and Powell, 2003).*
>700ºC, <16kb:	*CFMASH, excess qtz, high fO_2 (Spear, 1981b; Patterson, 2003).*
>600ºC, >8kb:	*CFMASH, qtz may be absent (Yang and Indares, 2005; Zeh et al., 2005).*
>700ºC, 6-18kb:	*CFMASH, qtz may be absent, tholeiites (Ringwood, 1975; Spear, 1993; Patterson, 2003; Green and Ringwood, 1972; Jamieson, 1981; Olafsson and Eggler, 1983; Nicollet and Goncalves, 2005).*
Fluid / Melt:	*Water is in excess throughout except at high-T above melting reactions.*
$XH_2O>>XCO_2$.	*H_2O not represented for clarity.*
Quartz:	*Quartz is in excess throughout and not represented for clarity.*
Plagioclase:	*Na-Ca feldspar is present throughout,*
Scapolite:	*Scapolite may be present in CMASHC systems with $XCO_2>0.1$. At T>550ºC and pressures below ttn-in and grt-in reactions.*

Figure 34: *Figure on next page. Simple mafic petrogenetic grid based on (Figure 33) with the following additional reactions in red.*

Reaction 1:	*Calculated equilibria in NCFASH for metabasite and $aH_2O=0.3$ (Pattison, 2003). Minimum-T limit of almandine (i.e.limit of all garnet).*
Reaction 2:	*Calculated equilibria in NCFMASH for metabasite and $aH_2O=0.3$ (Pattison, 2003). Maximum-T/minimum-P limit of general garnet.*
Reaction 3:	*Minimum-T limit of wet melting in metabasite (Wyllie and Wolf, 1993).*
Reaction 4:	*Minimum-T limit of clinopyroxene, for HM-buffer (Spear, 1981b).*
Reaction 5:	*Experimental minimum-T limit of orthopyroxene, for WM- and QFM-buffers (Spear, 1981b; Nair and Chacko, 2000).*
Reaction 6:	*Experimental minimum-P limit of titanite, for WM-buffer (Spear, 1981b). Highest-P lower limit of titanite (i.e QFM and HM at lower P).*
Reaction 7:	*Experimental minimum-P limit of garnet, for quartz-tholeiite B with XMg=60% (Green and Ringwood, 1967a).*
Reaction 8:	*Experimental minimum-P limit of garnet, for olivine-tholeiite (Ito and Kennedy, 1971; Cohen et al., 1967).*

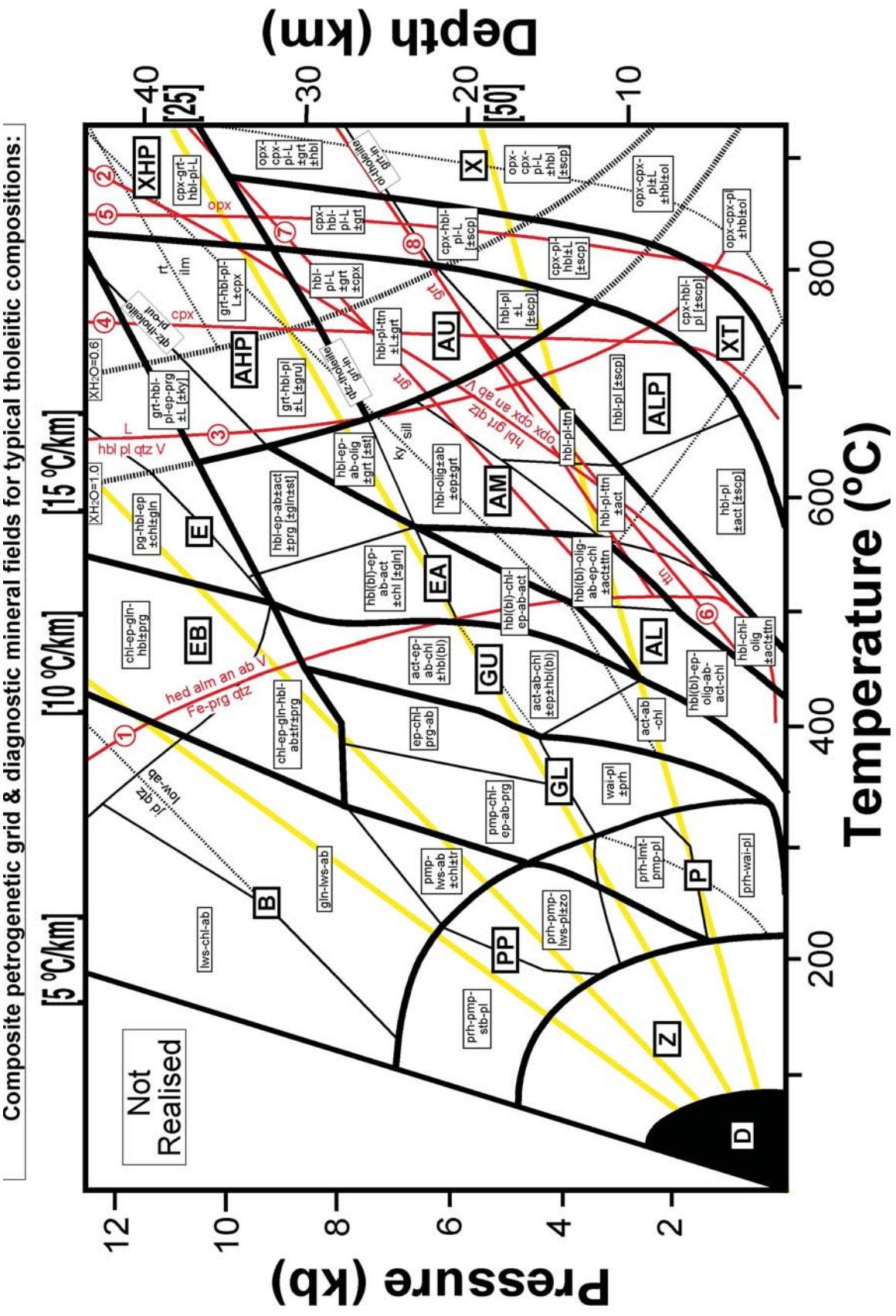
Composite petrogenetic grid & diagnostic mineral fields for typical tholeiitic compositions:
[5 °C/km]
[10 °C/km]
[15 °C/km]
Pressure (kb)
Temperature (°C)
Depth (km)
Not Realised
XHP
AHP
E
EB
B
EA
GU
GL
PP
Z
D
AU
AM
AL
ALP
X
XT
P
XH2O=0.6
XH2O=1.0
hbl pl qtz V
hed alm an ab V
Fe-prg qtz
opx
cpx
grt
ky
sill
rt
ilm
tln
hbl grt qtz
opx cpx an ab V

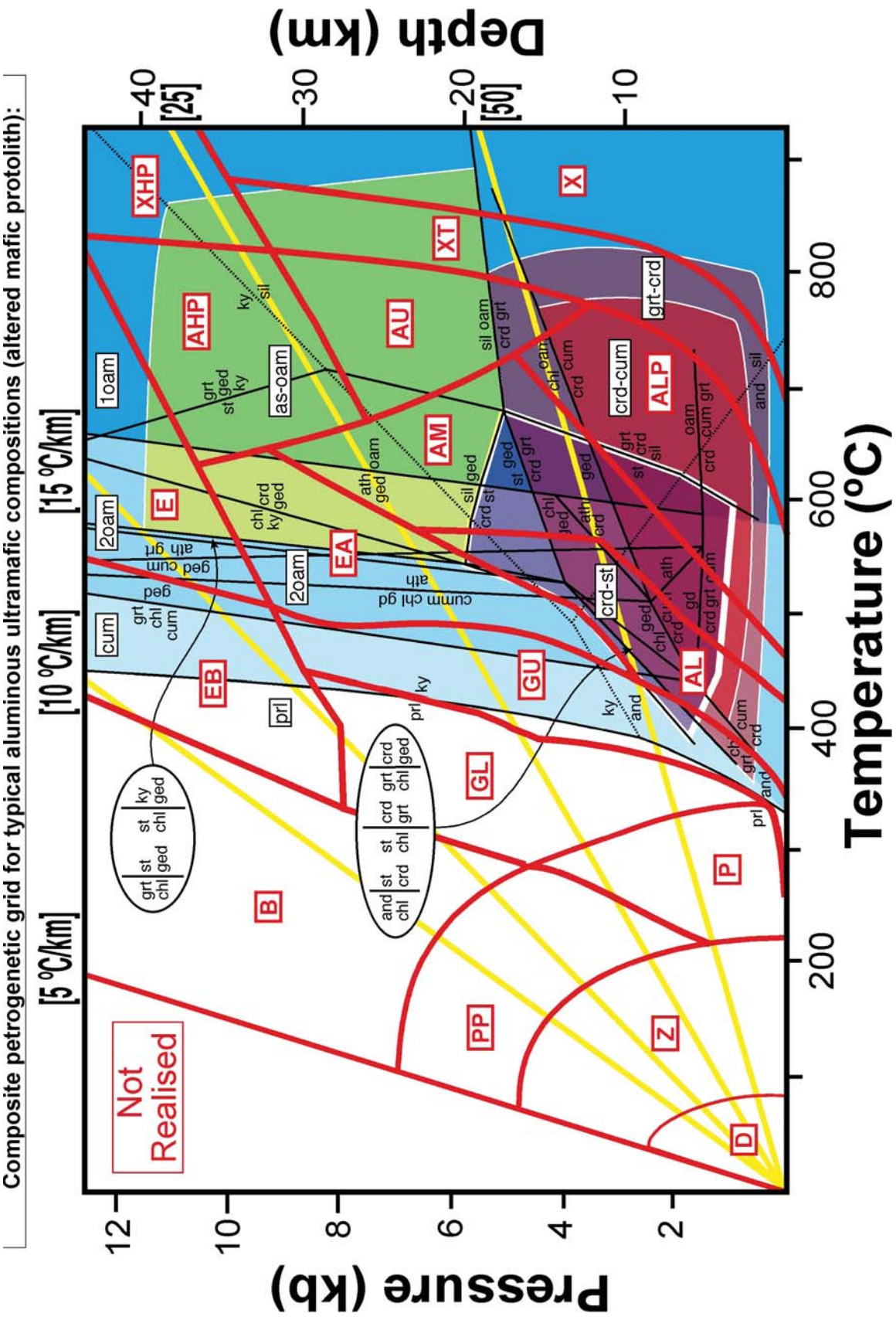
Composite petrogenetic grid for typical aluminous ultramafic compositions (altered mafic protolith):
Pressure (kb)
Depth (km)
Temperature (°C)
[5 °C/km]
[10 °C/km]
[15 °C/km]
[25]
[50]
Not Realised
XHP
AHP
E
EB
B
EA
2oam
1oam
cum
prl
AU
AM
XT
X
GU
GL
PP
P
Z
D
AL
ALP
crd-cum
grt-crd
crd-st
as-oam

Figure 35: *Figure on previous page. Semi-quantitative PT petrogenetic grid for typical aluminous-ultramafic or altered mafic protolith compositions based on published experimental studies and calculated reactions. Because of the large range of possible bulk compositions, general quantitative pseudosections cannot be developed and generalized grids and reactions are used.*

Red grid: *Metamorphic facies based on mafic parageneses (Figure 33).*

Black grid: *SiO_2-Al_2O_3-MgO-FeO-CaO-Na_2O-H_2O theoretical grid for cordierite-anthophyllite rocks (Spear, 1993), modified from Spear and Rumble (1986). Excess quartz, andesine and H_2O.*

Polygons: *Over-lapping key mineral parageneses.*

Figure 36: *Figure on next page. Semi-quantitative PT petrogenetic grid for calcsilicate rocks based on published experimental studies and calculated reactions. Because of the large range of possible bulk compositions, general quantitative pseudosections cannot be developed and generalized grids and reactions are used.*

Red grid: *Metamorphic facies based on mafic parageneses (Figure 33).*

Black lines: *Calculated reactions in SiO_2-MgO-CaO-H_2O (Spear, 1993).*

Reaction 1: *Maximum zoisite stability field at XCO_2=0.05 (Brunsmann et al., 2000).*

Reaction 2: *cal+qtz=wo+CO_2, XCO_2=0.5 and 1.0 (Ghent et al., 1979).*

Reaction 3: *cal+qtz=wo+CO_2, XCO_2=0.2 (Ghent et al., 1979).*

Reaction 4: *an+cal=scp (me80), (Harley and Buick, 1992).*

Reaction 5: *qtz+grs=wo+an (Harley and Buick, 1992).*

Reaction 6: *grs+cal+qtz=me+wo (Fitzsimons and Harley, 1994).*

Reaction 7: *czo+qtz=an+grs+H_2O (Spear, 1993).*

Reaction 8: *rt+cal+qtz=ttn+CO_2 (Spear, 1993).*

Reaction 9: *ep=grt+an+qtz+H_2O (Ernst, 1966).*

Reaction 10: *czo+qtz=grs+an+H_2O (Ghent, 1988).*

Reaction 11: *rt+cal+qtz=ttn+CO_2 (Reviews in Mineralogy, V9B).*

Reaction 12: *qtz+ky+zo=an30/100+H_2O (Spear, 1993).*

Reaction 13: *czo+qtz=grs+ant, NCFASH (Begin, 1992).*

Reaction 14: *prh=zo+grs+qtz (Liou et al., 1983; Schiffman and Liou, 1983).*

Reaction 15: *prh=czo+grs+qtz (Liou et al., 1983; Schiffman and Liou, 1983).*

Reaction 16: *Mg-pumpellyite (Bevins andMerriman, 1988; Nitsch, 1971; Liou etal, 1985).*

Reaction 17: *prh=zo+grs+qtz+H_2O (Chatterjee et al., 1984).*

Reaction 18: *prl+zo=an (Nitsch, 1971).*

Reaction 19: *arg=cal (Spear, 1993).*

Reaction 20: *zo+qtz=an+grs+H_2O (Ghent et al., 1979).*

Reaction 21: *zo+qtz=an+grs+H_2O (Liou et al., 1971).*

Reaction 25: *Upper limit of titanite, QFM buffer (Wones, 1989).*

Reaction 26: *act+chl=act+cal (Bassias and Triboulet, 1992).*

Reaction 27: *Lower limit of pumpellyite (Liou et al., 1971).*

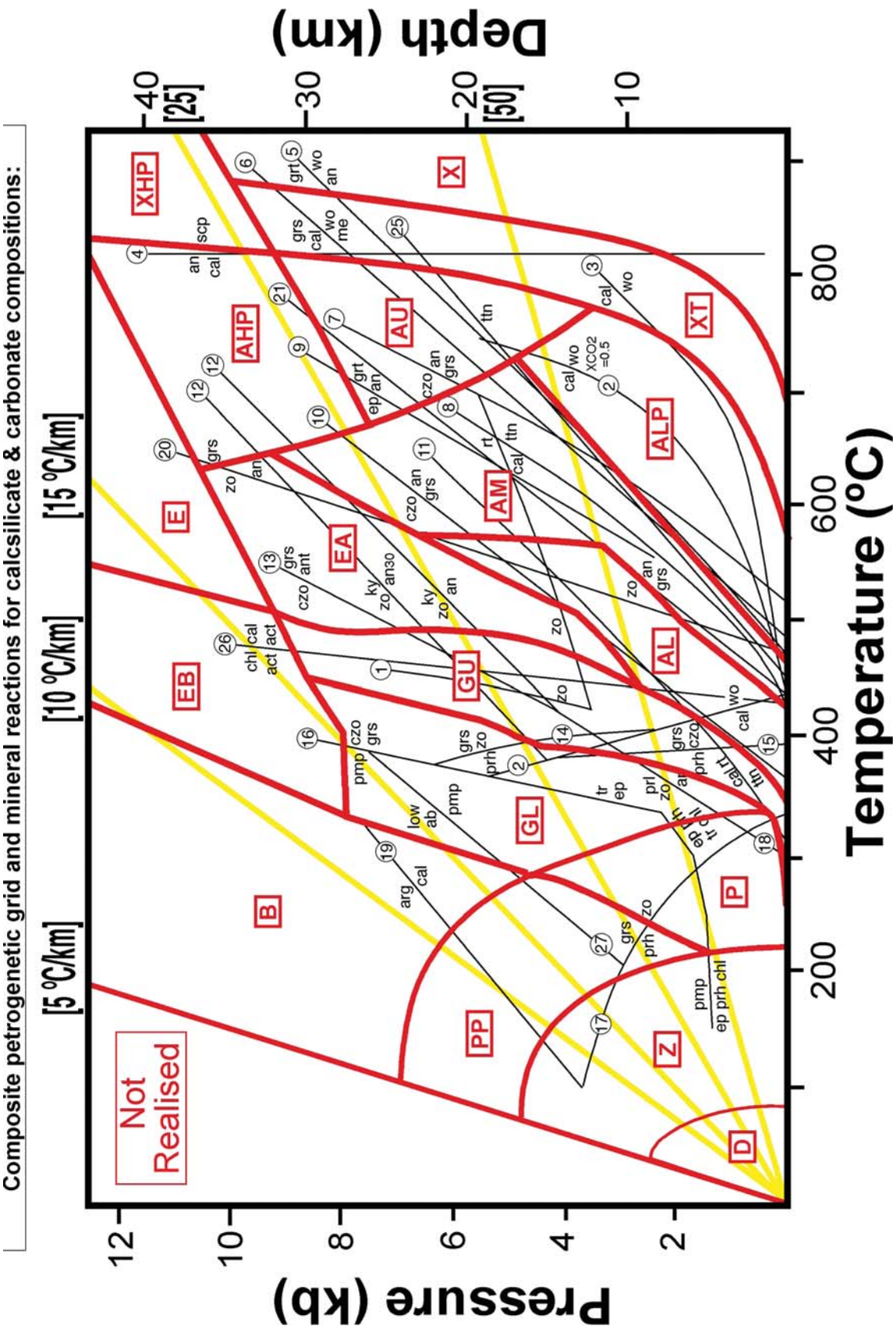
Composite petrogenetic grid and mineral reactions for calcsilicate & carbonate compositions:
[5 °C/km]
[10 °C/km]
[15 °C/km]
Pressure (kb)
Depth (km)
Temperature (°C)
Not Realised
XHP
AHP
E
EB
B
EA
GU
GL
PP
Z
D
P
AM
AU
X
XT
ALP
AL

Coupled Facies and P-Series Metamorphic Maps (CFPS)

Metamorphic Map Rationale

Metamorphic maps of the EYC have been generated by a simplified version of the DMF rationale (Goscombe and Blewett, 2009; Appendix 2). This methodology simply employs a coupled metamorphic facies – pressure-series (CFPS) assignment at each site. Adoption of this method is primarily for three reasons. [1] The vast bulk of peak metamorphic and alteration PT conditions in the EYC fall within medium-pressure series conditions (defined as G between 30 and 50 ºC/km). [2] Assignment of pressure-series to large groups of aligned localities is significantly easier and more efficient than assigning a diagnostic mineral field to each sample. [3] Assignment of diagnostic mineral field is not possible in most cases because most localities have only very simple non-diagnostic assemblages available.

CFPS assignment is made at each locality by assigning metamorphic facies coupled with an independent assessment of pressure-series (i.e., temperature/depth ratio = G). Peak metamorphic PT calculations from the EYC show that most parageneses and localities fall into medium pressure-series conditions, independent of metamorphic grade. Consequently, a *prima facie* assumption is initially made that all sites are of medium pressure-series. The few localities which fall into different pressure-series can be confidently documented using key diagnostic mineral assemblages and absolute PT calculations. The resultant combination of metamorphic facies (i.e., proxy for T) and pressure-series (i.e., proxy for P) is used to assign the metamorphic map polygons from site data in the MDB. The CFPS method outlined above is the prime constraint on producing the peak metamorphic maps.

Definition of Pressure-Series

[1] Very, low pressure metamorphic series (VLP): >70 ºC/km.

[2] Low pressure metamorphic series (LP): 50-70 ºC/km.

Diagnostic of extreme dominance of heat conduction with respect to advection of material, such as in contact aureoles, or high heat flow environments with magma accretion and thermal blanketing such as magmatic arcs.

[3] Medium pressure metamorphic series (MP): 30-50 ºC/km. [i.e., Buchan Series]

Diagnostic of slow exhumation rates and/or high heat flow due to either; mantle lithosphere thinning, magmatic accretion, high radiogenic heat generation or efficient thermal blanketing by thick sedimentary sequences.

[4] High-pressure metamorphic series (HP): 15-30 ºC/km. [i.e., Barrovian Series]

Diagnostic of continental collisional orogens experiencing relatively fast exhumation rates with advection of material in quasi-equilibrium with conduction of heat.

[5] Very high pressure metamorphic series (VHP): <15 ºC/km

Diagnostic of settings where the fast advection of material out competes the conduction of heat, such as within subduction regimes. Is not represented in the EYC.

Temporal Layers in Metamorphic Maps

The generation of meaningful metamorphic maps has historically been hampered by different aged metamorphic parageneses being presented together as a “composite” metamorphic map pattern. Rarely does a metamorphic terrane record only one metamorphic cycle or event. The EYC is no exception and the EYCMP has documented different metamorphic periods (see below). Over-printing relationships, time constraints offered by stratigraphy and relative age determinations have allowed a preliminary framework of the broad metamorphic periods to effect the EYC. At least 5 temporally distinct metamorphic periods of contrasting metamorphic style, conditions and possible tectonic setting are recognised in different parts of the EYC. These periods are defined simply here, the full details and arguments for each is contained in the Metamorphic Interpretation section.

Criteria for assigning metamorphic parageneses to these metamorphic periods are discussed later. Unlike stress fields, switching between different thermal periods involves slow rates, conductive delays and a history less punctuated than the structural evolution: necessitating broad thermal events and also the possibility of continuums between them (i.e., the M2-M3a-M3b continuum).

Ma (2720-2685 Ma and Older?)

High temperature/depth ratio metamorphism (G ≥ 70ºC/km) associated with high heat flow in magmatic arc environments and possibly also near surface seafloor alteration during formation of the volcanic pile. Most plausibly, M*a* parageneses will be spatially restricted and there may be a number of different aged magmatic arcs with associated metamorphic parageneses. A metamorphic map isolating M*a* parageneses and conditions is possible because the temperature/depth ratio of metamorphism is extreme and distinct from all other mineral parageneses. This is true particularly for the few granulite grade sites, but recognising early seafloor alteration parageneses for shallower crustal levels will be indistinguishable from late-stage alteration (M3b) parageneses unless over-printed.

M1 (2720-2685 Ma)

Low temperature/depth ratio (G < 25ºC/km), high-P and moderate-T metamorphic parageneses with very restricted distribution that are now exposed only in crustal-scale shear zone settings. Tectonic setting is not entirely understood, but these rocks are over-printed by regional parageneses and preliminary age dating indicates that these parageneses formed prior to the regionally extensive M2 parageneses. A metamorphic map isolating M1 parageneses and conditions can be attempted because the temperature/depth ratio conditions are very low and distinct from all other mineral parageneses. This can be achieved by applying a cut off of G<25ºC/km.

M2 (2685-2670 Ma)

Regional, moderate thermal gradient metamorphism (G = 30-50ºC/km) associated with volumous granite emplacement. Associated with a very heterogeneous distribution of strain. After peeling away the M*a* and M1 episodes of metamorphic parageneses, this leaves wide spread regional metamorphic parageneses. These parageneses are the result of both M2 and M3a thermal events. Consequently, at best, the "left over" metamorphic parageneses constitute a M2-M3 composite metamorphic map.

M3a (2670-2650 Ma)

Static metamorphic parageneses formed by elevated thermal gradient metamorphism (G = 40-70ºC/km) associated with lithospheric extension, indicated by post-volcanic turbiditic basin (PVTB) deposition and metamorphism. Distribution and conditions of M3a metamorphism can be constrained by PVTB rocks that have been metamorphosed. The true extent of the M3a thermal over-print may have been more extensive, though possibly localised to zones of maximum extension. In stratigraphy below the PVTB's, distinguishing whether a mineral assemblage is M2 or M3a is only possible if the P-T path can be determined. Consequently, outlining the true extent of the M3a thermal overprint is probably not possible though would constitute a good Au exploration tool as discussed later.

M3b (2650-2620 Ma)

Overprinting, late-stage, fluid-rich alteration parageneses constitute M3b and typically involved alteration and metasomatism of the bulk rock composition. Accompanying temperature/depth ratio conditions are generally moderate to elevated (G = 40-90 ºC/km) and crustal levels are shallow, ranging from 4.0 down to 1.0 kb. A metamorphic map isolating M3b parageneses and conditions is possible on the basis of correct assignment of alteration by the authors that the MDB has drawn from. "Alteration" in legacy data is accepted to mean; (i) late-stage, (ii) overprinting, (iii) hydrothermal, (iv) down-graded metamorphic assemblages and (v) altered bulk compositions. Assignment in the literature appears to generally follow this definition but some authors have used "alteration" to mean low-grade regional metamorphic parageneses.

GIS Map Products

The structural and metamorphic GIS maps produced, have been interpreted from three sources of data: [1] point data contained in the MDB (Appendix 3), [2] GSWA 100K map polygons labelled with some level of metamorphic information and [3] published metamorphic isograd maps (Binns et al., 1976; Archibald and Bettenay, 1977; Archibald et al., 1978; Hallberg, 1985; Clark et al., 1986; Ahmat 1986; Swager et al., 1990; Witt, 1991; Ridley, 1992; Swager et al., 1992; Williams and Whitaker, 1993; Witt, 1993; Ridley, 1993; McNaughton et al., 1993; Williams and Whitaker, 1993; Williams and Currie, 1993; Swager, 1994a; Swager, 1994b; Swager, 1994c; Witt, 1994; Smithies, 1994; Swager, 1995; Swager and Nelson, 1997; Bloem et al., 1997; Witt, 1997; Wilkins, 1997; Swager, 1997; Witt and Davy, 1997; Witt et al., 1997b; Langford and Farrell, 1998; Libby and DeLaeter, 1998; Dalstra, 1999; Groenewald et al., 2000; Painter and Groenewald, 2001; Stewart, 2001; Wyche et al., 2001; Mikucki and Roberts, 2003; Jones, 2006).

The ArcGIS v9.2 project for the EYCMP contains a select number of data layers that map the attributes and distribution of the most significant parameters. These data layers are also available as PDF format outputs contained in Appendix (2) along with a text file outlining legends for these data layers. These select numbers of data layers have been used to compile the final interpretive maps, which are also contained in Appendix (2) and published (Goscombe and Blewett, 2009). The ArcGIS v9.2 project for the EYCMP can be used to plot the distribution of a larger number (~230) of other parameters (e.g., amphibole type, age data etc). The final interpretive maps that have been produced are outlined below. These interpretive maps are available in draft form as pdf's in Appendix (2), and maps [1] and [5] incorporated into Plate 1 (Goscombe and Blewett, 2009).

[1] Peak metamorphic map: Metamorphic CFPS polygons are constrained by site data, 100K polygons and published metamorphic maps. Different hatching is superimposed to indicate documented static metamorphism and gneissic domains. Different symbols are used at sites to indicate Ma, M1, M2 and M3a metamorphic periods. Strings of absolute T-P-G data calculated at key sites are superimposed. Insets indicate metamorphic maps during M*a*, M1 and M3a periods and metamorphic field gradients along profiles across the EYC.

[2] Key mineral assemblage maps: Separate maps have been produced that indicate key mineral assemblages in mafic, metapelite and ultramafic rocks.

[3] Alteration map: Map outlines the total extent of alteration (M3b) parageneses and hydrothermal veining. Different hatching is superimposed to indicate the extent of alteration facies defined by Witt (1993). Strings of absolute T-P-G data calculated for alteration conditions are superimposed.

[4] Redox-pH map: Polygons outline the extent of the following combinations of redox and pH determined from alteration mineral parageneses: oxidized-acid, oxidized-alkali, reduced-acid and reduced- alkali. Different symbols are superimposed to indicate the dominant fluid type: CH_4, CO_2 and H_2O.

[5] Bulk strain map: Contoured map of qualitative foliation intensity index (QFII) with calculated strain ratio (R) and Flynn ratio (k) values superimposed at select key sites.

[6] Structural grain map: Map of trace lines for strike of the main foliation, superimposed on a contoured background indicating variation in dip of the main foliation.

[7] Maximum extension direction map: Map of arrow lines indicating the direction of plunge of stretching lineations, with shear sense indicated at select key sites. Lineation traces superimposed on a contoured background indicating variation in plunge of stretching lineations.

[8] Obliquity map: Contoured map of the degree of obliquity between the strike of the main foliation and stretching lineation direction.

Metamorphic Methodology

METAMORPHIC DATABASE (MDB)

Database Rationale

ITAR has been in the process of developing a geological database over the last 16 years; to enable the collation, organization and calculation of a near comprehensive suite of geological parameters that may be generated in and utilised by any integrated geological study (i.e., Structure – Metamorphism – Chronology – Stratigraphy – Geochemistry - Rock Type - Field Relationships – Mineralization – Geophysical Properties). This database has been extensively modified and tailored for the Yilgarn Craton and particularly for the metamorphic aspects of the EYCMP and labelled the Metamorphic Database (MDB). The aims of the constructed MDB was to parameterise almost all geological data that can be collected or generated at a point locality, organise this large range of data types in a geologically sensible and self explanatory way, and arrange for efficient data entry. Only previously defined attributes can be entered (Appendix 1), making the database uniquely interrogatable. Furthermore, ranges, limits and internal consistencies are encoded so that only sensible and plausible data can be entered, greatly reducing the chance of incorrect data entry. Approximately 600 unique parameters can be inputted or calculated / generated by the database, storing a near comprehensive range of geological data. The MDB is easily modified for the specific geographic location and stratigraphy of any geological project worldwide. The MDB is the foundation for the Integrated Terrane Analysis method. Parametization of geological variables, in an internally consistent way, across whole orogenic systems will facilitate both the documentation of structural and metamorphic patterns and both the temporal and spatial integration of different data types on a large scale.

All site or point data generated and captured for the EYCMP has been both processed through the MDB for the calculation and generation of additional parameters and the complete point dataset for the project is stored within the MDB. Because of the large scope of the project, covering approximately 40,691 data points, the MDB has been sub-divided in the following sub-datasets. [1] GSWA data from the central EYC n=1957); [2] GSWA data from the extreme south EYC (n=1241); [3] GSWA data from the north EYC (n=1825); [4] GSWA data from the south EYC (n=1984); [5] The Mikucki and Roberts (2003) petrological dataset (n=1848); [6] Quantitative data generated by Goscombe in the EYCMP (n=1894); [7] Quantitative data available in literature (n=1702); [8] GA petrological dataset (n=1372); [9] GSWA data from the Southern Cross Terrane part 1 (n=1599), [10] GSWA data from the Southern Cross Terrane part 2 (n=1581); [11] GA structural dataset (n=6592); [12] GSWA structural dataset part 1 (n=5699); [13] GSWA structural dataset part 2 (n=5701); [14] GSWA structural dataset part 3 (n=5696). Preliminary databases for the Southern Cross, Narreyer, Murchison and Southwest Terranes have also been partially compiled in the course of the EYCMP.

Parameters relevant to the outcomes of the EYCMP have been extracted from these MDB's and compiled as a single data table (Appendix 3) for uploading into the ArcGIS v9.2 GIS platform for spatial analysis and mapping. These 230 relevant parameters form the basis of all GIS projects and are listed in Appendix (6). Appendix (1) contains all possible attributes and codes for the selected relevant parameters. These attribute lists can be used to interrogate the data table for the EYCMP. The data table was divided at longitude 120º; data to the east in Zone 51 gives complete coverage of the EYC and data to the west in Zone 50 constitutes a very preliminary dataset for the western Yilgarn Craton. The final data table for the EYC contains 230 geological parameters and 36,367 data points. To aid uploading into ArcGIS v9.2 redundancy was removed reducing the size of the data table considerably, by dividing into two tables containing metamorphic data only or structural data only.

Database Structure

Location Sheet

A Unique Site Number (USN) is automatically generated for each new row of data, linking all data from the same location throughout the entire database. This sheet contains all spatial location information available, including map sheets, grid reference, location accuracy, original field site number, date of capture, identification of data entry personnel, originator of data, type of data source and reference details. All grid references have been converted to the GDA94 datum.

Stratigraphy Sheet

This sheet contains a simple informal categorization of rock unit stratigraphy based on broad groups of distinct stratigraphic association. Information on the detailed GSWA stratigraphy and GSWA rock codes was not available for almost all locations and was not captured in the EYCMP. All localities have been assigned to the current Domain and Terrane definition of Cassidy et al. (2006). West of the Ida Fault, structural Domains have been defined on the basis of distinct greenstone belts.

Rock Sheet

This sheet contains rock and outcrop description, rock name and rock classification. Rock names are largely based on the GA's OZROX database with extensive modifications and additions for metamorphic rocks. The details of collected samples; including the type of sample collected, the intended and undertaken analysis such as lapidary, geochemistry and geochronology, and the current storage locality.

Petrography Sheet

This sheet contains all petrographic, mineral and metamorphic data. Also included are analytical and calculation details (i.e., analysis sites used for PT calculation), robustness of data source (e.g., full or partial descriptions etc), and details of microscope images (i.e., microphotographs, compositional maps and sketches of mineral textures). Petrographic parameters include; thin section descriptions, rock textures (e.g., gneissose etc), mineral textures (e.g., pseudomorphs etc), grain size, leucocratic segregations and mineral assemblages at different stages of growth such as igneous, inclusion, matrix, secondary (e.g., reaction textures, late foliations etc) and alteration parageneses. Rock and mineral textures are mostly defined after Passchier and Trouw (2005). More interpretive petrological parameters include; the sequence of mineral growth, assignment to diagnostic mineral fields (DMF), metamorphic facies, pressure series and metamorphic style (e.g., dynamic, regional, contact, static etc). Quantitative metamorphic parameters are pressure, temperature and temperature/depth ratio estimates and calculations for different stages of rock evolution, mineral names, garnet zoning and fluid parameters (i.e., fluid and melt phases present, redox and pH). Interpretive metamorphic parameters are P-T paths and assignment of the metamorphic event (i.e., Ma, M1, M2, M3a and M3b).

Metamorphic facies are after Spear (1993) with the additional subdivisions of middle-amphibolite (i.e., staurolite-garnet metapelite), upper-amphibolite facies (i.e., sillimanite or partial melt in metapelite), high-P upper-amphibolite, "sub-metamorphic" for unmetamorphosed sedimentary rocks and "supra-metamorphic" to indicate rocks derived from melt (i.e., igneous) that have not been appreciably modified by metamorphism, but by nature of their mid-crustal emplacement have seen metamorphic conditions.

Temperature/depth ratio (G) is simply the temperature (T in ºC) divided by depth (z in km), where depth is calculated from pressure (P in kb) assuming a density of 2.8 g/cm^3. Temperature/depth ratio is not to be confused with the instantaneous thermal gradient or metamorphic field gradients (Figure 20). Temperature/depth ratio was calculated using [T/(P*3.5)] and the 2σ error on G was calculated using [G*($\sqrt{((\pm T/T)^2 + (\pm P/P)^2)}$)].

Mineral names are recorded in full in the database to avoid ambiguities. Mineral assemblage strings are automatically generated using the international convention for mineral abbreviations (Kretz,

1983). All mineral abbreviations are listed in Appendix (1) and new mineral abbreviations for the EYCMP have 4 characters. Sequence of mineral growth strings use + to indicate coeval phases and > to indicate temporal progression.

Interpretive composite P-T paths are also recorded by a sequential combination of documented P-T trajectories at different stages of evolution of the rock (Figure 37). The fundamental trajectories used to describe P-T paths are loading (L), decompression (D), cooling (C), heating (H), isobaric (IB), isothermal (IT), anticlockwise (ACW) and clockwise (CW) trajectories.

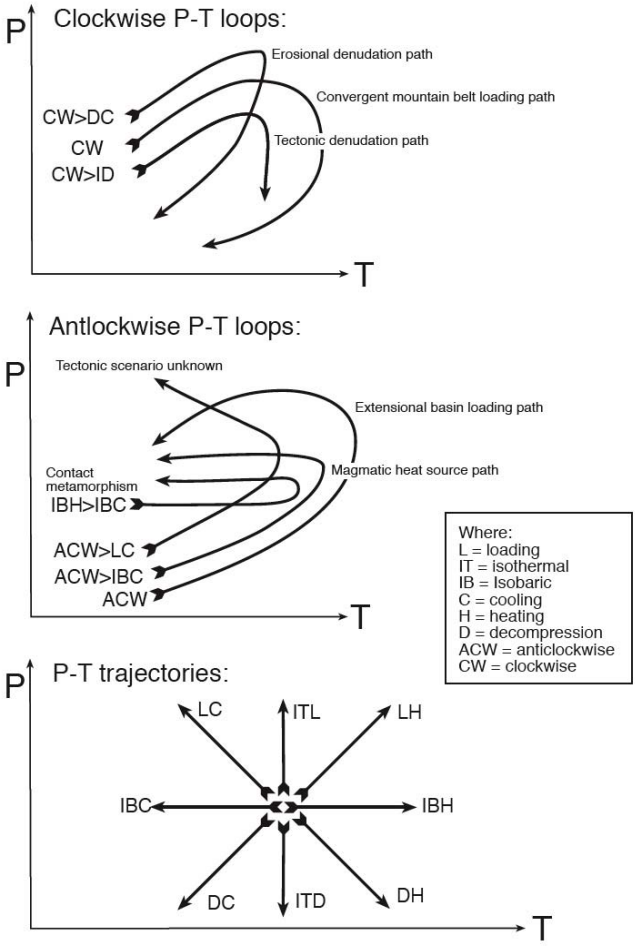

Figure 37: *Composite P-T paths and P-T trajectories with possible tectonic interpretations modified after Spear (1993).*

Chemistry Sheet

This sheet contains whole rock analyses including major oxides and trace elements and analytical details. Useful ratios, sums, normalization for triangle plots and normalization for primordial mantle (Wood et al., 1979a, 1981; McDonough et al., 1991) and chondrite (Sun, 1980; Wood et al., 1979b; Thompson, 1982) are automatically generated. Different combinations of total FeO, total Fe_2O_3 and analysed FeO and Fe_2O_3 are all recorded and different versions of XMg calculated. The order of major and minor oxides has a long historical precedence. Trace element order is based on convenient groupings (e.g., LILE, HFSE, REE, Transition elements, Noble metals etc) with each arranged in order of increasing atomic number.

Isotope Sheet

This sheet contains the details of isotopic analysis and geochronology. This includes the relevant genetic relationship of analysed phase (e.g., magmatic etc), analysed minerals, analysis site, isotopic system, analytical method, age determination, 2σ error, MSWD, type of age constraint (e.g., isochron age, plateau age, pooled mean age etc), number of analytical determinations, available geochronology images, model ages, initial ratios and interpretation of age (e.g., maximum deposition age etc).

Structure Sheet

This sheet contains the description, quantification and orientation of all planar and linear structures, quantification of the intensity of deformation (e.g., strain), directional data (i.e., younging, vergence and shear sense) and interpretation of EYC deformation event (Blewett and Czarnota, 2007c). Descriptions and details of field photos are recorded. All planar and linear structures are classified in a two-tiered system of class (e.g., magmatic, foliation etc) and type (e.g., dyke, schistosity etc). GA structure symbol codes are automatically assigned. Relative ages of different structures at the same locality determined by over-printing criteria are recorded as outcrop generation number. This organises the time sequence of deformation and magmatic events at a specific location and does not attempt correlations between different localities. Bulk strain is recorded as qualitative foliation intensity index (QFII) and semi-quantitative estimates are calculated automatically from structural parameters measured in outcrop (e.g., angle between S-C foliations). The angle of obliquity (β) between the plunge direction of the maximum extension axis (e.g., stretching lineation etc) and strike of a related plane (e.g., shear plane etc) is calculated automatically.

Shear sense is captured by two parameters: [1] the relative shear sense of the hanging wall (i.e., sinistral, dextral, normal and reverse), and [2] shear sense of the hanging wall with respect to the stretching lineation (i.e., up-plunge, down-plunge and no-plunge in case of strike-slip). These parameters, combined with obliquity (β), automatically assign categories of shear sense (e.g., dextral strike-slip, dextral-reverse oblique, normal dip-slip etc). Obliquities <6º determine strike-slip shear couples, obliquities >60º determine dip-slip shear couples and all other fields are oblique-slip. Two types of vergence are recorded. Fold asymmetry vergence is the direction of transport of the antiform in the top-plate, when looking down plunge. Bedding-foliation vergence is the direction (left or right) from the young plane (i.e., foliation) to the older plane (i.e., bedding) in the top-plate, when looking down the intersection lineation.

Data Sources

Background

The approach taken by the EYCMP has been to compile a near comprehensive database from all available pre-existing data and add to this with intensive analysis of a select number (n=493) of key metamorphic locations (Appendix 7). The alternative approach of detailed petrographic description of all easily available thin sections (i.e., GA and GSWA collections), similar to the sub-set described by Mikucki and Roberts (2003), was considered inefficient for the scale of the entire EYC. A detailed re-description approach would have taken >4 years to describe the ~12,000 thin sections available. Consequently, the thin section and field descriptions by the original geologists have been used as the basis for extracting different data for the database. Industry datasets were not made available, restricting the resolution of the MDB to documenting regional patterns and not being able to bring out patterns at the near camp scale. The following parameters among others have been extracted from legacy descriptions: partial peak assemblages, partial alteration assemblages, primary minerals, metamorphic facies, metamorphic style, rock texture, mineral textures, protolith rock type, qualitative strain and sequence of mineral growth.

A more detailed range of metamorphic data has also been complied for many additional locations by extracting parameters from the published literature (Gower and Boegli, 1977; Bunting et al., 1978; Willett et al., 1978; Purvis, 1978; Clark, 1980; Henderson, 1981; Woad, 1981; McQueen, 1981; Phillips and Groves, 1982; Elias et al., 1982; Ion, 1982; Gee, 1982; Chin and Smith, 1983; Walker

and Blight, 1983; Scantlebury, 1983;Phillips and Groves, 1983; Purvis, 1984; Chin et al., 1984; Ho, 1984; Phillip and Groves, 1984; Phillips, 1985; Hallberg, 1985; Spray, 1985; Bickle and Archibald, 1986; Ho, 1986; Clark et al., 1986; Phillips, 1986; Martyn and Johnson, 1986; Ho, 1987; Allen, 1987; Neall and Phillips, 1987; Skwarnecki, 1988; Jurasky, 1989; Bennett, 1989; Clark et al., 1989; Skwarnecki, 1990; Ho et al., 1990; Groves et al., 1992; McNaughton et al., 1992; McQueen, 1992; Hagemann and Ridley, 1993; McCuaig et al., 1993; Hunter, 1993; Phillips and Powell, 1993; Mikucki and Ridley, 1993; Williams and Currie, 1993; Knight et al., 1993; Bloem et al., 1994; Bloem, 1994; Morris, 1994; Bagas, 1994; Swager, 1994; Wyche and Witt, 1994; Ahmat, 1995; Ojala, 1995; Dalstra, 1995; Knight et al., 1996; Witt and Davy, 1997; Mikucki, 1997; Witt, 1997; Swager, 1997; Wilkins, 1997; Hall, 1997; Liu et al., 1998; Westaway, and Wyche, 1998; Witt, 1998; Wyche, 1998; Cassidy et al., 1998; McCuaig and Kerrich, 1998; Dalstra, 1999; Dalstra et al., 1999; Chen, 1999; Wyche, 1999; Langford, 2000; Barnes and Hill, 2000; Knight et al., 2000; Dugdale and Hagemann, 2001; Witt, 2001; Farrell, 2001; Polito, 2001; Huston et al., 2001; Riganti, 2002; Duuring, 2002; Mikucki and Roberts, 2003; Hagemann and Luders, 2003; White et al., 2003; Mason, 2004; Roberts, 2004; Groenewald et al., 2006; Evans et al., 2006; Elmer et al., 2006; Hodge, 2007).

The most comprehensive range of metamorphic and structural data was generated by intensive analysis of key localities specifically sampled for the EYCMP (n=493). The analysis of these samples is described in the Metamorphic Methodology, Metamorphic Description and Metamorphic Results chapters below. These key sampling sites were selected after compilation of the available legacy and published data, which highlighted localities with rocks and mineralogy appropriate for intensive analysis. The MDB can be further populated with data generated in future metamorphic programs, increasing the resolution, scope and quality of the documented metamorphic patterns.

GA mapping programs in the EYC utilised GPS, all sites are accurately located (±60 m) and this has been confirmed in the field during the EYCMP. The majority of data in GSWA legacy datasets were captured prior to GPS and inaccurately located (±600 m), which has been confirmed in the field where some sites could not be relocated. Location errors were further compounded by rounding off of grid references to the nearest kilometre and the original field mapping was translated onto the AGD66 datum. A few GSWA 100K map sheets have a portion of nonsensical site locations presumably introduced by data entry errors.

Assignment of Minerals and Metamorphic Facies From Legacy Data

Text descriptions of outcrops and thin sections in GA and GSWA datasets have been used as a basis for identifying the minerals present and assigning metamorphic facies. All mineral assemblages determined in this way are designated partial assemblages in the database. Because legacy descriptions are typically very abbreviated, all described minerals are assumed to constitute a single assemblage. Temporal relations between minerals are recorded when indicated by the originator or if the minerals occupy incompatible P-T fields. Sausuritized is recorded as albite and epidote, uralitized as actinolite and rodingite as grossular. The following assumptions have been made: amphibolite or mafic gneiss contains hornblende and plagioclase; porphyroblastic metapelite contains andalusite; shale and siltstone contains clay minerals; phyllite, phyllonite, slate, argillite and K-metasomatism contain sericite; metapelite schist contains quartz and muscovite; mafic schist contains chlorite. The criteria for assigning metamorphic facies are summarized in Table (3).

Table 3: *Table summarizing the criteria for assigning metamorphic facies from legacy datasets. Assignments have been made from text descriptions of outcrops and thin sections in GA and GSWA datasets.*

Metamorphic Facies	Text from outcrop & thin section descriptions in Government databases: Felsic & Granitoid	Calcsilicate	Ultramafic	Aluminous	Mafic	Metapelite	BIF
Sub-metamorphic					basalt		
Prehnite-Pumpellyite					cleaved basalt	shale slate meta-siltstone meta-sandstone	
Lower Greenschist	slate		carbonated carb-chl		chlorite sericite±carb	silty schist±graphite chloritic siltstone sericite phyllite phyllonite	
Undifferentiated Greenschist	phyllitic epidote sericite chlorite qtz-stp-ab schist altered phyllitic phyllonitic		altered talc-chl talc-carb talc-serp-chl serpentine ultramafic schist rodingite sausserite	chlorite pyrophyllite	sausserite epidote meta-basalt altered foliated sheared basalt	ms-qtz chlorite graphitic pelite altered tourmaline veins alteration	chl
Upper Greenschist	schist siliceous mylonite epidote siltstone	tremolite	trem±talc±chl uralitized act±chl		bt-act-qtz bt±chl±carb act / trem amphibole chlorite schist mafic schist	ctd schist ctd pelite ctd-and qtz-kyn-ms / seri kyn-and±seri schist qtz-ms-and	qtz-grun
Lower Amphibolite	mylonite grt-bt-chl-olig gneiss biotite foliated granite chl-amph felsic grt-ms-alb-qtz gneiss	hbl-grt±pl	bt-tlc grunerite-chlorite ol-trem chl-trem-ol trem-carb-ol phlogopite-trem serp-grunerite bt-tlc	cumm-crd-anth cumm	amphibolitic meta-basalt biotite-hornblende alkali-amphibole reibeckite	grt-ms fib-ms fib-bt andalusite biotite	qtz-chl-grun-bt chl-bt
Undifferentiated Amphibolite	gneiss recrystallized metamorphosed sheared grt-bt-ms gneiss hbl-bt-pl gneiss	skarn hornfels gneiss			diopside amphibolite hornfels hornblende	hornfels spotted porphyroblastic	Ca-amph
Epidote Amphibolite		qtz-diop-epi	sausserite-hbl		epi-hbl sausserite-hbl		
Middle Amphibolite	grt-amph grt-bt gneiss	cpx-grt cpx-grt-pl±hbl grunerite-cpx hbl-cpx	grunerite±olivine cumm / grun	anth / ged	grt-amphibolite epi-cpx grun-amphibolite	sillimanite rutile-biotite crd±gd staurolite	grt-grun-qtz grun-hbl-qtz
Upper Amphibolite	migmatite cpx-hbl gneiss		cpx-hbl enst-ol-tlc	grt-crd	cpx-amphibolite grt-amphibolite mafic gneiss		
High-Pressure Amphibolite				kyn-ged / anth	grt-cpx amphibolite		

Assignment of Metamorphic Style From Legacy Data

Metamorphic style is assigned from legacy outcrop descriptions. Dynamic regional metamorphism is assigned if any deformation fabric is described and is the default assignment where no other diagnostic information is available. Static regional metamorphism is assigned where recognised by the originator and where igneous textures have been described: such as ophitic, gabbro, dolerite, spinifex texture, cumulate texture, amygdales, and plagioclase-phyric. Contact metamorphism is assigned only where recognised by the originator.

Alteration is taken to mean either down grading with respect to regional conditions, retrogression, metasomatic fluid influx, veining, change in bulk composition and mineralization. Alteration is assigned where recognised by the originator, where veining and metasomatism have been described and where change of bulk composition is inferred, such as carbonated and silicified. Alteration is often described as assemblages over-printing matrix regional metamorphism and the two assemblages are separated in the database. A few legacy originators have used the term “alteration” for regional metamorphic assemblages. In most cases this ambiguity is recognised from the outcrop description, developed minerals or by context with respect to adjacent samples. Alteration assemblages are assigned to an alteration facies after the scheme of Witt (1993) for altered mafic

rock types. This assignment has been made using the criteria summarized in Table (4). The alteration facies approximately correspond to increasing temperature, though developed assemblages are influenced by a large range of variables, such as proximal versus distal sites, fluid chemistry and bulk chemistry of host rock.

Table 4: *Table summarizing the criteria for assigning alteration facies from legacy datasets. Alteration facies are after Witt (1993).*

Alteration Mineral	Alteration Facies assignment: A (~300ºC)	B (~400ºC)	C (~500ºC)	D (~600ºC)
Flourite	fl			
Talc	tlc			
Prehnite	prh			
Serpentine	serp			
Fe-oxide	feox			
Clay / illite	ill			
Epidote	ep	ep		
White mica	sericite	ms		
Chlorite	chl	chl		
Carbonate	sd / ank / cc	ank / cc	cc	cc
Ilmenite	ilm	ilm	ilm	ilm
Sulphides	sulph	sulph	sulp	sulp
Plagioclase	ab	ab	Ca-pl	Ca-pl
Actinolite	act	act-hbl		
Amphibole	gln	cum	rbk / gru	
Hornblende			hbl	hbl
Quartz		qtz	qtz	
Monazite		mnz	mnz	mnz
Ti-minerals		rt / ttn	ttn	ttn
Stilphenomelane		stp	stp	
Biotite		bt	bt / phl	bt / phl
Garnet			±grs / adr	alm
K-feldspar				mic
Diopside				di
Zircon				zrn

Assignment of Alteration Redox and pH

A qualitative assessment of redox and pH has been made from alteration assemblages based on John Walshe's composite pH-redox pseudosection constructed at 500 ºC and 4 kb. This assignment has been made using the criteria summarized in Table (5). These assignments are necessarily very interpretive as modal proportions of mineral phases and mineral compositions are typically unknown and some phases form across a wide range of redox-pH space. Best considered interpretations are given simply as either oxidised or reduced (boundary approximately at log fO2 –27) and either acid or alkali (boundary at pH of 7). Neutral or intermediate conditions are not recorded. Thus an assessment of "acid" means the assemblage indicates higher probability of pH<7.0. This same logic is applied to the other simple categories.

Table 5: *Table summarizing the criteria for assigning alteration redox and pH from legacy datasets. Assignment based on the composite pseudosection contructed by John Walshe pers. comm. (2006).*

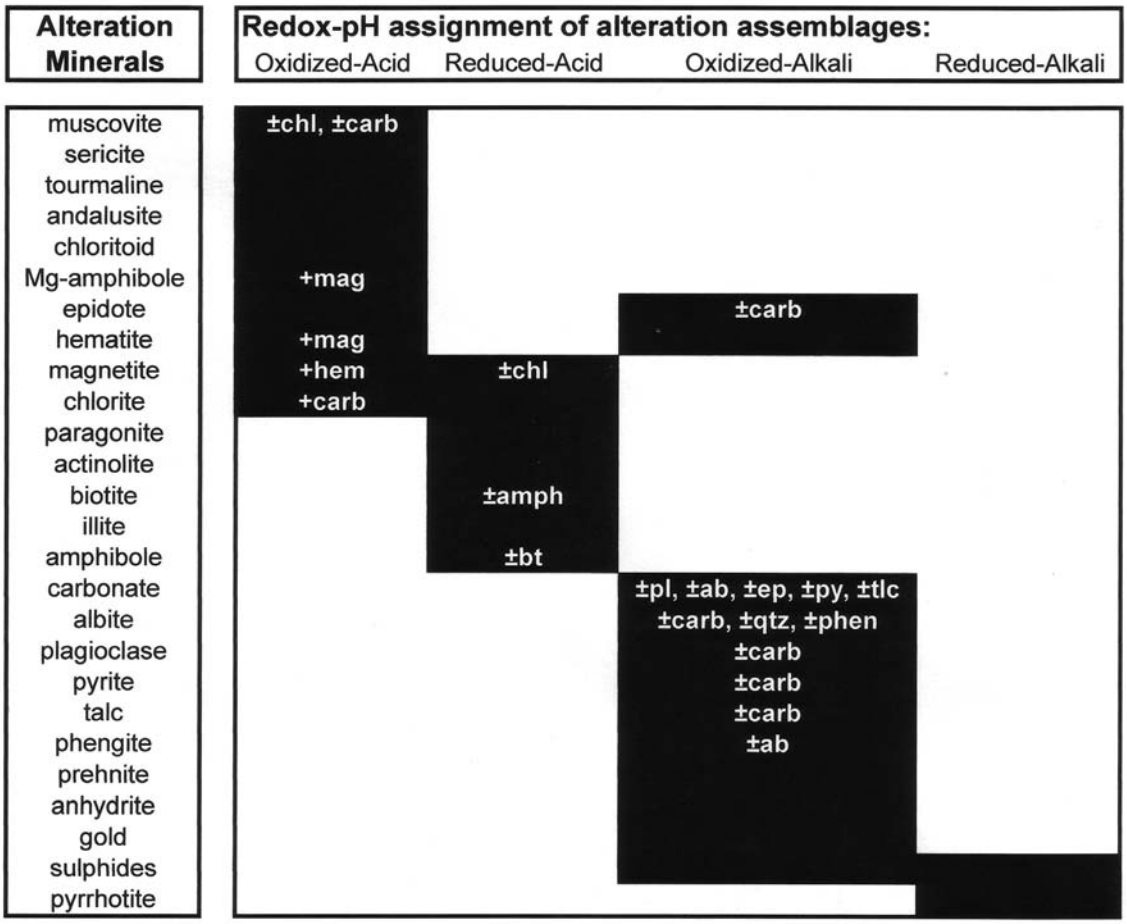

Assignment of Diagnostic Assemblages and Pressure-Series

Key minerals and diagnostic mineral assemblages have been assigned to assemblages developed at localities with sufficient information. These diagnostic assemblages for different common bulk rock compositions are listed by increasing grade in Table (6). Interpretive metamorphic maps are based on metamorphic facies as a proxy for temperature and pressure-series (i.e., temperature/depth ratio; Figure 19) as a proxy for pressure at different grades. The five categories of pressure-series used are defined in the following way:

- Very low-pressure series (VLP): >70ºC/km.
- Low pressure-series (VLP): 50-70ºC/km.
- Medium pressure-series (VLP): 30-50ºC/km.
- High pressure-series (VLP): 15-30ºC/km.
- Very high pressure-series (VLP): <15ºC/km, not represented in the EYC.

Pressure-series has been assigned where sufficient data exists using two criteria: [1] calculated pressures where available, and [2] some key minerals and diagnostic assemblages. Where there is insufficient information, medium pressure-series is assumed. Key assemblages that indicate low pressure-series are: chloritoid-andalusite, cordierite-biotite, cordierite-andalusite-biotite, cordierite-sillimanite-biotite and cordierite-garnet-biotite in metapelites, orthopyroxene-clinopyroxene-

hornblende-plagioclase in mafic granulite and cordierite-cummingtonite and cordierite-garnet in aluminous Fe-rich protoliths. Key assemblages that indicate high pressure-series are: lawsonite, epidote-hornblende-plagioclase, Na-amphiboles, garnet-hornblende-plagioclase, garnet-clinopyroxene-hornblende-plagioclase and clinopyroxene-hornblende-plagioclase in mafic rocks and kyanite-orthoamphibole and grunerite-garnet in aluminous Fe-rich protoliths.

Table 6: *Table of key minerals and diagnostic assemblages. Metamorphic grade increases downward.*

Listing of Key Minerals & Key Assemblages; metamorphic grade increases downwards				
Pelite	Mafic	Calcsilicate	Ultramafic	Fe-Al rich rocks
Illite / clay	Zeol		Dol	Prl
Prl, ±ms	Carb	Carb	Chl, ± carb	Stp
Chl-ms	Lws		Srp	Cum
Ms, ±chl, bt-absent	Pump-ab		Tlc, ±chl, ±carb, ±serp	Crd-cum / ath
Ctd-ms	Prh-ab	Prh-ab	Grs	Crd-st
Ctd-and-ms	Chl - Na-pl	Chl - Na-pl	Tr, ±chl, ±tlc	Ath / ged
Ctd-kyn-ms	Ep - Na-pl	Ep - Na-pl	Phl	Ky-ath / ged
Bt	Act - Na-pl	Act - Na-pl	Ol-tr	Grt-crd
Crd-bt	Act-epi-pl	Act-epi-pl	Ol-tlc	Grun
Crd-and-bt	Chl-grt-pl	Chl-grt-pl	Ol-ath	Grt-grun
Crd-sill-bt	Act-grt-pl	Act-grt-pl	Ol-cpx	
Crd-grt-bt	Epi-hbl-pl	Epi-hbl-pl	Di	
Crd-grt-st-bt		grs-hbl, ±ep	Opx-ath / tr	
Grt-bt	Hbl-pl	Hbl-pl	Opx-ol	
Grt-and-bt		grs-cpx, ±ep	Cpx-hbl, ±opx	
Grt-sill-bt	Grt-hbl-pl			
St-bt	Grt-cpx-hbl-pl			
St-and-bt	Cpx-hbl-pl			
St-grt-bt	Opx-cpx-hbl-pl			
St-grt-and-bt				
And, ±bt				
Ky, ±bt				
Sil, ±bt				
Ky-sill, ±bt				
Ky-and-sill, ±bt				
Ky-and, ±bt				
Sil-and, ±bt				
Kfs-bt				
Grt-kfs-bt				
Melt				

Assignment of Bulk Strain From Legacy Data

The arguments for the assignment of a qualitative foliation intensity index (QFII) based on observation of fabrics in outcrop, has been made in the Structural Framework section above. Specific application of this method to assigning QFII from legacy descriptions has been made using the criteria summarized in Table (7). It is noted that most outcrops in the EYC have low strains indicated by QFII ≤4 (Figure 5), giving an assumed background value where no strain data is available. Where legacy descriptions contain strain information it is typically where noteworthy and at high strains. Granitoids, gabbro and dolerite with no fabric described or igneous textures preserved have QFII value of 0 assigned.

Table 7: *Table summarizing the criteria for assigning qualitative foliation intensity indices (QFII) from legacy datasets. Assignments have been made from text descriptions of outcrops and thin sections in GA and GSWA datasets.*

QFII	Text from outcrop descriptions in Government databases: Granitoids	Mafic rocks	Metapelites	Structure datasets
0	granite massive	gabbro dolerite		joint
1				spaced fracture cleavage
2	very weakly foliated			spaced cleavage fracture cleavage
3	weakly foliated subgrains partially recrystallised	acicular recrystallised	siltstone	crenulation
4	metamorphosed foliated recrystallised grainshape fabric migmatite	foliated basalt	shale foliated mudstone granoblastic	generic cleavage
5	gneissic banded		phyllite schistose rock slate measurable foliation	generic foliation
6	weakly sheared foliation schistose	sheared basalt schist	sheared schist	schist
7	sheared		strong schist	intense fabric c-plane
8	mylonite		mylonite	mylonite
9				
10				

PETROGRAPHY METHODOLOGY

New and Legacy Petrographic Data

Partial descriptions of the petrography of rocks have been made by identification of mineral phases in outcrop and hand specimen. These partial descriptions are sufficiently confident in most cases to make an assessment of metamorphic facies and in some cases also the timing of growth of different mineral phases. Partial petrographic descriptions have greatly increased the scope and data density of the EYCMP and significantly reduced lapidary costs. Partial petrographic descriptions contained in literature and in GSWA and GA legacy databases have been reinterpreted to generate metamorphic parameters such as metamorphic facies and entered into the Metamorphic Database (MDB). These partial descriptions come from both field descriptions and from petrographic analysis by microscope. Metamorphic parametization of legacy datasets constitutes 12,300 of the 14,400 metamorphic sites in the MDB. In comparison, detailed full descriptions made by Ed Mikucki (n=1,842) and those made in the coarse of the EYCMP (n=245) constitute only 15% of the MDB. The distinction between partial petrographic descriptions and full accurate descriptions made by microscope is transparently labelled in the MDB. All new samples collected and studied intensely for the EYCMP are located in Figure 38.

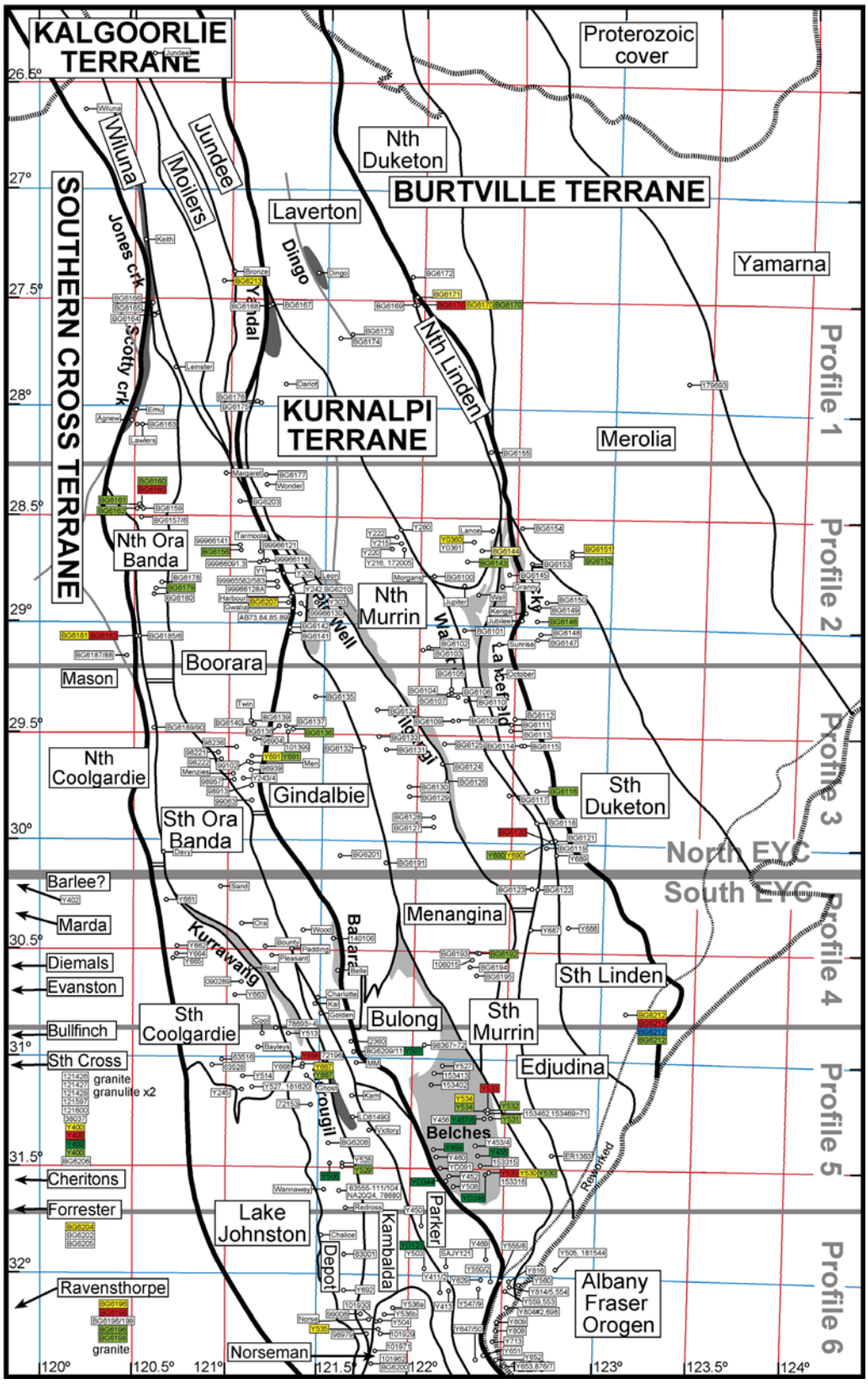

Figure 38: *Map with all sample localities and key metamorphic sites indicated. Larger and more legible image available in Appendix (9).*

Samples with mineralogy suitable for either; [1] PT calculations from mineral analyses or [2] showing a detailed evolution in the growth of mineral phases, typically recognised by the presence of porphyroblasts or reworking fabrics, were selected for thin section or polished thin section. Samples collected in 2003-2004 were thin sectioned by Petro-Lab as part of the ongoing GSWA work program. Samples collected in 2006 were thin sectioned by Ian Pontifex and Associates as part of the EYCMP. As an additional cost saving, pairs of billets of fine and homogeneous 2006 samples were glued together on a single thin-section slide. Though this experiment worked, the differential flex of the rock wafer during the polishing stage made these samples hard to prepare, and the process probably will not be repeated.

Detailed descriptions (n=245) of new samples collected for the EYCMP in 2003, 2004 and 2006 and a select number of samples from the GSWA and GA legacy thin section collections are contained in the MDB and tabulated separately with all details in Appendix (8). Details of the new samples collected for the EYCMP are contained in Appendix (9). Transmitted light optical microscope work and digital microphotographs were undertaken between 2003 and 2007 at the ITAR office, Adelaide University, Adelaide Microscopy, Alice Springs office of the Northern Territory Geological Survey and Kalgoorlie office of GSWA. Confirmation and identification of very fine mineral phases, feldspar and amphibole type, opaques, exsolution relationships and accessory phases were made in the course of electron microprobe work. In some samples, confident identification of haematite versus magnetite has not been made and the presence or absence of quartz and plagioclase has not always been confirmed by electron microprobe.

A select number of samples (n=12) were submitted to GA for XRD analysis, undertaken by Liz Webber and Bill Pappas (Appendix 10). All samples selected were low-grade schists with very fine grain size or inter-leaved phases, making optical identification difficult. XRD analysis was undertaken on a Siemens D500 Diffractometer by scanning between 2º and 70º at 40kV and 30mA. Mineral identification was carried out using BrukerDiffrac^{Plus}Eva and mineral proportions estimated using Siroquant®.

Appendix (8) draws all streams of mineral identification together into a detailed description of each sample. The relative timing and textural setting of each generation of each mineral phase is encoded in this table. For example, distinction is made between; inclusions, matrix phases, porphyroblasts of different generations, porphyroblast over-growths, main schistosity, late foliations, over-printing phases, retrogressive phases and reaction texture phases such as in coronas, moats and symplectites. Also included is a detailed petrological description, summary of the sequence of mineral growth (SMG), overall rock texture and the textural relationships between different minerals. The interpretive SMG string is the raw data used to constrain the P-T path of the rock by interpretation within published P-T pseudosections (see below). All mineral abbreviations used throughout the EYCMP are after Kretz (1983). Minerals not listed in Kretz (1983) have been given new 4 character abbreviations to distinguish them. All mineral abbreviations are listed in the attribute lists of the MDB (Appendix 1).

MINERAL CHEMISTRY METHODOLOGY

Mineral Analyses

New mineral analyses were undertaken on the Cameca SX51 electron microprobe at Adelaide Microscopy, Adelaide University (March 2004, September 2004, December 2006 and March 2007). Approximately 30% of the new mineral analyses were undertaken in the ARRC complex, CSIRO, Perth (November 2003, June 2005, September 2006). An operating voltage of 15 kV and 30 nA was used for all phases except micas (10 nA) and feldspar (15 nA) and a beam radius of 2 μm for most phases and 4 μm for micas and feldspars. Natural silicates were used as standards and checked periodically. Raw and recalculated mineral analyses are contained in Appendix (11).

The EYCMP also draws upon mineral analyses from previously published sources (Phillips and Groves, 1982; Neall and Phillips, 1987; Purvis, 1978; Dalstra, 1995, 1999; McQueen, 1981; Witt and Davy, 1997; Witt, 1998; Knight et al., 1993, 1996, 2000; Williams and Currie, 1993; Bloem et

al., 1994; Spray, 1985; Clark et al., 1989). An attempt has been made to collate a comprehensive database of all available silicate mineral analyses from both the EYC and Southern Cross Terrane. The only exceptions are data in Bloem (1994), Ojala (1995) and Mikucki (1997), no other sources of silicate mineral data is thought to be available.

Mineral Recalculation

All new and published mineral analyses (n=4193) have been recalculated in programs written for each mineral species (Goscombe unpublished). All recalculated analyses are contained in a large mineral database organised by sample (Appendix 11). The ranges of mineral compositions in different rock types and at different metamorphic grades, is described in the Metamorphic Description section. The mineral database contains values for the following groups of parameters.

[1] All details of the electron microprobe analysis including analysis site etc.

[2] All details of the rock sample.

[3] Official nomenclature of amphiboles (Leake, 1978), chlorite (Hey, 1954), feldspar (Deer et al., 1962), pyroxenes (Poldervaart and Hess, 1951), epidote minerals (Deer et al., 1962) and biotites (Deer et al., 1962).

[4] Weight percent of oxides.

[5] Number of cations recalculated for standard, mineral specific number of O and OH.

[6] Calculated mole fractions on crystallographic sites; tetrahedral T1 and T2 sites, octahedral M1, M2 and M3 sites, A-sites and V-sites and assumed values for OH, CO_3 and H_2O sites.

[7] Calculated ideal activities of mineral end-members.

[8] Proportions of the different mineral end-members.

[9] Specific compositional ratios such as Mg/(Mg+Fe) and Al/(Al+Si)

[10] Fe^{3+} is recalculated by charge balance on cations in the following minerals: garnet, pyroxene, spinel, ilmenite and cordierite. Otherwise a fixed proportion of total Fe that is assumed to be Fe^{3+} is based on the typical range in nature (Roger Powell pers. comm., 1989; Cesare et al., 2005). These assumptions are: 100% Fe^{3+} in aluminosilicates, feldspar and epidote minerals, 15% Fe^{3+} in amphiboles and biotite, 10% Fe^{3+} in chlorite and staurolite and 60% Fe^{3+} in muscovite. Muscovite and chlorite are also recalculated assuming 0% Fe^{3+}, because some of the applied conventional geothermobarometers do not account for Fe^{3+}. All chlorite and muscovite analyses are described without any Fe^{3+} assignment.

Garnet Compositional Maps

Qualitative, garnet compositional maps (Ca, Fe, Mg and Mn) from 14 representative samples covering a range of garnet-bearing rock-types in the EYC, was undertaken by Angus Netting at Adelaide Microscopy. The SX51 microprobe was used at a current of 100 nA and voltage of 15 kV, and average spacing between spots was 5 μm. Mg counts were collected on the TAP crystal, Ca on PET crystal and Mn and Fe on LiF crystal. These representative garnet maps are crucial to both the selection of probe sites used in PT calculations in different rock-types and metamorphic grades and the interpretation of PT calculation results (see below). The garnet maps also record an extended period of mineral growth, near the peak of metamorphism, that is useful in documenting the prograde P-T evolution of rock samples that is otherwise lost from the rock record. Garnet compositional maps are presented and described in the Petrography Description section.

WHOLE ROCK ANALYSES METHODOLOGY

Whole rock analyses of typical metapelite and meta-mafic rocks were made for comparison with the bulk composition used to calculate P-T pseudosections in the literature. These analyses have facilitated the selection of appropriate pseudosections for interpreting the petrology of specific samples. Furthermore, characterization of the compositional range of different rock-types in the

EYC, has allowed for selection of general P-T pseudosections from the literature that all other EYC samples can be interpreted within.

New whole rock analyses were undertaken on 30 metapelite and 12 meta-mafic rocks from the EYCMP (Appendix 12). All new whole rock analyses were undertaken using standard XRF techniques at the GA laboratories in Canberra. Total Fe is reported as Fe_2O_3 and FeO was analysed by titrimetry. In addition, an extensive dataset has been compiled of existing whole rock analyses from published EYC metamorphic rocks (Appendix 12). Published analyses include 280 meta-mafic samples, 44 metapelites, 13 calc-pelites, 4 calc-silicates, 7 Fe-rich sediments and 89 quartzo-feldspathic gneisses. An extensive dataset of the bulk composition of published calculated P-T pseudosections has also been compiled (Appendix 12). These include 118 metapelites, 3 quartzo-feldspathic gneisses and 19 mafic compositions. Appendix (12) contains major oxides and trace elements and all analyses have been recalculated for mole fractions in a variety of different chemical systems for comparison to published P-T pseudosections.

PT CALCULATION METHODOLOGY BY THERMOCALC V3.1

Absolute PT conditions from peak metamorphic parageneses have been determined by the statistically robust average PT approach of Powell and Holland (1994) using THERMOCALC v3.1 (Powell and Holland, 1988) with the v3.21 thermodynamic dataset (Powell et al., 1998).

PT calculation experiments using THERMOCALC require as input; [1] activities of the mineral end-members present in what is interpreted to be the equilibrium assemblage and [2] assumptions about the presence and composition of fluid and [3] knowledge on what mineral analysis sites and mineral phases are interpreted to be in equilibrium. The latter is crucial to the application of all PT calculation methods. Establishing likely equilibrium assemblages and the suite of mineral analysis sites that represent this, is drawn from textural interpretation under the microscope, garnet compositional maps and inferences on timing of growth and resorption of the different mineral phases (Spear, 1993).

Non-ideal mineral end-member activities were calculated from mineral analyses by the method of Holland and Powell (1990) using the program AX (Holland et al., 1998). Ideal mineral activities of 1.0 are assumed for sillimanite, kyanite, andalusite, rutile, titanite and quartz. The following P and T assumptions were made to calculate mineral end-member activities in different samples. All typical medium grade samples assume 550 ºC and 4.0 kb, all garnet-bearing or clinopyroxene-bearing amphibolites assume 620 ºC and 6.0 kb and all granulite samples assume 700 ºC and 6.0 kb. Resultant AX output files for different P and T assumptions are contained in Appendix (13).

PT calculation experiments using THERMOCALC have been applied to all possible samples with sufficient mineral end-members. Because the same internally consistent thermodynamic dataset is used for all of these PT calculation experiments the results are considered directly comparable across all samples across the EYC, and between different rock-types and metamorphic grades. For each suite of analysis sites in each sample (see below), average-PT, average-P and average-T calculations were made. In some samples this was an iterative process where suspect mineral end-members identified by high e• values (most with values >2.0 and all with values >2.5) are deleted from subsequent runs. All accepted experimental runs have good statistics with low e* values and all results satisfy the chi-squared test, indicated by the sigfit value being less than the cut off value for 95% confidence. The THERMOCALC thermodynamic dataset has also been used to calculate T using Fe-Mg-exchange between the following mineral pairs; garnet-biotite, garnet-cordierite, orthopyroxene-clinopyroxene, garnet-hornblende, garnet-chlorite, hornblende-clinopyroxene, garnet-clinopyroxene and hornblende-biotite. All output files from THERMOCALC runs are available from Goscombe. All results from THERMOCALC PT calculations are collated in a large database that summarizes; ave-PT results, ave-T results, ave-P results, Fe-Mg-exchange T results, errors, statistics, fluid assumptions, PT assumptions for activity calculations and the mineral end-members used (Appendix 14). Error propagations undertaken by THERMOCALC incorporate both uncertainties on mineral end-member activities and errors on thermodynamic parameters. For all PT

calculations undertaken for the EYCMP (n=575), the average of all errors from individual calculations are ±30 ºC and ±1.0 kb (Appendix 14).

Fluid Assumptions

All THERMOCALC PT calculation experiments require assumptions about the presence or absence of fluid and the fluid composition. For simplicity, all low and medium grade metapelite and amphibolite samples are assumed to have XH_2O=1.0 fluid compositions because dehydration reactions prvail. For low and medium grade samples devoid of carbonate minerals, variation in XH_2O does not effect the PT calculations and assumptions about fluid composition do not constitute a significant variable effecting PT calculations. All samples that contain minor amounts of carbonate are assumed to have XH_2O=XCO_2=0.5 fluid compositions. Assumptions about fluid XCO_2 composition, does greatly affect PT calculation results in carbonate and calc-silicate samples, and consequently both rock-types have been avoided in this study. Upper-amphibolite facies samples (i.e., muscovite-absent and sillimanite ± melt in metapelites and clinopyroxene ± melt in mafics) are assumed to be absent of a fluid phase and a value of aH_2O=0.5 is assumed. Granulite samples (i.e., presence of orthopyroxene) are assumed to be absent of a fluid phase and a value of aH_2O=0.25 is assumed. This estimate is based on independent estimates of aH_2O from granulite facies rocks in the literature (n=40), ranging between 0.1 and 0.5 and averaging 0.27±0.10 (Goscombe, unpublished data). PT calculations in high-grade samples are significantly influenced by aH_2O assumptions and thus all high-grade PT calculations are considered best estimates on a P-T-aH_2O array.

Calculation Assemblages

Different suites of analysis sites are used to calculate either; prograde, peak and post-peak metamorphic conditions in different rock-types. The criteria used to define the different analysis suites and the interpreted metamorphic period they possibly represent, are listed below.

[1] In typical metapelite and some mafic rocks with porphyroblastic garnet, peak metamorphic conditions were derived from garnet rims in conjunction with the cores of matrix feldspar, pyroxene, staurolite and micas (Spear, 1993). Garnet rim analyses were taken from the furthest extent of prograde growth and typically 15-50 μm in from the garnet edge, to avoid post-peak altered garnet compositions due to either re-equilibration or resorption (Spear, 1993; Kohn and Spear, 2000; Goscombe et al., 2005a). Garnet compositional maps and spot analysis profiles across garnets show typical growth zoning patterns and very few samples show re-equilibrated or resorbed margins as indicated by very thin Mn-rich outer rims. An alternative analysis assemblage for extracting peak metamorphic conditions is to use the inner rims of garnet combined with biotite inclusions within matrix quartz or feldspar and the cores of other matrix minerals (Donohue and Essene, 2005).

[2] Attempts were made to calculate post-peak metamorphic conditions in porphyroblastic samples using the re-equilibrated compositions in the outer-most garnet rims in conjunction with rim analyses in the matrix phases. If in equilibrium, these PT calculations possibly represent either reworking during a second metamorphic event or some arbitrary point in the evolution of retrograde re-equilibration between minerals.

[3] Attempts were made to calculate metamorphic conditions during mylonitization or enveloping reworking foliation development. In reworked samples containing relict porphyroclasts, peak reworking conditions were calculated using the re-equilibrated compositions in the outer-most garnet porphyroclast rims in conjunction with core analyses from phases in the enveloping fabric. Core analyses from relict porphyroclast assemblages were used in an attempt to calculate the pre-mylonitization peak metamorphic conditions. Calculations from reworking assemblages were often in equilibrium giving reliable and accurate results. However, pre-mylonitization parageneses were typically not in equilibrium and PT calculations were unsuccessful.

[4] Mineral phases in mafic and calc-silicate samples with polygonal granoblastic matrix textures, high-grade gneissic samples and granulite samples, all show little or no core to rim compositional zoning. At low and medium metamorphic grades these textures are interpreted to indicate that all phases grew in equilibrium. Consequently, core analyses were used to calculate peak metamorphic

conditions, to avoid any retrograde re-equilibration effects at grain margins. At high metamorphic grades, mineral compositions are typically homogenised at, or immediately after, the peak of metamorphism (Tuccillo et al., 1990; Spear, 1993; Goscombe et al., 1998, 2003, 2005a; Goscombe and Hand, 2000). At very high metamorphic grades, adjacent grains continued to re-equilibrate during post-peak cooling until closure of cation exchange (Frost and Chako, 1989). Consequently, peak metamorphic conditions in high-grade samples are best represented by analyses from the inner portion of mineral grains, away from the effects of post-peak mineral re-equilibration. Core PT calculations at best represent peak metamorphic conditions or more likely, conditions at some stage during post-peak re-equilibration and so are best considered minimum estimates of the peak. Garnet compositional maps of high-grade samples show that re-equilibration is predictably concentrated at grain margins but can also be highly irregular due to crystallographic heterogeneity, strain and fractures. Consequently, in the absence of mineral compositional maps, finding primary compositional domains is hit and miss in some samples, and PT calculations can give anomalously low results (Goscombe et al., 1998; Goscombe and Hand, 2000). Attempts to document post-peak metamorphic conditions, and thus constrain a portion of the retrograde P-T path, have been made using re-equilibrated rim analyses for PT calculations.

[5] The conditions of formation of symplectite assemblages were calculated using the cores of symplectite phases in conjunction with the outer-most re-equilibrated rims of the reactant primary phases.

[6] Attempts have been made to document conditions at an arbitrary stage in the prograde evolution using PT calculations from inclusion assemblages. Garnet core analyses are used in conjunction with inclusion core analyses, to avoid re-equilibration effects at grain margins. In most cases the PT results have large errors suggesting the suite of analyses are not in equilibrium.

[7] Further attempts to document prograde conditions have been made using garnet porphyroblast core analyses to estimate PT conditions at the time of initiation of garnet growth. Metapelite garnet core analyses (n=39) have been plotted on PT pseudosections with garnet compositional isopleths for both general metapelite (Spear, 1993) and a sample specific metapelite composition (Gaidies et al., 2006). Results are only considered estimates because the garnet isopleths have been calculated for typical metapelite compositions that may not closely resemble the bulk composition of all EYCMP samples. Nevertheless, most samples give plausible results with T-estimates invariably lower than calculated peak metamorphic conditions. Prograde P-estimates by this method give results similar to peak metamorphic conditions or 1.0-3.0kb higher, suggesting a possible over-estimation of prograde pressures in some samples.

High-Grade Samples

PT calculations from samples of low and medium metamorphic grade, are largely independent of assumptions about fluid composition and largely free of re-equilibration effects, and thus considered generally reliable. In contrast, PT calculations from high grade samples must consider the additional variable of aH_2O and have the potential for mineral re-equilibration, resorption and cation exchange resulting in deleterious effects on PT calculations (Frost and Chako, 1989; Goscombe et al., 1998: Kohn and Spear, 2000). Consequently, PT calculations from high-grade samples must be treated with circumspect and if not representative of the real conditions are most plausibly minimum estimates. PT calculations have been tested against the stability field of the matrix assemblage (Appendix 8) and all correlate within errors, and are thus considered plausible estimates of the equilibration conditions.

Final Best-Considered PT Loci

For the purpose of building up a quantitative database of peak metamorphic conditions at localities across the whole EYC: the following method was employed to establish the best-considered PT conditions for each sample (Appendix 15). The complete suite of PT calculation results available for each sample, including ave-PT, ave-P, ave-T, Fe-Mg-exchange thermometry, garnet core compositional isopleths and a range of conventional thermobarometers (see below), were plotted together and the intersections used as the basis for the best-considered results for each sample.

THERMOCALC results are considered the most reliable and ave-PT, ave-P and ave-P results are generally mutually supportive. Conventional thermobarometry has been used in two ways: [1] to independently verify the THERMOCALC results, and [2] to constrain the best-considered PT conditions only where insufficient mineral end-members were available to calculate both P and T by THERMOCALC. This process of plotting all results also identifies samples where ave-P and ave-T arrays intersect at very acute angles, resulting in inaccurate intersection constraints such as very high P results as an artefact. The application and reliability of individual conventional thermobarometers are discussed in detail below. All best-considered PT estimates have been used to calculate the temperature/depth ratio (G in ºC/km), which is defined simply as the ratio temperature/depth ratio assuming an average rock density of 2.8 g/cm^3.

Best-considered PT loci from the different mineral parageneses represented in a single sample; prograde, peak, post-peak and retrograde (Appendix 15), have been used to put constraints on the P-T evolution of the sample (Appendix 7). Because of the error range on individual PT calculations and the potential for mineral re-equilibration and other deleterious effects on these calculations, using PT calculations to document P-T trajectories can only be considered preliminary. Where possible, reliable P-T paths need to be documented from petrological analysis involving the reconstruction of the SMG (Appendix 8) and interpretation within an appropriate P-T pseudosection (see below).

PT CALCULATION METHODOLOGY BY CONVENTIONAL THERMOBAROMETRY

Because of low metamorphic grades and simple metamorphic assemblages, many samples have an insufficient number of mineral end-members to write enough independent reactions to give results in THERMOCALC. Consequently, a wide range of conventional thermometers and barometers covering the wide diversity of assemblages in the EYC, have been applied to the entire mineral analyses database (Appendix 11). Of the many resulting calculations covering many different samples, very few of the results have been used in constraining the best-considered PT loci inputted into the MDB. The different conventional thermobarometers and calibrations that have been used are listed below and all results are tabulated in Appendix (16). For mineral pairs in equilibrium, the errors on most conventional thermometers and barometer calibrations are approximately ±25 ºC and 0.5 kb.

The MDB has also drawn upon previous PT estimates in the literature from across all terranes in the Yilgarn Craton. These have been primarily derived from phase stability constraints and also a large range of conventional thermobarometers. Geothermometer calibrations that have been applied in literature are; garnet-biotite (Thompson, 1976; Ferry and Spear, 1978; Hodges and Spear, 1982; Newton and Haselton, 1981; Indares and Martignole, 1985), chlorite thermometry (Cathelineau and Nieva, 1985; Cathelineau, 1988), carbonate thermometry (Powell et al., 1984), plagioclase-hornblende (Spear, 1981a; Blundy and Holland, 1990), garnet-chlorite, δO^{18} for calcite-quartz and quartz-magnetite pairs, garnet-hornblende, orthopyroxene-clinopyroxene, olivine-orthopyroxene thermometry and garnet-cordierite (Perchuk and Lavrent'eva, 1983). Geobarometer calibrations that have been applied are sphalerite barometry, hornblende-plagioclase-epidote and garnet-cordierite (Currie, 1971; Wells, 1977; Lonker, 1981; Martignole and Sisi, 1981).

Mono-Mineral Geobarometers and Geothermometers

Total Al-in hornblende geobarometer (Schmidt, 1992) has been empirically calibrated for granodiorite bulk compositions and offers the only method for estimating crustal depth during crystallization of granitoids in the EYC. This geobarometer has been applied to 18 samples. Individual errors are approximately ±0.6 kb, which was reduced in individual samples by pooling multiple results. Hornblendes in amphibolite bulk compositions have been empirically calibrated for the correlation between pressure and Al^{6+}, total Al and Si cations (Spear, 1981b). These empirical geobarometers have been applied to approximately 100 samples, and pooled results give P estimates that are reasonable and are often the only available P estimate for a sample. The phengite (Si) content in white mica geobarometer of Massonne and Schreyer (1987) has been applied to 23 white mica-bearing parageneses. This geobarometer requires an independent estimate of T and most of the

results appear to be reasonable or under-estimate pressures. Al^{4+} and vacant-site chlorite geothermometer calibrations of Cathelineau and Nieva (1985) and Cathelineau (1988) have been applied to low-grade retrograde and alteration parageneses. The chlorite, calcite, biotite-muscovite and biotite-chlorite geothermometers have been the primary constraints on T estimates for late-stage retrogression and alteration.

Solvus Geothermometers

The geothermometer based on Ca-Mg partitioning in calcite with coexisting dolomite (Powell et al., 1984) has been widely applied to low-grade retrograde and alteration parageneses. The Ca-Mg partitioning between coexisting orthopyroxene and clinopyroxene thermometer (Brey and Kohler, 1990; Nickelm and Brey, 1984) has been applied to 3 samples with results similar to THERMOCALC.

Exchange Geothermometers

Calibrations of Fe-Mg exchange geothermometers that have been applied are: garnet-clinopyroxene (Ellis and Green, 1979), garnet-muscovite Fe and Mg calibrations (Green and Hellman, 1982; Hynes and Forrest, 1988), garnet-ilmenite (Pownceby et al., 1991), garnet-cordierite (Perchuk, 1985), clinopyroxene-ilmenite (Bishop, 1980) and hornblende-clinopyroxene and hornblende-orthopyroxene (Perchuk, 1985). The number of samples with assemblages suitable for the application of each geothermometer is low (between 1 and 17), but where applied, all except garnet-ilmenite give reasonable results that confirm THERMOCALC results. Biotite-muscovite (Hoisch, 1989), biotite-chlorite (Laird, 1989) and tourmaline-biotite (Colopietro and Friberg, 1987) thermometers have been applied to a few (7, 10, 3 respectively) low-grade schist samples and all give results approximately 25ºC lower than expected. The conventional garnet-biotite geothermometer (i.e., Ferry and Spear, 1978) has not been universally applied because T calculations by Fe-Mg exchange from this mineral pair have been undertaken using THERMOCALC (see above).

Net Transfer Equilibria Geobarometers and Geothermometers

Net transfer geobarometers were applied to a large range of assemblages listed below. The clinopyroxene-plagioclase barometer (Rollinson, 1981; Holland, 1980) was applied to 16 samples with reasonable results from most samples. Garnet-cordierite barometers (Thompson, 1976; Bhattacharya, 1986) were applied to 10 samples with only half giving reasonable results. Both Fe and Mg calibrations of the garnet-hornblende-plagioclase barometer (Kohn and Spear, 1990), was applied to 11 samples and gave very reasonable results in most samples. The garnet-clinopyroxene-plagioclase (Ghent et al., 1983) and biotite-muscovite-chlorite (Powell and Evans, 1983) barometers were applied to only one sample each with reasonable results. The net transfer hornblende-chlorite-epidote-albite-quartz thermobarometer (Triboulet, 1992) was applied to 3 samples, all with very reasonable results. Different calibrations of the hornblende-plagioclase net transfer thermometer have been applied to approximately 80 samples (Spear, 1981a; Holland and Blundy, 1994). Both the edenite-tremolite and edenite-riebeckite calibrations were calculated using the program HBPLAG (Holland and Blundy, 1997) and the results are typically 10-50ºC higher than expected. Hornblende-plagioclase thermometry results have been used to constrain the best-considered PT loci in many samples because this method offers the only T constraint in simple amphibolite assemblages. The Ca-in orthopyroxene thermometer (Brey and Kohler, 1990) has been applied to 1 high-grade ultramafic sample with reasonable results.

FLUID INCLUSION PT ESTIMATES

PT estimates from the lowest grade parageneses and domains, such as alteration assemblages and the broad low-grade domains in the cores of greenstone belts, are very difficult to determine because the assemblages developed are generally not suitable for THERMOCALC or conventional PT calculations. Illite crystallinity studies may be applicable to rocks metamorphosed below 400 ºC, but has not been applied in the Yilgarn Craton. Otherwise low-grade PT estimates are best made by fluid inclusion studies, assuming that the P results reflect lithostatic pressures and that the temperatures of

the entrapped fluids were thermally buffered by the rock mass and represent ambient T conditions. Numerous fluid inclusion studies have been undertaken in the Yilgarn Craton (Henderson, 1981; Woad, 1981; Ho, 1986; Scantlebury, 1983; Allen, 1987; Clark et al., 1989; Bennett, 1989; Jurasky, 1989; Clark, 1980; Skwarnecki, 1990; Ho et al., 1990; Bloem, 1994; Ojala, 1995; Mikucki, 1997; Duuring, 2002; Hodges, 2007). All are from vein events associated with alteration, within mineral deposits and represent the conditions of different episodes of alteration. All known fluid inclusion based PT estimates and fluid compositions, in the different alteration episodes documented at each mine site, have been collated in the MDB (n = ~130). A few studies (i.e., Hodges, 2007) have documented a sufficient number of sequential veining events at a specific locality to constrain a portion of the P-T path the rock mass evolved through.

PHASE STABILITY CONSTRAINTS ON PT CONDITIONS

The best-considered PT loci were constrained in a very select number of samples with assemblages not suitable for PT calculations, but diagnostic of a restricted range in P-T space. For example: pumpellyite (350 ºC, 4.0 kb), pyrophyllite-paragonite-kyanite (380 ºC, 3.0 kb), chlorite-paragonite-chloritoid-kyanite (≤490 ºC, >3 kb approximating 4.2 kb), biotite-muscovite-kyanite (550 ºC, ~5.0 kb), andalusite-kyanite-muscovite±biotite (480 ºC, 3.5 kb), andalusite-sillimanite-kyanite-muscovite±biotite (500 ºC, 4.0 kb), sillimanite-kyanite-muscovite-biotite (600 ºC, 6.5 kb), andalusite-chloritoid (≤480 ºC, 3.0 kb), garnet-biotite-plagioclase-K-feldspar migmatitic gneiss (680 ºC, 5.0 kb) assemblages. Other seemingly diagnostic assemblages were not used to constrain PT loci for the following reasons. Garnet-bearing or epidote-bearing amphibolite and calc-silicate assemblages are strongly influenced by both bulk composition and fluid composition. Similarly the presence of diagnostic minerals may be controlled by trace components, such as MnO stabilization of garnet and ZnO stabilization of staurolite in metapelites.

METHODOLOGY OF DETERMINING P-T PATHS OF METAMORPHIC EVOLUTION

Bulk Composition Comparisons

A range of whole rock samples from the EYC were analysed for major oxides at the GA laboratories. These analyses have been recalculated for mole fractions in a range of different chemical systems and compiled along with all available whole rock analyses from metamorphic rocks in the Yilgarn Craton available in literature and GSWA and GA datasets (Appendix 12). A comparison of all available whole-rock analyses from metamorphic rocks in the EYC and bulk compositions used to calculate published P-T pseudosections are contained in Figures 39 to 46. Mafic, calc-silicate and quartzo-feldspathic samples are compared in ACF and Al_2O_3 – CaO - (FeO+MnO+MgO) diagrams. Metapelite, calc-pelite and meta-psammopelite samples are projected from muscovite and compared in AFM and Al_2O_3-FeO-MgO diagrams. This comparison is used to select the appropriate pseudosection for interpreting the petrology of EYC metamorphic samples.

All whole rock analyses cluster strongly by rock-type when plotted in ACF (Figures 39 to 41). In particular all EYC mafic analyses cluster centrally, near hornblende, in the plagioclase-garnet-orthopyroxene-clinopyroxene field. These samples are equally distributed either side of the hornblende-plagioclase and garnet-clinopyroxene tielines (Figure 40). The available published pseudosections for mafic rocks cover this same broad range of bulk compositions (Figure 43). Consequently, a set of pseudosections has been chosen to represent compositional clusters in the EYC mafic dataset, separated by hornblende-plagioclase, garnet-clinopyroxene, clinopyroxene-hornblende, hornblende-actinolite and hornblende-biotite tielines (Figure 42). All quartzo-feldspathic rocks plot in the K-feldspar-plagioclase-hornblende field, with many of these in the plagioclase-hornblende-garnet field (Figure 39). Almost all pelite and psammopelite rocks plot in the Al_2SiO_5-garnet-biotite field, with a portion below the garnet-biotite tieline (Figure 41).

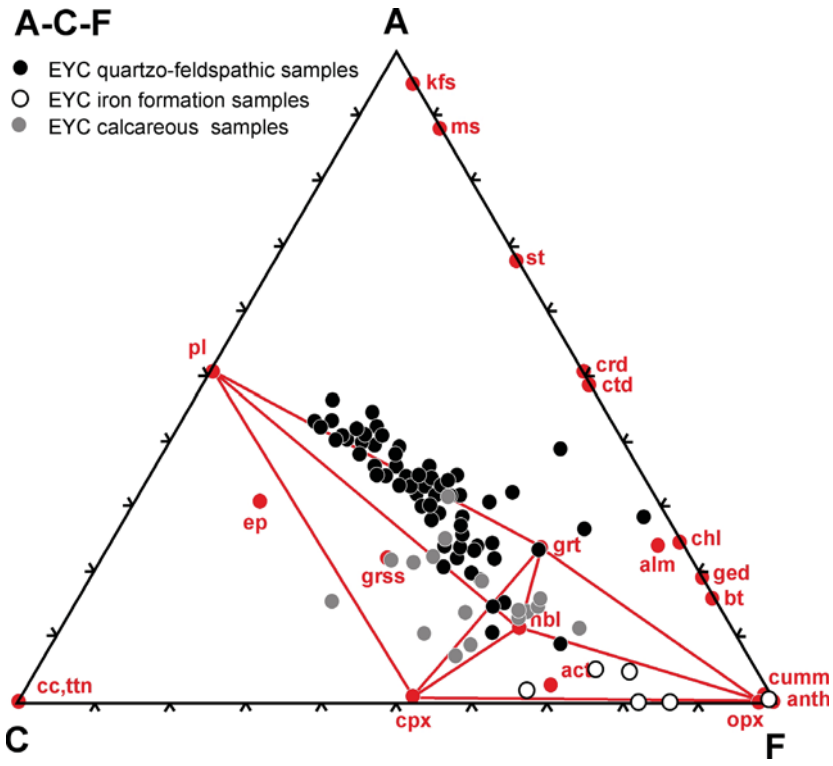

Figure 39: *Bulk compositions of samples of quartzo-feldspathic, calcsilicate and iron formation rocks from the EYC, plotted in ACF space.*

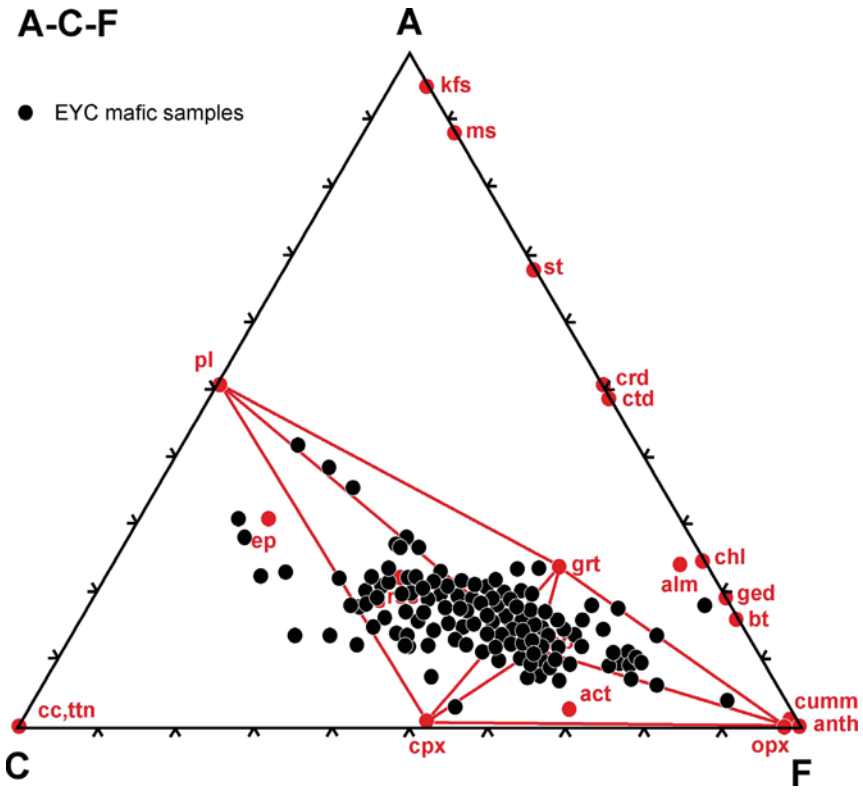

Figure 40: *Bulk compositions of mafic samples from the EYC, plotted in ACF space.*

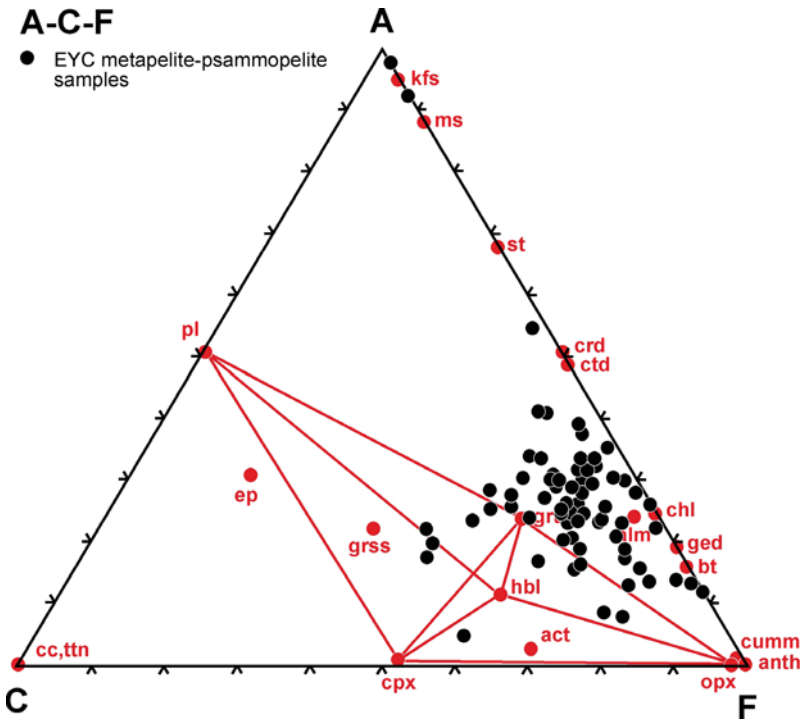

Figure 41: *Bulk compositions of metapelite and psammopelite samples from the EYC, plotted in ACF space.*

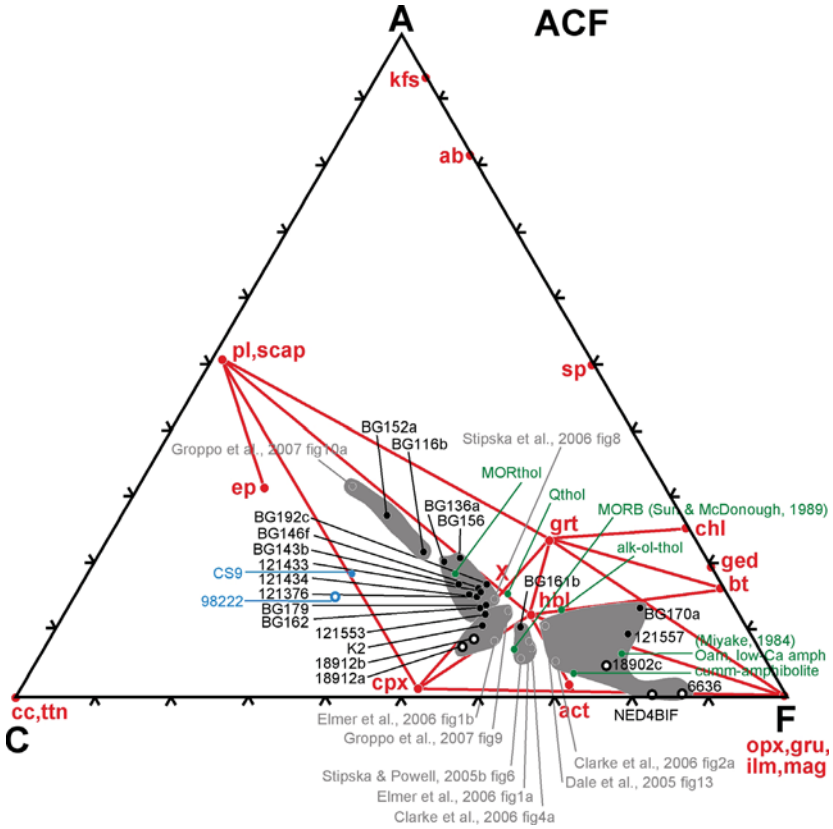

Figure 42: *Groupings of similar mafic samples in ACF, and the published P-T pseudosections used to interpret the petrology of the samples in each grouping.*

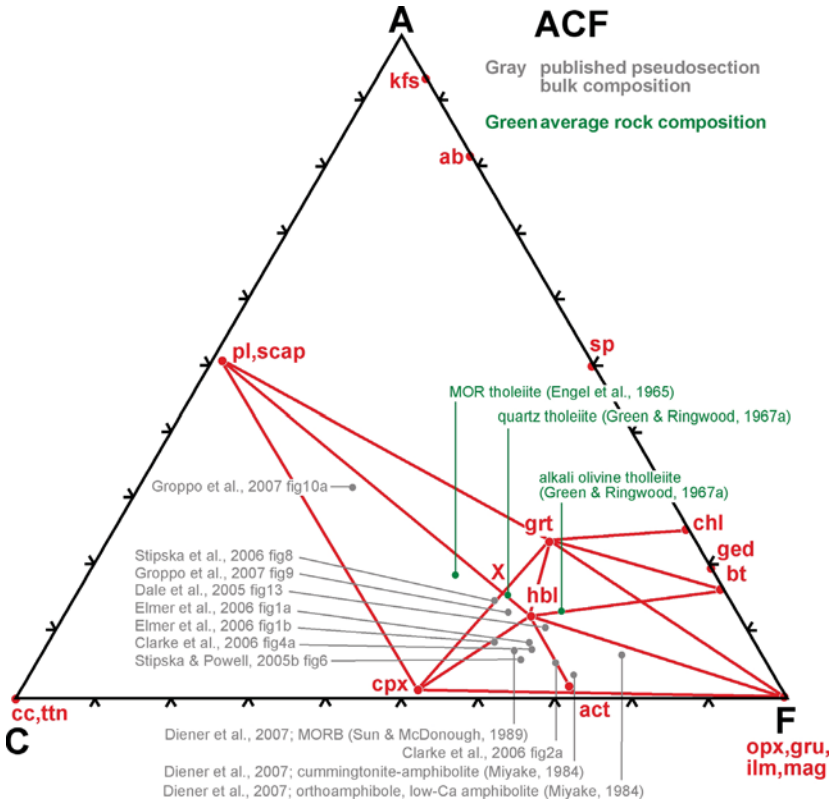

Figure 43: *Published P-T pseudosections and average mafic bulk compositions in literature, plotted in ACF.*

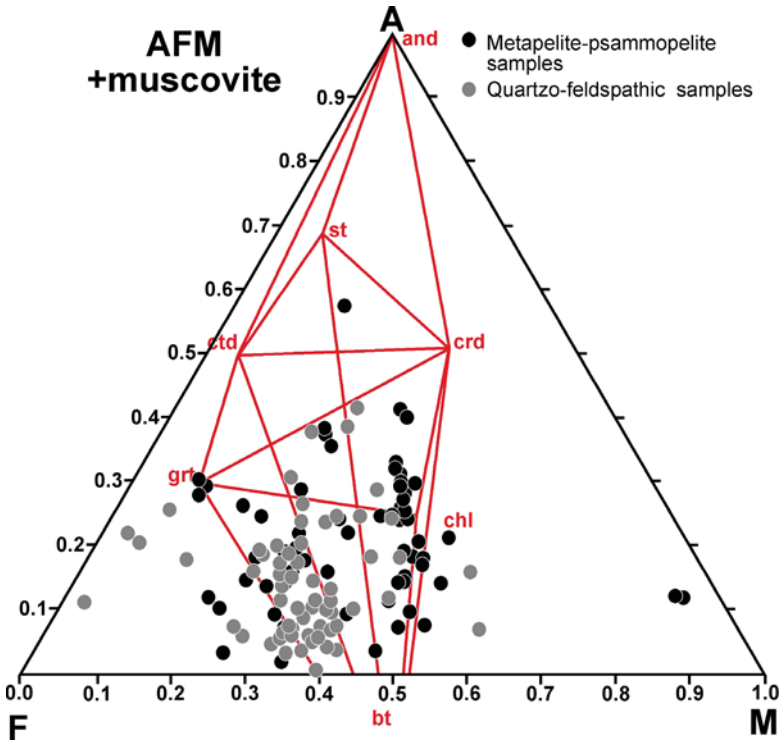

Figure 44: *Bulk compositions of metapelite, psammopelite and quartzo-feldspathic samples from the EYC, plotted in AFM space.*

Both quartzo-feldspathic and pelite-psammopelite rocks in the EYC have wide compositional variation in AFM (Figure 44). Fortunately, published pseudosections cover an equally large range of bulk compositions (Figure 46). Pseudosection have been chosen that represent different clusters of analyses and compositional fields in AFM (Figure 45). Fields of decreasing Al_2O_3 contents are separated by the chloritoid-cordierite, garnet-cordierite and garnet-chlorite tielines. Similarly fields of increasing XMg are separated by garnet-biotite, chloritoid-biotite, staurolite-biotite and cordierite-biotite tielines (Figure 45).

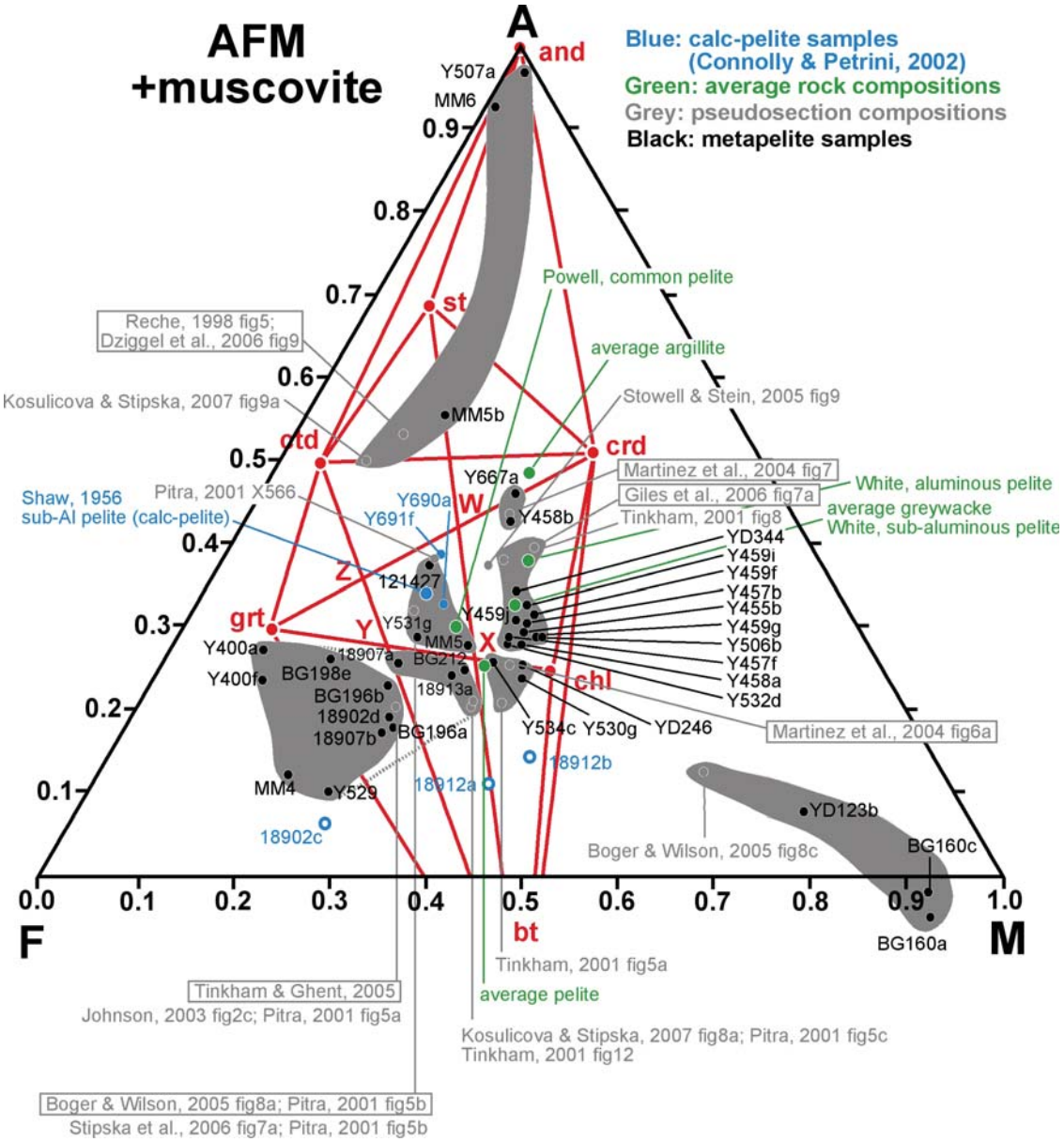

Figure 45: *Groupings of similar metapelite and psammopelite samples in AFM, and the published P-T pseudosections used to interpret the petrology of the samples in each grouping.*

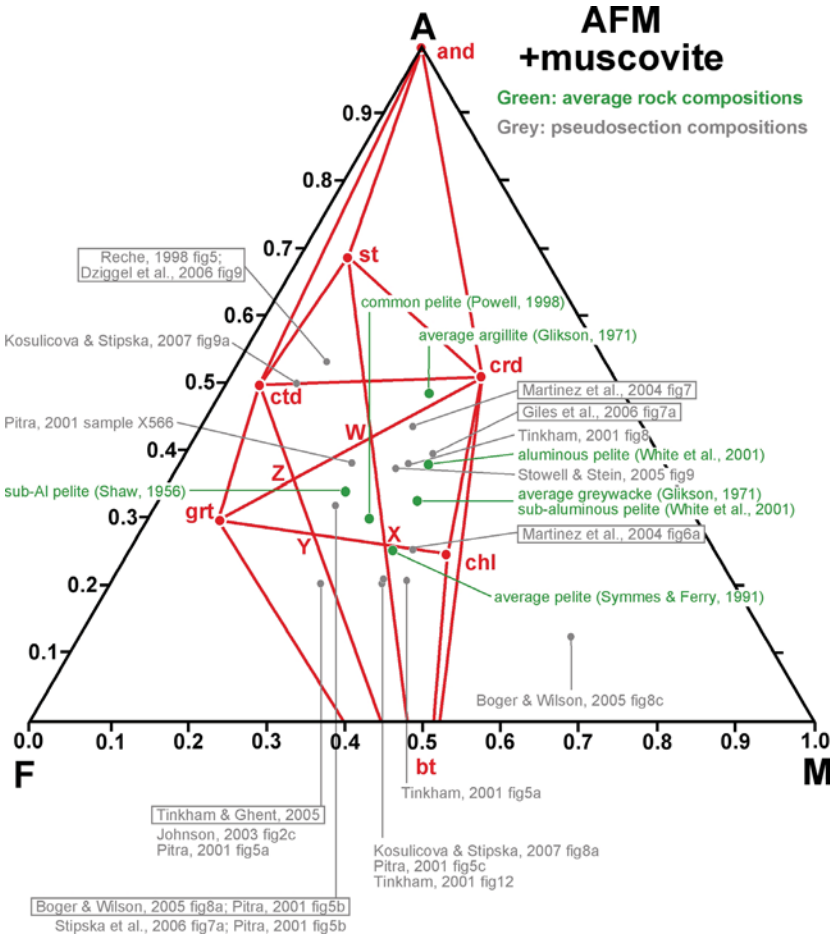

Figure 46: *Published average rock compositions and P-T pseudosections for metapelite and psammopelite bulk compositions, plotted in AFM.*

PT Pseudosections Used

A comprehensive library of the utilised calculated P-T pseudosections that are appropriate for EYCMP samples are not presented here, but are available in Appendix 5 and figures are labelled with the prefix - ps. The bulk composition used to calculate each pseudosection is compared with analysed EYC samples (see above). Rock samples with similar bulk compositions to the pseudosection are listed on each model pseudosection in the library. Typically the difference in composition is only 1-5%, with a few as high as 10% between sample and model compositions. All interpreted samples are on the correct side of key tielines in AFM space (for pelite samples) and ACF space (for mafic samples). Consequently, the topology of the selected model pseudosection will be very similar to a pseudosection calculated specifically for each sample. The selected model pseudosections are used to interpret the evolving mineral parageneses in each sample, to constrain both peak metamorphic conditions and P-T paths (Appendix 7). P-T path interpretations are based on petrology, sequence of mineral growth and diagnostic assemblages. Circles in the pseudosections are recognised mineral parageneses. Crosses are PT calculations by different methods, with typical errors of ±25ºC and ±0.5kb.

Mafic samples have been interpreted in P-T pseudosections for NCFMASH±K space, based on low-Al and high-Mg+Fe mid-ocean ridge basalt bulk compositions (Figures ps1, ps6 in Appendix 5; Clarke et al., 2006; Stipska and Powell, 2005; Dale et al., 2005) and low-Al and moderate-Mg+Fe ocean island basalt bulk compositions (Figures ps2, ps7, ps8 in Appendix 5; Clarke et al., 2006; Stipska and Powell, 2005; Elmer et al., 2006; Stipska et al., 2006). High-grade mafic samples have been interpreted in P-T pseudosections for NCKFMASHTO space, based on low-Al and moderate-

Mg+Fe bulk compositions (Figure ps9 in Appendix 5; Elmer et al., 2006; Groppo et al., 2007) and high-Al and low-Mg+Fe ocean island basalt bulk compositions (Figure ps10 in Appendix 5; Groppo et al., 2007). A range of general composite pseudosections in NCFMASH and NCFMASHTO for mafics, have been used where the bulk composition of the sample is unknown (Figures ps34, ps35, ps37, ps38 in Appendix 5). These include low-Al, moderate-Fe compositions (Diener et al., 2007), and low-Al, low-Fe compositions (Diener et al., 2007; Elmer et al., 2006; Groppo et al., 2007; Clarke et al., 2006). A composite pseudosection for diagnostic mineral fields covering all of P-T space has been constructed for typical tholeiite bulk compositions (Figure ps30 in Appendix 5). This general mafic grid is based on pseudosections and metamorphic reactions from many sources (Thompson, 1971; Liou et al., 1971; Liou, 1971a, b, c; Perkins et al., 1980; Spear, 1993; El-Shazly, 1994; Liou, 1973; Liou et al., 1974; Apted and Liou, 1983; Zeh et al., 2005; Ballevre et al., 2003; Carson et al., 1999; Marmo et al., 2002; Wei and Powell, 2003; Spear, 1981b; Patterson, 2003; Yang and Indares, 2005; Ringwood, 1975; Green and Ringwood, 1972; Jamieson, 1981; Ollafsson and Eggler, 1983; Nicollet and Goncalves, 2005; Wyllie and Wolf, 1993; Nair and Chacko, 2000; Green and Ringwood, 1967; Ito and Kennedy, 1971; Cohen et al., 1967). A composite grid for mafic bulk compositions that contain grunerite (Figures ps11, ps39 in Appendix 5) is based on a theoretical petrogenetic grid in CFMASH (Zeh et al., 2005) and those with cummingtonite (Figure ps36 in Appendix5) is based on a pseudosection in NCFMASHTO (Diener et al. 2007).

Pelite samples have been interpreted in P-T pseudosections for NCKFMASH±Mn±Ti space, based on high-Fe bulk compositions above the garnet-chlorite tieline in AFM (Figures ps12, ps23 in Appendix 5; Boger and Wilson, 2005; Kolulicova and Stipska, 2007; Stipska et al., 2006; Pitra and De Waal, 2001), high-Fe bulk compositions below the garnet-chlorite tieline (Figures ps17, ps18, ps22, ps26, ps27 in Appendix 5; Johnson et al., 2003; Kosulicova and Stipska, 2007; Pitra and De Waal, 2001; Tinkham et al., 2001; Tinkham and Ghent, 2005), low-Fe bulk compositions below the garnet-chlorite tieline (Figures ps13, ps20, ps24 in Appendix 5; Boger and Wilson, 2005; Martinez et al., 2004; Tinkham et al., 2001) and low-Fe bulk compositions above the garnet-chlorite tieline (Figures ps16, ps21, ps25 in Appendix 5; Giles et al., 2006; Martinez et al., 2004; Tinkham et al., 2001). The Fe-rich, sub-aluminous pelite pseudosection (Figure ps27 in Appendix 5; Tinkham and Ghent, 2005) is used as the general pseudosection for metapelites for which the bulk composition is not known. A composite pseudosection for diagnostic mineral fields covering all of P-T space has been constructed for typical pelite bulk compositions (Figure ps29 in Appendix 5). This general pelite grid is based on pseudosections and reactions from many sources (Cartwright and Buick, 1995; Chatterjee et al., 1984; Spear and Cheney, 1989; Wei and Powell, 2003, Wei et al., 2004; Proyer, 2003; Tinkham et al., 2001; Johnson et al., 2003; White et al., 2001; Kelsey et al., 2003; Powell and Holland, 1990).

Calc-pelite samples have been interpreted in a P-T pseudosection for NCKFMASH space (Figure ps14 in Appendix 5; Connolly and Petrini, 2002). Quartzo-feldspathic felsic bulk compositions that contain garnet are interpreted in a pseudosection constructed for high-grade metapelite (Figure ps28 in Appendix 5; White et al., 2001) and a theoretical petrogenetic grid in MnNCKFMASH space (Figure ps26 in Appendix 5; Stowell and Stein, 2005). A composite grid for diagnostic mineral fields covering all of P-T space has been constructed for highly aluminous altered bulk compositions appropriate for cordierite-anthophyllite rocks (Figure ps31 in Appendix 5). This general grid is based on published metamorphic reactions and petrogenetic grids (Spear, 1993; Spear and Rumble, 1986). Highly aluminous rocks are interpreted within P-T pseudosections for MnKFMASH, based on low-Fe bulk compositions above the chloritoid-cordierite tieline (Figure ps15 in Appendix 5; Dziggle et al., 2006; Reche, 1998) and for NCKFMASH, based on high-Fe bulk compositions above the chloritoid-cordierite tieline (Figure ps19 in Appendix 5; Kosulicova and Stipska, 2007). A composite grid for diagnostic mineral fields covering all of P-T space and T-XCO_2 space has been constructed for calc-silicate bulk compositions (Figure ps32 in Appendix 5). This general grid is based on metamorphic reactions and petrogenetic grids from many sources (Spear, 1993; Brunsmann et al., 2000; Ghent et al., 1979; Harley and Buick, 1992; Fitzsimons and Harley, 1994; Ernst, 1966; Ghent, 1988; Begin, 1992; Liou et al., 1983; Schiffman and Liou, 1983; Bevins and Merriman, 1988; Nitsch, 1971; Chatterjee et al., 1984; Wones, 1989; Bassias and Triboulet, 1992; Spear, 1993).

Metamorphic Description

PETROGRAPHY

Below are representative descriptions of samples covering the spectrum of rock types collected and studied for the EYCMP. More complete descriptions including sample specific data, of all described samples (n=~480) are contained in site-specific data sheets within Appendix (7). The samples that were selected for intensive analysis and description in the EYCMP are not comprehensive of all rock-types (i.e., calc-silicates, felsics and ultramafics not described) and not comprehensive of all metamorphic grades (i.e., greenschist and lower grades are largely not described). Only a very select number of samples from the Southern Cross Terrane have been described for comparison, a more comprehensive description of samples from regions west of the Ida Fault will be presented in Phase-2 of the EYCMP. The descriptions below are supported by representative microphotographs, field photos and garnet maps. Also see Appendix (8) for detailed petrology descriptions and table of petrology. All available microphotographs, field photographs and garnet compositional maps are contained in Appendix (7). SMG indicates the sequence of mineral growth recognised in the sample and all mineral abbreviations are after Kretz (1983).

Mafic Rocks

High-P Clinopyroxene-Amphibolite Mafics

Upper amphibolite facies zones are invariably highly strained, though subsequently annealed, and partially reworked by lower-grade schists indicating high-grade relicts in lower grade shear zones. Consequently, two metamorphic events are recognised in high-grade amphibolite gneisses. M1 parageneses are represented by porphyroblasts and coarse-grained granoblastic hornblende, clinopyroxene, garnet and plagioclase. M2 parageneses are represented by the enveloping schistose to aligned granoblastic hornblende-plagioclase matrix. Foliated matrix minerals may be in equilibrium with re-equilibrated outer rims of the porphyroblastic phases.

Sample BG6-178b: Medium-grained clinopyroxene amphibolite gneiss from Ora Banda Domain in the Kalgoorlie Terrane. Medium-grained granoblastic gneissic matrix assemblage consists of quartz – labradorite – green ferroan pargasitic hornblende – salite clinopyroxene (Figure 47c, d). Epidote occurs as coronas around quartz near hornblende.

SMG: hbl-pl-qtz-cpx > ep

Sample BG6-105a: Sheared clinopyroxene amphibolite from Murrin Domain in the Kurnalpi Terrane. Sample contains coarse K-feldspar – clinopyroxene – green hornblende – pyrite augen-shaped porphyroclasts up to 8 mm long. A very fine-grained, foliated matrix assemblage of quartz – plagioclase – grunerite – pale green actinolite – apatite envelops the porphyroclasts. Early clinopyroxene is partially replaced by actinolite and early hornblende by actinolitic hornblende. Relationships suggest a high-grade metamorphic assemblage downgraded in a second metamorphic event accompanying deformation.

SMG: hbl-cpx-kfs-py > qtz-pl-gru-act-act/hbl-ap

Sample Y280: Clinopyroxene-amphibolite gneiss from Laverton Domain in the Kurnalpi Terrane. Medium-grained polygonal granoblastic matrix with weak grain-shape alignment, has matrix assemblage of quartz? – zoned andesine – green edenitic hornblende – pale green salite clinopyroxene – rutile? - apatite - zircon. Epidote occurs as coronas on hornblende (Figure 47a).

SMG: hbl-pl-qtz?-cpx-rt?-ap-zrn > ep

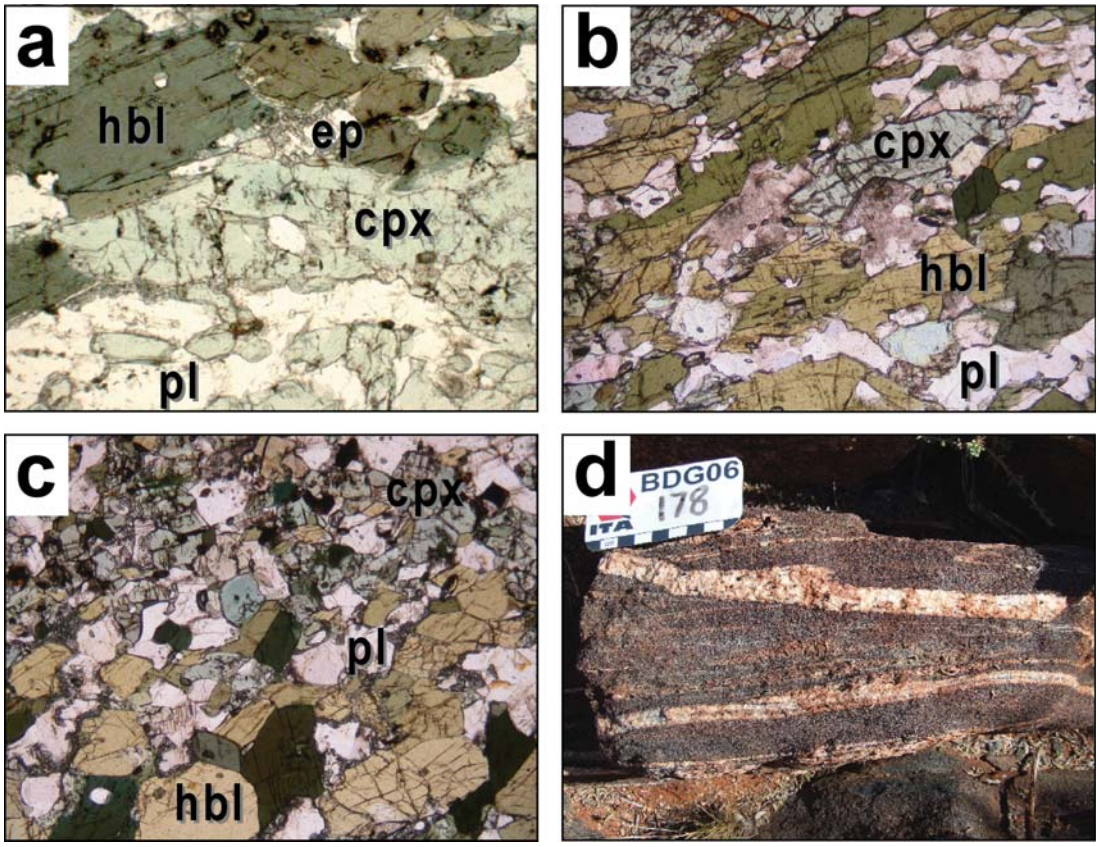

Figure 47: *Mineral textures in high-P clinopyroxene amphibolites. (a) Aligned coarse-grained polygonal granoblastic matrix with thin partial coronas of late-stage epidote (Y280; x2.5 ppl). (b) Aligned coarse-grained polygonal granoblastic matrix (BG6-159k; x5 ppl). (c) Gneissic banding defined by clinopyroxene proportions in polygonal granoblastic matrix (BG6-178b; x5 ppl). (d) Gneissic banding defined by variation in clinopyroxene/hornblende proportions and felsic layers. Note discordant low-angle granite vein (BG6-178).*

High-P Garnet-Amphibolite Mafics

Sample Y0360: Medium-grained garnet-hornblende-quartz amphibolite selvedge adjacent to granite. Sample collected by Kevin Cassidy in WMC drill core from the Laverton Domain in the Kurnalpi Terrane. All phases are in textural equilibrium within a polygonal granoblastic texture (Figure 48a). Matrix assemblage consists of quartz, biotite, garnet, magnetite, hematite, Mn-ilmenite, blue-green ferro-pargasite, chalcopyrite, titanite and calcite. Garnet porphyroblasts are syn-kinematic? and up to 6 mm in diameter. Inclusions within garnet include calcite, hornblende, ilmenite, hematite, magnetite and biotite.

SMG: cc-hbl-ilm-hem-mag-bt inclusions > grt-hbl-qtz-bt-mag-hem-ilm-cpy-cc-ttn

Sample Y0361: Medium-grained garnet amphibolite collected by Kevin Cassidy in WMC drill core from the Laverton Domain in the Kurnalpi Terrane. Aligned polygonal granoblastic matrix assemblage consists of quartz – biotite – ferro-hornblende – rutile? – titanite - pyrite. The matrix is layered as hornblende-rich versus biotite-rich bands. There are two episodes of post-kinematic garnet porphyroblast growth (Figure 48b, c, d). Garnet1 occurs as medium sized (2.5 mm diameter) poikiloblasts with inclusion trails and grew across the main foliation. Garnet2 occurs as small idioblastic porphyroblasts across main foliation biotite. There is minor resorption of some garnet margins. Epidote occurs as both a porphyroblastic phase and as coronas around titanite. Both settings of epidote growth post-date the matrix assemblage ad may be coeval with garnet1 growth.

SMG: hbl-bt-qtz-rt?-ttn-py > grt1-ep > grt2

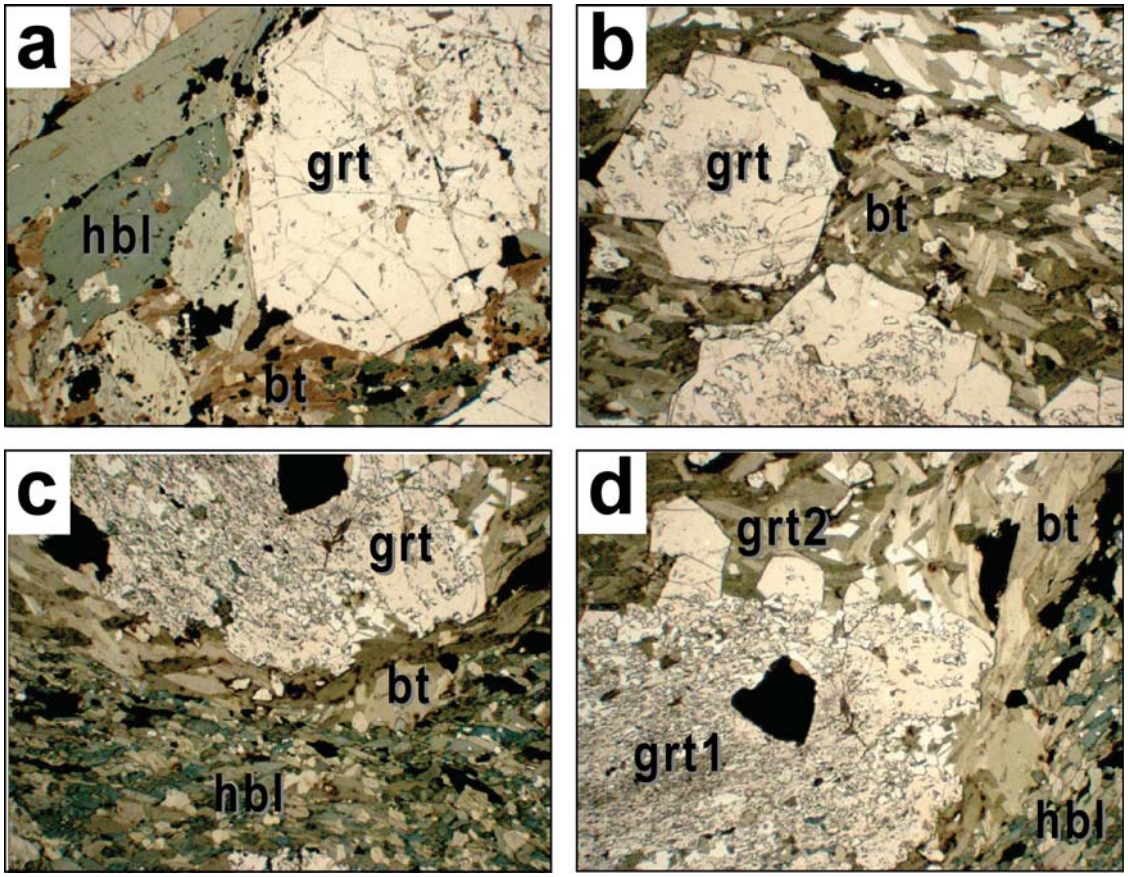

Figure 48: *Examples of high-P garnet amphibolites. (a) Polygonal granoblastic assemblage of garnet-hornblende-ilmenite-biotite (Y0360, x2.5 ppl). (b) Second stage post-kinematic garnet porphyroblast in biotite-rich domain within amphibolite (Y0361, x2.5 ppl). (c) First stage garnet porphyroblast in biotite-rich domain within foliated amphibolite. Note early fabric preserved by garnet inclusion trails (Y0361, x2.5 ppl). (d) Idioblastic second stage garnet overgrowth on first stage garnet, in foliated biotite amphibolite. Note early fabric preserved by garnet inclusion trails (Y0361, x2.5 ppl).*

Sample BG6-185b: Garnet amphibolite with medium-grained, well aligned polygonal granoblastic matrix. From Coolgardie Domain in the Kalgoorlie Terrane. Foliated granoblastic matrix assemblage consists of quartz – bytownite – ferro-tschermakite. Garnets are poikiloblasts up to 1.9 mm diameter with idioblastic margins. There is minor resorption of some garnet margins. Garnet compositional mapping indicates typical, though weak, single garnet growth patterns of decreasing Ca and Mn and increasing Fe with growth (Figure 49). Aligned quartz and minor opaque inclusion trails are continuous with the main foliation. There is minor post-garnet flattening of the main foliation around garnet porphyroblasts.

SMG: hbl-pl-qtz > grt

Sample BG6-106c: Garnet-epidote amphibolite from Murrin Domain in the Kurnalpi Terrane. Fine-grained, layered, aligned granoblastic matrix assemblage in textural equilibrium consists of quartz – andesine – biotite – green ferroan-pargasitic hornblende2 – garnet2 – rare ilmenite – epidote. Sample contains early syn-kinematic hornblende1, garnet1 and apatite porphyroblasts (0.6 mm diameter) enveloped by the main foliation. Most porphyroblasts abut main foliation minerals and are also enveloped by the main foliation and few are relict porphyroclasts. Biotite is retrogressively replaced by chlorite

SMG: grt1-hbl1-ap porphyroblasts > hbl2-grt2-pl-qtz-bt-ilm-epi > chl

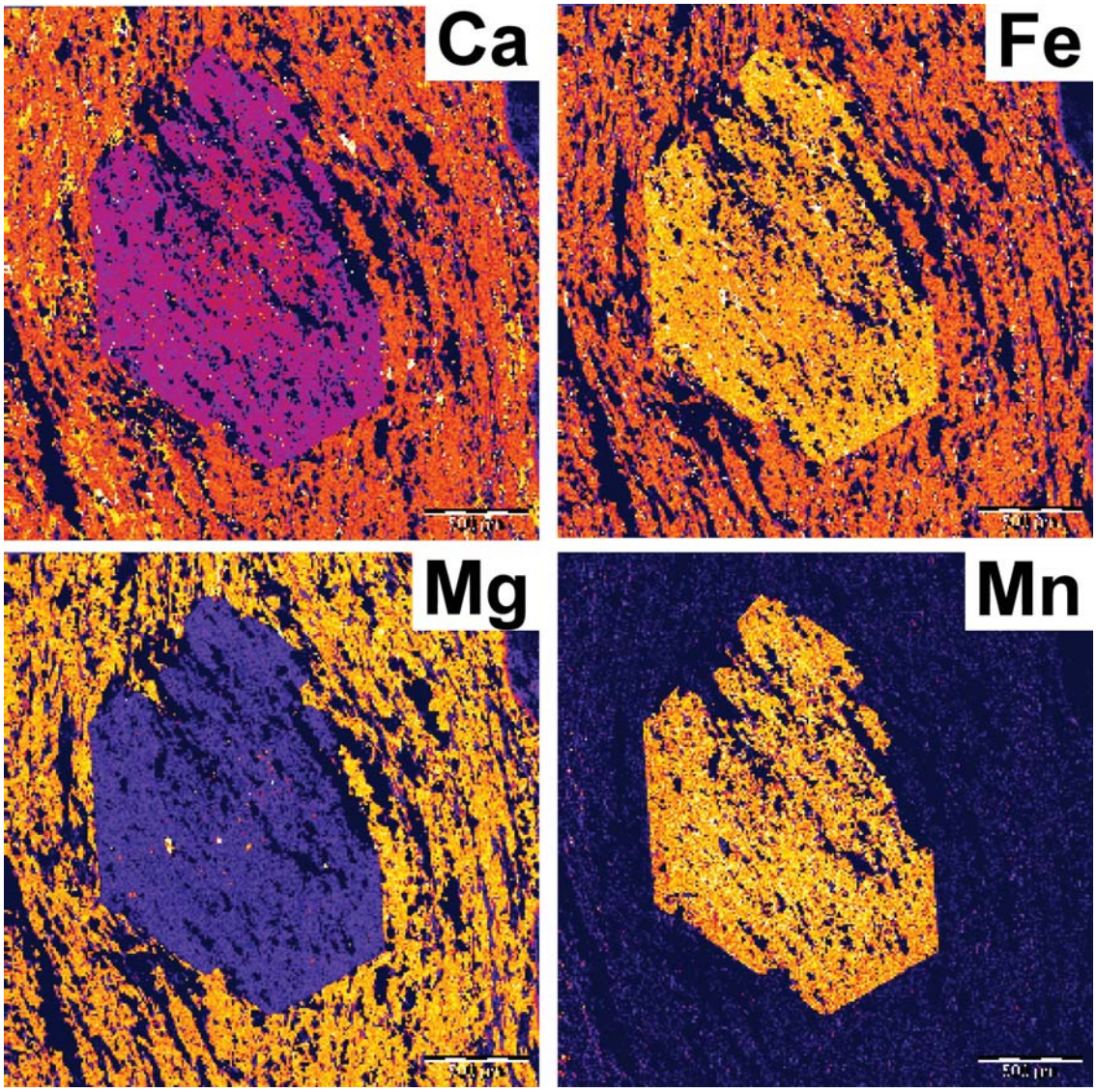

Figure 49: *Garnet compositional maps for sample BG6-185b.*

Sample BG6-192a: Garnet-amphibolite from Menangina Domain in the Kurnalpi Terrane. Fine-grained, aligned granoblastic matrix consists of quartz - plagioclase – garnet – magnetite – taramite hornblende – iron oxide. All phases are in textural equilibrium. Garnet occurs as small (1.8 mm) porphyroblasts and hornblende is aligned, defining the foliation. Gneissic banding defined by hornblende-quartz-plagioclase layers versus hornblende-garnet—plagioclase layers. Garnet compositional mapping indicates typical growth zoning with a smooth decrease in Ca and Mn and increase in Mg from core to rim. Fe is nearly compositionally flat with a weak decrease towards the rims. Garnet rims are highly irregular and resorbed, with minor Mn-enrichment in only small parts of the outer rim (Figure 50). Sample BG6-192b is garnet-chlorite-rich static metamorphosed mafic. Randomly oriented, static metamorphosed granoblastic matrix consists of garnet – chlorite – ilmenite – green-blue edenitic hornblende. Garnet porphyroblasts are poikiloblastic and up to 3.8 mm diameter and hornblende forms as radial fans. Sample BG6-192c contains: 0 ppm La, 0 ppm Th, 106 ppm Zr, 21 ppm Ce, and 14 ppm Nd.

SMG:	BG6-192a	qtz-pl-grt-mag-hbl-feox
	BG6-192b	grt-chl-ilm-hbl

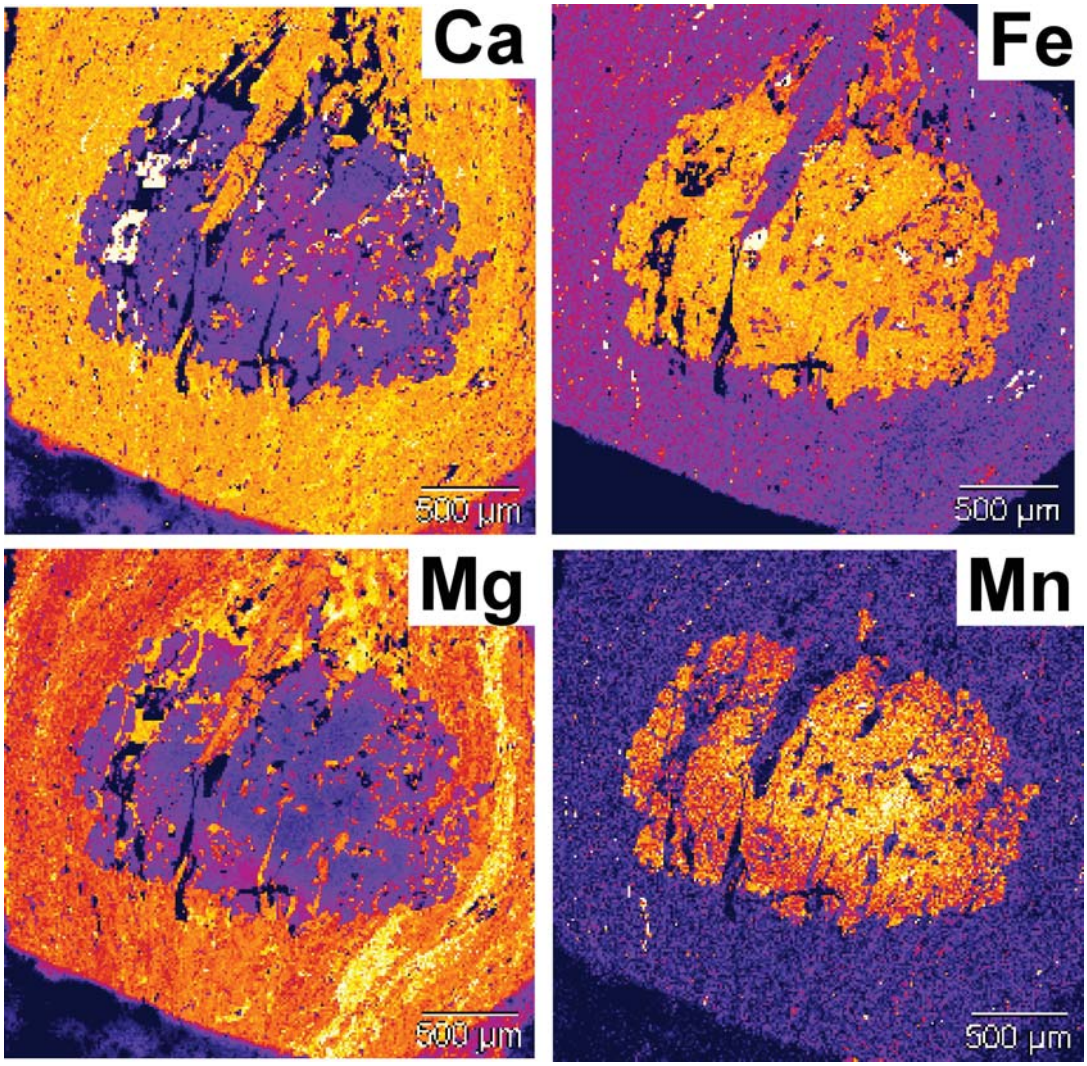

Figure 50: *Garnet compositional maps for sample BG6-192a.*

Sample Y691f: Sheared garnet amphibolite from Boorara Domain in the Kalgoorlie Terrane. Medium-grained aligned granoblastic matrix assemblage consists of quartz – plagioclase – magnetite – hematite – ilmenite – rutile? – dark blue-green to yellow-green ferro-tschermakite hornblende2 – garnet2. Rock has experienced two metamorphic events. Poikiloblastic garnet1 and hornblende1 porphyroclasts of 1.2 mm diameter are enveloped by the main foliation. Second-stage garnet2 and hornblende2 growth occurs as idioblastic overgrowths on porphyroclasts. Garnet2 and hornblende2 over-growths are in textural equilibrium with the main foliation. Epidote forms on garnet margins. Retrogressive chlorite partially replaces garnet. Sample contains: 49 ppm Zr.

SMG: hbl1-grt1 porphyroclasts > hbl2-grt2-qtz-pl-mag-ilm-hem-rt? matrix > ep-chl

High-P Garnet-Clinopyroxene Mafics

Sample BG6-171b: Garnet-clinopyroxene calcareous amphibolite from the north Linden Domain within the Kurnalpi Terrane. Medium-grained aligned granoblastic matrix assemblage in textural equilibrium, consists of quartz – oligoclase – green ferro-pargasitic hornblende – hedenbergite clinopyroxene – grossular garnet – ilmenite – rare biotite (Figure 51). Garnets are in textural equilibrium with the matrix assemblage. Ilmenite is enclosed by titanite coronas and manganese oxide may be late-stage.

SMG: hbl-pl-qtz-cpx-grt-ilm-bt > ttn-MnO

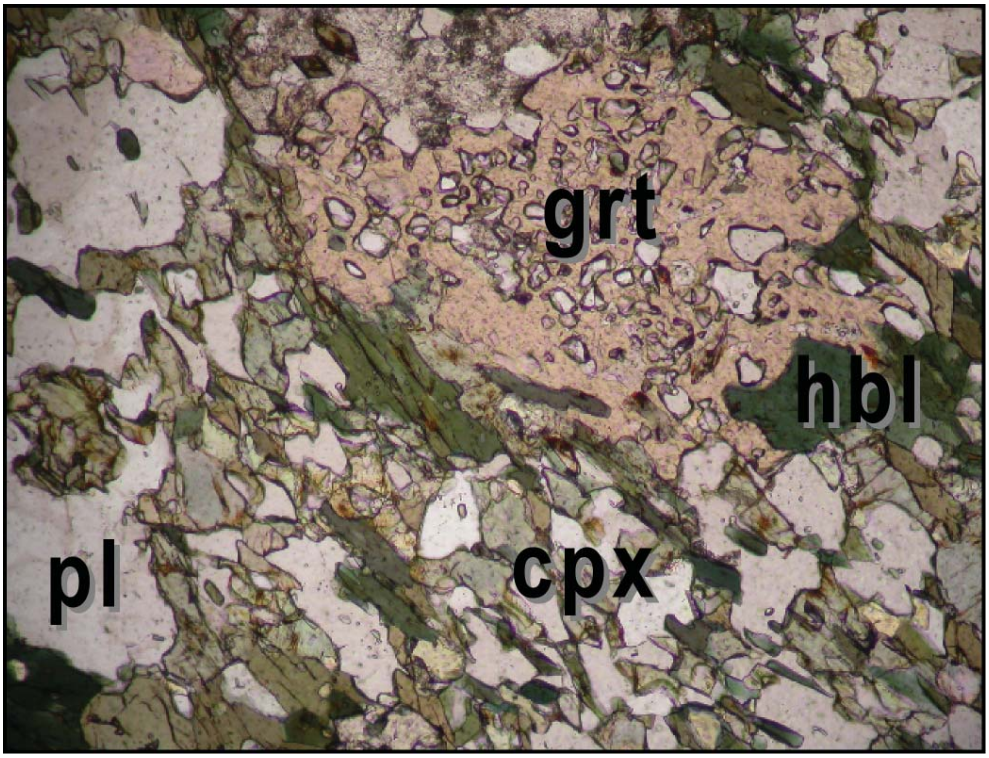

Figure 51: *High-P garnet-clinopyroxene amphibolite sample with aligned polygonal granoblastic matrix (BG6-171b, x10 ppl).*

High-P Garnet-Grunerite-Amphibolite Mafics

Sample BG6-171i: Garnet-grunerite amphibolite from the north Linden Domain within the Kurnalpi Terrane. Aligned granoblastic matrix assemblage consists of ilmenite – green ferro-pargasitic hornblende – clear grunerite (Figure 52d). Garnet occurs as 1-3 mm diameter post-kinematic porphyroblasts across the foliation and with grunerite inclusions. Early clinopyroxene? Is pseudomorphed by hornblende and grunerite. Most grunerite occurs as inclusions and a minor portion in the main foliation. Secondary grunerite2 and hornblende2 corrode garnet margins. Epidote appears to be in textural equilibrium with the matrix assemblage. Chlorite is retrogressive. Other retrogressive phases recognised by XRD include periclase and brucite.

SMG: cpx? > hbl1-gru1-ilm > grt > gru2-hbl2

Sample BG6-171j: Garnet-grunerite amphibolite from the north Linden Domain within the Kurnalpi Terrane. Coarse-grained weakly aligned granoblastic matrix assemblage consists of quartz – albite to oligoclase - ilmenite – bright green to blue ferro-edenitic hornblende – grunerite (Figure 52a, b, c). Garnet occurs as 1.8 mm diameter post-kinematic poikiloblasts across the foliation. Garnet has thin oligoclase coronas. Apatite and grunerite2 occurs as late laths across the main foliation. Secondary hornblende2 occurs as fine aggregates replacing grunerite. Other retrogressive phases recognised by XRD include kaolin.

SMG: hbl1-gru-ilmp-qtz-pl > grt-ap porphyroblasts ≥ gru2-hbl2 > pl coronas > kaolin

Sample BG6-171d: Static metamorphosed grunerite-hornblende amphibolite from the north Linden Domain within the Kurnalpi Terrane. Unaligned granoblastic matrix assemblage in textural equilibrium consists of quartz? – oligoclase – green ferro-edenitic hornblende – clear grunerite - ilmenite.

SMG: gru-hbl-pl-qtz?-ilm

Sample BG6-170a, b: Coarse-grained, foliated intermediate gneiss from northern Linden Domain in the Kurnalpi Terrane. Aligned granoblastic matrix assemblage consists of brown biotite1 – green ferro-pargasitic hornblende1 - quartz - albite to oligoclase – ilmenite – minor clear grunerite2 – zircon - apatite. An early generation of grunerite1 occurs as abundant large inclusions within garnet porphyroblasts. A second generation of biotite2 occurs medium-grained laths across the main foliation. Minor hornblende2 occurs on the margin of grunerite2 within the main foliation. There is minor retrograde chlorite and antigorite. All garnet is post-kinematic, idioblastic porphyroblasts up to 2 mm in diameter. A single atypical, small highly resorbed relict garnet grain was compositionally mapped. This garnet grain is compositionally flat in all components. Garnet rims are highly irregular and resorbed, with a very thin outer rim paralleling the irregular surface that is enriched in Mn and low in Fe (Figure 53). Garnet resoption and accumulation of Mn at the margins is due to metamorphic reactions as the rock evolved, and not due to deformation (Kim, 2006). Sample BG6-170c is a coarse-grained, foliated intermediate to calc-pelite gneiss with polygonal granoblastic matrix assemblage of biotite-grunerite-hornblende-quartz-feldspar with late idioblastic garnet. Sample BG6-170a contains 14 ppm La, 0 ppm Th, 294 ppm Zr, 59 ppm Ce and 45 ppm Nd and was submitted for monazite chronology. Sample BG6-170c has no thin section and was submitted for garnet chronology

SMG: BG6-170a: gru1 > bt1-hbl1-qtz-feld?-ilm-gru2-zrn > grt-bt2-hbl2

BG6-170b: gru? > gru?-bt-qtz-pl-ilm-grt-chl? > chl

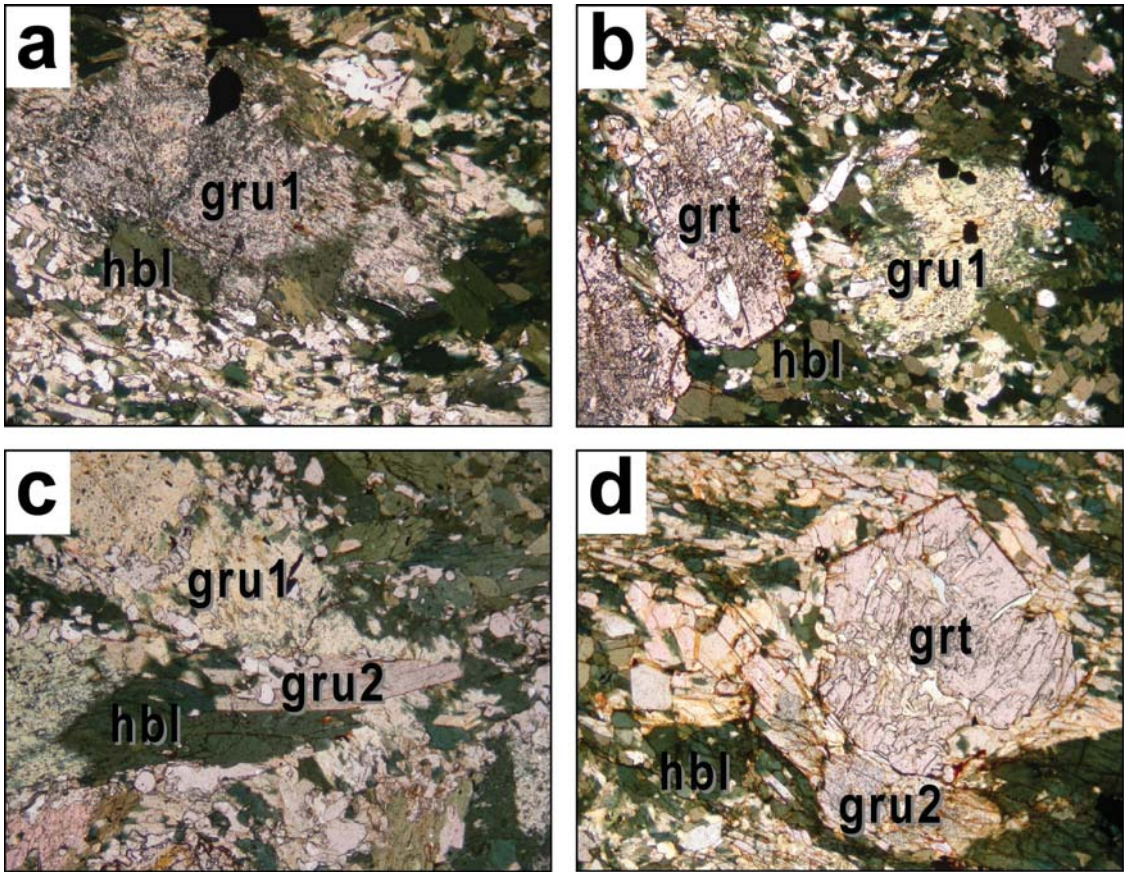

Figure 52: *High-P garnet-grunerite amphibolite samples. (a) Early grunerite partially replaced by matrix hornblende (BG6-171j, x5 ppl). (b) Early grunerite partially replaced by hornblende in a garnet-hornblende matrix assemblage (BG6-171j, x5 ppl). (c) Second-stage grunerite lath in equilibrium with matrix hornblende, over-growing first-stage grunerite (BG6-171j, x5 ppl). (d) Equilibrium matrix assemblage of garnet, hornblende and second-stage grunerite laths (BG6-171i, x5 ppl).*

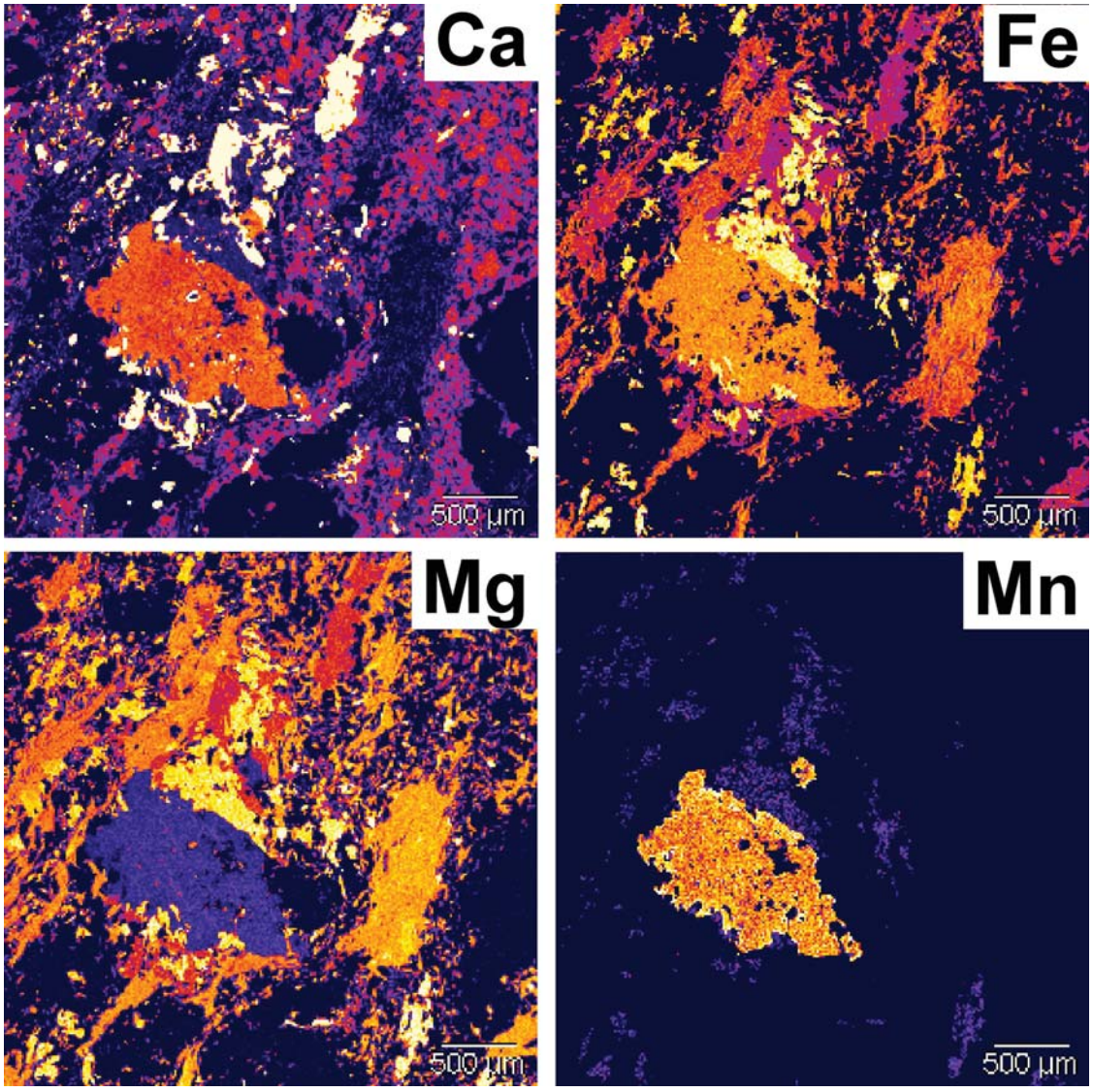

Figure 53: *Garnet compositional maps for sample BG6-170a.*

Low-P Granulite Facies Mafics

Samples BG6-146a, b, c, g: Medium-grained mafic granulite with relict ophitic texture preserved in samples BG6-146c, g and interlocking plagioclase laths in samples BG6-146a, b (Figure 54a, b). A cluster of granulite samples came from outcrops in the south Duketon Domain of the Burtville Terrane. GA site database reported kyanite at this locality. The presence of kyanite would be inconsistent with both the rock types described and the calculated PT conditions. It is worth pursuing the GA thin section collection to verify this observation. All collected samples are medium-grained polygonal granoblastic metamorphic matrix assemblage consists of bytownite – green-brown to brown magnesio-hornblende – orthopyroxene – salite to augitic clinopyroxene - ilmenite ± rutile ± quartz? Orthopyroxene and clinopyroxene occur as poikiloblastic ameboid masses. Hornblende and orthopyroxene also occur as polygonal granoblastic grains interstitial to the ameboid masses. Plagioclase occurs as recrystallized relict inter-locking lath shapes. Rare hornblende2 occurs as thin coronas on orthopyroxene. Similar sample BG6-146f contains: 0 ppm La, 0 ppm Th, 32 ppm Zr, 0 ppm Ce and 12 ppm Nd.

SMG: BG6-146a: opx-cpx-pl-hbl-op-rt

BG6-146b: opx-cpx-pl-hbl-ilm-rt > hbl corona

BG6-146c: opx-cpx-pl-hbl-ilm-qtz?

BG6-146g: opx-cpx-pl-hbl-ilm-qtz?

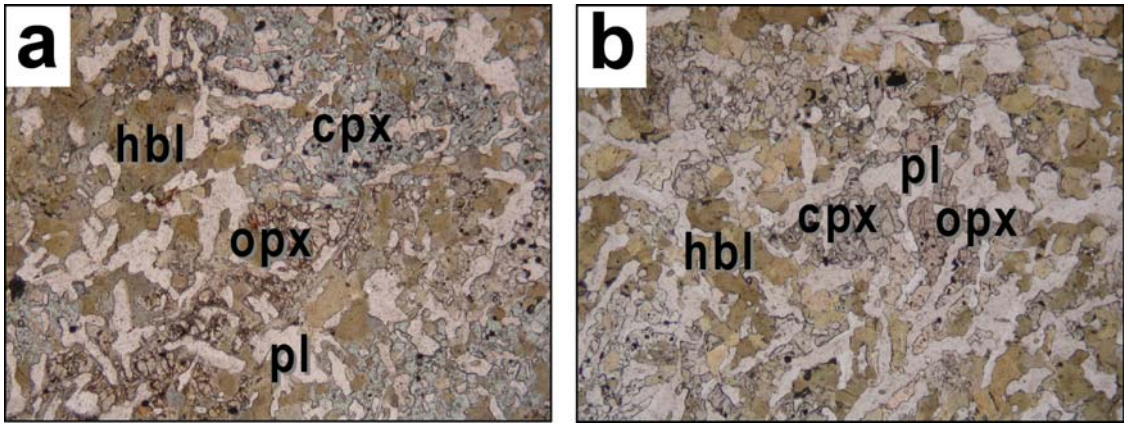

Figure 54: *Mafic granulite samples. (a) Polygonal granoblastic mafic granulite with orthopyroxene-clinopyroxene-hornblende-plagioclase assemblage. Note the ghosted ophitic texture indicating static metamorphism of ophitic gabbro protoliths (BG6-146a, x5 ppl). (b) Same as (b) (BG6-146g, x5 ppl).*

Epidote Amphibolite Mafics

Sample 99966091.3: Epidote amphibolite legacy GA thin section from the Boorara Domain in the Kalgoorlie Terrane. Aligned granoblastic matrix assemblage in apparent textural equilibrium, consists of quartz – labradorite – magnesio-hornblende – epidote1. Sample is devoid of opaques. Epidote1 is aligned in the main foliation and a second generation of epidote2 occurs as late-stage laths across the main foliation.

SMG: hbl-pl-qtz-ep1 > ep2

Sample 99966118: Epidote amphibolite legacy GA thin section from the Boorara Domain in the Kalgoorlie Terrane. Unaligned polygonal granoblastic matrix assemblage in apparent textural equilibrium consists of quartz – andesine – common green ferro-tschermakite hornblende1 – rare blue-green hornblende2 - chlorite – magnetite – ilmenite – epidote. There are apparently two coexisting hornblendes in the sample.

SMG: hbl1-hbl2-pl-qtz-chl-mag-ilm-ep

Sample 99966121B: Epidote amphibolite legacy GA thin section from the Boorara Domain in the Kalgoorlie Terrane. Polygonal granoblastic matrix assemblage in apparent textural equilibrium consists of quartz – oligoclase – ilmenite – epidote – blue-green ferro tschermakite hornblende. Titanite occurs as coronas on ilmenite.

SMG: hbl-pl-qtz-ilm-ep > ttn

Low-P Mafics with Clockwise Evolution

Sample Y535d: Garnet-hornblende-grunerite-chlorite static metamorphosed mafic from Norseman Domain in the Kalgoorlie Terrane. Random orientated to slightly foliated matrix assemblage consists of chlorite – hematite/magnetite – plagioclase? The matrix is overgrown by randomly oriented and fanning porphyroblasts of garnet, grunerite and hornblende. Grunerite is coarse-grained, occurs as radial fans and contains opaque inclusion trails. Garnet occurs as late idioblastic porphyroblasts of 2 mm diameter and contains opaque inclusion trails (Figure 55). Hornblende laths are ferro-tschermakite.

SMG: chl-pl?-qtz > hbl-grt-gru

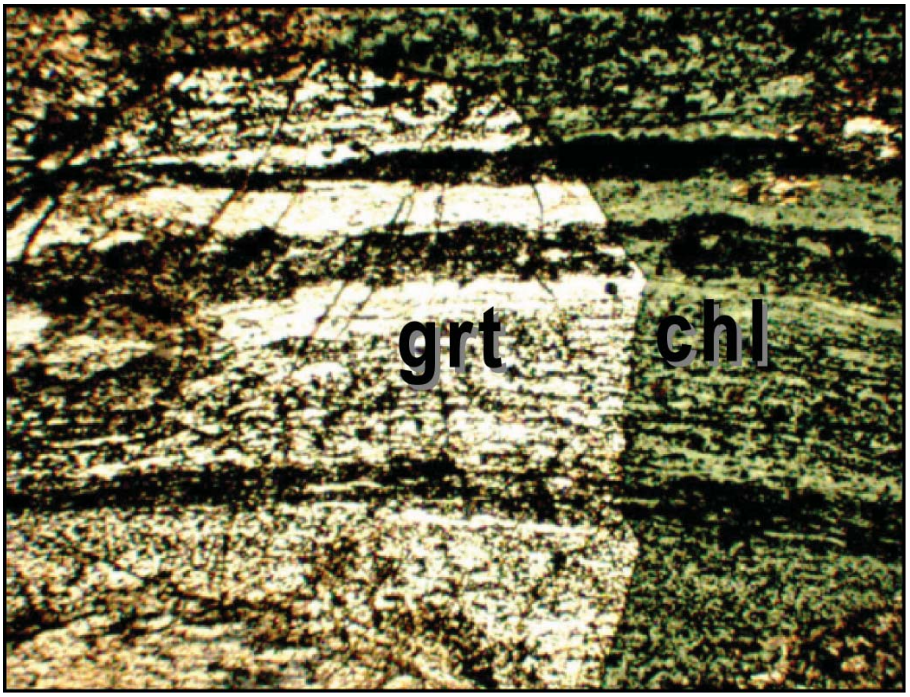

Figure 55: *Low-P Fe-rich garnet-hornblende-grunerite-chlorite mafic sample Y535d that experienced a clockwise P-T path. Note post-kinematic, idioblastic garnet porphyroblast over grows an early fine-grained chlorite-magnetite (or hematite) foliation (x2.5 ppl).*

Sample Y504: Amphibolite from Norseman Domain in the Kalgoorlie Terrane. Well-foliated matrix assemblage consists of plagioclase – chlorite - opaque. The main foliation is defined by well-aligned chlorite grains and granoblastic aggregate lenses of plagioclase. Post-kinematic pale green grunerite/cummingtonite prisms and radial fans over-grow the main foliation. Late-stage actinolite over-grows the main foliation and corrodes grunerite margins.

SMG: chl-pl-op > cumm/gru > act

Sample BG6-114g: Coarse static metamorphosed actinolitic-hornblende amphibolite from south Linden Domain in the Kurnalpi Terrane. The static metamorphic matrix assemblage consists of randomly orientated and inter-locking amphiboles with interstitial plagioclase. This assemblage consists of quartz? – plagioclase – pale green actinolite1 - opaque. Blue-green hornblende forms rims on pale green actinolite cores. Chlorite is retrogressive and sample has late prehnite veins.

SMG: act1-pl-qtz? > hbl2 > chl > prh vein

Sample BG6-121: Medium-grained amphibolite from south Linden Domain in the Kurnalpi Terrane. Medium-grained, well-aligned granoblastic matrix assemblage consists of quartz – bytownite1 – green ferro-hornblende – biotite – tan chlorite? – ilmenite - titanite. All chlorite may be retrogressive and occurs replacing biotite. Hornblende is enclosed by thin plagioclase2 coronas. .

SMG: hbl-pl1-qtz-ilm-ttn-[chl?] > pl2 corona > chl

Sample BG6-163e: Static metamorphosed actinolitic-hornblende amphibolite from Ora Banda Domain in the Kalgoorlie Terrane. Randomly oriented granoblastic matrix assemblage consists of quartz? – plagioclase – green-blue hornblende2 – pale blue-green actinolitic-hornblende1 – opaque – actinolite1. Sample contains at least two coexisting amphiboles. Pale blue-green actinolitic hornblende laths are common and some grains have darker green-blue hornblende2 rims. Plagioclase is interstitial to interlocking actinolite and actinolitic-hornblende.

SMG: qtz?-pl-act/hbl1-act1-op > hbl2 rims

Sample BG6-163f: Coarse-grained, statically metamorphosed epidote amphibolite from Ora Banda Domain in the Kalgoorlie Terrane. Coarse-grained unaligned granoblastic matrix assemblage consists of quartz? – andesine1 – green ferro-pargasitic hornblende – ilmenite – epidote - calcite. Hornblende occurs as coarse-grained porphyroblasts and fine-grained randomly oriented laths. Epidote is enclosed by thin plagioclase2 coronas.

SMG: hbl-pl-qtz?-ilm-ep-cc > pl2 corona

Forrestania Domain Garnet Amphibolite

Sample BG6-204: Garnet-biotite schist interleaved with garnet-amphibolite from Forrestania Belt in Southern Cross Terrane. Well-aligned granoblastic matrix assemblage in textural equilibrium, consists of quartz – anorthite – biotite – pale green ferro-hornblende – garnet - ilmenite - minor pyrite - minor carbonate ± chlorite (Figure 56a). Garnet porphyroblasts (5 mm diameter) are elongate, syn-kinematic poikiloblasts in textural equilibrium with the matrix assemblage. Garnet contains ilmenite and quartz inclusions and occurs in both amphibole-rich and biotite-chlorite-rich layers. Chlorite occurs in the main foliation of biotite-rich layers and also retrogressively replaces biotite. Carbonate occurs both as large grains and as sub-grains. Sample submitted for garnet chronology.

SMG: qtz-pl-bt-grt-ilm±hbl±chl-carb±py > chl

Sample BG6-205: Garnet-biotite amphibolite from Forrestania Belt in Southern Cross Terrane. Fine-grained foliated granoblastic matrix assemblage consists of quartz – bytownite – green ferro-tschermakitic hornblende – brown biotite – ilmenite (Figure 56b). Garnet occurs as post-kinematic poikiloblasts of up to 3.0 mm diameter and with idioblastic margins. There is some rotation and flattening of the foliation around garnet porphyroblasts. Garnet is present in all hornblende-rich, biotite-rich and hornblende-biotite layers.

SMG: hbl-pl-qtz-bt-ilm > grt porphyroblast

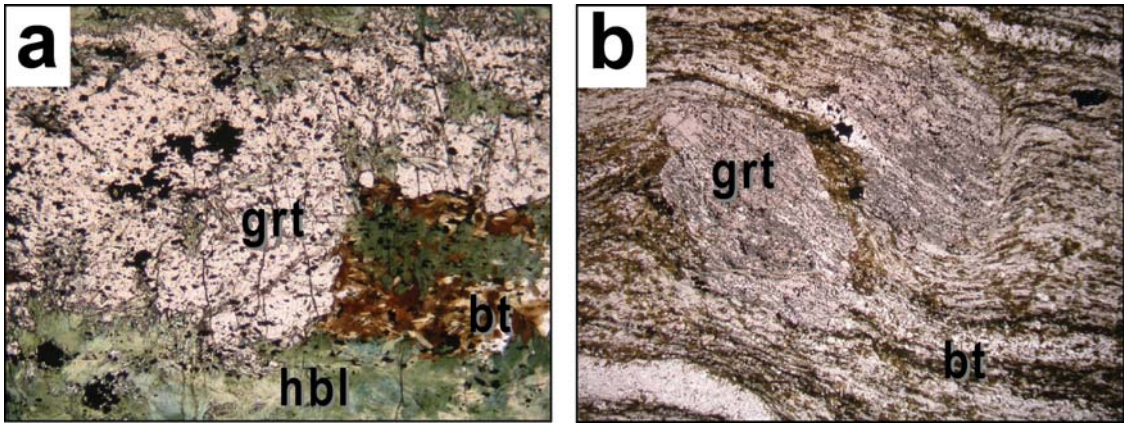

Figure 56: *Representative samples from the Forrestania belt. (a) Garnet-biotite amphibolite, showing that garnet growth continued after deformation and fabric development (BG6-204, x5 ppl). (b) Garnet-biotite metapelite schist showing garnet growth after main phase fabric development and before further deformation and folding of garnets and foliation (BG6-205, x5 ppl).*

Metapelite Schists

Belches Formation Metapelite with Anticlockwise Evolution

Sample Y533d: Pelite sample from Mt Belches Formation in the northeast Bulong Domain in the Kurnalpi Terrane. No thin section available and sample was submitted for monazite geochronology. Andalusite-staurolite-biotite-quartz-plagioclase metapelite schist with rare chlorite pseudomorphs after early-formed flattened cordierite porphyroblasts.

Samples Y533a, e, f, i: Pelite samples at the same locality contain very small garnet porphyroblasts between 0.2-0.7 mm in diameter. These samples have a foliated matrix assemblage of quartz, plagioclase (oligoclase to labradorite), biotite1 and ilmenite. Post-kinematic porphyroblasts are sieve staurolite with idioblastic margins, random orientated blocky brown biotite2 laths, andalusite poikiloblasts and less common idioblastic garnet porphyroblasts (Figure 57a, b, d). Andalusite occurs as inclusions within staurolite and pre-dates both staurolite and garnet growth. Biotite2 laths form both together with andalusite and also with staurolite in different samples. Quartz aggregate clots are enclosed by biotite moats (Figure 57c). Pseudomorphed cordierite is rare and early-formed, and defined by clots of biotite-chlorite-muscovite-quartz aggregates. Where present, garnet pre-dates andalusite porphyroblasts and some round chlorite-muscovite pseudomorphs may be after garnet. Muscovite occurs as late-stage laths across the main foliation, on the margins of andalusite and in aggregates after garnet and cordierite. Chlorite occurs in pseudomorphs and retrogressive replacement of biotite grains. Garnet compositional mapping from similar sample Y533a, are small compositionally flat (Figure 58) post-kinematic idioblastic garnets. There are very minor amounts of very fine quartz, chlorite? and monazite? inclusions. Garnets are not resorbed, re-equilibrated or retrograded.

SMG:	Y533a:	qtz-bt1-pl > and > st-grt-bt2 > ms
	Y533e:	qtz-bt1-pl-ilm > and > st-bt2 > ms-chl
	Y533f:	qtz-bt1-pl-ilm-crd > st-and-bt2 > ms-chl-bt-qtz
	Y533i:	qtz-bt1-pl-ilm > and-bt2 > st-grt? > ms-chl

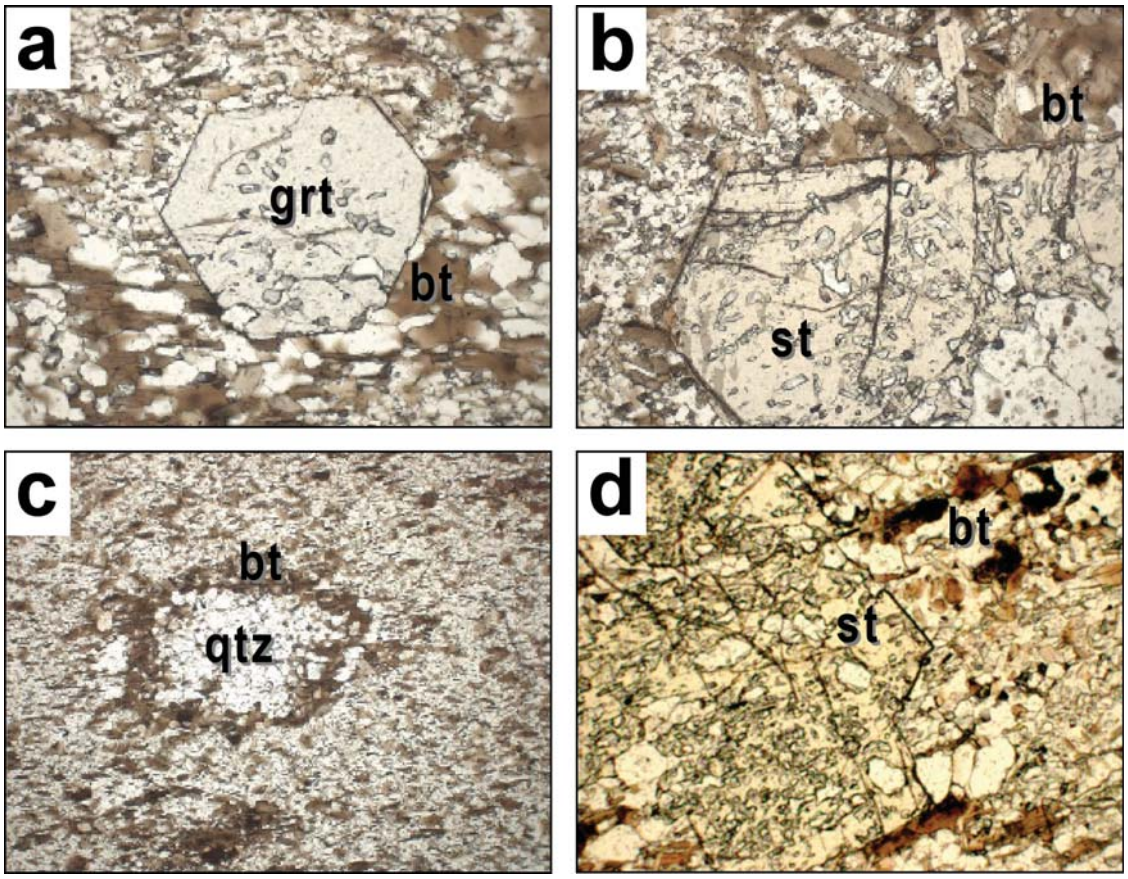

Figure 57: *Metapelite samples from the Mount Belches Formation showing anti-clockwise P-T paths. (a) Small post-kinematic garnet with quartz inclusions defining trace of the main foliation (Y533a, x10 ppl). (b) Post-kinematic staurolite (Y533a, x10 ppl). (c) Aggregate clot of quartz with a moat of biotite (Y533a, x10 ppl). (d) Post-kinematic staurolite over printing the main biotite foliation (Y533e, x6.3 ppl).*

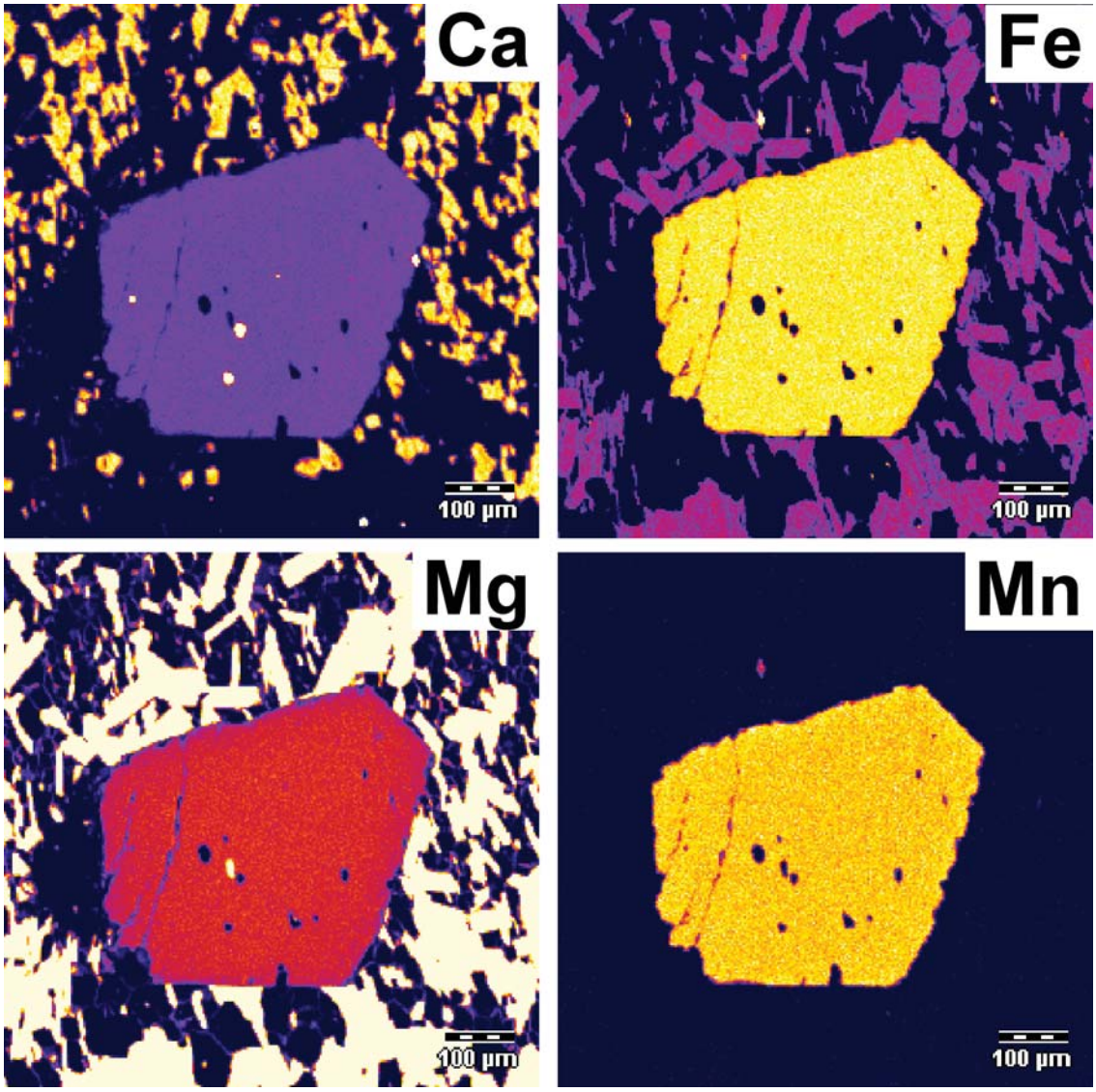

Figure 58: *Garnet compositional maps for sample Y533a.*

Sample Y534a: Fine-grained garnet-staurolite metapelite schist from Mt Belches Formation in northeast Bulong Domain in the Kurnalpi Terrane. Similar sample Y534b shares similar relationships. Foliated granoblastic matrix assemblage consists of quartz – oligoclase – biotite1 – muscovite - ilmenite. Second-stage biotite2 occurs as blocky laths across the main foliation and a third phase of biotite occurs as large porphyroblasts that contain main foliation inclusion trails (Figure 59d). Staurolite porphyroblasts are partially relaced by sericite moats and pseudomorphed to sericite clots (Figure 59a). Garnet occurs as small (1.0 mm), post-kinematic, idioblastic porphyroblasts with inclusion trails (Figure 59b). Garnet contains inclusions of quartz, monazite and ilmenite. Garnet compositional maps show typical smooth growth zoning of decreasing Ca and Mn, and increasing Fe and Mg towards rims (Figure 60, 61). Both muscovite and chlorite form late-stage grains that grew across the foliation and on the margins of biotite and garnet. Similar sample Y534b contains chlorite-muscovite aggregates interpreted to be pseudomorphs after cordierite (Figure 59c). Similar sample Y534c contains 134 ppm Zr.

SMG: bt1-qtz-pl-ilm-ms-mnz > bt2-grt-st > ms > chl.

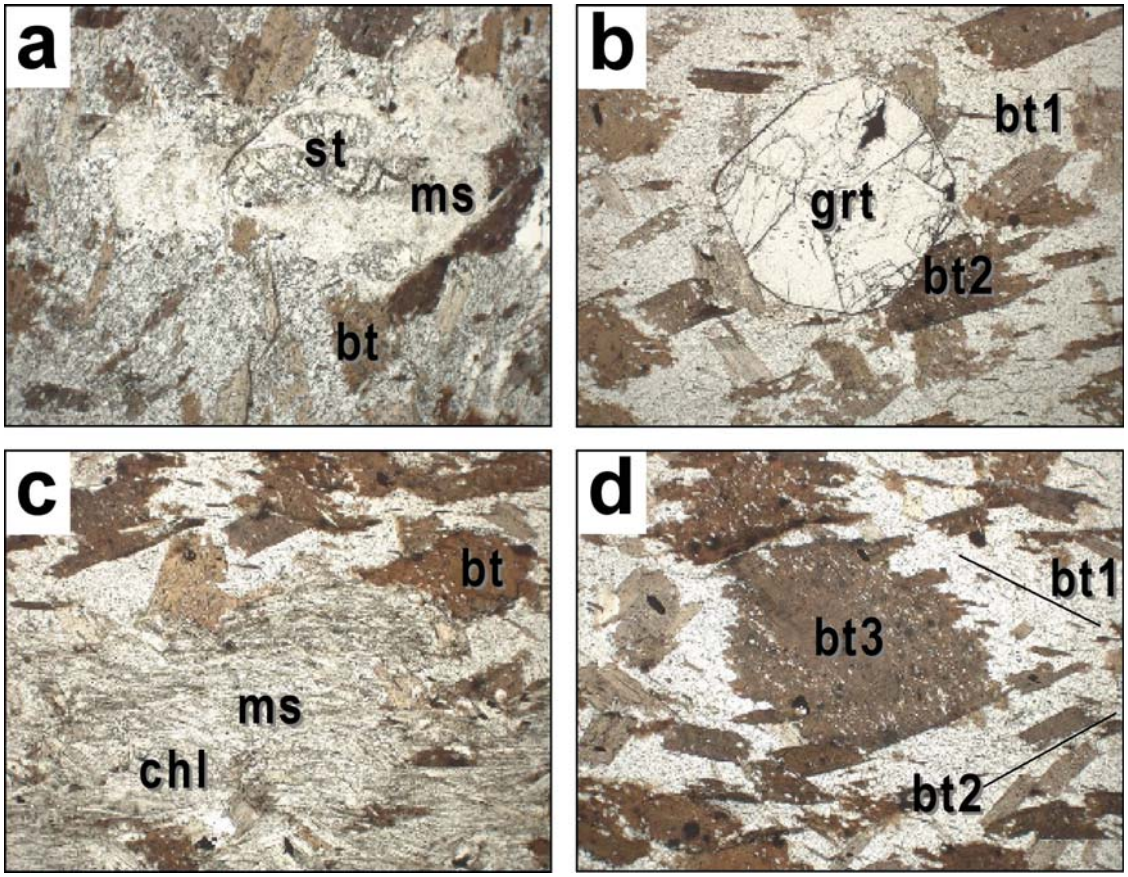

Figure 59: *Metapelite samples from the Mount Belches Formation showing anti-clockwise P-T path. (a) Relict grains of a staurolite porphyroblast partially replaced by fine muscovite (Y534a, x2.5 ppl). (b) Small post-kinematic idioblastic garnet over grows biotite2 laths (Y534b, x2.5 ppl). (c) Aggregate of chlorite-muscovite pseudomorph after cordierite (Y534b, x2.5 ppl). (d) Three generations of biotite growth. Very fine biotite1 defines the main matrix foliation, biotite2 laths are aligned defining a second foliation at high-angle and biotite3 is post-kinematic porphyroblast growth with inclusion trails of the early main foliation (Y534b, x2.5 ppl).*

Samples 153469, 153470, 153471: Metapelite schist in Belches Formation from the northeast Bulong Domain within the Kurnalpi Terrane. These samples have been described by Mickuki and Roberts (2003). All samples have a matrix of quartz – biotite – muscovite ± chlorite. The matrix is overgrown by flattened ellipsoid poikiloblasts of cordierite. Both the matrix foliation and cordierite poikiloblasts and pseudomorphs are over-grown by randomly oriented, coarse blocky biotite2 laths and post-kinematic porphyroblasts of garnet, andalusite and staurolite. Some cordierite poikiloblasts are pseudomorphed by chlorite.

SMG:	153469:	bt1-chl1 > crd > bt2-grt-st > chl2
	153470:	bt1-ms > crd > bt2-and-st > chl
	153471:	bt1-ms > crd > and-bt2-grt-st

Samples Y459a, i, j: Fine grey-brown metapelite schists from Mount Belches Formation in the west Bulong Domain in the Kalgoorlie Terrane. Foliated granoblastic matrix assemblage consists of andesine – orange-brown biotite1 – magnetite/hematite – tourmaline ± quartz ± muscovite1. Biotite1 is medium-grained and well aligned. Biotite2 occurs as blocky laths across the main foliation. Muscovite2 occurs as later laths across all generations of biotite. Garnet occurs as post-kinematic porphyroblasts of 0.8 mm diameter across the foliation (Figure 62b). Tourmaline occurs as porphyroblasts with inclusion trails, across the main foliation. Sample Y459i similar to Y459a contains: 22.75 ppm La, 7.3 ppm Th, 120 ppm Zr, 5.04 ppm Sm, 48.82 ppm Ce, 26.14 ppm Nd, 0.23 ppm Lu and 3.4 ppm Hf. Sample Y459j contains: 31.07 ppm La, 8.2 ppm Th, 115.1 ppm Zr, 5.95 ppm Sm, 64.88 ppm Ce, 31.45 ppm Nd, 0.26 ppm Lu and 3.2 ppm Hf.

SMG: Y459a: pl-bt-op-tur > grt

Y459i: qtz-pl?-bt1-tur-ms1 > bt2-tur > ms2

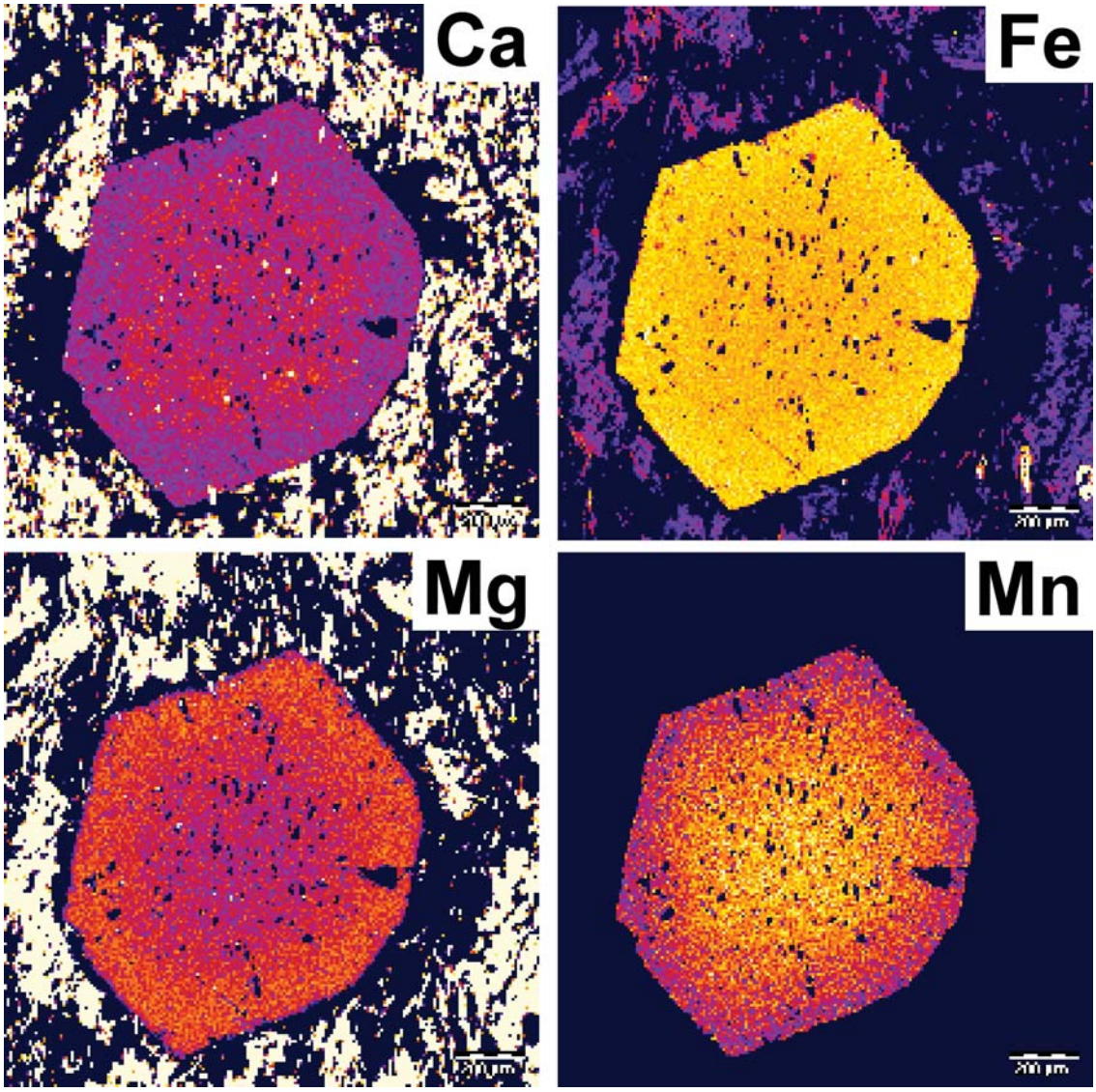

Figure 60: *Garnet compositional maps for sample Y534a.*

Samples Y459e, g: Fine grey metapelite schists from Mount Belches Formation in the west Bulong Domain in the Kalgoorlie Terrane. Fine-grained foliated granoblastic matrix assemblage consists of quartz – plagioclase – biotite1 – elliptical opaque – graphite – olive tourmaline ± chlorite ± muscovite. Both samples contain post-kinematic biotite2 laths across both the main foliation and cordierite pseudomorph assemblages that occur as dark clots at locality Y458 (Figure 62d). Sample 459g contains andalusite poikiloblasts and flattened ovoid pseudomorphs of muscovite-chlorite-biotite aggregates after cordierite. Retrogressive chlorite replaces biotite. Sample Y459g contains: 34.76 ppm La, 6.8 ppm Th, 107.1 ppm Zr, 6.13 ppm Sm, 76.5 ppm Ce, 34.79 ppm Nd, 0.23 ppm Lu and 3.3 ppm Hf.

SMG:	Y459e:	qtz-pl-ms-bt1-gr-tur > bt2 laths > chl
	Y459g:	qtz-pl-bt1-gr-tur-op > crd > bt2-ms-chl pseudomorph > bt3 laths

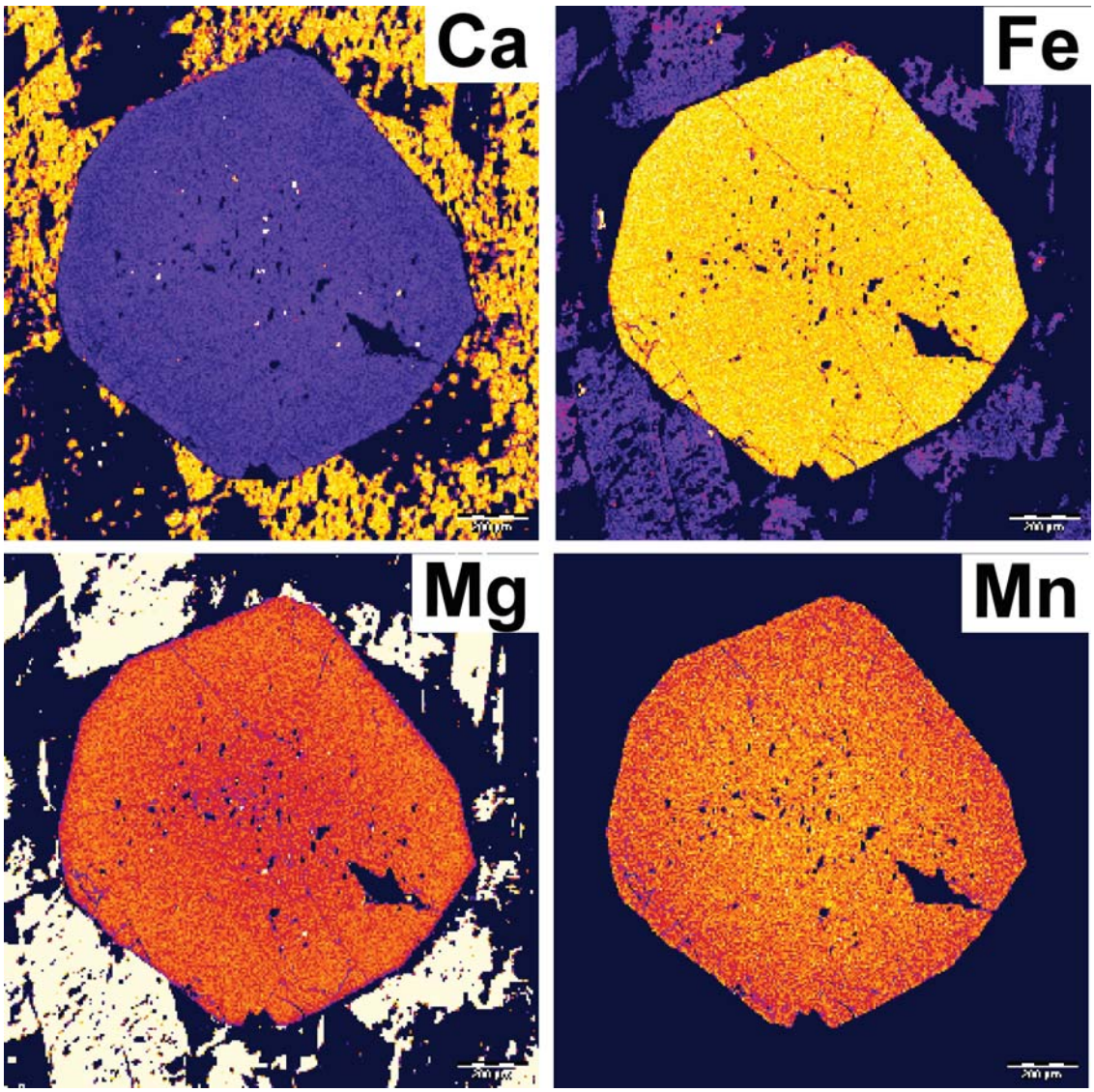

Figure 61: *Garnet compositional maps for sample Y534b.*

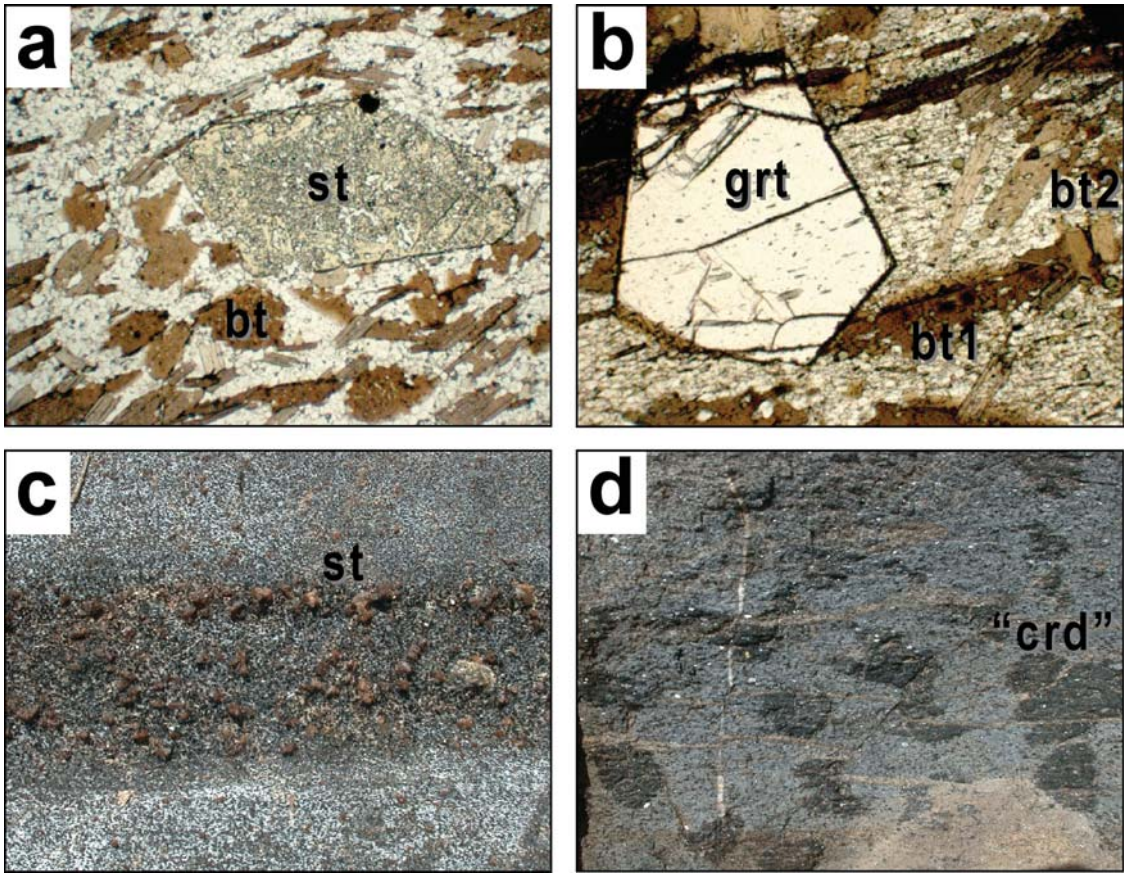

Figure 62: *Metapelite samples from the Mount Belches Formation showing anti-clockwise P-T path. (a) Post-kinematic staurolite (Y455c, x2.5 ppl). (b) Small post-kinematic idioblastic garnet over-printing biotite1 in the main foliation. Note biotite2 laths overprinting biotite1-tourmaline foliation at a high-angle (Y459i, x10 ppl). (c) Staurolite porphyroblasts in outcrop outlining a metapelite band in psammite (Y455, field of view 7 cm). (d) Dark chlorite pseudomorphs in outcrop after cordierite porphyroblasts in metapelite (Y458, field of view 10 cm).*

Sample Y530b(ii): Dark grey, fine-grained metapelite schist from Mt Belches Formation in the southeast Bulong Domain in the Kurnalpi Terrane. Foliated matrix assemblage of quartz-biotite1-albite with small (1.0 mm) post-kinematic garnet porphyroblasts (Figure 63a). There are also post-kinematic blocky brown biotite2 porphyroblasts at high angles across the foliation and muscovite growth across both biotite2 and the main foliation (Figure 63c). Garnet porphyroblasts post-date both biotite2 and muscovite. Staurolite occurs as post-kinematic poikiloblasts in sample Y530b (Figure 63b, d). Retrograde chlorite replaces biotite. Garnet compositional mapping from similar sample Y530b, are small compositionally flat (Figure 64), post-kinematic and sub-idioblastic garnets. There are minor amounts of fine monazite? grains in both the matrix and as inclusions in garnet. Garnets may be slightly resorbed, but are not re-equilibrated or retrograded. Sample was submitted for monazite chronology

SMG: qtz-pl-bt1 > bt2 > ms > grt-st > chl

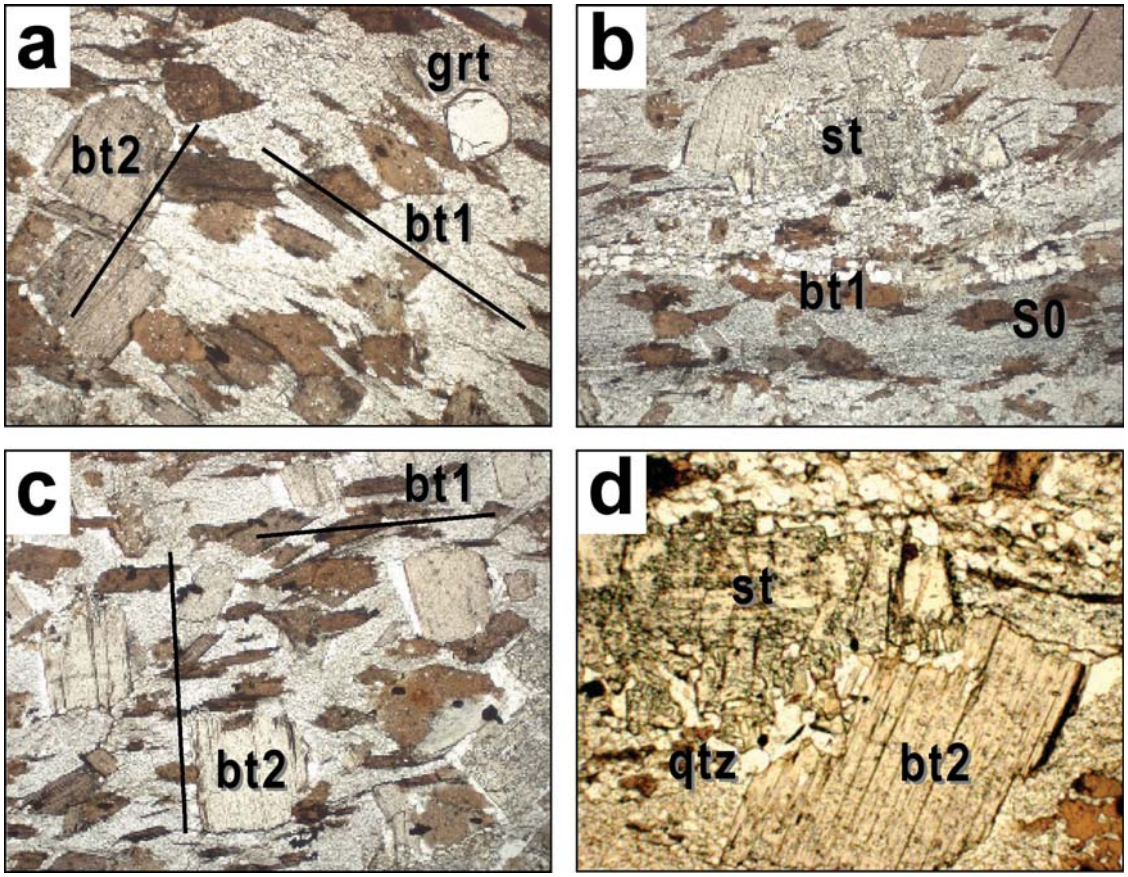

Figure 63: *Metapelite samples Y530b(ii) and Y530b from the Mount Belches Formation showing anti-clockwise P-T path. (a) Small garnet idioblasts and biotite2 laths over-print the main foliation (x2.5 ppl). (b) Post-kinematic staurolite porphyroblast. Note main foliation defined by biotite1 is parallel to bedding compositional layering (x2.5 ppl). (c) Fine-grained biotite1 defining main foliation and over-printing coarse biotite2 laths define a second foliation at high angle (x2.5 ppl). (d) Post-kinematic staurolite over growing both biotite2 lath and main foliation. Note quartz moat around staurolite (x6.3 ppl).*

Samples Y530a, g: Fresh and dark, medium-grained metapelite schist from Mount Belches Formation in southeast Bulong Domain in the Kurnalpi Terrane. Foliated granoblastic matrix assemblage in sample Y530a consists of quartz – plagioclase – biotite1 – ilmenite – graphite - tourmaline. Most biotite1 is fine grained with some early biotite grains in the foliation having pressure shadows. Blocky biotite2 and ilmenite2 occur as coarse post-kinematic porphyroblasts across the main foliation. Late-stage chlorite laths grow across the main foliation. The main foliation is axial planar to isoclines. No garnet described from thin section but described in outcrop. Sample was submitted for garnet chronology. Sample Y530g contains 117 ppm Zr.

SMG: bt1-qtz-pl-ilm1-gr-tur > bt2 laths > ilm2 laths > chl plates

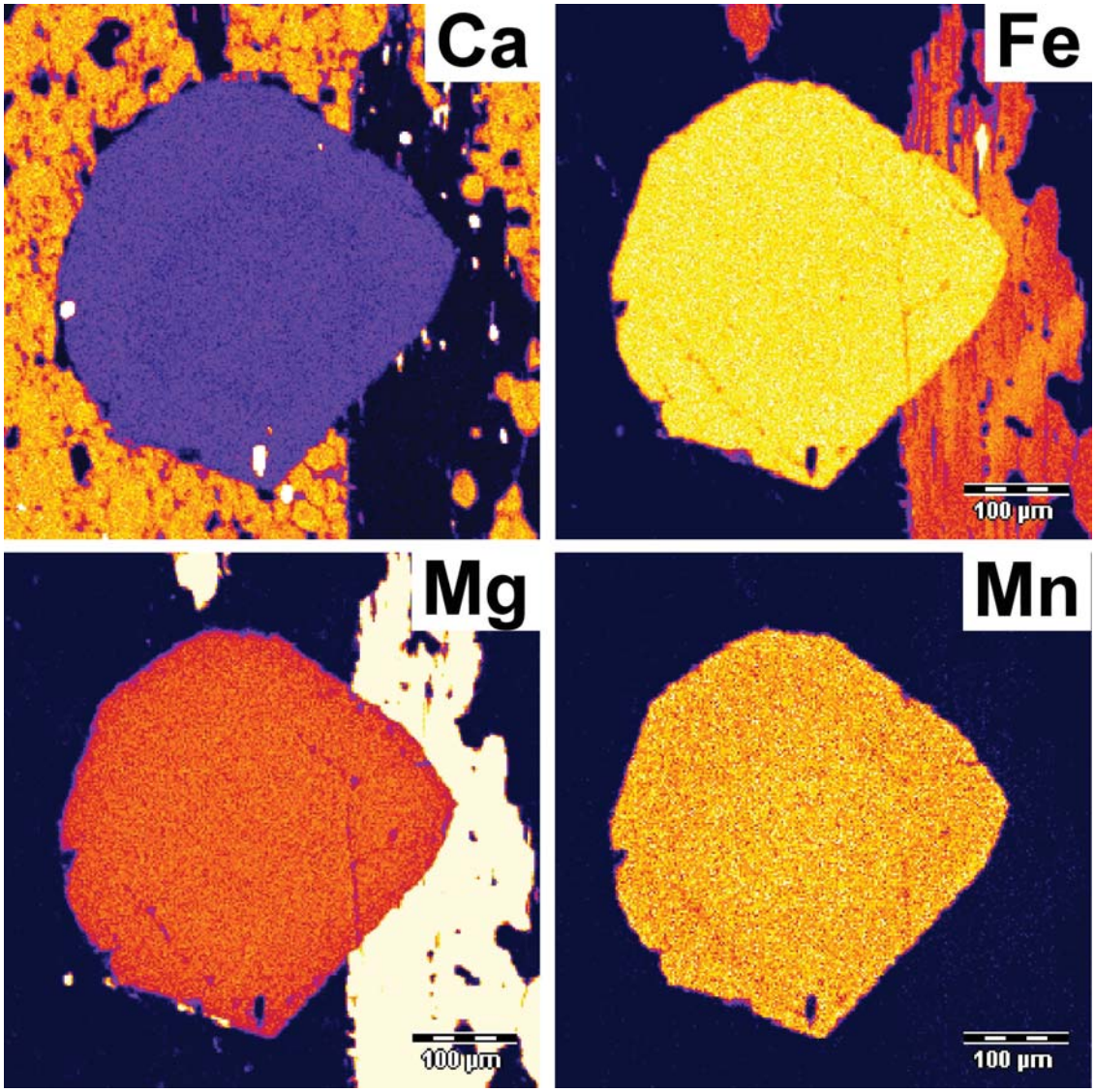

Figure 64: *Garnet compositional maps for sample Y530b.*

Samples Y455b, c, f: Staurolite-andalusite metapelite schists in the Mount Belches Formation from southeast Bulong Domain in the Kalgoorlie Terrane. All samples have a fine- to medium-grained foliated granoblastic matrix assemblage consisting of quartz – oligoclase – biotite ± rare muscovite ± ilmenite. Andalusite occurs as rare large post-kinematic poikiloblasts up to 10 mm diameter, some with quartz moats. Staurolite is common and occurs as post-kinematic poikiloblasts up to 6 mm in diameter (Figure 62a, c). Biotite is mostly aligned and also forms across the foliation. Muscovite in sample Y455b is late-stage across biotite grains. Chlorite is retrogressive and replaces biotite. All samples are devoid of garnet. Sample Y455b contains: 27.05 ppm La, 6.7 ppm Th, 116.1 ppm Zr, 5.14 ppm Sm, 57.88 ppm Ce, 28.28 ppm Nd, 0.22 ppm Lu and 3.3 ppm Hf.

SMG:	Y455b:	qtz-pl-bt-op > st-and porphyroblasts > ms > chl
	Y455c:	qtz-pl-bt-ms-op > st porphyroblasts
	Y455f:	qtz-pl-bt-ms-ilm-and > st porphyroblasts > chl

Sample Y531g: Fresh medium-grained, garnet-metapelite schist from Mt Belches Formation in the central east Bulong Domain in the Kurnalpi Terrane. Matrix assemblage consists of quartz, oligoclase, biotite and muscovite-margarite? Garnets are small (2.3 mm diameter), idioblastic to rounded, poikiloblastic post-kinematic porphyroblasts. Garnet contains pyrite and quartz inclusions. Elongate andalusite porphyroblasts that over-grew the foliation and pre-date garnet, are pseudomorphed by muscovite-margarite? clots with biotite moats. Retrograde chlorite replaces biotite. Sample contains 117 ppm Zr. Microphotographs are available from similar samples Y531a and c.

SMG: qtz-bt1-pl-chl-[ms] > and-bt2 porphyroblasts > grt porphyroblasts > ms

Samples Y458b, c: Fine-grained grey metapelite schists from Mount Belches Formation in the central east Bulong Domain in the Kalgoorlie Terrane. Fine-grained foliated granoblastic matrix assemblage consists of quartz – plagioclase – biotite1 – muscovite - ilmenite ± graphite. Biotite1 are medium-grained laths aligned parallel with the early fine muscovite foliation. Garnet occurs in sample Y458c as post-kinematic poikiloblasts of 1.4 mm diameter. Sample Y458c also contains post-kinematic block laths of biotite2 across the main foliation. Sample Y458b contains flattened ovoid chlorite-sericite-plagioclase-quartz pseudomorphs after cordierite (Figure 62d). The cordierite porphyroblast is interpreted to be syn-kinematic with parallel inclusion trails and flattened shapes that are enveloped by the main foliation. Chlorite forms post-kinematic plates across the foliation and retrogressively replaces biotite. Sample Y458b contains: 15.69 ppm La, 8 ppm Th, 135.5 ppm Zr, 3.75 ppm Sm, 27.36 ppm Ce, 16.92 ppm Nd, 0.26 ppm Lu and 3.8 ppm Hf. Similar sample Y458a contains: 18.53 ppm La, 6.9 ppm Th, 133.8 ppm Zr, 3.63 ppm Sm, 38.56 ppm Ce, 21.47 ppm Nd, 0.23 ppm Lu and 3.6 ppm Hf.

SMG: Y458b: qtz-pl-ms-gr > crd porph > flatten > qtz-pl-chl-ms pseudo > bt-op > chl

Y458c: qtz-pl-ms-ilm > bt1 > bt2 laths> grt porphyroblasts > chl1 laths > chl2

Belches Formation Metapelite with Clockwise Evolution

Sample Y508: Grey garnet metapelite schist from Mount Belches Formation in the south central Bulong Domain in the Kurnalpi Terrane. Foliated granoblastic matrix assemblage consists of quartz – andesine – K-feldspar – biotite - pyrite. Garnet occurs as post-kinematic, idioblastic porphyroblasts up to 0.8 mm diameter without inclusions (Figure 65a). Retrogressive chlorite replaces biotite.

SMG: bt-pl-qtz-kfs-py > grt > chl

Sample YD246: Fine-grained garnet-staurolite-biotite metapelite schist from Mount Belches Formation in the central Bulong Domain in the Kurnalpi Terrane. Sample collected by Sarah Jones. Fine-grained, foliated matrix assemblage consists of quartz – oligoclase – biotite1 - ilmenite – graphite - staurolite. Garnet occurs as 1.2 mm diameter, post-kinematic porphyroblasts across the main foliation (Figure 65b). Biotite2 and andalusite also occur as porphyroblasts across the main foliation. Staurolite is fine-grained and early formed within the main foliation and preserved as inclusions within pseudomorphs after cordierite. Cordierite porphyroblasts over-grow all other porphyroblastic phases and the main foliation. No fresh cordierite is preserved and all has been pseudomorphed to chlorite-muscovite aggregates. Staurolite is resorbed by muscovite (Figure 65c, d). All chlorite is retrogressive after biotite and staurolite and in pseudomorphs after cordierite. Late-stage muscovite and chlorite grains grow across the main foliation and pseudomorph assemblages. Sample contains 18.24 ppm La, 6.9 ppm Th, 141.3 ppm Zr, 4.55 ppm Sm, 38.45 ppm Ce, 21.71 ppm Nd, 0.24 ppm Lu and 3.7 ppm Hf.

SMG: qtz-pl-bt1-ilm-gr-st > grt-bt2-and > crd > chl1-ms1 pseudomorph > chl2-ms2 late

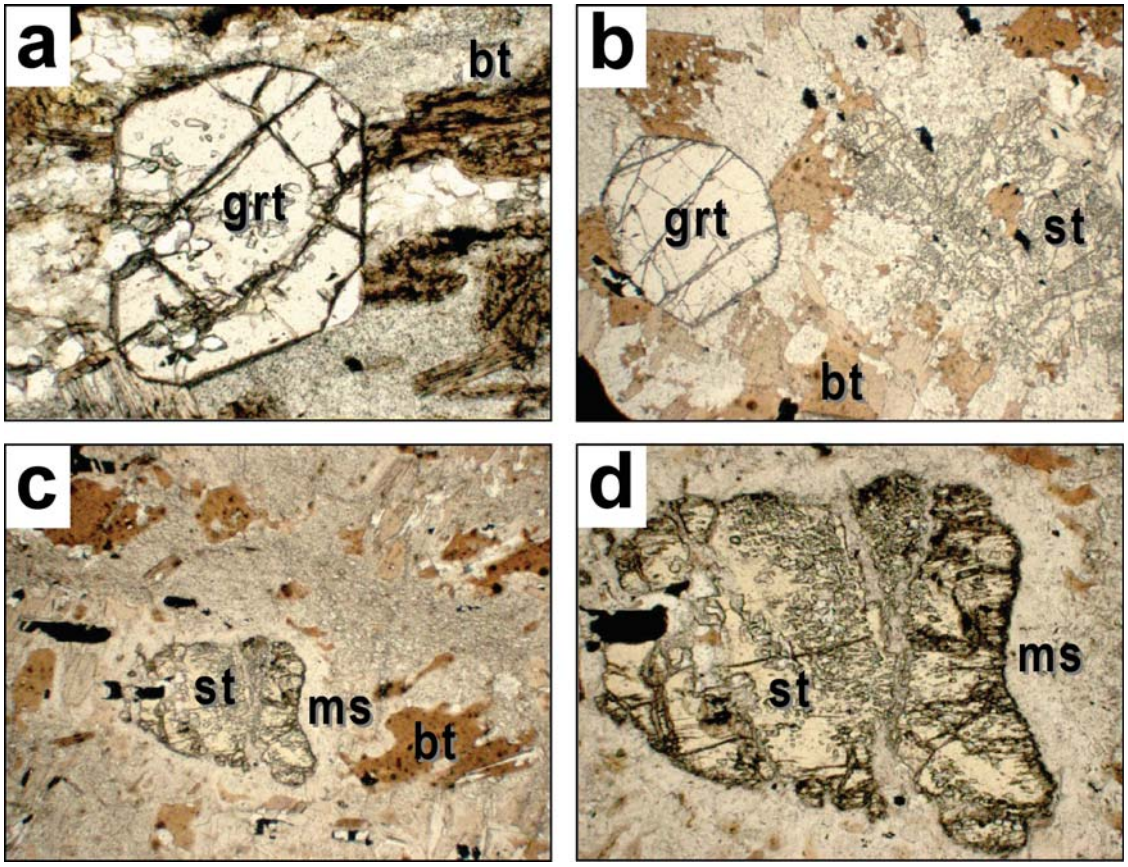

Figure 65: *Metapelite samples from Mount Belches Formation that show clockwise P-T paths. (a) Late garnet over-printing biotite foliation (Y508; x6.3 ppl). (b) Late garnet and staurolite (YD246; x2.5 ppl). (c) Staurolite resorbed by muscovite (YD246; x2.5 ppl). (d) Close up of staurolite resorbed by muscovite (YD246; x6.3 ppl).*

Sample PBGMB0201: Coarse biotite-cordierite-staurolite metapelite from Mount Belches Formation in the central Bulong Domain in the Kurnalpi Terrane. Sample collected by Bruce Groenewald. Coarse-grained, randomly orientated granoblastic matrix assemblage consists of quartz – plagioclase – random red-brown blocks of biotite – opaque – tourmaline – zircon/monazite - staurolite. Sample is devoid of garnet. Staurolite occurs as early poikiloblasts associated with the matrix assemblage and is found as inclusions within cordierite (Figure 66a). Staurolite inclusions within cordierite are enclosed by quartz moats (Figure 66a). Andalusite occurs as large poikiloblasts that over-grow the matrix assemblage (Figure 66b). Staurolite also occurs as late-stage porphyroblasts with quartz moats (Figure 66c, d). Cordierite is fresh and occurs as large poikiloblasts that over-grow the matrix assemblage and staurolite and andalusite (Figure 66a). Cordierite margins are corroded by chlorite-sericite aggregates. All muscovite is late-stage, growing across biotite and cordierite and partially replacing andalusite. Retrogressive chlorite forms on the margins of staurolite and cross biotite grains.

SMG: qtz-pl-bt-st-tur-op > and > crd > ms > chl

Sample 153402: Metapelite schist from Mount Belches Formation in the north central Bulong Domain within the Kurnalpi Terrane. This sample has been described in detail by Mikucki and Roberts (2003). A foliated matrix assemblage contains fine-grained aligned biotite1 and quartz. The foliation is overgrown by coarse stubby biotite2 laths aligned at a high-angle to the foliation. Both episodes of biotite are overgrown by post-kinematic cordierite and biotite3 porphyroblasts. Some cordierite porphyroblasts are pseudomorphed by an opaque mineral, chlorite and muscovite.

SMG: foliation bt1 > stubby bt2 > crd-bt3 > ms-chl-op

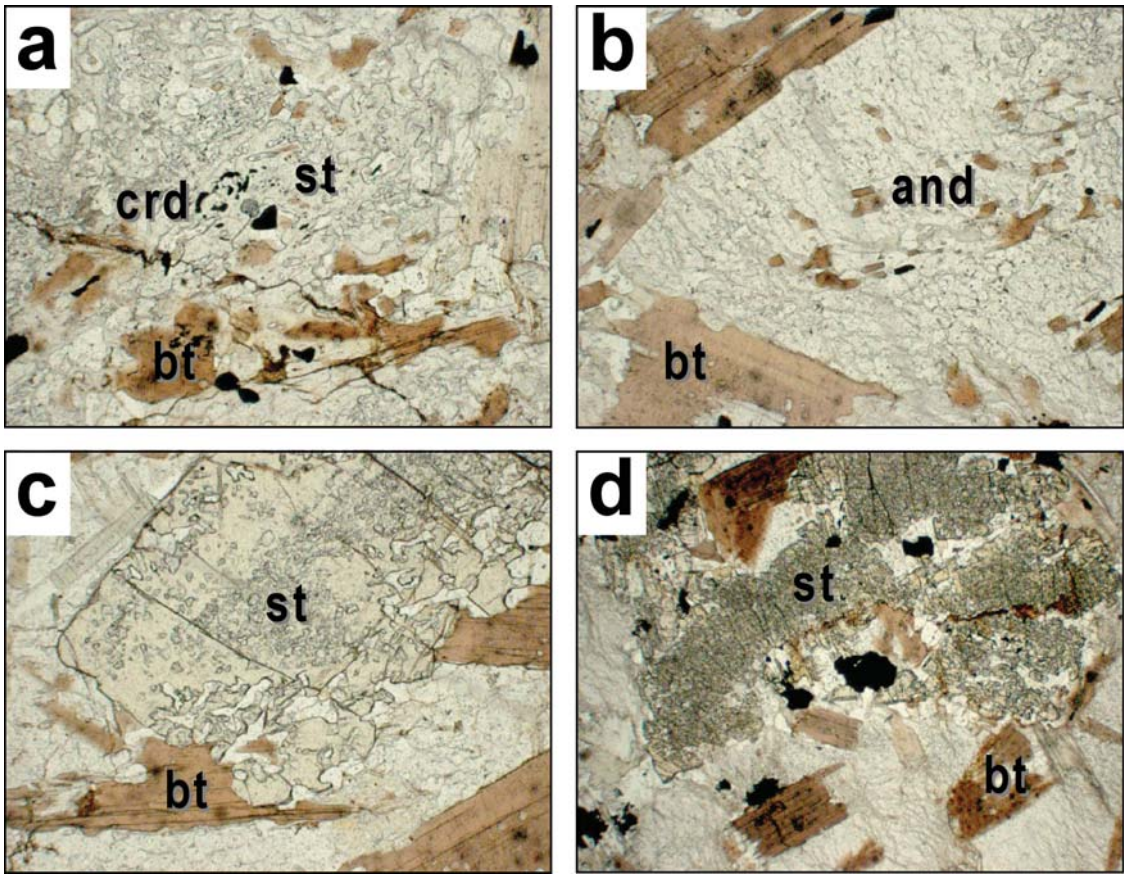

Figure 66: *Metapelite sample PBGMB0201 from the Mount Belches Formation that shows a clockwise P-T path. (a) Early formed amoeboid cordierite in andalusite-phlogopite-staurolite metapelite, Note relict andalusite and staurolite overgrown by amoeboid cordierite (x2.5 ppl). (b) Andalusite porphyroblast (x2.5 ppl). (c) Late staurolite porphyroblast (x2.5 ppl). (d) Late-stage staurolite and quartz moat (x2.5 ppl).*

Pre-Late Basin Stratigraphy Metapelite with Anticlockwise Evolution

Other samples from pre-Late Basin stratigraphy near the Ockerburry shear zone and with anticlockwise P-T paths, but highly aluminous bulk compositions (i.e., Y242, BG6-209, Y507a, b, e, f) are described in the aluminous rock section below.

Sample 98957: Garnet-staurolite-cordierite metapelite schist. Legacy GSWA polished thin section from near Bardoc shear zone in north Boorara Domain in the Kalgoorlie Terrane. Well-foliated, fine-grained granoblastic matrix assemblage consists of quartz – bytownite – chlorite – biotite? - ilmenite. Biotite has not been confidently identified. Both garnet and staurolite are mostly in textural equilibrium and occur as idioblastic post-kinematic porphyroblasts across the main foliation and some garnet over-prints staurolite (Figure 67a). Garnet has thin Ca-plagioclase coronas. Cordierite occurs as large poikiloblasts that apparently enclose garnet and are either late-formed, or alternatively garnet over-grows the cordierite.

SMG: qtz-chl-ilm-pl-bt? foliation > [crd?] > grt-st > [crd?] > pl corona

Sample BG6-142c: Very fine-grained chloritoid-metapelite schist from near the Ockerburry shear zone in Gindalbie Domain in the Kurnalpi Terrane. Foliated matrix assemblage consists of quartz – muscovite1 – ilmenite - biotite. Sample is devoid of plagioclase. Chloritoid occurs as idioblastic

post-kinematic porphyroblasts across the main foliation (Figure 67b). Quartz inclusions in chloritoid define inclusion trails. There is minor flattening of the main foliation around chloritoid porphyroblasts. Second stage muscovite2 is illite and occurs as medium-grained plates across the foliation and either pre-dates or is coeval with chloritoid growth.

SMG: qtz-ms1-bt-ilm > ms2 ≥ ctd porphyroblasts

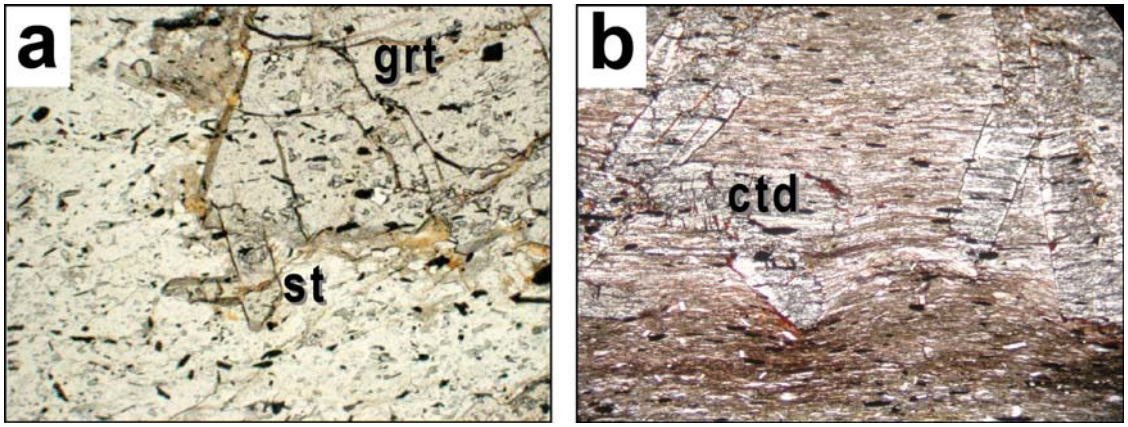

Figure 67: *Metapelite samples from pre-late basin stratigraphy and showing anticlockwise P-T paths. (a) Small post-kinematic staurolite over-printed by garnet porphyroblast (98957; x6.3 ppl). (b) Post-kinematic chloritoid porphyroblast over-printing biotite-ilmenite-quartz foliation (BG6-142c; x2.5 ppl).*

Samples 140106, 140107: Metapelite schist from near the Ockerburry shear zone in the South Boorara Domain within the Kalgoorlie Terrane. These samples have been described by Mikucki and Roberts (2003). A foliated matrix assemblage consists of quartz – muscovite – rutile. The main foliation is overgrown by post-kinematic andalusite porphyroblasts, which are in turn overgrown by chloritoid laths.

SMG: ms-rt > and > ctd

Pre-Late Basin Stratigraphy Metapelite with Clockwise Evolution

Sample Y667a: Fresh metapelite from the Depot Domain within the Kalgoorlie Terrane. Fine-grained metapelite schist with quartz-biotite1-oligoclase-graphite foliated matrix assemblage. Small (0.8 mm) garnet porphyroblasts are rounded and may be pre-kinematic. Blocky red-brown biotite2 porphyroblasts cut the main foliation. Sample contains 116 ppm Zr and was submitted for garnet chronology

SMG: qtz-bt1-pl-gr-grt > bt2 laths

Samples Y667b(ii), (v): Very fine grey metapelite schists from the Depot Domain within the Kalgoorlie Terrane. Weakly foliated granoblastic matrix assemblage consists of quartz – oligoclase – fine brown biotite1 ± ilmenite ± tourmaline. Biotite1 and tourmaline occur in lenses that may be pseudomorphs. Second-stage biotite2 occurs as medium-grained red-brown blocky laths across the main foliation. Sample Y667b(v) is devoid of garnet but has andalusite poikiloblasts and skeletal box-work growth, all with quartz, ilmenite and biotite inclusions. Andalusite over-grows both biotite2 laths and the main foliation and is retrogressively replaced by muscovite at margins and internally. Garnet in Y667b(ii) is very small (0.5 mm diameter), rounded, possibly resorbed and possibly pre-kinematic. Garnets are mostly free of inclusions except for minor quartz.

SMG: Y667b(ii): bt1-qtz-pl-ilm±tur-grt > bt2

Y667b(v): bt1-qtz-pl?-op > bt2 > and > ms.

Sample NA20: Static metamorphosed semi-pelite matrix to conglomerate from the central Depot Domain within the Kalgoorlie Terrane. Sample described by Bickle and Archibald (1984) and reinterpreted here. Fine-grained matrix contains ilmenite – biotite – quartz – plagioclase and large

chloritoid laths. Chloritoid laths are in part over-grown by medium-grained garnet, biotite and staurolite porphyroblasts that appear to have grown across the chloritoid grain margin. An alternative interpretation would be that the chloritoid lath partially overgrows earlier garnet and staurolite. Though textural relations are ambiguous, the former interpretation is preferred for internal consistency with the evolution in other samples at the same locality. Staurolite grains have biotite2 coronas where in contact with chloritoid and retrograde muscovite and chlorite are described from the rock.

SMG: ilm-bt1-pl-qtz-ctd > grt-st-bt1 > bt2 > ms-chl

Sample 63555-111: Static metamorphosed pelite-greywacke from the central Depot Domain within the Kalgoorlie Terrane. Sample described by Bickle and Archibald (1984) and reinterpreted here. Fine-grained matrix assemblage consists of quartz – biotite – muscovite – ilmenite with medium-grained staurolite. The matrix contains large irregular shaped relict chloritoid that is enclosed by a moat of fine-grained muscovite-chlorite aggregate. This moat embays the relict chloritoid and is interpreted to be a pseudomorphed cordierite moat that partially replaced the chloritoid. The pseudomorph assemblage preserves the outline of the original rectangular chloritoid laths, the margin of which was over-grown by garnet porphyroblasts. Garnet also overgrows matrix staurolite. All cordierite in the sample is late-formed and has been entirely pseudomorphed by muscovite and chlorite.

SMG: ilm-bt-st-ms1-qtz-ctd > grt > crd > ms2-chl

Sample 63555-104: Static metamorphosed pelite from the central Depot Domain within the Kalgoorlie Terrane. Sample described by Bickle and Archibald (1984) and reinterpreted here. Fine-grained matrix consists of biotite – ilmenite – quartz with large staurolite porphyroblasts and scattered garnet porphyroblasts. Andalusite porphyroblasts over-grow the staurolite porphyroblasts. All cordierite in the sample is late-formed and has been entirely pseudomorphed by chlorite.

SMG: bt-st-ilm-qtz-grt > and-crd > chl

Sample 83001: Coarse-grained metapelite schist from the south Depot Domain within the Kalgoorlie Terrane. Sample described by Bickle and Archibald (1984) and reinterpreted here. The weakly foliated granoblastic matrix assemblage consists of biotite - muscovite – quartz – ilmenite with andalusite porphyroblasts in textural equilibrium with the matrix. Andalusite porphyroblasts contain relict, irregular shaped staurolite inclusions from an earlier parageneses. Andalusite margins are partially embayed by cordierite moats containing relict ilmenite and biotite1 inclusions. Andalusite is also partially enclosed by coarse-grained moats of inter-grown muscovite, sillimanite and biotite2. Late-stage, fine-grained fibrolite and muscovite replace biotite in these moats.

SMG: st > and-bt1-ms1-ilm-qtz > crd-bt2-ms2-sill > fib-ms3

Samples 63516, 63528: Metapelite schists from the western South Coolgardie Domain within the Kalgoorlie Terrane. These samples have been described by Mikucki and Roberts (2003). The matrix assemblage consists of sillimanite – biotite – quartz. The matrix is overgrown by cordierite porphyroblasts, which are in part replaced by secondary biotite, chlorite and sericite.

SMG: 63516 sill-bt1 > crd > bt2-chl

63528 sill-bt > crd > seri

Samples 78694, 78693: Metapelite schists from the eastern South Coolgardie Domain within the Kalgoorlie Terrane. These samples have been described by Mikucki and Roberts (2003). The foliated matrix is dominated by muscovite and quartz with biotite and chlorite present in sample 78693. Sample 78694 contains andalusite and biotite porphyroblasts that overgrow the main foliation. Both samples contain post-kinematic cordierite after the matrix and porphyroblastic phases. Retrograde muscovite and chlorite partially replace andalusite and cordierite.

SMG: 78694 ms1 > and-bt > crd > ms2-seri

78693 bt-ms1-chl > crd > ms2-chl

Sample BG6-207: Garnet-chloritoid metapelite from Sons of Gwalia drill core 20-30 km south of Leonora, Boorara Domain in Kalgoorlie Terrane. Foliated matrix assemblage consists of quartz-plagioclase?-muscovite-chlorite-ilmenite-dolomite-pyrite. Complex evolution of porphyroblastic phases, all pre-date main foliation and are enveloped. Earliest formed are deformed chloritoid porpyroblast fish; followed by rounded garnet porphyroblasts and last formed are muscovite, chlorite and rare dolomite porphyroblasts. Garnet porphyroblasts are up to 4 mm in diameter. Garnet compositional mapping indicates that the garnets are compositionally flat for Ca, Fe and Mg with typical growth zoning patterns for Mn. Margins are slightly resorbed and show thin rims of elevated Mn, as is common in garnets overprinted by later strain (Kim, 2006). Though complex the garnets show one phase of growth (Figure 68). Garnets are in part idioblastic and also have resorbed and corroded margins. Aligned quartz inclusion trails at high angles to the enveloping foliation indicate pre-kinematic garnet growth followed by later main phase foliation development after most garnet growth. Garnets contain numerous quartz and minor opaque inclusions and very fine monazite? inclusions. Sample submitted for garnet chronology.

SMG: ctd > grt > ms-chl-cc porphyroblasts > ms-chl-ilm-qtz-cc

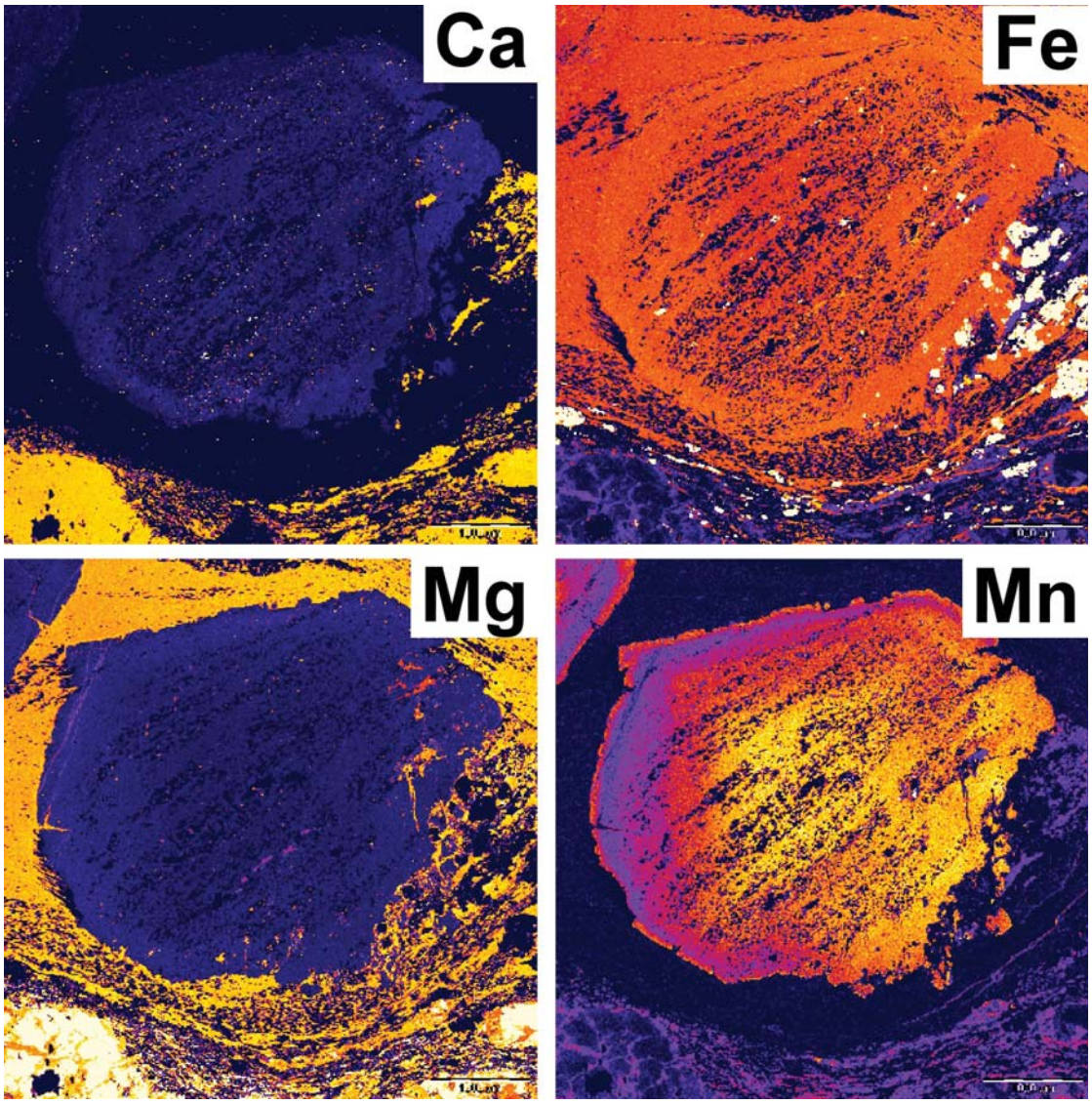

Figure 68: *Garnet compositional maps for sample BG6-207.*

Sample 98939: Weathered dark metapelite schist from north Boorara Domain in the Kalgoorlie Terrane. Sketches and description from a legacy GSWA polished thin section. Foliated granoblastic matrix assemblage consists of quartz – plagioclase? – biotite – opaque - graphite. Garnet occurs as inclusions within andalusite and as post-kinematic porpyroblasts of up to 1.6 mm diameter across the main foliation. There is flattening of the foliation around the garnet porphyroblasts and most garnet has been pseudomorphed to aggregates of iron oxides. Andalusite porphyroblasts over-grow both garnet and the main foliation. Deformation continued after andalusite growth, kinking andalusite and the main foliation is flattened around and envelops the andalusite crystals. All muscovite is late formed and overgrows the main foliation.

SMG: qtz-pl?-bt-op-gr foliation > grt > and > flattening > ms > Feox

Sample BG6-164b: Very fine-grained, pale grey metapelite schist with andalusite porphyroblasts from Boorara Domain in the Kalgoorlie Terrane. Very fine-grained, strongly foliated matrix assemblage consists of quartz – plagioclase? – muscovite - opaque. Andalusite occurs as cm-scale post-kinematic porphyroblasts across the main foliation. There is minor flattening of the foliation around the porphyroblasts.

SMG: ms-op-pl?-qtz > and porphyroblasts > flattening

Sample ER1363: Metapelite schist collected by Sarah Jones, from the south Murrin Domain in the Kurnalpi Terrane. Foliated granoblastic matrix assemblage consists of quartz – andesine – biotite – muscovite – chlorite – ilmenite – magnetite/hematite – rutile – graphite. Garnet occurs as small post-kinematic? porphyroblasts. Biotite is partially retrogressed by chlorite and plagioclase is partially sericitized.

SMG: qtz-pl-bt-ms-chl-ilm-mag/hem-rt-gr > grt > chl-ms

Sample BG6-167a: Very fine-grained, pale grey metapelite schist with andalusite porphyroblasts from Murrin Domain in the Kurnalpi Terrane. Very fine-grained, strongly foliated matrix assemblage consists of quartz – plagioclase? – muscovite - opaque. Andalusite occurs as cm-scale post-kinematic porphyroblasts across the main foliation. There is minor flattening of the foliation around the porphyroblasts and they are deformed by late-stage shear bands. Andalusite is partially pseudomorphed by sericite.

SMG: ms-op-pl?-qtz > and porphyroblasts > flattening-shear bands > sericite

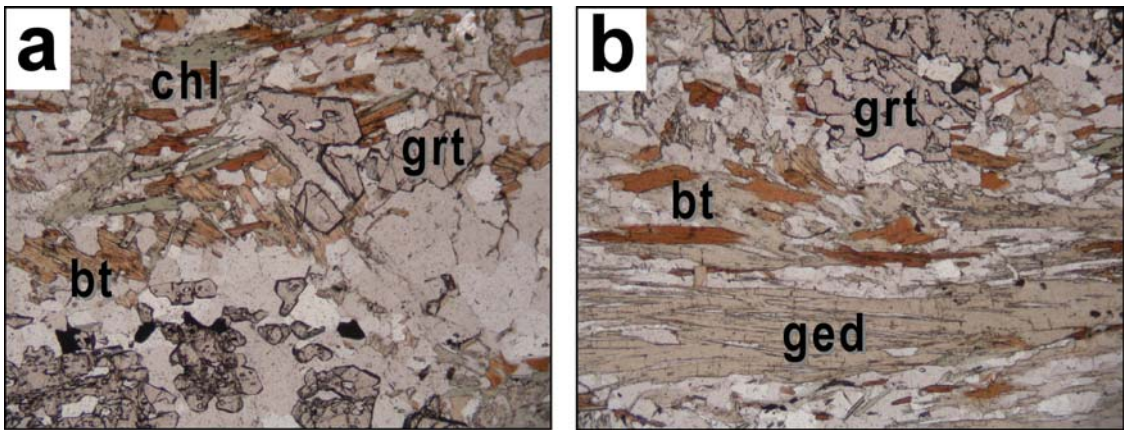

Figure 69: *(a) Post-kinematic garnet over-printing biotite (BG6-213a; x5 ppl). (b) Garnet-gedrite-biotite aluminous rock (BG6-213a; x5 ppl).*

Sample BG6-213a: Medium-grained static metamorphosed aluminous rock from Anxiety Bore drill core in Moilers Domain of the Kalgoorlie Terrane. Polygonal granoblastic matrix assemblage with all phases in textural equilibrium consists of garnet, cordierite, biotite, quartz, andesine, ilmenite and tan-grey gedrite (Figure 69b). Garnet porphyroblasts (2.5 mm diameter) are elongate and skeletal

with idioblastic margins. Garnet is the latest formed phase and grows across gedrite (Figure 69a). Retrograde chlorite growth at the margin of gedrite. Sample submitted for garnet chronology

SMG: ged-crd-qtz-pl-ilm-bt > grt > chl

Sample BG6-213b: Medium to coarse-grained garnet-staurolite metapelite from Moilers Domain in the Kalgoorlie Terrane. Weakly foliated granoblastic matrix assemblage consists of quartz – andesine – weakly aligned orange biotite - ilmenite ± tourmaline. Staurolite occurs as elongate poikiloblasts that grow across the foliation and contains aligned inclusion trails of quartz. Garnet porphyroblasts are up to 2 mm in diameter. There are two stages of garnet growth and both grow across the foliation Second-stage garnet is idioblastic outgrowths from the margins of garnet1, and possibly post-date staurolite. Garnet compositional mapping shows a complex growth zoning pattern with a core recording smooth variation in components and a wide compositionally flat over-growth and thin resorbed outer margin. The core records a smooth decrease in Ca and Mn and increase in Fe and Mg from core to rim. Over-growths are flat with low Mn and Ca and high Fe and Mg compositions. Garnet rims are smooth and rounded to idioblastic, with minor Mn-enrichment in the outer rim (Figure 70).

SMG: bt-qtz-pl-ilm > st-grt1 > grt2.

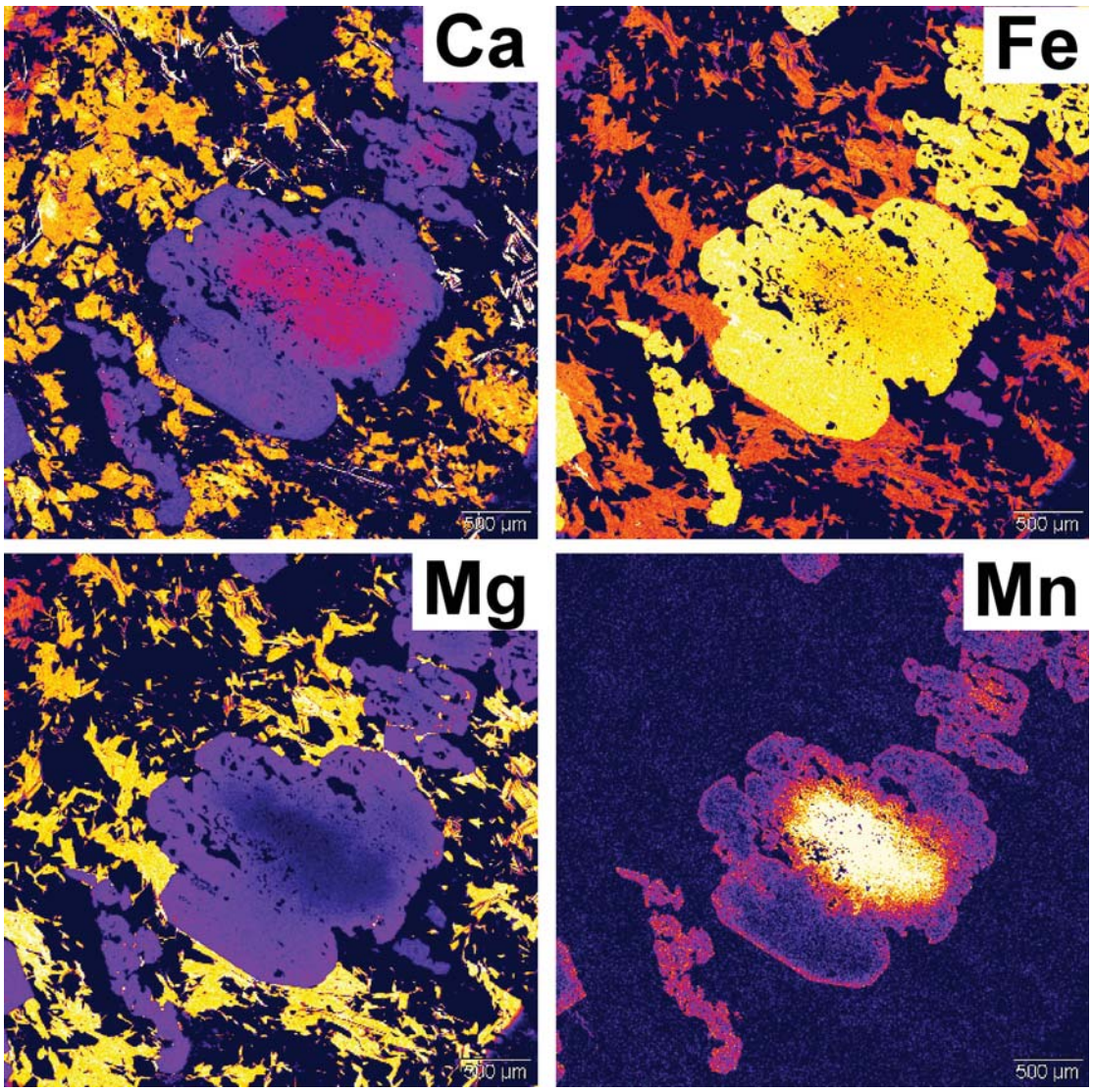

Figure 70: *Garnet compositional maps for sample BG6-213b.*

High-P Metapelite with Clockwise Evolution

Sample BG6-183A: Thin metapelite schist band (30 cm) within a mafic unit, from Coolgardie Domain in the Kalgoorlie Terrane. Foliated matrix assemblage of muscovite (with 1% BaO) – quartz – chlorite – ilmenite – rutile - plagioclase? ± biotite? All rutile occurs near staurolite. Staurolite porphyroblasts over-grow the main foliation and occur as inclusions within garnet (Figure 71). Andalusite was not confirmed and may be staurolite. Garnet porphyroblasts are skeletal with idioblastic margins, are post-kinematic, over-grow both staurolite and the main foliation and are up to 10 mm in diameter. Sample submitted for monazite chronology.

SMG: chl-ms-qtz-pl?-ilm-rt [±bt?] >st-[and?] >grt

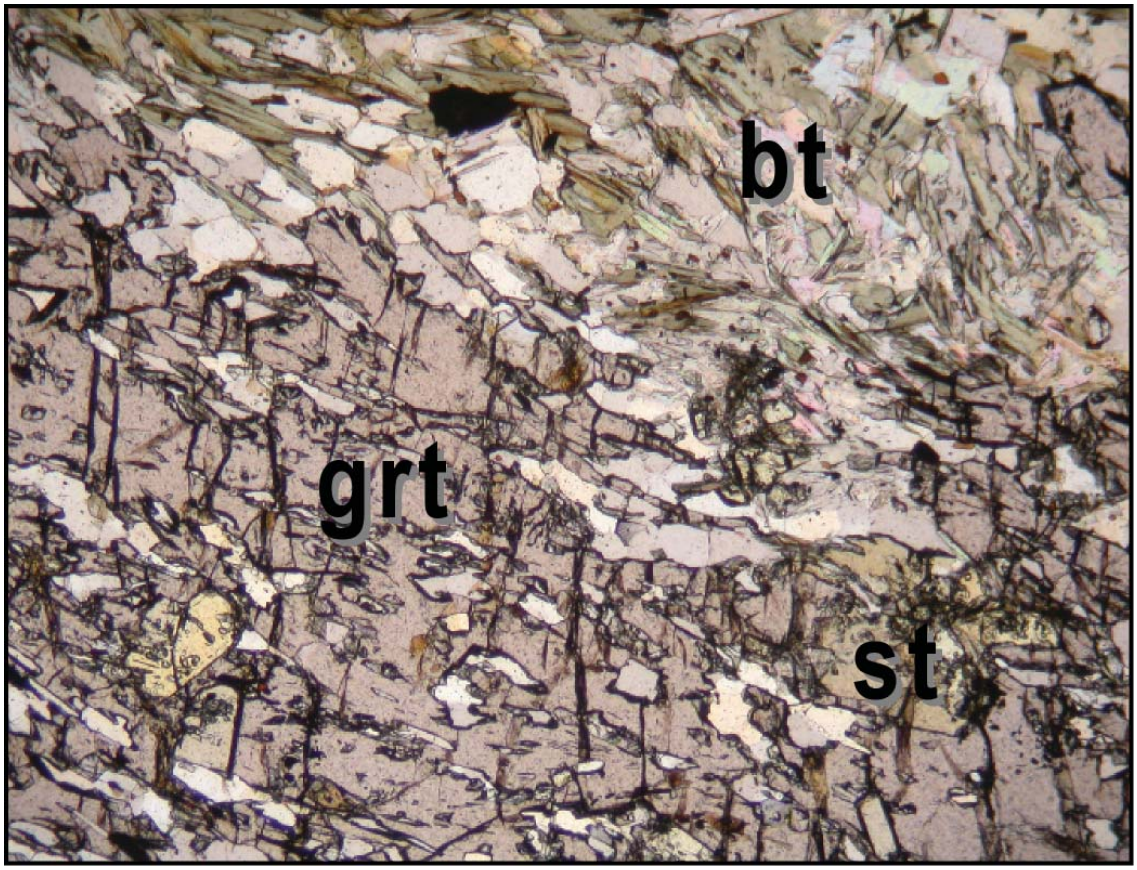

Figure 71: *High-P metapelite sample BG6-183a. Early staurolite grains over grown by a post-kinematic garnet porphyroblast (x5 ppl).*

Southern Cross Metapelite with Clockwise Evolution

Sample Y400f: Dark fine-grained metapelite schist with post-kinematic idioblastic garnet and andalusite porphyroblasts. Sample collected by Steven Wyche from the Transvaal mine in Southern Cross Belt within the Southern Cross Terrane. No thin section is available.

Samples Y400a, c, e: Dark fine-grained metapelite schists. Samples collected by Steven Wyche from the Transvaal mine in Southern Cross Belt within the Southern Cross Terrane. Samples have main

foliation assemblages consisting of quartz, biotite, graphite, tourmaline, Cr-magnetite or ilmenite and staurolite or andesine (Figure 72b, c). Small idioblastic, post-kinematic garnets of 1.0-2.6 mm diameter overgrow the foliation and staurolite (Figure 72a, b, c). Garnets are in turn overgrown by cm-scale, idioblastic, post-kinematic andalusite porphyroblasts (Figure 72d). Retrograde muscovite forms in cracks in andalusite. Rare, late-stage cordierite? pseudomorphs are indicated by tan amorphous moats around chloritoid and andalusite. Garnet compositional mapping from similar sample Y400a, indicate simple, single stage growth, post-kinematic idioblastic garnets with typical growth zoning patterns of decreasing Ca and Mn and increasing Fe and Mg with growth (Figure 73). There are minor amounts of very fine quartz inclusions. Garnets are not resorbed, re-equilibrated or retrograded. Similar samples Y400a and Y400f contain 15 ppm La, 5.3 ppm Th, 78-83 ppm Zr, 2.66 ppm Sm, 28 ppm Ce, 13 ppm Nd, 0.22 ppm Lu and 2.1 ppm Hf, and were submitted for garnet and monazite geochronology.

SMG:	Y400a:	qtz-bt-gr-st-ctd? > crd? > grt
	Y400c:	qtz-bt > grt > and
	Y400e:	qtz-bt-gr-st > and-grt > crd? > ms

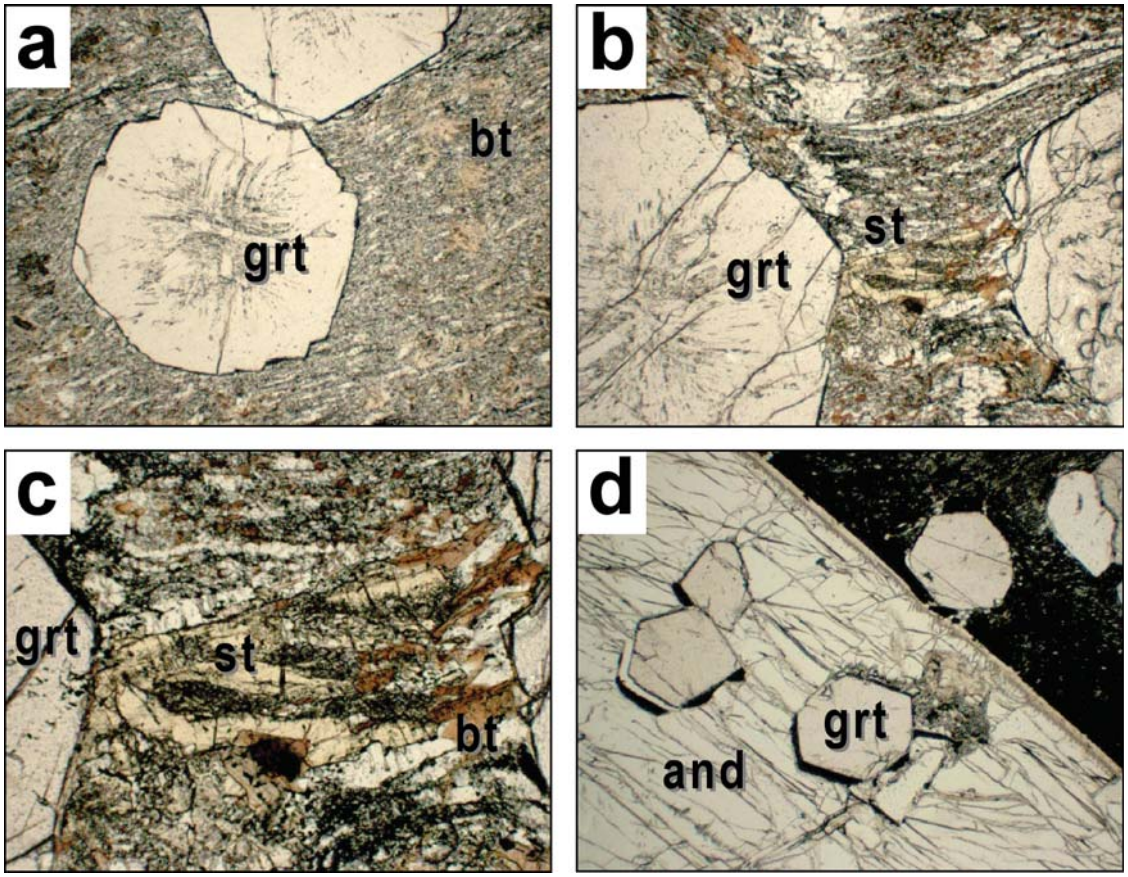

Figure 72: Metapelite samples from Southern Cross belt showing clockwise P-T paths. (a) Post-kinematic garnet porphyroblast over printing matrix foliation (Y400a; x2.5 ppl). (b) Skeletal staurolite aligned within a main foliation that also contains biotite. Matrix foliation is over grown by post-kinematic garnet (Y400a; x6.3 ppl). (c) Close-up of (b) (x10 ppl). (d) Partial view of a very large, late-stage andalusite porphyroblast that over-grows smaller post-kinematic garnets (Y400c x2.5 ppl).

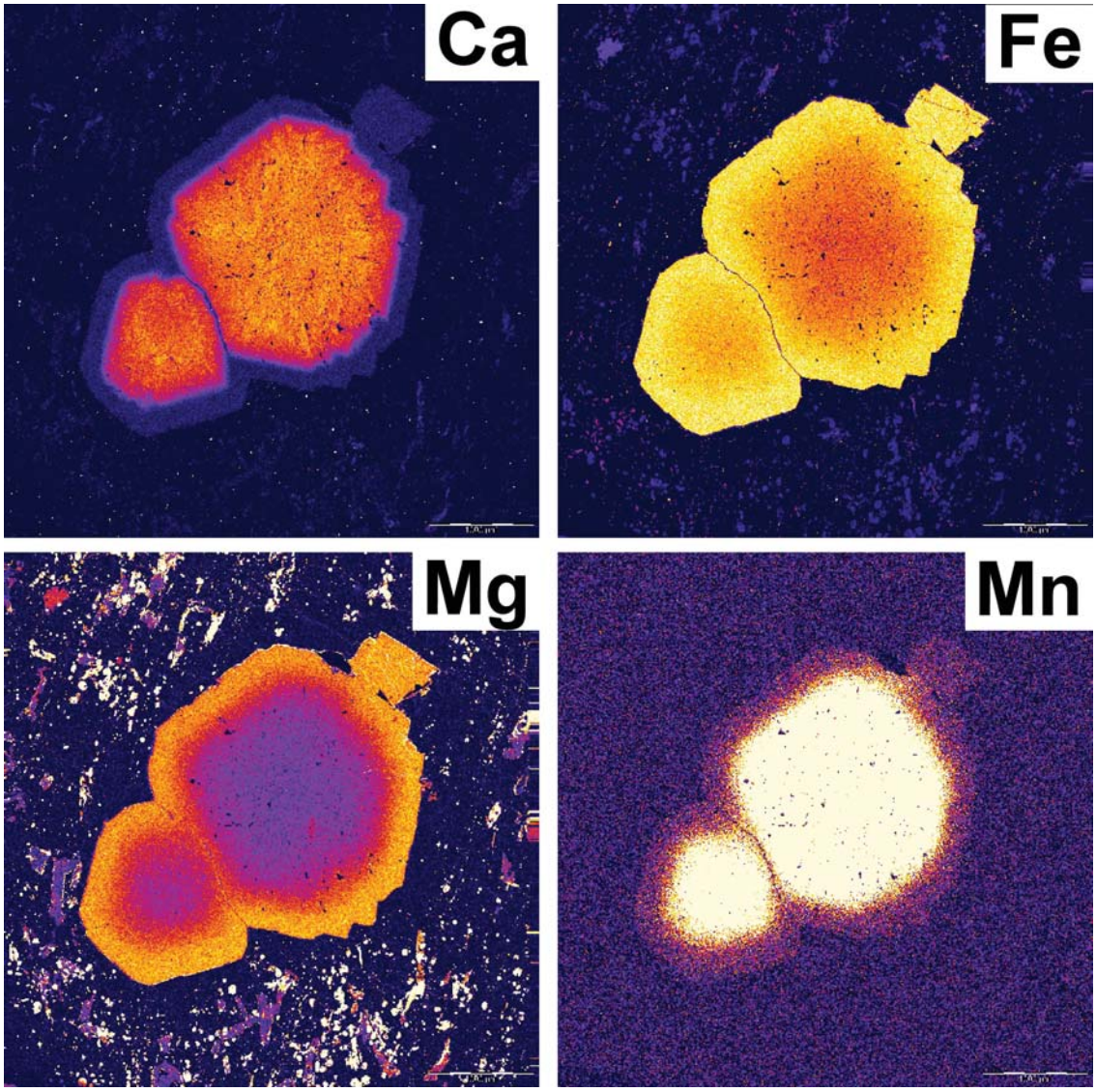

Figure 73: *Garnet compositional maps for sample Y400a.*

Ravensthorpe Metapelite with Anticlockwise Evolution

Sample BG6-198e: Well-foliated quartz – phlogopitic biotite – chlorite metapelite schist from Ravensthorpe Belt within the Southern Cross Terrane. Sample contains: 11 ppm La, 1 ppm Th, 103 ppm Zr, 16 ppm Ce and 12 ppm Nd.

Sample BG6-198f: Porphyroblastic garnet-staurolite-andalusite metapelite schist from Ravensthorpe Belt within the Southern Cross Terrane. Medium-grained foliated granoblastic matrix assemblage consists of quartz – plagioclase? – biotite1 – chlorite1 – opaque – rare rutile. All porphyrobasts grow across the main foliation and range from late-syn-kinematic to post-kinematic. The sequence of porphyroblast formation is from andalusite followed by biotite2, staurolite, garnet, chlorite2 and finally muscovite. Andalusite occurs as early elongate poikiloblasts that grow across the foliation. Blocky biotite2 laths occur both along and across the main foliation and most pre-date staurolite growth. Staurolite occurs as elongate poikiloblasts aligned in and across the main foliation and may be late-syn-kinematic. Garnets are post-kinematic and occur as idioblastic poikiloblasts up to 7 mm

in diameter (Figure 74d). Late-stage chlorite2 and muscovite laths grow across the main foliation. Retrogressive muscovite replaces andalusite and grows near andalusite margins

SMG: qtz-pl?-bt1-chl1-op-rt > and-bt2 porphyroblasts > st porphyroblasts > grt porphyroblasts > chl2 > ms

Sample BG6-198a: Medium-grained garnet metapelite schist from Ravensthorpe Belt within the Southern Cross Terrane. Medium-grained moderately aligned granoblastic matrix assemblage with straight grain margins, consists of quartz – plagioclase? – brown biotite1 – muscovite1 – chlorite – magnetite/hematite. Garnet occurs as post-kinematic, equi-dimensional poikiloblasts with idioblastic margins and diameters up to 6.0 mm. Staurolite occurs as idioblastic porphyroblasts across the foliation and also as elongate skeletal domains with numerous quartz inclusions. Second stage biotite2 laths grew across the main foliation. Andalusite occurs as large poikiloblasts across the foliation. Chlorite occurs as concentrations in the main foliation, the timing of which is uncertain and is also late-formed on the margins of garnet. Muscovite is rare and some grew across the main foliation. Plagioclase is rare and has not been confirmed and the opaque phase is not been determined.

SMG: qtz-pl?-ms1-bt1-op-[chl?] > st-and-ms2-bt2 porphyroblasts > grt porphyroblasts > chl

Sample BG6-198b: Garnet metapelite schist from Ravensthorpe Belt within the Southern Cross Terrane. Medium- to fine-grained, aligned granoblastic matrix assemblage with straight grain margins consists of quartz – plagioclase – brown biotite – opaque. Garnet occurs as post-kinematic, equi-dimensional poikiloblasts with idioblastic margins and grew across the main foliation. Garnet porphyroblasts have diameters up to 4.0 mm and numerous quartz and opaque inclusions. Chlorite retrogressively replaces biotite. Muscovite is absent. Plagioclase is rare and the opaque phase is not been determined.

SMG: qtz-pl-bt-op > grt porphyroblasts > chl

Sample BG6-198c: Garnet-staurolite-chloritoid metapelite schist from Ravensthorpe Belt within the Southern Cross Terrane. Medium-grained, aligned granoblastic matrix assemblage consists of quartz – plagioclase – brown biotite – magnetite. Garnet occurs as late-syn- to post-kinematic, elongate poikiloblasts and skeletal domains that grew across the main foliation (Figure 74a). Garnet porphyroblasts have diameters up to 3.0 mm, have been bent and contain numerous inclusions. There is two-stages of biotite growth; blocky post-kinematic biotite2 grows across the main foliation. Staurolite occurs as post-kinematic poikiloblasts with idioblastic margins that mostly grow across the main foliation but some are also elongate and bent (Figure 74a). Blue, twinned chloritoid occurs as pre-kinematic porphyroblasts (Figure 74b, c). These are elongated parallel with the foliation, contain inclusion trails at angles to the enveloping main foliation and are kinked. Chlorite occurs both parallel to and across the main foliation and retrogressively replaces biotite. Muscovite is absent and plagioclase is rare.

SMG: qtz-pl-bt1-mag > ctd deformed porphyroblasts > grt syn-post-kinematic porphyroblasts > st-bt2 post-kinematic porphyroblasts > chl

Sample BG6-198d: Garnet-chloritoid metapelite schist from Ravensthorpe Belt within the Southern Cross Terrane. Medium-grained, aligned granoblastic matrix assemblage consists of quartz – plagioclase? – rare biotite – common chlorite – ilmenite – magnetite/hematite – rare olive tourmaline. Garnet occurs as post-kinematic, poikiloblasts with idioblastic margins and grew across the main foliation. Garnet porphyroblasts have diameters up to 7.0 mm and contain numerous opaque, quartz and chloritoid inclusions defining inclusion trails. Chlorite inclusions are absent in garnet indicating resorption of all local chlorite during garnet growth. Chloritoid occurs as syn-kinematic elongate porphyroblasts within the granoblastic matrix and also over-grew the main foliation. Muscovite is absent and plagioclase has not been confirmed.

SMG: qtz-pl-bt-mag/hem-ilm-tur-chl-ctd > ctd porphyroblasts > grt post-kinematic porphyroblasts

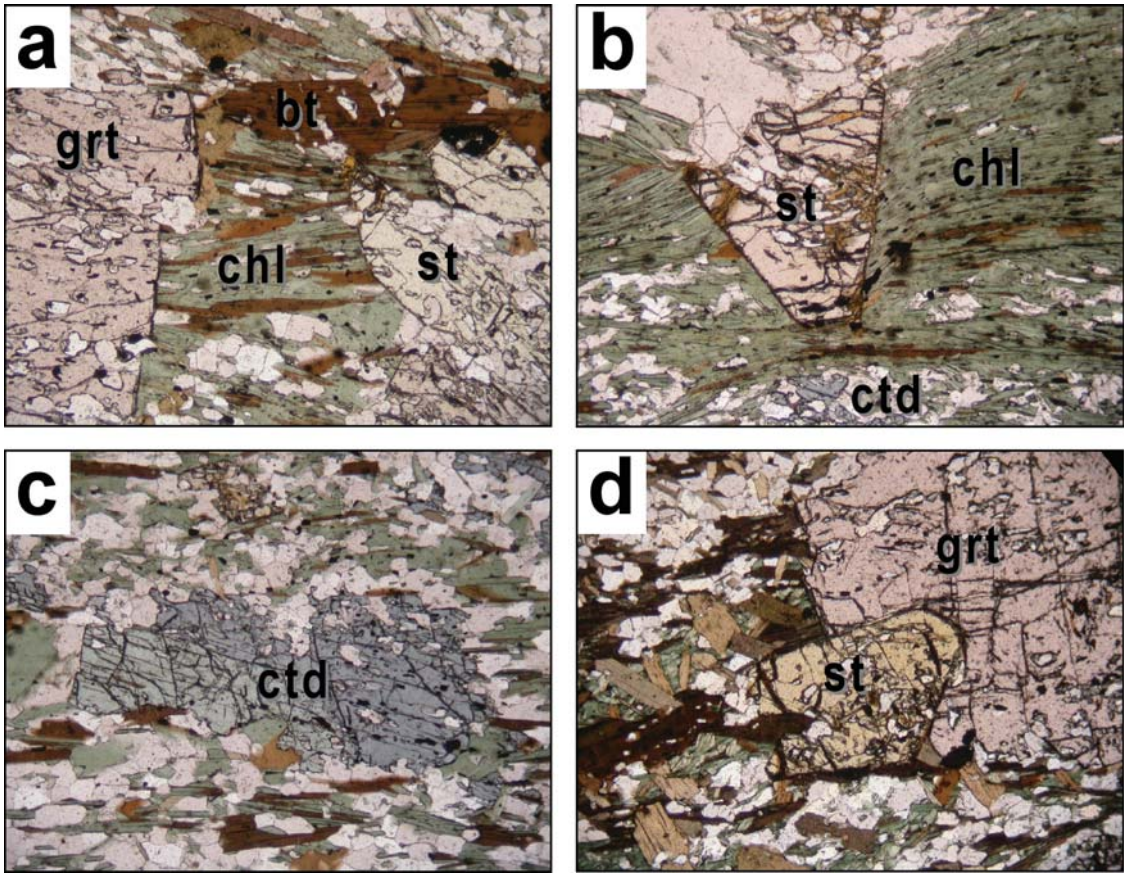

Figure 74: *Metapelite samples from Ravensthorpe belt that show anti-clockwise P-T path. (a) Post-kinematic garnet and staurolite porphyroblasts in chlorite-biotite schist (BG6-198c; x1.5 ppl). (b) Early chloritoid enveloped by chlorite-biotite foliation and late-stage post-kinematic staurolite porphyroblast (BG6-198c; x1.5 ppl). (c) Chloritoid in the main matrix assemblage (BG6-198c; x1.5 ppl). (d) Post-kinematic garnet and staurolite, with garnet being the latest formed (BG6-198f; x5 ppl).*

Sample BG6-196a: Medium-grained foliated metapelitic gneiss with quartzo-feldspathic segregations from Ravensthorpe Belt in Southern Cross Terrane. Weakly foliated granoblastic matrix assemblage consists of quartz – andesine – brown biotite - ilmenite. Post-kinematic garnet porphyroblasts are up to 2.6 mm in diameter and poikiloblastic with idioblastic margins. Garnet compositional mapping indicates that the garnets are compositionally flat for Ca, Fe and Mg with typical growth zoning patterns for Mn (Figure 75). Garnets are idioblastic, over-grow the main foliation, show one phase of growth and are not re-equilibrated, resorbed or retrograded. Garnets contain numerous quartz inclusions. Sample BG6-196a contains 0 ppm La, 2 ppm Th, 129 ppm Zr, 0 ppm Ce and 7 ppm Nd and was submitted for monazite chronology. Hand specimen BG6-196b is medium-grained foliated felsic gneiss with polygonal granoblastic matrix assemblage of quartz-feldspar-garnet-biotite and quartzo-feldspathic segregations. Sample BG6-196b contains 0 ppm La, 3 ppm Th, 119 ppm Zr, 0 ppm Ce and 10 ppm Nd.

SMG: BG6-196a: qtz-pl-bt-ilm > grt

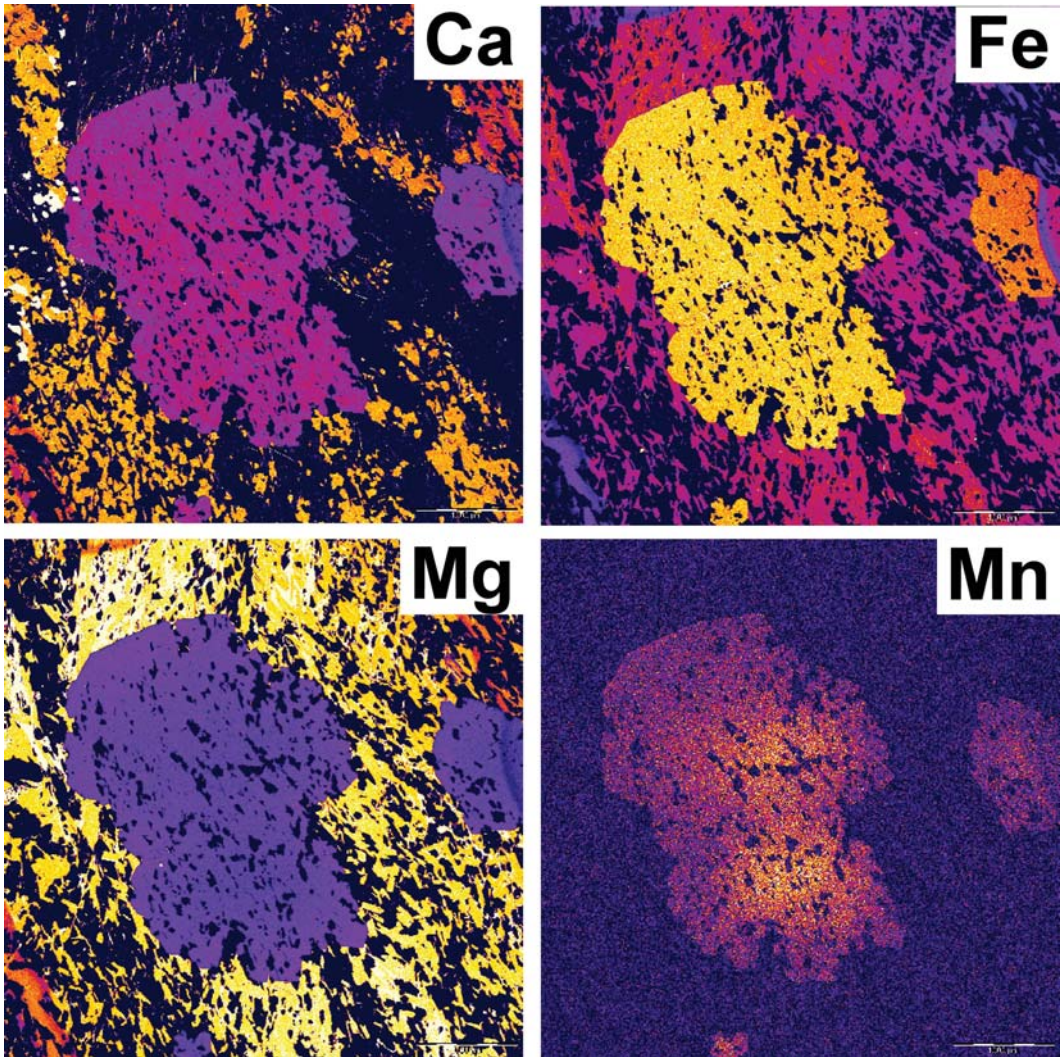

Figure 75: *Garnet compositional maps for sample BG6-196a.*

Samples BG6-197a,b: Biotite metapelite schists from the Ravensthorpe belt in the Southern Cross Terrane. Schistose matrix assemblage with aligned and granoblastic texture, consists of quartz – oligoclase1 – orange phlogopitic biotite1 – olive tourmaline. Both samples are devoid of garnet. Secondary plagioclase2 occurs as poikiloblasts that over-grow the main foliation. Pale cream chlorite clots (BG6-197b) and fibrolite-biotite2 clots (BG6-197a) are interpreted as early-formed cordierite pseudomorphs and these are elongate lenses within the main foliation. Andalusite has not been confirmed by electron-probe or XRD; but has been interpreted as poikiloblasts in BG6-197b and relict grains in domains replaced by plagioclase in BG6-197a. Sample BG6-197a contains late-stage fine shear bands of fibrolite-biotite2 and sillimanite grows across andalusite? and plagioclase poikiloblasts. Retrogressive antigorite and kaolin are identified by XRD.

SMG: qtz-pl1-bt1-tur-crd? > and? > pl2 > bt2-fib±chl pseudomorph = bt2-fib shear bands

Sample BG6-197c: Cordierite-sillimanite metapelite schist from the Ravensthorpe belt in the Southern Cross Terrane. Well-aligned granoblastic matrix assemblage with aggregate ribbons, consists of quartz – oligoclase – red-orange biotite2 – sillimanite1 – opaque – tourmaline - zircon. Sample is devoid of garnets and staurolite. There are three episodes of biotite growth. Early coarse-grained biotite1 occurs in low-strain domains and is in equilibrium with early cordierite and andalusite. Biotite2 in the main foliation is over-printed by thin fine-grained shear bands with biotite3 and fibrolite2 assemblages. All muscovite is late-stage, post-dates the main foliation and is

rare. Early, coarse-grained ovoid porphyroblasts of cordierite, plagioclase and andalusite are enveloped by the main foliation (Figure 76a, b). Cordierite is not confirmed by electron microprobe, but is indicated by ovoid porphyroblasts that are partially replaced by sericite-yellow chlorite-iddingsite (Figure 76a, b).

SMG: pl-crd-and-bt1 porphs > bt2-qtz-pl-tur-op-sill1 foliation > fib2-bt3 shear bands > ms

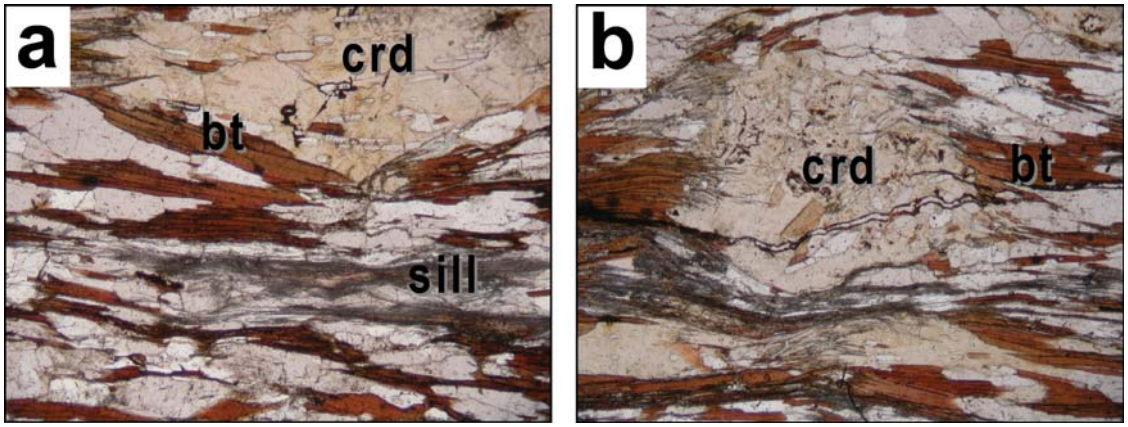

Figure 76: *Cordierite metapelite sample BG6-197c from Ravensthorpe belt that show anti-clockwise P-T path. (a) Early cordierite porphyroblast enveloped by biotite-sillimanite main foliation. Cordierite contains early foliation defined by rounded quartz inclusions. (x5 ppl). (b) Early cordierite porphyroblast enveloped by biotite-sillimanite main foliation (x5 ppl).*

Ravensthorpe Metapelite with Clockwise Evolution

Sample BG6-199: Very fine-grained garnet-andalusite metapelite schist from the Ravensthorpe belt in the Southern Cross Terrane. Very fine-grained foliated matrix assemblage consists of quartz – oligoclase – brown biotite – muscovite - ilmenite. The schistose foliation is crenulated prior to porphyroblast growth. Garnet occurs as small (0.5 mm diameter), inclusion-free, post-kinematic idioblasts that over-grew the foliation (Figure 77a). Andalusite occurs as large post-kinematic poikiloblasts with quartz and garnet inclusions and inclusion trails of the over-grown main foliation. Garnet inclusions in andalusite domains indicate andalusite post-dates the garnet and both are post-dated by some flattening strain (Figure 77a, b).

SMG: qtz-pl-bt-ms-ilm > crenulation > grt porphyroblasts > and porphyroblasts

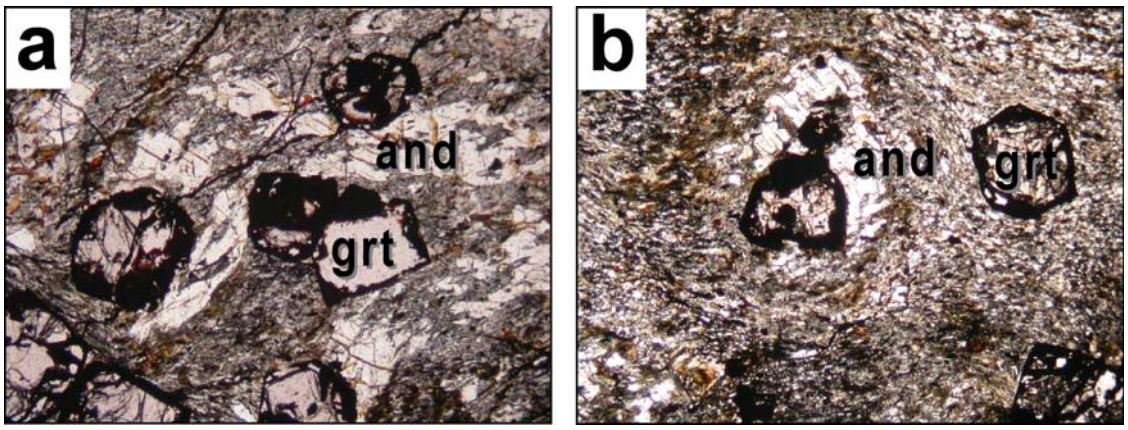

Figure 77: *Andalusite metapelite sample BG6-199 from the Ravensthorpe belt that shows a possible clockwise P-T path. (a) Post-kinematic garnet that is possibly over-grown by andalusite (x5 ppl). (b) Post-kinematic garnet that is possibly over-grown by andalusite and the matrix foliation is later flattened around both minerals (x5 ppl).*

Hybrid Between Calc-Pelite and Mafic

Sample Y690a: Mylonitized intermediate to mafic biotite amphibolite from Edjudina Domain in Kurnalpi Terrane. Has an annealed medium-grained polygonal granoblastic matrix of quartz, anorthite, orange biotite, weakly aligned hornblende, magnetite, hematite, ilmenite and carbonate. Garnet occurs as syn- to post-kinematic porphyroblasts up to 3.2 mm in diameter and with quartz inclusion trails. Grey-blue-green ferro-hornblende also occurs as porphyroblasts. Sample Y690g(i) is mylonitized garnet-rich mafic, with garnet-hornblende-plagioclase matrix assemblage and no thin section is available. Sample Y690a contains 104 ppm Zr and was submitted for garnet geochronology.

SMG: qtz-pl-bt-hbl1-mag-hem-ilm-carb > grt-hbl2

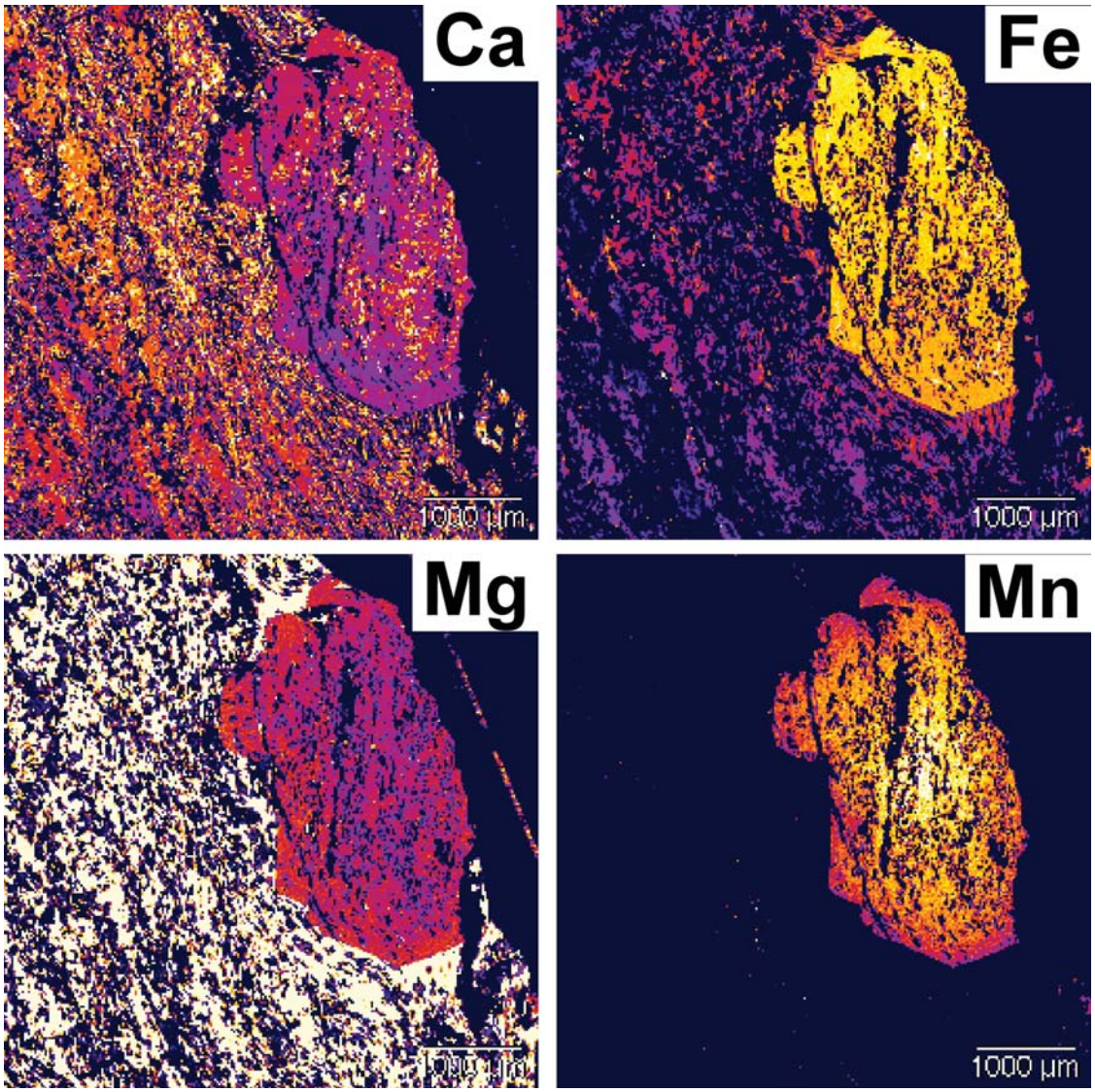

Figure 78: *Garnet compositional maps for sample BG6-120e.*

Sample BG6-120c: Medium-grained calc-pelite schist with matrix assemblage of biotite-sericite-quartz and garnet-hornblende porphyroclasts from Edjudina Domain in Kurnalpi Terrane. Foliated granoblastic matrix assemblage consists of quartz – plagioclase – orange-brown biotite – muscovite – minor grunerite. The matrix assemblage envelops deformed porphyroclastic fish of green hornblende and garnet. Garnets are elongate, poikiloblastic, rotated, have rounded resorbed margins and are enveloped by the foliation. Garnet porphyroblasts are up to 5 mm in diameter. These pre-

kinematic porphyroblasts, now porphyroclasts, may indicate an early metamorphic parageneses that have been reworked by a later metamorphic event represented by the foliated matrix. Plagioclase is partially replaced by sericite. Sample submitted for monazite chronology.

SMG: hbl-grt fish > qtz-pl-ms-bt-gru > seri

Sample BG6-120e: Fine-grained garnet-biotite-hornblende calc-pelite schist from Edjudina Domain in the Kurnalpi Terrane. Foliated granoblastic matrix assemblage consists of quartz – plagioclase – orange biotite – muscovite/margarite? - ilmenite. Green magnesio-hornblende and garnet are poikiloblasts in equilibrium with the matrix assemblage. Garnet porphyroblasts are up to 3.8 mm diameter. Some while mica is late-stage across the main foliation and sericite partially replaces plagioclase. Retrogressive chlorite replaces biotite and there is rare retrogressive calcite. Garnet compositional mapping of BG6-120e indicates weak growth zoning with a smooth decrease in Mn and increase in Mg from core to rim. Fe and Ca are nearly compositionally flat with a weak increase in Ca towards the rims (Figure 78). Garnet rims are idioblastic, not resorbed and are devoid of Mn-enrichment in the outer rim.

SMG: grt-hbl-bt-qtz-pl-ilm±ms/marg > marg > chl-cc.

Samples BG6-120k, l: Medium-grained, foliated and layered calcareous garnet amphibolite from Edjudina Domain in the Kurnalpi Terrane. Medium-grained, well-aligned granoblastic matrix assemblage consists of quartz – plagioclase – green-blue to green ferro-tschermakitic hornblende – ilmenite – magnetite – garnet1 - calcite. There are possibly two stages of garnet growth; garnet1 is syn-kinematic poikiloblasts (1.3-2.5 mm) that are in equilibrium with and enveloped by the main foliation (Figure 79). Garnet2 growth is represented by idioblastic garnet margins that abut the main foliation minerals. Plagioclase is partially replaced by muscovite.

SMG: hbl-pl-qtz-grt1-mag-ilm-cc > grt2 > ms

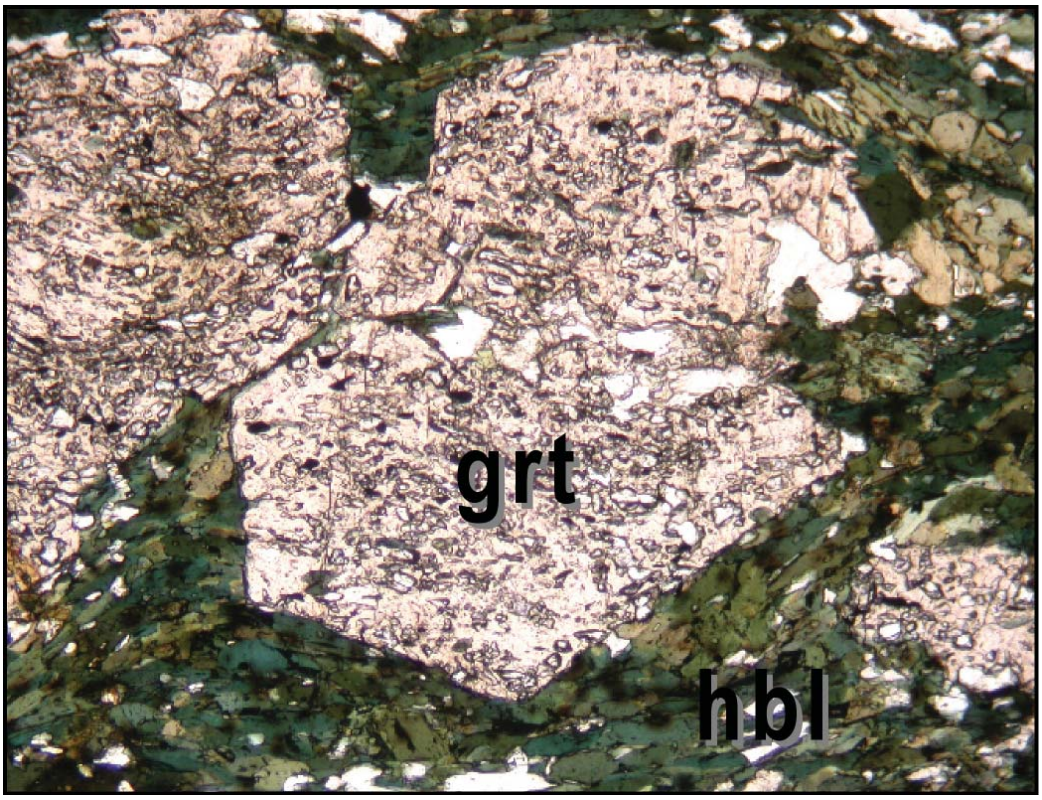

Figure 79: *Poikiloblastic garnet porphyroblast in hornblende-quartz matrix of sample BG6-120k (x5 ppl).*

Calc-Pelite Schists

Samples 99966130e,g, h, i, k, l: Well-foliated calc-pelite schists in legacy GA polished thin sections, from the Gindalbie Domain within the Kurnalpi Terrane. Schistose matrix assemblage in all samples consists of quartz – bytownite – green biotite – muscovite – dolomite – pyrite ± chlorite ± graphite. Quartz and plagioclase form granoblastic matrix and muscovite define a well-developed schistosity. Early porphyroblasts, enveloped by the chlorite foliation include biotite, muscovite and small albite poikiloblasts in samples 99966130e,I, l. Sample 99966130k contain post-kinematic laths of dolomite, ilmenite and green magnesio-hornblende across the main foliation. Sample 99966130e contains post-kinematic laths of biotite and ilmenite? across the main foliation. The post-kinematic porphyroblasts suggest either post-deformation thermal peak or a second metamorphic event. Epidote is common (5-10%) in sample 99966130g and forms part of the main foliation assemblage, otherwise absent in other samples. Retrogressive chlorite2 replaces biotite. Interpreted as pre-Late Basin stratigraphy with clockwise P-T evolutions.

SMG:	99966130e:	qtz-dol-bt-ms-pl porphyroblasts > chl foliation > ilm-bt porphs.
	99966130g:	qtz-dol-bt-ms-py-epi-pl porphyroblasts and foliation > chl2
	99966130h:	qtz-dol-ms-py porphyroblasts and foliation
	99966130i:	qtz-dol-bt-ms-chl-py-pl porphyroblasts and foliation
	99966130k:	qtz-pl-bt?-chl foliation > ilm-dol-hbl porphyroblasts
	99966130l:	qtz-pl-dol-bt-ms?-py-gr porphyroblasts and foliation

Highly Aluminous Rocks

Muscovite-Kyanite Schist Within Granitoid

Samples BG6-159e, j: Coarse-grained muscovite-biotite metapelitic schist from the Ora Banda Domain in the Kalgoorlie Terrane. Coarse-grained well-foliated granoblastic matrix assemblage consists of quartz – ± plagioclase – tan brown biotite – muscovite ± chlorite – rutile – apatite ± zircon ± monazite. Muscovite aggregate clots may be pseudomorphed andalusite or kyanite. Rutile and apatite grains are large and rounded, inclusion-free apatite grains of 1-7 mm diameter grew across the main foliation. Late fibrolite and peak metamorphic kyanite are recognised in the field indicating decompression.

SMG: and or ky > qtz±pl-bt-ms±chl-rt-ap±zrn±mnz > ms-fib > ap

Kyanite Hill Locality, Leonora

Samples Y242a, b: Kyanite-andalusite aluminous schist from the Gindalbie Domain in the Kurnalpi Terrane. Strongly foliated matrix assemblage consists of quartz aggregate ribbons – graphite – skeletal andalusite – skeletal kyanite ± muscovite. Andalusite occurs as syn-kinematic poikiloblastic and as skeletal masses containing inclusion trails aligned with the foliation (Figure 80a). The early andalusite poikiloblasts are boudinaged, flattened and enveloped by the foliation, by continuing deformation (Figure 80b). Late-stage sillimanite? forms within the foliation in sample Y242a. In sample Y242b, post-kinematic kyanite laths grow across the foliation at high angles (Figure 80d). Some kyanite grains are kinked during late-stage flattening across the foliation (Figure 80c). Retrogressive muscovite2 forms on kyanite margins. Skeletal andalusite2 grows out from kyanite margins, growing preferentially along foliation planes (Figure 80d).

SMG: qtz-gr±ms1-and1-ky1? > sill > ky2 > ms2-and2

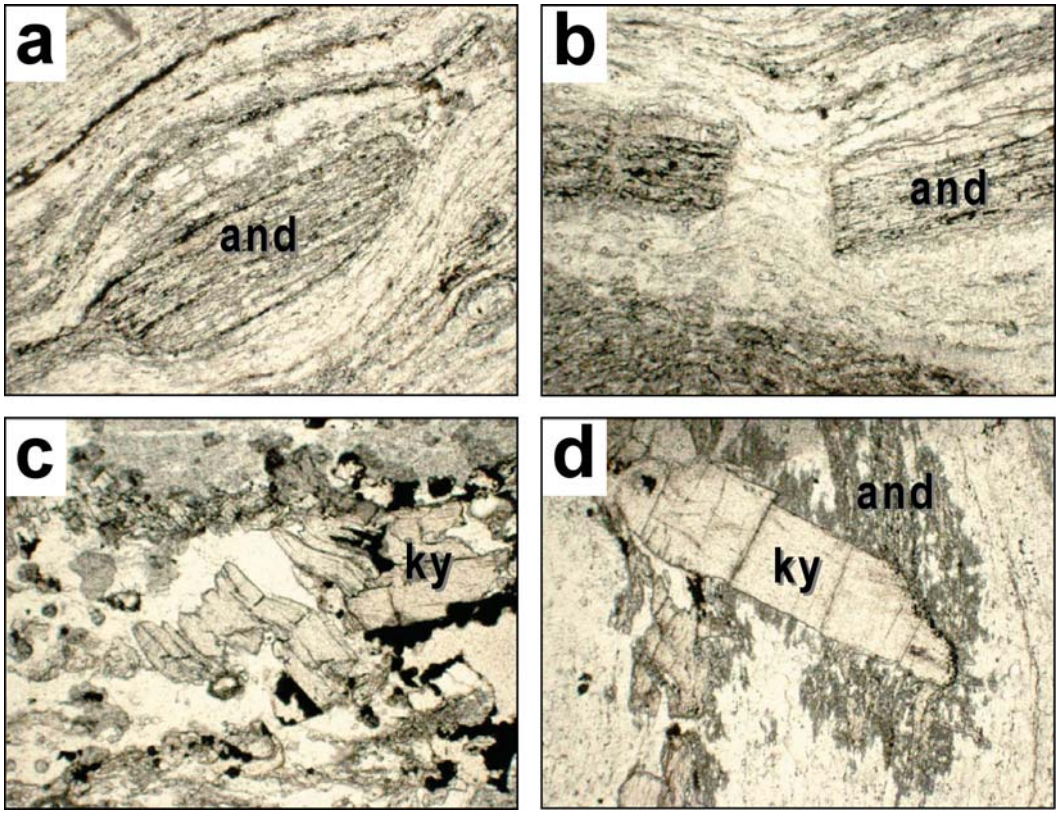

Figure 80: *Microphotos from aluminous schists at Kyanite Hill, Leonora. (a) Early enveloped andalusite (Y242a; x2.5 ppl). (b) Boudinaged andalusite in (Y242a; x2.5 ppl). (c) Kinked kyanite (Y242b; x6.3 ppl). (d) Late skeletal andalusite2 growth on the margin of post-kinematic kyanite (Y242b; x6.3 ppl).*

Mount Martin locality

Other samples from this locality (i.e., MM1 to MM4) are described in detail in Purvis (1978, 1984).

Sample BG6-209: Kyanite-andalusite aluminous schist from Boorara Domain in the Kalgoorlie Terrane. Strongly foliated, fine-grained granoblastic matrix assemblage consists of quartz and muscovite with domains of intimate thin, elongate skeletal andalusite. Quartz forms granoblastic aggregate ribbons and muscovite is well aligned. Skeletal andalusite is interpreted to be syn-kinematic, growing during foliation development. There are two episodes of kyanite porphyroblast growth. Kyanite1 occurs as large laths, parallel to and over-growing the main foliation preserving inclusion trails. Kyanite1 laths are deformed by boudinage; sub-domains are rotated and have undulose extinction, and are interpreted to be late kinematic. Fine, high-strain ductile shear bands post-date kyanite1 laths. Kyanite2 occurs as laths across both the main foliation and shear bands and is post-kinematic. Retrogressive muscovite grows at the margins of kyanite. Early long laths of apparent chloritoid and feldspars have not been confirmed by XRD.

SMG: qtz-ms-and > ky1 porphyroblasts > shear bands > ky2 porphyroblasts > ms

Samples Y507a, b, e, f: Pale green kyanite-andalusite aluminous schists. Samples are from the Zuleika shear zone in the Boorara Domain within the Kalgoorlie Terrane. Fine-grained, strongly foliated matrix assemblage consists of quartz – muscovite – sillimanite1 – pale pink andalusite – pale blue kyanite1 ± chlorite? ± opaque ± graphite. Kyanite1-quartz-muscovite±sillimanite1 defines the early main foliation. Syn-kinematic elongate andalusite poikiloblasts and skeletal stringers are slightly later-formed and overprint the main foliation, containing kyanite inclusions. Both kyanite and andalusite porphyroblasts are drawn boudinaged and enveloped by further flattening of the main foliation. Sillimanite1 is in the earliest formed filiation and occurs as inclusions in kyanite. Sillimanite2 occurs in late-stage shear bands. Kyanite2 occurs as laths enveloping andalusite (Figure

81a) and as laths across the main foliation. Retrogressive muscovite forms on the margins and pressure shadows of kyanite and andalusite. Sample Y507e contains discrete biotite seams within the main foliation. Sample Y507b contains discordant biotite foliations formed by dissolution and accumulation in seams of secondary biotite (Figure 81b). Sample Y507a contains: 0.59 ppm La, 0.5 ppm Th, 58.8 ppm Zr, 0 ppm Sm, 1.11 ppm Ce, 0.49 ppm Nd, 0 ppm Lu and 1.6 ppm Hf.

SMG: Y507a: qtz-ms-sill1 > ky1 > and > flatten > ky2 > ms-sill2 shear band > ms

Y507b: qtz-ms-sill1 > and > flatten

Y507e: qtz-ms-chl?-gr?-bt > and > flatten > ms

Y507f: qtz-ms-op > and > flatten > ms

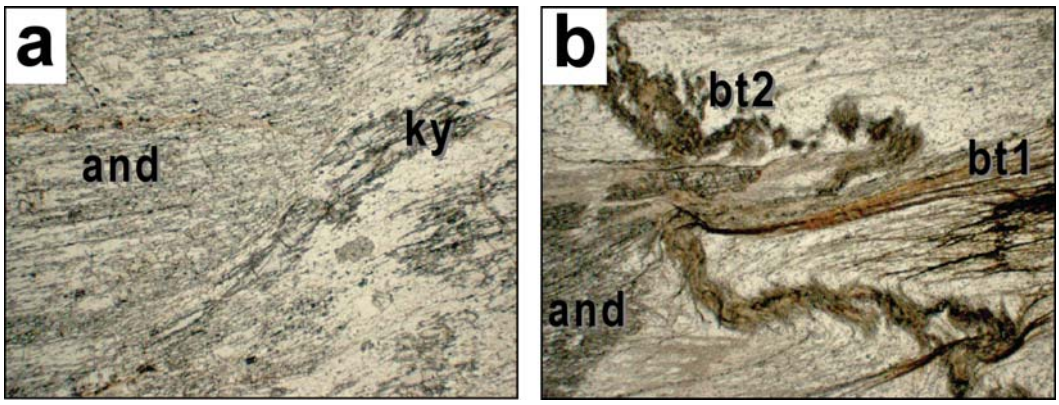

Figure 81: *Microphotos from aluminous schists at Mount Martin. (a) Large, early poikiloblastic andalusite, enveloped by the matrix foliation that contains kyanite on poikiloblast margins (Y507a; x2.5 ppl). (b) Two biotite foliations and andalusite. A late biotite foliation is discordant and "stylolitic", formed by dissolution (Y507b; x2.5 ppl).*

Felsic Rocks

High-Grade Quartzo-Feldspathic Gneiss

Sample BG6-212: Migmatized garnet-biotite-quartz-plagioclase-K-feldspar gneiss with coarse-grained polygonal granoblastic texture. Sample is from the Southern Linden Domain within the Kurnalpi Terrane. Two stages of melting are evident: early stromatic melt parallel to a gneissic banding defined by variation in garnet-biotite proportion (Figure 82a, b). Second melting event produces segregations discordant to gneissic banding. Later ductile shear bands transect both stages of melt segregations. Zircon is recognised in thin section. Rock is of upper-amphibolite grade with >20% partial melt and thus possibly contains metamorphic zircons. Biotite is aligned and dark brown. Plagioclase is partially replaced by symplectites of quartz-K-feldspars. Garnets are large poikiloblasts up to 9mm diameter and have textures suggesting two stages of growth; syn-matrix cores with idioblastic post-kinematic over-growths. Second-stage garnet overgrowths have thin plagioclase coronas. Garnet compositional mapping indicates very complex garnet growth and re-equilibration histories. Though garnets now show heterogenous patchy compositional patterns, relict signs of initial typical garnet growth patterns are evident, with cores on average relatively high in Mn and low in Mg. Superimposed on this growth pattern is a very patchy distribution due to partial post-growth re-equilibration, strong corrosion and resorption of margins and very thin Mn-enriched outer-rims (Figure 83). Garnet resoption and accumulation of Mn at the margins is due to metamorphic reactions as the rock evolved, and not due to deformation (Kim, 2006). Coarse quartz, plagioclase, K-feldspar, biotite, clinozoisite, apatite? or monazite? inclusions are common in garnet. Coarse apatite and monazite? or clinozoisite? grains are also common in the polygonal granoblastic matrix. Sample contains 43 La, 13 ppm Th, 206 ppm Zr, 99 ppm Ce and 42 ppm Nd and was submitted for garnet, monazite and zircon geochronology

SMG: ep-pl-bt-qtz-kfs inclusions > grt1-bt-kfs-pl-PM-qtz-ttn > grt2 > pl coronas

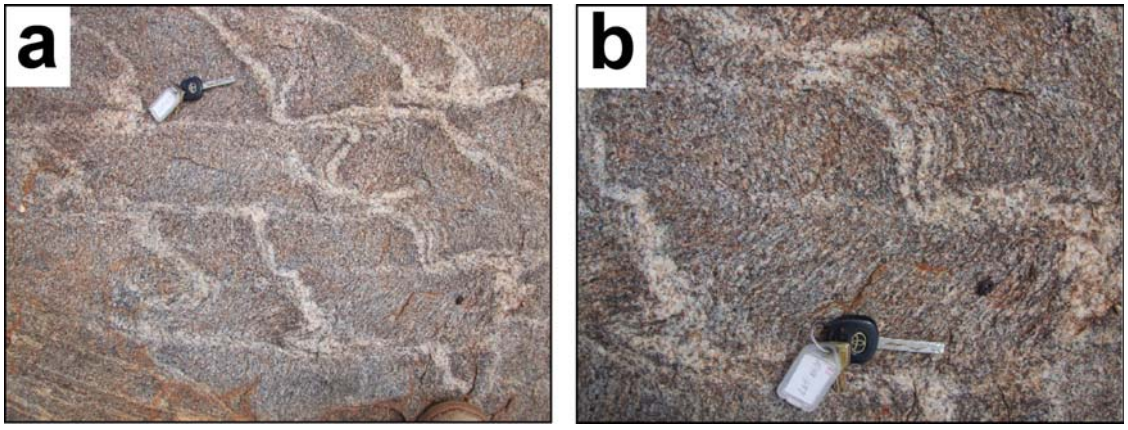

Figure 82: *(a) Two generations of partial melt in high-grade garnet-biotite quartzo-feldspathic gneiss at locality BG6-212. (b) Close up view of same outcrop.*

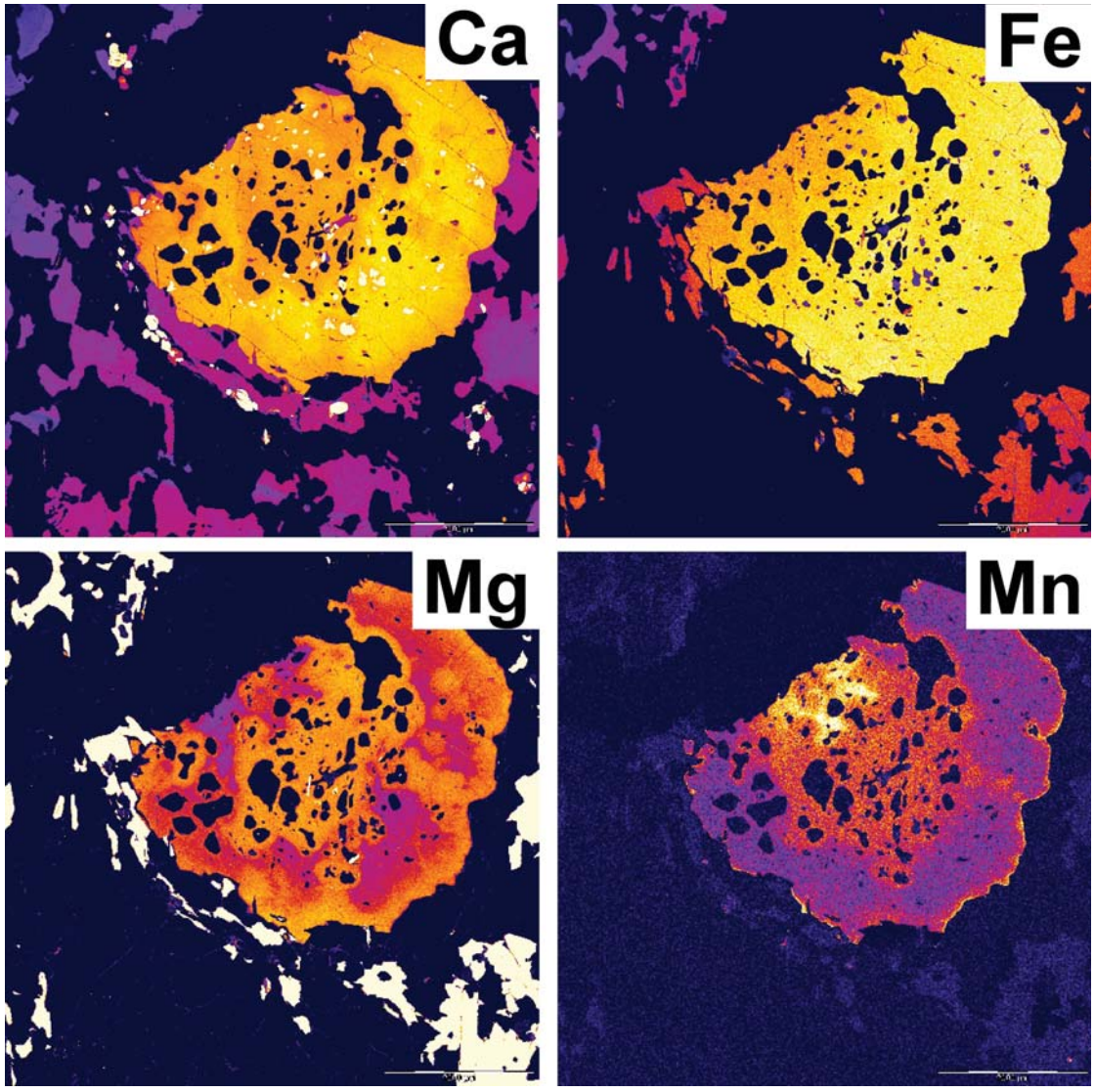

Figure 83: *Garnet compositional maps for sample BG6-212.*

Calcsilicate Rocks

High-Grade Calcsilicate Gneisses in Burtville Terrane

Sample BG6-151a: Very coarse-grained and layered calc-silicate polygonal granoblastic gneiss. Sample from the Merolia Domain in the Burtville Terrane and no thin section is available. Sample contains grossular-diopside-plagioclase-hornblende-quartz layers and hornblende-plagioclase layers. Similar sample BG6-151b at the same locality has andesine-grossular-salite-titanite-zircon assemblages and garnet porphyroblasts up to 8 mm in diameter. Garnet makes up to 50% of the rock and is partially replaced by epidote-quartz symplectites (Figure 84). Sample BG6-151a was submitted for garnet geochronology.

SMG: BG6-151a: grt-di-pl-hbl-qtz

BG6-151b: pl-grt-cpx-ttn-zrn-grt > qtz-ep

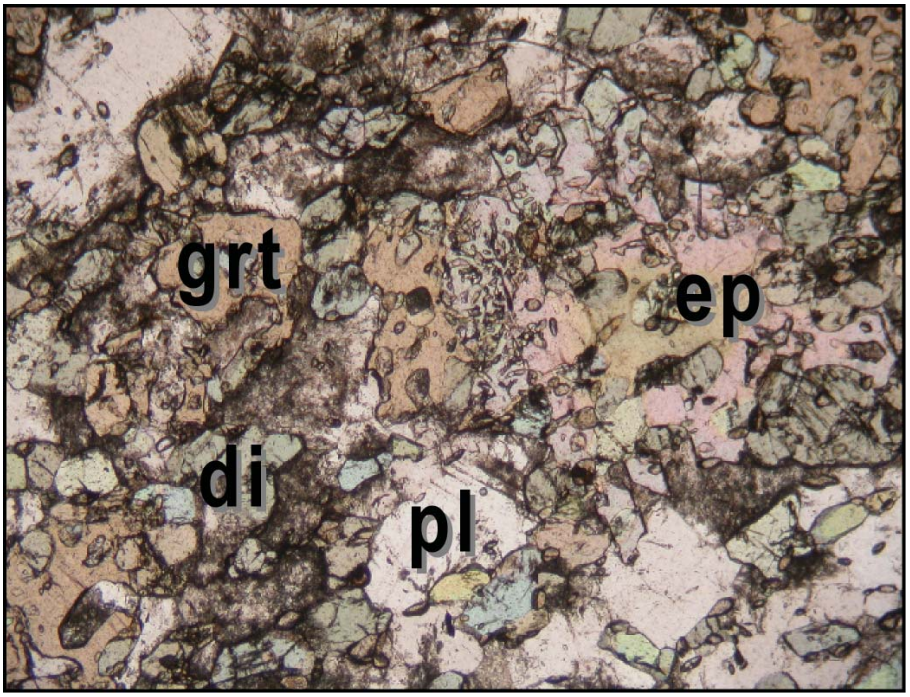

Figure 84: *Polygonal granoblastic grossular-plagioclase-diopside calcsilicate with large, secondary poikiloblastic and zoned epidote on the right (BG6-151b; x5 ppl).*

Sample BG6-152c: Granoblastic clinopyroxene-bearing intermediate gneiss from the Merolia Domain in the Burtville Terrane. Medium-grained polygonal granoblastic matrix assemblage consists of quartz – oligoclase – opaque – clinopyroxene – green ferroan pargasitic hornblende - apatite. Epidote-quartz symplectites are secondary. Similar sample BG6-152a contains: 57 ppm La, 8 ppm Th, 178 ppm Zr, 103 ppm Ce and 45 ppm Nd.

SMG: qtz-pl-cpx-hbl-ap > ep-qtz

Sample 179693B: Intermediate clinopyroxene-amphibolite gneiss sample collected by Charlotte Hall, from the Merolia Domain in the Burtville Terrane. Aligned polygonal granoblastic matrix assemblage consists of quartz? – andesine – green magnesio-hornblende – salite clinopyroxene. Sample is devoid of garnet and presence of quartz has not been confirmed. Clinozoisite only occurs as late-stage coronas.

SMG: hbl-pl-qtz?-cpx > czo

MINERAL CHEMISTRY

The composition of metamorphic minerals from the EYC is described below as summaries based on the different rock-types mafic, calcsilicate, calc-pelite and metapelite, in different structural or stratigraphic settings. Southern Cross Terrane mineral compositions are only described from the select number of samples described in the Petrography section above. A comprehensive description of minerals from regions west of the Ida Fault will be presented in Phase-2 of the EYCMP.

Garnet

Garnets in high-P garnet-amphibolite are almandine-grossular and have the following total composition range: XFe^{2+} (0.33 to 0.72), XMg (0.01 to 0.21), XCa (0.07 to 0.36), XMn (0.04 to 0.40) and Fe/(Mg+Fe) ratios (0.746 to 0.961). Half of these samples show typical growth-zoning patterns of increasing Fe^{2+} and Mg, decreasing Mn and Fe/(Mg+Fe) and decreasing to flat Ca, towards the rims. The remainder show inverse growth zoning of decreasing or increasing Fe^{2+}, opposite increasing or decreasing Mn and Mg and increasing or decreasing Ca, towards the rims. Some garnets have very thin outer re-equilibration rims (<20 μ) showing slightly lower Fe and higher Ca and Mg or lower Mg and higher Mn. Garnet in high-P garnet-clinopyroxene mafics are of two types. Almandine-grossular in BG6-171b has the following total composition range: XFe^{2+} (0.40), XMg (0.001 to 0.002), XCa (0.55 to 0.54), XMn (0.05) and Fe/(Mg+Fe) ratios (0.994 to 0.998). These porphyroblasts are compositionally flat, showing no systematic patterns. Mn-rich almandine in BG6-206 has the following composition range from core to rim: XFe^{2+} (0.51 to 0.50), XMg (0.05 to 0.07), XCa (0.15 to 0.26), XMn (0.29 to 0.21) and Fe/(Mg+Fe) ratios (0.906 to 0.885). This garnet shows irregular inverse growth zoning of decreasing then increasing Fe^{2+} and Mg, decreasing Mn and Fe/(Fe+Mg) and increasing then decreasing Ca, towards the rim. Garnets in high-P garnet-grunerite-amphibolite have the following composition range from core to rim: XFe^{2+} (0.71 to 0.78), XMg (0.01 to 0.03), XCa (0.18 to 0.12), XMn (0.10 to 0.06) and Fe/(Mg+Fe) ratios (0.965 to 0.984). Most porphyroblasts show irregular typical growth-zoning patterns of increasing Fe^{2+}, increasing then decreasing Mg and Fe/(Mg+Fe) and decreasing Mn and Ca, towards the rims. Some of these garnets have very thin outer rims showing slightly higher Mn and Ca.

Garnet in low-P garnet-amphibolite has the following composition range from core to rim: XFe^{2+} (0.84), XMg (0.04), XCa (0.10), XMn (0.016 to 0.023) and Fe/(Mg+Fe) ratios (0.951 to 0.955). This porphyroblasts is essentially compositionally flat with only a slight increase in Mg and Ca and decrease in Mn.

Garnets in moderate-P garnet-amphibolite in the Forrestania Belt have the following composition range from core to rim: XFe^{2+} (0.52 to 0.67), XMg (0.04 to 0.25), XCa (0.27 to 0.10), XMn (0.23 to 0.03) and Fe/(Mg+Fe) ratios (0.946 to 0.716). Most porphyroblasts show a typical growth-zoning pattern of increasing Fe^{2+} and Mg and decreasing Mn, Ca and Fe/(Mg+Fe), towards the rims. These typical garnets have very thin outer rims showing slightly lower Fe. A single garnet shows inverse growth zoning of decreasing Fe^{2+} and Fe/(Fe+Mg) and increasing Mg, Ca and Mn.

Garnets in Mount Belches Formation metapelites showing anticlockwise P-T paths (n=15) have the following total range from core to rim: XFe^{2+} (0.61 to 0.86), XMg (0.06 to 0.12), XCa (0.16 to 0.03), XMn (0.23 to 0.00) and Fe/(Mg+Fe) ratios between 0.842 and 0.929. Most of these small porphyroblasts show a consistent and typical growth-zoning pattern of increasing Fe^{2+} and Mg, decreasing Fe/(Mg+Fe) and Mn and decreasing to flat Ca towards the rims. Half of these typical zoned garnets have very thin outer rims showing slightly lower Mg and higher Mn. Four samples show atypical inverse growth-zoning patterns of decreasing Mg with increasing or decreasing Fe^{2+}, Mn, Ca and Fe/(Mg+Fe) towards the rims. Garnets in Mount Belches Formation metapelites showing clockwise P-T paths have the following range from core to rim: XFe^{2+} (0.65 to 0.78), XMg (0.12 to 0.14), XCa (0.04 to 0.05), XMn (0.17 to 0.06) and Fe/(Mg+Fe) ratios (0.834 to 0.865). These porphyroblasts show a consistent and typical growth-zoning pattern of increasing Fe^{2+}, Mg and Fe/(Mg+Fe), decreasing Mn and decreasing to flat Ca towards the rims. Some of these garnets have very thin outer rims showing slightly lower Mg and higher Mn.

Garnet in metapelite from pre-Late Basin stratigraphy showing anticlockwise P-T paths has the following range from core to rim: XFe^{2+} (0.73 to 0.80), XMg (0.07 to 0.09), XCa (0.07 to 0.05), XMn (0.14 to 0.06) and Fe/(Mg+Fe) ratios (0.910 to 0.902). This porphyroblast shows a typical growth-zoning pattern of increasing Fe^{2+} and Mg and decreasing Mn, Ca and Fe/(Mg+Fe) towards the rims. This garnet does not have a thin outer rim showing re-equilibration. Large garnet porphyroblasts (2-9 mm) in metapelite from pre-Late Basin stratigraphy showing clockwise P-T paths have the following total range from core to rim: XFe^{2+} (0.59 to 0.87), XMg (0.03 to 0.12), XCa (0.15 to 0.03) and XMn (0.22 to 0.01) and Fe/(Mg+Fe) ratios between 0.851 and 0.958. Half of these porphyroblasts show typical growth-zoning patterns of increasing Fe^{2+}, Mg and decreasing Mn, Ca and Fe/(Mg+Fe) towards the rims. The remainder show atypical inverse growth-zoning patterns of decreasing Mg and increasing or decreasing Fe^{2+} and Fe/(Mg+Fe) and decreasing Mn and Ca towards the rims. Some garnets have very thin outer rims (<20-40 μ) showing slightly lower Mg and higher Mn. Large garnet (8 mm) in high-P metapelite from pre-Late Basin stratigraphy showing a clockwise P-T path (BG6-183a) has the following range from core to rim: XFe^{2+} (0.68 to 0.77), XMg (0.04 to 0.05), XCa (0.05 to 0.06), XMn (0.22 to 0.13) and Fe/(Mg+Fe) ratios (0.937 to 0.933). This porphyroblast shows a typical growth-zoning pattern of increasing Fe^{2+}, Mg and Ca and decreasing Mn and Fe/(Mg+Fe) towards the rim. This garnet has a very thin outer rim (<25 μ) showing slightly lower Mg and Ca and higher Fe/(Fe+Mg).

Small idioblastic garnets from metapelite in the Southern Cross Belt have the following total range from core to rim: XFe^{2+} (0.66 to 0.92), XMg (0.02 to 0.08), XCa (0.08 to 0.01), XMn (0.23 to 0.00) and Fe/(Mg+Fe) ratios (0.969 to 0.919). These porphyroblasts show a consistent and typical growth-zoning pattern of increasing Fe^{2+} and Mg and decreasing Mn, Ca and Fe/(Fe+Mg) towards the rims. These garnets do not have thin outer rims showing re-equilibration. Large garnets porphyroblasts (3-5 mm) in metapelite from the Ravensthorpe Belt have the following total range from core to rim: XFe^{2+} (0.67 to 0.86), XMg (0.04 to 0.10) and XMn (0.23 to 0.01) and XCa between 0.03 and 0.08 and Fe/(Mg+Fe) ratios between 0.955 and 0.890. These porphyroblasts show a consistent and typical growth-zoning pattern of increasing Fe^{2+}, Mg and decreasing Fe/(Mg+Fe) and Mn towards the rims and irregular decreasing and increasing Ca patterns. Most of these garnets have very thin outer rims (<20-30 μ) showing slightly lower Mg and higher Mn and Fe/(Fe+Mg).

Garnets in hybrid rock between mafic and calc-pelite are almandine-grossular and have the following composition range from core to rim: XFe^{2+} (0.51 to 0.60), XMg (0.04 to 0.09) and XMn (0.14 to 0.05) and XCa between 0.22 and 0.32 and Fe/(Mg+Fe) between 0.864 and 0.940. Most porphyroblasts show typical growth-zoning patterns of increasing Fe^{2+} and Mg and decreasing Mn, Ca and Fe/(Mg+Fe) towards the rims. One sample has atypical growth zoning of decreasing then increasing Mg and Mn and increasing Fe^{2+} and Ca towards the rims. Some garnets have very thin outer rims (<15-40 μ) showing slightly lower Mg and higher Mn.

The large garnets (9 mm) in migmatitic quartzo-feldspathic gneiss are almandine-grossular and have the following composition range from core to rim: XFe^{2+} (0.45 to 0.48), XMg (0.08 to 0.12), XCa (0.38 to 0.44), XMn (0.05 to 0.01) and Fe/(Mg+Fe) ratios (0.843 to 0.799). This porphyroblast shows a typical growth-zoning pattern of increasing Fe^{2+} and Mg and decreasing Mn and Fe/(Mg+Fe) and increasing to decreasing Ca towards the rim. This garnet has a very thin outer re-equilibration rim (<40 μ) showing slightly lower Mg and higher Ca and Fe/(Fe+Mg).

The large garnets (8 mm) in high-grade calc-silicate gneiss are grossular and have the following composition range from core to rim: XFe^{2+} (0.05 to 0.04), XMg (0.005 to 0.003), XCa (0.92 to 0.91), XMn (0.03 to 0.02) and Fe/(Mg+Fe) ratios (0.897 to 0.949). This porphyroblast shows an inverse growth-zoning pattern of decreasing Fe^{2+} and Mg, increasing Fe/(Mg+Fe) and flat Ca and Mn towards the rim. This garnet has a very thin outer re-equilibration rim (<30 μ) showing slightly higher Fe.

Clinopyroxene

Clinopyroxene in high-P clinopyroxene amphibolite samples are zoned salite with high-Mg rims. Mg/(Mg+Fe) ratios range 0.587-0.708, moderate Al_2O_3 contents of 0.661-1.949 wt% and moderate

Na_2O contents of 0.354-0.634 wt%. Clinopyroxene in high-P garnet-clinopyroxene mafic gneiss is unzoned hedenbergite, with Mg/(Mg+Fe) ranging 0.064-0.075, low Al_2O_3 contents of 0.366-0.397 wt% and low Na_2O contents of 0.187-0.249 wt%.

Clinopyroxene in mafic granulite samples are unzoned augite and salite, with Mg/(Mg+Fe) ranging 0.658-0.777, low Al_2O_3 contents of 0.834-1.856 wt% and low Na_2O contents of 0.246-0.379 wt%.

Clinopyroxene in moderate- to low-P amphibolite samples have a large range in compositions, though most grains are essentially unzoned salite and rare diopside. Mg/(Mg+Fe) ratios range 0.550-0.824, moderate Al_2O_3 contents of 0.406-2.131 wt% and low Na_2O contents of 0.125-0.774 wt%. There is no systematic difference in clinopyroxene composition from amphibolites, whether they containing epidote or not.

Clinopyroxene in calc-silicate gneisses in the Burtville Terrane are unzoned salite, with Mg/(Mg+Fe) ranging 0.637-0.787, low Al_2O_3 contents of 0.549-1.280 wt% and low Na_2O contents of 0.222-0.478 wt%.

Orthopyroxene

All orthopyroxene in mafic granulite samples are hypersthene with Mg/(Mg+Fe) ratios ranging 0.520-0.649 and Fe_2O_3 ranging 0.804-2.122 wt%. Al_2O_3 contents are very low, most range 0.514-1.147 wt% and a few are between 1.855-2.755 wt%. All other orthopyroxene reported from the EYC is enstatite in metamorphosed ultramafic. This enstatite has Mg/(Mg+Fe) ratios of 0.86-0.89 and 0.23-0.33 wt% Al_2O_3.

Calcic Amphibole

Hornblende in high-P clinopyroxene-amphibolite is of edenitic and ferro-edenitic hornblende and ferroan pargasitic hornblende compositions (Leake, 1978). These have Mg/(Mg+Fe) ratios ranging 0.49-0.54, Si-cations range 6.45 to 6.58, Na+K cations range 0.58-0.67, Ca+Na cations range 2.26-2.34 and weight percent TiO_2 is 0.63-1.10. Hornblende in high-P garnet-amphibolite is of taramite, ferro-tschermakite, ferroan pargasite, ferro-pargasite, ferro-hornblende, ferroan pargasitic hornblende and edenitic hornblende compositions (Leake, 1978). These have Mg/(Mg+Fe) ratios ranging 0.20-0.57, Si-cations range 5.86 to 6.82, Na+K cations range 0.36-0.59 and 0.69-0.86, Ca+Na cations range 2.09-2.39 and weight percent TiO_2 is 0.13-0.82. Hornblende in high-P garnet-clinopyroxene mafics is ferro-pargasitic and ferroan pargasitic hornblende (Leake, 1978), and has a Mg/(Mg+Fe) ratios of 0.03 and 0.42, Si-cations of 6.29 and 6.40, Na+K cations range 0.53-0.54 and 0.66, Ca+Na cations range 2.16-2.20 and 2.49 and weight percent TiO_2 is 0.55-0.89. Hornblende in high-P garnet-grunerite-amphibolite is of ferro-edenitic and ferro-pargasitic hornblende compositions (Leake, 1978). These have Mg/(Mg+Fe) ratios ranging 0.09 to 0.19, Si-cations range 6.26 to 6.56, Na+K cations range 0.58-0.68, Ca+Na cations range 2.20-2.41 and weight percent TiO_2 is 0.07-0.69.

Hornblende in mafic granulite is essentially unzoned and of edenitic- and magnesio-hornblende compositions (Leake, 1978), and has Mg/(Mg+Fe) ratios ranging 0.56-0.67, Si-cations range 6.56 to 7.08, Na+K cations range 0.33-0.64, Ca+Na cations range 2.01-2.28 and weight percent TiO_2 is 1.30-2.17.

Hornblende in moderate-P epidote-amphibolite is of magnesio-hornblende, ferro-tschermakite, ferro-tschermakitic hornblende and actinolite compositions (Leake, 1978). These have Mg/(Mg+Fe) ratios ranging 0.19-0.72, Si-cations range 6.06 to 7.51, Na+K cations range 0.15-0.22, 0.39-0.45 and 0.56-0.58, Ca+Na cations range 2.00-2.19, 2.22-2.26 and 2.36-2.42 and weight percent TiO_2 is 0.09-0.61. Hornblende in low-P amphibolite is of ferro-tschermakite, ferro-hornblende and ferro-tschermakitic and ferro-pargasitic hornblende compositions (Leake, 1978). These have Mg/(Mg+Fe) ratios ranging 0.21-0.44, Si-cations range 6.14 to 6.57, Na+K cations range 0.25-0.35 and 0.41-0.57, Ca+Na cations range 1.92-2.15 and 2.16-2.35 and weight percent TiO_2 is 0.20-0.64.

Hornblende in moderate-P garnet-amphibolite in the Forrestania Belt is of ferro-tschermakitic and ferro-hornblende compositions (Leake, 1978). These have Mg/(Mg+Fe) ratios ranging 0.27-0.45, Si-

cations range 6.27 to 6.76, Na+K cations range 0.18-0.21 and 0.35-0.37, Ca+Na cations range 1.92-2.00 and 2.08-2.10 and weight percent TiO_2 is 0.33-0.73.

Hornblende in hybrid rock between mafic and calc-pelite is of magnesio- and ferro-hornblende and tschermakitic and ferro-tschermakitic hornblende compositions (Leake, 1978). These have Mg/(Mg+Fe) ratios ranging 0.30-0.52, Si-cations range 6.40 to 6.52, Na+K cations range 0.34-0.48, Ca+Na cations range 2.08-2.25 and weight percent TiO_2 is 0.45-0.84.

Hornblende in high-grade calc-silicate gneiss is of edenite and ferroan pargasitic, ferro-edenitic and magnesio-hornblende compositions (Leake, 1978), and have Mg/(Mg+Fe) ratios ranging 0.47-0.64, Si-cations range 6.45 to 6.83, Na+K cations range 0.48-0.51 and 0.58-0.63, Ca+Na cations range 2.19-2.23 and 2.25 and weight percent TiO_2 is 0.42-0.61.

Igneous hornblende in granitoids of the EYC is of edenite and magnesio-hornblende compositions (Leake, 1978). These have Mg/(Mg+Fe) ratios ranging 0.60-0.68, Si-cations range 6.91 to 7.19, Al-cations range 0.88-1.28, Na+K cations range 0.39-0.74, Ca+Na cations range 2.05-2.32 and weight percent TiO_2 is 0.42-2.10. A range of metamorphic amphiboles in these samples, have magnesio-hornblende, ferro-edenite, ferroan pargasitic hornblende, actinolitic hornblende, cummingtonite and actinolite compositions. Igneous hornblende in granitoids in the Ravensthorpe Belt is of magnesio-hornblende composition (Leake, 1978), and has Mg/(Mg+Fe) ratios ranging 0.54-0.67, Si-cations range 6.86 to 7.24, Al-cations range 1.06-2.02, Na+K cations range 0.16-0.39, Ca+Na cations range 1.77-2.20 and weight percent TiO_2 is 0.19-1.36. A range of metamorphic amphiboles in these samples, have magnesio-hornblende, ferro-hornblende, ferro-tschermakitic and tschermakitic hornblende, ferro-pargasitic hornblende, ferroan pargasitic hornblende, ferro-edenitic hornblende, actinolitic hornblende, cummingtonite and actinolite compositions.

Actinolite and tremolite are widely reported from low-grade metamorphosed mafics and ultra-mafics and from alteration parageneses. All have Na_2O less than 0.67 wt% and actinolite has Mg/(Mg+Fe) ratios greater than 0.60 and tremolite greater than 0.90. All actinolites have Al_2O_3 contents of 0.20-6.68 wt% and 7.46-7.97 Si-cations and all tremolites have Al_2O_3 contents of 0.39-3.37 wt% and 7.66-8.10 Si-cations.

Fe-Mg Amphibole

Grunerite in high-P garnet-grunerite amphibolite has Mg/(Mg+Fe) ratios ranging 0.12 to 0.25, Si-cations range 7.91 to 8.03, Na+K cations range 0.01-0.03, Ca+Na cations range 0.08-0.11 and weight percent TiO_2 is 0.00-0.04. Grunerite in low-P amphibolite has Mg/(Mg+Fe) ratios ranging 0.30-0.34, Si-cations range 7.62 to 8.00, Na+K cations range 0.02-0.03, Ca+Na cations range 0.05-0.13 and weight percent TiO_2 is 0.00-0.06.

Grunerite is also widely reported from metamorphosed iron formations and Fe-rich mafics, and has Mg/(Mg+Fe) ratios of 0.15-0.35, Al_2O_3 contents of 0.32-5.26 wt% and Na_2O contents less than 0.70 wt%. Cummingtonite is reported from metamorphosed iron formations, mafics and ultra-mafics and alteration parageneses, and has Mg/(Mg+Fe) ratios of 0.39-0.66, Al_2O_3 contents of 0.71-4.87 wt% and Na_2O contents less than 0.39 wt%.

Gedrite in pre-Late Basin metapelite has Mg/(Mg+Fe) ratios ranging 0.35-0.36, Si-cations of 6.27, weight percent Na_2O of 1.35-1.73 and weight percent TiO_2 is 0.11-0.14. Purvis (1978) presents numerous other gedrite and anthophyllite analyses from metamorphosed highly altered rocks in the Forrestania Belt and Mount Martin area. Anthophyllite and gedrites group as Al-rich and Al-poor compositions. Al-rich gedrites have 5.97-6.27 Si-cations, Mg/(Mg+Fe) ratios of 0.24-0.40 and Na_2O contents of 1.64-3.16 wt%. Al-poor gedrites have 6.39-6.97 Si-cations, Mg/(Mg+Fe) ratios of 0.34-0.58 and Na_2O contents of 1.26-1.70 wt%. Al-rich anthophyllites have 7.33-7.66 Si-cations, Mg/(Mg+Fe) ratios of 0.57-0.60 and Na_2O contents of 0.22-1.10 wt%. Al-poor anthophyllites have 6.92-8.26 Si-cations, Mg/(Mg+Fe) ratios of 0.82-0.90 and Na_2O contents of 0.00-0.13 wt%.

Feldspar

Plagioclase in high-P clinopyroxene-amphibolite is of labradorite and andesine compositions with Xan ranging 0.35-0.55 and zoning to lower Ca in the rims. Plagioclase in high-P garnet-amphibolite is of andesine and bytownite compositions with Xan ranging 0.42-0.88 and weak zoning to lower Ca in the rims. Plagioclase within high-P garnet-clinopyroxene mafic is of two types. Plagioclase in BG6-171b is of oligoclase composition with Xan ranging 0.15-0.20 and weak zoning to higher Ca in the rims and re-equilibrated albite outer rims. Plagioclase in BG6-206 is of anorthite composition with Xan ranging 0.95-0.94 and weak zoning to lower Ca in the rims. Plagioclase in high-P garnet-grunerite-amphibolite is of oligoclase and albite compositions with Xan ranging 0.05-0.18 and weak zoning to higher or lower Ca in the rims of different grains.

Plagioclase in low-P mafic granulite is of labradorite and bytownite compositions with Xan ranging 0.52-0.80 and weak zoning to lower Ca in the rims of most grains.

Plagioclase in moderate-P epidote-amphibolite is of a large range in compositions of andesine, labradorite, bytownite and oligoclase. The total range in Xan is 0.24-0.38 and 0.67-0.74 and weak zoning to higher or lower Ca in the rims occurs in different grains. Plagioclase in low-P amphibolites, some with documented clockwise evolutions, have a very large range of compositions of labradorite, bytownite, oligoclase and andesine. Xan ranges are 0.18-0.33, 0.39-0.59 and 0.77-0.89. Zoning is mostly to lower Ca in the rims, though some grains have higher Ca and re-equilibrated outer rims and coronas of anorthite occur. One sample (AB85) contains sanidine grains with Xab of 0.11.

Plagioclase in moderate-P garnet-amphibolite in the Forrestania Belt is of anorthite to bytownite compositions with Xan ranging 0.89-0.96 and weak zoning to higher or lower Ca in the rims of different grains.

Matrix plagioclase in Mount Belches Formation metapelites showing anticlockwise P-T paths is of oligoclase to andesine composition with rare inclusion labradorite. Matrix plagioclase shows a total Xan range of 0.20-0.33. Most grains are small and zoning is not evident except in a few showing slightly lower Ca in the rims and rare re-equilibrated rims of albite. Plagioclase in Mount Belches Formation metapelites showing clockwise P-T paths is of andesine to oligoclase composition with Xan ranging 0.26-0.37 and zoning to lower Ca in the rims. One sample (Y508) contains sanidine grains with Xab ranging 0.02-0.18.

Plagioclase in metapelite from pre-Late Basin stratigraphy showing anticlockwise P-T paths is of bytownite composition with Xan of 0.87. Plagioclase in metapelite from pre-Late Basin stratigraphy showing clockwise P-T paths is of oligoclase and andesine compositions with Xan ranging 0.19-0.49 and weak zoning to higher or lower Ca in the rims of different grains.

Plagioclase in metapelite from the Ravensthorpe Belt is of andesine and oligoclase compositions with Xan ranging 0.21-0.37 and weak zoning to higher or lower Ca in the rims of different grains.

Plagioclase in hybrid rock between mafic and calc-pelite is of anorthite composition with Xan greater than 0.90 and no zoning is evident. One sample (Y666b) contains sanidine grains with Xab of 0.05. Plagioclase in calc-pelite schist is of two compositions, oligoclase and bytownite. Xan ranges are 0.17-0.29 and 0.83-0.91 in different samples and weak zoning to higher or lower Ca in the rims of different grains.

Metamorphic K-feldspar only occurs in migmatitic quartzo-feldspathic gneiss (BG6-212) and is sanidine with Xor ranging 0.88-0.92. Plagioclase in this rock is andesine with Xan ranging 0.29-0.34 and zoning to higher Ca in the rims and coronas.

Plagioclase in high-grade calc-silicate gneiss from the Burtville Terrane is of andesine composition with Xan ranging 0.30-0.45 and weak zoning to higher or lower Ca in the rims of different grains.

Metamorphic plagioclase over-growths and outer rims within granitoids of the Ravensthorpe Belt are of andesine and labradorite compositions, with Xan ranging 0.32-0.55.

Epidote

Secondary epidote in high-P clinopyroxene-amphibolite has Xep compositions of 0.60-0.68, with almost no MgO and TiO2, $Fe^{3+}/(Fe^{3+}+Al)$ ratios of 0.208-0.224, Al/(Al+Si) ratios of 0.377-0.433 and weight percent MnO contents of 0.05-0.15%. Secondary epidote in high-P garnet-amphibolite has Xep compositions of 0.54-0.81, with almost no MgO and 0.03-0.24% TiO2, $Fe^{3+}/(Fe^{3+}+Al)$ ratios of 0.191-0.287, Al/(Al+Si) ratios of 0.416-0.455 and weight percent MnO contents of 0.22-0.45%. Secondary clinozoisite in high-P garnet-amphibolite has an Xcz composition of 0.62, with 0.13% MgO and 0.15% TiO2, $Fe^{3+}/(Fe^{3+}+Al)$ ratio of 0.049, Al/(Al+Si) ratio of 0.40.

Epidote in moderate-P epidote-amphibolite has Xep compositions of 0.52-0.72, with almost no MgO and 0.05-0.13% TiO2, $Fe^{3+}/(Fe^{3+}+Al)$ ratios of 0.165-0.240 and Al/(Al+Si) ratios of 0.357-0.456. Weight percent MnO contents are 0.06-0.37%, with highest MnO in cores. Epidote in low-P amphibolite has Xep compositions of 0.74-0.93, with almost no MgO and TiO2, $Fe^{3+}/(Fe^{3+}+Al)$ ratios of 0.25-0.31, Al/(Al+Si) ratios of 0.414-0.460 and weight percent MnO contents of 0.01-0.15%. Clinozoisite in low-P amphibolite has an Xcz composition of 0.59-0.66, with no TiO2, $Fe^{3+}/(Fe^{3+}+Al)$ ratio of 0.10-0.13, Al/(Al+Si) ratio of 0.47-0.48 and weight percent MnO contents of 0.14-0.25%.

Epidote in calc-pelite schists have Xep compositions of 0.52-0.55, with almost no MgO and TiO2, $Fe^{3+}/(Fe^{3+}+Al)$ ratios of 0.18-0.19, Al/(Al+Si) ratios of 0.447-0.450 and weight percent MnO contents of 0.04-0.06%.

Epidote inclusions in high-grade quartzo-feldspathic gneiss has Xep compositions of 0.37-0.44, with almost no MgO and 0.16-0.27% TiO2, $Fe^{3+}/(Fe^{3+}+Al)$ ratios of 0.14-0.16, Al/(Al+Si) ratios of 0.46-0.47 and weight percent MnO contents of 0.06-0.08%.

Epidote in high-grade calc-silicate gneiss has Xep compositions of 0.61-0.74, with 0.07-0.13% TiO2, $Fe^{3+}/(Fe^{3+}+Al)$ ratios of 0.21-0.25, Al/(Al+Si) ratios of 0.431-0.444 and weight percent MnO contents of 0.01-0.87%.

Muscovite

Matrix muscovite is common to uncommon in highly aluminous schists, metapelite and calc-pelite schists and is a common late-stage phase in most rock-types and rare retrograde phase in mafics. Most analyses are from cores; nevertheless most samples show little compositional variation suggesting muscovite grains are essentially unzoned. Where zoned, muscovite rims typically have slightly higher Mg/(Mg+Fe), Si cations and paragonite contents in samples with anticlockwise P-T paths, and the opposite for samples with clockwise P-T paths. Some highly aluminous metamorphic rocks from altered protoliths also contain paragonite in the matrix foliation and have been described in detail by Purvis (1978).

Retrograde muscovite in mafic samples, have Si cations ranging 3.08-3.18; Mg/(Mg+Fe) ratios of 0.39 and 0.63, Al/(Al+Si) ratios of 0.45-0.48 and the proportion of Na cation in the A-site is 0.006, indicating essentially no paragonite content.

Muscovite in metapelites from the Mount Belches Formation, showing anticlockwise P-T paths, have Si cations ranging 3.014-3.482, Mg/(Mg+Fe) ratios of 0.373-0.587 and Al/(Al+Si) ratios of 0.398-0.493. The proportion of Na cations in the A-site range 0.010-0.192 indicating low to moderate paragonite contents, which is highest in rims and late-stage grains.

Muscovite in metapelites from pre-Late Basin stratigraphy, showing anticlockwise P-T paths, have Si cations ranging 3.104-3.107; Mg/(Mg+Fe) ratios of 0.266-0.310, Al/(Al+Si) ratios of 0.476 and the proportion of Na cations in the A-site range 0.126-0.133 indicating moderate paragonite contents. Muscovite in metapelites from pre-Late Basin stratigraphy, showing clockwise P-T paths, have Si cations ranging 3.04-3.21; Mg/(Mg+Fe) ratios of 0.234-0.443 and 0.552-0.671, Al/(Al+Si) ratios of 0.439-0.484 and the proportion of Na cations in the A-site range 0.016-0.092 indicating low paragonite contents. Muscovite in high-P metapelites from pre-Late Basin stratigraphy, showing clockwise P-T paths, have Si cations ranging 2.989-3.035; Mg/(Mg+Fe) ratios of 0.32-0.38,

Al/(Al+Si) ratios of 0.486-0.495 and the proportion of Na cations in the A-site range 0.116-0.128 indicating moderate paragonite contents.

Retrograde muscovite in metapelites from the Southern Cross Belt has Si cations of 3.34; Mg/(Mg+Fe) ratios of 0.47, Al/(Al+Si) ratios of 0.419 and the proportion of Na cations in the A-site is 0.016, indicating low paragonite contents. Muscovite in metapelites from the Ravensthorpe Belt, have Si cations ranging 3.02-3.14; Mg/(Mg+Fe) ratios of 0.17-0.56, Al/(Al+Si) ratios of 0.459-0.486 and the proportion of Na cations in the A-site range 0.083-0.126, indicating moderate paragonite contents.

White micas in hybrid rocks between calc-pelite and mafic are either margarite or muscovite in different samples. Muscovite Si cations of 3.128; Mg/(Mg+Fe) ratios of 0.179, Al/(Al+Si) ratios of 0.472 and the proportion of Na cations in the A-site are 0.007, indicating essentially no paragonite content. Margarite has Si cations ranging 2.727-2.984; Mg/(Mg+Fe) ratios of 0.285-0.414, Al/(Al+Si) ratios of 0.396-0.456, Ca/(Ca+K+Na) ratios of 98-99% and the proportion of Na cations in the A-site range 0.000-0.005 indicating essentially no paragonite content. Muscovite in calc-pelite schists has Si cations ranging 3.14-3.17; Mg/(Mg+Fe) ratios of 0.38-0.40, Al/(Al+Si) ratios of 0.460-0.462 and the proportion of Na cations in the A-site range 0.033-0.044 indicating low paragonite contents.

Muscovite in aluminous schists layers within granitoids, have Si cations ranging 3.04-3.05; Mg/(Mg+Fe) ratios of 0.59-0.67, Al/(Al+Si) ratios of 0.484-0.486 and the proportion of Na cations in the A-site range 0.028-0.043 indicating low paragonite contents. White mica in highly aluminous schists from Mount Martin is paragonite and has been described by (Purvis, 1978). These paragonites have Si cations ranging 2.973-3.117; Mg/(Mg+Fe) ratios of 0.53-0.58 and 0.87, Al/(Al+Si) ratios of 0.476-0.493 and the proportion of Na cations in the A-site range 0.566-0.622 indicating high paragonite contents.

Chlorite

Main phase matrix chlorite is uncommon in the metapelites and mafic samples investigated. However, matrix chlorite is common in low-grade mafics and hydrothermally altered rocks and as a secondary or retrograde phase in all rock types.

Matrix chlorite in garnet amphibolites is ripidolite and has Mg/(Mg+Fe) ratios of 0.42-0.52, Al/(Al+Si) ratios of 0.49-0.53 and weight percent MnO of 0.21%. Retrograde chlorite in these rocks is pseudothuringite and has Mg/(Mg+Fe) ratios of 0.21, Al/(Al+Si) ratios of 0.54 and weight percent MnO of 0.13-0.70%. Retrograde chlorite in garnet-grunerite amphibolite is daphnite and has Mg/(Mg+Fe) ratios of 0.141, Al/(Al+Si) ratios of 0.50-0.51 and weight percent MnO of 0.12-0.37%.

Matrix chlorite in epidote amphibolite is ripidolite and has Mg/(Mg+Fe) ratios of 0.51-0.52, Al/(Al+Si) ratios of 0.49-0.50 and weight percent MnO of 0.20-0.22%. Chlorite in low-P amphibolites, some with clockwise P-T paths, is ripidolite with a large range in Mg/(Mg+Fe) ratios of 0.29-0.70, Al/(Al+Si) ratios of 0.46-0.52 and weight percent MnO of 0.00-0.35%.

Retrograde chlorite in amphibolite from the Forrestania Belt is ripidolite and has Mg/(Mg+Fe) ratios of 0.64, Al/(Al+Si) ratios of 0.48 and weight percent MnO of 0.05%.

Matrix chlorite in metapelite samples from the Mount Belches Formation, showing anticlockwise P-T paths, is ripidolite and pycnochlorite and has Mg/(Mg+Fe) ratios of 0.42-0.59, Al/(Al+Si) ratios of 0.44-0.54 and weight percent MnO of 0.16-0.43%. Chlorite in metapelite samples from the Mount Belches Formation, showing clockwise P-T paths, is pycnochlorite and has Mg/(Mg+Fe) ratios of 0.48-0.52, Al/(Al+Si) ratios of 0.44-0.45 and weight percent MnO of 0.10-0.18%.

Matrix chlorite in metapelite from the pre-Late Basin stratigraphy, showing anticlockwise P-T paths, is ripidolite and pseudothuringite and has Mg/(Mg+Fe) ratios of 0.06-0.41, Al/(Al+Si) ratios of 0.54-0.66 and weight percent MnO of 0.07-2.11%. Matrix chlorite in metapelite samples from pre-Late Basin stratigraphy, showing clockwise P-T paths, is ripidolite and pseudothuringite and has Mg/(Mg+Fe) ratios of 0.23-0.38, Al/(Al+Si) ratios of 0.51-0.54 and weight percent MnO of 0.11-

0.37%. Matrix chlorite in high-P metapelite from pre-Late Basin stratigraphy, showing clockwise P-T paths, is ripidolite and pseudothuringite and has Mg/(Mg+Fe) ratios of 0.26-0.27 and Al/(Al+Si) ratios of 0.54-0.55. MnO contents range 0.09% to 0.30% from cores to rims.

Chlorite in metapelite samples from the Southern Cross Belt is pseudothuringite and brunsvigite and has Mg/(Mg+Fe) ratios of 0.11, Al/(Al+Si) ratios of 0.60-0.66 and no MnO. Matrix chlorite in metapelite samples from the Ravensthorpe Belt is ripidolite and pseudothuringite and has Mg/(Mg+Fe) ratios of 0.26-0.30, Al/(Al+Si) ratios of 0.54-0.55 and weight percent MnO of 0.06-0.22%.

Retrograde chlorite in hybrid rocks between calc-pelite and mafics is pycnochlorite and has Mg/(Mg+Fe) ratios of 0.50-0.53, Al/(Al+Si) ratios of 0.37-0.39 and weight percent MnO of 0.12-0.28%. Matrix chlorite in calc-pelite is ripidolite and has Mg/(Mg+Fe) ratios of 0.54-0.67, Al/(Al+Si) ratios of 0.48-0.49 and weight percent MnO of 0.08-0.13%.

Chlorite in aluminous schists at Mount Martin is ripidolite and has Mg/(Mg+Fe) ratios of 0.57, Al/(Al+Si) ratios of 0.55 and weight percent MnO of 0.12-0.33% (Purvis, 1978).

Retrograde chlorite in granitoids from the Ravensthorpe Belt is ripidolite and pynochlorite and has Mg/(Mg+Fe) ratios of 0.52-0.62, Al/(Al+Si) ratios of 0.37-0.51 and weight percent MnO of 0.15-0.31%.

Chlorites in altered mafics are ripidolite, clinochlore and pycnochlorite with a large range in Mg/(Mg+Fe) ratios of 0.19-0.25, 0.48-0.60 and 0.67-0.85, Al/(Al+Si) ratios of 0.40-0.54 and weight percent MnO of 0.07-0.32%. Chlorite in altered ultramafics is Mg-rich penninite and clinochlore with Mg/(Mg+Fe) ratios of 0.87-0.95, Al/(Al+Si) ratios of 0.16-0.39 and weight percent MnO of 0.02-0.26%.

Staurolite

All staurolite analyses from metapelite in the EYC are essentially unzoned. The compositional range of staurolite from metapelite in the Mount Belches Formation is Mg/(Mg+Fe) ratios of 0.157-0.240, Al/(Al+Si) ratios of 0.698-0.713, moderate weight percent MnO of 0.36-0.65% and low to moderate weight percent ZnO contents of 0.13-3.86%.

The compositional range of staurolite from metapelite in pre-Late Basin stratigraphy from throughout the EYC is Mg/(Mg+Fe) ratios of 0.075-0.146, Al/(Al+Si) ratios of 0.699-0.716 and low weight percent ZnO contents of 0.05-1.00% in most samples and 2.38% reported by Bickle and Archibald (1984). Most samples have low weight percent MnO of 0.04-0.22%, except the high-P sample (BG6-183a) with 0.24-0.48%.

The compositional range of staurolite from metapelite in the Southern Cross Belt is Mg/(Mg+Fe) ratios of 0.104-0.134, Al/(Al+Si) ratios of 0.699-0.704, low weight percent MnO of 0.00-0.05% and low weight percent ZnO contents of 0.37-0.90%. The compositional range of staurolite from metapelite in the Ravensthorpe Belt is Mg/(Mg+Fe) ratios of 0.105-0.121, Al/(Al+Si) ratios of 0.696-0.710, moderate weight percent MnO of 0.12-0.19% and low weight percent ZnO contents of 0.04-0.11%.

Chloritoid

All samples of chloritoid are essentially unzoned. Chloritoid from metapelite in pre-Late Basin stratigraphy of the EYC is very Fe-rich with Mg/(Mg+Fe) ratios of 0.061-0.073, Al/(Al+Si) ratios of 0.659-0.663 and is relatively rich in MnO with 0.82-1.95 wt%. ZnO contents are low with 0.06-0.25 wt%.

Chloritoid from metapelite in the Ravensthorpe Belt are very Fe-rich with Mg/(Mg+Fe) ratios of 0.079-0.094, Al/(Al+Si) ratios of 0.661-0.666 and lower MnO of 0.26-0.31 wt%. ZnO contents are low with 0.07-0.13 wt%.

Chloritoid from aluminous schists at Mount Martin (Purvis, 1978) are moderately Fe-rich with Mg/(Mg+Fe) ratios ranging 0.063-0.251, Al/(Al+Si) ratios of 0.658-0.668 and MnO contents of 0.25-0.78 wt%.

Fe-Ti oxides

In the absence of unambiguous constraints from reflected light microscopy, the Fe-oxide analyses may be magnetite or hematite. All Fe-oxide analyses from metapelite have Mg/(Mg+Fe) ratios ranging 0.008-0.036 and insignificant TiO_2 of 0.00-0.39 wt%. Chromite is reported by Purvis (1978) from the Mount Martin aluminous schists.

Ilmenite analyses show a significant range of compositions, reflecting exsolution textures and solid-solutions with the Mn-end member and rutile and hematite. Mg-end member solid solutions are insignificant in most samples. Rutile is present in some metapelite samples from pre-Late Basin stratigraphy (e.g., ER1363, BG6-159e, 140106, 140107, BG6-183a) and some high-grade mafic samples (e.g., Y280, BG6-146b). High-grade quartzo-feldspathic gneiss and calc-silicate gneiss do not contain ilmenite, where all Ti is partitioned into titanite.

Garnet amphibolite samples have impure ilmenite with Xilm ranging 0.741-0.926, Xhem ranging 0.000-0.022, XMn-ilm ranging 0.058-0.173 and XMg-ilm ranging 0.001-0.002. Garnet-clinopyroxene amphibolite have impure Mn-rich ilmenite with Xilm ranging 0.737-0.911, Xhem ranging 0.032-0.105, XMn-ilm ranging 0.044-0.117 and XMg-ilm ranging 0.000-0.005. Garnet-grunerite amphibolite samples have impure ilmenite with Xilm ranging 0.857-0.970, Xhem ranging 0.001-0.091, XMn-ilm ranging 0.015-0.057 and XMg-ilm of 0.000.

Mafic granulite samples have impure ilmenite with Xilm ranging 0.867-0.948, Xhem ranging 0.000-0.063, XMn-ilm ranging 0.009-0.049 and XMg-ilm ranging 0.003-0.023.

Epidote amphibolite samples have impure ilmenite with Xilm ranging 0.835-0.936, Xhem ranging 0.015-0.074, XMn-ilm ranging 0.037-0.117 and XMg-ilm ranging 0.000-0.002. Mafic amphibolite samples have impure ilmenite with Xilm ranging 0.877-0.929, Xhem ranging 0.000-0.067, XMn-ilm ranging 0.013-0.095 and XMg-ilm ranging 0.001-0.008.

Garnet amphibolite samples from the Forrestania Belt have impure ilmenite with Xilm ranging 0.829-0.854, Xhem ranging 0.088-0.121, XMn-ilm ranging 0.023-0.040 and XMg-ilm ranging 0.000-0.007.

All metapelite samples from the Mount Belches Formation have impure ilmenite with significant Mn. Xilm ranges 0.845-0.933, Xhem ranges 0.017-0.046, XMn-ilm ranges 0.039-0.110 and XMg-ilm ranges 0.000-0.007.

Metapelite samples from pre-Late Basin stratigraphy have impure ilmenite with Xilm ranging 0.848-0.975, Xhem ranging 0.000-0.123, XMn-ilm ranging 0.000-0.1297 and XMg-ilm ranging 0.000-0.007.

The metapelite sample from the Southern Cross Belt has impure ilmenite with Xilm ranging 0.903-0.932, Xhem ranging 0.060-0.083, XMn-ilm ranging 0.001-0.003 and no XMg-ilm. Metapelite samples from the Ravensthorpe Belt have impure ilmenite with Xilm ranging 0.844-0.952, Xhem ranging 0.001-0.139, XMn-ilm ranging 0.001-0.026 and no XMg-ilm.

Hybrid samples between calc-pelite and mafic have impure ilmenite with Xilm ranging 0.839-0.905, Xhem ranging 0.024-0.033, XMn-ilm ranging 0.038-0.129 and XMg-ilm ranging 0.000-0.005. Calc-pelite samples have impure ilmenite with Xilm ranging 0.884-0.940, Xhem ranging 0.000-0.074, XMn-ilm ranging 0.031-0.052 and XMg-ilm of 0.002.

Biotite

Multiple generations of biotite is the dominant matrix phase in the EYC metapelites investigated and biotite is present in some mafic samples. Most biotite grains are small and show insignificant zoning, though stubby biotite porphyroblasts in metapelites show weak compositional zoning.

Matrix biotite in clinopyroxene±garnet amphibolite gneisses have phlogopite and annite compositions with high Mg/(Fe+Mg) ratios of 0.45-0.67 and high weight percent TiO_2 of 1.87-3.84% and Al/(Al+Fe+Mg) ratios of 0.34-0.38. Matrix biotite from garnet amphibolites have annite compositions with moderate Mg/(Fe+Mg) ratios of 0.35-0.46 and low weight percent TiO_2 of 0.97-2.24% and Al/(Al+Fe+Mg) ratios of 0.34-0.37. Matrix biotite from garnet-grunerite amphibolites have annite and siderophyllite compositions with low Mg/(Fe+Mg) ratios of 0.16-0.18 and high weight percent TiO_2 of 1.54-2.79% and Al/(Al+Fe+Mg) ratios of 0.34-0.37.

Matrix biotite from low-P mafics and amphibolites have annite and siderophyllite compositions with high Mg/(Fe+Mg) ratios of 0.51-0.64 and high weight percent TiO_2 of 1.59-1.81% and Al/(Al+Fe+Mg) ratios of 0.35-0.39.

Matrix biotite from garnet amphibolite in the Forrestania Belt have annite and phlogopite compositions with moderate to high Mg/(Fe+Mg) ratios of 0.36-0.67 and high weight percent TiO_2 of 0.92-2.86% and Al/(Al+Fe+Mg) ratios of 0.34-0.39.

Matrix biotite from metapelites in the Mount Belches Formation showing anticlockwise P-T paths, have a narrow range of siderophyllite compositions with high Mg/(Fe+Mg) ratios of 0.44-0.59 and low weight percent TiO_2 of 1.08-1.94% and Al/(Al+Fe+Mg) ratios of 0.40-0.46. Mg/(Mg+Fe) ratios are generally highest in early fine-grained foliation biotite, and the second-generation blocky biotite porphyroblasts are weakly zoned with higher Mg/(Mg+Fe) ratios in the rims. Matrix biotite from metapelites in the Mount Belches Formation showing clockwise P-T paths, have siderophyllite compositions with moderate Mg/(Fe+Mg) ratios of 0.39 and low weight percent TiO_2 of 1.27-1.28% and high Al/(Al+Fe+Mg) ratios of 0.41-0.42.

Matrix biotite from metapelites in pre-Late Basin stratigraphy showing clockwise P-T paths, have siderophyllite compositions with a large range in moderate Mg/(Fe+Mg) ratios of 0.34-0.57 and moderate weight percent TiO_2 of 0.97-1.76% and Al/(Al+Fe+Mg) ratios of 0.39-0.46.

Matrix biotite from metapelites in the Southern Cross Belt have siderophyllitic compositions with low Mg/(Fe+Mg) ratios of 0.32-0.37 and moderate weight percent TiO_2 of 1.28-2.07% and Al/(Al+Fe+Mg) ratios of 0.44-0.49. Matrix biotite from metapelites in the Ravensthorpe Belt, showing clockwise and anticlockwise P-T paths, have siderophyllite and minor annite compositions with moderate Mg/(Fe+Mg) ratios of 0.25-0.57 and moderate to high weight percent TiO_2 of 1.20-2.72% and Al/(Al+Fe+Mg) ratios of 0.38-0.45. Mg/(Mg+Fe) ratios are highest in early fine-grained foliation biotite, and the second-generation blocky biotite porphyroblasts are weakly zoned with higher Mg/(Mg+Fe) ratios in the rims.

Matrix biotite from hybrid rocks between calc-pelite and mafic, have siderophyllite compositions with high Mg/(Fe+Mg) ratios of 0.55-0.57 and high weight percent TiO_2 of 1.49-2.26% and Al/(Al+Fe+Mg) ratios of 0.35-0.38. Matrix biotite from calc-pelite has phlogopite and siderophyllite and phlogopite compositions with high Mg/(Fe+Mg) ratios of 0.58-0.66 and 0.81 and low weight percent TiO_2 of 0.41-1.58% and Al/(Al+Fe+Mg) ratios of 0.41-0.43 and 0.30.

Matrix biotite from highly aluminous schist within granitoid, have phlogopite compositions with high Mg/(Fe+Mg) ratios of 0.86-0.93 and low weight percent TiO_2 of 0.74-1.06% and Al/(Al+Fe+Mg) ratios of 0.37-0.39.

Matrix biotite from migmatitic quartzo-feldspathic gneiss has annite compositions with high Mg/(Fe+Mg) ratios of 0.55-0.59 and high weight percent TiO_2 of 1.78-3.62% and Al/(Al+Fe+Mg) ratios of 0.37.

Matrix biotite in ultramafic chlorite±talc schists have phlogopite compositions with high Mg/(Fe+Mg) ratios of 0.71-0.88 and low weight percent TiO_2 of 0.44-1.50% and low Al/(Al+Fe+Mg) ratios of 0.28-0.29.

Biotites in alteration parageneses group as two distinct compositional ranges. Phlogopite and eastonite compositions have high Mg/(Fe+Mg) ratios of 0.72-0.78 and low weight percent TiO_2 of 0.19-1.57% and low Al/(Al+Fe+Mg) ratios of 0.32-0.43. Annite compositions have high

Mg/(Fe+Mg) ratios of 0.53-0.64 and moderate weight percent TiO_2 of 1.54-1.89% and low Al/(Al+Fe+Mg) ratios of 0.34-0.41.

Cordierite

Cordierite in metapelite from the Mount Belches Formation is relatively Fe-rich with Mg/(Mg+Fe) ratios ranging 0.56-0.68 and weight percent Na_2O range 0.18-0.38%.

Cordierite in metapelite from pre-Late Basin stratigraphy is relatively Fe-rich with Mg/(Mg+Fe) ratios ranging 0.60-0.61 and a weight percent Na_2O range of 0.87-1.21% in most samples. Higher-grade sillimanite-cordierite pelites have Mg/(Mg+Fe) ratios of 0.68-0.75 and a weight percent Na_2O range of 0.20-0.53% (Bickle and Archibald, 1984),

Titanite

Titanite analyses in all EYC samples contains minor solid solution with grothite end-member indicated by Al in the T1 and M1 sites. The analyses show weight percent Al_2O_3 of 0.53-4.27% and significant FeO ranging 0.33-1.55%.

Tourmaline

Tourmaline is a moderately common accessory mineral in EYC metapelite samples. All analyses have typical dravite compositions with Mg/(Mg+Fe) ratios ranging 0.39-0.68 and Al/(Al+Si) ratios ranging 0.52-0.54. All samples are nearly devoid of MnO, low in TiO_2 (0.57-0.90%) and have Na_2O contents ranging 1.40-2.10%.

Carbonate

Carbonate rarely occurs as a metamorphic matrix mineral in the EYC, but is a very common and widespread alteration and retrograde phase. Carbonate analyses reported from the EYC span a large range in compositions that group as: calcite ($Xcc>0.83$), dolomite ($0.56>Xcc>0.48$, $Xmgs>0.32$), ankerite ($Xcc>0.51$, $Xmgs<0.31$, $Xsid<0.24$), siderite1 ($0.45>Xmgs>0.34$, $Xsid>0.55$), siderite2 ($Xsid>0.79$) and magnesite ($Xmgs>0.50$). Calcite analyses from all rock types in the EYC have XFe ratios ranging 0.34-1.00. Dolomite analyses from all rock types in the EYC have XFe ratios ranging 0.11-0.28. Ankerite analyses from all rock types in the EYC have XFe ratios ranging 0.21-0.69. Siderite analyses from all rock types in the EYC have XFe ratios ranging 0.37-0.98.

Alumino-silicates

Matrix sillimanite in metapelite samples from the EYC contain 0.19% Fe_2O_3 and in the Ravensthorpe Belt 0.3-0.6% Fe_2O_3. All andalusite porphyroblasts in EYC metapelites, contain appreciable Fe_2O_3 ranging 0.12-0.97% and averaging 0.43% (n=24).

Other Minerals in Mafic and Ultra-mafics

All reported metamorphic olivine is of forsterite compositions. All late-stage vein and alteration prehnite has Si-cations ranging 5.97-7.30. Only one pumpellyite analysis is reported from the EYC (18913) with 5.42 Si-cations and 5.63 Al-cations. Metamorphic and alteration serpentine minerals are widely reported in mafic and ultra-mafic rocks, though few analyses exist. Those reported are of chrysotile, lizardite and antigorite compositions with Mg/(Mg+Fe) greater than 0.95. Na-K meionitic scapolite has been identified in only one amphibolite sample (BG6-111). Metamorphic and alteration talc minerals are widely reported in mafic and ultra-mafic rocks, though few analyses exist. These have Mg/(Mg+Fe) greater than 0.80 and Al_2O_3 contents between 0.06-0.70 wt%. A single iowaite analysis is reported by Purvis (1978).

Metamorphic Results

PT CALCULATION RESULTS BY THERMOCALC V3.1

All average PT, average T, average P and Fe-Mg exchange T calculations by THERMOCALC are tabulated in Appendix (14). All of the utilised THERMOCALC results return good statistics with fit values below the cut off for 95% confidence. Similarly all mineral end-members that have been used have low e* values, less than 2.5, indicating they are not giving deleterious results. The intersections of these experiments are compared with conventional thermobarometry and the resultant "best-considered" PT loci are tabulated in Appendix (15) and plotted in Figure (85). All accepted best-considered estimates of peak metamorphic conditions are verified as compatible with the matrix parageneses in the sample (Appendix 7). THERMOCALC experiments form the basis for almost all "best considered" results and these are discussed below for natural groups based on rock-type, metamorphic grade and stratigraphic and structural context. The mean peak metamorphic condition for each of these groups is summarized in Table (8).

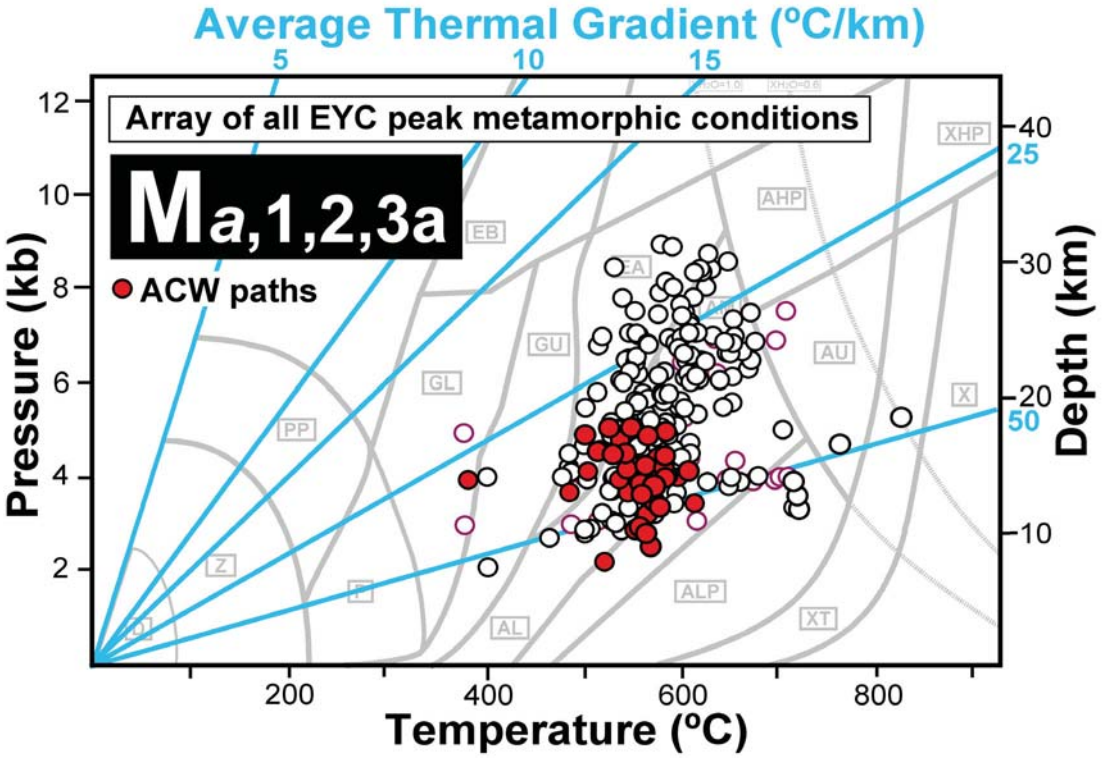

Figure 85: *Plot of all calculated peak metamorphic PT loci.*

High-P clinopyroxene amphibolite (Y280) and garnet-clinopyroxene amphibolite (BG6-206, BG6-171b) samples have well constrained average PT results of 642±44 ºC / 8.5±1.4 kb, 625±41 ºC / 7.6±1.1 kb and 594±71 ºC / 8.2±1.2 kb respectively. Average P, average T and Fe-Mg exchange T calculations intersect at the average PT result in all samples, significantly reducing the errors. Conventional thermobarometry results are similar and mutually support the average PT results, which form the basis for the peak metamorphic conditions in these samples. The mean of these results is approximately 620±33 ºC / 8.1±1.2 kb, corresponding to a temperature/depth ratio between 20.7-23.5 ºC/km.

Calculations from garnet amphibolite and hybrid mafic samples in the EYC fall into high-P and low-P groups. High-P garnet amphibolite samples (Y0360, Y690, Y120e, k, BG6-106c, BG6-192a, b) have moderately constrained average PT results of 579±110 ºC / 6.8±2.9 kb, 510±15 ºC / 6.6±1.9 kb, 563±36 ºC / 6.2±1.2 kb, 613±51 ºC / 7.3±2.0 kb, 623±61 ºC / 7.2±1.6 kb, 550±55 ºC / 8.0±2.0 kb

and 594±24 ºC / 6.8±2.8 kb respectively. Average P, average T and Fe-Mg exchange T calculations intersect near the average PT results, slightly adjusting the accepted PT loci and significantly reducing the errors in most cases. Conventional thermobarometry results are similar and mutually support the average PT results. Average PT calculations on sample (Y0361) gave inaccurate constraints on P and was constrained at 547±36 ºC / 7.1 kb by average T calculations and P estimates from amphibole chemistry. The accepted peak metamorphic condition in each sample is based on the average PT in combination with the intersection between the average P and average T arrays. The mean of these results is approximately 571±32 ºC / 7.0±1.7 kb, corresponding to a mean temperature/depth ratio of 23.3 ºC/km. Low-P garnet amphibolite samples (Y531j, Y691f, BG6-185b) have moderately constrained average PT results of 549±37 ºC / 4.5±0.7 kb, 525±52 ºC / 4.4±1.0 kb and 515±71 ºC / 3.7±1.2 kb respectively. Average P, average T and Fe-Mg exchange T calculations intersect near the average PT results, adjusting the accepted PT loci to slightly higher P and T, and significantly reducing the errors in most cases. Conventional thermobarometry results are similar and mutually support the average PT results. Individual average PT calculations from sample (Y535d) gave large errors on P, which were reduced by averaging multiple PT calculations, constraining the sample at 596±26 ºC / 4.2±2.7 kb. The accepted peak metamorphic condition in each sample is based on the average PT in combination with the intersection between the average P and average T arrays. The mean of these results is approximately 563±31 ºC / 4.5±1.5 kb, corresponding to a mean temperature/depth ratio of 36.3 ºC/km.

High-P garnet-grunerite amphibolite samples (BG6-170b, BG6-171j, BG6-184b) have moderately constrained average PT results of 513±13 ºC / 7.4±1.1 kb, 600±149 ºC / 6.8±2.1 kb and 611±93 ºC / 8.4±2.1 kb respectively. Average T calculations intersect at the average PT results and significantly reduce the errors in most cases. Average PT calculations on sample (BG6-171i) gave inaccurate constraints on P and has been constrained at 530±53 ºC / 7.7 kb by average T calculations and P estimates from garnet isopleths and conventional geobarometry. The accepted peak metamorphic condition in the other samples is based on the average PT in combination with the intersection with average T arrays. The mean of these results is approximately 568±50 ºC / 7.6±1.8 kb, corresponding to a mean temperature/depth ratio of 21.6 ºC/km.

Mafic granulite samples (BG6-146b, BG6-146c, BG6-146g, BG6-147, BG6-148) have moderately constrained average PT results of 710±38 ºC / 4.0±1.8 kb, 731±129 ºC / 2.5±2.0 kb, 716±51 ºC / 4.6±3.6 kb, 824±49 ºC / 5.2±1.7 kb and 761±48 ºC / 4.8±2.0 kb respectively. Average P, average T and Fe-Mg exchange T calculations intersect near the average PT results, slightly adjusting the accepted PT loci and significantly reducing the errors in all cases. Conventional thermobarometry results are similar and mutually support the average PT results. The accepted peak metamorphic condition in each sample is based on the average PT in combination with the intersection between the average P, average T and Fe-Mg exchange T arrays. The mean of these results is approximately 740±31 ºC / 4.0±1.6 kb, corresponding to a mean temperature/depth ratio of 55.5 ºC/km.

Moderate-P epidote amphibolite samples (99966118, 98965829h) have well constrained average PT results of 555±33 ºC / 7.1±1.3 kb and 539±48 ºC / 6.4±1.8 kb respectively. Average P and average T calculations intersect at the average PT results and significantly reduce the errors. Conventional thermobarometry results are similar and mutually support the average PT results. The accepted peak metamorphic condition in each sample is based on the average PT in combination with the intersection between the average P and average T arrays. The mean of these results is approximately 546±40 ºC / 6.8±0.6 kb, corresponding to a mean temperature/depth ratio of 22.9 ºC/km. Moderate-P clinopyroxene-epidote amphibolite samples (BG6-159k, BG6-162) have well constrained average PT results of 607±54 ºC / 6.2±1.6 kb and 607±58 ºC / 6.0±1.7 kb respectively. Average P and average T calculations intersect at the average PT results and significantly reduce the errors. Conventional thermometry results are similar and mutually support the average PT result in (BG6-159k). The accepted peak metamorphic condition in each sample is based on the average PT in combination with the intersection between the average P and average T arrays. The mean of these results is approximately 607±15 ºC / 6.1±1.3 kb, corresponding to a mean temperature/depth ratio of 28.4 ºC/km.

Low-P amphibolite samples (BG6-108, BG6-121, BG6-122, BG6-143b, 99965583a) have moderately constrained average PT results of 479±∞ ºC / 4.7±∞ kb, 477±40 ºC / 3.7±2.2 kb, 482±83 ºC / 4.4±1.2 kb, 518±18 ºC / 5.2±0.7 kb and 462±76 ºC / 3.4±1.8 kb respectively. Average P and average T calculations intersect near the average PT results, slightly adjusting the accepted PT loci and significantly reducing the errors in most cases. The accepted peak metamorphic conditions are based on the average PT in combination with average P and average T intersections and hornblende geobarometry in sample (BG6-122). The mean of these results is approximately 497±40 ºC / 4.3±0.9 kb, corresponding to a mean temperature/depth ratio of 33.7 ºC/km. Conventional thermobarometry results are similar and mutually support the average PT results. Average PT calculations on sample (BG6-136b) gave inaccurate constraints on P and was constrained at 626 ºC / 4.5 kb by average PT and geothermobarometry.

Garnet amphibolites in the Forrestania Belt also give similar high-P and low-P results. Sample (BG6-204) gives an average PT of 619±19 ºC / 7.1±1.3 kb and (BG6-205) gives an average PT of 574±65 ºC / 4.4±1.0 kb. A gedrite-cordierite-garnet aluminous rock (WR120) in the Forrestania Belt gave a similar high-P average PT result of 626±73 ºC / 6.7±1.0 kb. Average P, average T and conventional thermobarometry calculations confirm these results. Intersection of average P and average T arrays reduce errors slightly and the average PT results are taken to constrain the peak metamorphic conditions in these samples.

Metapelite samples from the Mount Belches Formation that show anticlockwise P-T paths (Y459a, Y530b, Y530b(ii), Y531j, Y533a, Y533e, Y534a#1, Y534a#2, Y534b), have well constrained average PT results of 511±88 ºC / 4.5±1.7 kb, 567±17 ºC / 3.5±0.5 kb, 577±15 ºC / 4.5±1.0 kb, 575±49 ºC / 5.3±1.3 kb, 581±61 ºC / 4.0±1.9 kb, 553±18 ºC / 3.5±0.7 kb, 564±17 ºC / 4.1±1.0 kb, 565±18 ºC / 4.0±1.0 kb and 570±15 ºC / 4.0±0.7 kb respectively. Average P, average T and Fe-Mg exchange T calculations intersect at the average PT results significantly reducing the errors in all cases. Conventional thermobarometry results are similar and mutually support the average PT results. The accepted peak metamorphic condition in each sample is based on the average PT in combination with the intersection between the average P, average T and Fe-Mg exchange T arrays. The mean of these nine results is approximately 563±14 ºC / 4.2±0.7 kb, corresponding to a mean temperature/depth ratio of 39.3 ºC/km. Metapelite sample (YD246) with clockwise P-T path, from the Mount Belches Formation, has a poorly constrained average PT result of 588±99 ºC / 4.4±2.0 kb. Average P and average T calculations intersect at the average PT, significantly reducing the errors. The accepted peak metamorphic condition in each sample is based on the average PT in combination with the intersection between the average P and average T arrays, resulting in 588±41 ºC / 4.4±1.3 kb, corresponding to an temperature/depth ratio of 38.2 ºC/km.

Metapelite sample (98957) with anticlockwise P-T path, from pre-Late Basin stratigraphy, has a well-constrained average PT result of 572±20 ºC / 3.2±0.6 kb, corresponding to an temperature/depth ratio of 51.1 ºC/km. Metapelite samples with clockwise P-T paths, from pre-Late Basin stratigraphy in the EYC, fall into moderate-P and low-P groups. Moderate-P pelite samples (Y667a, BG6-207, BG6-213a) have poor to well-constrained average PT results of 544±∞ ºC / 6.4±∞ kb, 487±10 ºC / 6.4±0.7 kb and 540±20 ºC / 6.0±0.7 kb respectively. Average P, average T and Fe-Mg exchange T calculations intersect at the average PT results and significantly reduce the errors. The accepted peak metamorphic condition in each sample is based on the average PT in combination with the intersection between the average P, average T and Fe-Mg exchange T arrays. The mean of these results is approximately 524±16 ºC / 6.3±0.6 kb, corresponding to a mean temperature/depth ratio of 23.9 ºC/km. Low-P pelite samples (YD091c, ER1363, BG6-213b) have well-constrained average PT results of 565±95 ºC / 3.6±1.7 kb, 537±21 ºC / 4.1±1.5 kb and 570±17 ºC / 5.1±1.0 kb respectively. Average P, average T and Fe-Mg exchange T calculations intersect at the average PT results and significantly reduce the errors. The accepted peak metamorphic condition in each sample is based on the average PT in combination with the intersection between the average P, average T and Fe-Mg exchange T arrays. The mean of these results is approximately 557±32 ºC / 4.3±1.3 kb, corresponding to a mean temperature/depth ratio of 38.0 ºC/km. High-P metapelite sample (BG6-183A) with clockwise P-T path, from pre-Late Basin stratigraphy, has a well-

constrained average PT result of 527±14 ºC / 8.5±1.8 kb, corresponding to an temperature/depth ratio of 17.7 ºC/km. Conventional thermometry results are similar and mutually support the average PT result.

Metapelite samples with anticlockwise P-T paths, from the Ravensthorpe Belt (BG6-198a, BG6-198c, BG6-198d, BG6-198f), have poor to well-constrained average PT results of 539±16 ºC / 2.3±0.5 kb, 541±13 ºC / 4.9±1.9 kb, 537±23 ºC / 3.5±3.8 kb and 542±18 ºC / 2.3±0.6 kb respectively. Average P, average T and Fe-Mg exchange T calculations intersect at the average PT results and significantly reduce the errors. Garnet compositional isopleths mutually support the average PT results in sample (BG6-198c). The accepted peak metamorphic condition in each sample is based on the average PT in combination with the intersection between the average P, average T and Fe-Mg exchange T arrays. The mean of these results is approximately 540±11 ºC / 3.3±0.8 kb, corresponding to a mean temperature/depth ratio of 52.4 ºC/km.

Moderate-P calc-pelite sample (BG6-130l) has a poorly constrained average PT result of 545±124 ºC / 5.5±1.4 kb. Fe-Mg exchange T and geobarometer calculations intersect near the average PT results significantly reducing the T error to ±11 ºC. Sample (BG6-130g) was constrained at 500 ºC / 4.7 kb by geothermometry and geobarometry. The mean of these two results is approximately 523±18 ºC / 5.1±1.0 kb, corresponding to a mean temperature/depth ratio of 29.3 ºC/km.

Calc-silicate samples from the Burtville Terrane (179693b, BG6-151b, BG6-152c) have moderately constrained average PT results of 503±79 ºC / 5.0±2.4 kb, 518±88 ºC / 3.8±2.3 kb and 609±56 ºC / 6.4±1.7 kb respectively. Average P, average T, geobarometers and geothermometers intersect near the average PT results and significantly reducing the errors. The accepted peak metamorphic condition in each sample is based on the intersection of these calculated arrays. The resultant best considered estimates are 510±10 ºC / 5.2±0.4 kb, 518±15 ºC / 3.8±1.0 kb and 609±16 ºC / 6.4±1.0 kb respectively, corresponding to temperature/depth ratio ranging 27.2 to 38.9 ºC/km.

Table 8: *Summary of mean peak metamorphic conditions in distinct groups based on rock-type, stratigraphic and structural setting and P-T paths. These mean values are derived only from PT calculations by THERMOCALC.*

Terrane	Rock Group	P-T Path	n	Peak T (ºC)	Peak P (kb)	Peak G (ºC/km)
Ma metamorphic event (2720-2685 Ma):						
EGST: Pre-Late Basin	Mafic granulite	high-T ACW	5	740±31	4.0±1.6	55.5
M1 metamorphic event (2720-2685 Ma):						
EGST: Pre-Late Basin	Clinopyroxene±garnet amphibolite	high-P CW	2	620±33	8.1±1.2	22.1
EGST: Pre-Late Basin	Garnet amphibolite	high-P CW	8	571±32	7.0±1.7	23.3
EGST: Pre-Late Basin	Garnet-grunerite amphibolite	high-P CW	4	568±50	7.6±1.8	21.6
EGST: Pre-Late Basin	Metapelite	high-P CW	1	527±14	8.5±1.8	17.7
M2 metamorphic event (2685-2665 Ma) - Moderate thermal gradient :						
EGST: Pre-Late Basin	Epidote amphibolite	mod-P CW	2	546±40	6.8±0.6	22.9
EGST: Pre-Late Basin	Clinopyroxene-epidote amphibolite	mod-P/high-T CW	2	607±15	6.1±1.3	28.4
EGST: Pre-Late Basin	Metapelite	mod-P CW	3	524±16	6.3±0.6	23.9
EGST: Pre-Late Basin	Calc-pelite	mod-P CW	2	523±18	5.1±1.0	29.3
M2 metamorphic event (2685-2665 Ma) - High thermal gradient :						
EGST: Pre-Late Basin	Garnet amphibolite	low-P CW	4	563±31	4.5±1.5	36.3
EGST: Pre-Late Basin	Amphibolite	low-P CW	5	497±40	4.3±0.9	33.7
EGST: Pre-Late Basin	Amphibolite	low-P/high-T CW	1	626	4.5	39.7
EGST: Pre-Late Basin	Metapelite	low-P CW	3	557±32	4.3±1.3	38.0
M3a metamorphic event (2665-2650 Ma):						
EGST: Mt Belches Basin	Metapelite	low-P ACW	9	563±14	4.2±0.7	39.3
EGST: Mt Belches Basin	Metapelite	low-P CW	1	588±41	4.4±1.3	38.2
EGST: Pre-Late Basin	Metapelite	low-P ACW	1	572±20	3.2±0.6	51.1
Unknown metamorphic events:						
Burtville Terrane	Calc-silicate	low-P CW	2	514±12	4.5±0.7	33.5
Burtville Terrane	Calc-silicate	mod-P CW	1	609±16	6.4±1.0	27.2
Forrestania Belt	Garnet amphibolite & pelite	high-P CW	2	623±46	6.9±1.1	25.8
Forrestania Belt	Garnet amphibolite	low-P CW	1	574±65	4.4±1.0	37.3
Ravensthorpe Belt	Metapelite	low-P ACW	4	540±11	3.3±0.8	52.4

PT CALCULATION RESULTS BY CONVENTIONAL THERMOBAROMETRY

All PT calculations by conventional geothermometers and geobarometers are contained in Appendix (16). These results and evaluation of their utility has been discussed in the Conventional Thermobarometry Methodology section above.

METAMORPHIC CONDITIONS (P, T, G) AND EVENTS

PT calculations and estimates from the EYC span a large proportion of PT space between 150-760 ºC and 0.5-8.7 kb. There is a marked clustering of the PT calculations and these groupings correspond to different rock-type and distinct stratigraphic and structural settings (Figure 86). Most significantly the range of PT conditions preserved, document a large range in temperature/depth ratio ranging from 18 to 100 ºC/km indicating that entirely distinct thermal regimes were operating. A very large range in thermal regime is also evident for peak metamorphic conditions only (18 to 70 ºC/km) with late-stage alteration parageneses removed (Figure 85). These different metamorphic conditions and thermal regimes were strongly spatially partitioned and heterogeneously distributed into different parts of the EYC. For example:

[1] The highest P rocks of 7.0-8.7 kb and 570-640 ºC also had the lowest thermal regimes of 18-23 ºC/km indicating high advection/conduction ratios and sub-subduction zone conditions. These conditions are only found within crustal scale shear zones.

[2] The highest T rocks are granulites of 4.0 kb and 740 ºC, with the highest peak metamorphic thermal regimes in the EYC of 56 ºC/km. These conditions are only found in two small clusters within metamorphosed mafic intrusive complexes.

[3] A narrow range of low-P/moderate-T metamorphic conditions (550-580 ºC / 3.5-4.5 kb) with high thermal regimes of 39 ºC/km are consistently found in the Late-Basin stratigraphy such as the Mount Belches Formation.

[4] Late-stage, over-printing hydrothermal alteration parageneses have a wide range of conditions from 0.5-4.5 kb and 150-600 ºC, indicating moderate to very high thermal regimes. Alteration parageneses are not widespread but strongly spatially partitioned on 100's m to km scale and are typically associated with fault zones.

[5] Otherwise, the only exception is widespread peak metamorphic parageneses of medium- to low-P (3.5-6.5 kb) that span a wide range in temperate from greenschist to upper amphibolite facies. These regional metamorphic conditions indicate a range from moderate to moderately high thermal regimes of 24-38 ºC/km.

Overprinting criteria and the incompatibility of widely different thermal regimes strongly suggest that the five different metamorphic groupings outlined above, were not necessarily time equivalent and represent different metamorphic events. The granulite conditions are thought to be the earliest formed and are labelled M*a*. The high-P parageneses are reworked by regional metamorphic parageneses and interpreted to be early formed, and have been labelled M1. The medium- to low-P regional metamorphic parageneses are widespread throughout pre-Late Basin stratigraphy and associated with the granite bloom, and are labelled M2. Metamorphic parageneses in the Late-Basins are tightly constrained in time and have been labelled M3a. Alteration parageneses everywhere overprint peak metamorphic assemblages and are clearly late formed. Hydrothermal alteration occurs during a multiple of local events over a period of diminishing P and T, and together these local events are collectively labelled M3b. The temporal relationships between these five different metamorphic events is explored in detail with respect to overprinting criteria, structural setting, stratigraphic context and correlations with geochronology in the Assigning Metamorphic Event section below.

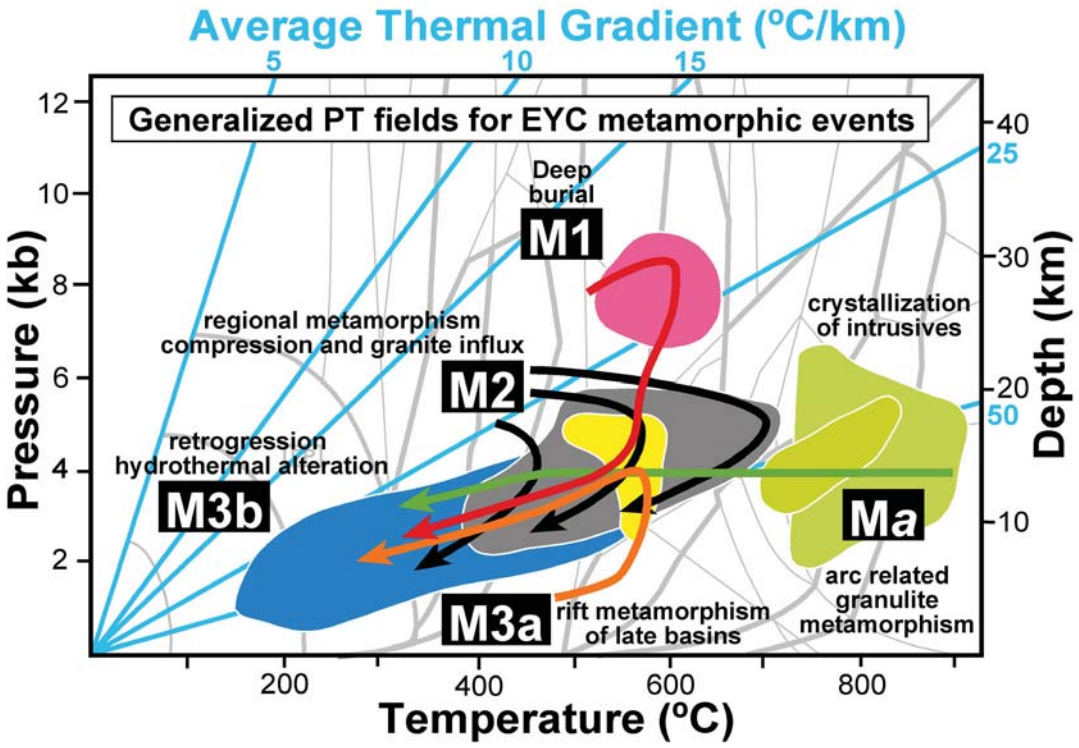

Figure 86: *Generalized PT fields and representative P-T paths for different aged and distinct metamorphic events recognized in the EYC.*

P-T EVOLUTION PATHS

The P-T paths for groupings of samples with distinct stratigraphic or structural settings that allow temporal classification are interpreted below. P-T paths are based on the sequence of mineral growth described in the petrography section, interpreted within published pseudosections. These interpretations are also constrained by PT calculations and core to rim compositional isopleths in garnet where available. The P-T paths described below collectively represent the range of P-T evolutions recognised. Arguments governing the interpretation of P-T paths are presented only for the best-constrained and representative samples. Representative P-T paths for each sample grouping are presented in figures based on published PT pseudosections. Details of the published PT pseudosection are contained within the figure. Circles in the figures represent documented mineral parageneses and crosses are constraining PT calculations by different methods, with a typical general error of ±25ºC and ±0.5 kb. The interpretive P-T paths for all investigated samples are contained in Appendix (7).

Ma Intrusive and Granulite Cooling P-T Paths

Garnet-absent, two-pyroxene mafic granulite assemblages with magnesio hornblende, bytownite to labradorite and ilmenite ± rutile, indicate low-P granulite grade conditions in meta-gabbros at locations BG6-135 and BG6-146 to 148. Localities BG6-173, BG6-174, BG6-178, BG6-179 and BG6-180 also formed at high-T/low-P peak metamorphic conditions indicated by PT calculations and quartz, salite clinopyroxene, labradorite to bytownite and magnesio hornblende assemblages. High-T/low-P samples have arrays of PT calculations suggesting post-peak isobaric cooling. Retrograde mineral growth is restricted to hornblende, actinolite and epidote and secondary plagioclase is not recognised, which is consistent with isobaric cooling. There is no constraint on the prograde path. The absence of garnet precludes clockwise P-T paths through high-P prograde conditions. Consequently, the P-T paths are interpreted to have been tight anticlockwise loops terminated by isobaric cooling (Figures 87, 88). Alternatively, the high-grade metamorphic parageneses formed during isobaric cooling after crystallization of these mafic intrusives.

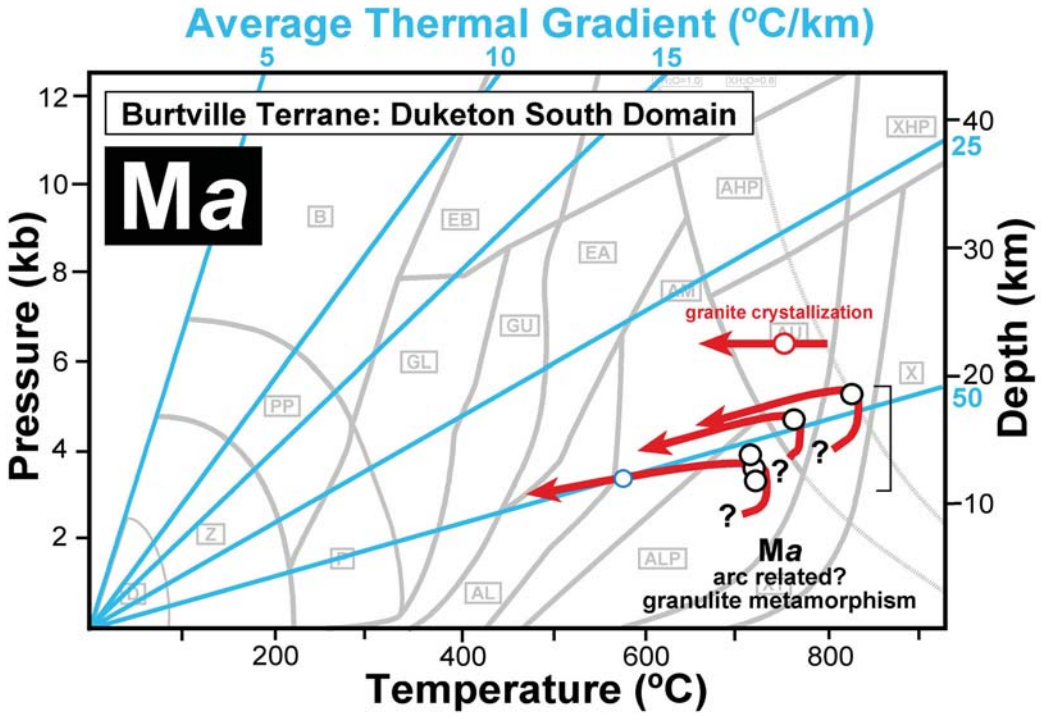

Figure 87: *Peak PT loci and P-T evolutions from granulite facies static metamorphosed gabbros in the South Duketon Domain.*

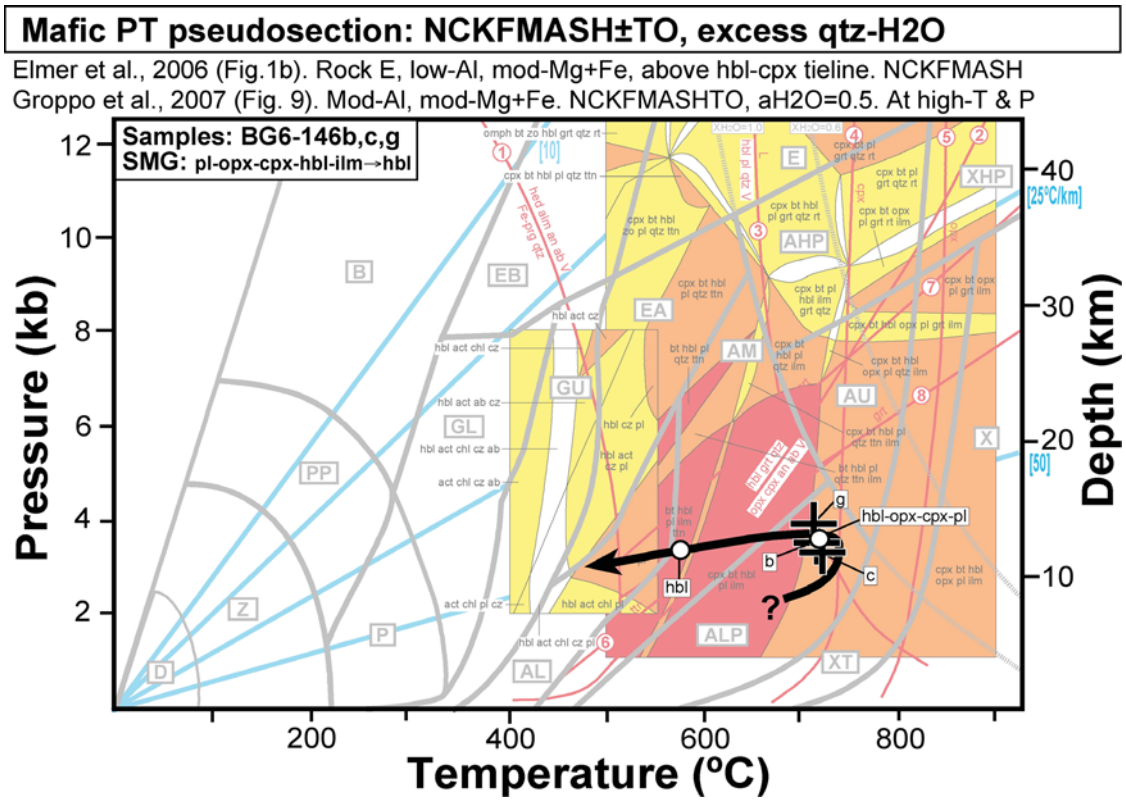

Figure 88: *PT pseudosection for interpretation of mafic granulite samples BG6-146. Details of published pseudosection are listed in header. Cross - calculated PT results, circles - documented mineral parageneses.*

M1 Clockwise P-T Paths with Isothermal Decompression

Many of the crustal-scale shear zones in the EYC contain localities with high-P upper-amphibolite facies parageneses. Upper-amphibolite facies parageneses are often annealed polygonal granoblastic gneisses that invariably occur in high-strain shear zones. These outcrops are typically partially reworked low-strain shear lenses within lower grade shear zones. Consequently, two metamorphic parageneses are recognised in these high-grade amphibolite gneisses. M1 parageneses are represented by porphyroblastic phases, and by coarse-grained polygonal granoblastic matrix of hornblende, clinopyroxene, garnet and plagioclase. M2 parageneses are represented by the enveloping schistose to aligned granoblastic hornblende-plagioclase matrix. Foliated matrix minerals may be in equilibrium with re-equilibrated outer rims of the earlier porphyroblastic phases.

High-P, upper-amphibolite conditions are documented by both PT calculations, and different diagnostic assemblages from a range of mafic bulk compositions.

[1] Rare garnet-clinopyroxene-hornblende-plagioclase-quartz-ilmenite (BG6-171b; Figure 89).
[2] Garnet-hornblende-grunerite-plagioclase-quartz-ilmenite (BG6-171d, i, j, BG6-170a, b; Figure 90).
[3] Hornblende-clinopyroxene-plagioclase-quartz ± K-feldspar (BG6-178b, BG6-105a, Y280; Figure 91).
[4] Garnet-hornblende-quartz-plagioclase-ilmenite±rutile±magnetite±hematite±biotite (Y0360, Y0361, BG6-185b, BG6-106c, BG6-192a, Y691f; Figure 92).

These peak-P parageneses are over-printed by secondary parageneses containing garnet2, grunerite, hornblende2, actinolitic hornblende, epidote and coronal plagioclase. Secondary parageneses formed at similar temperatures but lower pressures, indicating isothermal decompression. Near isothermal decompression is supported by steep arrays of PT calculations in many samples. Retrograde actinolite, epidote, titanite and chlorite indicate cooling after decompression (Figure 93).

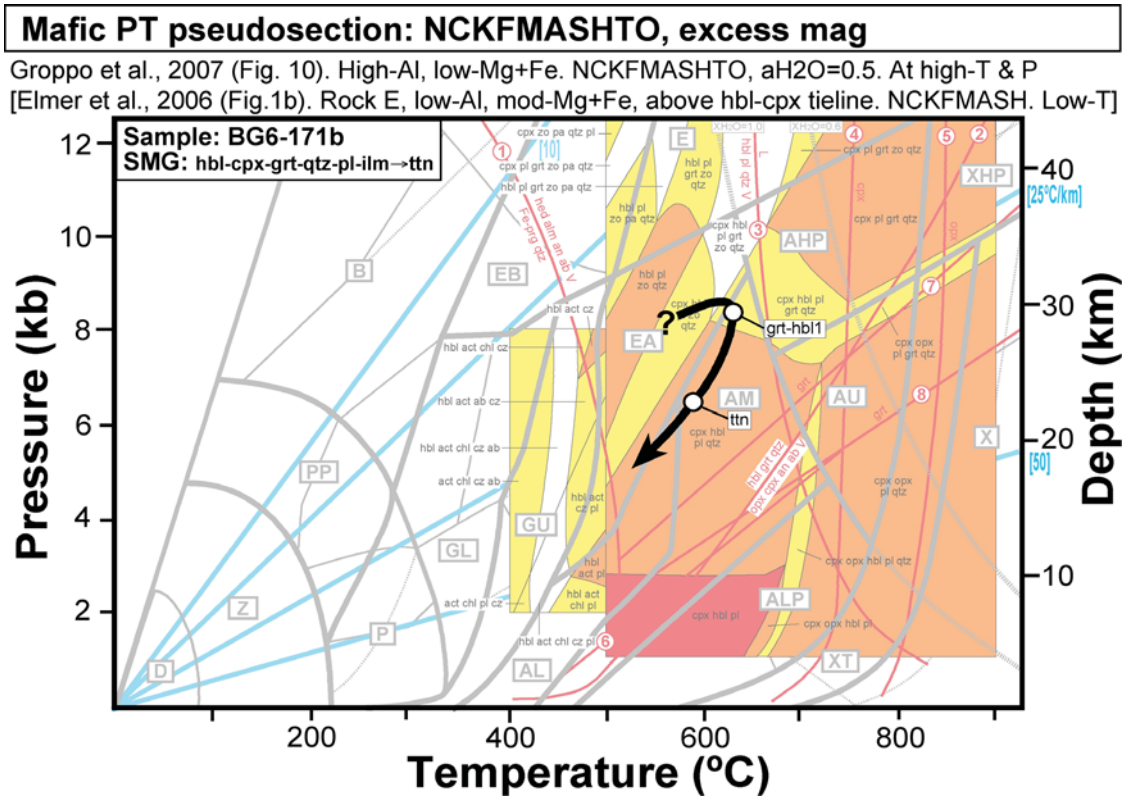

Figure 89: *PT pseudosection for interpretation of high-P garnet-clinopyroxene mafic samples BG6-171b. Details of published pseudosection are listed in header. Cross - calculated PT results, circles - documented mineral parageneses.*

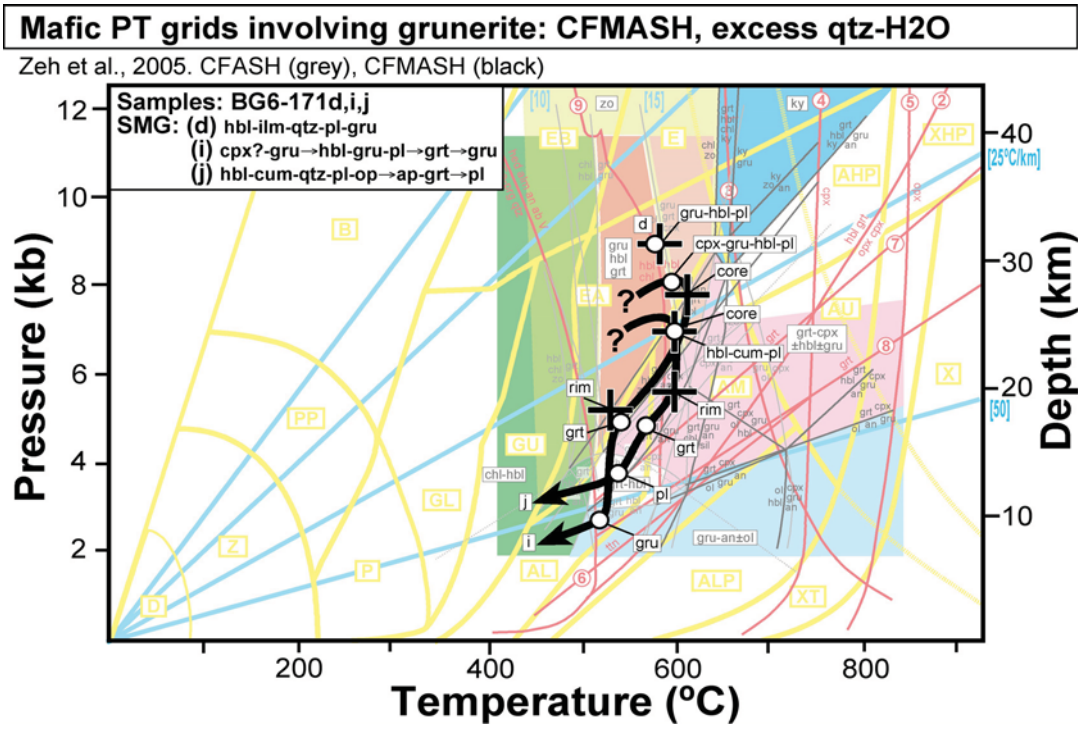

Figure 90: *PT pseudosection for interpretation of high-P hornblende-garnet-grunerite mafic BG6-171. Details of published pseudosection are listed in header. Cross - calculated PT results, circles - documented mineral parageneses.*

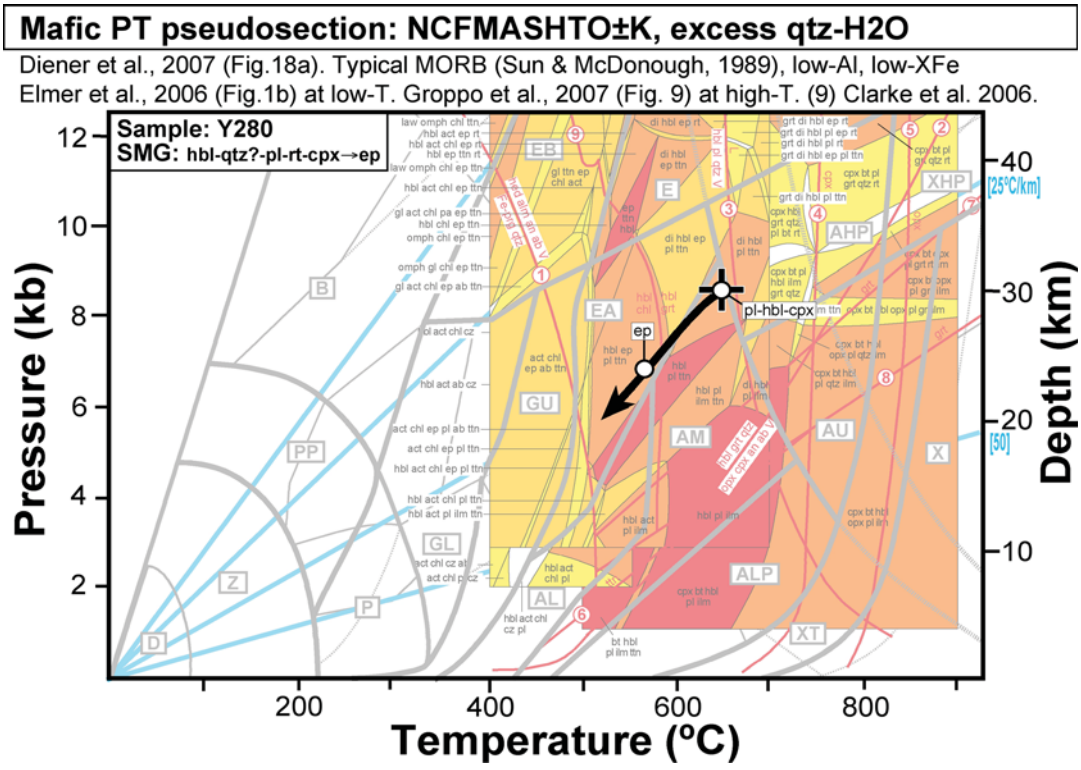

Figure 91: *PT pseudosection for interpretation of high-P hornblende-clinopyroxene mafic samples Y280. Details of published pseudosection are listed in header. Cross - calculated PT results, circles - documented mineral parageneses.*

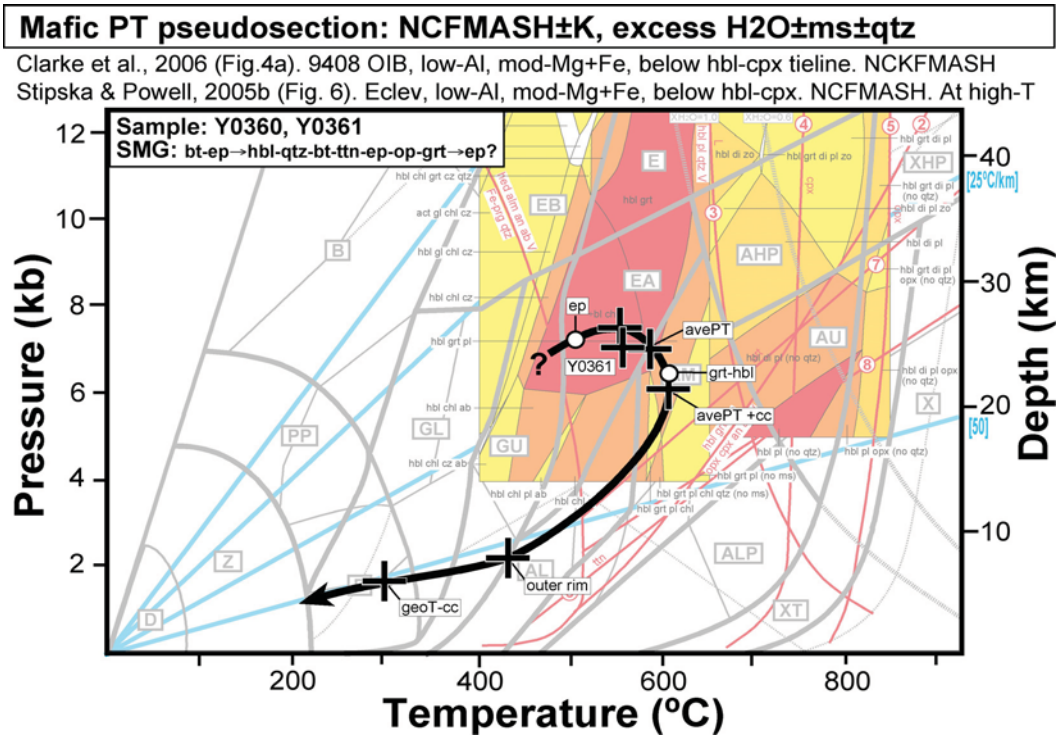

Figure 92: *PT pseudosection for interpretation of high-P hornblende-garnet mafic samples Y0360. Details of published pseudosection are listed in header. Cross - calculated PT results, circles - documented mineral parageneses.*

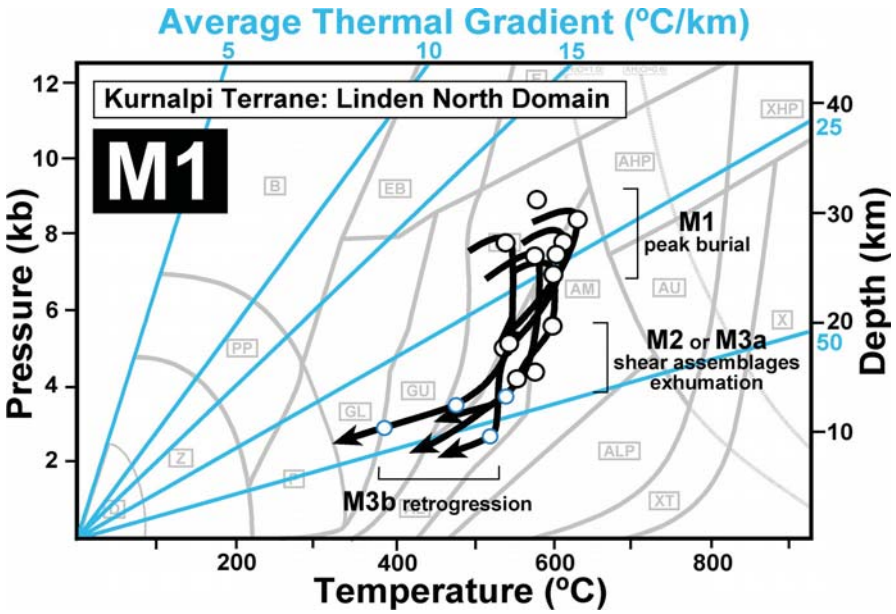

Figure 93: *Peak PT loci and P-T evolutions from high-P rocks in the major shear zone in the north Linden Domain.*

Hybrid rocks with bulk compositions between calc-pelite and mafic occur within the Laverton Shear Zone between the Edjudina and South Linden Domains. These preserve high-P peak metamorphic parageneses of garnet-hornblende-plagioclase-biotite-quartz-ilmenite ± grunerite (Y690a, BG6-120c, e, k). These samples have secondary muscovite chlorite and calcite. PT calculation arrays indicate near isothermal decompression (Figure 94).

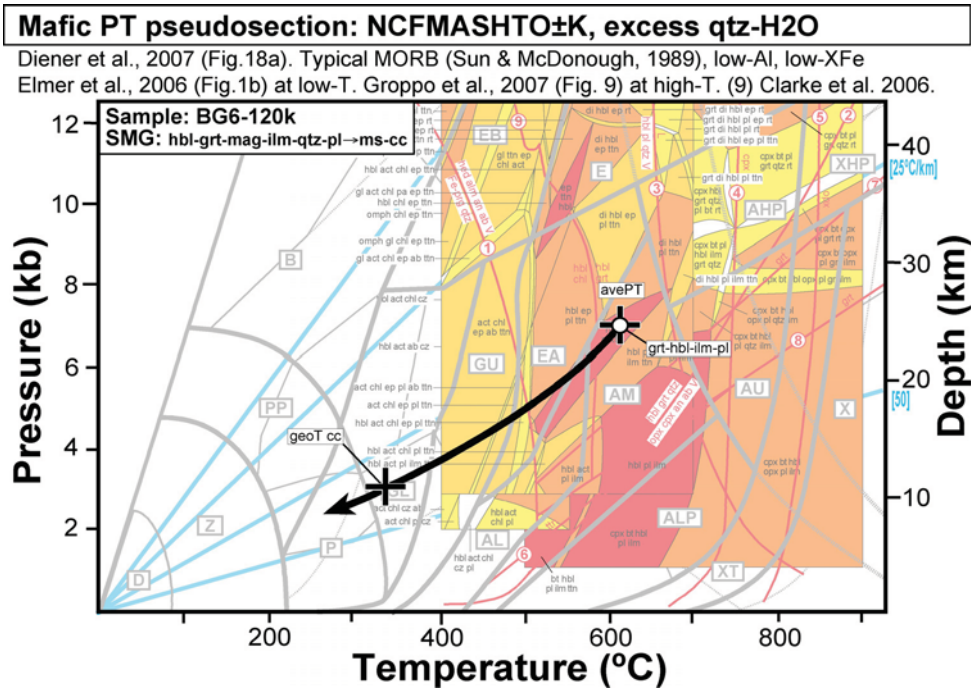

Figure 94: *PT pseudosection for interpretation of high-P hybrid mafic samples BG6-120k. Details of published pseudosection are listed in header. Cross - calculated PT results, circles - documented mineral parageneses.*

Metapelite rocks preserving evidence for high pressures are very rare, with only one unambiguous sample (BG6-183A) from the Ida Shear Zone in the North Coolgardie Domain. The peak metamorphic assemblage of garnet-staurolite-chlorite-muscovite-quartz-ilmenite-rutile and returns high-P PT calculations (Figure 95).

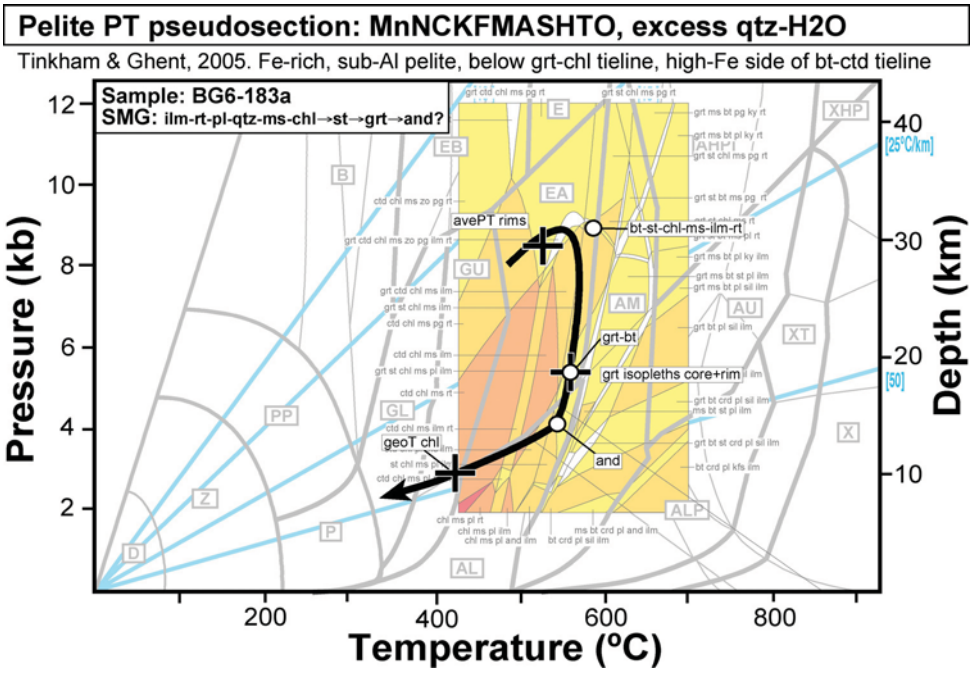

Figure 95: *PT pseudosection for interpretation of high-P metapelite samples BG6-183. Details of published pseudosection are listed in header. Cross - calculated PT results, circles - documented mineral parageneses.*

M2 Granite Cooling P-T Paths

The metamorphic database for the EYC suffers from very few constraints from granitoids that may constrain the crustal level of emplacement (Figure 15). This information is crucial because the crustal level of granite emplacement is crucial to determining between competing tectonic models. For example granites in a lower-plate domain within extended crust will be of similar crustal levels to adjacent domains, where as diapiric granitoid masses should contain evidence for significantly deeper crustal levels (Figure 17). PT constraints from granitoids are hard to obtain and there are only three sources available. PT calculations can be obtained from granitoids that have been metamorphosed to gneissic assemblages. Suitable assemblages containing garnet, micas and aluminosilicate have not been documented in the EYC. Metamorphosed xenoliths of metasediment or mafic bulk compositions can be potentially used to calculate PT conditions in granite-gneiss batholiths. Xenolith PT constraints are problematic because these assemblages may have formed in the source region and are not representative of granite emplacement conditions. The third method available is to apply the Al-in hornblende geobarometer to igneous hornblendes in granitoids. This method also has limited applicability because not all granitoids contain igneous hornblende and most igneous hornblende has retrograded margins with blue-green metamorphic hornblende or actinolitic amphibole growth.

Igneous hornblende pressure estimates from the EYC range from 2.0 to 6.0 kb and most between 3.5-4.0 kb. These pressures are similar to those during M2-M3a metamorphism in the host rock units. PT calculations from secondary and retrograde mineral parageneses in granitoids define a shallow PT array indicating near isobaric cooling (Figure 96). Lower pressures of 2.0-2.5 kb have been calculated from hornblende in the Granny Smith Granodiorite (Kevin Cassidy, pers. comm. 2006). The Granny Smith Granodiorite intrudes a fluviatile late basin and so represents crustal levels subsequent to M3a metamorphism

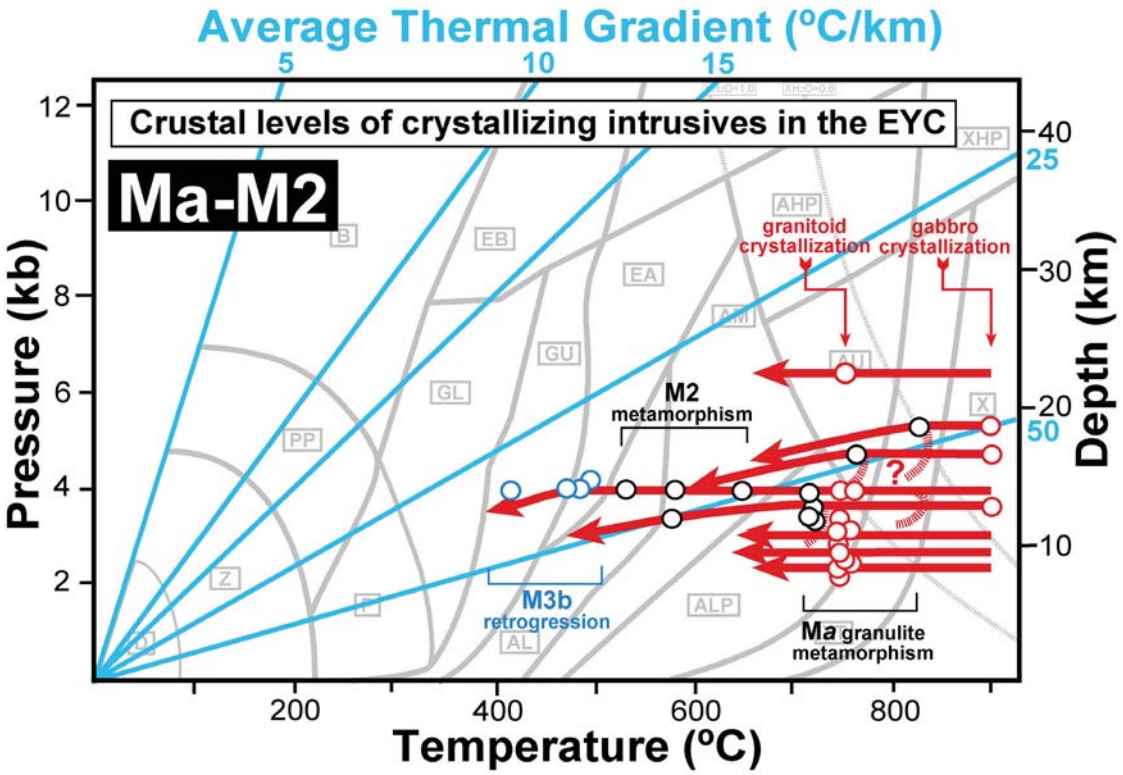

Figure 96: *Crystallization PT loci and cooling trajectories for EYC granitoids and gabbro intrusives.*

M2 Tight Clockwise P-T Paths

P-T evolutions from the widespread regional matrix parageneses are consistently of tight clockwise paths at medium-P to low-P conditions (Figure 97). These P-T paths of evolution are recorded from metamorphic parageneses in stratigraphic units below Late Basin stratigraphy and away from major shear zone structures.

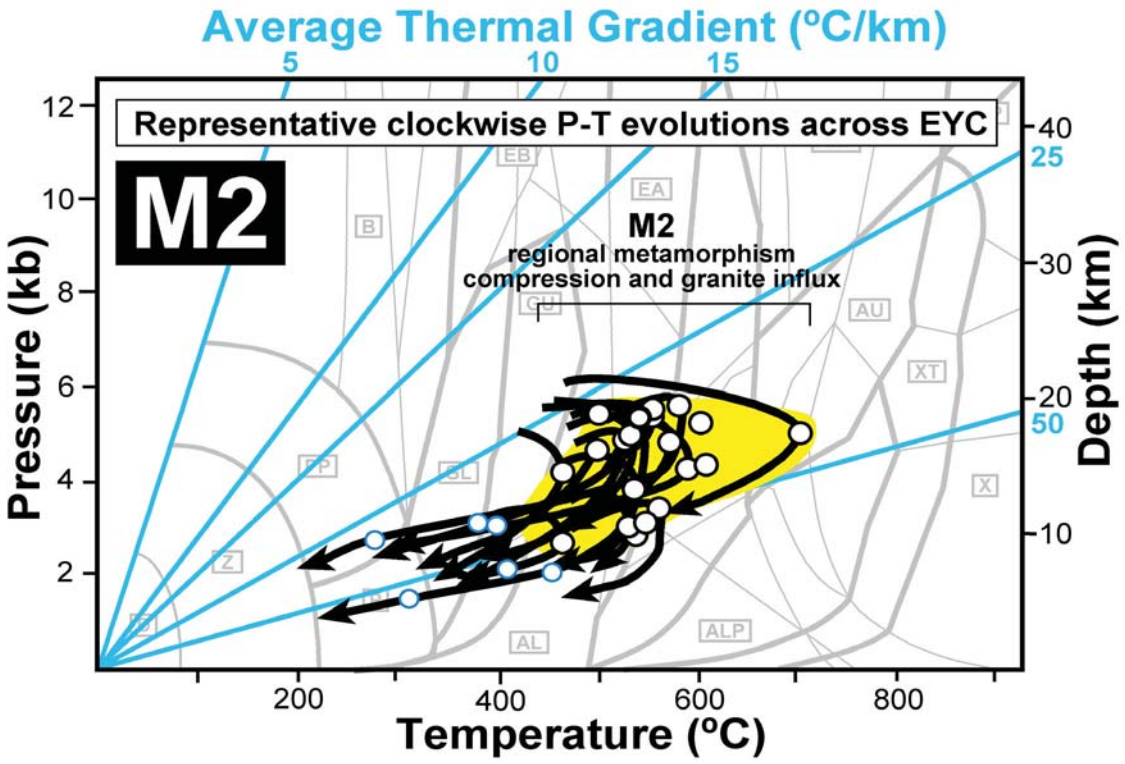

Figure 97: *Representative clockwise P-T evolutions from the EYC.*

Low-P amphibolite facies mafics are widespread and preserve a range of peak metamorphic assemblages containing hornblende, actinolitic hornblende, actinolite, plagioclase, quartz, ilmenite, chlorite and rare garnet and grunerite (Y535d, Y504, BG6-114g, BG6-121, BG6-163e, f). Peak metamorphic hornblende and grunerite over-print the prograde parageneses containing chlorite and actinolite. Reaction textures such as plagioclase coronas on hornblende (BG6-121, BG6-163f) and PT calculations indicate decompression through the peak of metamorphism and clockwise P-T paths (Figure 98). Retrograde chlorite and actinolite followed by prehnite veins define decompressive cooling paths.

Medium-P, epidote amphibolite conditions are documented by both PT calculations and diagnostic hornblende-epidote-plagioclase-quartz-ilmenite assemblages in a cluster of samples in the North Boorara Domain (99966091.3, 99966118, 99966121b). These samples contain titanite coronas indicating decompression (Figure 99).

Numerous metapelite samples from pre-Late Basin stratigraphic units widely scattered across all domains, document clockwise P-T paths at low-P and medium-P conditions. Clockwise P-T paths are documented by different sequence of mineral growth in different bulk compositions, in combination with PT calculations and garnet compositional isopleths (Figure 100). Most commonly matrix assemblages of quartz-biotite-plagioclase-opaque-graphite with small garnet porphyroblasts are overprinted by post-kinematic biotite and andalusite porphyroblasts (Y667a, b, 98939, BG6-164b, ER1363, BG6-167a). Late-stage andalusite indicates decompression at the peak of metamorphism and retrogressive muscovite, chlorite and sericite document post-peak cooling.

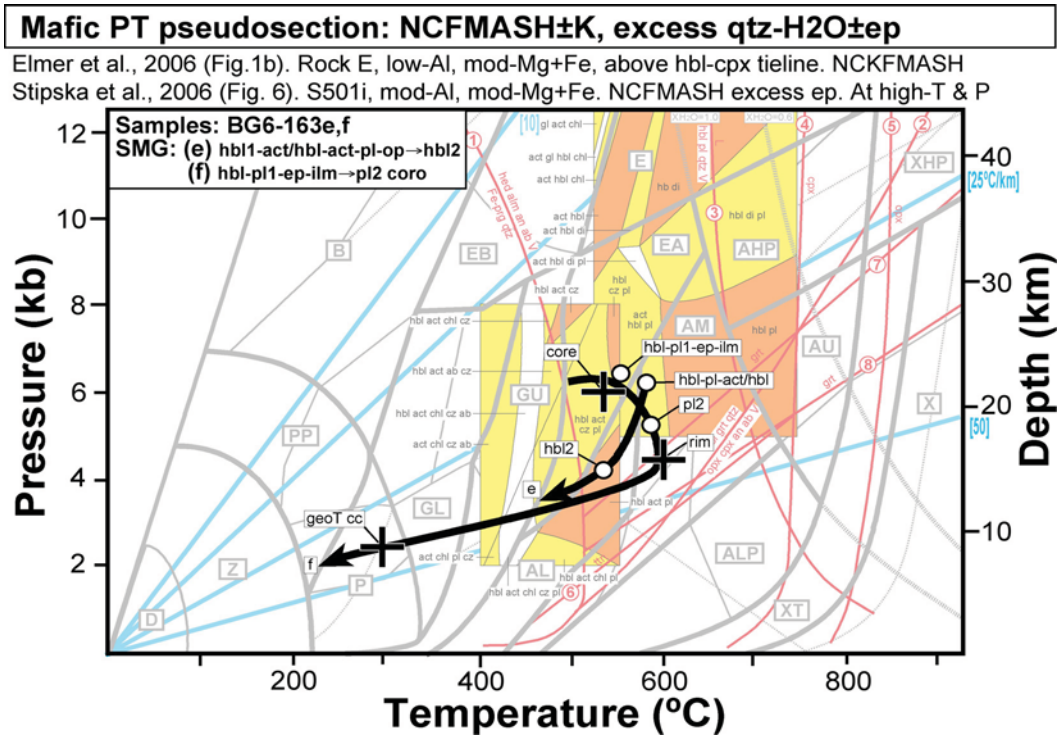

Figure 98: *PT pseudosection for interpretation of M2 clockwise P-T paths samples BG6-163. Details of published pseudosection are listed in header. Cross - calculated PT results, circles - documented mineral parageneses.*

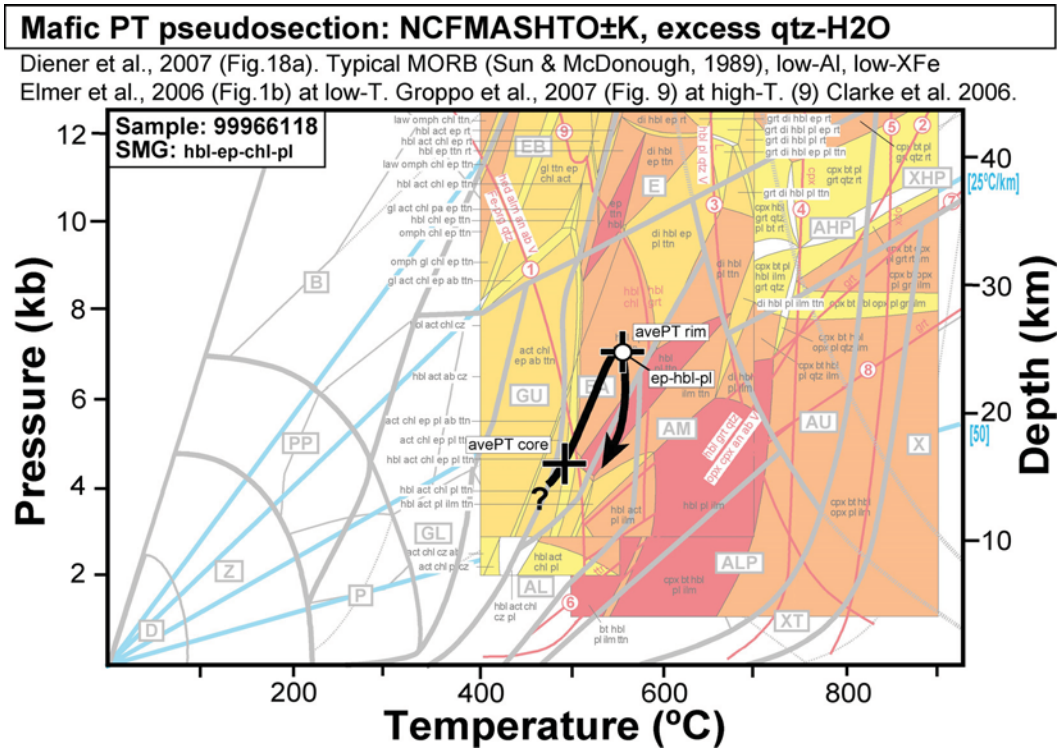

Figure 99: *PT pseudosection for interpretation of M2 clockwise P-T paths samples 99966118. Details of published pseudosection are listed in header. Cross - calculated PT results, circles - documented mineral parageneses.*

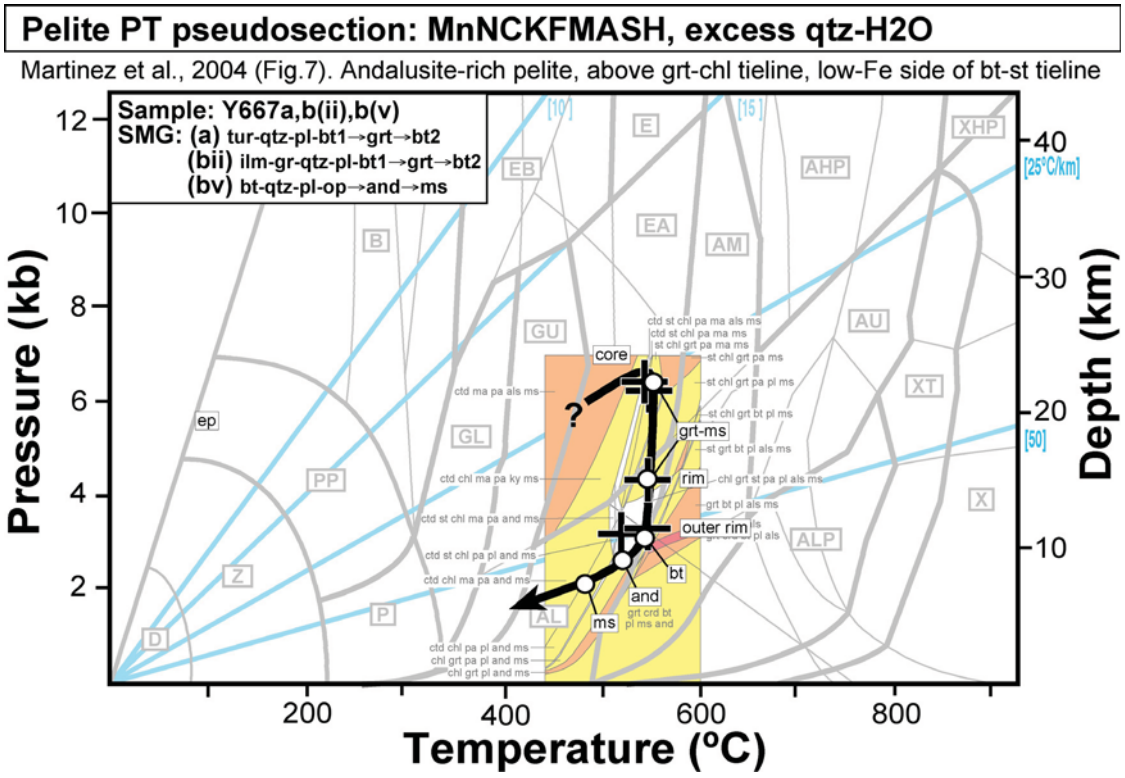

Figure 100: *PT pseudosection for interpretation of M2 clockwise P-T paths samples BG6-Y667. Details of published pseudosection are listed in header. Cross - calculated PT results, circles - documented mineral parageneses.*

Metapelite samples that contain relict early chloritoid (NA20, 63555-111, BG6-207) have matrix assemblages of biotite-quartz-plagioclase-ilmenite ± muscovite. Matrix parageneses are over-printed by post-kinematic, peak metamorphic staurolite, garnet and biotite porphyroblasts. Peak metamorphic parageneses are in turn over-printed by secondary biotite and cordierite in some samples and by retrograde muscovite and chlorite. Early chloritoid and peak garnet-staurolite document prograde trajectories followed by decompression into the cordierite field (Figure 101).

Staurolite-bearing metapelite samples (63555-104, 83001, BG6-213b) have matrix assemblages containing garnet, quartz, biotite, ilmenite and plagioclase with staurolite either as a relict prograde or peak metamorphic phase. Staurolite is either over-grown by garnet or cordierite parageneses containing andalusite or sillimanite, indicating decompression through prograde and peak metamorphism (Figures 102, 103). Late-stage fibrolite, muscovite and chlorite growth document post-peak cooling.

Metapelite samples with matrix assemblages containing sillimanite and biotite (63516, 63528) are over-printed by cordierite indicating decompression followed by cooling into the biotite, chlorite and muscovite fields (Figure 104).

Metapelites with matrix assemblages containing muscovite, biotite and andalusite (78693, 786934) are over-printed by cordierite indicating decompression followed by cooling into the muscovite-chlorite field (Figure 105).

The highly aluminous sample BG-213a documents a clockwise P-T path involving decompression from the cordierite-gedrite field to the garnet field followed by retrograde cooling into the chlorite field (Figure 106).

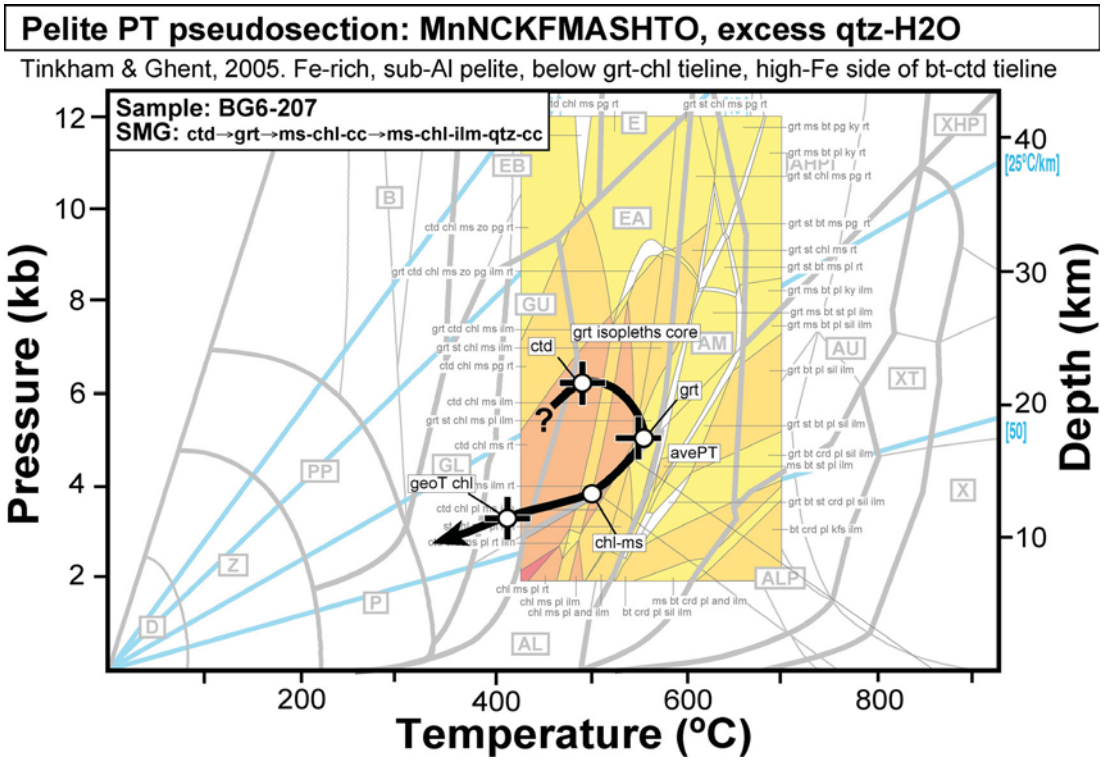

Figure 101: *PT pseudosection for interpretation of M2 clockwise P-T paths samples BG6-207. Details of published pseudosection are listed in header. Cross - calculated PT results, circles - documented mineral parageneses.*

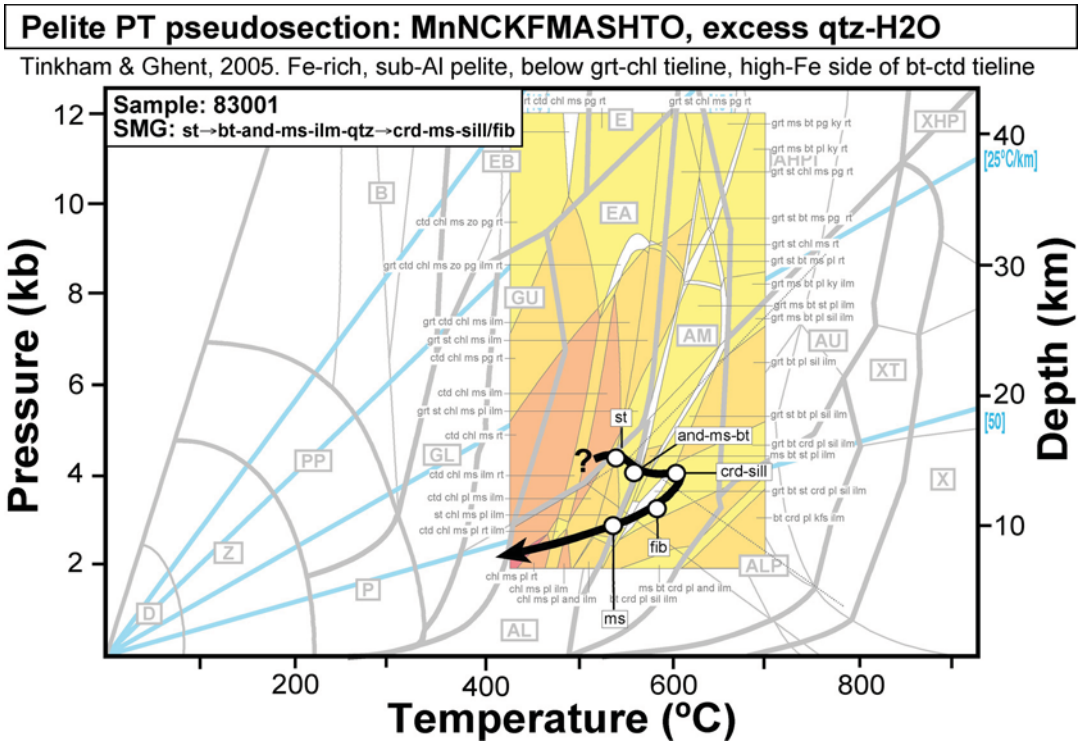

Figure 102: *PT pseudosection for interpretation of M2 clockwise P-T paths samples 8301. Details of published pseudosection are listed in header. Cross - calculated PT results, circles - documented mineral parageneses.*

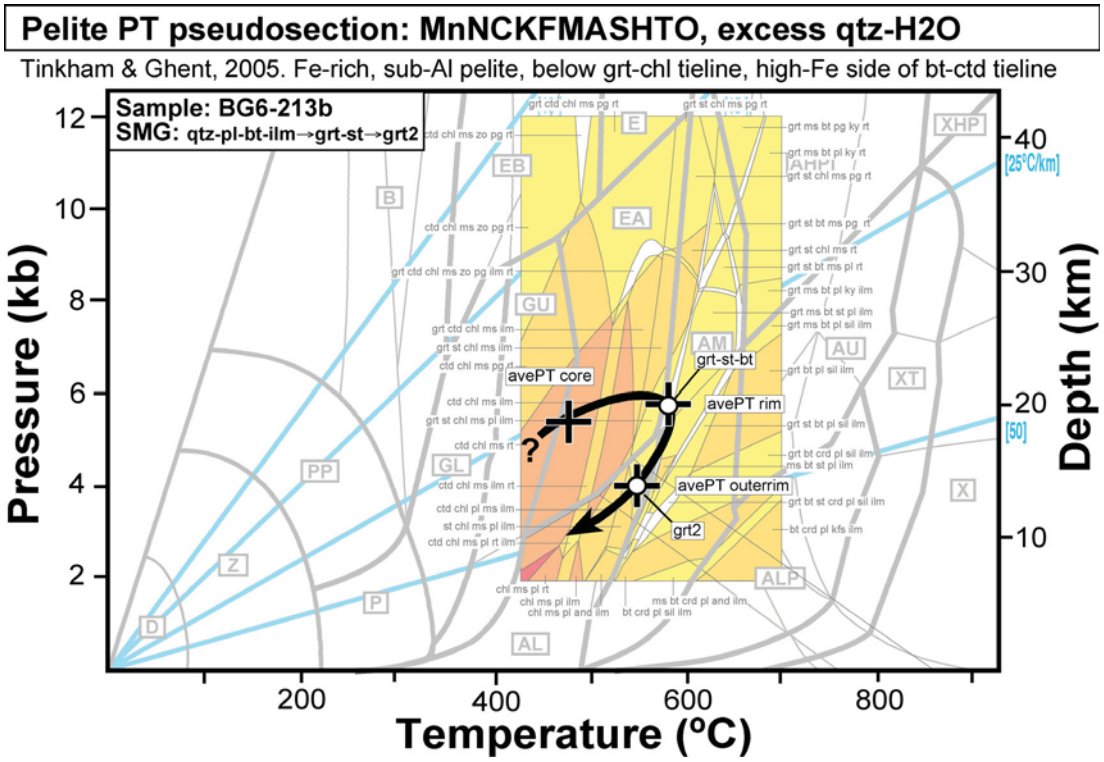

Figure 103: *PT pseudosection for interpretation of M2 clockwise P-T paths samples BG6-213b. Details of published pseudosection are listed in header. Cross - calculated PT results, circles - documented mineral parageneses.*

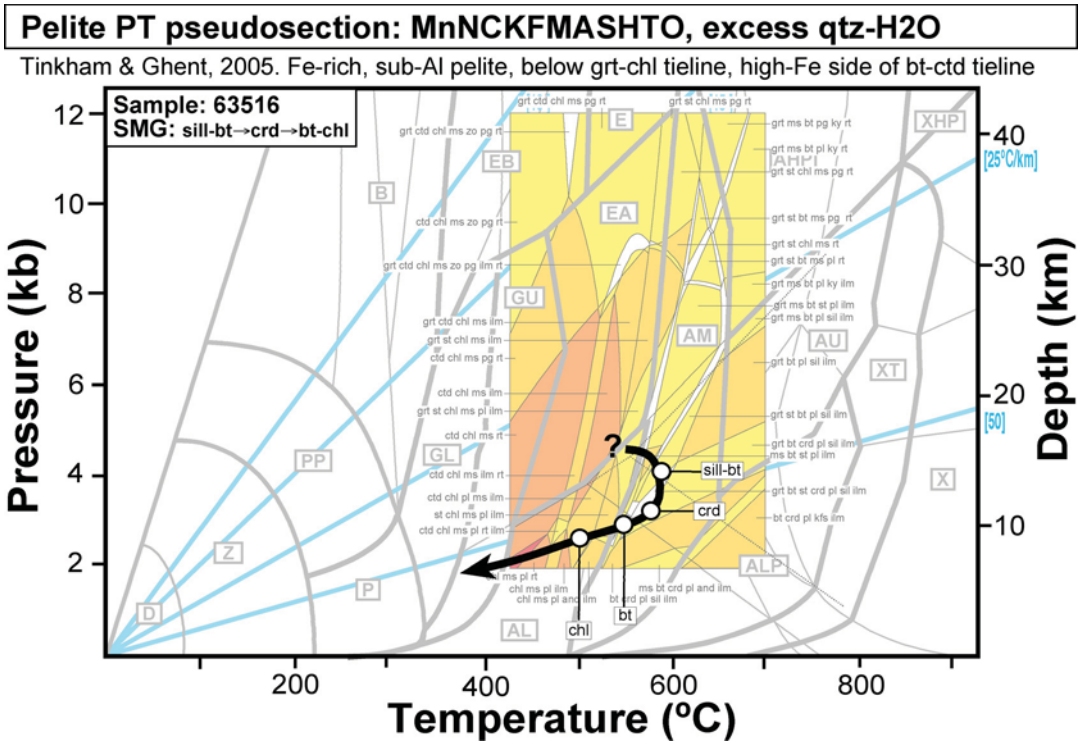

Figure 104: *PT pseudosection for interpretation of M2 clockwise P-T paths samples 63516. Details of published pseudosection are listed in header. Cross - calculated PT results, circles - documented mineral parageneses.*

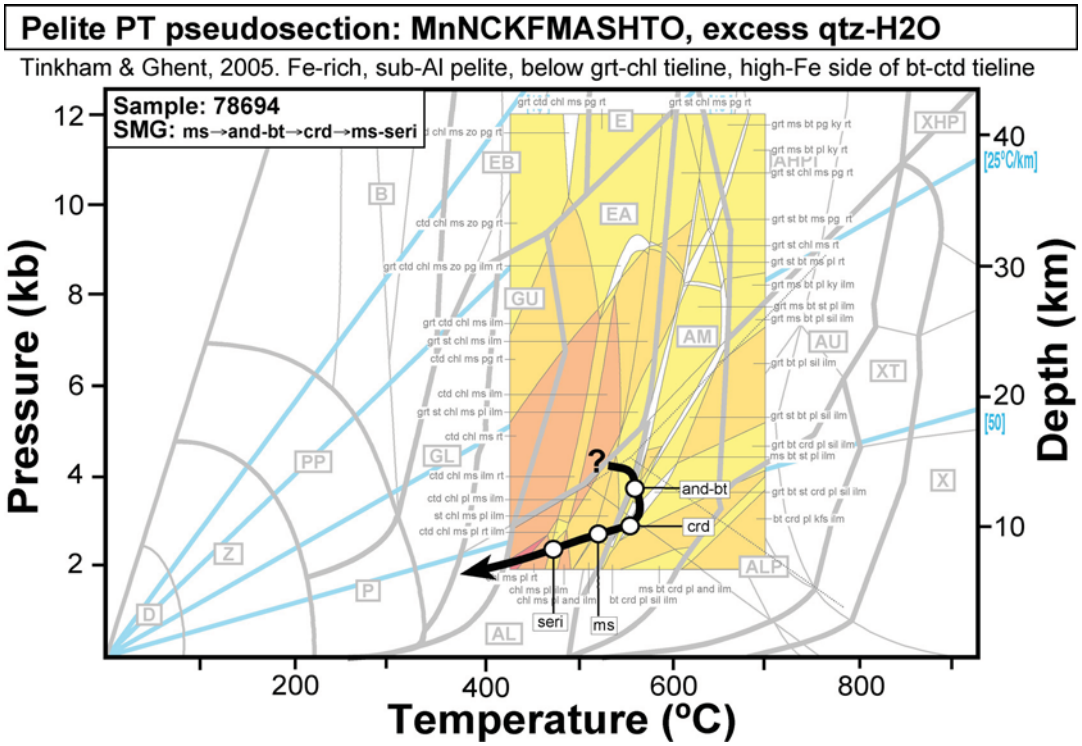

Figure 105: *PT pseudosection for interpretation of M2 clockwise P-T paths samples 78694. Details of published pseudosection are listed in header. Cross - calculated PT results, circles - documented mineral parageneses.*

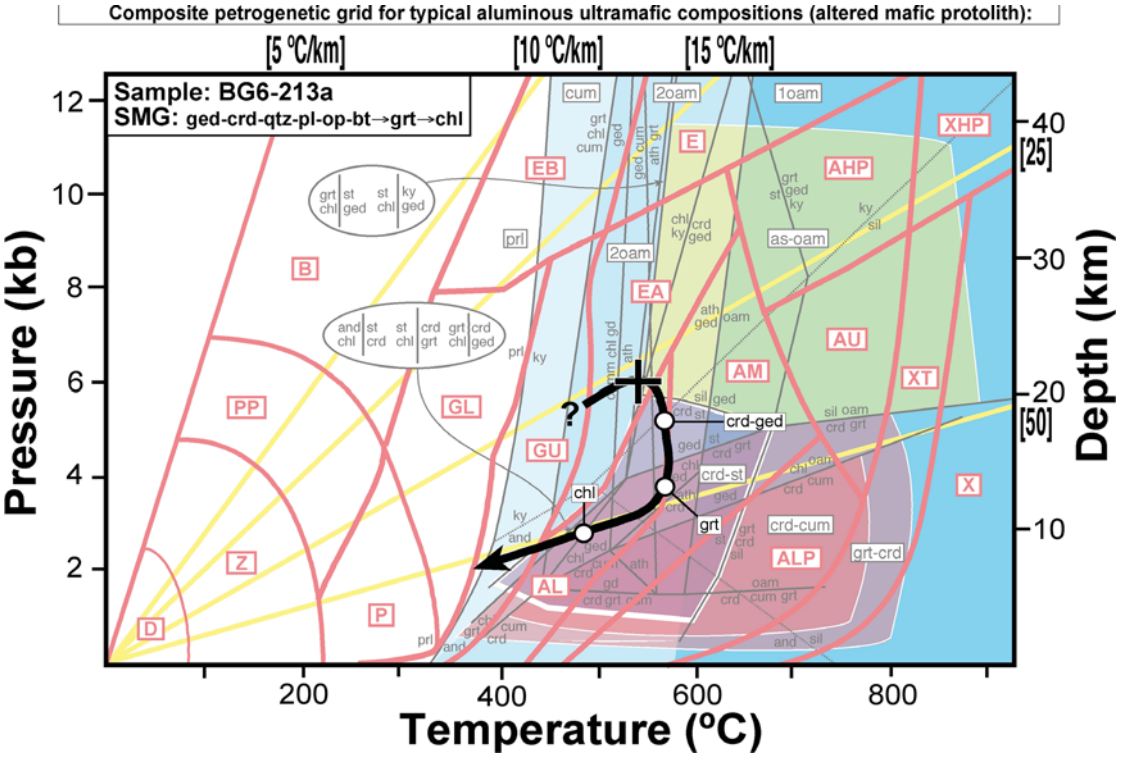

Figure 106: *PT pseudosection for interpretation of M2 clockwise P-T paths samples BG6-213a. Details of published pseudosection are listed in header. Cross - calculated PT results, circles - documented mineral parageneses.*

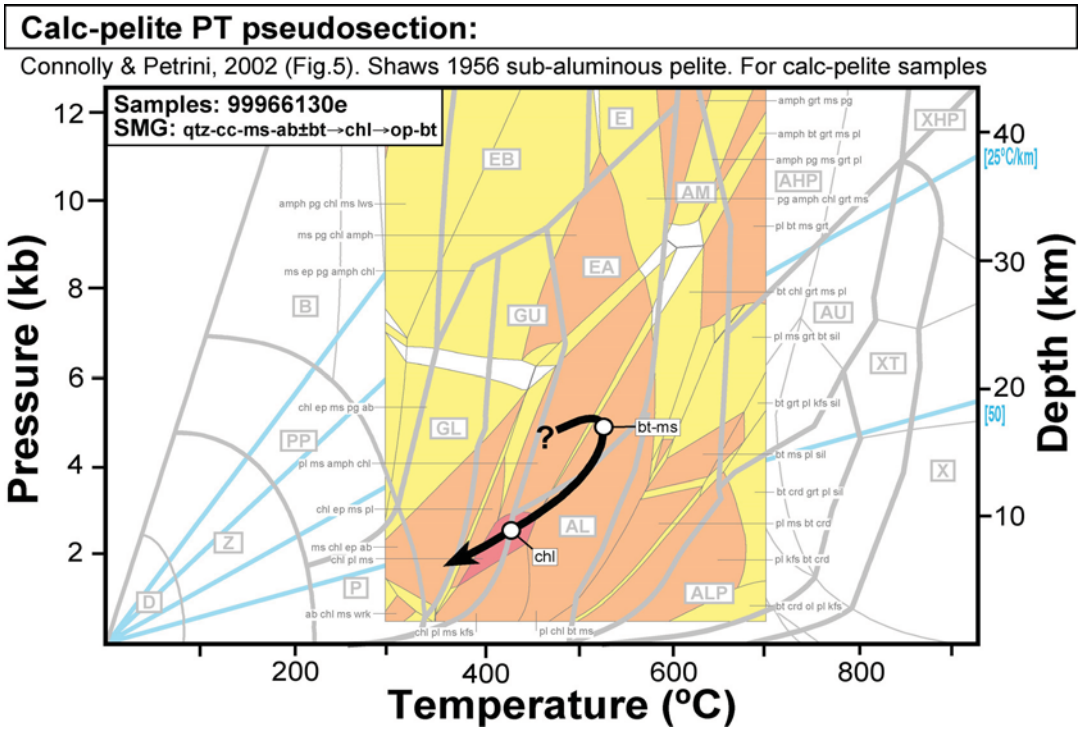

Figure 107: *PT pseudosection for interpretation of M2 clockwise P-T paths samples 99966130. Details of published pseudosection are listed in header. Cross - calculated PT results, circles - documented mineral parageneses.*

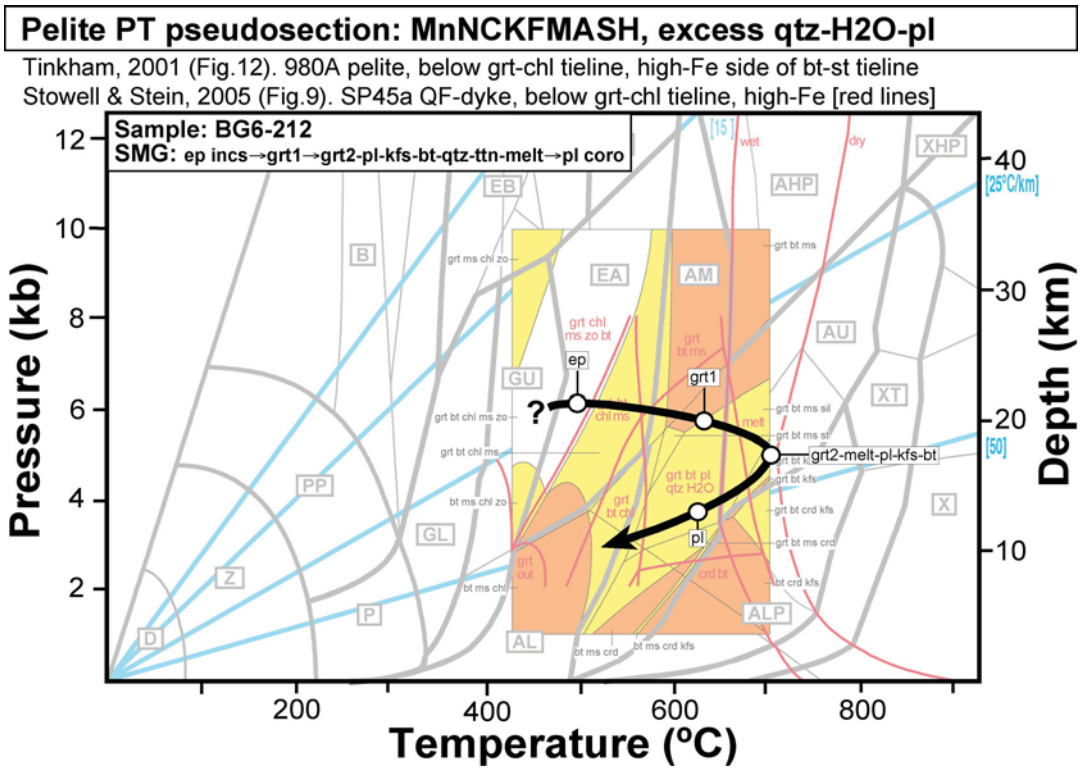

Figure 108: *PT pseudosection for interpretation of felsic migmatite samples BG6-212. Details of published pseudosection are listed in header. Cross - calculated PT results, circles - documented mineral parageneses.*

Calc-pelite schists from a single locality (99966130) in northern Boorara Domain document a clockwise P-T path. Peak metamorphic assemblages of quartz-dolomite-biotite-muscovite-plagioclase ± chlorite porphyroblasts and foliation are overprinted by late-stage ilmenite, dolomite, biotite and hornblende porphyroblasts and retrograde chlorite (Figure 107).

Coarse-grained aluminous schist layers within granite (BG6-159e) document a clockwise P-T path. Peak metamorphic assemblages of kyanite-muscovite-biotite-quartz-rutile, are overprinted by late-stage, fine-grained muscovite-fibrolite shear bands indicating decompression. High-grade migmatized quartzo-feldspathic gneiss in the South Linden Domain (BG6-212) documents a tight clockwise P-T path. Prograde parageneses are preserved as epidote and biotite inclusions within garnet. The peak metamorphic assemblage of garnet-melt-quartz-plagioclase-K-feldspar-biotite is over-printed by garnet overgrowths and plagioclase coronas (Figure 108).

Clockwise P-T Paths in Mount Belches Formation

The eastern central part of the Belches Formation in the Bulong Domain has four metapelite samples (Y508, YD246, PBGMB0201, 153402) that show evidence for clockwise P-T evolutions (Figure 109). Clockwise P-T paths showing decompression through the peak are defined by arrays of PT calculations and core to rim garnet isopleths record a decompressive prograde path in Y508. Phase relations support these clockwise paths. Early matrix parageneses containing biotite1, quartz, plagioclase, ilmenite, graphite, tourmaline, K-feldspar and staurolite are over-grown by peak metamorphic garnet and biotite2 porphyroblasts tracking a prograde trajectory. Early staurolite parageneses are recorded from YD246 and PBGMB0201. The peak parageneses in both of these samples are in turn over-printed by andalusite and later cordierite. Late stage cordierite with a third episode of biotite growth is also recorded in 153402. Late-stage andalusite and latest-stage cordierite growth are diagnostic of peak to post-peak decompression (Figure 110). Late-stage cooling trajectories are recorded by retrograde chlorite, muscovite and opaque.

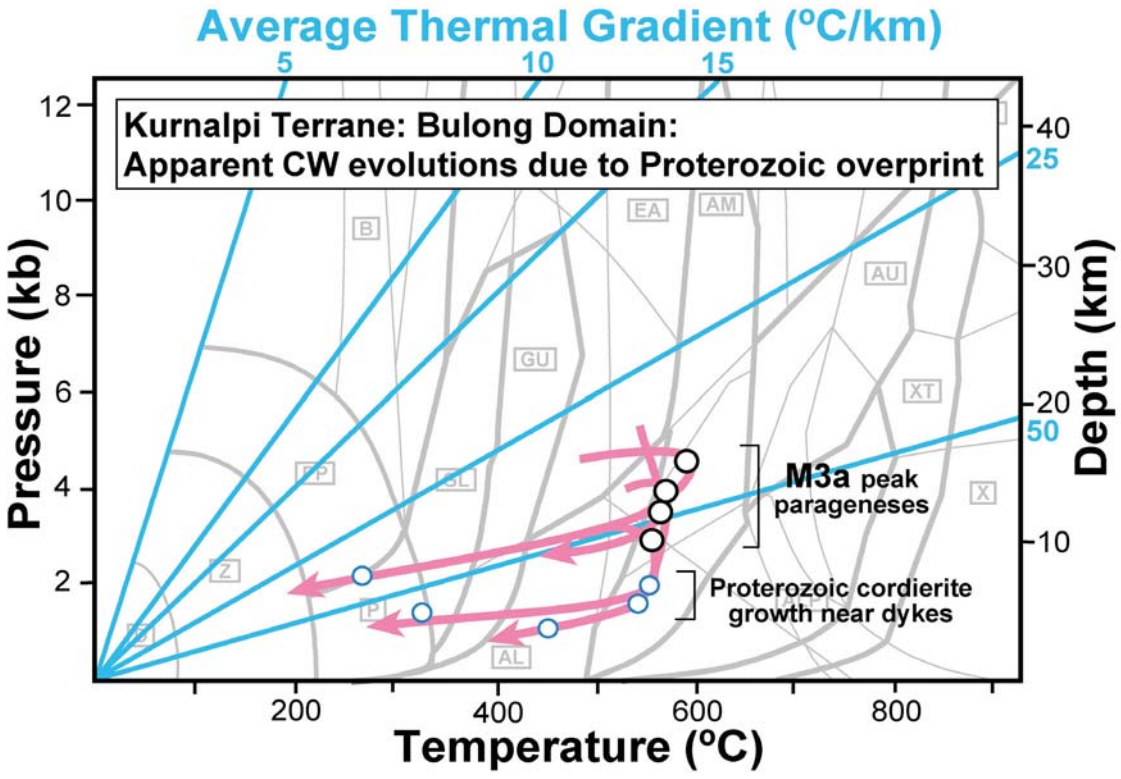

Figure 109: *Peak PT loci and apparent CW P-T evolutions from Belches Formation in the Bulong Domain. Apparent P-T paths are possibly an artifact of two metamorphic events such as M3a peak parageneses and M4 Proterozoic cordierite growth in contact aureoles at shallow crustal levels.*

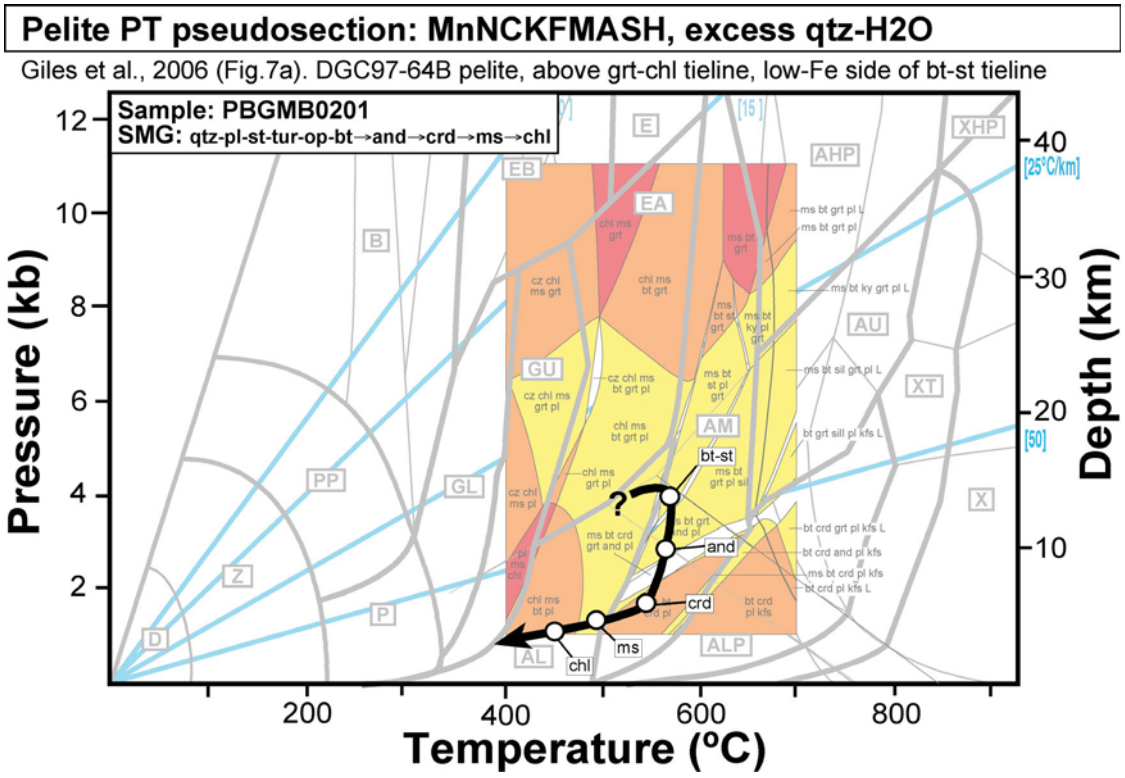

Figure 110: *PT pseudosection for interpretation of clockwise Mt Belches samples PBGMP0201. Details of published pseudosection are listed in header. Cross - calculated PT results, circles - documented mineral parageneses.*

These samples outline a narrow N-S arcuate zone devoid of anticlockwise evolutions, which are ubiquitous to both the east and west elsewhere in the Belches Formation. This zone of anomalous clockwise evolutions may be due to any of the following five explanations.

[1] Samples may be from an older stratigraphic unit below the Mt Belches formation, and thus recording M2 clockwise evolutions.

[2] The zone may be an up-thrust older stratigraphic unit recording M2 parageneses.

[3] The zone may be the lower-plate, decompressing rocks bound by extensional faults governing the burial trajectories of upper-plate rocks elsewhere in the Belches Formation. In this scenario both the clockwise and anticlockwise parageneses are time equivalent representing M3a parageneses, both in Mt Belches Formation stratigraphy.

[4] An alternative scenario of both P-T evolutions being in the same Mt Belches Formation stratigraphic units would require the clockwise P-T paths to be slightly earlier formed in the M2 metamorphic period. The corollary of this scenario is that either M2 metamorphism is long-lived and transitions into M3a, or the Mt Belches Formation is older than other Late Basins and was deposited before the end of M2 metamorphism. The maximum deposition age of 2666 Ma reported by Hall (2006) would preclude this scenario.

[5] The most plausible interpretation is that the mineral reaction textures do not represent a single metamorphic event and the different episodes of mineral growth cannot be linked in the one P-T path. Samples 153402 and PBGMB0201 are located 300-600 m from Proterozoic dolerite dykes of moderate 200 m widths. Samples YD246 and Y508 are located 1000 m from the 2000 m wide Paleoproterozoic Jimberlana mafic-ultramafic dyke. The apparent clockwise P-T paths could possibly be explained by late-stage ameboid cordierite growth in a transient thermal pulse at shallow crustal levels resulting from

emplacement of Proterozoic mafic-ultramafic intrusives in the vicinity. There is a high spatial density of Proterozoic dykes and intersection of multiple dyke swarms in the Mt Belches Basin region (Figure 3), coinciding with the domain containing samples with Proterozoic overprint. Late-stage cordierite growth is inconsistent with the anticlockwise P-T evolutions in the Mt Belches Formation and so the Proterozoic thermal overprint was readily recognised. Elsewhere out of the Mt Belches Formation, late-stage cordierite growth is typical of the widespread M2 clockwise P-T evolutions and thus Proterozoic mineral growth will remain unrecognised.

M3a Anticlockwise P-T Paths in Mount Belches Formation

Metapelites record unambiguous anticlockwise P-T paths from most samples of the Mt Belches Formation (Figure 111). Apart from the zone of clockwise evolutions described above, samples across the remainder of the Mt Belches Formation indicate ubiquitous anticlockwise evolutions.

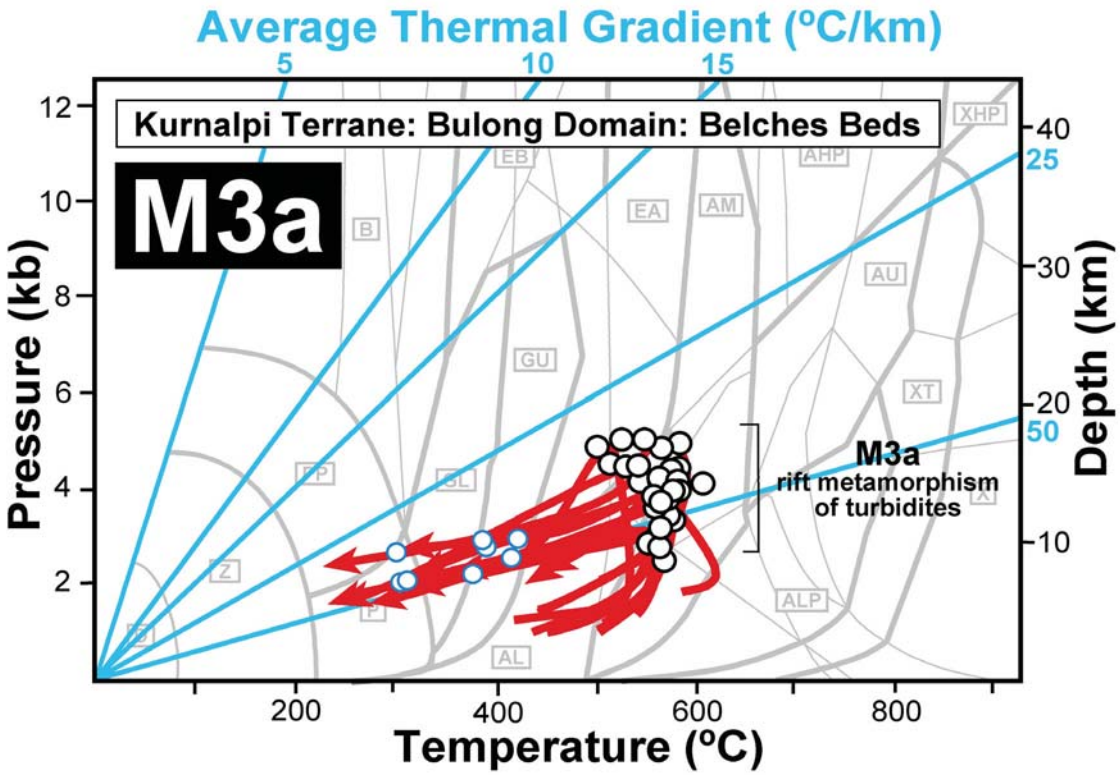

Figure 111: *Peak PT loci and ACW P-T evolutions from Belches Formation.*

Andalusite metapelites (Y533a, i, Y531g) have foliated fine-grained matrix assemblages of quartz-plagioclase-biotite1±ilmenite±chlorite that are over-printed by andalusite and biotite2 porphyroblasts. These very low-P parageneses are over-printed by post-kinematic porphyroblasts of garnet, staurolite and biotite2, constituting the peak metamorphic parageneses. These relations indicate burial with prograde metamorphism, followed by cooling and retrograde chlorite and muscovite growth (Figure 112).

Staurolite metapelites (Y533e, Y455b, c, f) have foliated fine-grained matrix assemblages of quartz-plagioclase-biotite1-ilmenite±muscovite that are over-printed by andalusite grains and porphyroblasts. These very low-P parageneses are over-printed by post-kinematic porphyroblasts of staurolite and biotite2, constituting the peak metamorphic parageneses. These relations indicate burial with prograde metamorphism, followed by cooling and retrograde chlorite and muscovite growth (Figure 113).

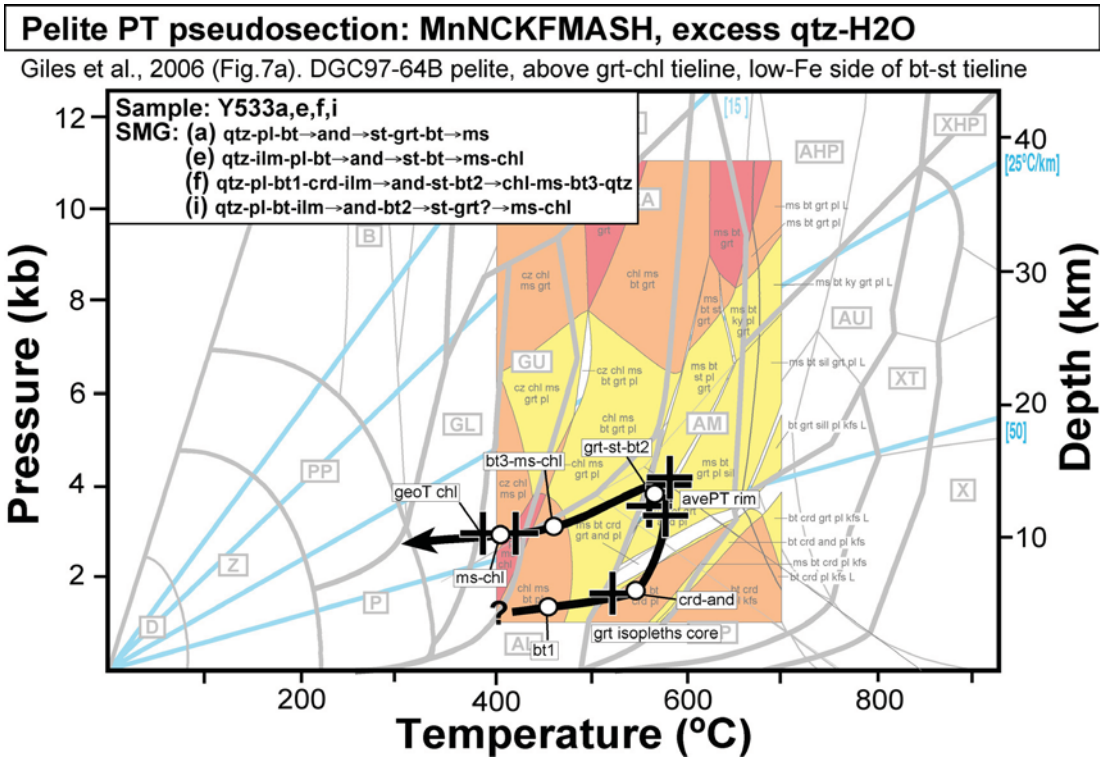

Figure 112: *PT pseudosection for interpretation of anticlockwise Mt Belches samples Y533. Details of published pseudosection are listed in header. Cross - calculated PT results, circles - documented mineral parageneses.*

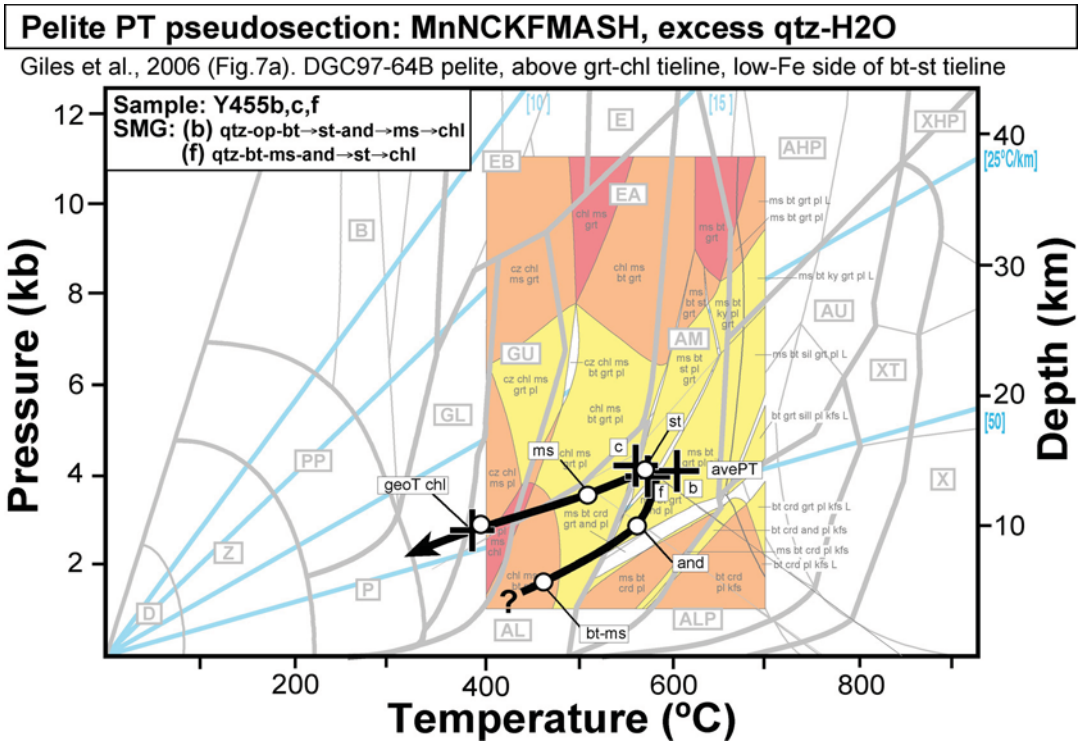

Figure 113: *PT pseudosection for interpretation of anticlockwise Mt Belches samples Y455. Details of published pseudosection are listed in header. Cross - calculated PT results, circles - documented mineral parageneses.*

Complex cordierite metapelites (153469, 153470, 153471, Y533f) have foliated fine-grained matrix assemblages of quartz±plagioclase-biotite1±ilmenite±chlorite±muscovite that are over-printed by cordierite porphyroblasts. These very low-P parageneses are over-printed by post-kinematic porphyroblasts of garnet, staurolite, andalusite and biotite2, constituting the peak metamorphic parageneses. These relations indicate burial with prograde metamorphism, followed by cooling and retrograde chlorite, biotite and muscovite growth (Figure 114).

Simple cordierite metapelites (Y459g, Y458b) have foliated fine-grained matrix assemblages of quartz-plagioclase-graphite±biotite1±muscovite that are over-printed by flattened cordierite porphyroblasts. The cordierite is pseudomorphed to chlorite-muscovite±biotite. Both matrix and pseudomorph assemblages are over-printed by stubby biotite3 and ilmenite laths constituting peak metamorphic mineral growth. These relations indicate further burial from the very low-P cordierite field, followed by cooling and retrograde chlorite growth (Figure 115).

Garnet metapelites (Y534a, Y459a, Y458c, Y530b(ii)) have foliated fine-grained matrix assemblages of quartz-plagioclase-biotite1-ilmenite ± muscovite that are over-printed by stubby biotite2 laths. These prograde parageneses are over-printed by post-kinematic porphyroblasts of garnet and uncommonly staurolite, constituting peak metamorphic mineral growth (Figure 116). These relations indicate prograde metamorphism but with no constraint on pressure trajectories. Retrograde chlorite growth is common in garnet metapelites.

Biotite metapelites (Y459i, e, Y530a, g) have foliated fine-grained matrix assemblages of quartz-plagioclase-biotite1-graphite-tourmaline±ilmenite±muscovite. The matrix is over-printed by post-kinematic blocky biotite2 and ilmenite porphyroblasts, constituting peak metamorphic minerals (Figure 117). These relations indicate prograde metamorphism but with no constraint on pressure trajectories. Retrograde chlorite ± muscovite growth is common.

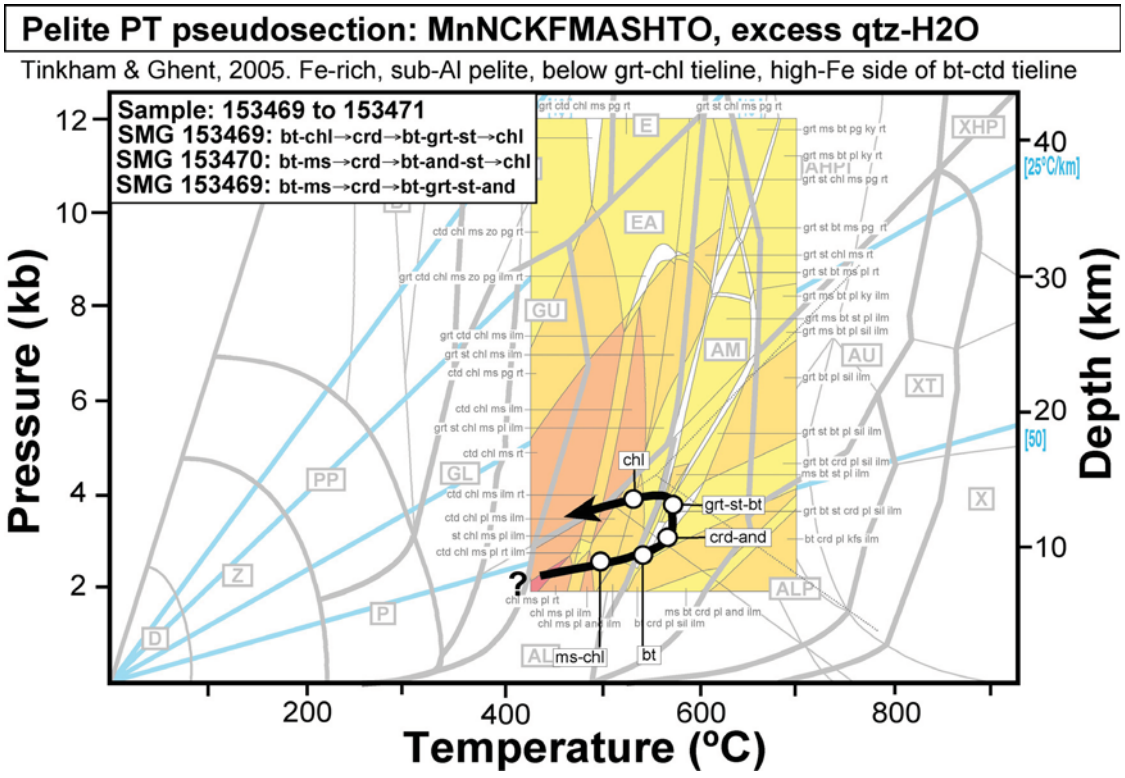

Figure 114: *PT pseudosection for interpretation of anticlockwise Mt Belches samples 153470. Details of published pseudosection are listed in header. Cross - calculated PT results, circles - documented mineral parageneses.*

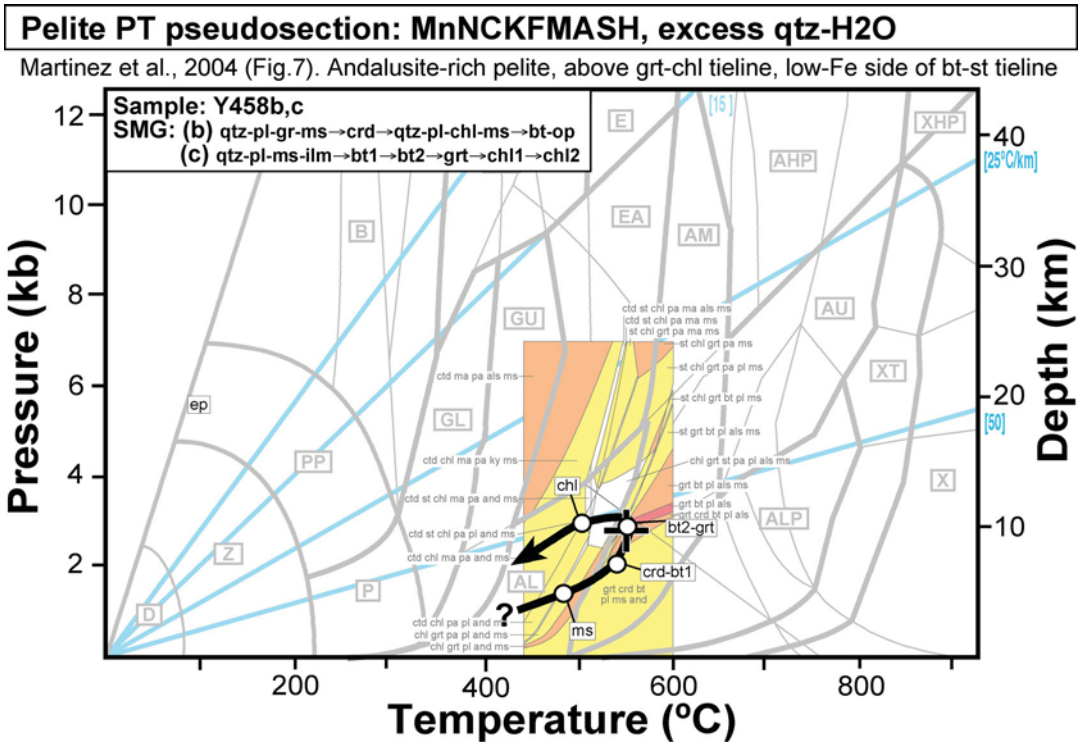

Figure 115: *PT pseudosection for interpretation of anticlockwise Mt Belches samples Y458. Details of published pseudosection are listed in header. Cross - calculated PT results, circles - documented mineral parageneses.*

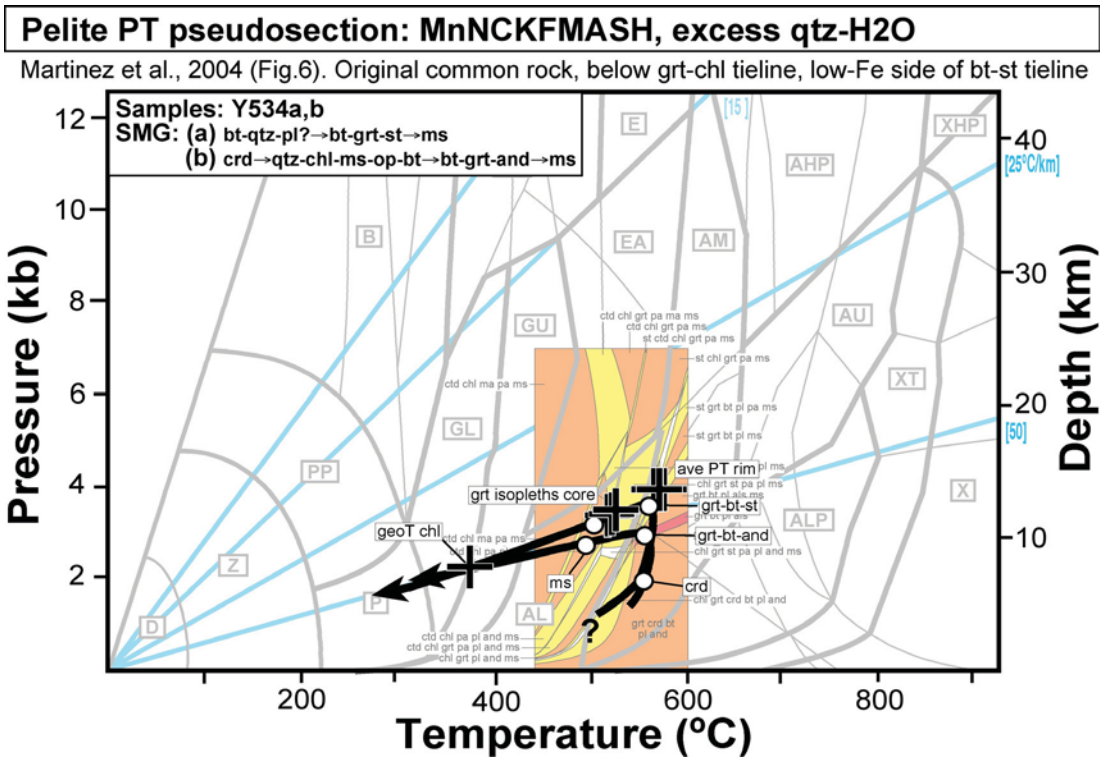

Figure 116: *PT pseudosection for interpretation of anticlockwise Mt Belches samples Y534. Details of published pseudosection are listed in header. Cross - calculated PT results, circles - documented mineral parageneses.*

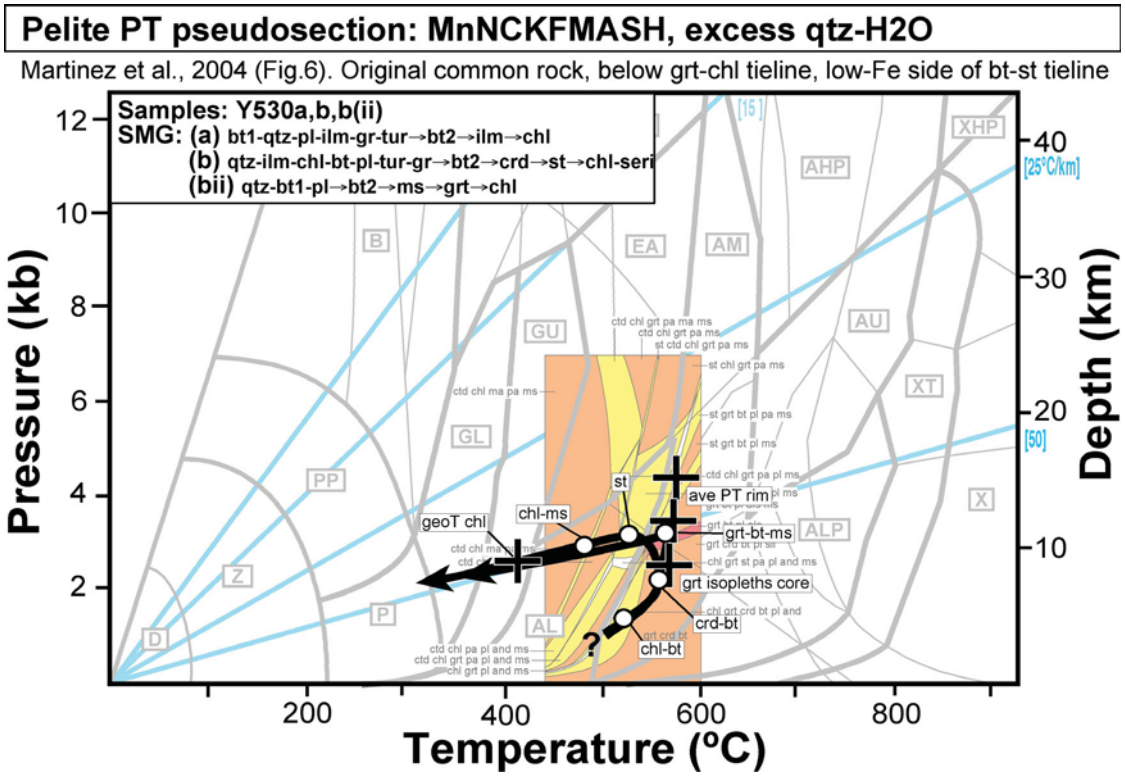

Figure 117: *PT pseudosection for interpretation of anticlockwise Mt Belches samples Y530. Details of published pseudosection are listed in header. Cross - calculated PT results, circles - documented mineral parageneses.*

M3a Anticlockwise P-T Paths near Ockerburry Shear Zone

Anticlockwise P-T paths are also recorded from metapelite samples that are apparently from pre-Late Basin stratigraphy (Figure 118). Almost all of these samples (BG6-142c, 140106, 140107, Y242a, b, BG6-209, Y507a, b, e, f) are located within or close to the Ockerburry Shear Zone, from four distinct localities along its length.

An additional anticlockwise evolution (98957) is recorded from immediately east of the Bardoc Shear Zone. This sample has a matrix foliation of chlorite-biotite-quartz-plagioclase-ilmenite that is over-printed by cordierite, which is in turn over-printed by peak metamorphic garnet and staurolite porphyroblasts enclosed by plagioclase coronas. These mineral relations indicate burial trajectories through the peak of metamorphism and an anticlockwise turn around (Figure 119).

Two metapelite localities (BG6-142c, 140106, 140107) on the Ockerburry Shear Zone have late-stage, post-kinematic chloritoid growth. Matrix assemblages are dominantly muscovite1 and quartz with minor rutile, biotite and ilmenite. The matrix is over-printed by peak metamorphic andalusite and muscovite2 porphyroblasts, which are inturn over-printed by chloritoid, indicating burial followed by cooling, tracking an anticlockwise path (Figure 120).

Rocks with highly aluminous bulk compositions from Kyanite Hill at Leonora (Y242a, b) record an unambiguous anticlockwise turn around the alumino-silicate triple junction. The fine-grained and skeletal matrix foliation contains quartz, muscovite, graphite and andalusite1. This foliation also contains later-stage sillimanite growth and is over-printed by post-kinematic kyanite laths. These relations indicate burial with heating through the peak of metamorphism. Kyanite laths are partially enveloped by late-stage andalusite beards, indicating post-peak decompression with cooling back into the andalusite field (Figure 121).

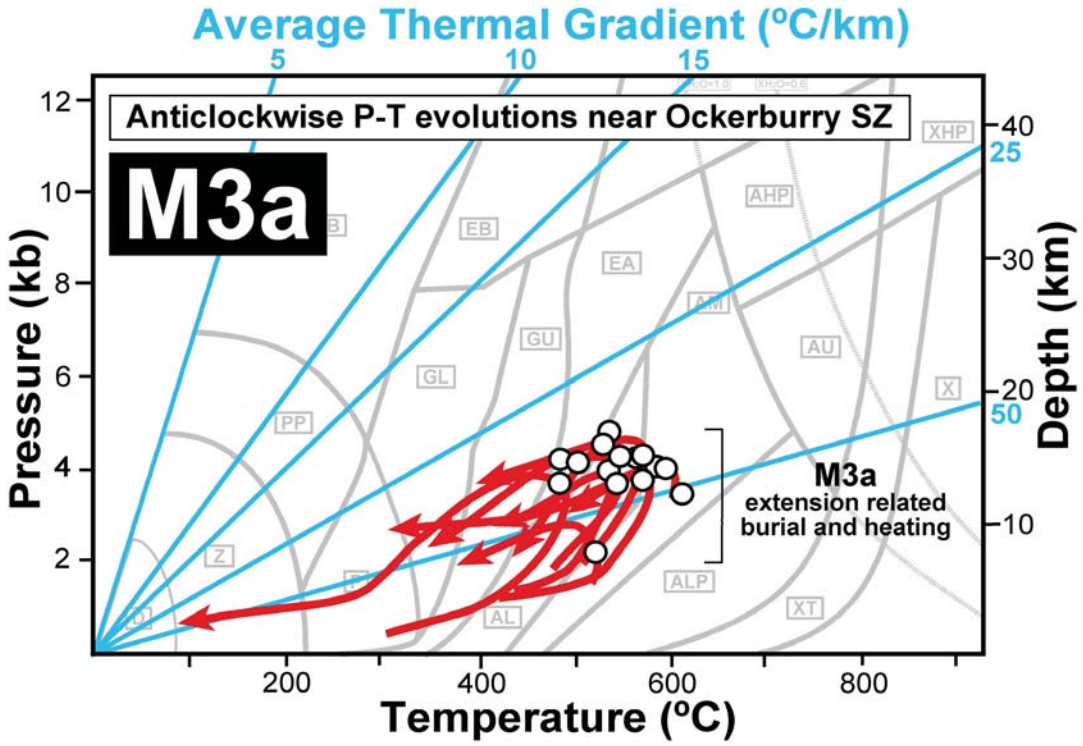

Figure 118: *Peak PT loci and P-T evolutions from samples with ACW P-T evolutions in the vicinity of the Ockerburry shear zone.*

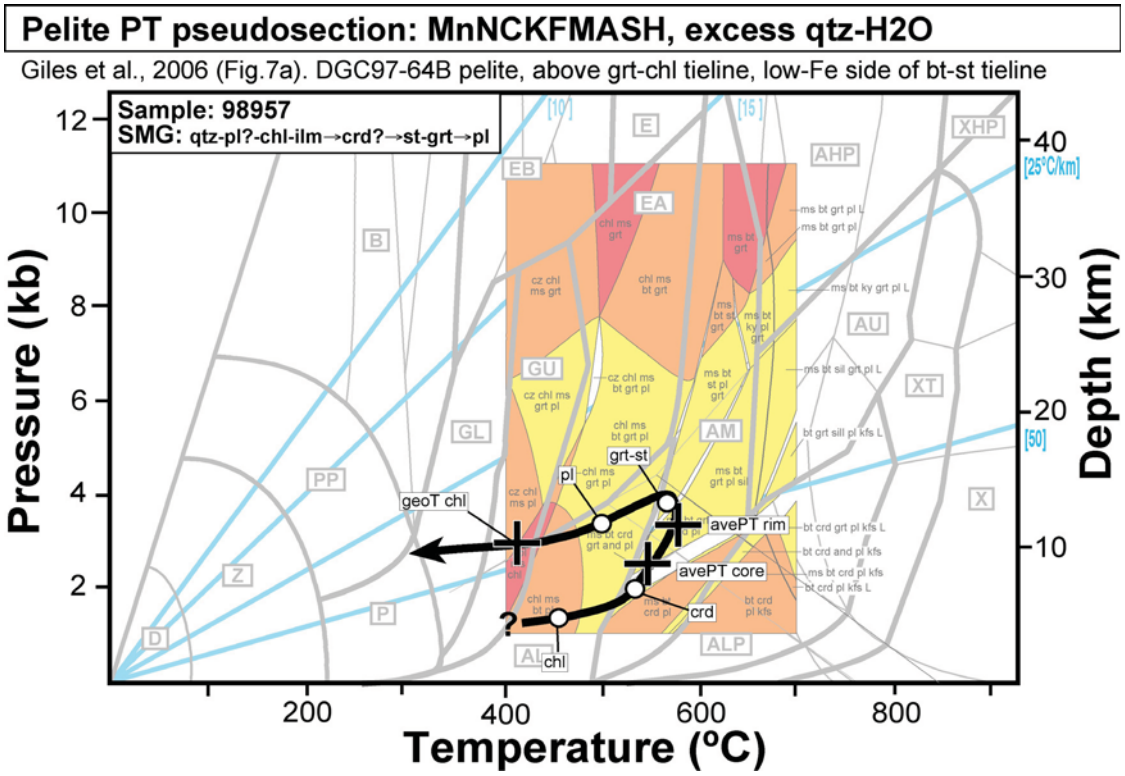

Figure 119: *PT pseudosection for interpretation of anticlockwise Ockerburry samples 98957. Details of published pseudosection are listed in header. Cross - calculated PT results, circles - documented mineral parageneses.*

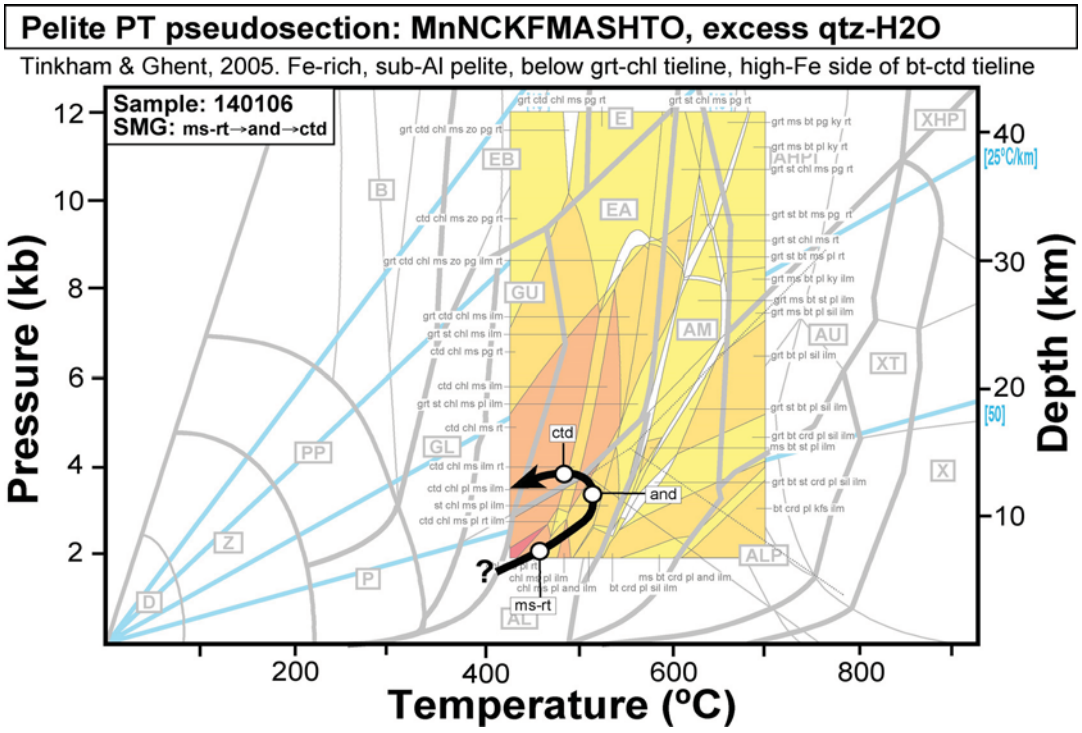

Figure 120: *PT pseudosection for interpretation of anticlockwise Ockerburry samples 140106. Details of published pseudosection are listed in header. Cross - calculated PT results, circles - documented mineral parageneses.*

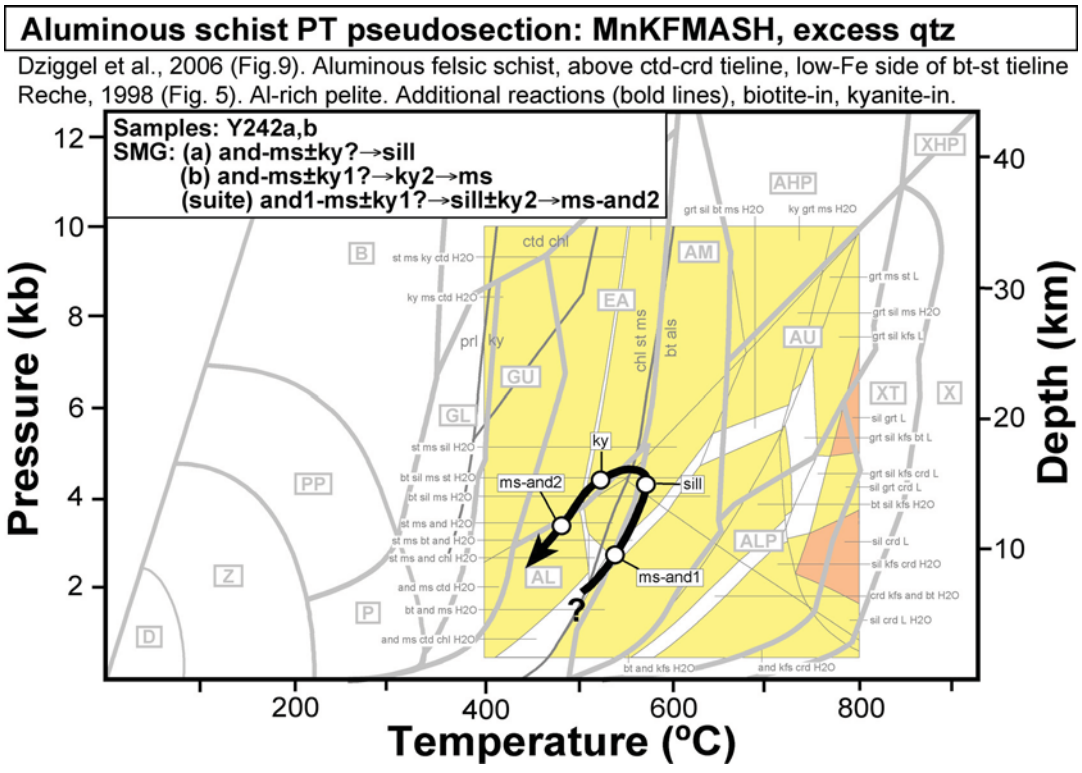

Figure 121: *PT pseudosection for interpretation of anticlockwise Ockerburry samples Y242. Details of published pseudosection are listed in header. Cross - calculated PT results, circles - documented mineral parageneses.*

Rocks with highly aluminous bulk compositions from Mount Martin, south of Kalgoorlie (BG6-209, Y507a, b, e, f) record an unambiguous anticlockwise turn around the alumino-silicate triple junction. Additional samples at this locality (MM1 to MM5) have been described in detail by Purvis (1978, 1984). The unusual bulk compositions are interpreted to indicate rocks that were highly altered early in the geological history, prior to metamorphism (Purvis, 1978, 1984). These rocks record complex mineral relations and may have experienced more than one thermal event. Matrix assemblages are dominated by quartz, muscovite, paragonite and biotite and contain syn-kinematic sillimanite1 or andalusite. These parageneses are over-printed by two-stages of kyanite-growth separated by further flattening and shear bands. The latest stage of shear bands contains sillimanite-muscovite assemblages and retrograde muscovite is common. The overall P-T evolution indicated by these relations is burial during prograde metamorphism and multiple deformation and heating pulses at the peak of metamorphism (Figure 122).

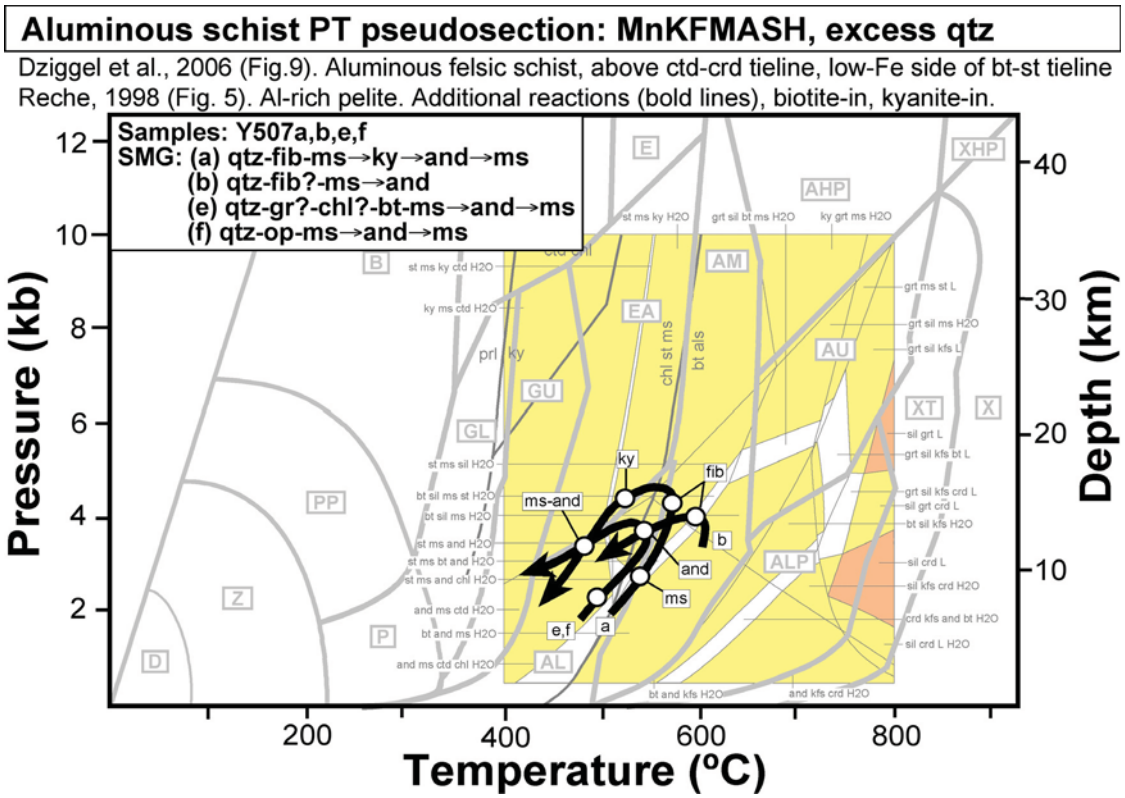

Figure 122: *PT pseudosection for interpretation of anticlockwise Ockerburry samples Y507. Details of published pseudosection are listed in header. Cross - calculated PT results, circles - documented mineral parageneses.*

M3b Alteration P-T Paths

Alteration parageneses are due to the high fluid to rock ratios in localised domains. New mineral growth to give theses parageneses are due primarily to the influx of fluids into a regional ambient thermal regime that is undergoing retrograde cooling after the peak of regional metamorphism. Consequently the M3b P-T path is interpreted in many cases to be a mineral growth event superimposed on a cooling and decompressive regional P-T path. In addition to this simple framework, there are altered domains associated with late-stage igneous intrusives (i.e., syenites and Low-Ca granites). Consequently, there is possibly short-lived transient heat pulses associated with some alteration events. This is confirmed by the large range in temperatures estimated for alteration assemblages, up to 600ºC (Figure 123) and temperature estimates of associated fluids from fluid inclusion studies, up to 550ºC (Ho, 1987). We would interpret that the superimposed M3b alteration events, in many cases probably followed transient and short-lived isobaric heating followed by

isobaric cooling paths, superimposed on the background regional decompressive cooling path. It is worth noting that during the M3b alteration events there is a large drop in pressure of 3 kb from 4 kb to 1 kb, documented fluid inclusion studies. This indicates a step in the decompression of the EYC region through a stage of higher rates of decompression between early and late alteration parageneses.

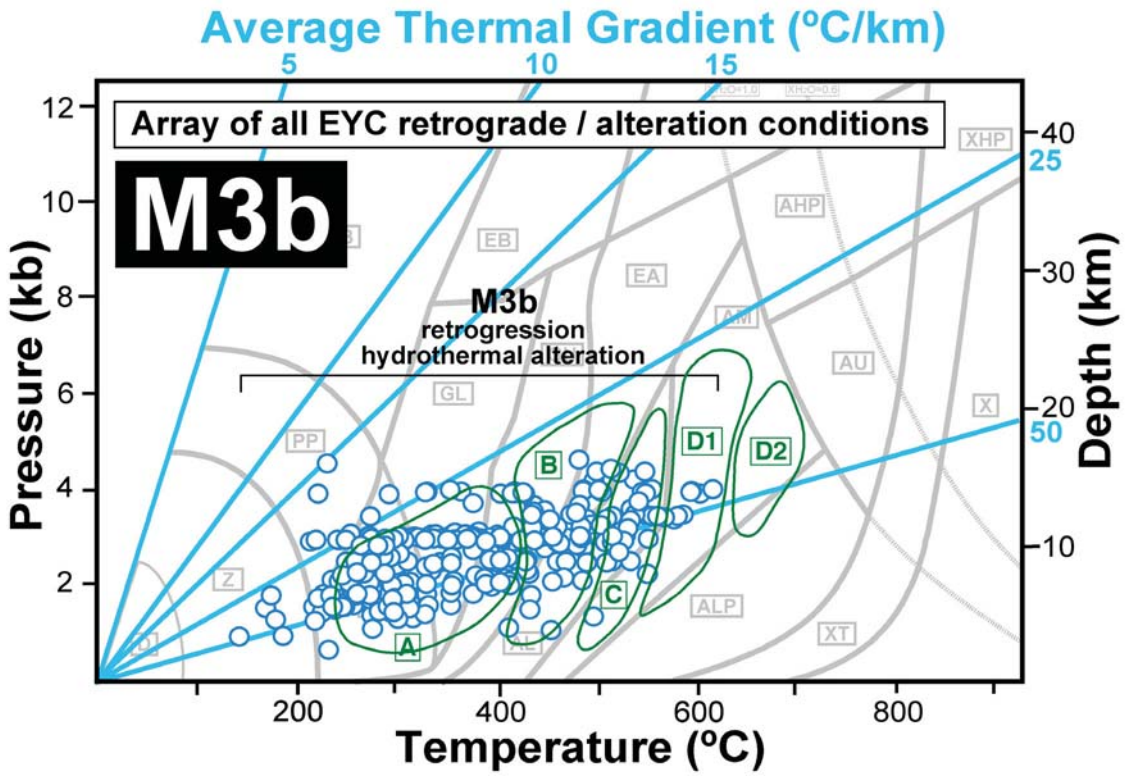

Figure 123: *PT loci from retrograde and alteration parageneses in the EYC. The approximate ranges of alteration facies defined by Witt (1993) are indicated in green.*

Southern Cross Terrane P-T Paths

Southern Cross Domain P-T Path

Mid-amphibolite facies metapelites from the Southern Cross Belt are only described in detail from the Transvaal Mine (Y400a, c, e). PT calculations and mineral relations accurately constrain a clockwise P-T path at low-P, mid-amphibolite conditions. Calculated peak metamorphic conditions for Y400 samples are centred on 575±12 and 3.8±0.75 kb (Appendix 17; GArecord_App17Tab_DomainAnal.xls). These are similar to published PT estimates of 560 ºC and 3.2 kb from the Transvaal area (Dalstra et al., 1999). There are no stratigraphic, geochronologic or structural constraints to determine the age of these metamorphic parageneses and correlation with the metamorphic periods defined for the EYC. The fine-grained and foliated matrix in these samples is a quartz-biotite-graphite assemblage with fine elongate staurolite grains in equilibrium. Some samples also contain fine chloritoid laths in equilibrium with the matrix. The matrix foliation is over-printed by small post-kinematic garnet porphyroblasts representing peak metamorphic mineral growth. Garnets are over-grown and enclosed by large andalusite porphyroblasts and possibly also by cordierite in some samples. This sequence of mineral growth tracks a decompressive prograde path from the chloritoid and staurolite fields at medium pressures. Andalusite and cordierite after garnet, indicates decompression through the peak of metamorphism and a clockwise turn around, followed by retrograde muscovite growth (Figure 124).

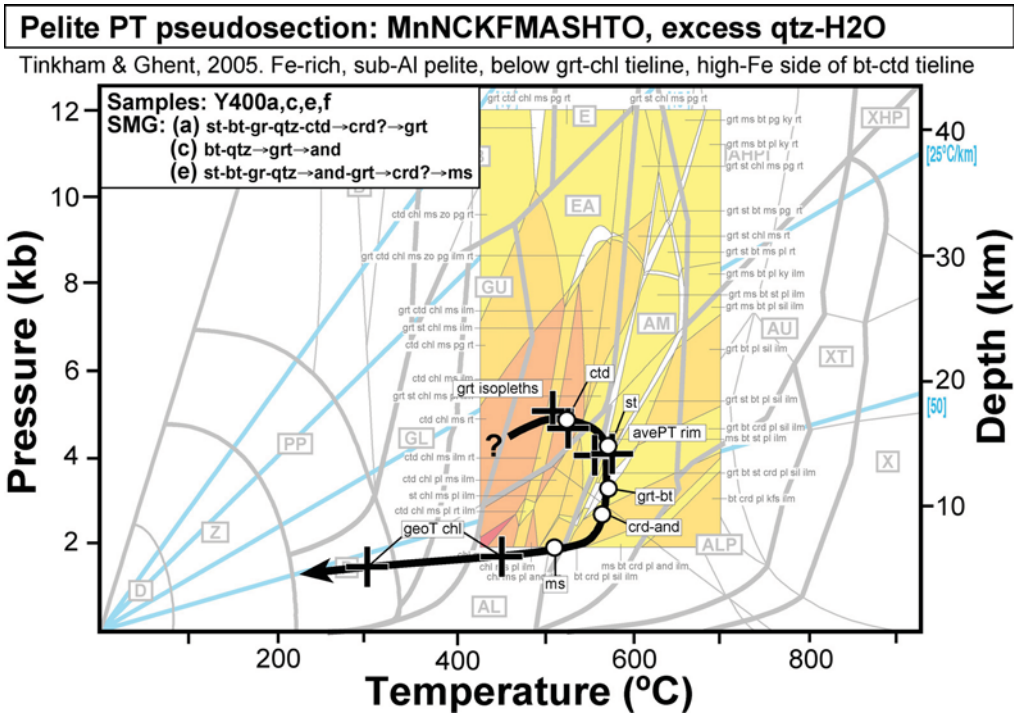

Figure 124: PT pseudosection for interpretation of Southern Cross metapelite samples Y400. Details of published pseudosection are listed in header. Cross - calculated PT results, circles - documented mineral parageneses.

Forrestania Domain P-T Path

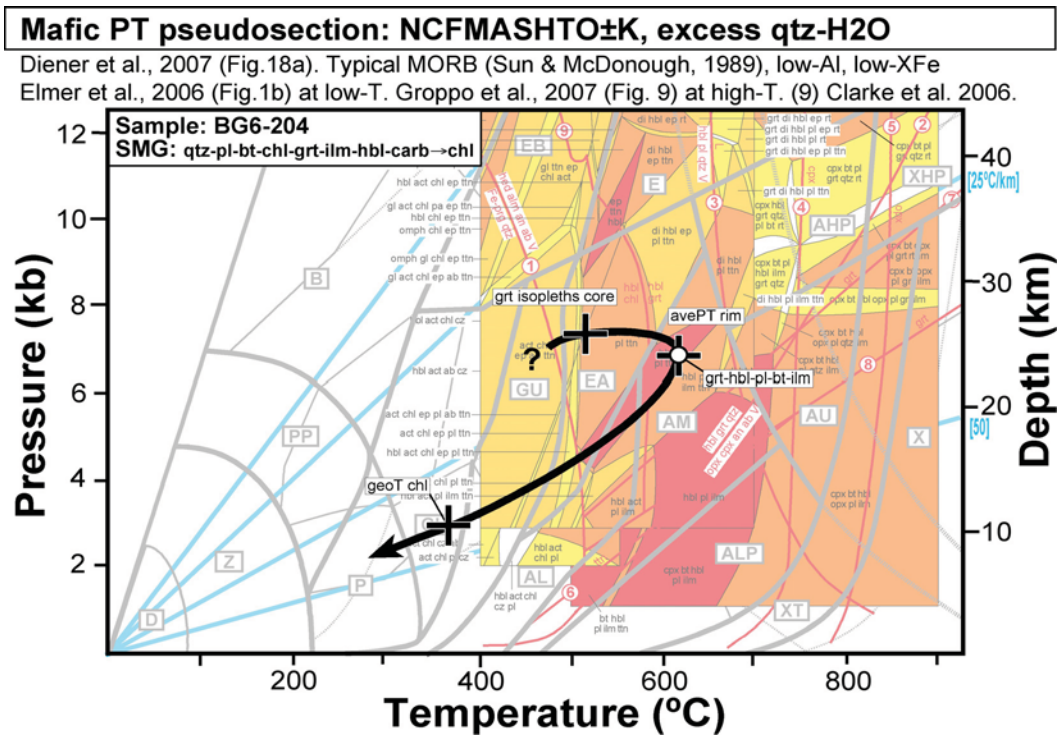

Figure 125: PT pseudosection for interpretation of Forrestania belt samples BG6-204. Details of published pseudosection are listed in header. Cross - calculated PT results, circles - documented mineral parageneses.

Upper-amphibolite facies mafics from the Forrestania Belt are only described in detail from two localities (BG6-204, BG6-205). PT calculations and mineral relations accurately constrain a clockwise P-T path at high-P, upper-amphibolite conditions followed by decompressive cooling. There are no stratigraphic, geochronologic or structural constraints to determine the age of these metamorphic parageneses and correlation with the metamorphic periods defined for the EYC. These samples have aligned granoblastic matrix assemblages of quartz-plagioclase-hornblende-ilmenite-biotite. Garnet porphyroblasts are syn- to post-kinematic but in textural equilibrium with the matrix, indicating isobaric heating prograde trajectories (Figure 125). Chlorite and calcite growth occurs on the post-peak decompressive cooling path documented by PT calculations.

Ravensthorpe Domain P-T Paths

Well-constrained anticlockwise P-T paths are documented from mid-amphibolite facies metapelites at two localities in the Ravensthorpe Belt (BG6-198, BG6-197). The P-T evolutions are defined by detailed mineral relationships and sequence of mineral growth and are confirmed by PT calculations. There are no stratigraphic, geochronologic or structural constraints to determine the age of these metamorphic parageneses. These samples have foliated medium-grained matrix assemblages of quartz-plagioclase-biotite1-ilmenite±muscovite±rutile±chlorite. Medium-grained chloritoid grains occur in the matrix of some samples and early-formed and deformed chloritoid porphyroblasts are in equilibrium with the matrix. Chloritoid-bearing samples have garnet porphyroblasts that range from syn- to post-kinematic, which are in turn over-printed post-kinematic staurolite and biotite2 porphyroblasts. In chloritoid-free samples the matrix assemblage is over-printed by andalusite, muscovite2 and biotite2 porphyroblast, which are in turn over-printed by post-kinematic staurolite and then garnet porphyroblasts. These relationships track burial prograde P-T paths from very low-P chloritoid-andalusite stability field to peak metamorphism at higher pressures in the garnet-staurolite field. Late-stage staurolite in chloritoid-bearing samples, indicate a clockwise turn around, followed by retrograde chlorite and muscovite growth (Figure 126).

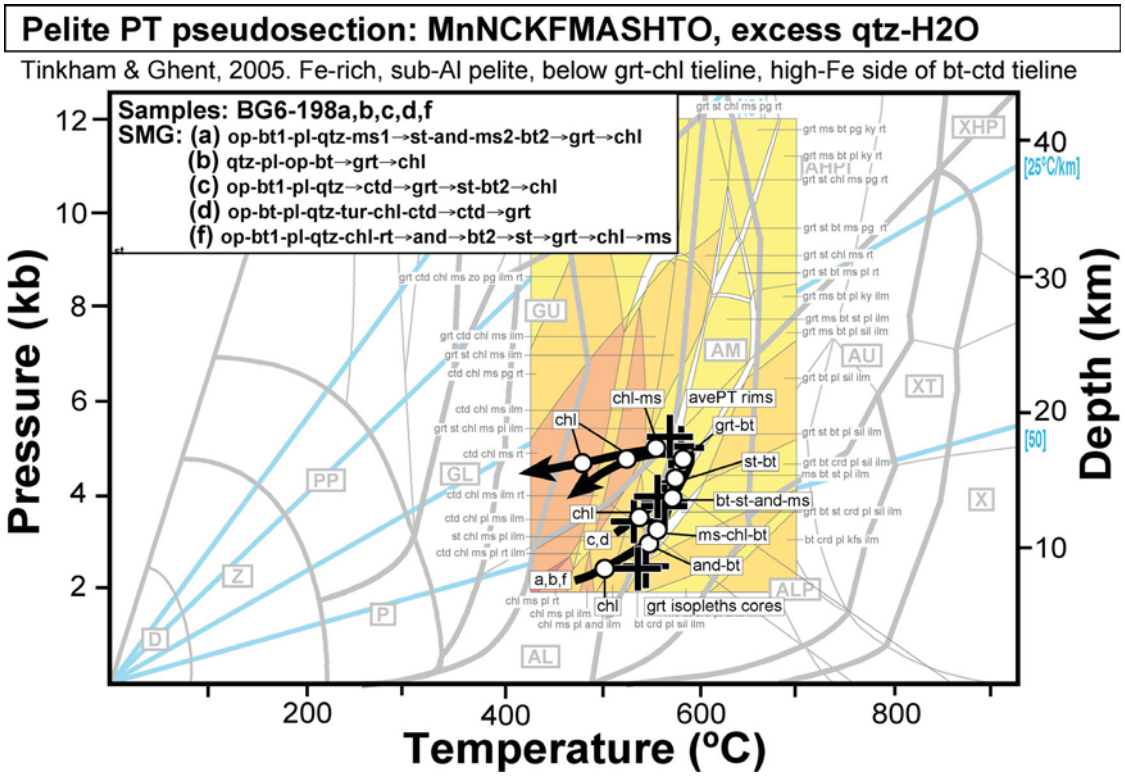

Figure 126: *PT pseudosection for interpretation of Ravensthorpe metapelite samples BG6-198. Details of published pseudosection are listed in header. Cross - calculated PT results, circles - documented mineral parageneses.*

Anticlockwise P-T paths are also documented from cordierite-sillimanite metapelites at BG6-197. The matrix assemblage at this locality is quartz-plagioclase-biotite1±muscovite±tourmaline. Syn-kinematic porphyroblasts of cordierite are in equilibrium with the matrix. Early parageneses are over-printed by andalusite porphyroblasts and in turn by peak metamorphic parageneses containing sillimanite, biotite2 and plagioclase. Peak assemblages are overprinted by fine-grained fibrolite and biotite3. These mineral relationships indicate a prograde path with burial from cordierite-andalusite into the sillimanite field followed by anticlockwise turn around and isobaric cooling and fibrolite growth (Figure 127).

Other localities in the Ravensthorpe Domain have less robust clockwise P-T paths defined by PT calculations, core to rim garnet isopleths, late growth of garnet in amphibolite (BG6-196c) and metapelite (BG6-196a) and andalusite after garnet in metapelite (BG6-199; Figure 128).

Granite orthogneiss in the Ravensthorpe Domain have igneous hornblendes indicating crystallization at pressures of 3.0-5.9kb by Al-in hornblende geobarometers. PT calculations from secondary metamorphic plagioclase and hornblende indicate subsequent further burial to 5.5-8.0kb at 560-650ºC (Figure 129). These constraints indicate cooling trajectories for these intrusives that initially involved burial with cooling followed by decompressive cooling to retrograde parageneses. This P-T evolution suggests compressional reworking of the granitic orthogneiss domain. This is consistent with both the thrust stack structural geometries (Witt, 1998) and the clockwise P-T paths documented by some samples in the Ravensthorpe Domain.

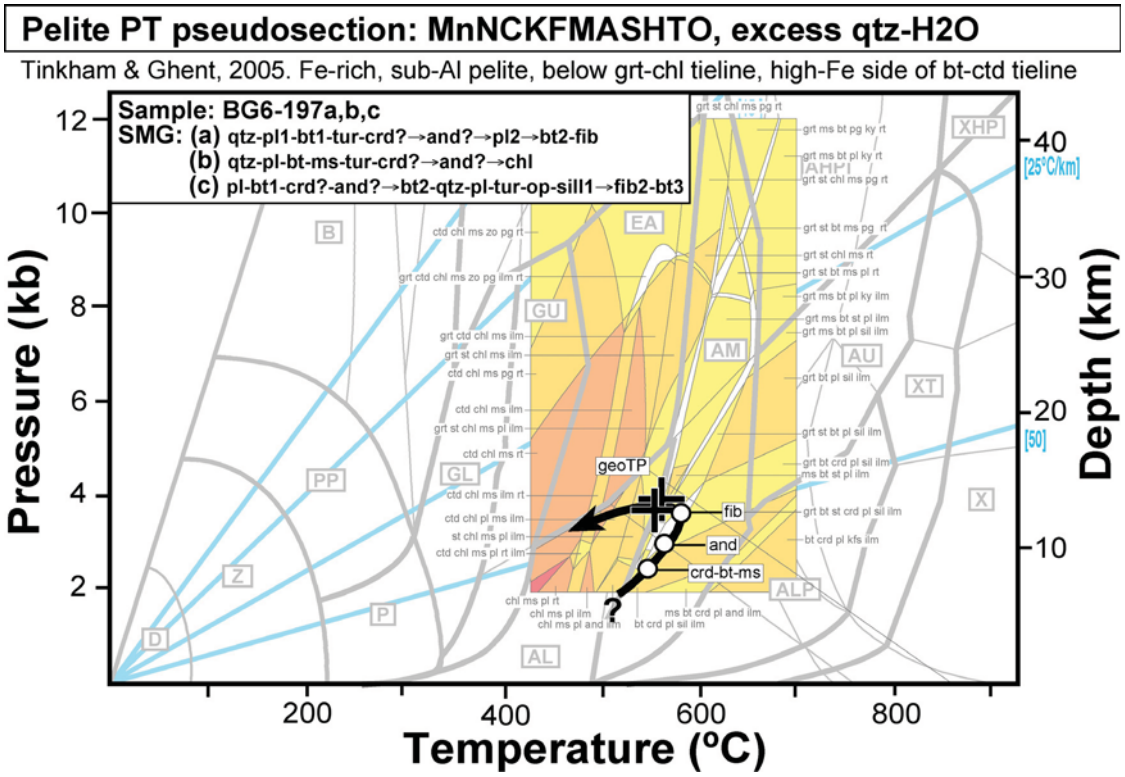

Figure 127: *PT pseudosection for interpretation of Ravensthorpe metapelite samples BG6-197. Details of published pseudosection are listed in header. Cross - calculated PT results, circles - documented mineral parageneses.*

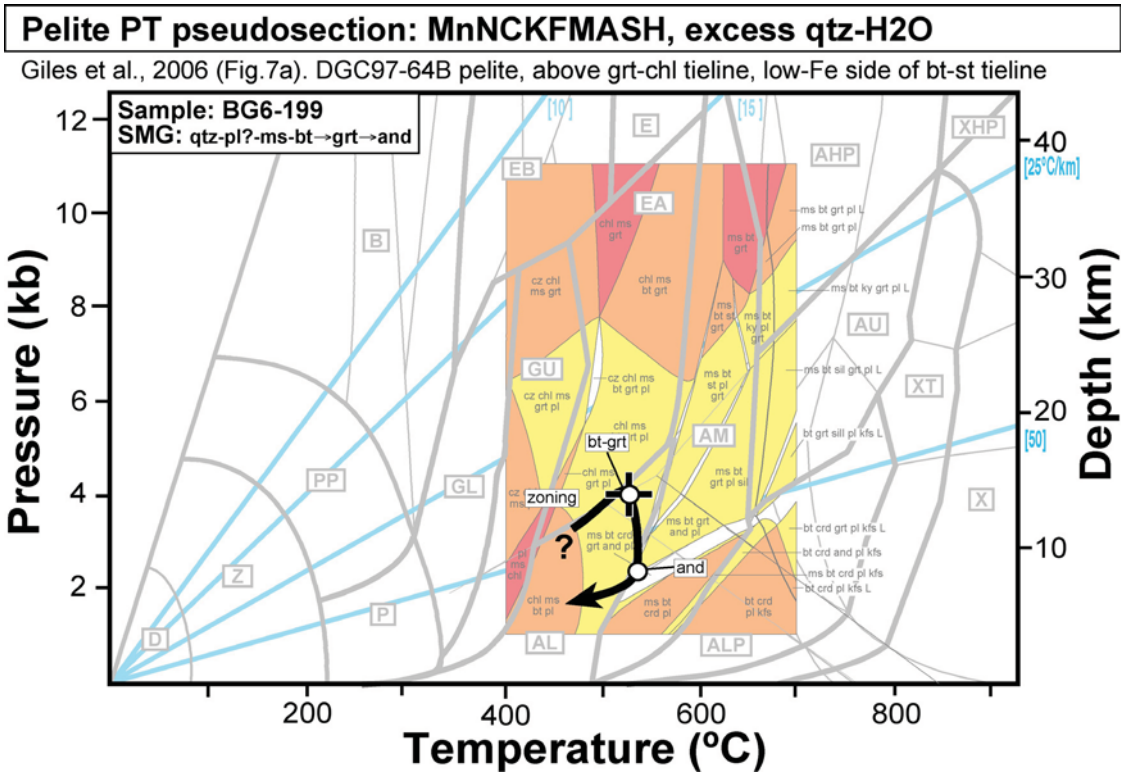

Figure 128: *PT pseudosection for interpretation of Ravensthorpe metapelite samples BG6-199. Details of published pseudosection are listed in header. Cross - calculated PT results, circles - documented mineral parageneses.*

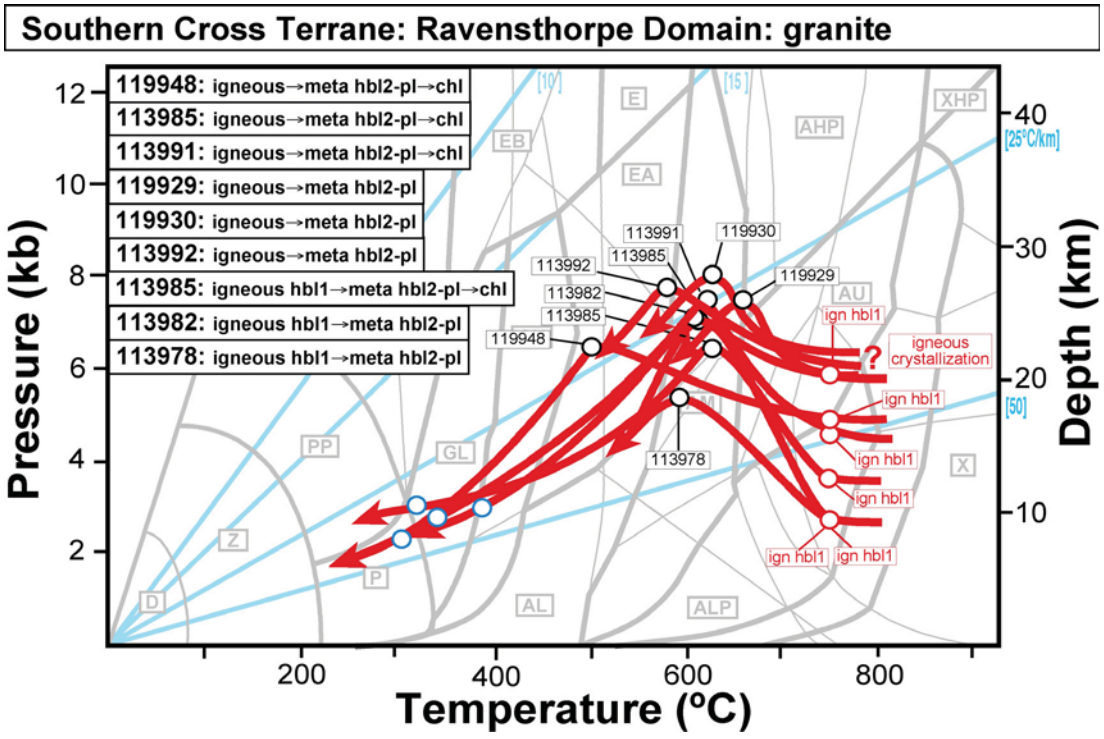

Figure 129: *Interpreted P-T evolution of granitoids in the Ravensthorpe belt. Pressures calculated from metamorphic hornblendes are higher than igneous hornblendes, inferring burial after igneous crystallization.*

Burtville Terrane P-T Paths

High-grade calc-silicate gneisses from the Burtville Terrane (BG6-151a, b, BG6-152c, 179693b), give PT calculations and mineral relations that document decompressive cooling trajectories from high-P, moderate-T conditions (Figures 130, 131). These samples have aligned polygonal granoblastic matrix of quartz-plagioclase-clinopyroxene-hornblende ± garnet. These assemblages are overprinted by secondary and coronal epidote, clinozoisite and quartz. There are no stratigraphic, geochronologic or structural constraints to determine the age of these metamorphic parageneses.

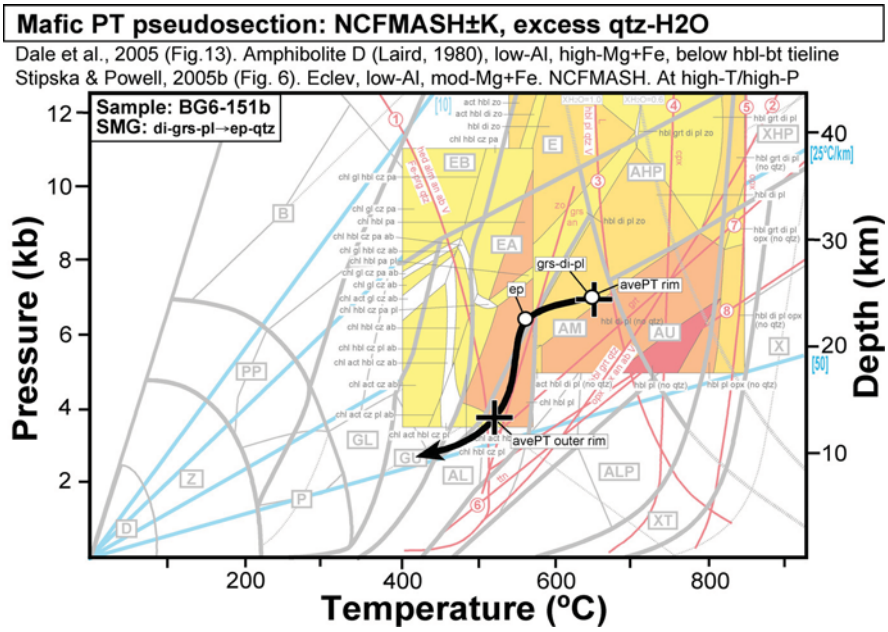

Figure 130: *PT pseudosection for interpretation of Burtville calcsilicate samples BG6-151. Details of published pseudosection are listed in header. Cross - calculated PT results, circles - documented mineral parageneses.*

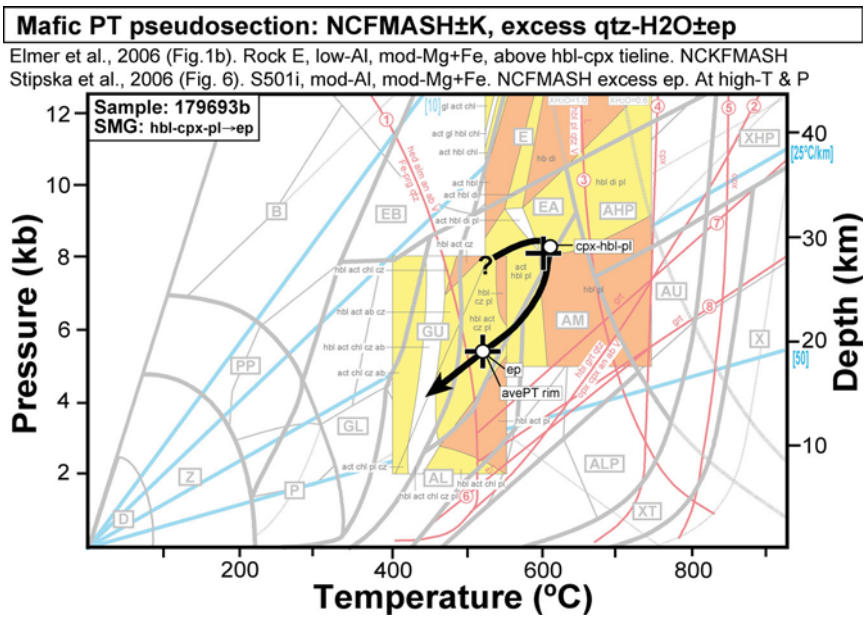

Figure 131: *PT pseudosection for interpretation of Burtville calcsilicate samples 179693b. Details of published pseudosection are listed in header. Cross - calculated PT results, circles - documented mineral parageneses.*

METAMORPHIC DOMAIN ANALYSIS

Metamorphic domain analysis is the process of recognizing distinctly different metamorphic domains within a broader orogenic system that shares metamorphic cycles in common. Metamorphic domains are recognised by a combination of metamorphic style, temperature/depth ratio, absolute PT conditions and the P-T paths that individual rocks evolved through. Metamorphic partitioning within orogenic systems can be very complex and is typically inter-related with deformation partitioning and crustal architecture (Figure 132).

Appendix (17) contains all PT calculations and P-T evolutions available from the Yilgarn Craton, plotted in PT space and grouped by Terrane, Domain and sub-domains. Only peak-T, peak-P and alteration PT estimates are included, all other PT loci that constrain the P-T paths have been removed for clarity. All errors are removed for clarity. Refer to Appendix (15) for full suite of PT loci that have been used to constrain each P-T loop. Grouping to sub-domains is based only on the new EYCMP data and not data from literature. Appendix (17) contains analysis of 144 sub-domains with distinct P-T evolutions in spatially distinct regions, within a total of 37 domains across the whole Yilgarn Craton. Analysis west of the Ida Fault is not comprehensive. The map (Figure 133) outlines the location and labels of the sub-domains in the EYC; domain prefix has been removed from these labels for clarity. A table (GArecord_App17Tab_DomainAnal.xls) summarising the labelling of sub-domains and their generalized metamorphic conditions and evolutions, is contained in Appendix (17).

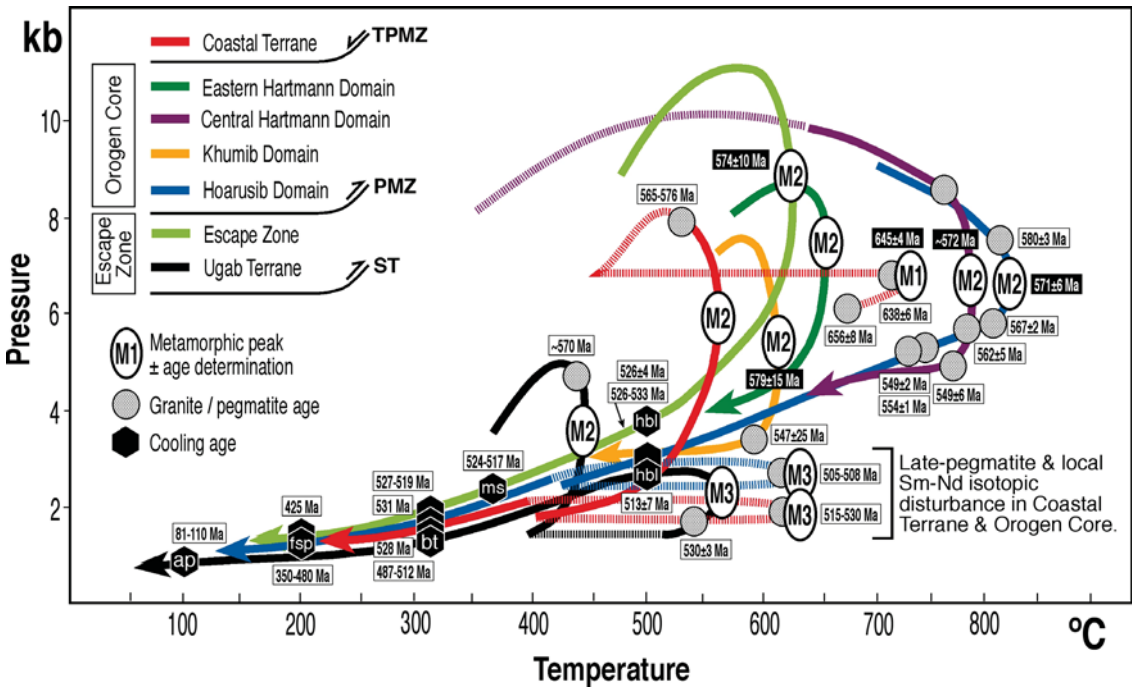

Figure 132: *Example of metamorphic domain analysis of a complex transpressional orogen (Kaoko Belt) composed of numerous distinct tectono-metamorphic domains (Goscombe et al., 2005b).*

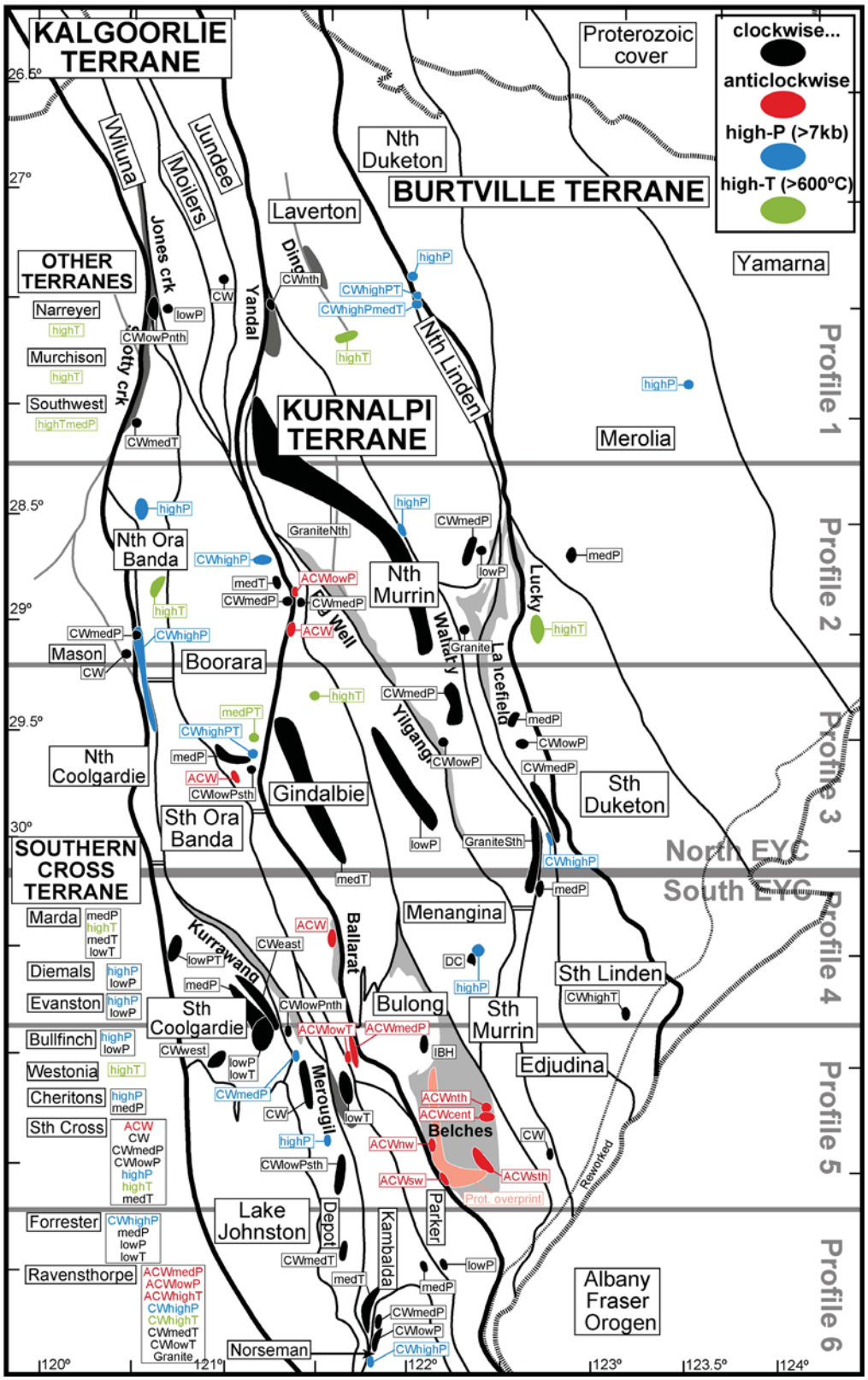

Figure 133: *Map summarizing the results of metamorphic domain analysis in the EYC. The small sub-domains represent the spatial distribution of distinct metamorphic PT conditions and P-T evolutions that are shared in common in these sub-domains.*

ASSIGNING METAMORPHIC EVENT

Interpretive assignment of the Metamorphic Event (i.e., M*a*, M1, M2, M3a, M3b) is made using the following method, constrained by salient characteristics listed in Table (9). Interpretive assignments have been made for all sites in the MDB. The key parameters in the MDB that are used to make these interpretive assignments are; metamorphic type, metamorphic facies, stratigraphic unit, P-T path and calculated peak metamorphic P and T.

Ma = Dry, static, granulite parageneses in metamorphosed dolerite-gabbro intrusives, constrained by T≥650ºC and P≤6.0kb.

M1 = High-P amphibolite and upper-amphibolite facies parageneses with clockwise P-T paths showing near isothermal decompression, constrained by T>600ºC and P>7.0kb.

M2 = Regional static and dynamic parageneses across a large P-T range and with clockwise P-T loops. Can only be directly constrained by contact parageneses associated with High-Ca granitoids.

M3a = Static, middle-amphibolite facies parageneses, constrained by anticlockwise P-T paths and being located in post-volcanic sedimentary basins.

M3b = Late-stage, retrogressive, alteration parageneses developed across a large P-T range.

Table 9: *Table on next page. Summary of the criteria used to assign metamorphic event. This matrix lists all the salient characteristics of each metamorphic event and has been used as the basis for assigning the interpretive metamorphic event in the MDB.*

Metamorphic Event*	Key Defining Constraints: P-T Path	Tpeak	Ppeak	Gpeak	Metamorphic Facies	Metamorphic Type	Stratigraphy	Granite	Additional Salient Characteristics: Strain	Tpeak timing	Fluid	Spatial Extent	Age Range#
Mseafloor					sub-greenschist greenschist	**seafloor**						evident in low-grade zones & odd bulk compositions	>2680
Ma	IBC±ACW?	**≥650°C**	**≤6.0kb**	high	**granulite** upper-amphibolite	**early contact**	**gabbro-dolerite intrusive**		static	Tpeak at Ppeak	fluid absent aH2O~0.25	very localized rare	>2680
Ma-M2?		<5.0kb	>630°C	>40°C/km	upper-amphibolite	**regional static** if upper-amphibolite							
M1	**CW-ITD**	**>600°C** >550°C if P>7.5kb	**>7.0kb** >6.0kb if T>650°C	low	**high-P amphibolite** upper-amphibolite				aligned granoblastic	Tpeak at Ppeak	±partial melt	localized major crustal structures	2720-2685
M1-M2?					**upper-amphibolite** middle-amphibolite								
Ma-M1-M2?					**upper-amphibolite**	**gneiss**	**SW Terrane** if granulite						
M2	tight CW	~350-710°C	~3.0-6.0kb	moderate	sub-greenschist greenschist amphibolite	**contact** regional static regional dynamic			static to dynamic heterogeneous	post-kinematic	H2O-CO2	widespread	2685-2666
M2?						**regional dynamic**							
M2?-granite						**intrusive**		**high-Ca HFSE granite** general granitoid					
M3a	**ACW** CW	500-580°C	3.0-5.0kb	moderate	lower-amphibolite upper-amphibolite	regional static regional dynamic	**post-volcanic basins**		low strain	post-S0//foliation	H2O	linear rifts	2666-2654
M3a?	**ACW**												
M3a?-granite						**intrusive**		**low-Ca, syenite, mafic granite**					
M3b	ACW?	150-600°C	1.0-4.0kb	high	sub-greenschist greenschist amphibolite	**alteration**			deformation & fault related	multiple post-peak parageneses	large fluid influx multiple fluids H2O-CO2-CH4-O2	multiple localized fault associated	2658-2620
M?-unassigned						**unassigned**							
M?-unmetamorphosed						**unmetamorphosed**							
Mprot	CW-ITD	650°C	8.0-kb		high-P amphibolite upper-amphibolite		**Albany-Fraser Margin**						
Mprot?		350-650°C?	3.0-8.0kb?		high-P amphibolite upper-amphibolite greenschist		**Reworked Yilgarn Margin**						

Bold text: Constraints used for interpretive metamorphic event assignment*.
Normal text: Salient characteristics of metamorphic events.
#Age Range in Ma: Interpreted age range of metamorphic parageneses by geological constraints, stratigraphic constraints, over-printing mineral parageneses, structure correlations, granitoid correlations and "relative" Lt-Hf garnet ages.

METAMORPHIC FIELD GRADIENTS

Six metamorphic field gradients across the EYC and the data used to constrain them. All reliable P, T and G data available, organized into 6 profile bands across the EYC with localities sorted by distance from the Ida Fault. Arbitrary distance scale is approximately 1 unit = 1.5 km. Profile lengths are based on the maximum width of each domain in each profile band. Only peak metamorphic T, P and G are used to plot metamorphic field gradients along the 6 profiles (Figure 134 to 139). The northern 3 profiles have been combined into a composite metamorphic field gradient for the north EYC (Figure 140) and the southern 3 for a composite south EYC field gradient (Figure 141). Locations of the six profile bands are outlined in (Figure 142). All errors have been removed from figures for clarity; error data is included in the table and typical ranges are ±25ºC, ±0.75kb and ±2ºC/km. These error ranges approximately correspond to the space between lines in the figures, for each parameter. Field gradients are based on the newly calculated EYCMP data. Data from literature have been ignored because pressures are typically unconstrained.

The metamorphic field gradients are not time equivalent, but have simply been fitted to all reliable PT loci available from each profile, including parageneses from M*a*, M1, M2 and M3a metamorphic events. In effect these field gradients show the variation in metamorphic parameters (PTG), of all ages, in E-W traverses across the current erosion surface. These field gradients show extreme variation in metamorphic parameters and also very steep gradients, i.e., rapid change in parameters with respect to distance travelled (i.e., ΔT/ΔX, ΔP/ΔX and ΔG/ΔX). Alteration and retrograde PT loci of the M3b event (coloured circles) are plotted separately from peak metamorphic data (coloured dots).

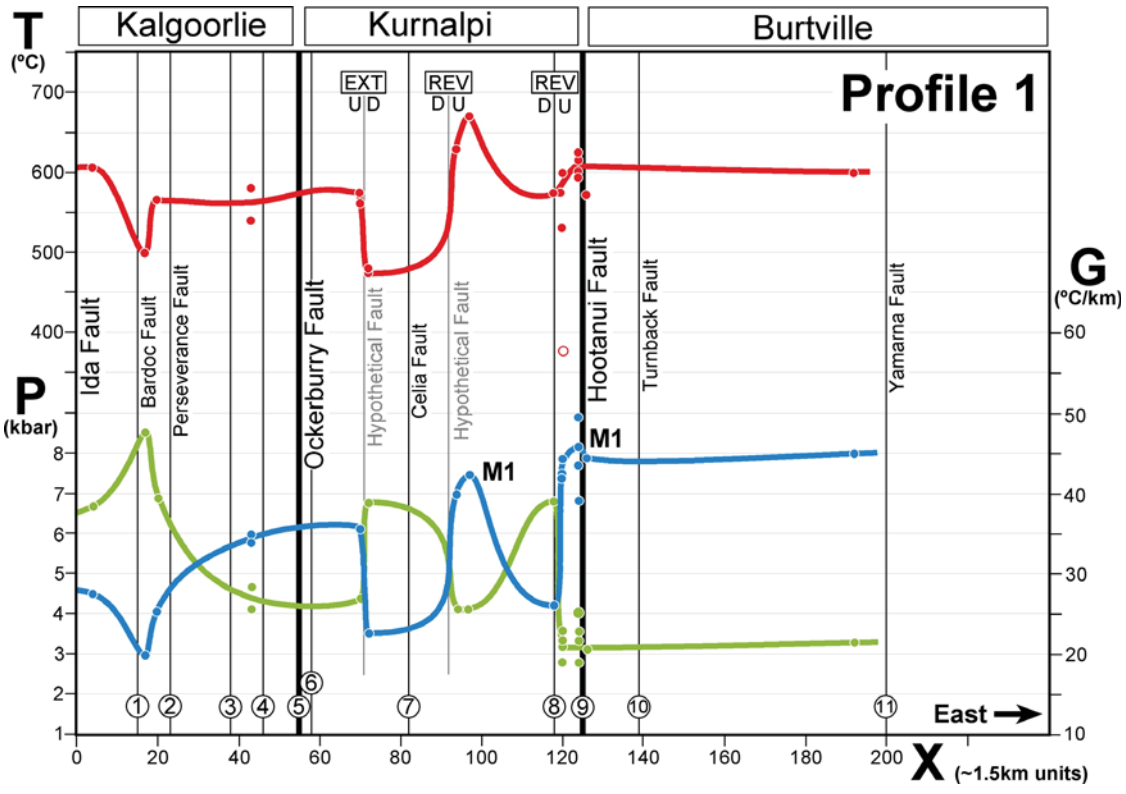

Figure 134: *Metamorphic field gradients for profile 1 (Figure 142) across the EYC.*

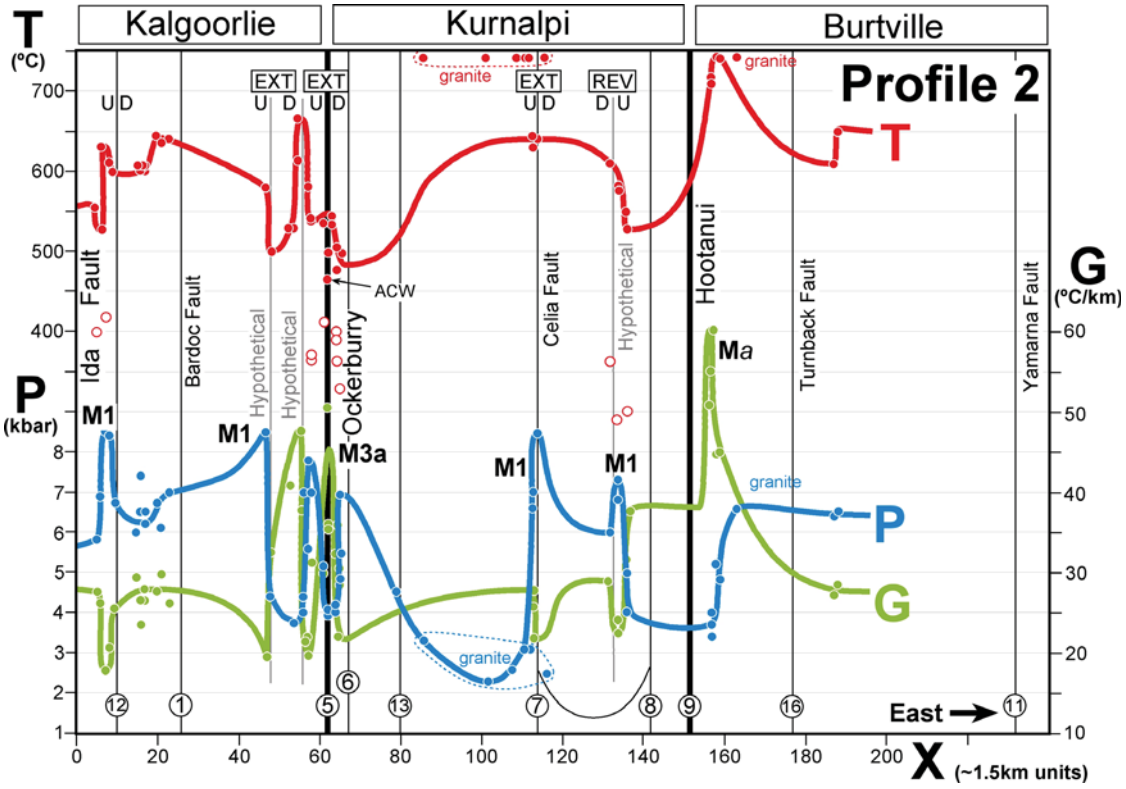

Figure 135: *Metamorphic field gradients for profile 2 (Figure 142) across the EYC.*

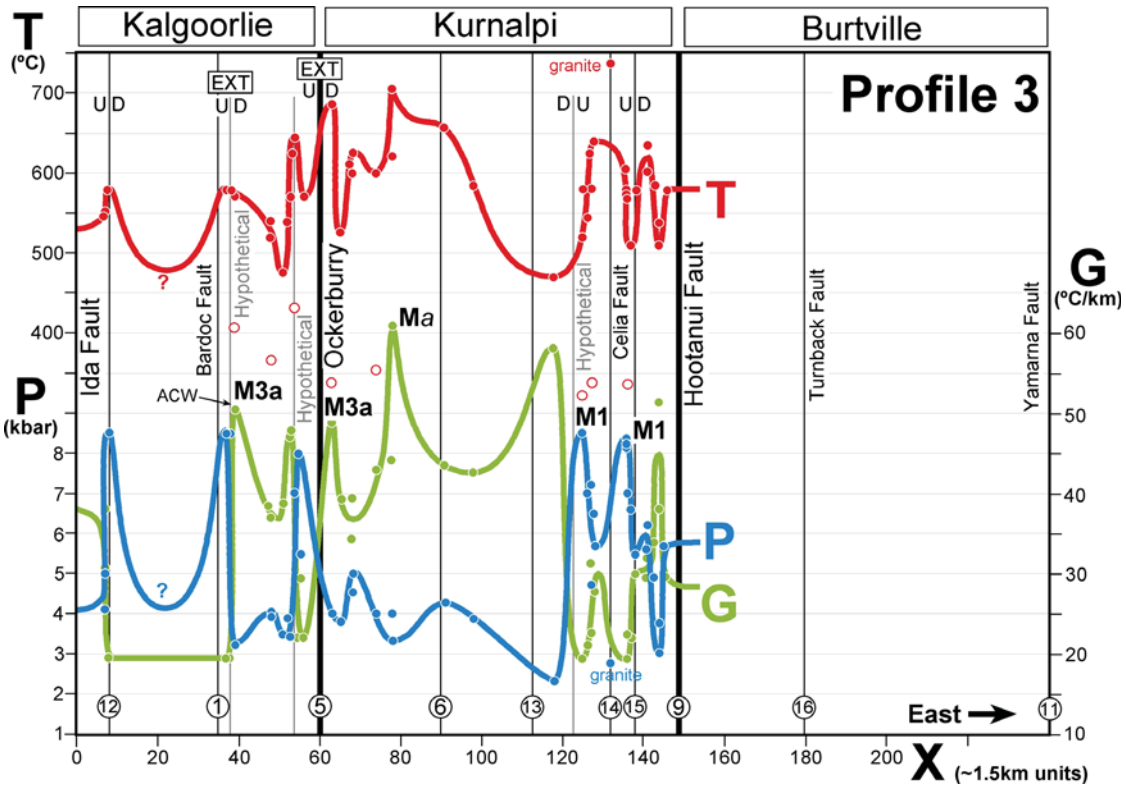

Figure 136: *Metamorphic field gradients for profile 3 (Figure 142) across the EYC.*

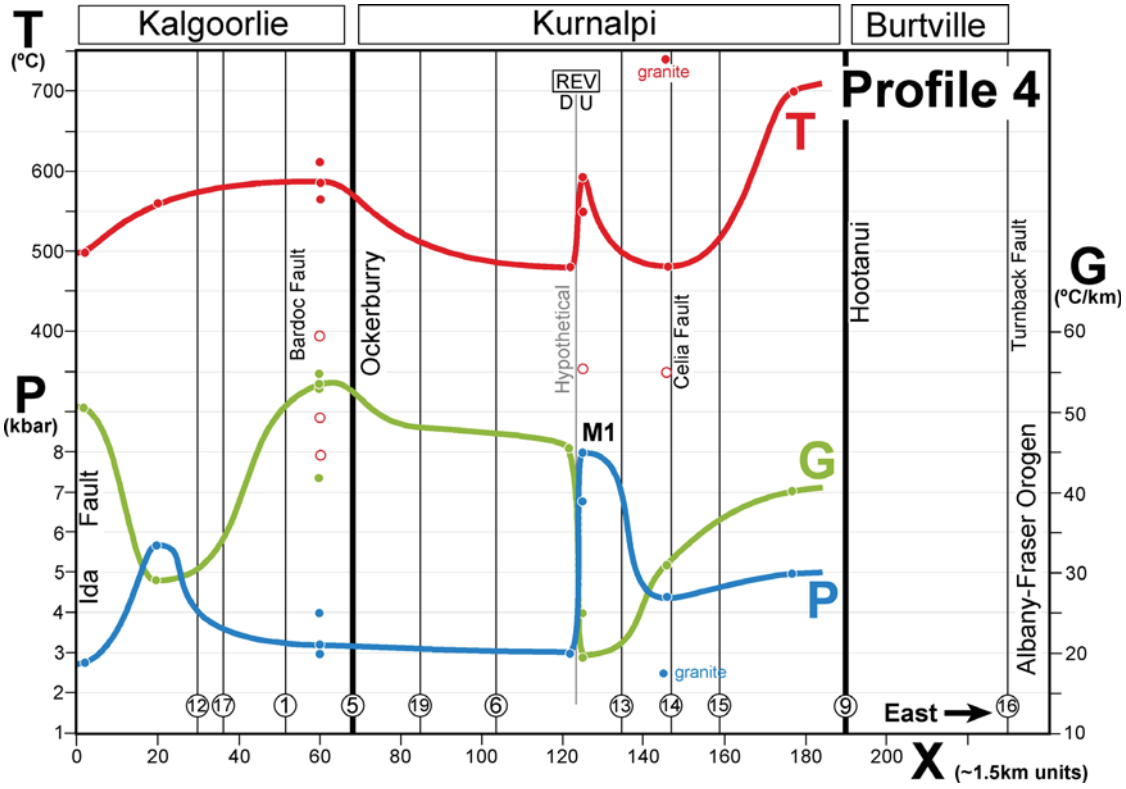

Figure 137: *Metamorphic field gradients for profile 4 (Figure 142) across the EYC.*

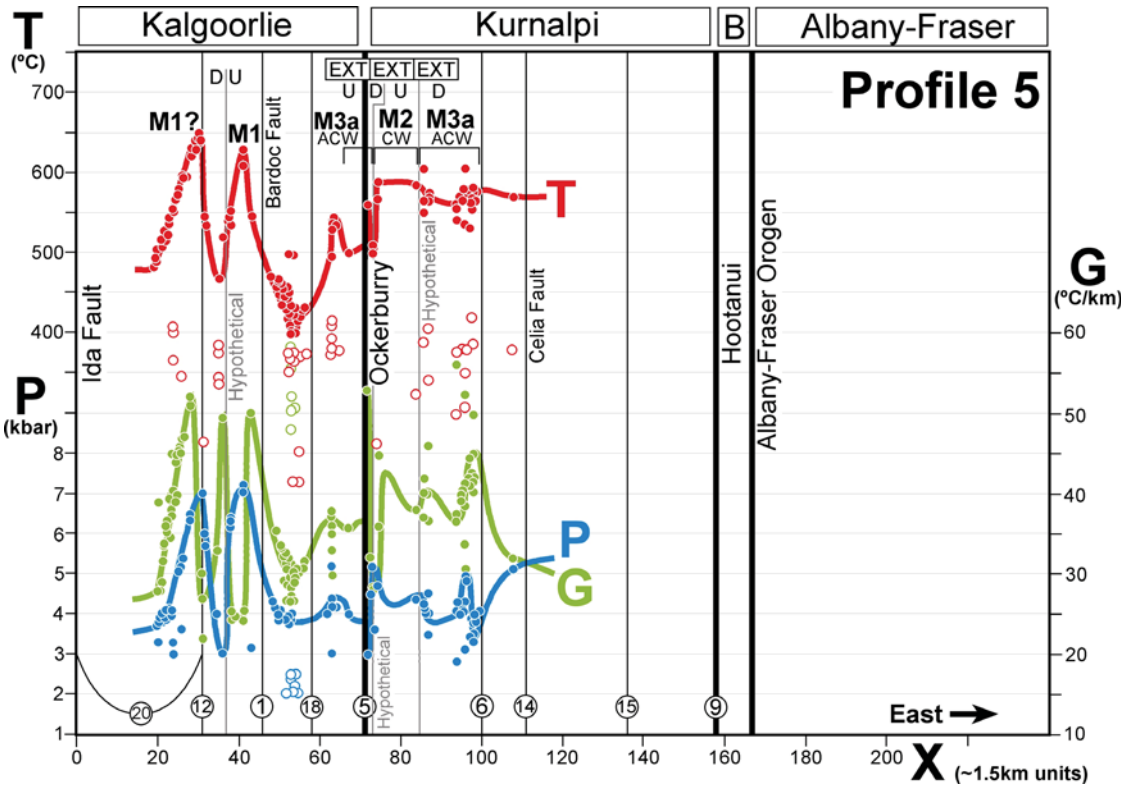

Figure 138: *Metamorphic field gradients for profile 5 (Figure 142) across the EYC.*

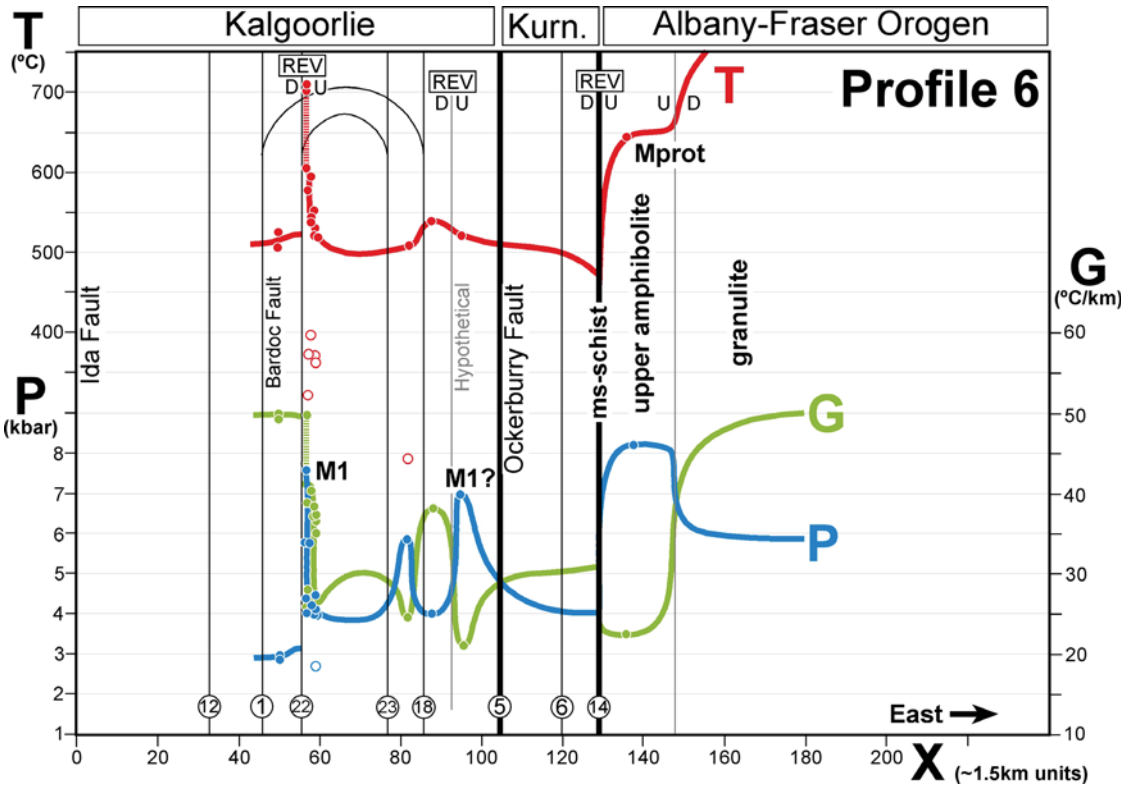

Figure 139: *Metamorphic field gradients for profile 6 (Figure 142) across the EYC.*

The metamorphic event can be inferred at certain points on the field gradient using the following criteria and are annotated on the metamorphic field gradient figures:

[1] M1 parageneses are indicated by high pressures (>7 kb), high temperatures (≥600 ºC) and low temperature/depth ratios (≤20 ºC/km).

[2] M3a parageneses are indicated by low pressures (3-5 kb), moderate temperatures (500-580 ºC) and high temperature/depth ratios (>40 ºC/km), in association with anticlockwise P-T paths and are sited on the down-thrown side of known or hypothetical extensional faults.

[3] M*a* parageneses are indicated by very high temperatures (>650 ºC), very high temperature/depth ratios (>50 ºC/km) and low pressures (<4 kb).

Hypothetical faults are inferred on the basis of metamorphic data alone, the structural and geological context is unknown and has not been considered in interpreting these hypothetical structures. In particular, steep pressure gradients that indicate juxtaposed different crustal levels, define the up-thrown and down-thrown blocks from pressures. An inference can also be made on whether a fault is extensional or reverse on the basis of the polarity and degree of change in P, T and G across the inferred fault. Figure 143 summarizes the possible suite of P, T and G field gradients that would be expected across extensional and reverse faults. Extensional faults can possibly by identified by higher temperatures on the down-thrown (upper-plate) block that has been extended and experienced a heat perturbation, possibly also with higher temperature/depth ratio than otherwise expect. Extensional structures are also evident by anticlockwise P-T paths in the upper-plate.

Note that the Ockerburry fault system appears to be extensional throughout its entire length and is possibly the main controlling extensional system during M3a lithospheric extension. Furthermore, most other inferred extensional structures, M3a parageneses and anticlockwise P-T paths occur in the vicinity of this structure, in a 40 km wide band that is mostly, but not only restricted to the upper-plate setting. Other hypothetical extensional structures and possible M3a parageneses occur in the central Boorara and central Murrin Domain (Figures 134 to 141).

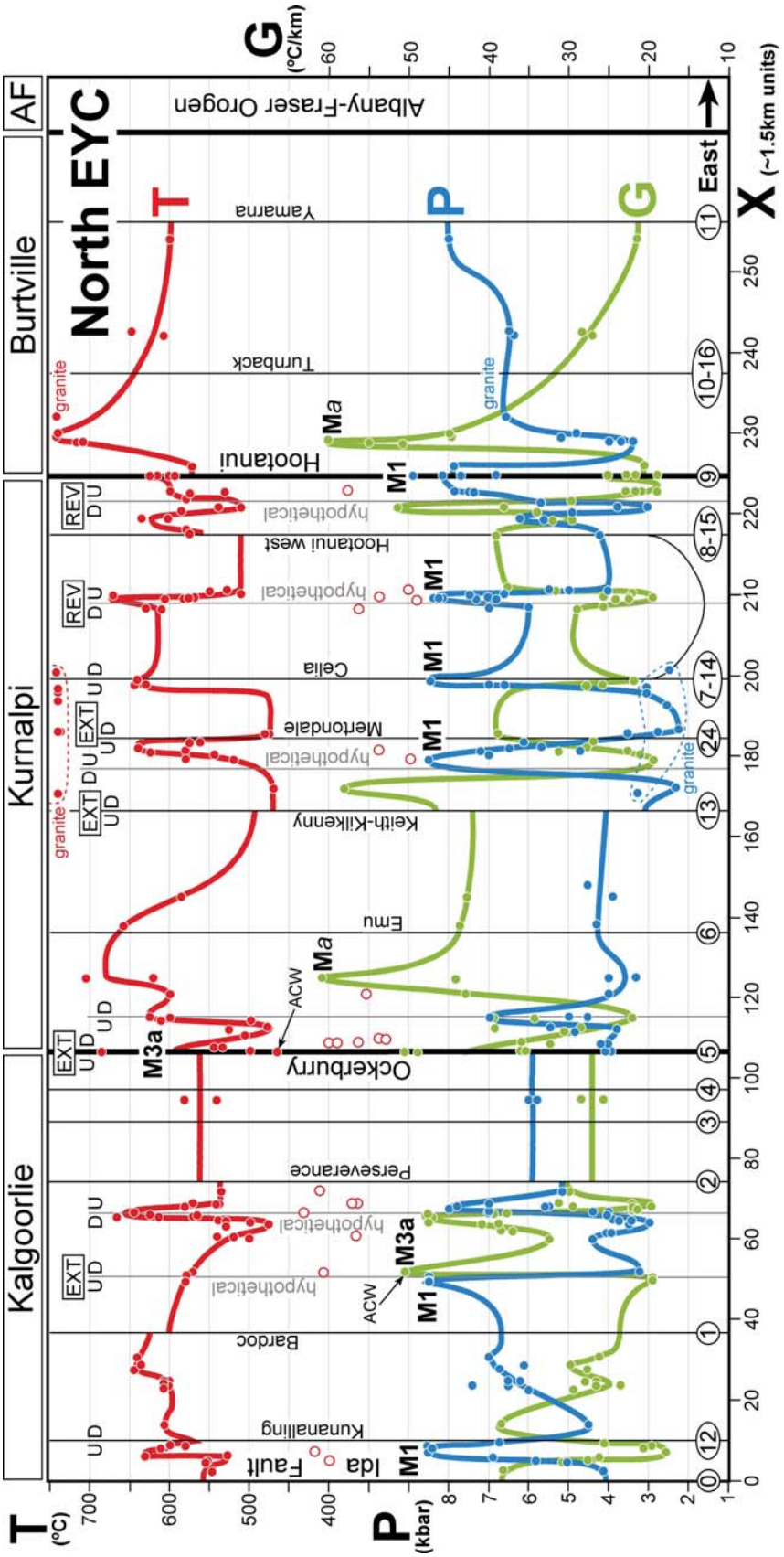

Figure 140: *Composite metamorphic field gradients across the northern EYC region.*

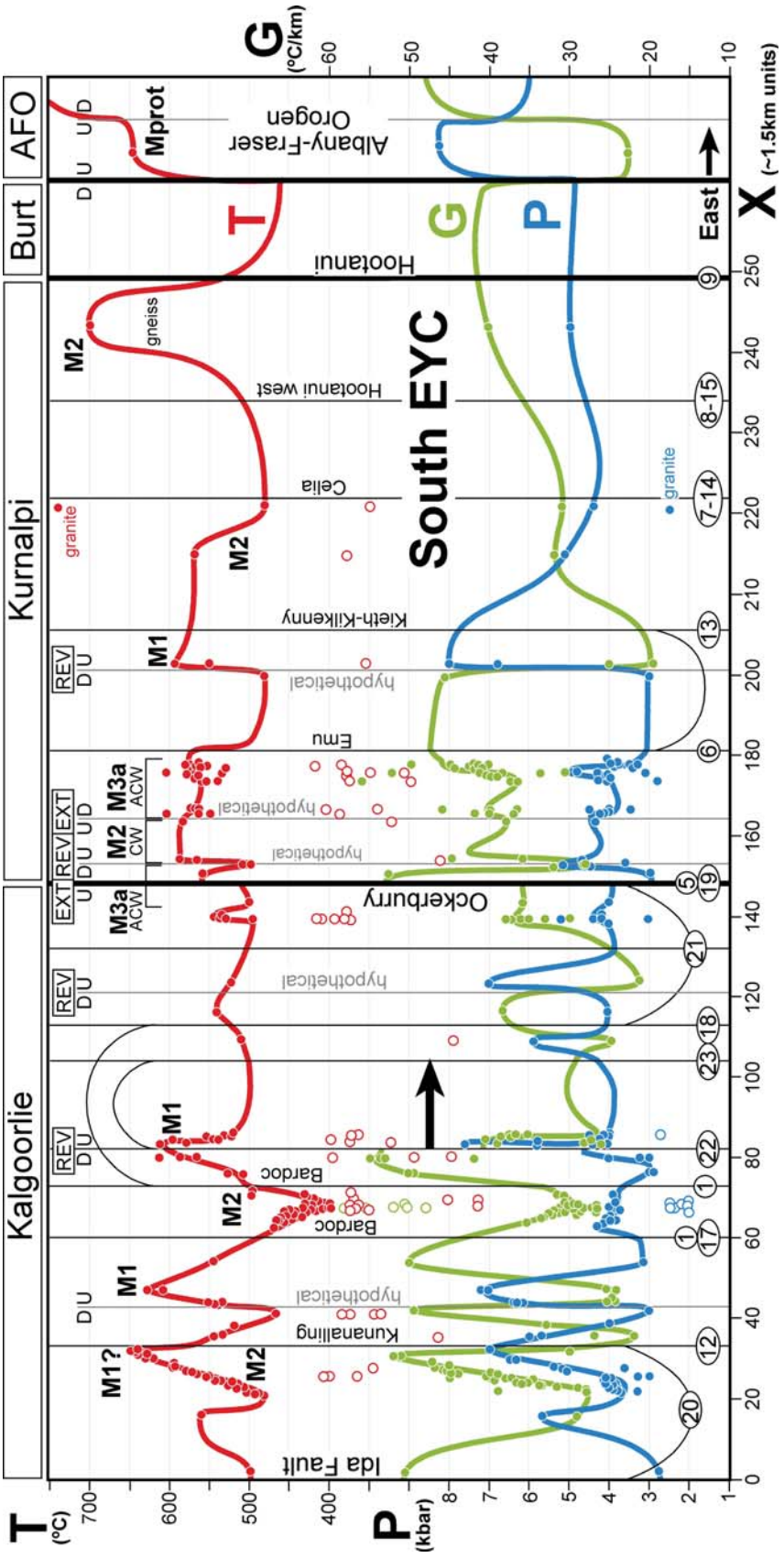

Figure 141: *Composite metamorphic field gradients across the southern EYC region.*

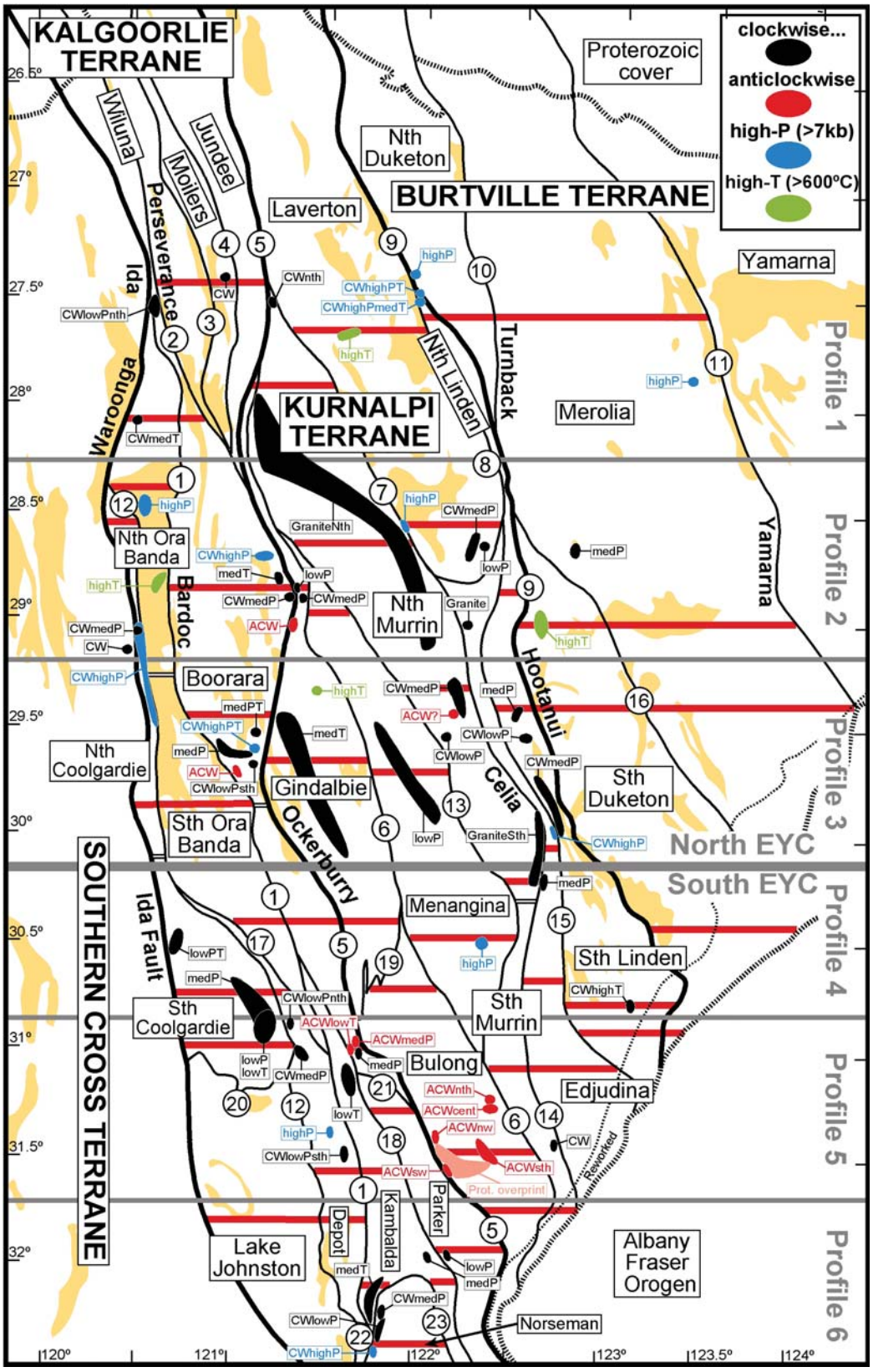

Figure 142: *Location of metamorphic field gradient profiles along the segmented red lines and drawing on data contained within the bands bounded by the grey lines.*

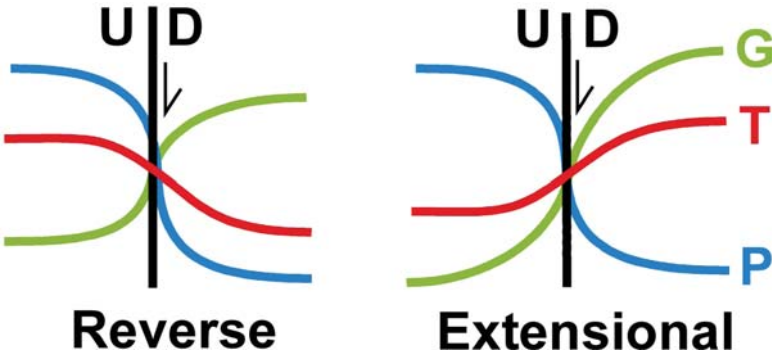

Figure 143: *Criteria for determining fault shear sense based on metamorphic field gradients.*

METAMORPHIC MAP PATTERNS

An attempt has been made to subdivide the composite metamorphic facies map of the EYC that encompasses all ages of metamorphic parageneses (Figure 30) into maps of the distribution of metamorphic parageneses for each metamorphic period (Goscombe and Blewett, 2009; Figures 144 to 146). In the absence of absolute age constraints from metamorphic parageneses, this undertaking is necessarily interpretive. Nevertheless, this can be done with some level of confidence because the different metamorphic periods experienced distinct metamorphic conditions, P-T evolutions and in some cases (M1 and M3a) formed in characteristic stratigraphic or tectonic settings. This has allowed a simple tentative assignment of peak metamorphic matrix parageneses at each site to the different metamorphic periods using criteria listed in Table (9) and discussed above. This classification process was initially made on the key metamorphic sites, for which quantitative PT data and P-T evolutions are available, resulting in the metamorphic domain analysis summarized in Figure 133. Because these metamorphic domains are constrained by robust metamorphic data, the age assignments are considered reliable and these domains serve as control points for the final interpretive maps (Figures 144 to 146).

Ma and M1 Metamorphic Patterns

The distribution of known M*a* granulite parageneses is simply the small cluster of outcrops at two widely separate localities in the Duketon and Gindalbie Domains (Hallberg, 1985; Figure 144). It is anticipated that more M*a* parageneses will be found in the vicinity of known magmatic arc complexes, such as at Welcome Well (Groenewald et al., 2006) and Yandal belt (Champion and Cassidy, 2007).

The possible maximum extent of M1 parageneses is defined by the distribution of high-grade peak metamorphic parageneses that formed at >600 ºC (Figure 144). The M1 metamorphic map is further constrained by localities with assemblages formed at pressures >6.0 kb. This is a minimum estimate of the extent of M1 because quantitative P-constraints are relatively rare for the size of the EYC, with only 480 localities distributed across 4,400 km^2. Nevertheless, the two end-member constraints on M1 distribution correlate well and indicate widely spaced elongate domains that are associated with major shear zone systems. The final detailed interpretive M1 map is published by GA (Goscombe and Blewett, 2009) and a draft version is contained in Appendix (2). In particular, M1 parageneses are associated with the Ida, Celia, north Hootanui, Laverton and Perseverance shear zones (Figure 144). Thin (<2 km wide), elongate and high-grade gneissic domains have been mapped previously in the Celia and Laverton shear zones, northern margin of the Gindalbie dome and southern margin of the Boorara dome (e.g., Hallberg, 1985; Swager, 1994c; Swager and Nelson, 1997). M1 parageneses also occur in arcuate to crescent shaped domains around the lateral termination of elongate granite-gneiss batholith domes, such as the Laverton, Gindalbie, Norseman and Boorara domes (Figure 144). Other more extensive high-grade domains with few high-pressured localities (>6 kb) indicate possible scattered M1 parageneses. These extensive and more problematical domains are at the southern extent of the Emu and Keith-Kilkenny shear zones and around the margin of the Lake Johnston Domain (Figure 144).

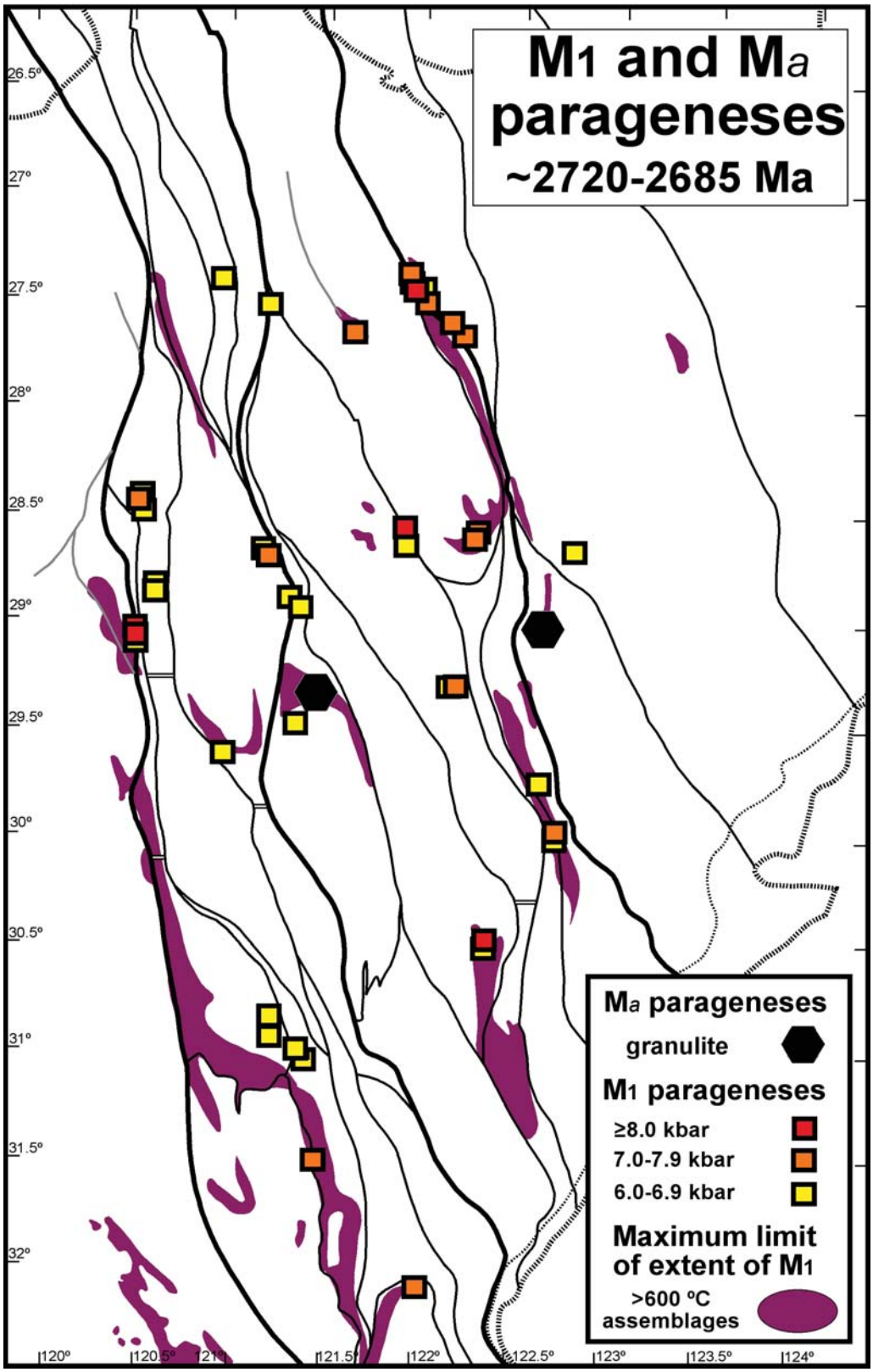

Figure 144: *Location of Ma granulites. Highly simplified distribution of possible M1 mineral parageneses based on high-T (>600ºC) and high-P (>6.0 kb) metamorphic conditions. See Appendix (2) and Goscombe and Blewett (2009) for the detailed interpretive map of M1 and Ma metamorphism.*

M2 Metamorphic Pattern

The distribution of M2 metamorphic conditions has been documented from literature (e.g., Binns et al., 1976; Mikucki and Roberts, 2003) and parameters in the MDB, by plotting metamorphic facies (Appendix 2; eycmp1_Meta_Facies.pdf), pressure-series (Appendix 2; eycmp1_DMF_Series.pdf), metamorphic event (Appendix 2; eycmp1_Meta_Event.pdf), quantitative PT conditions (Appendix 2; eycmp1_Peak_PTG.pdf) and diagnostic mineral assemblages and minerals (Appendix 2; eycmp1-Key-Alum.pdf, eycmp1-Key-Mafic.pdf, eycmp1-Key-Pelite.pdf, eycmp1-Key-Ultramafic.pdf). These many data sources and metamorphic parameters have been simplified into a composite map of peak metamorphic conditions, which has been modified to represent the distribution of M2 effects only (Figure 145). This highly simplified map suffices to illustrate the broad M2 metamorphic patterns. A detailed final version of the peak metamorphic map is available (Goscombe and Blewett, 2009; a draft version is in Appendix 2). The simple composite map is based on peak metamorphic parageneses from the M*a*, M1, M2 and M3a metamorphic periods. To generate the preliminary M2 map, Ma and M1 parageneses indicated by linear high-grade (>600 ºC) domains associated with major shear zones have been removed. The result is a composite M2-M3a metamorphic map. The localised M3a thermal overprint is of similar grade to the more widespread M2 parageneses, and consequently will not alter the M2 metamorphic map pattern appreciably.

The distribution of M2 metamorphic effects is widespread across all greenstones in the EYC. M2 metamorphism pre-dates all generations of post-volcanic clastic basins and Low-Ca granites, leaving these domains the only ones not recording M2 metamorphism. The extent of M2 metamorphic effects within the extensive granitoid domains cannot be accurately assessed. The granitic gneissic domains further extend the higher-grade M2 metamorphic domains. Otherwise, the majority of EYC granitoids are not obviously metamorphosed and so are interpreted to be broadly synchronous with M2 and do not pre-date the major M2 thermal anomaly. Granitic melts are typically 650-800 ºC when emplaced (Harrison et al., 2007). Consequently, the regions of High-Ca and other granites that pre-date the Low-Ca granites, in effect represent the highest-grade domains of the M2 thermal field.

Outside of the granitoids, M2 metamorphic patterns are characterized by broad, low-grade domains in the cores of large greenstone synforms, and show an increase in grade towards the granite batholiths (Figure 145). This metamorphic pattern is repeated throughout the EYC and has been confirmed by detailed metamorphic maps in sub-regions (Binns et al., 1976; Hallberg, 1985; Mikucki and Roberts, 2003). The main thermal lows are of lower greenschist and sub-greenschist facies conditions and are centred on Kalgoorlie, south Lake Cowan, east Lake Yindarlgooda, Lake Carey, Lake Violet, Wiluna, Thunderbox, Murrin Murrin and Granny Smith. M2 metamorphic isograds are broadly sub-parallel to the granite batholith margins and the lowest grade domains are most distal from the granites, indicating the close temporal and spatial association between M2 metamorphism and a coeval High-Ca granite bloom. Throughout most of the EYC, M2 isograds are also generally sub-parallel to major crustal structures. Some shear zones also correlate with significant changes in metamorphic grade and in effect represent isograds. Metamorphic variation across structures has been documented at the Ockerburry (Williams and Currie, 1993), Keith-Kilkenny (Williams and Whitaker, 1993), Kunanalling, Hootanui and Laverton shear zones (Figure 145). Elsewhere in the Kalgoorlie Region, the M2 metamorphic pattern shows isograds crossing major structures, indicating that the M2 thermal anomaly was long lived (Mikucki and Roberts, 2003). This pattern possibly also indicates that lateral displacement on these major structures may have been less than the resolution of the metamorphic mapping, as a result of strain being largely accommodated by shortening across these zones (see Rock Flow Regime section).

With M1 parageneses removed from the M2 metamorphic pattern, the remaining M2 regional parageneses show very little pressure variation. M2 pressures vary from ~3.0 kb in low-grade domains to ~4.5kb at the margin of granite-gneiss batholiths. This regional pressure gradient may be the result of post-M2 up doming of the granite-gneiss batholiths. Pressure increases in concert with temperature and indicates almost no variation in temperature/depth ratio (centred on ~38 ºC/km) from synforms to granite margins. This indicates a moderately elevated average thermal regime across the entire EYC during M2.

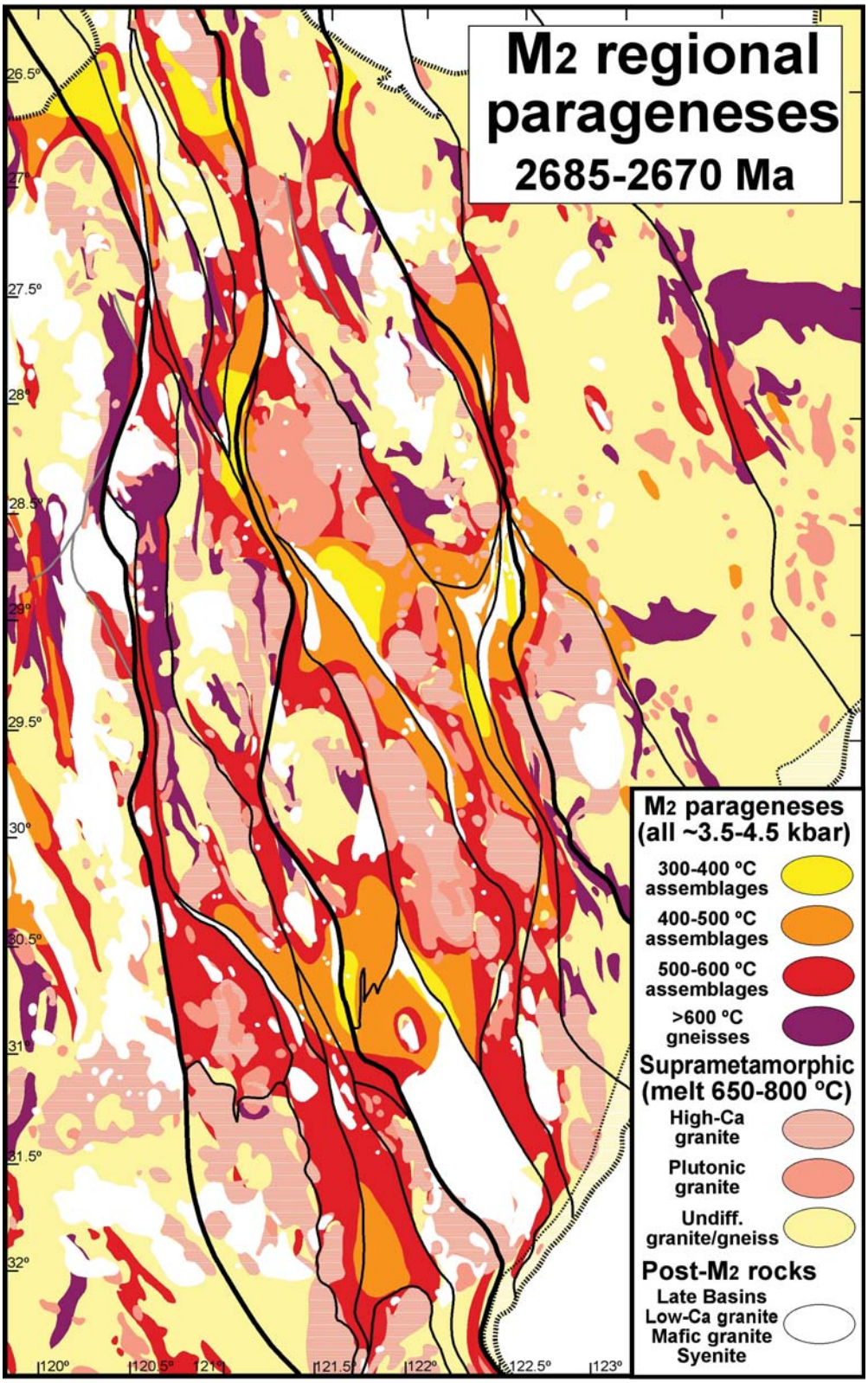

Figure 145: *Possible distribution of M2 metamorphism, based on 300-600ºC regional metamorphic parageneses at 3.5-4.0 kb, gneisses and granite gneisses and associated high-Ca and undifferentiated plutonic granites of ~2685-2670 Ma age. See Appendix (2) and Goscombe and Blewett (2009) for the detailed interpretive map of M2 metamorphism.*

M3a Metamorphic Pattern

The map of M3a thermal overprint (Figure 146) is very speculative and has been extended out from a limited number of control points by inference. M3a thermal overprint has been directly documented in the MDB from seven spaced localities along the Ockerburry shear zone and throughout the entire Mt Belches PVTB (Figure 133). M3a metamorphism occurs immediately after formation of all generations of post-volcanic clastic basins. All documented late basins have at least metamorphic biotite growth reported (Krapez et al., 2000; Blewett and Czarnota, 2005) indicating conditions >420 ºC. Consequently, it can be inferred that all late basins were metamorphosed during M3a and that the thermal foot print must extend beyond these erosional relicts to some degree (Figure 146). Additional M3a thermal footprints have been inferred on the basis of being upper-plate rift settings immediately adjacent to crustal-scale D3 extensional shear zones such as the Ida, Ockerburry and Hootanui shear zones and the extensional shear systems on the flanks of granite-gneiss domes (Blewett and Czarnota, 2005, 2007c). More tentative indicators of possible M3a thermal overprint are regions with high concentrations of the mantle-derived syenitic and mafic granitoids indicating extreme lithospheric thinning and high heat flow. The limit of M3a thermal anomalies are outlined to some degree by the exposure of old stratigraphy and/or exhumed mid-crustal rocks with M1 metamorphic parageneses >7 kb. Both the high-P rocks and old stratigraphy indicate zones of extreme exhumation of the lower-plate below extensional detachments. Other indicators of lower-plate settings are granite-gneiss domes, which also have a strong correlation with late-stage Low-Ca granites emplaced in their core (Figure 146). Lower-plate domal domains were exhumed during M3a extension and distal from the zone of maximum extension and high heat flow, which generally coincides with the upper-plate in asymmetric extensional settings (Buck et al., 1988; Issler et al., 1989; Ruppel, 1995). The final detailed interpretive M3a map is published by GA and a draft version is contained in Appendix (2).

M3b Alteration Distribution

The distribution of M3b alteration systems have been mapped out on the basis of indicators of hydrothermal alteration recorded at sites in the MDB (Appendix 2; eycmp1_Meta_Type.pdf). The distribution of documented alteration systems has been further sub-divided by temperature of alteration indicated by alteration facies (Appendix 2; eycmp1_Alt_facies.pdf) and by absolute PT calculations where available (Appendix 2; eycmp1_Alt_PTG.pdf). Similar alteration facies maps have been produced for the Kalgoorlie region (Witt, 1993a) and exploration company databases have no doubt produced alteration maps around individual mineral deposits. The distribution of alteration fluid composition is presented as maps of redox and pH conditions (Appendix 2; eycmp1_Redox_pH.jpg) and the dominant fluid species (i.e., H_2O, CO_2, CH_4), documented by fluid inclusions and alteration assemblages (Appendix 2; eycmp1_Fluid.pdf). All of these mapped alteration parameters show a highly patchy distributed pattern of different small-scale alteration systems. Nevertheless, the well known strong correlation between alteration systems and major shear zones is evident. Also of note is the close proximity and overlap of markedly different types and composition of alteration systems.

Figure 146: *Figure on next page. Inferred distribution of the effects of M3 lithospheric extension, and distribution of possible lower-plate domes (blue) versus upper-plate highly extended, high-heat flow domains (red). Flanks of lower-plate domes are indicated by exhumed old stratigraphy (hexagons) and high-P M1 parageneses (squares). Cores of lower-plate domes loosely coincide with low-Ca granites (green). Upper-plate domains of high extension coincide with by post-volcanic late basins (grey) and mafic and syenitic granites (dark blue) and define hypothetical zones of high M3 heat flow (red outline). See Appendix (2) and Goscombe and Blewett (2009) for the detailed interpretive map of M3a metamorphism.*

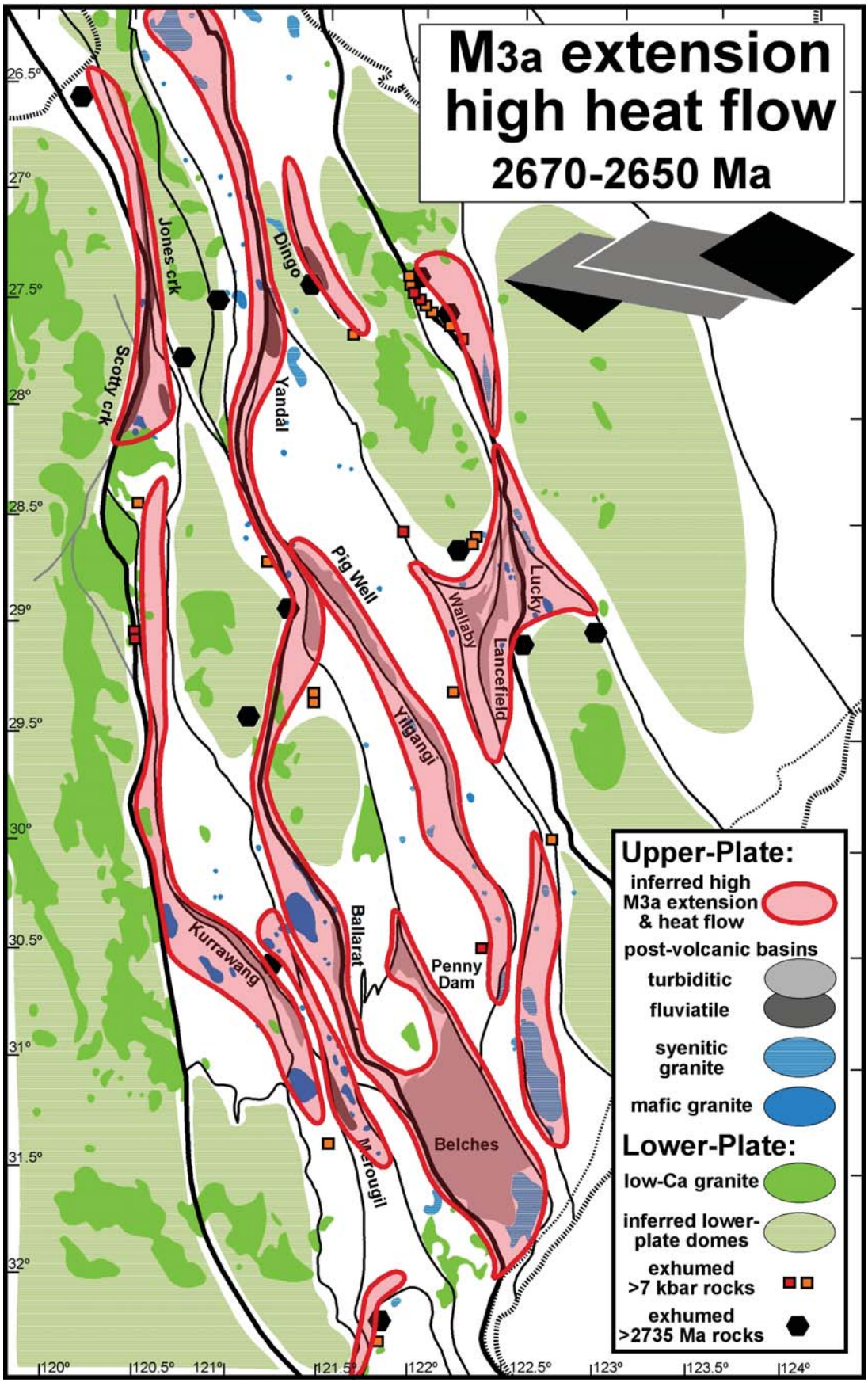
M3a extension
high heat flow
2670-2650 Ma
Jones crk
Scotty crk
Dingo
Yandal
Pig Well
Wallaby
Lancefield
Lucky
Yilgangi
Kurrawang
Ballarat
Penny Dam
Belches
Merougil
Upper-Plate:
inferred high M3a extension & heat flow
post-volcanic basins
turbiditic
fluviatile
syenitic granite
mafic granite
Lower-Plate:
low-Ca granite
inferred lower-plate domes
exhumed >7 kbar rocks
exhumed >2735 Ma rocks
26.5°
27°
27.5°
28°
28.5°
29°
29.5°
30°
30.5°
31°
31.5°
32°
120°
120.5°
121°
121.5°
122°
122.5°
123°
123.5°
124°

METAMORPHIC ARRAYS

Curvi-linear arrays were fitted to the population of calculated PT loci in each domain (Figure 147). These arrays represent the distribution of PT conditions in each Domain and Terrane (Figures 148 to 150). P versus T arrays are not necessarily time equivalent, but are simply fitted to all PT loci available from each domain, including parageneses from M*a*, M1, M2, M3a and M3b metamorphic events. Thus these are **time independent P versus T arrays**. All fitted P versus T arrays are contained in Appendix (18). These arrays are based on peak metamorphic and alteration conditions, secondary PT loci used to define P-T paths have not been included. The arrays are also primarily based on the new PT loci calculated for the EYCMP and literature datasets have only been used where little other data exists. The T versus G array of all calculated loci from the Yilgarn Craton is plotted in Figure 151. This T versus G array shows no trends or patterns but does well illustrates the range of depths in km's recorded by Yilgarn metamorphic rocks. The P versus G array of all calculated loci from the Yilgarn Craton is plotted in Figure 152. A very tightly constrained curvi-linear array has been fitted to this data, showing a non-linear decrease in temperature/depth ratio with increasing pressure.

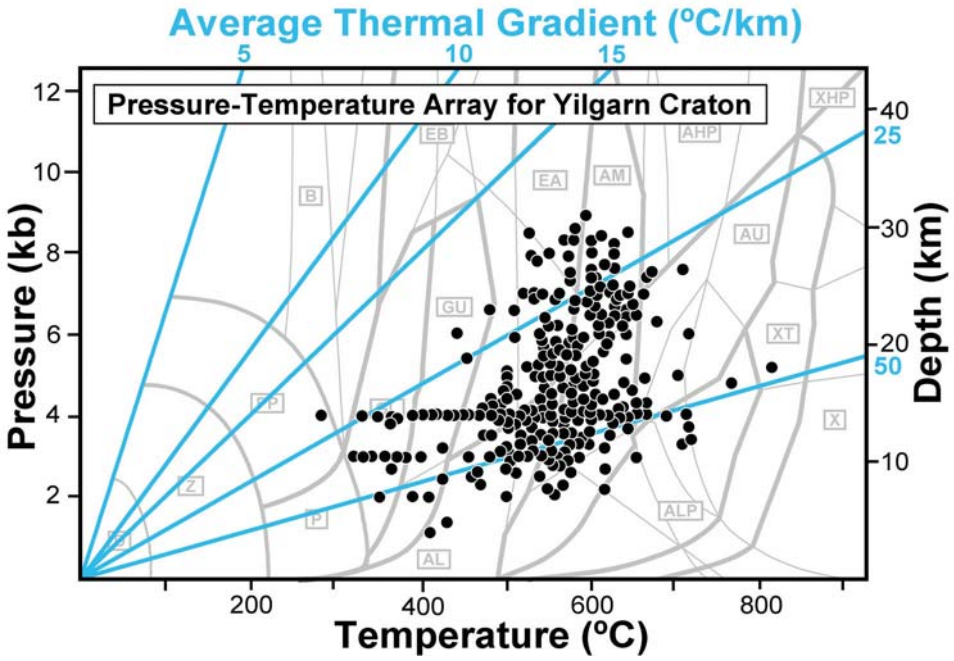

Figure 147: *All PT loci from the Yilgarn Craton that are used to constrain P versus T arrays. Note a significant number of legacy data with assumed 3.0 or 4.0 kb pressures.*

Almost all domains show P versus T arrays with characteristic J-curves showing much steeper slopes of increasing P with increasing T above 500-550 ºC than at lower temperatures. All Terranes with sufficient data (Southern Cross, Kalgoorlie and Kurnalpi) show very similar distributions of PT conditions and fitted time independent P versus T arrays (Figures 148 to 150). These P versus T arrays illustrate the two contrasted thermal regimes present in the Yilgarn Craton; regional and other parageneses with high temperature/depth ratio of 30-60 ºC/km and low temperature/depth ratio of 18-25 ºC/km in small domains within crustal-scale shear zones. These arrays show a thermally stratified crust with temperature/depth ratio higher at shallow crustal levels and lower temperature/depth ratio deeper in the crust (Figures 152, 153). Bearing in mind that the P versus T arrays are defined by PT loci that possibly span a significant period of time, there are three end-member processes that can give rise to this apparently stratified crust. Assuming the high- and low-P parageneses of M1 and M2 are nearly time equivalent and related in the same orogenic cycle, the thermal stratification would be real and related to high heat influx into the shallow crust by pooling volumous granites. Alternatively, if M1 and M2 metamorphic parageneses formed in temporally

distinct metamorphic events, stratification is apparent and the currently different thermal regimes occurred at different times and in different tectonic settings. A third alternative is that the two different thermal regimes occurred at the same time and in different settings within a larger tectonic setting, defining a paired orogenic system. In all of these scenarios the observation remains that over the span of time that is the EYC orogenic cycle, the crust was thermally stratified for most of that time with the highest thermal regimes recorded in the upper crust from Ma-M2-M3a-M3b and all rocks available from deeper crustal levels (M1), show much lower thermal regimes.

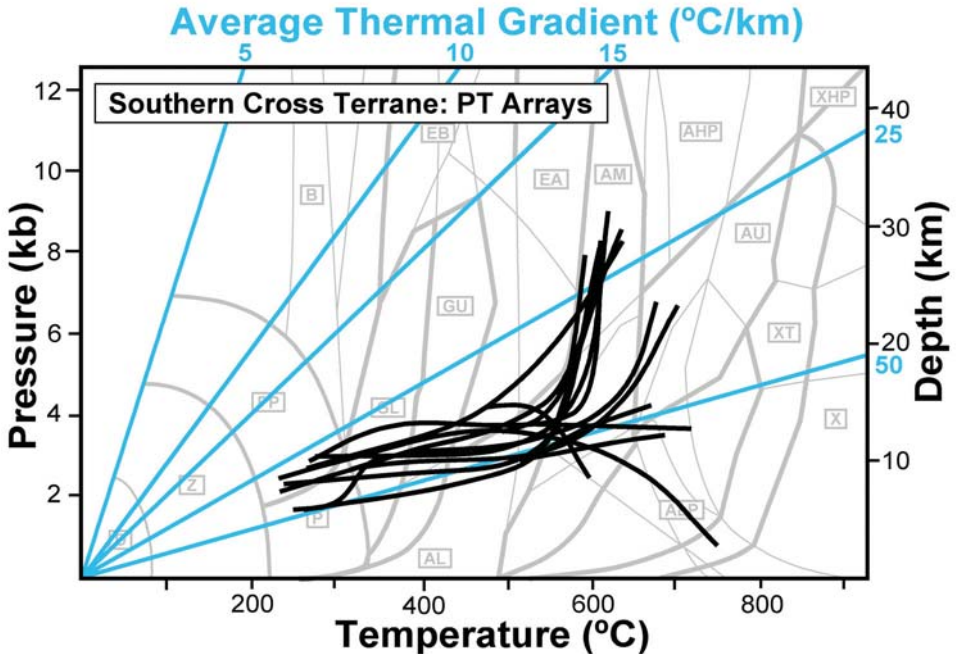

Figure 148: *Black lines are P versus T arrays fitted to the PT calculations from different domains within the Southern Cross Terrane.*

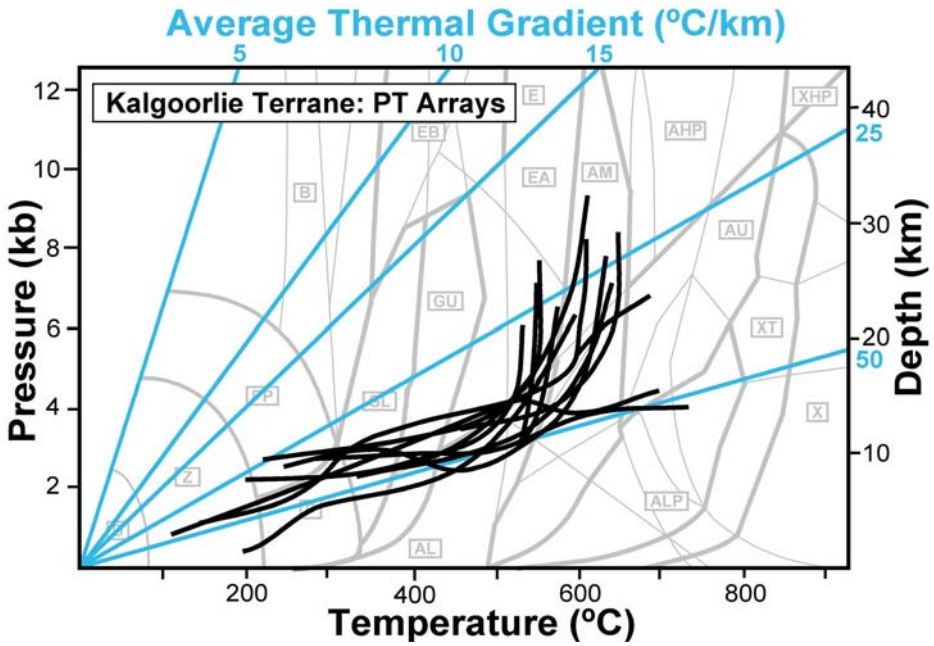

Figure 149: *Black lines are P versus T arrays fitted to the PT calculations from different domains within the Kalgoorlie Terrane.*

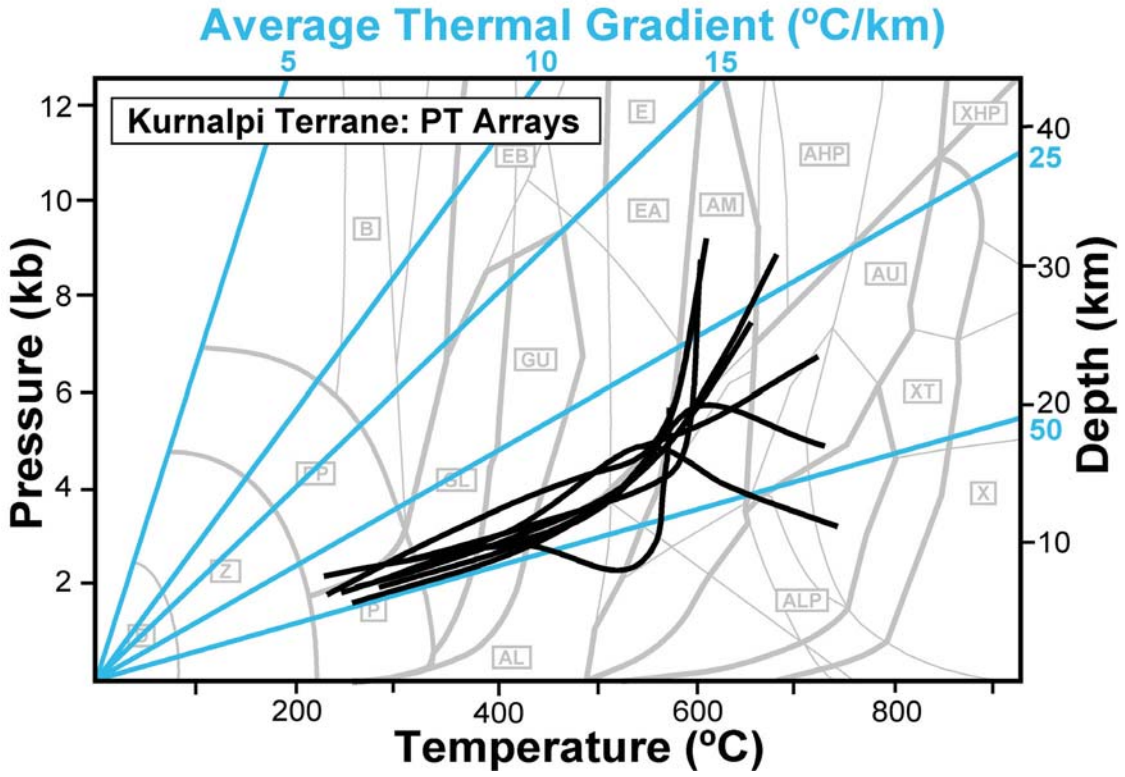

Figure 150: *Black lines are P versus T arrays fitted to the PT calculations from different domains within the Kurnalpi Terrane.*

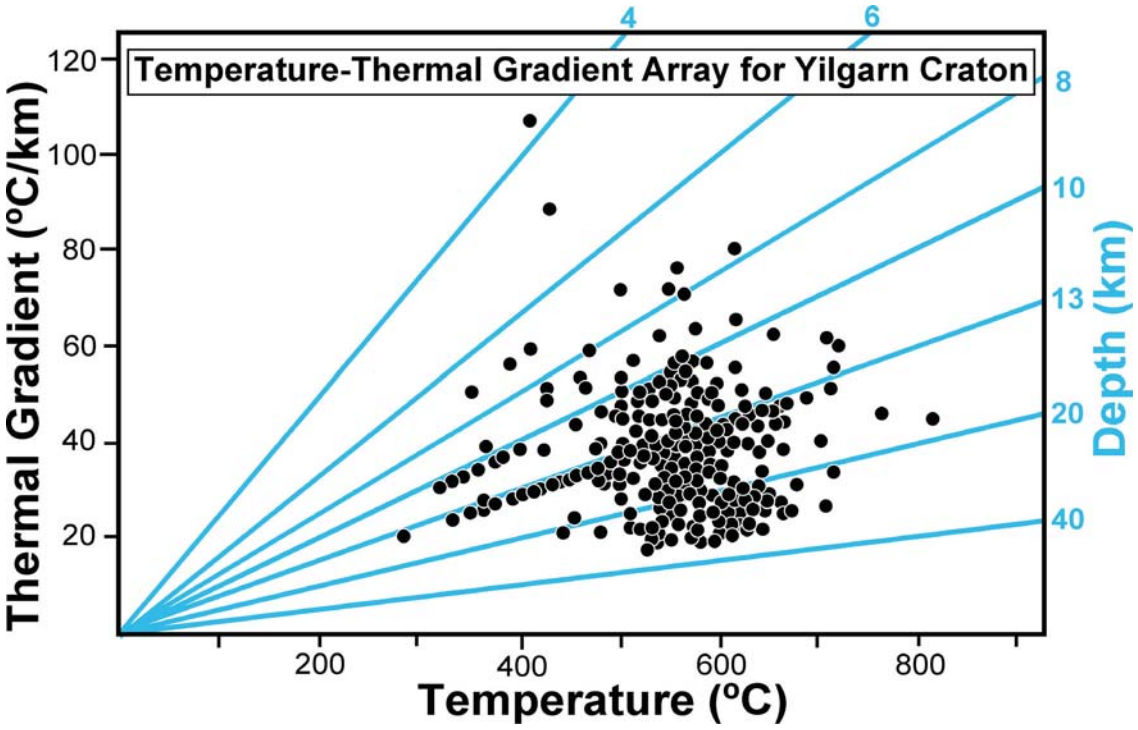

Figure 151: *All TG loci from the Yilgarn Craton. Note a significant number of legacy data with assumed 3.0 or 4.0 kb pressures.*

Both high-P garnet ± clinopyroxene upper amphibolite and epidote amphibolite samples define the relatively low temperature/depth ratio conditions at depth. These two rock groups define apparently nested J-curve arrays across a range of temperatures (Figures 149, 150). There is currently insufficient age data to test if the shapes of these time independent P versus T arrays are real or artefacts. With sufficient age constraints from both epidote amphibolite and high-P upper amphibolite parageneses, it may be possible to fit peak metamorphic data from the Yilgarn Craton to two independent, **time dependent P versus T arrays** (Figure 154). One monotonic array fitted to all the higher-P parageneses (M1) if they all prove sufficiently older than other Yilgarn parageneses. A second younger and also monotonic P versus T array would be fitted to the remaining low-P, high-G regional parageneses (M2-M3a). If age data does show two monotonic time dependent P versus T arrays in preference to the time independent J-curves, this will also support evidence for a thermally stratified crust. The spread between epidote- and upper-amphibolite high-P conditions would affirm low temperature/depth ratio conditions where widespread at depths > 6 kb and not restricted to areas where they currently outcrop. Furthermore, because these deep rocks have not been re-equilibrated at high temperature/depth ratio conditions, they show that the later high thermal gradient conditions were restricted to the upper crust where the volumous granite was pooling and not throughout the entire crustal column. Consequently, in the absence of age data constraints, the two most plausible scenarios indicate a thermally stratified crust showing different thermal regimes in the upper- and middle-crust.

The only plausible scenario that does not involve a thermally stratified crust must show that low thermal gradient conditions were not widespread at depth. The current exposure of M1 high-P /low-G rocks is restricted to small sub-domains within crustal-scale shear zones. Superficially, this restricted distribution suggests low thermal regimes formed in very specific settings within the Yilgarn Craton. For example in discrete zones with high advection rates leading to low-G conditions, such as zones showing “subduction” or down-advection transport of material. Possible settings may be shallow relatively slow subduction zones or down advection in keels at the margin of diapirs. There are currently insufficient constraints to assert that M1 parageneses were spatially restricted at formation and to speculate further on possible tectonic scenarios. It is equally plausible that the currently exposed restricted distribution of M1 parageneses represents the relatively rare and ad hoc sampling of the middle crust by later structural events, such as M2 up thrusting and M3a extensional detachments.

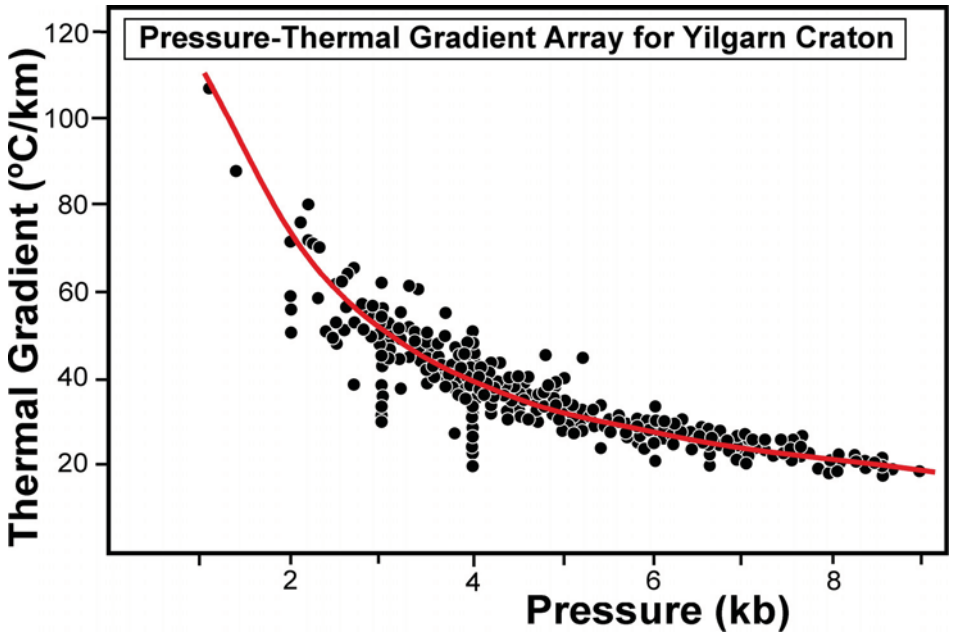

Figure 152: *P versus G array fitted to all PG loci from the Yilgarn Craton. Note a significant number of legacy data with assumed 3.0 or 4.0 kb pressures.*

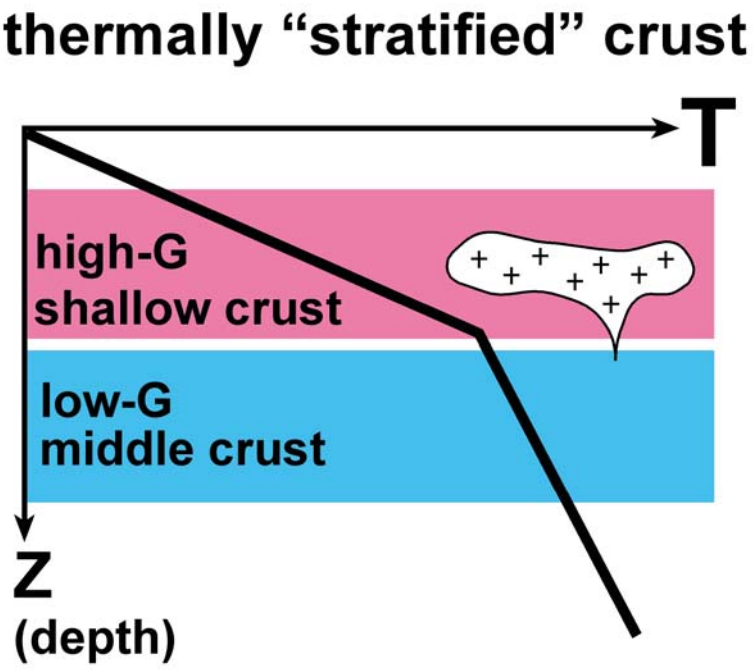

Figure 153: *Diagram illustrating the thermal gradient through a thermally stratified crust. : Model for regional M2 metamorphism involving a thermally stratified crust due to input of heat into shallow crustal levels by large volumes of granite. Note the change in slope of the crustal temperature gradient indicates different thermal regimes or average thermal gradient, which is highest in the shallow crust. Change in slope is at approximately 4.5 kb in the EGST and 3.5 kb in the Southern Cross Terrane.*

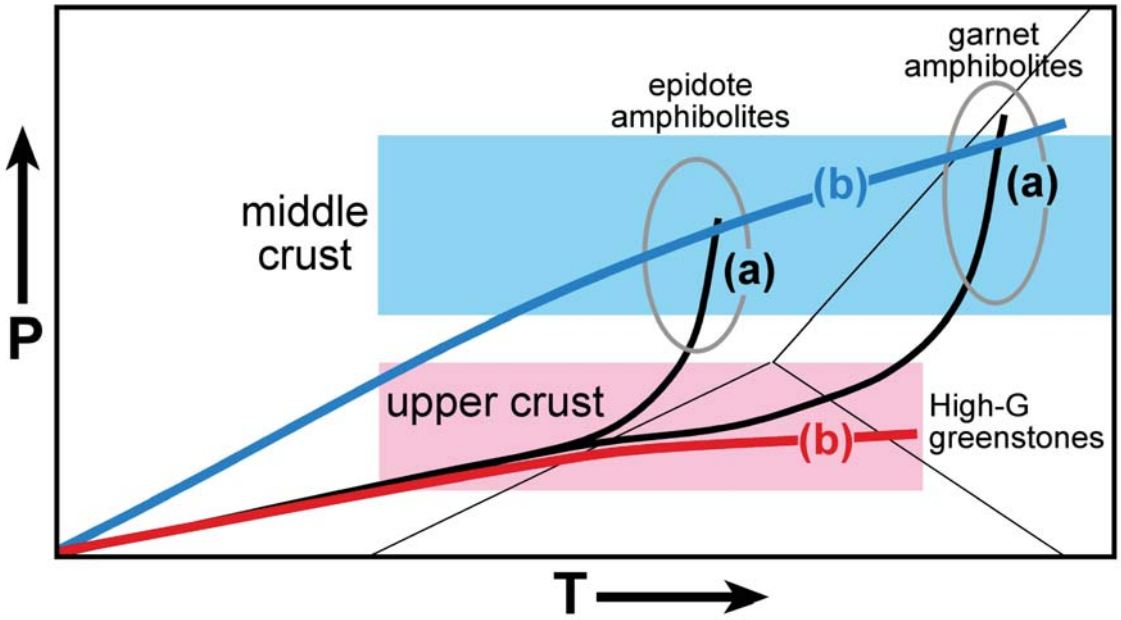

Figure 154: *Alternative hypotheses for P versus T arrays in the EYC. (a) J-curves linking high-G and low-G mineral parageneses, with the implication that they are the same age. (b) Preferred hypothesis of high-G and low-G parageneses on separate P versus T arrays of high-G shallow crust with voluminous granites, and low-G middle–crust. Both of the two arrays labelled (b) may be either the same age implying a thermally stratified crust, or alternatively represent two metamorphic events of different age.*

INTEGRATION OF METAMORPHIC AND STRUCTURAL DATASETS

Metamorphic data for the EYC has been integrated with other geological datasets (i.e., geochronology, structure, intrusives, stratigraphy, geodynamics) in four different ways.

Temporal Integration

Metamorphic data have been temporally integrated using **evolution curves**, which document the evolution in individual metamorphic parameters (P, T and G) with time (Figure 155). These evolution curves have been correlated with stratigraphy, magmatic evolution, deformation events, Au-mineralization and interpreted geodynamic settings (Figures 11, 155).

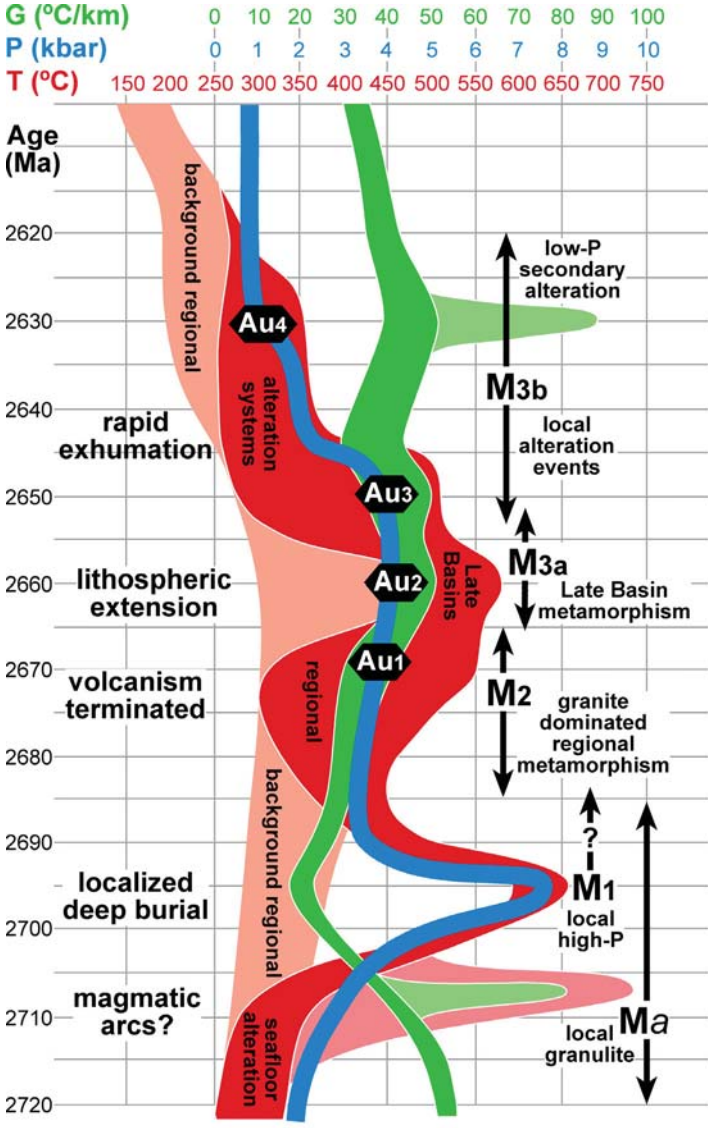

Figure 155: *Evolution curves for the fundamental metamorphic parameters temperature (T), pressure or crustal depth (P) and temperature/depth ratio or thermal regime (G). The curves illustrate change in these variables at the current exposure level for the span of EYC geological history. Curves are for a hypothetical composite of the EYC that experienced all regionally extensive metamorphic events and most localized events. Note that M3a in post-volcanic late basins and M1 high-P metamorphic events are localized to some degree. Evolution curves do not track a single real location. Stripped bands highlight very localized metamorphic events and pale shading represents the ambient regional metamorphic conditions at the time that more local metamorphic pulses are also operating. There may be multiple Ma and M1 metamorphic events and the M3b period experienced many alteration events in different places.*

Spatial Integration

Metamorphic data have been spatially integrated using **metamorphic field gradients**, which document the variation in metamorphic parameters ($\Delta T/\Delta x$, $\Delta P/\Delta x$, $\Delta G/\Delta x$) along profiles across the EYC (Figures 134 to 141, 156).

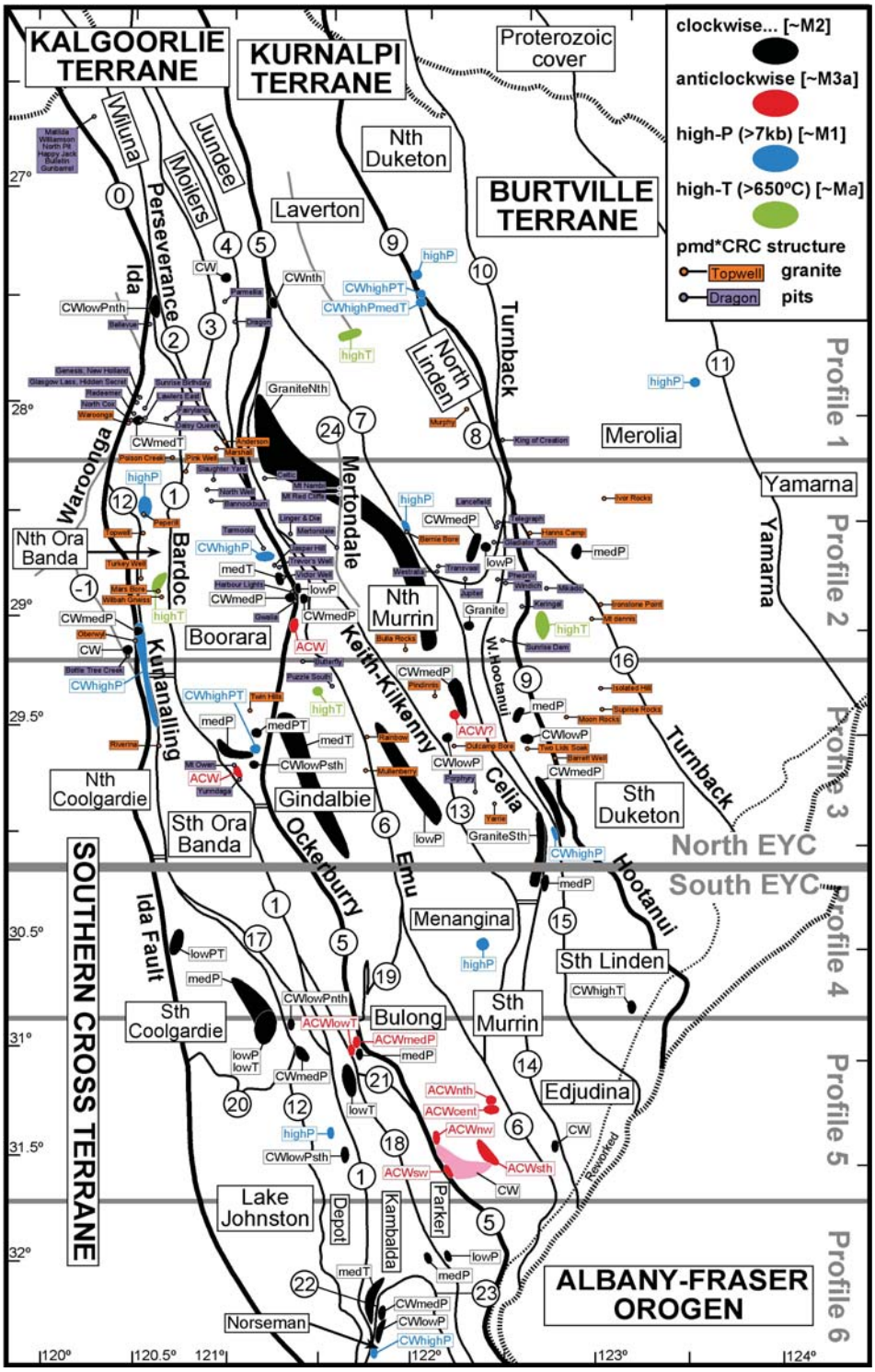

Figure 156: *Correlation between* ***pmd****CRC structural sites (Blewett and Czarnota, 2007c) and metamorphic domain analysis sites.*

Temporal and Spatial Integration

Metamorphic data have been temporally and spatially integrated by linking metamorphic evolutions (i.e., P-T-t paths), either with metamorphic field gradients (Figures 157, 158) or with the mapped distribution of distinct metamorphic domains (Figures 159 to 161). All available metamorphic evolution paths have been linked with the location of specific metamorphic domains sharing the same metamorphic evolution and PT conditions. These linkages have been classified for the different metamorphic periods: M*a* and M1 (Figure 159), M2 (Figure 160) and M3a (Figure 161).

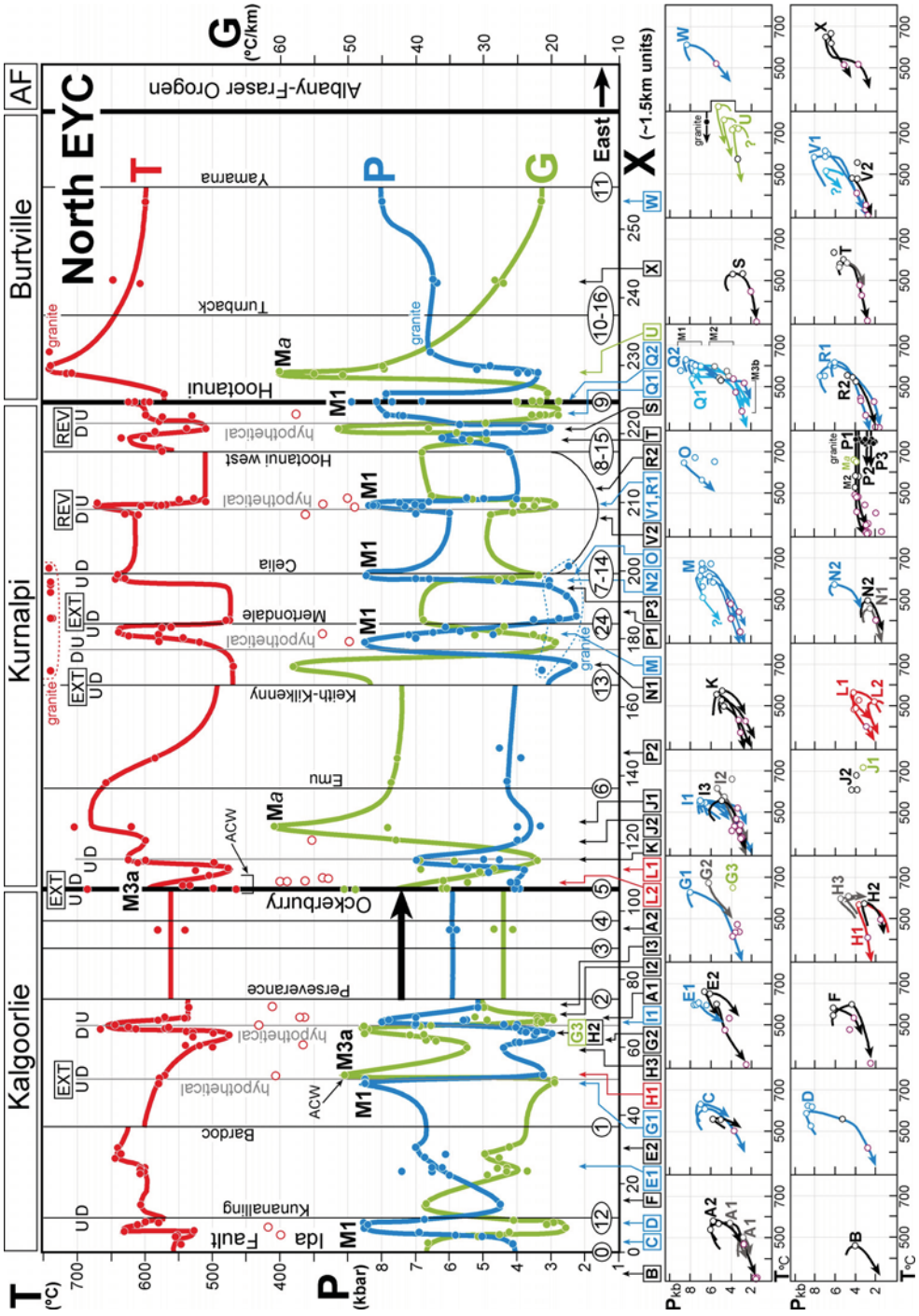

Figure 157: *Integration of the composite metamorphic field gradients for the northern EYC (Figure 140), with P-T loops at specific sites along this profile.*

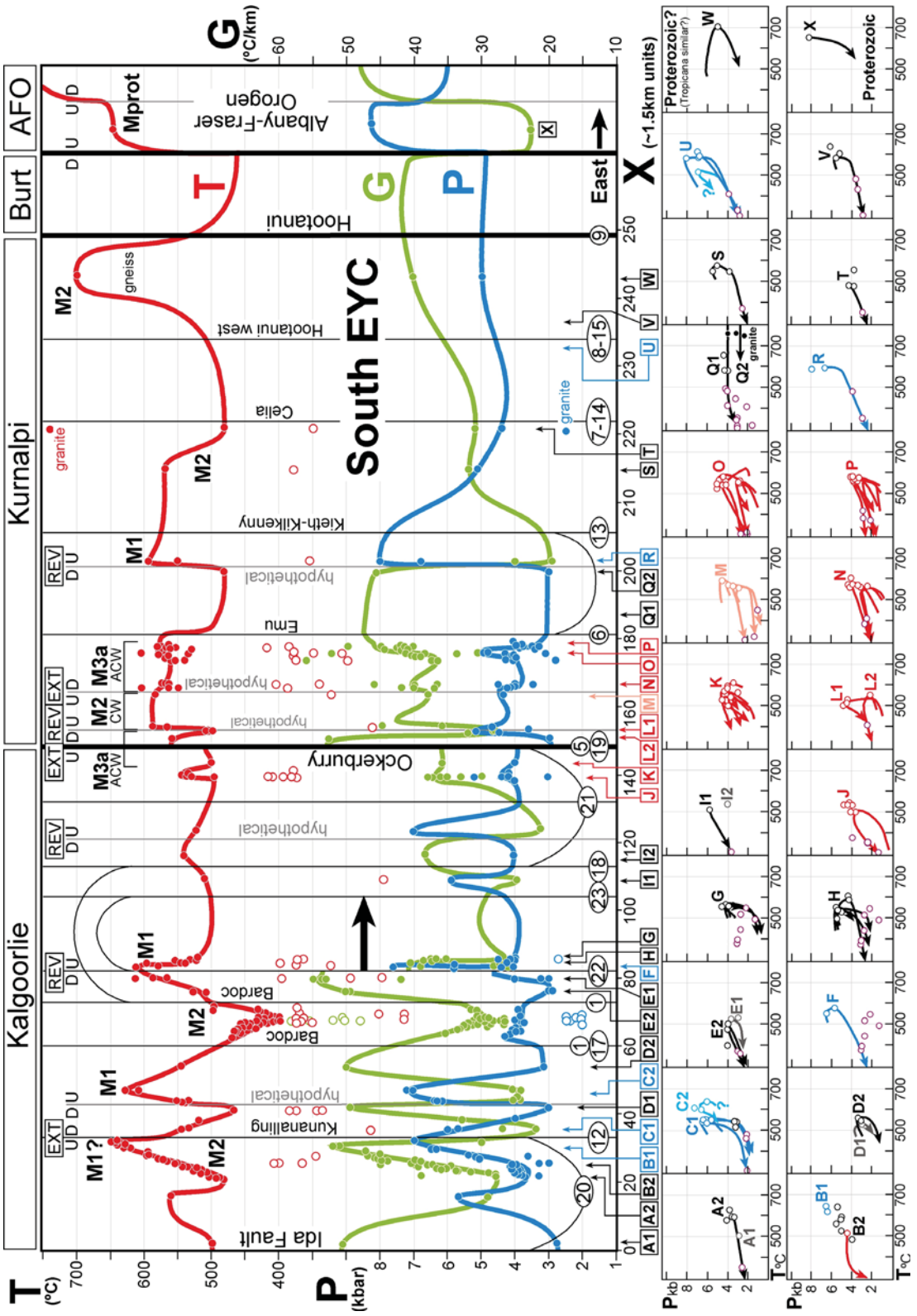

Figure 158: *Integration of the composite metamorphic field gradients for the southern EYC (Figure 141), with P-T loops at specific sites along this profile.*

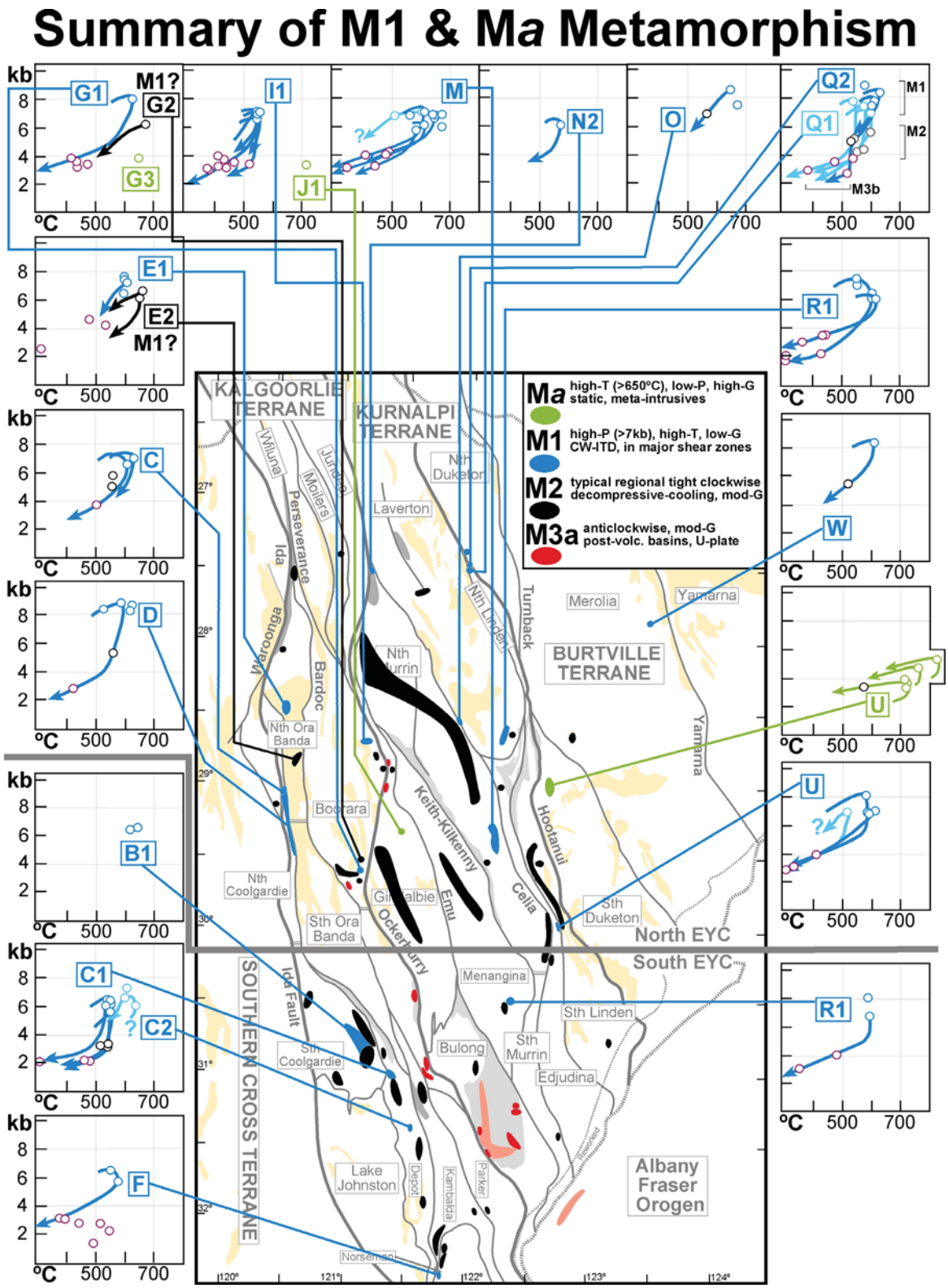

Figure 159: *Integration of the interpreted Ma and M1 P-T evolutions with the results of metamorphic domain analysis outlining regions that experienced common metamorphic histories.*

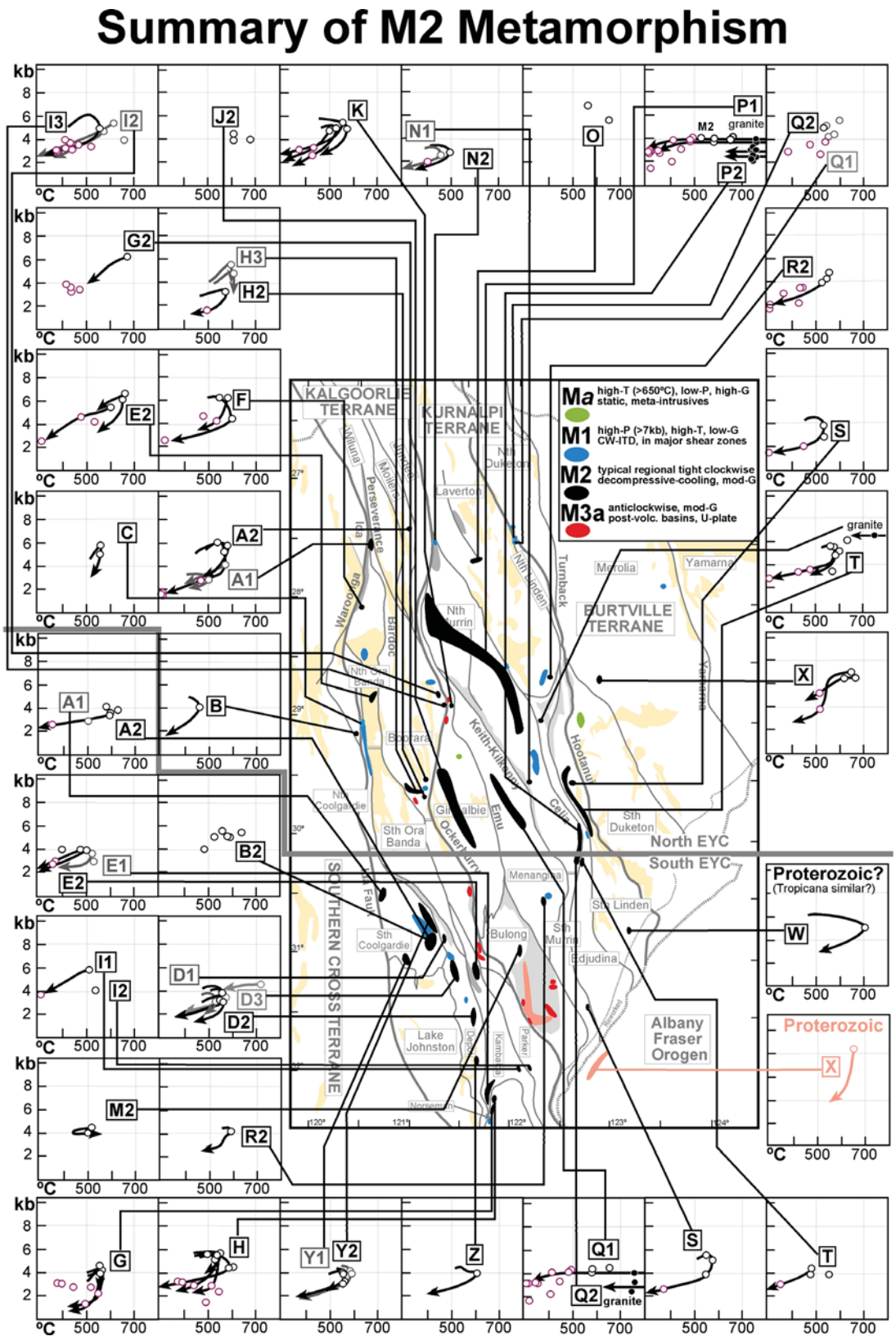

Figure 160: *Integration of the interpreted M2 P-T evolutions with the results of metamorphic domain analysis outlining regions that experienced common metamorphic histories.*

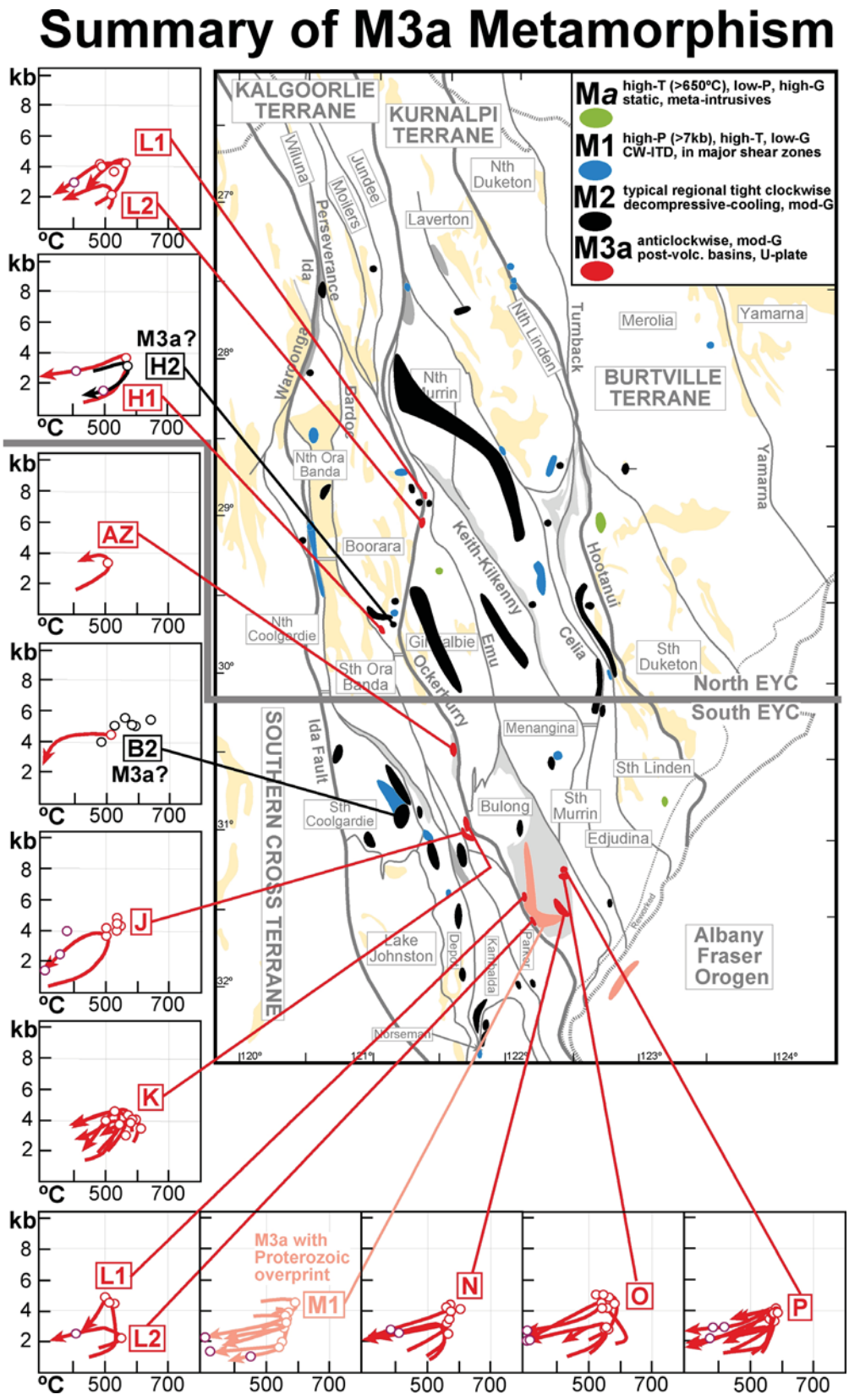

Figure 161: *Integration of the interpreted M3a P-T evolutions with the results of metamorphic domain analysis outlining regions that experienced common metamorphic histories.*

Metamorphism – Deformation Integration

Metamorphic data have been **temporally and spatially integrated with deformation evolution** by linking metamorphic field gradients with summaries of the structural evolution (Figure 162) documented at ***pmd****CRC* structural sites in the north EYC (Blewett et al., 2004b; Blewett and Czarnota, 2005). There is no internally consistent structural dataset across the south EYC region with which to integrate with metamorphic data. The ***pmd****CRC* structure data is from well exposed mine pit and granite outcrops (Figure 156). The ***pmd****CRC* structural data have been simplified to the essential elements; such as presence or absence of different deformation events, intensity of deformation, gold mineralization events and granitoid intrusive events, which are summarized in Figure 162. The full dataset of ***pmd****CRC* structural sites have been correlated with the metamorphic conditions and evolutions in the vicinity of these sites, where known (Appendix 17, GArecord_App17Tab_StructMetaInteg.xls). It is important to note that the ***pmd****CRC* structural sites are correlated only approximately with the location of the EYCMP metamorphic domains (Figures 133, 156). Furthermore, all metamorphic domains represent peak metamorphic conditions away from highly altered or mineralised sites, nor are they sited in granitoids. In contrast, all ***pmd****CRC* structural sites are located in mine pits or granitoids and invariably do not share the same metamorphic parageneses as those developed in the nearest-correlated metamorphic domain. Consequently, the metamorphic evolution and PT conditions in individual ***pmd****CRC* structure sites have not been determined directly. Metamorphic conditions in mine pits are commonly obliterated by pervasive hydrothermal alteration assemblages associated with mineralization (M3b). In granitoid structural sites metamorphic conditions cannot be determined because of the absence of suitable rock-types.

Figure 162: *Figure on next page. Composite metamorphic field gradients for the northern EYC (Figure 140) integrated with summaries of the structural evolution based on data from groups of similar sites along this profile (Blewett and Czarnota, 2005, 2007c).*

Grey shading:	*Indicates presence of deformation and density indicates deformation intensity. Black=high strain and ductile, medium grey=moderate ductile strain and light grey=low strains and brittle deformation.*
Stripes:	*Indicate deformation events not represented in all sites that have been grouped together.*
Green shading:	*Indicates amphibolite facies deformation, all of which is high strain.*
Yellow text:	*Au indicates presence of known and inferred (?) gold mineralization events.*
Red text:	*Indicates presence of granitoid intrusive events. T=tonolite, G⇑=High-Ca granite, G⇓=Low-Ca granite, G=undifferentiated granite or aplite, P=pegmatite, M=Mafic or HHFSE granites, S=syenite.*
Blue text:	*D indicates deposition of sedimentary sequences and maximum deposition ages.*
White text:	*Indicates alternative interpretation of deformation event.*

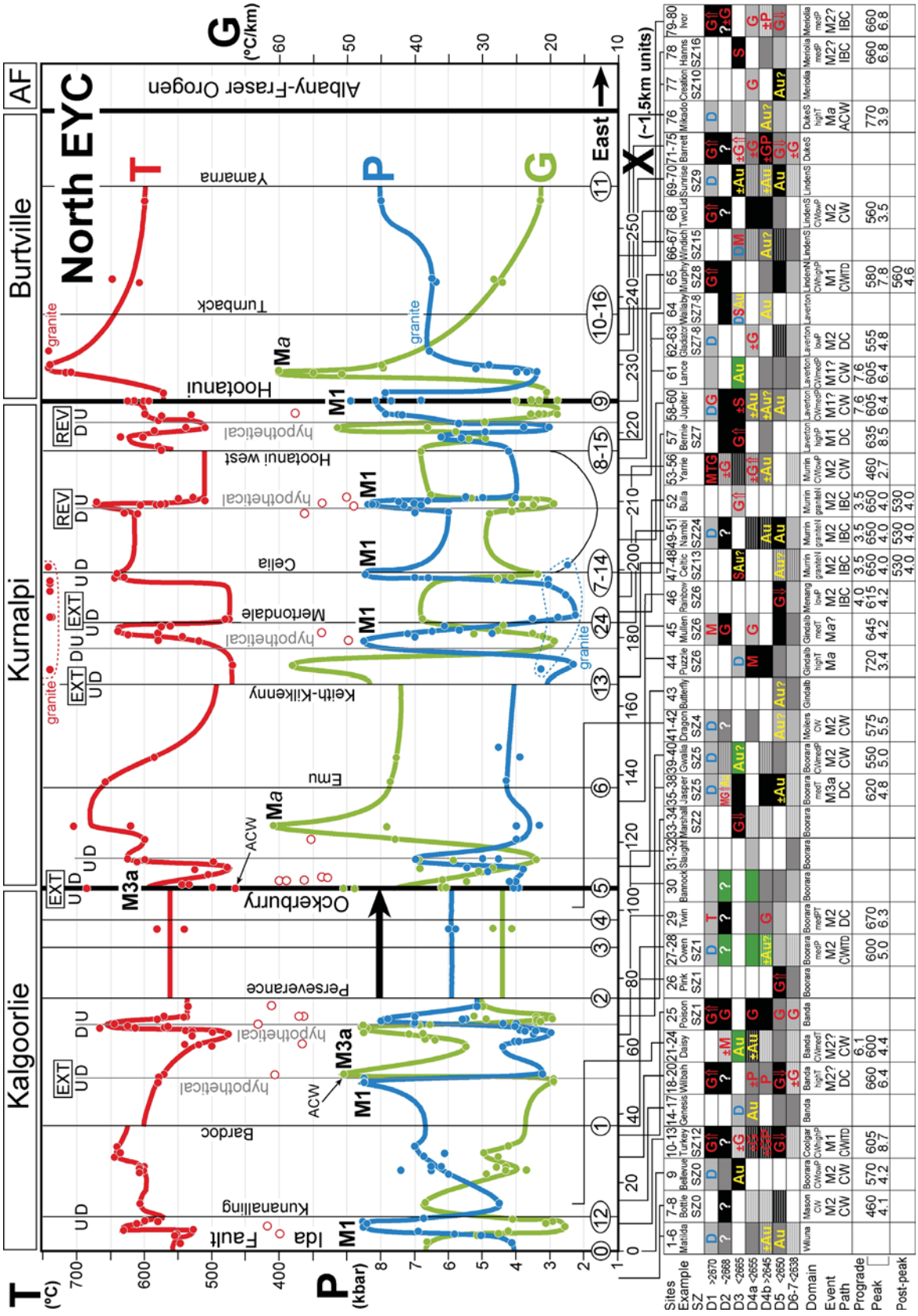
Kalgoorlie
Kurnalpi
Burtville
AF
North EYC
Albany-Fraser Orogen
T (°C)
P (kbar)
G (°C/km)
X (~1.5km units)
East
Ockerburry
Perseverance
Emu
Keith-Kilkenny
Celia
Mertondale
Hootanui west
Hootanui
Turnback
Yamarna
Bardoc
Kunanalling
Ida Fault
granite
hypothetical
ACW
M1
M2
M3a
Ma
Sites
Example
SZ
Domain
Event
Path
Prograde
Peak
Post-peak

Garnet Geochronology

Garnet Lu-Hf and Sm-Nd chronology was attempted to directly date the age of garnet growth during the M1, M2 and M3a metamorphic periods.

GARNET ANALYTICAL PROCEDURES

Garnet Lu-Hf and Sm-Nd isotope analyses were done at University of Melbourne. Garnet separates for samples Y530, Y531, Y667 and Y690 were prepared using standard procedures, i.e., heavy liquids, magnetic separator, and finally handpicking of small sub-sets. Representative powders of the garnet-poor rock matrix were prepared using an agate mill. Prior to the isotopic work, trace element data were obtained from all powders and garnet fractions using quadrupole-ICPMS. This was done to ascertain the suitability of the garnet separates for Lu/Hf and Sm/Nd dating, and to guide spike addition. For the isotopic work, two splits of whole rock powder were dissolved for each sample, one at high pressure (Krogh-type Teflon capsule, oven, 160ºC, 4 days), one at low pressure (in a Savillex beaker, hotplate, 120°C, 2 days). This was done to assess the influence of zircon on Lu-Hf budgets. Each split was spiked with mixed $^{176}Lu/^{180}Hf$ and ^{149}Sm-^{150}Nd spikes. Garnet fractions were ground into fine sand in an acid-cleaned agate mortar (under ethanol), followed by a clean-up step (warm 2M HNO_3, 1 hr) to remove surface contamination and easily soluble mineral impurities. Garnets Y530, Y534 and Y690 (which had low Sm/Nd ratios) were then leached with hot 6M HCl for 2 hours to remove soluble Nd-rich impurities (i.e., phosphates) and raise the Sm/Nd ratio of the resulting garnet residue. Garnets and garnet residues were then spiked (a Lu-Hf spike with high Lu/Hf ratio was used for the garnet fractions) and dissolved on a hotplate (HF-HNO_3, HCl). All samples produced visibly clear solutions (i.e., no gels). Leachates from the 6M HCl hot-leach were also spiked and then evaporated.

LREE were extracted from all samples using 0.1 ml beds of EICHROM RE resin. Sample matrix, along with Hf and part of the HREE, are not retained on this resin and were collected. Lu and Hf were then extracted using a single pass over 1 ml columns of EICHROM LN resin (Münker et al., 2001). Sm and Nd were purified on different columns of the same resin (Pin and Santos-Zaldegui, 1997). All beakers used in this work were cleaned with concentrated distilled HF to control Hf memory. Total analytical blanks were <30 pg for Lu-Hf-Sm, and <50 pg for Nd.

Isotopic analyses were carried out on a NU Plasma MC-ICPMS (Woodhead et al. 2001; Maas et al., 2005). Hf isotope ratios are corrected for interfering Lu, Yb and W, normalized to $^{179}Hf/^{177}Hf$=0.7325 and reported relative to JMC475=0.282160. Spike subtraction and iterative mass bias correction are done on-line. Spiked Lu fractions are corrected for Yb and mass bias based on the measured $^{173}Yb/^{171}Yb$ (natural ratio 1.1292, Vervoort et al., 2004); we obtain $^{175}Lu/^{176}Lu$=37.54 for natural Lu. Nd mass bias is corrected by normalizing to $^{146}Nd/^{145}Nd$=2.0719425 (equivalent to the more familiar $^{146}Nd/^{144}Nd$ = 0.7219, Vance and Thirlwall, 2002); data are reported relative to La Jolla=0.511860. Typical in-run precisions (2σ) for samples >20 ng Hf or Nd are ±0.000006 (Hf) and ±0.000010 (Nd); smaller samples yielded less signal and produce larger in-run errors (see Table 10). The external (2sd) precision, or reproducibility, is based on multiple runs of the same sample: ±0.000015 (Hf), ±0.000020 (Nd). Accuracy was assessed through isotope dilution analysis of USGS standard basalts with both Lu-Hf spikes and with our Sm-Nd spike. The results are consistent with those reported from other laboratories. ε_{Hf} and ε_{Nd} values are calculated relative to present-day CHUR parameters of 0.1967/0.512638 (Sm-Nd) and 0.0332/0.282772 (Lu-Hf, Blichert-Toft and Albarede, 1997). Age calculations used the most recent decay constant for ^{176}Lu is 1.865 10^{-11}/yr (Scherer et al., 2001), which supersedes the older one (1.93-1.94E-11/yr). The decay constant for $\lambda^{147}Sm$ is 6.54 10^{-12}/yr (e.g., Dickin, 1995). The 4 age determinations are based on the 2 Lu-Hf points for a whole rock powder (one dissolved on a hotplate, the other in a high-pressure bomb) and on variously treated garnet. Results of isotopic analysis are contained in Table (10) and apparent ages in Table (11).

GARNET SAMPLE DESCRIPTIONS

Sample Y530a

Sample is fresh, dark coloured and medium-grained metapelite schist from Mt Belches Formation in the Bulong Domain within the Kurnalpi Terrane. Foliated matrix assemblage of quartz-biotite-plagioclase-ilmenite-graphite-tourmaline with small post-kinematic blocky biotite laths across the foliation and ilmenite porphyroblasts across both biotite laths and foliation. There is late-stage chlorite growth across foliation. No garnet described from thin section but described in outcrop. Similar sample Y530g contains 152 ppm Zr.

Sample Y534b

Sample is fresh and dark coloured medium-grained metapelite schist from Mt Belches Formation in the Bulong Domain within the Kurnalpi Terrane. Matrix assemblage of quartz-biotite1-oligoclase-ilmenite with small muscovite grains across the main foliation. Post-kinematic porphyroblasts include poikiloblastic blocky biotite2 laths, garnet and poikiloblastic andalusite. Idioblastic garnet porphyroblasts are up to 1.0 mm in diameter and inclusion trails parallel the main foliation. Early flattened cordierite lenses up to 2 cm long are pseudomorphed by muscovite, quartz, ilmenite and chlorite that are aligned with the main foliation. Retrogressive chlorite replaces biotite. Garnet compositional mapping indicates that the garnets are compositionally flat for Ca and Fe with typical growth zoning patterns for Mg and Mn. Garnets in similar sample Y534A show typical growth zoning with decreasing Mn and Ca and increasing Fe and Mg with growth. Garnets are idioblastic, show one phase of growth and are not re-equilibrated, resorbed or retrograded. Garnets contain minor amounts of very fine quartz and monazite? inclusions. Similar sample Y534c contains 134 ppm Zr. Microphotographs are available.

Sample Y667a

Sample is fresh metapelite from Depot Domain within the Kalgoorlie Terrane. Fine-grained metapelite schist with quartz-biotite1-oligoclase-graphite foliated matrix assemblage. Small (0.8 mm) garnet porphyroblasts are rounded and may be pre-kinematic. Blocky red-brown biotite2 porphyroblasts cut the main foliation. Sample contains 116 ppm Zr.

Sample Y690a

Mafic-intermediate hybrid rock from the Edjudina Domain within Kurnalpi Terrane. Mylonite with an annealed medium-grained polygonal granoblastic matrix of quartz, anorthite, orange biotite, weakly aligned hornblende, magnetite, hematite, ilmenite and carbonate. Garnet occurs as syn- to post-kinematic porphyroblasts up to 3.2 mm in diameter and with quartz inclusion trails. Grey-blue-green ferro-hornblende also occurs as porphyroblasts. Sample contains 104 ppm Zr.

Table 10: *Table on next page. Sm-Nd and Lu-Hf isotopic results from Mt Belches, Black Flags and Yaboo rocks and their garnets.*

		Sm ppm	Nd ppm	$^{147}Sm/^{144}Nd$	$^{143}Nd/^{144}Nd$	ε_{Nd} now	T_{DM},Ga	Lu ppm	Hf ppm	$^{176}Lu/^{177}Hf$	$^{176}Hf/^{177}Hf$	ε_{Hf} now	T_{DM2} Hf
Y530 wr 1	hp	5.48	30.98	0.1070	0.511150	-29.0	2.84	0.22	3.89	0.00803	0.281558	-42.9	2.92
Y530 wr2	lp	5.47	30.87	0.1071	0.511158	-28.9	2.84	0.21	3.77	0.00793	0.281550	-43.2	2.92
Y530 gt1	lp	1.80	4.57	0.2386	0.513349	13.9		14.77	1.62	1.3089	0.348589	2328	
Y530gt2R	lp	1.00	0.34	1.7992	0.539717	528.2		13.77	1.48	1.3427	0.350360	2390	
Y530 gt2L	lp	0.83	4.29	0.1163	0.511272	-26.6		1.43	0.14	1.5292	0.360634	2754	
Y534 wr1	hp	5.52	29.89	0.1116	0.511112	-29.8	3.03	0.21	3.74	0.00818	0.281517	-44.4	3.02
Y534 wr2	lp	5.37	29.06	0.1117	0.511136	-29.3	3.03	0.20	3.72	0.00777	0.281498	-45.1	3.02
Y534 gt1	lp	2.22	8.06	0.1663	0.512054	-11.4		16.30	1.74	1.3532	0.350649	2400	
Y534gt2R	lp	0.89	0.69	0.7811	0.522361	189.7		15.40	1.70	1.3036	0.348131	2311	
Y534 gt2L	lp	1.88	10.46	0.1084	0.511048	-31.0		1.94	0.11	2.6240	0.416008	4712	
Y667 wr1	hp	4.35	23.12	0.1138	0.511054	-30.90	3.18	0.25	2.87	0.01219	0.281509	-45	3.47
Y667 wr2	lp	4.16	22.03	0.1140	0.511053	-30.92	3.19	0.24	2.85	0.01202	0.281504	-45	3.46
Y667 gt1	lp	0.74	0.96	0.4671	0.517093	86.90		15.00	0.86	2.5458	0.412938	4603	
Y690 wr1	hp	3.27	15.43	0.1280	0.511411	-23.94	3.08	0.30	2.93	0.01477	0.281826	-33	3.09
Y690 wr2	lp	3.23	15.26	0.1281	0.511419	-23.78	3.07	0.30	2.36	0.01785	0.281991	-28	3.07
Y690 gt R	lp	0.466	0.231	1.2265	0.530318	344.88		4.67	0.73	0.9203	0.329045	1636	
Y690 gt L	lp	0.150	0.451	0.2014	0.512719	1.58							

Dissolution of whole rocks by both high-pressure (hp) and low-pressure (lp); all garnet fractions dissolved on a hotplate (lp); suffixes R (residue) and L (leachate) mark fractions obtained by leaching of finely-ground garnet with hot 6M HCl to remove soluble (phosphate ?) Nd-rich impurities. All isotopic analyses done by isotope dilution multi-collector ICPMS. In-run precision (2se) for samples >20 ng Hf or Nd: ±0.000006 (Hf), ±0.000010 (Nd); smaller samples (e.g. Hf runs for leachates and for Y690 gtR; Nd run Y690 gtL) have in-run errors up to 3x greater. External (2sd) precision: ±0.000015 (Hf), ±0.000020 (Nd). Nd and Hf isotope ratios reported relative to LaJolla=0.511860 and JMC465+0.282160, respectively. External precision for $^{147}Sm/^{144}Nd$ and $^{176}Lu/^{177}Hf$ is ±0.2 and ±0.5%, respectively. CHUR parameters: $^{147}Sm/^{144}Nd$=0.1967, $^{143}Nd/^{144}Nd$=0.512638; $^{176}Lu/^{177}Hf$=0.0332, $^{176}Hf/^{177}Hf$=0.282772. T_{DM} for SmNd is the conventional Nd model age with present-day DM parameters of 0.2136/0.513151; T_{DM2} for LuHf is a 2-stage model age with present-day DM parameters 0.03829/0.283224 and default crustal $^{176}Lu/^{177}Hf$=0.0142

GARNET GEOCHRONOLOGY RESULTS

Lu-Hf Geochronology Results

Sample Y530

Two whole rock fractions with garnet give approximately the same result, suggesting no noticeable effect from zircon which would give variations in Lu/Hf and $^{176}Hf/^{177}Hf$. Analysed three garnet fractions to improve the Sm/Nd ratio. A bulk garnet washed with mild acids only, a heavily leached garnet (left in hot 6M HCl for 24 hours and leachate from this heavily leached garnet. The 3 garnet-based points have only limited dispersion in Lu/Hf but the garnet – whole rock dispersion is good. The age for all 5 points is 2691±29 Ma (MSWD 2.8). The leachate pair is off the mean isochron and so is omitted, giving 2681±9 (MSWD 0.059). This result is a good model 1 (perfect fit) isochron.

Sample Y534

The two whole rock fractions give very similar data, regardless of the mode of dissolution. Garnets were treated the same way as for Y530. The leachate has a much higher Lu/Hf than the garnets, which in turn has much higher Lu/Hf than the whole rock. All 5 points define a well-fitted line with age 2675±7 Ma (MSWD 0.051). There is virtually no change in age if the leachate is omitted. The leachate possibly carries the Lu/Hf characteristics of phosphate, perhaps apatite.

Sample Y667

The two whole rock fractions give almost identical data, regardless of dissolution method. For this sample, no leaching of the garnet was undertaken because the bulk garnet already had very high Sm/Nd and Lu/Hf and was suitable material. The two whole rock fractions are very close, giving a virtual 2-point isochron. The age is 2698±13 Ma (MSWD 0.21).

Sample Y690

The two whole rock fractions for this sample showed some differences. The bombed sample has lower Lu/Hf and lower $^{176}Hf/^{177}Hf$, indicative of a greater amount of zircon-held Hf. The hotplate sample did not dissolve as much zircon and shows lower Hf (2.36 vs. 2.94 ppm), higher Lu/Hf ratio and higher $^{176}Hf/^{177}Hf$ ratio. There was only sufficient clean garnet for 1 analysis. To provide a large range in Sm/Nd, this fraction was hot-leached with 6M HCl. The data is poor because the leachate has almost no Hf. The two whole rock fractions and the single garnet residue give a well-fitted line with an age of 2712±13 Ma (MSWD 0.26).

Sm-Nd Geochronology Results

Sm-Nd garnet - whole rock isochron age determinations are: 2561±11 Ma (Y530a), 2547±17 Ma (Y534b), 2593±13 Ma (Y667a) and 2610±16 Ma (Y690a).

Table 11: *Table of apparent garnet-whole rock ages from Sm-Nd and Lu-Hf data.*

sample			n	MSWD	SmNdage	$^{143}Nd/^{144}Nd_i$	ε_{Ndi}
530	Mt Belches	2665	5	3.5	2561±11	0.50933±4	0.3
534	Mt Belches	2665	5	2.6	2547±17	0.50925±3	-1.7
667	BlackFlags	2700	3	0.076	2593±13	0.50911±2	-3.3
690	Yaboo	2710	4	1.16	2610±16	0.50921±2	-0.7

sample			n	MSWD	LuHf age	$^{176}Lu/^{177}Hf_i$	ε_{Hfi}
530	Mt Belches	2665	4	0.062	2695±9	0.281143±8	2.9
534	Mt Belches	2665	5	0.022	2688±8	0.281097±8	1.1
667	BlackFlags	2700	3	0.21	2712±13	0.280878±9	-6.1
690	Yaboo	2710	3	0.26	2726±13	0.281058±10	0.6

GARNET GEOCHRONOLOGY INTERPRETATION

Interpretation of Lu-Hf Results

Possible Half-Life Effect

The apparent ages (2675, 2681, 2698, 2712 Ma) all have the expected nominal errors (<±0.5%) and are all based on garnets with high Lu/Hf ($^{176}Lu/^{177}Hf$ 0.9 - 2.5). Calibration of both spikes was undertaken in the previous week, giving identical results for USGS standard BCR2. Furthermore, garnet and whole rock Hf analyses are robust, without deleterious interference or blank issues. Consequently, these results are technically robust. However, the ages are older than expected for the age of metamorphism in the Eastern Goldfields, which is ~2660-2670 Ma, based on various geochronology from post-tectonic granites and syn-mineralization micas. Additionally, the results give a 37 Ma range in age determinations.

There are two half lives for Lu; based on meteorite and terrestrial data. Difference between the two half lives is ~4%, which is equivalent to 108 Ma for a 2700 Ma aged sample. The most recent Lu decay constant (1.867E-11/yr) was used, which supersedes the now discredited older one (1.93-1.94E-11/yr). Recalculation using the older half-life (1.93), gives ages that would be younger by ~87 Ma, which is too young for the eastern Yilgarn Craton.

Lu-Hf garnet dating has given ages that are consistently 20-25 Ma older that the expected age based on the stratigraphic association of the sample. This 20-25 Ma differential, amounts to only 0.9% of the age, which is well below the 4-5% difference between different estimates of the Lu decay constant. An earlier decay constant of 1.94E-11/yr has recently been revised to 1.865E-11/yr. The new constant is 3.8% lower (Scherer et al., 2000) and at 2700 Ma gives ages approximately 100 Ma older than the original decay constant. An intermediate decay constant between these two could theoretically give ages from the Yilgarn isotopic data that would match geological constraints. Nevertheless, the revised decay constant has been confirmed repeatedly and is considered accurate, discounting this explanation. The difference between determined age and expected age in different rock units is systematic and there are no indicators of micro-inclusions or other problems in the isotopic data. This systematic pattern suggests a geochronological explanation and not an ad hoc geological one (i.e., micro inclusions). Consequently. It is felt these age determinations can be used in a relative way to confirm the following. [1] There are multiple ages of metamorphic parageneses in the EYC (at least 3). [2] The distinct high-P and low-G metamorphic parageneses are unrelated to and older than all other metamorphic events. [3] Metamorphism of the post-volcanic late basins (M3a) was by an overprinting, late-stage thermal peak after the regional M2 metamorphic event.

Possible Zircon Effect

Zircon has 1 % Hf contents and the Lu/Hf ratio is close to zero, whereas garnet has <1 ppm Hf and very high Lu/Hf ratios. Any zircon will thus essentially freeze in the Hf isotope ratio it inherited from its parent melt or fluid at the time of its formation. Age-zoned zircons may have >1 Hf isotope signature. Inherited zircon populations such as those in metasediments should have a range of Hf isotope signatures, reflecting the provenance. Lu/Hf dating of such systems using metamorphic garnets can be difficult if zircon is abundant. The newly formed garnet may not equilibrate with all Hf isotope flavours in the rock (in unreacted zircons), producing fine-scale isotopic disequilibria. The slope of any isochron is in part controlled by the amount of zircon released in the analysis, in both the whole rock powder and the garnet. The age can be too old or too young. If the range of inherited zircon ages is small (say a few 100 Ma only), the range in zircon Hf isotope flavour may also be small; reducing the extent of any fine-scale disequilibrium to the point where 2700 Ma worth of ^{176}Hf growth in garnet swamps such effects, which is probably the case for the EYC samples.

To avoid these zircon effects, zircon-free systems are preferable. Alternatively, dissolution of zircon can be minimized on a hotplate, or in very strong HCl in a bomb, on a hotplate, without attacking the included zircon. It is plausible that the old ages could result from disequilibrium between garnet and some of the matrix Hf located in old zircon. However, this Hf was dissolved with the hydrofluoric acid. Sample Y690 shows a very small zircon effect, but is insufficient to make a difference which

whole rock was paired with the garnet. The Yilgarn garnets have ≈50 ppm Zr, indicating that they contain zircon (compare host metapelites 90-150 ppm). The matrix contains 90-150 ppm, indicating a greater proportion of Hf derived from ancient low-εHf zircon relative to the garnet. This would rotate the isochron to an older age. The only problem with this interpretation is the apparent coincidence of a similar effect in all samples, leaving an apparently undisturbed relative age sequence.

Interpretation of Sm-Nd Results

The Sm/Nd garnet ages are in the range 2610-2550 Ma, which is 60-100 Ma younger than expected. This differential between expected age and determined age is the opposite of Lu-Hf data, but similarly shows a systematic shift with respect to stratigraphic constraints on the age. Unlike Lu-Hf, very little Sm and Nd partition into zircon and Sm-Nd age determinations are insensitive to zircon. With the exception of sample Y667, the garnets were leached with hot 6M HCl to remove monazite and increase the Sm/Nd ratio towards that of the pure garnet. Garnet in sample Y667 has less monazite and did not require leaching to give the required high Sm/Nd. The isotopic dispersion in all samples is large, as was the case for the Lu/Hf system. Ages were derived from garnet - whole rock pairs, and these pairs were duplicated (one dissolved in high-pressure bomb, the other on hotplate). Scatter in the Sm/Nd isochrons (MSWD 0.1-3.5) is greater than for the Lu/Hf (<0.1 to 0.26) but is still comparatively modest. Rock standards run with the same procedure at the same time give the expected results, and the blanks are ok. Initial εNd for these "isochrons" were in the range -3.3 to +0.3, which is typical of Late Archaean metapelites. Like the Lu-Hf data, analytically there is no obvious explanation for the low Sm-Nd ages.

An alternative analytical explanation for the young Sm/Nd ages is by variation in the whole rock. Garnets in these samples were concentrated in particular layers reflecting compositional variation in these fine-grained sediments. It is preferential to work with fractions of just garnet-bearing material, to avoid biasing the system towards sedimentary layers that may not have been in equilibrium with the growing garnet. However, these samples were entirely crushed to get sufficient garnet material and the whole rock fraction was a small portion of this crush. It is possible that the whole rock fraction selected is not 100% representative of the Sm/Nd reservoir seen by the growing garnet. This effect was examined by adjustments to the Sm/Nd and $^{143}Nd/^{144}Nd$ ratios in both whole rock and garnet, and recalculating the age. Unreasonably large changes in either $^{143}Nd/^{144}Nd$ or Sm/Nd were required to get ages of 2650 Ma. To adjust the age into the expected range requires changes of 20 eNd units in either the whole rock or garnet, and/or large shifts (i.e., >>5%) in both Sm/Nd and $^{143}Nd/^{144}Nd$, which is unrealistic.

Possible geological explanations for low Sm-Nd garnet ages are: [1] slow cooling, [2] re-heating in second event, [3] presence of REE-rich phases that are much younger than the garnet indicating an open system. Slow cooling is unlikely in the EYC setting and possible reheating events (i.e., mineralization events) are in the range 2660-2615 Ma and thus to old to cause the young garnet ages. Open-system behaviour has been suggested for the consistently low Ar-Ar (e.g., Napier et al., 1998; Kent and McDougall, 1995) and Rb-Sr age data from the Yilgarn Craton (e.g., McNaughton, et al., 1992; Mueller and McNaughton, 2000). Though open system behaviour is possible, it is unlikely that all 4 samples should be affected in a systematically similar way. Furthermore, the apparently systematic deleterious behaviour on both Lu-Hf and Sm-Nd age determinations correlate perfectly between the two isotopic systems. There is no obvious geological or analytical explanation for this systematic pattern across two independent isotopic systems.

Young Sm-Nd mineral ages have been observed in some hydrothermal gangue scheelites from Late Archean mesothermal Au veins in both Canada and Australia. Brugger et al. (2002) suggested this is related to disturbance of Sm-Nd systems as a result of late introduction of secondary bastnaesite, a rare LREE-Y carbonate fluoride. Introduction of LREE some time after mineral formation would lower bulk-garnet Sm/Nd and $^{143}Nd/^{144}Nd$ ratios, producing a disturbed system with a young apparent mineral-wr age, exactly as is observed. Introduction of a REE-rich secondary mineral may also affect Lu-Hf systems, although it is difficult to generalize the likely effects.

The almost perfect correlation (r^2=0.99) between the Sm-Nd and Lu-Hf ages Is problematical, given the very different possible modes of disturbance (i.e., variable inherited zircon producing old Lu-Hf ages, secondary disturbance of Sm-Nd systems producing low Sm-Nd ages). The garnets from Black Flags and Yaboo, with depositional ages near 2690-2680 Ma, have the oldest Lu-Hf and Sm-Nd ages, while the two samples of Mt Belches metapelite, with the youngest depositional age (~2665 Ma), have the youngest Lu-Hf and Sm-Nd ages. Apparently, alteration in the younger rocks occurred later, or lasted longer, than in the older rocks. Regarding the good age vs age correlation, it is noted that for each pair of samples, apparent Lu-Hf ages overlap within error, as do their Sm-Nd ages. The 4-point correlation thus reduces to a 2-point system. Moreover, variation in Sm-Nd ages is 50% greater than variation in Lu-Hf ages, thus increasing the probability of correlation. Consequently, the age-age correlation should not be over-interpreted.

Initial εHf and εNd values contain useful provenance information. The older metapelites from Yaboo and Black Flags Formation have lower εHf (-6.1, +0.6), indicating an older provenance than the younger Mt Belches PVTB samples, which have higher εHf (+1.1, +2.9). Initial εHf values calculated for the apparent Lu-Hf ages vary strongly for all samples, from +2.9 to -6.6. They are within 0.5 εHf units of the depositional εHf for these metapelites. Hf model ages (2.92-3.47 Ga) directly reflect this range in provenance signatures. As bulk rock Hf isotope budgets are strongly controlled by zircon, this variation is likely to mirror the amount, age and Hf isotope signature of inherited zircon in these rocks. A greater number of older zircons with lower $^{176}Hf/^{177}Hf$ (lower εHf) should produce lower bulk rock εHf and older model ages, and apparently have also effected Lu-Hf grt-wr ages. Initial εNd calculated for the grt-wr Sm-Nd isochrons vary from -3.3 to +0.3, a little lower than depositional εNd (-2.1 to +1.8). This offset is simply the result of isotopic evolution between age of deposition and garnet growth over some 100 Ma. There is no obvious correlation of apparent Sm-Nd age and εNd. Overall, the εHf and εNd values are within the range expected for clastic sediments deposited within a late Archaean granite-greenstone terrane which, although formed near 2.7 Ga, contains detrital zircon as old as 3.4 Ga (Compston et al., 1984). εHf and εNd correlate, as is observed for the large majority of crustal lithologies (i.e., the Nd-Hf array).

Metamorphic Interpretation

At least five distinct metamorphic periods have been recognised for the EYC on the basis of over-printing relations, absolute PT conditions, contrasting P-T paths and distinct structural and stratigraphic settings. Interpretations of the absolute timing of these metamorphic periods have been made by correlations with extrusive, intrusive, basinal and deformation histories documented by numerous workers and summarized by Blewett and Czarnota (2005, 2007c). These temporal correlations are summarized in Figure 163, which attempts to summarize the evolution of fundamental metamorphic parameters (P, T and G) with time and with links to possible tectonic settings. Cartoons summarizing the spectrum of possible tectonic settings that are consistent with the know salient metamorphic, deformation and magmatic relationships are presented in Figure 164. Interpretation of the metamorphic findings for each of these five periods within plausible tectonic settings is discussed below.

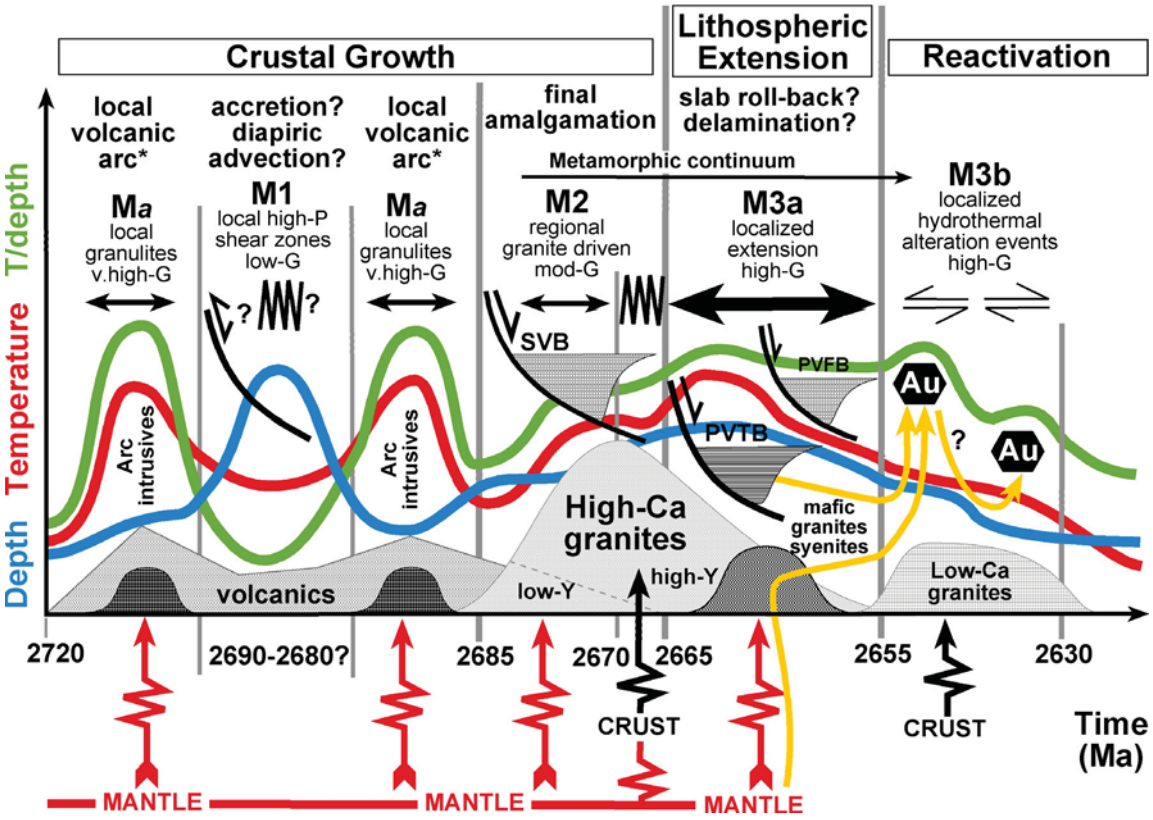

Figure 163: *Generalized evolution of metamorphic parameters (T, P or depth and temperature/depth ratio) with time, juxtaposed with crust formation events (volcanism, plutonism and sedimentary basins) and deformation events in the EYC. The pre-2685 Ma period is an entirely schematic representation of possible multiple local events distributed across a spatially complex mosaic of different tectonic settings. SVB - syn-volcanic clastic basin, PVTB - post-volcanic turbiditic basin, PVFB – post-volcanic fluvial basin.*

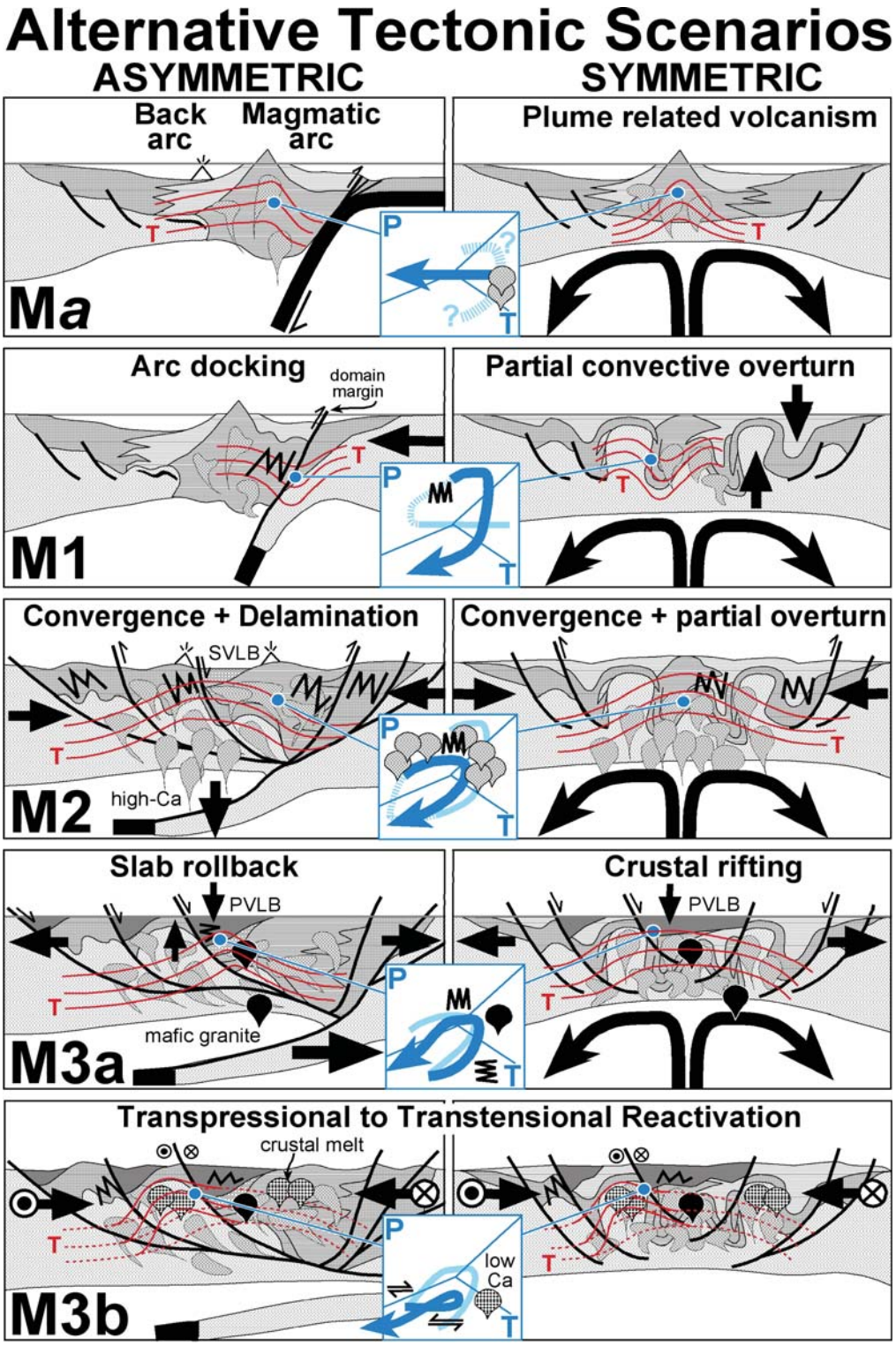

Figure 164: *Cartoons summarizing alternative tectonic scenarios for the different metamorphic episodes recognised in the EYC. The different tectonic settings are presented as end-member models: asymmetric tectonics of the plate tectonic paradigm and symmetric or vertical tectonics of plume related and diapiric paradigms. The tectonic settings of the EYC may have been either of these end-members or hybrid scenarios between the two, and it is also possible that tectonic setting alternated between different influences of these end-member scenarios as the EYC evolved.*

Ma METAMORPHISM (2720-2685 Ma)

Ma Metamorphic Conditions

The period of late crust formation and volcanic stratigraphy involved both multiple events and a spatially complex mosaic of subduction, magmatic arcs, back-arc and plume related environments and processes. Widespread near surface metamorphic parageneses that would have formed at this time are sea floor alteration (e.g., Phillips. 1986). These early alteration assemblages would have been largely obliterated during subsequent events, except possibly in the lowest grade parts of the EGST, typically in the cores of major greenstone synforms. Nevertheless, the resulting altered bulk compositions are preserved and these have strongly influenced the subsequent developed metamorphic parageneses in the EGST and Southern Cross Terrane (e.g., Purvis, 1984).

Granulite metamorphism is recognised in only two localities: a cluster in the northern part of the Southern Duketon Domain and one location in the northern part of Gindalbie Domain. These granulites are statically metamorphosed gabbros, preserving ghosted ophitic textures, recrystallised to polygonal granoblastic orthopyroxene-clinopyroxene-hornblende-plagioclase assemblages. Peak metamorphic conditions of ~730 ºC at low pressures between 2.5-5.0 kb, indicate very high temperature/depth ratio (G – simply the ratio T/depth assuming a density of 2.8 gm/cm^3) between 45-80 ºC/km. Peak-T was attained at peak-P conditions and was followed by near isobaric cooling (Figures 87, 159). Prograde evolutions are not well constrained. The absence of inclusion or mineral zoning evidence for higher-P parageneses, suggest heating paths with isobaric or shallow burial trajectories, implying tight anti-clockwise P-T paths (Figure 87). Tight anticlockwise P-T paths would be consistent with magmatic heat source paths (Spear, 1993).

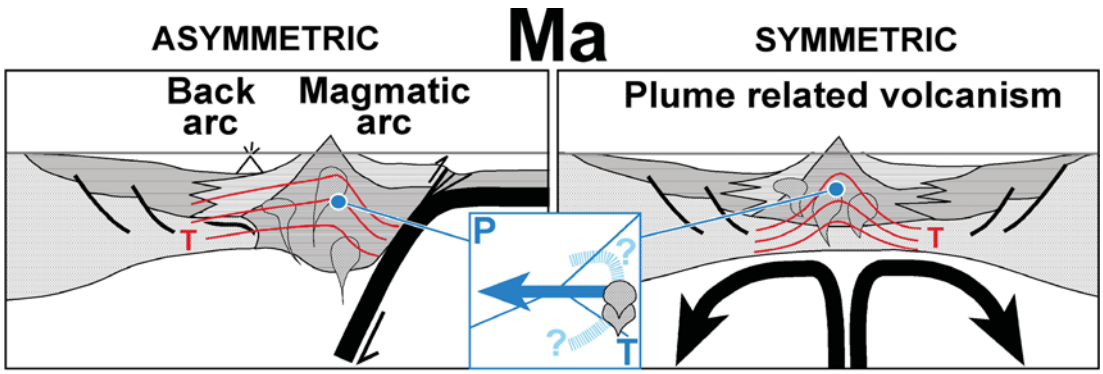

Figure 165: *Cartoons summarizing alternative tectonic scenarios for the Ma period.*

Ma Tectonic Setting

These high-T, high-G conditions (M*a*) in the upper crust are most plausibly formed in the high heat flow environment of magmatic arcs (Ernst, 1976; Kemp et al. 2007). Deeply eroded magmatic arc settings would result in a patchy distribution of small high-grade domains associated with arc volcanics and intrusives, such as documented in the Coastal Terrane in the Kaoko Belt, Namibia (Goscombe and Gray, 2007). The patchy distribution is due to a combination of a highly variable heat flow regime in arcs and later reworking obliterating the high-grade parageneses. Magmatic arc domains are anticipated to be widely scattered and of different ages, reflecting multiple magmatic arcs (Figure 163). Geochemical indicators of magmatic arc rocks are restricted to the Kurnalpi Terrane. The rare occurrences, small domains and association with mafic intrusives of Ma parageneses are consistent with magmatic arc settings. The alternative setting of formation in either a lithospheric extension or above a mantle plume setting would result in much larger domains and more widespread distribution of such metamorphic conditions. Consequently, the preferred tectonic setting for Ma parageneses is at upper crust levels within a magmatic arc, inferring subduction (Figure 165). If associated with magmatic arcs, these granulite parageneses were forming at the same time as the mafic and ultra-mafic extrusives and younger felsic volcanics between ~2720-2690 Ma. Furthermore, these early high-grade parageneses will be broadly time equivalent to sea floor

alteration of rock protoliths (Purvis, 1984) and what are interpreted to be seafloor metamorphic parageneses in low-grade parts of the EYC (Phillips, 1986). Contemporaneous early formation of these widely different metamorphic parageneses, that do however share high thermal gradient environments, would reflect a complex distribution of arcs and back arc environments, with superimposed plume-related magmatic processes during an extended period of crust formation.

M1 METAMORPHISM (2720-2685 Ma)

M1 Metamorphic Conditions

Rare, but widely distributed high-P (7.0-8.7 kb), high-T (570-640 ºC) and uniquely low temperature/depth ratio (G = 18-23 ºC/km) metamorphic parageneses are found almost exclusively associated with high-strain shear zones or Domain boundaries (e.g., Ida, Ockerburry, Celia and Hootanui shear systems). These upper-amphibolite parageneses have been labelled M1 and typically represented by garnet-clinopyroxene-hornblende, garnet-hornblende, clinopyroxene-hornblende and garnet-grunerite-hornblende mafic assemblages and rare garnet-staurolite-chlorite-muscovite-rutile metapelites. The documented pressures including typical errors (±1.0 kb) are significantly distinct from typical regional metamorphic conditions of 3.5-6.0 kb. These rocks experienced clockwise P-T paths where peak-T was attained at peak-P (Figure 159), and there is no evidence for deeper prograde histories preserved in the mineral parageneses. Peak conditions were followed by near isothermal decompression documented by PT calculations from outer-rim analyses and reaction textures such as plagioclase coronas. The timing of isothermal decompression is not confidently established. Most plausibly isothermal decompression was responsible for terminating metamorphism immediately after the peak and thus intimately associated with the tectonic processes responsible for metamorphism. Alternatively isothermal decompression occurred later, during an unrelated exhumation event such as M3a lithospheric extension.

A single Lu-Hf garnet age from one of these high-grade parageneses is 15 Ma older than Lu-Hf ages for garnets from regional metamorphic parageneses and 30-35 Ma older than Lu-Hf ages for metamorphic garnet in a post-volcanic late basin (see below). Consequently, these high-P, high-T parageneses are interpreted to have formed early, prior to pervasive regional metamorphic events. This is substantiated by overprinting of medium-P rocks within shear zones by lower grade shear assemblages and the formation of these rocks in thermal regimes entirely distinct from all younger events (i.e., within late basins) and over-printing (i.e., regional metamorphism and low grade shear events), all of which are characterized by higher temperature/depth ratios (G ≥40 ºC/km) than the M1 conditions (G = 18-23 ºC/km).

M1 Tectonic Setting

The tectonic setting for early, high-P, low-G parageneses is unknown, but can be explained by two competing end-member processes.

[1] A two-stage process involving late-stage selective exhumation of low thermal gradient parageneses that were originally more widespread and formed in a craton-wide tectonic setting. An example would be widespread low thermal gradients at mid-crustal levels such as in a thermally stratified crust (Figure 153). Or alternatively, low thermal gradient Barrovian metamorphism throughout the entire crustal column by craton-wide collisional orogenesis and crustal over-thickening. Either of these scenarios require that the currently restricted distribution of M1 assemblages are due to a small portion of the mid-crust being exhumed into the upper crust by late-stage processes. A possible exhumation scenario is during M3a lithospheric extension, telescoping the crust and exhuming M1 parageneses in the lower-plate of extensional shear zones below late basins. Nevertheless, a collisional setting would have formed widespread Barrovian assemblages, of which there is no preserved expression, and is thus considered an implausible scenario.

[2] Alternatively, single-stage processes would demand that the high-P, low-G conditions were spatially restricted at the time of formation similar to their current distribution. In which case the current spatial distribution of M1 parageneses becomes a significant observation, and the tectonic setting must account for discrete, thin, arcuate zones (Figure 144) of deep burial followed by rapid

exhumation (Figure 93). Possible tectonic settings (Figure 166) that match the metamorphic conditions and restricted spatial distribution are downward advection of attenuated margins of accreted terranes or arcs in "subductive"-like settings (e.g., Beyssac et al., 2008), or alternatively downward advection of greenstone keels during diapiric overturn (e.g., Collins and Van Kranendonk, 1999).

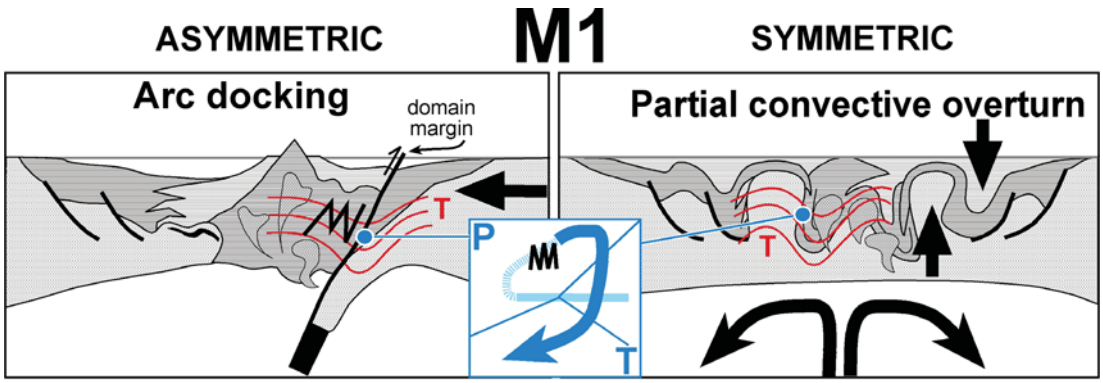

Figure 166: *Cartoons summarizing alternative tectonic scenarios for the M1 period.*

Diapiric overturn of TTG gneiss domes and downward advection of greenstone sequences at their margins can account for both the high-P and low-G metamorphic conditions and spatial association with margins of granite/gneiss domes (Van Kranendonk and Collins, 1998; Van Kranendonk et al., 2002, 2004). This gives effective downward advection of material into the mid-crust in greenstone keels and clockwise P-T paths (Warren and Ellis, 1996). The hornblende assemblages generated do not deform ductilely at the temperatures experienced (i.e., <700ºC), and adhere to upward advecting domes resulting in isothermal decompression paths into the upper-crustal (Collins and Van Kranendonk, 1999; Sandiford et al., 2004). Consequently, diapiric overturn scenarios invoke fast burial and exhumation rates and would be consistent with isothermal decompression paths. Diapirism is typically initiated late in crust formation, past a threshold of thermal weakening of the crust. Despite these correlations with documented features of M1 metamorphism, a diapiric model is contingent on early pressures >8.7 kb in the granite/gneiss domes for exhumation of the high-P mafic rocks to be due to diapiric rise of these domes. All pressures recorded from EYC granites and gneisses are lower than 6.0 KB. Furthermore, not all margins of domes preserve high-P parageneses, and high-P parageneses show a stronger correlation with shear zones. Furthermore, deep downward advection of the greenstone keels should result in evidence for more widespread evidence for high-pressure histories across all parts of the greenstone keels, and not just their margins (Warren and Ellis, 1996). Consequently, partial diapiric overturn models do not satisfy all M1 metamorphic features, and are inconsistent with the crustal structure of the EYC recorded by seismic profiles (Goleby et al., 1993, 2002a, 2002b; Blewett et al., 2002a,b; Henson and Blewett, 2006). There may also be more fundamental limitations to the convective model, which requires a mechanism to arrest the process, giving **partial** convective overturn. Downward advection of mafic material will eventually generate eclogitic assemblages increasing the density of the mafic keels further leading to runaway convective overturn.

Typical Phanerozoic to Proterozoic subduction settings, where advection out competes conduction, have temperature/depth ratio less than 13-18 ºC/km (Brown, 2007b,c). Tectonic settings involving the collision of magmatic arcs with normal thickness continental crust, such as in Taiwan, involve deep burial metamorphism in the suture region with temperature/depth ratios of 13-16 ºC/km (Beyssac et al., 2008). M1 parageneses record slightly higher average thermal regimes of 20 ºC/km, which are within the range for conductive response to thickening. Nevertheless, M1 temperature/depth ratios indicate a setting where advection of material and heat dominates over the conduction of heat. It is possible that the M1 parageneses represent an atypical high-T "subduction"-like setting, resulting from the higher ambient thermal gradients in the Neoarchaean or alternatively shallow or slow subduction. This explanation would need to argue the case that the metamorphic

expression of subduction of oceanic crust in the Neoarchaean was different to that in the Proterozoic and Phanerozoic. Alternatively, these high-P assemblages result from partial downward advection of the attenuated edge of magmatic arc terranes, where burial of the margin is arrested by buoyancy forces and thus do not attain the extreme pressures and low thermal gradients experienced during subduction of oceanic crust. Downward advection of the attenuated margin of a magmatic arc may occur during either collision of an arc terrane or accretionary shortening of a magmatic arc against contiguous and associated back arc or attenuated crustal margin settings. High rates of both downward advection and upward isostatic exhumation in either accretionary or collisional settings, would give rise to isothermal decompression paths similar to that experienced in M1. Partial downward advection of an attenuated magmatic arc margin during accretion against an attenuated crustal margin or back arc setting, best explains all M1 metamorphic features (i.e., P, T/depth and P-T path), their rare occurrence and distribution in discrete, elongate and arcuate zones (Figures 144, 159).

Though both M*a* and M1 have entirely distinct thermal regimes, it is possible that both formed at similar times in a co-genetic down-advected margin / magmatic arc tectonic system (Figure 167). M*a* metamorphic conditions experienced at shallow-crustal levels in magmatic arcs and M1 metamorphic conditions at deeper-crustal levels in an associated downward advection setting. M1 parageneses may have formed by down advection of the leading edge during collisional accretion of a magmatic arc (Figure 167). Collisional accretion would terminate volcanism and initiate crustal shortening and place the timing of M1 parageneses immediately prior to M2 crustal shortening, associated granite bloom and high heat flow. If related in this way, M1-M2-M3a periods form a metamorphic continuum in a sequence of causally inter-related but dissimilar tectonic settings.

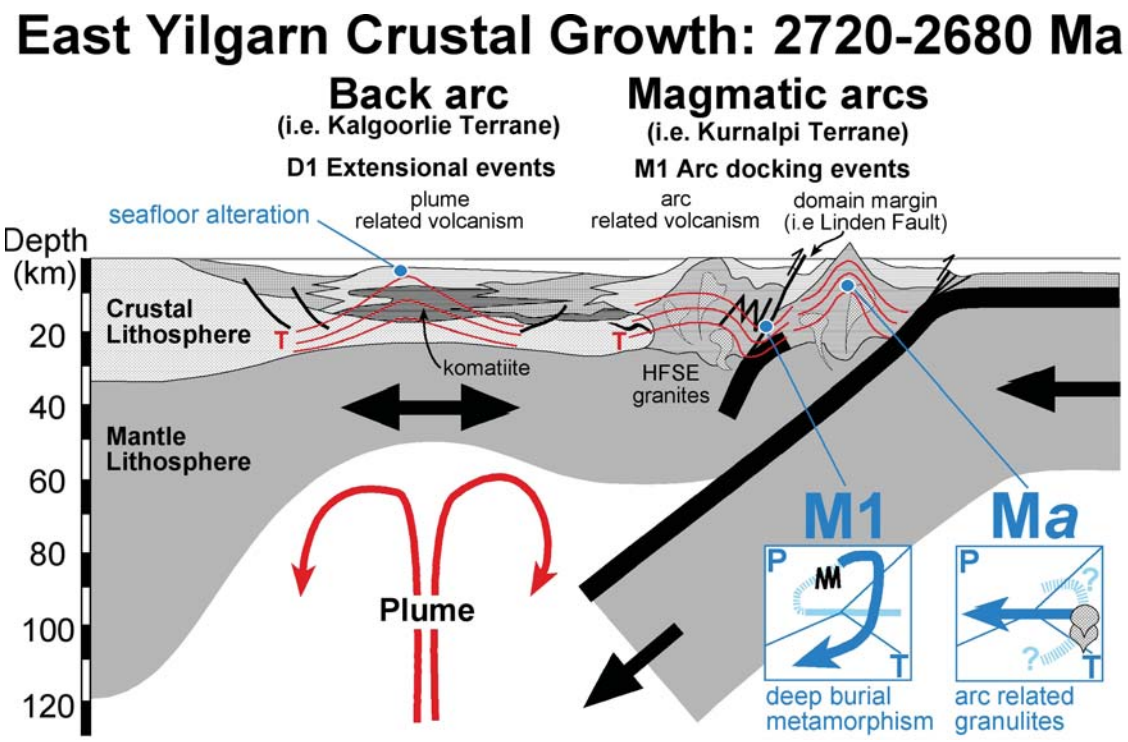

Figure 167: *Preferred model for the early crustal growth period for the EYC, with possible tectonic settings for M1 and Ma parageneses. The "plume" in this model is a linear zone of upwelling along the length of the back arc region.*

M2 METAMORPHISM (2685-2665 Ma)

M2 Metamorphic Conditions

M2 metamorphism was a pervasive, regionally extensive thermal peak that recrystallized all pre-Late Basin rock units, producing the matrix metamorphic assemblage. M2 parageneses range in temperatures from sub-greenschist to mid-amphibolite facies; 350-620 ºC. Peak metamorphic pressures are low, ranging from 3.5 kb at low grades to 5.0 kb at highest grades, resulting in elevated temperature/depth ratio of 30-40 ºC/km. Metamorphic temperatures increase toward granite/gneiss domes (Mikucki and Roberts, 2003) and the moderately elevated thermal gradients are consistent with a "regional-contact" type of metamorphism (Wilkins, 1997) dominated by conduction and advection of heat into the upper-crust by large volumes of (60-65%) High-Ca granitoids. This magmatic heat influx was further enhanced by the anomalously high Thorium contents of EYC granitoids contributing significant radiogenic heat (Champion, pers. comm. 2007).

M2 parageneses show tight clockwise P-T paths throughout the entire EYC (Figure 160). The widespread clockwise P-T paths are constrained by prograde garnet zoning, mineral reaction textures and PT calculations, all documenting decompression through the peak of metamorphism. The typical sequence of mineral growth in regional metamorphic metapelites is early biotite-muscovite foliation containing staurolite, which is over-printed by small post-kinematic garnet idioblasts and late-stage andalusite porphyroblasts. Maximum pressure conditions were attained before the thermal peak of metamorphism. Maximum limiting prograde pressures are 6.5 kb and typically only 5.0 kb in all parts of the EYC (Figure 160). The ubiquitous clockwise P-T paths indicate crustal shortening and thickening accompanying the M2 thermal anomaly. Decompression at the peak of metamorphism is also induced by destruction of compressive deviatoric stress around large magma bodies (Stüwe and Sandiford, 1994). The tightness of these paths, limited to pressures below 6.5 kb, indicates limited crustal thickening and precludes the crustal over-thickening experienced during major collisional orogenesis. The limited nature of crustal thickening experienced during M2 is consistent with the characteristic heterogeneous distribution of strain and highly partitioned distribution of deformation fabrics in the EYC, in stark contrast with the pervasive reworking and high strains of collisional orogens. Thickening due to inflation by the influx of High-Ca magmas is not considered to have been sufficiently significant to result in crustal over-thickening. The addition of 50% volume of High-Ca magma at 12-18 km depth (current exposure level), is due to neutral buoyancy pooling in the upper crustal, and is not representative of the entire crustal column.

M2 metamorphism pre-dates the deposition of post-volcanic late basins, which do not contain M2 metamorphic parageneses. Lu-Hf garnet ages are consistent with stratigraphy; and suggest that the regional, main-phase matrix parageneses in greenstone sequences grew 17-23 Ma before assemblages within turbiditic post-volcanic late basins (Figures 155, 163). Regional metamorphism prior to the post-volcanic late basins, and thus older than ~2665 Ma, is supported by the peak of High-Ca granitoids in the Kalgoorlie and Kurnalpi Terranes being between 2683-2670 Ma (Figure 11). The regional M2 thermal anomaly possibly continued over a protracted period in concert with the broad peak of granitoid emplacement (Figure 11), leading to a continuum with the more localised thermal anomalies associated with M3a metamorphism in the post-volcanic late basins (Figure 163). Outside of the post-volcanic late basins, it is difficult to distinguish outcrops that experienced the M3a thermal over-print from regional M2 metamorphic parageneses (Figure 145).

M2 metamorphic mineral growth accompanied deformation conditions ranging widely from essentially no strain to syn-kinematic well-developed fabrics. M2 metamorphism broadly overlaps in age with the heterogeneously distributed D2 compressional deformation (Blewett et al., 2004a). Ridley (1993) recognised that the universally low pressures and elevated temperature/depth ratio of regional M2 metamorphism is not compatible with widespread crustal over-thickening, such as in a collisional orogen as had been previously suggested for the Yilgarn Craton (Groves and Phillips, 1987). The spatial association of M2 field gradients and distribution of High-Ca granites (Figure 145) of broadly similar age (Figure 163), infer that metamorphism was in an inversely thermally stratified crust with elevated temperature/depth ratio in the upper crust due to the neutral buoyancy pooling of large volumes of granite below the Kambalda Sequence (Figure 153).

M2 Tectonic Setting

M2 regional metamorphism was induced in part by advection of heat into the upper crust by repeated ascent of felsic magma, repeated transient heating events contributing to pervasive metamorphism (Stüwe et al., 1993) associated with the High-Ca granite bloom (Figure 168). An additional contribution to the high geothermal gradient metamorphism is by moderate crustal thickening during contraction of a previously thinned lithosphere (thinned during D1 volcano-stratigraphy), particularly if thermally insulated by overlying sediments (Thompson, 1989). Being of Archaean age, the High-Ca granitoids of the EYC were initially enriched in radiogenic heat-producing elements in general, and were relatively enriched in Th with respect to other Neoarchaean terranes such as the Superior Province (Beakhouse, 2007). Consequently, the High-Ca magmatic bloom not only advected magmatic heat into the upper crust but also contributed radiogenic heat production that would have extended the M2 thermal anomaly.

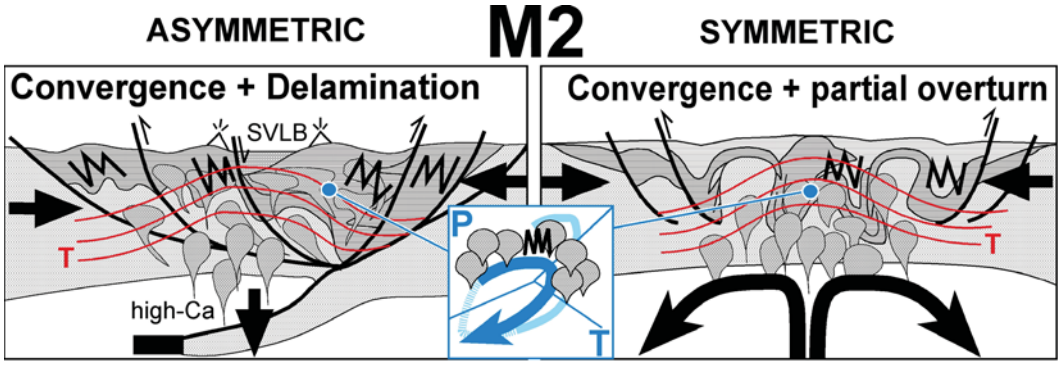

Figure 168: *Cartoons summarizing alternative tectonic scenarios for the M2 period.*

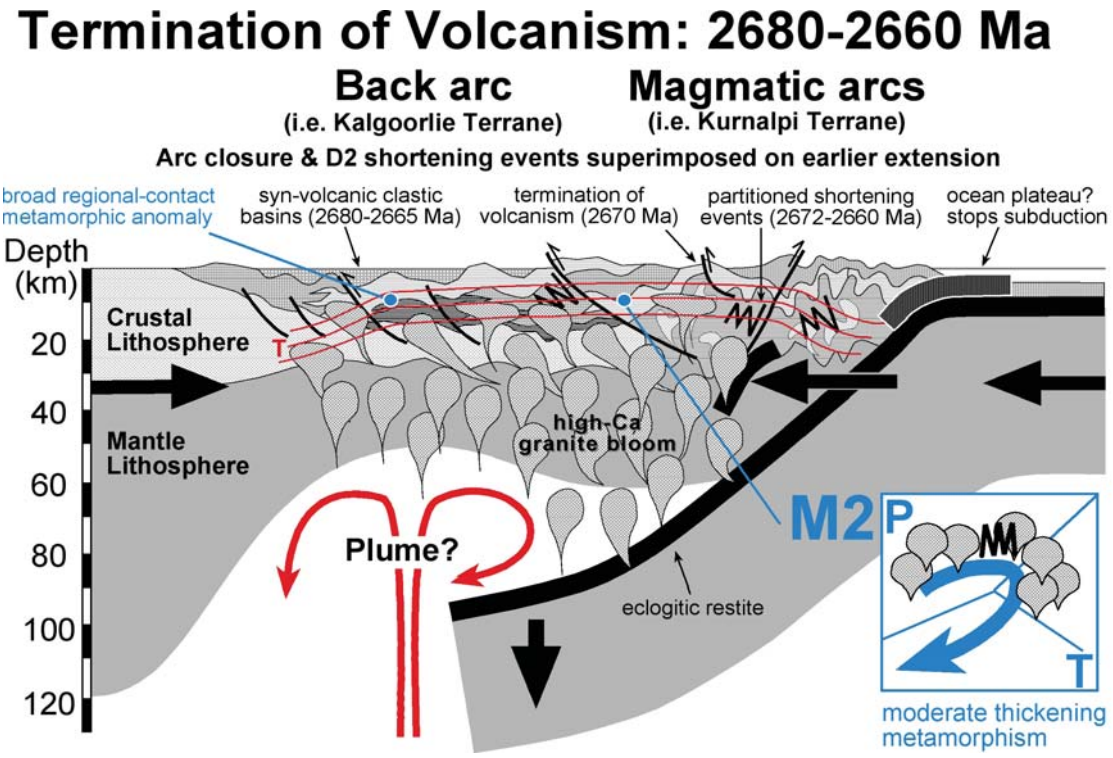

Figure 169: *Cartoon summarizing the preferred tectonic setting for the M2 period encompassing the high-Ca bloom, D2 crustal shortening and termination of volcanism.*

The tectonic setting and cause for the granite bloom has been interpreted as related to lower crust delamination (Blewett and Czarnota, 2007c). The mechanism for delamination is speculative, but its timing would accompany both regional crustal shortening during D2 and the termination of volcanism. Both fundamental changes are possibly related to cessation of subduction (i.e., due to choking of the subduction zone by oceanic plateau), giving rise to propagation of compressive stress through the EYC lithosphere and the initiation of delamination (Figure 169). Cessation of subduction will lead to down sagging of the subducted slab, inducing inflow and melting of the mantle wedge and further contributing to the granite bloom (Figure 169). The catastrophic termination of down-going subduction in this way may in turn give rise to roll back of the subduction hinge resulting in a delayed onset of lithospheric extension during M3a approximately 5-7 Ma later. This would further enhance the high heat flow and granite flux. Lithospheric extension, once initiated by slab roll back, could give rise to run away lithospheric extension leading into the M3a metamorphic period. Furthermore, M2 regional metamorphism thermally prepared the crust for M3a lithospheric extension. The large volume of granite emplaced and the elevated thermal gradient thermally softened the upper crust, leaving it sufficiently ductile to be primed ready for subsequent D3 lithospheric extension. Consequently, M2 and M3a are causally linked by an extended thermal perturbation related to magma influx, thermal softening and run away lithospheric extension, all contributing to elevated thermal regimes during this protracted period.

M3a METAMORPHISM (2665-2650 Ma)

Extensional M3a Metamorphism

M3a Metamorphic Conditions

Post-volcanic turbiditic basins (PVTB), such as Mt Belches Formation, are distinctive well-constrained rock units that are diagnostic of extensional settings. Metamorphism of these stratigraphic units offers a unique opportunity to document the thermo-barometric evolution of a specific well-constrained time period (2665-2650 Ma) in the evolution of the EYC. Peak metamorphism of the Mt Belches Formation was at 500-580 ºC and 4±1 kb, indicating high temperature/depth ratio of 40-50 ºC/km. Post-kinematic porphyroblasts indicate that peak metamorphism accompanied a static stress regime, subsequent to formation of an early burial, bedding-parallel mica foliation. P-T paths follow anticlockwise loops of heating with burial, followed by near isobaric cooling paths (Figure 111). Most samples have up-P prograde-burial trajectories, from early cordierite-andalusite parageneses, to peak garnet and post-peak staurolite growth, indicating anticlockwise P-T loops. Recognition of a post-2665 Ma high-heat flow thermal anomaly accompanying turbiditic basinal infill, has implications for driving basinal brine circulation, and release of large volumes of hydrous fluid by both dewatering and dehydration reactions (Figures 170, 171).

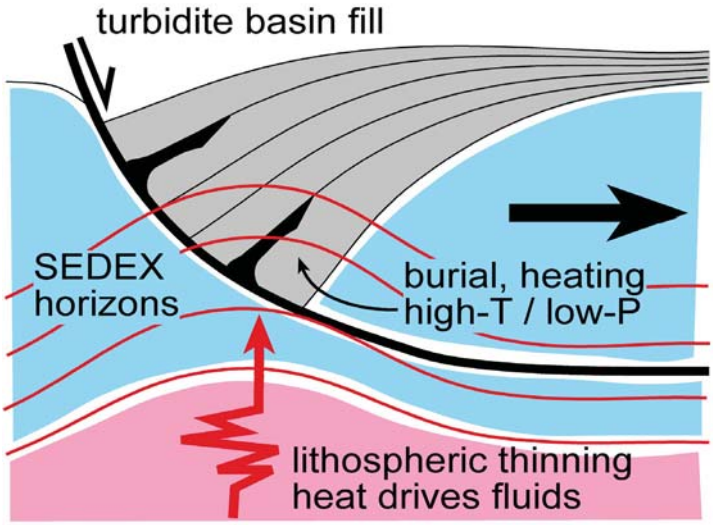

Figure 170: *Simplified model for syn-sedimentary exhalative Pb-Zn-Ag±Cu deposits in extensional basins.*

Extent of M3a Thermal Anomaly

The PVTB's are a crucial time marker that "samples" the PT conditions and thermal regime in operation between 2665-2650 Ma. Metamorphic parageneses in all older stratigraphy (volcanics) could potentially be a combination of both M2 and M3a metamorphic mineral growth – depending on the extent of M3a thermal effects. There are two possibilities for the extent of the M3a thermal overprint. [1] Either M3a has a wide regional thermal footprint, in which case the EYC metamorphic pattern is a combination of both M2-M3a effects. [2] Or alternatively, M3a thermal effects are restricted to spaced elongate domains of high heat flow associated with maximum rifting, coinciding roughly with exposed (and also below eroded) PVTB's (Figure 171). It is argued that the M3a thermal anomaly must be localised because the characteristic anticlockwise P-T paths are developed only in post-M2 stratigraphy or rarely in older rocks that have experienced D3 extensional deformation induced mineral growth (Figure 146). A widespread M3a thermal anomaly would obliterate the widely developed M2 mineral relationships indicating clockwise P-T paths (Figure 145).

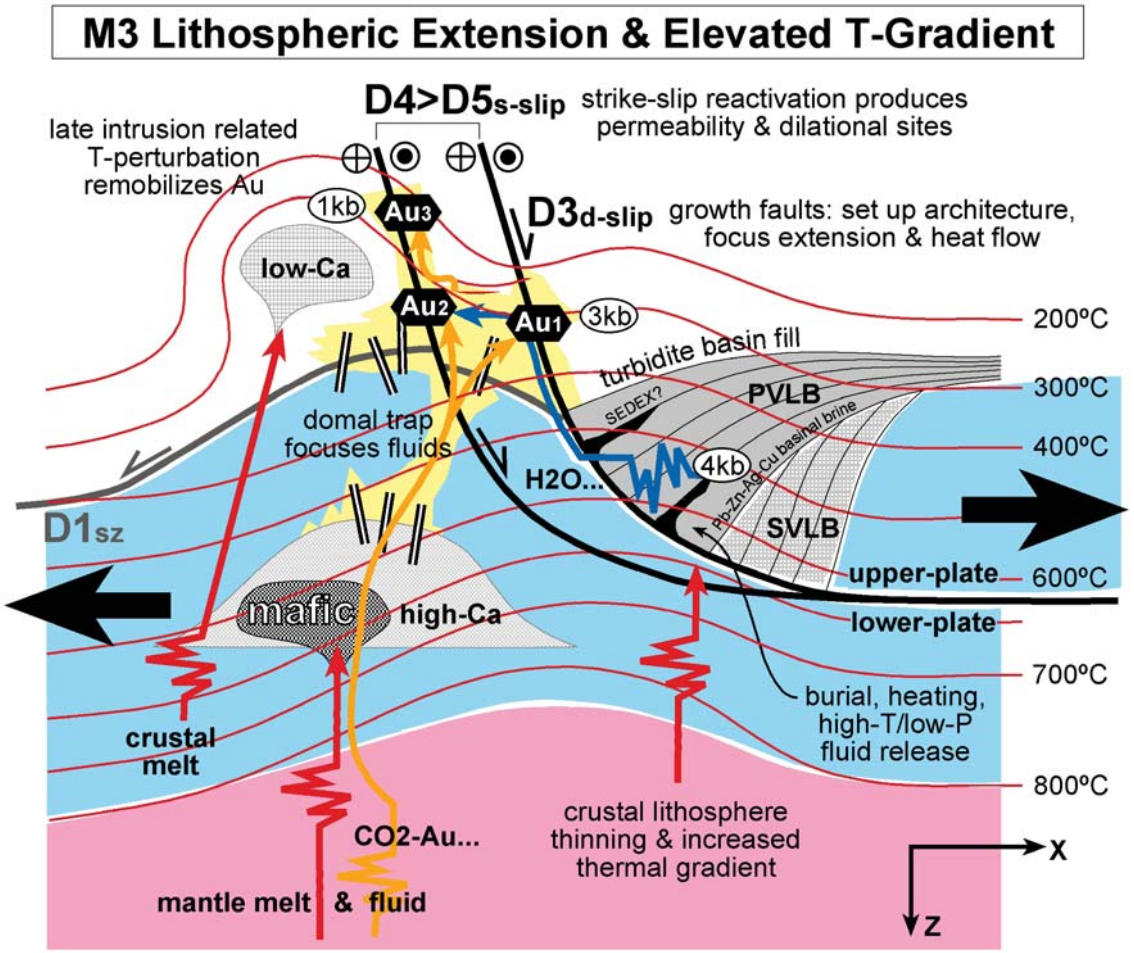

Figure 171: *Model for M3a lithospheric extension at ~2665-2650 Ma, and the consequent outcomes of: post-volcanic late basin rifts; listric growth fault architecture; input of mantle components into the shallow crust such as mafic granites and CO_2-metal-rich fluid; M3a post-kinematic thermal perturbation resulting in low-Ca crustal melting; H_2O-rich fluid release and fluid driving and ultimately resulting in fluid mixing and primary Au-mineralization. A lagging effect is later phases of Au-mineralization, by remobilisation during successive M3b thermal perturbations associated with emplacement of the low-Ca crustal melts and development of suitable mineralization sites by strike-slip reactivation of structures.*

Outlining the extent of M3a rifting and thermal overprint is hampered by there being only remnants of PVTB's currently exposed and the original extent of stratigraphic markers deposited between M2 and M3a is not known. An additional complication is that lower-plate rocks in an extensional setting such as M3a may experience clockwise P-T paths that are not distinguishable from M2 metamorphic parageneses. Consequently, outside of PVTB's, M2 versus M3a parageneses will be hard to resolve. This resolution is important because of the geodynamic contrast between these two events (compression versus extension), but is of little significance in absolute metamorphic conditions which are similar and the age of the events, which are separated by only ~5-10 Ma. However, in light of the causal relationship between gold and M3a extension (see below), defining the extent of the M3a thermal anomaly is crucial to recognition of Au-mineralization corridors on a large scale.

If high-P M1 parageneses and old (>2735 Ma) stratigraphic units were exhumed by M3a extensional telescoping of the upper-crust, these rock units will serve as good indicators of the lower-plate margin to zones of extreme M3a extension (Figures 146, 172). Spaced distribution of basins suggests M3a extension was locally partitioned by growth faults controlling development of the PVTB depositional basins. Squire et al., (2007) has shown that some of these growth faults may have reactivated older growth structures that controlled the development of syn-volcanic basins (SVB; Figure 146). Metamorphic patterns are consistent with extensional telescoping of the upper crust during M3a, with transport away from lower-plate domal cores, stepping outwards to successively younger extensional structures (Blewett and Czarnota, 2007c). These geometries resulted in exhumation of panels of deeper crustal levels and their juxtaposition against shallow crustal level rocks, as movements on different extensional structures migrate across this margin. The presence of old (>2735 Ma) stratigraphic units and high-P M1 parageneses indicate that the margin of lower-plate settings, and the young PVTB's (<2665 Ma) occupy upper-plate settings, in extensional shear systems (Figure 146). An extensional shear system with PVTB in the upper-plate is well illustrated by the seismic profile across the Ockerburry shear zone at Leonora (Blewett and Czarnota, 2007c). Additional, unrecognised domains of M3a high heat flow probably exist in settings where PVTB's at slightly higher crustal levels have been subsequently eroded. The similar peak metamorphic conditions of M2 and M3a mean that these cryptic M3a domains will be hard to locate, distinguished only by their contrasted P-T paths. Other post-volcanic basins in addition to the Mt Belches Basin, such as Scotty Creek and Wallaby have biotite and chloritoid parageneses, indicating temperatures >420 ºC. Further work is required to document the P-T evolutions of all known post-volcanic basins to test the extent of M3a effects and commonality of P-T evolutions.

M3a P-T Evolutions in Older Stratigraphy

Anticlockwise P-T paths through peak conditions of ~570 ºC and 3.2-4.0 kb are also documented from a number of sites outside PVTB's, within the under-lying stratigraphy (Figure 161). These experienced identical high thermal gradient metamorphic evolutions to those in PVTB's. All are distributed along a narrow zone within and in close proximity to the Ockerburry shear zone (Figure 161). The main sites are Kyanite Hill at Leonora, New Celebration Mine (Hodge, 2007), Gordon Mine and Mt Martin, linking with the Mt Belches basin and defining a linear domain of 360 km length. These parageneses are interpreted as further expressions of M3a metamorphism because of the uniquely similar P-T paths, which are distinct from P-T paths in all other metamorphic episodes in the EYC. At present, all correlated M3a parageneses have only been identified in association with the Ockerburry shear zone, indicating that this structure was the dominant crustal structure accommodating M3a lithospheric extension in the EYC. It is anticipated that further metamorphic work may recognise M3a effects associated with other crustal structures showing extensional histories, such as the Mt Ida and Hootanui shear zones and arcuate shaer zones around the lateral terminations of granitoid-gneissic domes (Blewett and Czarnota, 2007c).

M3a Metamorphism in Extensional Basins

Crucially, metamorphism of the PVTB's in high temperature/depth ratio regimes (40-50 ºC/km) at 10-12 km depth is diagnostic of lithospheric extensional settings. Cambrian examples of extensional basins show that basin fill, burial and metamorphism can occur in short time frames of 2-10 Ma in

the 10-15 km deep Kanmantoo Basin in South Australia (Foden et al., 2006), and ~40 Ma in the >20 km deep Irindina Province in the east Arunta (Buick et al., 2005). The Kanmantoo Basin example of extensional basin metamorphism shows an anticlockwise P-T path of heating with burial followed by isobaric cooling (Alias et al., 2002), almost identical to those developed in the Mt Belches basin (Figure 111). Consequently, M3a metamorphism is interpreted to have broadly accompanied basin infill, with a lagging peak in metamorphism between 2665 and 2650 Ma. Thermal modelling of lithospheric extension show that elevated temperature/depth ratio and metamorphic conditions like that experienced in M3a, can be attained within 10 Ma in the upper crust only if blanketed by an insulating layer of sediments (Buck et al., 1988; Issler et al., 1989; Sandiford et al., 1998). The documented 10-12 km thickness of Mt Belches Formation during metamorphism would have sufficiently incubated the high heat flow generated by lithospheric extension. The thermal anomaly recorded by PVTB rocks may have had a larger footprint than the currently exposed basins. Evidence for a wider extent will be difficult to determine because pre-existing M2 parageneses formed at very similar PT conditions (though through different P-T paths of evolution). If PVTB's occupied elongate, growth-fault controlled settings indicting domains of maximum M3a extension, the zones with highest M3a heat flow (and consequent fluid flow) will also be spaced elongate domains mirroring the distribution of exposed and eroded PVTB's.

M3a Deformation History and Clockwise P-T Paths

Clockwise P-T paths are described from a small number (n=4) of samples defining a narrow N-S sub-domain east of the centre of the Mt Belches Formation (Figures 133, 161). This narrow N-S zone is otherwise devoid of anticlockwise evolutions, which are ubiquitous to the rest of the Belches Formation. The clockwise P-T paths have been documented by PT calculations, garnet zoning and textural relationships such as early foliations containing staurolite being over-grown by peak metamorphic garnet and later andalusite and cordierite (Figure 109).

The apparently contrasted burial-heating-exhumation histories in different parts of the Mt Belches basin can be explained in three competing hypothetical scenarios. Either the clockwise P-T paths represent older metamorphic parageneses (i.e., M2), or are coeval and co genetically related to the processes that generated the ubiquitous M3a anticlockwise P-T paths or the clockwise P-T paths are not real.

[1] Older clockwise evolutions such as M2 are plausible only if the Mt Belches Basin is older than other PVTB's or alternatively if the basin is more complex than currently mapped and contains unrecognised older stratigraphy in parts of the basin. The maximum deposition age of 2666 Ma (Hall, 2006) precludes the whole basin being old enough to record M2 metamorphic parageneses. Outcrop exposure and the currently available mapping (Painter and Groenewald, 2000) are sufficiently detailed to show a single basinal sequence. There is no evidence for different rock units or structures delineating the N-S sub-domain with clockwise P-T paths.

[2] Alternatively, clockwise P-T paths may be experienced in lower-plate settings cotemporaneous with anticlockwise paths in the upper-plate, during M3a lithospheric extension. Lower-plate rocks below an extensional detachment will experience decompression accompanying the thermal anomaly generated by lithospheric thinning, giving rise to clockwise P-T paths. Such a scenario probably does not apply to the Mt Belches basin because there is no evidence for major extensional faults internally within the basin (Painter and Groenewald, 2000).

[3] The preferred interpretation is that clockwise P-T paths are invalid because they have been constructed from unrelated mineral parageneses formed in different metamorphic events. All samples come from within 600m of significant Proterozoic dolerite dykes or within 1000m of the major Palaeoproterozoic Jimberlana mafic-ultramafic dyke. Late-stage ameboid cordierite growth, that underpins the clockwise P-T path in three samples, is interpreted to have formed in a transient thermal pulse associated with dyke emplacement. Consequently, the apparent clockwise P-T paths are a composite of more that one metamorphic event and considered invalid interpretations for these rocks. Garnet compositional isopleths in the fourth sample shows isobaric heating and contains a

rare example of metamorphic K-feldspar. Both observations are consistent with a heating pulse at shallow crustal levels associated with Proterozoic intrusions.

The map pattern of the Mt Belches basin is dominated by upright chevron folding with inter-limb angles of 23-60º (Painter and Groenewald, 2000). These fold the main fine-grained bedding-parallel foliation containing prograde mineral parageneses. This foliation is interpreted to have formed during vertical shortening and extension during basin formation, infill and prograde heating. This main foliation is associated with least one generation of early isoclinal folding locally developed in parts of the Mt Belches basin (Painter and Groenewald, 2000). These are interpreted to have been recumbent isoclines formed during basin extension and vertical shortening, similar to early isoclines and flattening fabrics described from other extensional metamorphic basins (Webb, 2001; Alias et al., 2002; Foden et al., 2006; Buick et al., 2005; Hand and Maidment, 2006). The dominant upright folding of the basin is correlated with D4a ENE-WSW shortening episode of Blewett and Czarnota (2007). This shortening apparently post-dates the thermal peak in the Mt Belches basin and is expressed as minor flattening of the pre-existing main foliation, particularly evident around the post-main foliation, peak metamorphic garnet and staurolite porphyroblasts. No new penetrative foliation was developed during shortening of the basin and the developed axial planar crenulations are rare and did not involve appreciable new mineral growth. Despite post-peak shortening of the Mt Belches basin in the order of 65% there is no significant new fabric development or mineral growth. As a result, the metamorphic consequence of shortening and the P-T paths followed by samples, were not captured in the rock record. It is anticipated that the post-peak shortening of the basin would result in minor burial during cooling possibly giving slightly up-P cooling trajectories, such as described by Clarke et al., (1987) from the Olary Province.

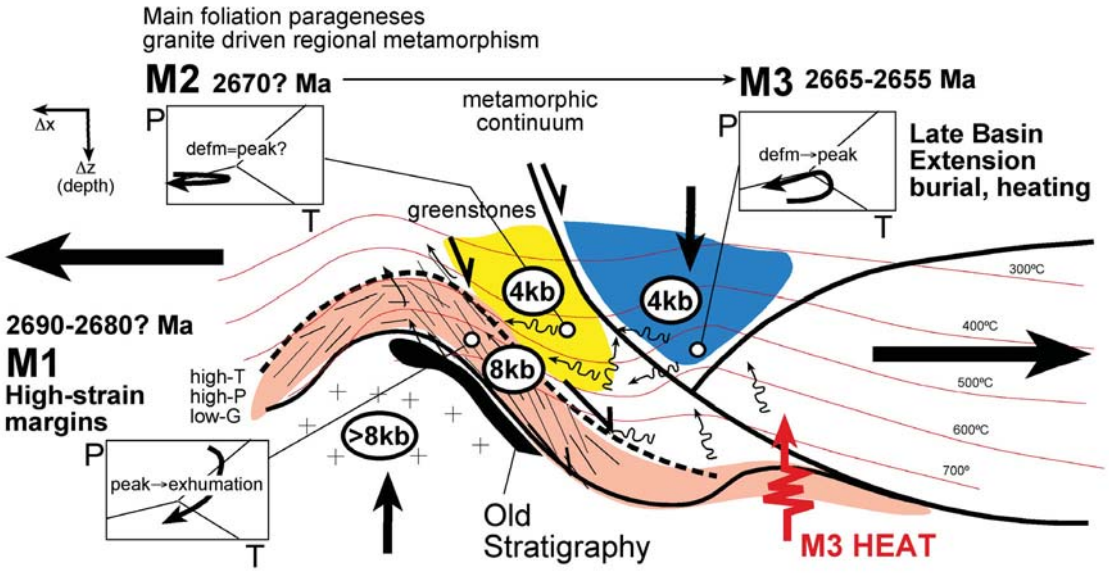

Figure 172: *Cartoon illustrating a model for the metamorphic consequences of lithospheric extension during the M3a period accompanying granitoid domes and late-basin development. Note this model also explains the juxtaposition of M1, M2 and M3a metamorphic parageneses into the same crustal level.*

M3a Tectonic Setting

A model for the crustal architecture during M3a lithospheric extension and metamorphism is presented in Figure 171 that summarises all barometric, thermal, magmatic and fluid consequences of lithospheric extension. The structural architecture developed by lithospheric extension produces upward transport by domal culminations in the lower-plate and downward transport by depositional basins in the upper-plate, separated by low-angle extensional shear zones or growth faults (Figures 17, 172). The flanks of lower-plate domes may be recognised by exhumed high-P M1 parageneses and old stratigraphy (>2750Ma). Lower-plate domal cores will be recognised by exhumed High-Ca

granite batholiths and high proportions of later Low-Ca granites triggered in part by the M3a thermal anomaly and decompressional melting in the lower-plate (Figure 146). The upper-plate domain accommodated lithospheric extension and subsidence, focused the high-heat flow, and will be recognised by post-volcanic turbiditic basins, mantle sourced syenite, lamprophyre, carbonatite and mafic granites and rifts bound by growth faults.

A repeated pattern showing the features of lower-plate domes, dome flanks, extensional shear zones and upper-plate basins, is seen in different parts of the EYC. The transition from lower-plate domes to margins contain outcropping old (>2750 Ma) stratigraphy and at higher structural levels are major extensional shear zones that contain the high-P M1 metamorphic parageneses and at higher structural levels still, above the shear zones are upper-plate PVTB troughs (Figure 146). This pattern is consistent with extensional telescoping of the crust with transport away from lower-plate domal cores and progressive stepping outwards of successively younger extensional structures, such that previously upper-plate domains become slivers in a new lower-plate. This telescoping process would result in the exhumation of panels of deeper crustal levels (old stratigraphy, high-P rocks) and would juxtapose them against shallower crustal levels as extensional structures migrate across this margin. The maximum pressure experienced by the currently exposed level of granitic/gneissic domes is unknown. Consequently the presence of old (>2750 Ma) stratigraphic units, act as a proxy to indicate that rocks from deeper crustal levels are being exhumed by the domes. Crucial further work required is the documentation of the pressure history in the domal regions. It is also crucial that stratigraphic and metamorphic datasets are integrated with structural datasets to better define lower-plate vs. upper-plate domains during M3a extension, throughout the EYC. Outlining upper-plate vs. lower-plate domains will be an important contribution towards defining the distribution of high heat flow domains during M3a and thus help constrain potential mineralization corridors.

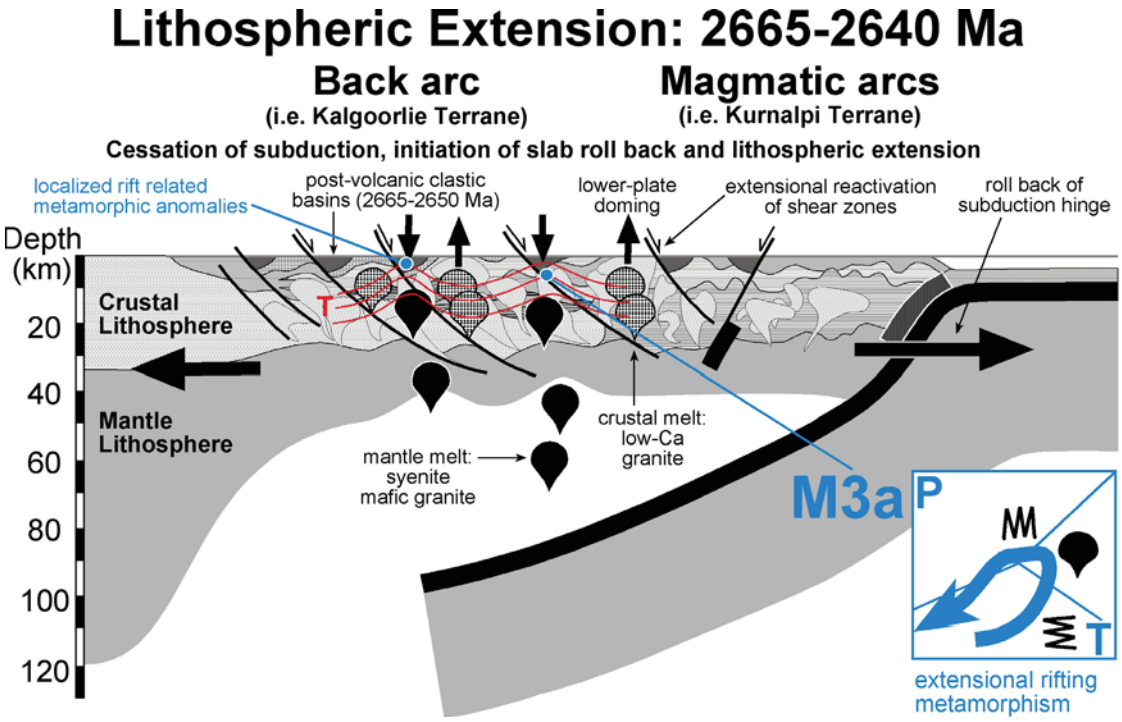

Figure 173: *Cartoon summarizing the preferred tectonic setting for the M3a period encompassing lithospheric extension induced by roll back of the subduction hinge.*

It is unlikely that M3a lithospheric extension was homogeneously partitioned across the ~300 km width of the EYC, but heterogeneously distributed into a number of crustal-scale extensional shear zones. M3a lithospheric extension would have been locally controlled and partitioned by dip-slip reactivation of the pre-existing widely spaced network of arcuate shear zones. Deep seismic profiles indicate most crustal structures have listric form and are inclined to the east (Goleby et al., 1993,

2002a). These pre-existing structures include growth faults associated with SVB's, and their reactivation lead to development of PVTB depositional troughs. The PVTB troughs are sited at zones of maximum lithospheric extension during M3a and will approximately coincide with the zone of highest geothermal gradients and heat flow. The form of the domains of high heat flow and rifting is anticipated to be relatively narrow and elongate, arcuate to curvi-linear zones interspersed by wide lower-plate domains of doming (Figure 146).

The ultimate driver for increased M3a lithospheric extension is necessarily speculative. The timing of M3a metamorphism post-dates both EYC volcanism and the main peak of the High-Ca granitoid bloom. This timing indicates M3a extension started after cessation of down-going subduction and consequently, it is possible that gravity driven slab roll back induced lithospheric extension of the EYC during M3a (Figure 173). An alternative scenario of delamination of the lower crust as suggested for M2 metamorphism and the granite bloom, can potentially explain the elevated M3a thermal gradients but does not explain features indicative of crustal lithosphere extension, such as extensional basins and growth faults. Another alternative model for lithospheric extension is by gravitational spreading in response to lithospheric over-thickening, producing a wide Basin and Range-type setting (Figure 174; Tirel et al., 2006). There is no evidence that the pre-M3a lithosphere was over-thickened to the degree that gravitational collapse could be induced. D2 contraction accompanying M2 metamorphism did not result in deep burial and crustal over-thickening such as in continent collision. Furthermore, earlier lithospheric thinning during D1 events meant that subsequent minor and partitioned D2 contraction was merely thickening a previously thin crustal lithosphere.

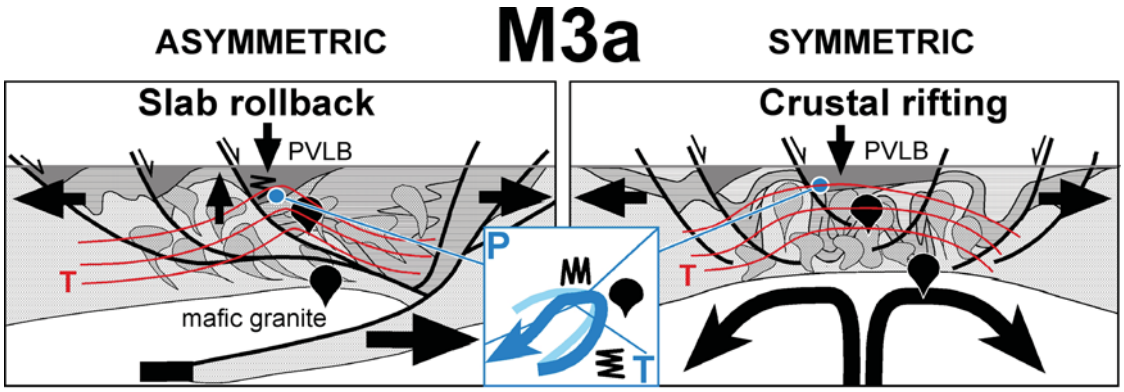

Figure 174: *Cartoons summarizing alternative tectonic scenarios for the M3a period.*

Extensional Depositional Basins

Extensional basins controlled by crustal-scale growth faults were already developing during M2 and prior to the post-volcanic turbiditic basins associated with M3a lithospheric extension. Four and possibly five, distinct groups of extensional basins have been recognised. Most of these basins have distinct geodynamic settings and should be distinguished by more diagnostic nomenclature than "late basins". Squire (2006, 2007) has documented at least two and possibly three, generations of mafic to felsic, feldspar-rich, coarse clastic granule beds and conglomerates, some of which are volcanoclastic. Deposition was in long-lived basins controlled by growth faults (i.e., Playa Fault) and maximum deposition ages of 2686 and 2680 Ma indicate deposition synchronous with mafic and felsic volcanism in the EYC, which was terminated at ~2670 Ma. For simplicity, these depositional basins are collectively labelled syn-volcanic basins (SVB), of which the Black Flags Formation is an example. There are two types of clastic basins formed subsequent to termination of volcanism in the EYC. Post-volcanic turbiditic basins (PVTB) are dominated by turbiditic sequences and contain rare intrusives. Examples are Merougil, Kanowna Belle, Granny Smith, Wallaby and Mount Belches basins. Maximum deposition ages are 2665 Ma for Granny Smith and Wallaby and 2666 Ma for the Mt Belches basin. The Mt Belches basin over-laps some growth faults and may be slightly younger than other PVTB (Charlotte, 2006). Very similar large-scale ensialic rift basins, with high

sedimentation rate turbidite fill of identical age (2680-2660 Ma), are developed in the Slave Craton (Bleeker, 2003). An older PVTB sequence is the White Flag Formation in the Kalgoorlie Terrane, with a maximum deposition age of 2669 Ma. The youngest basin type is post-volcanic fluvial basins (PVFB), *sensu stricto* "late basins", with the Pig Well basin and Kurrawang Formation as examples and maximum deposition age of 2659 Ma.

M3a Fluid Flow and Mineralization

M3a metamorphism and lithospheric extension has crucially led to the formation of three new fluid sources and reservoirs and controlled the processes for their transportation and flux into similar levels in the upper crust. The three fluid types are:

[1] Metamorphic fluid released by dehydration of hydrous minerals during the M3a prograde metamorphic event. Dehydration fluid will be released from both new turbiditic basinal sequences and also underlying stratigraphy that has not been substantially dehydrated in earlier metamorphic events.

[2] The new post-volcanic turbiditic basins in extensional rifts are responsible for dropping large volumes of basinal fluids to crustal levels of 10-15 km depth. Dewatering during burial will release large volumes of saline basinal fluids, possibly also with high metal ion loads (i.e., Pb, Zn, Ag, Cu). Both dehydration and basinal sources will create new large volume reservoirs of hydrous fluids in the upper crust, contributing to an ambient high fluid to rock ratio during M3a. This ambient hydrous fluid regime is temporally overwhelmed by the localised and transient flux of anhydrous mineralising fluids and returns back to the ambient hydrous fluid regime by back-flow into the flushed domain (Neumayr pers. comm. 2008). In contrast to the usually short-lived nature of fluid regimes (Thompson, 1983; Yardley and Valley, 1997), it is argued that the ambient hydrous fluid regime is relatively long-lived because of the extensional stress regime during M3a. Furthermore, continuous fluid generation due to prograde heating in a long-lived M3a thermal anomaly extends the period of ambient hydrous fluid.

[3] Lithospheric extension will facilitate the generation and transport of dry CO_2-rich and H_2-CH_4-rich fluids, possibly also with high metal ion loads (i.e., Au), from the mantle into upper crust.

Lithospheric extension and thermal anomaly associated with M3a metamorphism will not only generate these three new fluid sources, but will also be crucial in the driving of fluid flow during M3a. Fluid flow will by influenced in this way by three processes: [1] by creating steep localised thermal gradients to drive fluid flow, [2] by forming extensional deformation structures to channel fluid flow and dynamic pumping by movent within these structures and [3] the extensional stress regime will direct lateral and downward fluid flow.

The extensional stress regime is crucial to mineralization processes because this regime allows both horizontal and in part downward fluid flow trajectories. In contrast, static or convergent stress regimes model steep upward fluid flow trajectories (Sheldon et al., 2007, 2008). Numerical modelling of M3a settings similar to those described above, show patterns of horizontal and downward fluid flow and focusing into extensional shear zones (Sheldon et al., 2007, 2008). These flow patterns will facilitate both the juxtaposition and mixing of different fluid sources and the focusing into deformation structures (dynamic permeability creation), leading to precipitation and mineralization. In particular the extensional stress regime facilitates downward transport of fluids out of PVTB's in the upper-plate, tapping this distinct saline metal-rich fluid reservoir. Consequently, extensional settings provide a mode that can mix both deep and shallow fluids. Furthermore, fluid circulation cells associated with cooling magmatic intrusions remain longer-lived in extensional stress regimes (Sheldon et al., 2008), further increasing the temporal window for mineralization coinciding with formation of suitable structural sites.

The M3a thermal anomaly coincides in age with the second Au-mineralization event (Au2) and immediately pre-dates the main Au-mineralization events (Au3 to Au4) during M3b by only ~10 Ma (Figure 155). The close temporal association suggests important causative links between M3a lithospheric extension and metamorphism and Au-mineralization events. The M3a thermal anomaly

was ultimately the first-order cause for hydrothermal alteration (and Au) events in M3b by both generating the large hydrous fluid reservoirs in the upper crust (by dewatering and dehydration) and the long-lived and waning M3a thermal anomaly remained important in driving fluid circulation in conjunction with superimposed punctuated deformation events. M3a lithospheric extension gave rise to both architectures and processes allowing the mixing of different fluid types such as hydrous fluids, metal-rich CO_2–SO_2 magmatic fluids and possibly Au-bearing, dry and reduced H_2-CH_4 fluids from the mantle, leading to precipitation in suitable dilational sites produced by accompanying deformation (Figure 171).

Decompression of the lower-plate with anomalous heat flow during M3a lithospheric extension generated lower crustal melting. Slow accumulation and transport of this melt would have resulted in a significant delay before pooling in the shallow crust (3-10 km). This delay is approximately 10-15 Ma in the EYC. The effect of decompression of the lower-plate domes would have further enhanced partial melt production at these sites, resulting in the greater concentration of Low-Ca granites in the domes. Recognition of the delayed by co-genetic association between M3a lithospheric extension and Low-Ca granites (and Au4 mineralization) has important Yilgarn-wide implications. Late-stage Low-Ca granites of broadly similar age are found throughout the Yilgarn Craton. This implies that M3a lithospheric extension was propagated through the entire width of the Yilgarn Craton. If true, the model for gold mineralization in parts of the Southern Cross and Murchison Terranes may be similar to the EYC (Figure 171). Craton-wide M3a effects indicated by Low-Ca granites should drive a future program to explore for extensional shear zones and PVTB's to guide large-scale exploration for Au.

The Phanerozoic analogue for post-volcanic turbiditic basins in an extensional rift setting is the 520 Ma Kanmantoo Basin sitting unconformably on the Adelaidean Sequence. This basin has many salient features in common with PVTB's of the EYC; turbidite sequences, extensional growth fault margin, anticlockwise P-T path, 12-15 km burial, peak temperatures of 580 ºC, high temperature/depth ratio, burial with heating, late-stage basin shortening and associated granitoids containing mantle component. Deep turbiditic basins bound by growth faults have the high heat flow and basinal brines appropriate for sourcing and driving fluids for generation of syn-sedimentary exhalative deposits (Figure 170). The Kanmantoo Basin contains SEDEX Pb-Zn-Ag-Cu mineralization typical of these settings in the Palaeozoic and Proterozoic.

M3b ALTERATION (2650-2620 Ma)

M3b Alteration Conditions

The M3b period, subsequent to metamorphism of the PVTB's, is characterised by a switch from dip-slip extensional kinematics to multiple strike-slip kinematic episodes (Blewett and Czarnota, 2005) through a protracted period of high but waning thermal gradients and multiple Au-mineralization events. Metamorphic mineral growth was within hydrothermal alteration assemblages that over-print regional metamorphic parageneses (M2-M3a) and was strongly partitioned into restricted domains and is associated with veining. Hydrothermal alteration associated with main phases of Au-mineralization (~2650-2640 Ma) occurred across a wide range of temperatures 250-500 ºC but similar crustal depths of 3.0-3.5 kb, across most parts of the EYC, indicating moderately elevated thermal gradients of 30-50 ºC/km. This represents crustal levels only 3 km shallower than peak metamorphism during M2 and M3a. Later episodes of alteration and Au-mineralization (~2630-2620 Ma) occurred at pressures as low as 1 kb, while still at relatively elevated alteration temperatures (250-350 ºC) indicating very high apparent temperature/depth ratio (G >70ºC/km). This event coincides with a secondary peak of shallow crustal, Low-Ca granites, which possibly supplied the heat necessary to drive fluid circulation and gold remobilisation.

For typical conditions of fluid to rock ratios and flow rates, the fluid and host rock remain thermally equilibrated. Any transient thermal difference between fluid and rock will be short lived and equilibrated quickly. Consequently, given the typical error range in metamorphic studies, temperatures derived from alteration assemblages and trapped fluid inclusions will be representative of the temperature conditions within the alteration system. In most conditions, fluid flow through

permeability pathways and along grain margins is typically not a significant mechanism for transporting heat and modifying thermal gradients and ambient temperature of the rock mass on a regional scale. However, on the scale of an alteration system, the transient thermal difference between fluid and rock in high volume, high flow rate and high fluid to rock ratio conditions may be sufficient to locally re-equilibrate the rock mass at higher temperatures. The local thermal anomaly within an alteration system gives an apparent very high temperature/depth ratio, when compared with the ambient conditions at the same crustal level outside the alteration system (Figure 155). Similarly, pressures recorded by fluid inclusions are continuously equilibrated with changing conditions and should generally represent minimum estimates of crustal depth at entrapment (Hagemann and Luders, 2003). However, in dynamic alteration systems the common scenario of fluid over-pressure (Cox, 1995) can potentially lead to over estimation of the crustal depth at entrapment.

Multiple fluid generations and fluid types, ranging from reduced H_2O-rich to oxidized CO_2-SO_2-rich to reduced H_2-CH_4-rich (Walshe et al., 2008), are evident in different alteration systems (see Mineralization Fluids section below). Alteration systems are highly variable, showing strong spatial (i.e., patchy) and temporal (i.e., numerous alteration and veining events) partitioning of different alteration assemblages, reflecting fluids of different vapour composition, cation composition, redox and pH, all in close proximity. Alteration assemblages vary on scales too small to have experienced significant differences in T and P and are primarily controlled by fluid chemistry, pH and redox (e.g., Mikucki, 1997; Neumayr et al., 2007). Alteration systems on the whole reflect a pattern of pervasive hydrous alteration, and Au-mineralization within this broad system is associated with gradients between different fluid types: inparticular between oxidized-alkaline CO_2–SO_2 and reduced-alkaline H_2–CH_4 fluids (Neumayr et al., 2007; Neumayr, 2008; Walshe et al., 2008a,b). Most zones of alteration are barren, implying that alteration systems primarily involved a large flux of a single fluid type that may have been Au-free or lack mechanisms for precipitation. These general ambient alteration systems are either from Au-free hydrous fluids such as those sourced from late basins and metamorphic dehydration reactions or carbonic fluids from magmatic sources.

Multiple mineral growth events throughout M3b, define a broad continuum of elevated temperature/depth ratio that persisted from M3a (Figure 155). This long-lived high thermal budget is due to a combination of factors, such as conductive thermal lag from M3a, continuing lithospheric extension or transtension and emplacement of significant (35%) volumes of Low-Ca granites. Low-Ca crustal melts were initiated during M3a lithospheric extension, followed by pooling, emplacement and crystallization in the upper crust ~10 Ma later, representing a causal link between M3a and M3b thermal periods. Similarly, M3a fluid production by dewatering of PVTB brines and dehydration of hydrous minerals in both PVTB sediments and low-grade regional (M2) metamorphic domains sourced the large volumes of hydrous fluid responsible for much of M3b alteration. This causal link is supported by stable isotope and fluid inclusion salinity data indicating meteoric fluid that has undergone exchange in post-volcanic sedimentary basins. (e.g., Mikucki, 1997). The large ambient fluid volumes produced were possibly important in setting up permeability pathways and alteration systems where mixing with secondary, metal-rich, fluids could occur. A third causal link between M3a and M3b is the formation of [1] mantle-derived magmas (Mafic granites and Syenites) and [2] pathways for dry and reduced mantle-derived fluids in response to M3a lithospheric extension; both being possible sources for bringing Au into the upper crust (Figure 171).

D5 Transtensional Exhumation

Most Au-mineralization events (Au1-Au3) record pressures from fluid inclusions and alteration mineral parageneses of 3-4 kb. Whereas a series of young Au-mineralization events, collectively labelled Au4, occur at pressures of 1 kb recorded primarily in fluid inclusions across many ore deposits. Consequently, exhumation of the EYC from 10-14 km (3-4 kb) to 3.5 km (1 kb) crustal levels occurred in the period between 2645 Ma (Au3) and 2630 Ma (Au4). This exhumation event stripped 7-10 km of crust in less than 15 Ma. Indicating a specific concentrated event responsible for ~70% of EYC exhumation, in contrast to the slow protracted denudation before and after this event.

Temperatures from the low-P alteration assemblages were only slightly lower than earlier alteration events, resulting in very high temperature/depth ratio (up to 70 ºC/km) due to the large pressure reduction. Away from the alteration systems, no new mineral parageneses were formed and the ambient background temperatures cannot be estimated. Nevertheless, background pressures were equivalent to those recorded by fluid inclusions in the alteration assemblages. EYC exhumation is also recorded by Al-in hornblende geobarometer calculations from late-stage granitoids recording pressures as low as 2kb (Figure 96). The late-stage low-P Au-mineralization events and exhumation event coincide in age with D5 dextral transtension (Blewett and Czarnota, 2007c). Transtensional modes are a common scenario leading to exhumation late in orogenic histories. For example the Cambrian transpressional Kaoko Belt progressed into transtension with a small shift in stress fields at cessation of supercontinent assembly and initiation of subduction at the margin of Gondwana (Goscombe and Gray, 2008). Or alternatively correlates with sub-vertical shortening indicated by the formation of sub-horizontal crenulations during the last structural episode called D6.

M3b Tectonic Setting

The strong causal relationships between M3a and M3b intimately links Au-mineralization with the thermal evolution of the crust (Figure 155). This period follows on from a significant switch in lithospheric response to far field tectonic processes: from crustal growth (volcanism-subduction-arc accretion?) to lithospheric extension. Lithospheric extension was possibly first initiated at ~2685 Ma with the formation of growth fault controlled syn-volcanic late basins (SVB), steep increase in the volume of High-Ca granitoids and regionally extensive elevated thermal gradient (M2). Coincident with the termination of volcanism, accelerated lithospheric extension from ~2665 Ma generated the M3a thermal perturbation and PVTB rifts. Lithospheric extension may have generated mantle magmas that both transported Au and possibly set up conduits for dry metal-rich fluids to bring Au into the upper crust. M3a rifting generated both the PVTB's that brought large hydrous fluid reservoirs down into the upper crust and resulted in the high thermal gradients that permitted both dehydration and dewatering of juvenile and pre-existing low-grade rocks, and the thermal energy to drive fluid circulation. Modelling indicates that lithospheric extension is conducive to downward fluid flow trajectories, further facilitating movement of basinal brine fluids down into the upper crust (Sheldon et al., 2007). The thermally weakened and thinned crust, with a crustal architecture established by M2 and M3a growth faults, was conducive to strike-slip and thrust reactivation (Figure 175) in appropriate stress fields (D4 to D6). Reactivation generated dynamic fluid pumping, permeability pathways and deposition sites for Au-mineralization. By comparison with Phanerozoic earth history, a plausible first-order cause for the switch from continental growth to lithospheric thinning is sudden plate reconfiguration caused by the final assembly of a super-continent (e.g., Squire and Miller, 2003). Termination of super-continent assembly may have resulted in slab roll back and M3a lithospheric thinning at ~2665 Ma, with similar lagging causal effects resulting in Au-mineralization events from ~2650-2620 Ma in other Neoarchaean terranes worldwide.

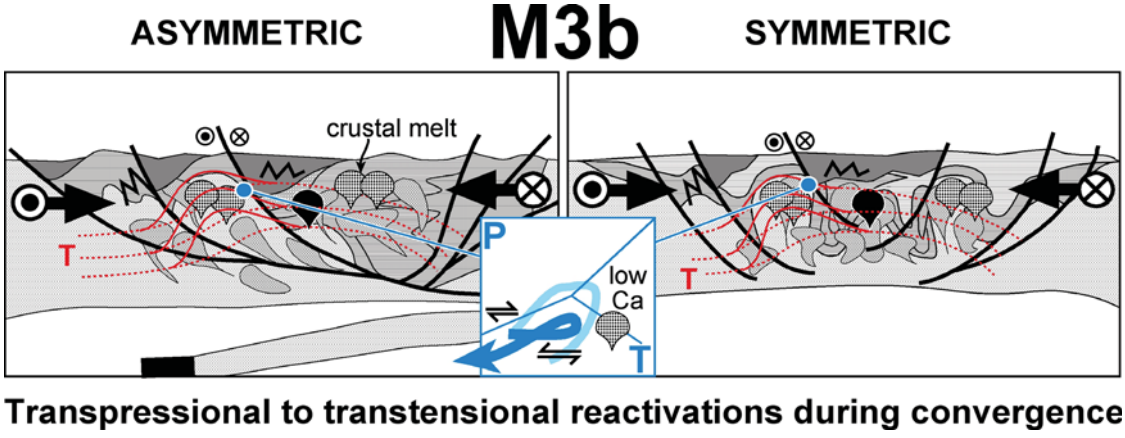

Figure 175: *Cartoons summarizing alternative tectonic scenarios for the M3b period.*

M4 PROTEROZOIC METAMORPHIC OVERPRINTS

Late-stage ameboid cordierite grew during the Proterozoic (M4a) in metapelites close (<1 km) to large (200-2000 m wide) Meso- to Palaeoproterozoic dolerite and ultramafic dykes. This cordierite formed below 2 kb at conditions of ~550 ºC, indicating that the current exposure level of the EYC was at <7 km depth during the Palaeoproterozoic.

Deformational and metamorphic reworking of the southern Yilgarn Craton by the Mesoproterozoic Albany-Fraser Orogen (M4b) was strongly heterogeneous along this margin. In the west and central regions there is evidence for pervasive high-grade reworking of Archaean protoliths. In contrast, parts of the eastern sector experienced only minor shortening of the Archaean rocks (Jones, 2006) and restricted low-grade metamorphic overprint (Goscombe, unpublished data; Goscombe and Blewett, 2009). In Archaean granitoids the Proterozoic thermal over-print is indicated by random late-stage muscovite growth in a zone only 2-5 km wide along the margin of the craton. The craton edge is a steep, 100 m wide muscovite-biotite schist zone that is interpreted to have been derived by complete reworking and retrogressive down grading of Archaean rocks (Goscombe, unpublished data). Southeast of the craton margin is high-P garnet-clinopyroxene amphibolites in a highly sheared 10 km wide margin of the Albany Fraser Orogen. PT calculations by THERMOCALC v3.21 indicate that these rocks equilibrated at 645±51 ºC and 8.3±3.5 kb (Goscombe, unpublished data). The internal part of the orogen in this region is the granulite grade mafic Fraser Complex that shows evidence of two granulite events (Goscombe, unpublished data).

Further north along the southeast margin, is a zone of high-grade rocks along the craton margin stretching between locality BG6-212 and Tropicana Mine. This zone has a unique magnetic response due to demagnetisation of the Archaean rocks. Both localities share upper-amphibolite facies metamorphic assemblages. Locality BG6-212 is migmatized garnet-biotite quartzo-feldspathic gneiss (Pseudo BG6-212). Tropicana Mine contains hornblende and garnet-biotite quartzo-feldspathic gneisses, garnet-grunerite siliceous ironstones and garnet amphibolites. These metamorphic parageneses indicate significant pressures, possibly greater than 6 kb. These assemblages are more typical of the Albany Fraser Orogen and in the absence of age constraints, are possibly Proterozoic parageneses.

GOLD MINERALIZATION

M3a-M3b Gold Mineralization Events

It could be argued that the EYC would not be as endowed in world class gold mineralization without the late orogenic switch from compression to lithospheric extension in M3a. All of the processes, architectures and juxtapositions required for world class gold deposits formed during M3a-M3b follow from this significant event. M3a lithospheric extension thinned the crustal lithosphere resulting in a higher flux of energy from the mantle lithosphere that then drove many of the key processes leading to mineralization (Figure 171). Lithospheric extension was heterogenous, resulting in basinal rifts and partitioned zones of high heat flux resulting in steep thermal gradients that drove fluid flow. The extensional stress field also modified fluid flow trajectories, giving both horizontal and downward paths in part (Sheldon et al., 2007) allowing the mixing of multiple fluid sources in the upper crust. Extensional rifting dropped basinal fluids into the upper crust significantly increasing the ambient fluid volume and introduced a new fluid type into the crust. Lithospheric extension and associated deep penetrating structures facilitated both the generation of mafic granitoid and syenitic melts and dry CO_2-rich fluids in the mantle and transport up into the upper crust. These mantle derived melts and fluids are possibly a major primary source of the gold and mixing of this distinct fluid type with ambient hydrous fluids in the upper crust ultimately resulted in precipitation and mineralization. Lithospheric extension both created and reactivated older crustal shear zone structures, generating suitable structural architectures such as extensional growth faults and footwall domes. These architectures allowed the focusing of fluids from different sources facilitating mixing and ultimately precipitation and mineralization, both during M3a lithospheric extension and by subsequent reactivation of these structures in D4 and D5.

There are four broad but distinct periods of Au-mineralization in the EYC (Figure 11; Roberts et al., 2005; Blewett and Czarnota, 2007a) that have been labelled Au1 to Au4 in Figure 155.

[1] Au1 Mineralization Event: Early rare mineralization events prior to PVTB's accompanied the High-Ca granite bloom and M2 regional metamorphism after cessation of volcanism at ~2670 Ma.

[2] Au2 Mineralization Event: The first major mineralization event accompanied M3a lithospheric extension at ~2665-2655 Ma, and is temporally and spatially closely associated with PVTB development and mafic granite, syenitic and carbonic intrusions. Isotopic indicators from acidic and reducing alteration fluids at Sunrise Dam, indicate post-volcanic sedimentary basins sources (Neumayr et al., 2007). Similarly, oxygen and hydrogen isotopes and salinity in late-stage fluids documented at Great Western (Mikucki, 1997), indicate meteoric fluid that has undergone exchange in a sedimentary basin. Most Au-mineralization in the EYC occurs at crustal levels <3 km shallower than the peak of metamorphism in regional metamorphics (M2) and PVTB's (M3a). The age of world class gold deposits in the EYC corresponds to cessation of late basin deposition in the adjacent region and occur within 1-2 km of late basin unconformities (Hall, 1997).

[3] Au3 Mineralization Event: There is a continuum from M3a metamorphism into a long-lived M3b period of numerous local alteration and mineralization events, which can be sub-divided into the dominant early Au3 events and later minor Au4 events. Au3 constitutes the second major mineralization period from 2655 to 2640 Ma in association with a deformation switch to sinistral transpression (D4). This period also coincides with the initial peak of Low-Ca granitoid intrusions. This period also straddles a period of rapid exhumation and transition to dextral transtension (D5).

[4] Au4 Mineralization Event: A long period from 2640 to 2615 Ma of less numerous mineralization events at shallow crustal levels accompanies the waning stages of Low-Ca granite intrusion. This episode of Au-mineralization occurred at pressures as low as 1 kb, while still at relatively elevated alteration temperatures (250-350 ºC) indicating very high apparent thermal gradients in these latest stage fluid events (G >70ºC/km). Shallow crustal, Low-Ca granitoid intrusions possibly supplied the heat necessary to drive the fluids and remobilise gold in this latest mineralization event.

There is a continuum from M3a to M3b thermal periods with associated Au2 to Au4 mineralization events. This broader 2665-2615 Ma metamorphic period is characterised by high temperature/depth ratio accompanying a switch from extension to a period of exhumation and cooling punctuated by transpression and transtension deformation events. Structural reactivation, recrystallization and fluid flow during these deformation events extended the geological visibility of the dissipating thermal anomaly. Significant volumes (35%) of Low-Ca granite plutons (Figures 10, 146) were emplaced late in this thermal period, extending the duration of the elevated thermal anomaly. These lower crustal melts were generated earlier during M3a lithospheric thinning and finally emplaced into the upper crust ~10 Ma later, from 2650 Ma onwards.

Similarly, there may also be temporal lags between the generation of fluid reservoirs in the upper crust and later association with mineralization events. Hydrous fluid reservoirs were being generated over a period from M2 to M3a by the dewatering of basinal brines in PVTB's and dehydration reactions in both these juvenile sediments and older (M2) low-grade hydrous metamorphic parageneses. The large volumes of hydrous fluid generated during M3a may have been important to Au-mineralization. Firstly by establishing high ambient fluid to rock ratios and large reservoirs to aid permeability and establish large-scale alteration systems. Secondly, these large alteration systems set up the suitable background conditions for mixing with different metal-rich (Au, Mo, Cu, Te) fluids, such as dry oxidized-alkaline CO_2-SO_2-rich magmatic fluids and mantle-derived reduced-alkaline, H_2-CH_4-rich vapour-rich fluids, leading to mineralization. Consequently, mineralization will require a close spatial association with PVTB rifts, or similar sources of large volumes of reduced-acid hydrous fluid and high heat flow to both release and drive fluid flow and generate conduits for mantle derived metal-rich fluids.

Mineralization Fluids

Four broad fluid types can be postulated and are evident in the EYC (e.g., Mikucki, 1997; Neumayr et al., 2007; Walshe et al., 2008a,b; Sheldon et al., 2008). Though few of these fluids are the source and transport medium for the gold, all fluid types ultimately played a hand in being responsible for mineralization to greater and lesser degrees; by their interactions in setting up permeability pathways, altering host rock chemistry and mineralogy, gold transport, fluid mixing and gold precipitation.

[1] Most alteration systems and most regional metamorphic rock types have an ambient background hydrous fluid (Ferry, 1987) that is reduced and acidic and has XCO_2 generally below 0.25 in the EYC (Ho et al., 1990; Cuaig et al., 1993; Cuaig and Kerrich, 1998; White et al., 2003; Elmer et al., 2006). This fluid is derived from the volcano-sedimentary rock mass by dehydration reactions during prograde metamorphism (Connolly and Thompson, 1989). Maximum fluid production by dehydration reactions in mafic and pelite bulk compositions occurs at temperatures between 420-470 ºC in the upper greenschist to lower amphibolite facies transition (Thompson, 2005; Elmer et al., 2006; Sheldon et al., 2008). There are two periods of hydrous fluid generation by prograde dehydration reactions: during the granite bloom related M2 thermal anomaly from 2685-2655 Ma and the superimposed M3a thermal anomaly from 2665-2645 Ma (Figure 155). These two periods also had different sources and so possibly different chemistries and signatures. M2 dehydration fluids are generated exclusively from a predominantly acid-mafic-ultramafic volcanic and volcanoclastic sequence with minor clastic sediment. In contrast, M3a dehydration fluids can be generated from both the volcanic-volcanoclastic sequence, where it has not previously been dehydrated, and from clastic sedimentary sequences in late basins.

[2] A second reduced and acidic hydrous fluid with higher salinity is also common. These fluids have oxygen and hydrogen isotopes indicating derivation by dewatering of basinal sequences during burial (Mikucki, 1997). Deep marine basin fluids are typically saline and transport metals such as Pb, Zn, Ag and Cu (McGoldrick and Large, 1998; Yardley and Graham, 2002). Dewatering fluids from the main volcanic-volcanoclastic stratigraphy will be released and lost from the crustal column early in the history of the EYC. Much younger dewatering fluids will be released into the upper crust from clastic sediment fill in the late basin rifts: at the same time as major gold mineralization events, between 2665-2645 Ma.

[3] Granitic magma typically contains on average 7% volatiles and fluid (Sheldon et al., 2008), most of which is released into the crustal column on crystallization. In contrast, typical metapelite and mafic rocks contain in the order of 2-4% H_2O-CO_2 locked in the structure of metamorphic minerals, of which only a portion is released during prograde metamorphism. Furthermore, because the High-Ca granite bloom accounts for 60% of the volume at the crustal level exposed, the contribution of magmatic fluids into the crustal column far outweighs dehydration fluids from the volcano-sedimentary sequences (Sheldon et al., 2008). Dry magmatic fluid is volatile-rich CO_2-SO_2 with oxidized and moderately alkaline chemistry (Walshe et al., 2008a). Magmatic fluids typically transport Mo, Bi and W and may have transported gold, particularly where associated with mantle-derived magmas such as syenites, lamprophyres, carbonatite and mafic granites (Neumayr et al., 2007). Magmatic fluids from High-Ca granitoids are also effectively mantle-derived via a two-stage process, by being transported within magma from the mantle into upper crust. CO_2-rich fluids are strongly implicated in the formation of gold-rich laminated quartz veins (Cleverley, 2008).

[4] A low volume but significant fluid type is dry, strongly reduced and alkaline volatile fluid that is interpreted to have been derived directly from the mantle (Walshe et al., 2008a). Highly reduced and alkaline volatile fluid is a mix of H_2-H_2S-CH_4 and other volatiles and is typically metal-rich and transports Au, Mo, Cu, As and Te (Neumayr et al., 2007). This fluid derived directly from the mantle and indirectly mantle-derived magmatic fluids are both possible sources for the transport of gold into the upper crust (Walshe et al., 2008a,b).

There are at least five main mechanisms for precipitating gold resulting in mineralization and of these only fluid mixing appears valid across most deposits in the EYC (Neumayr et al., 2007;

Walshe et al., 2008b). Reactions between injected fluid and different wall rock compositions (i.e., iron-rich lithologies) are processes that occur locally on small scales but are not responsible for high-grade deposits (Neumayr et al., 2007; Walshe et al., 2008b). Phase separation occurs where fluids enter a site of dilation and deposit gold. This process occurs in reworked fault zones with suitable geometries, but is unlikely to be the dominant process in major deposits. Rapid decrease in temperature will precipitate gold. It is unlikely this process is relevant to the EYC, given the long-lived M3a-M3b thermal anomaly with high heat flow regime and associated Low-Ca granites. Rapid decrease in pressure will condense CO_2 vapour and precipitate transported gold. This process is unlikely to be regionally significant in the EYC because there is no regional exhumation during the major mineralization events Au1-Au3. Significant exhumation of 7-10 km preceded or accompanied Au4 mineralization and may be significant. At smaller scales, cycles from local over-pressuring to rapid pressure drops due to earthquake events giving dilation and damage zones in the vicinity of faults with appropriate geometries (Sheldon and Micklethwaite, 2007; Crawford and Cox, 2007). Long-term repetition of this process can potentially accumulate significant volumes of the precipitated gold in veins but not in the wall rock, which hosts the gold in most deposits (Crawford and Cox, 2007).

The mixing of two or more different fluid-vapour compositions with different salinity, cation composition, redox and pH explains most observations in large-scale gold deposits in the EYC (Neumayr et al., 2007; Neumayr, 2008; Walshe et al., 2008b). There are numerous relationships at mineral and outcrop scale for fluid mixing mechanisms. For example, highest ore grades are at the intersection between different vein types defined by different mineral assemblages, mineral growth relationships and relationships to different deformation structures. These observations are extended to interpret patterns at map scales. The general observation is that mineralization is on redox gradients between different oxidising and reducing fluids (Neumayr et al., 2007; Neumayr, 2008; Walshe et al., 2008b). The different fluids could be reduced-acid basinal hydrous fluids that mixed with the dry reduced-alkaline H_2-CH_4 and Au-bearing mantle-derived fluids. Or alternatively these reduced mantle fluids mixed with oxidized-alkaline CO_2–SO_2 magmatic fluids that also were ultimately also mantle-derived but by a two-stage process. The mapping of alteration assemblages will document the distribution of different fluid types, leading to identification of steep gradients and overlaps between them, indicating prospective domains at regional scale (Appendix 2; eycmp1_Redox_pH.jpg) and camp scale (Stolz and Roache, 2007; Neumayr et al., 2007; Walshe et al., 2008a,b).

Exploration Targeting with Respect to Metamorphism

Current exposures of PVTB's and the spaced crustal-scale growth fault architecture of the EYC (Blewett and Czarnota, 2005; Squire, 2007), suggest M3a extension was heterogeneously partitioned into elongate rifts with accompanying high heat flow. These extensional domains are also closely coincident with mantle derived magmas and fluids (Figure 146). Earlier hydrous fluid reservoirs formed by dehydration reactions during M2. Most dehydration reactions and fluid release occurs between 400-500 ºC, in pelites at the lower range and in mafics at the top of the range (Figure 29). A mineralization potential map has been compiled that illustrates the juxtaposition between the M3a and M2 hydrous fluid reservoirs and overlap of zones of maximum M3a extension, maximum M3a heat flow and mantle-derived magmas, which may be proxies for mantle derived fluids (Figure 176). The mixing of different fluid types required for Au-mineralization (Neumayr et al., 2007) and necessary steep thermal gradients to drive fluid flow, give rise to clear spatial associations that will aid exploration for Au2-Au3 mineralization during or immediately after M3a lithospheric extension (Figure 171). A thermo-mechanical model for Au-mineralization (Figure 171) would predict the following well-known close spatial associations to be important in large-scale targeting:

[1] Close proximity to exposed or inferred and eroded PVTB's, which indicate both a fluid source and these extensional basinal rifts indicate of a high heat flow footprint (Figure 176). Many large gold deposits are within a few km's of post-volcanic basin margins.

[2] Where PVTB sequences are absent (i.e., due to erosion): domains of M3a rifting and high heat flow can be discerned by major extensional shear zones or the presence of metamorphic parageneses

showing anticlockwise P-T paths. A fluid inclusion study of New Celebration Mine near Ockerburry Fault indicates a tight anti-clockwise P-T loop (Hodge, 2007).

[3] Major extensional structures resulting in significant differential exhumation, may also be delineated by older stratigraphy (i.e., >2720 Ma) or high-P M1 metamorphic parageneses exposed in the lower plate.

[4] Close proximity to the 400 to 500ºC transition through upper greenschist into lower amphibolite facies coincides with maximal fluid release by dehydration reactions (Figure 29; Thompson, 2006) and is mapped in Figure 176.

[5] Mantle derived magmas of mafic granite, syenite and carbonatite, indicate zones of maximal lithospheric extension and are possible sources of, or associated with conduits for, associated metal-rich mantle fluids.

[6] Growth faults documented by variation in stratigraphic thickness (Squire, 2006, 2007) indicate zones that partitioned crustal rifting and extension. Pre-M3a syn-volcanic generations of growth faults are typically also reactivated during M3a extension and later strike-slip deformation events. Extensional growth faults also indicate potential zones of high heat flow and established upper-plate / lower-plate architectures suitable for later strike-slip and thrust reactivation and mineralization.

[7] Steep metamorphic field gradients indicate thermal energy gradients for driving fluid circulation. Consequently, the shape, spacing and gradients within metamorphic map patterns should also reflect fluid circulation patterns and distribution of mineralization. Large ore deposits are on steep metamorphic gradients between high- and low-grade domains, and typically spaced 30-35 km, indicating the scale of fluid circulation cells (Hall, 1997). The scale of circulation cells is also influenced by the size and depth of the greenstone basins, larger deposits are found in larger and deeper basins (Hall, 1997). Fluid circulation paths are also strongly influenced by magmatic intrusions from which fluids emanate and thermal gradients drive flow. This fluid flow is dependent on the cooling history of the intrusion. Initially fluid flow is upwards and streaming away, followed by fluid circulation cells when the intrusion cools below a critical threshold (Sheldon et al., 2008).

[8] At smaller scales, steep gradients or overlap between different alteration fluid chemistries will indicate mixing of different fluid types and high mineralization potential. The spatial distribution of Redox and pH states of alteration assemblages have been mapped (Appendix 2; eycmp1_Redox_pH.jpg), indicating prospective zones of overlap between reduced and oxidised fluids. Mapping mica alteration is an accurate near-camp indicator of gradients between different fluid types (Halley, 2007; Neumayr et al., 2007; Stolz and Roche, 2007).

Later, Au4 mineralization may be indicated by Low-Ca granitoids, which locally perturbed thermal gradients and influenced fluid flow. Low-Ca granite associated mineralization will be narrowed down further by suitable structural settings in the vicinity of perturbed thermal fields.

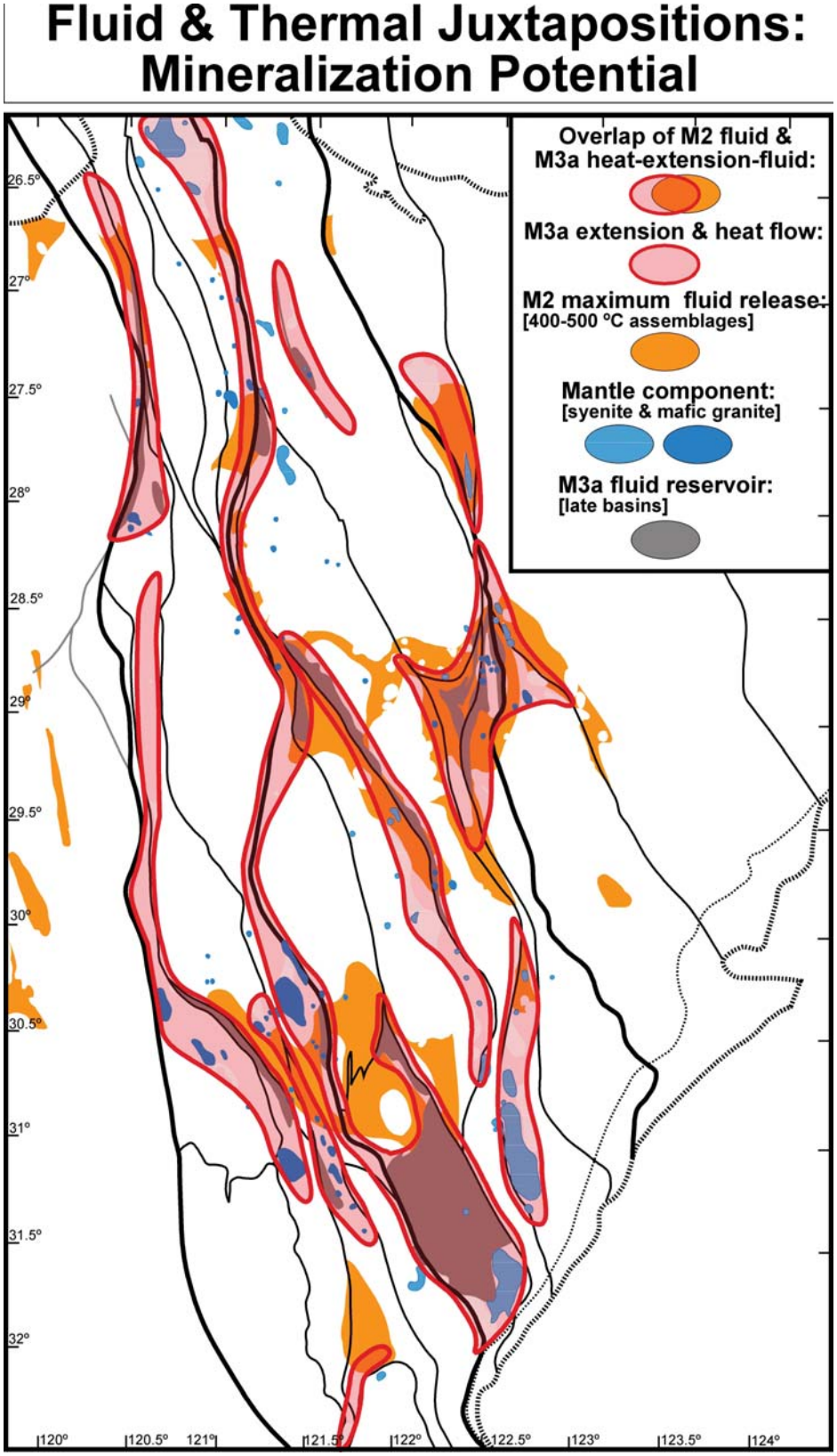

Figure 176: *Map outlining the M2 and M3a fluid reservoirs and juxtapositions with hypothetical zones of maximum M3a heat flow, extension and mantle-derived magmas and fluids.*

First-Order Mineralization Drivers

At a large-scale the first-order processes required for generating major gold deposits are listed in approximate descending order of scale and fundamental importance of controls (Barnicoat, 2006). Even with all of these first-order parameters satisfied, major mineralization will not necessarily occur without a fortuitous juxtaposition of second-order, site-specific ad hoc variables.

[1] Plate Configuration: Suitable tectonic plate reconfiguration with an accretionary margin containing magmatic arc, back arc and subduction settings (Groves, 2002; Squire and Miller, 2003).

[2] Lithosphere Age: Thinned juvenile lithosphere with short pre-history (Cassidy et al., 2002; Groves, 2002; Bierlein et al., 2006; Champion et al., 2006).

[3] Orogenic Regime: Late orogenic lithospheric extension is the crucial event from which follows all other subsidiary drivers leading to mineralization: such as high heat flow, mantle and crustal melting, crustal architecture and the juxtaposition of different fluids and crustal levels, as listed below (Figure 171). The tectonic setting for lithospheric extension is speculative, but at accretionary margins the simplest scenario is probably termination of subduction followed by rollback of the hinge (Squire and Miller, 2003), or alternatively lower-crust delamination (Czarnota et al., 2008).

[4] Heat: The elevated thermal gradients resulting from thinning of the lithosphere will drive partial melting in the mantle lithosphere, giving rise to mafic granite and syenite melts possibly enriched in gold. This thermal anomaly will also drive partial melting of the lower crustal lithosphere, which with delayed emplacement in the upper crust will prolong the thermal anomaly. Elevated thermal gradients are fundamental to the generation of fluids reservoirs in the upper crust by dewatering and dehydration and supplying the energy to drive lateral gradient and convective fluid flow (Oliver, 1996). The elevated thermal regime associated with gold mineralization events (2665-2615 Ma) post-dates all volcanism and cannot be related to high heat flow during komatiite volcanism between 2708-2692 Ma.

[5] Architecture: Lithospheric extension produces a heterogeneous strain pattern consisting of low strain domes and belts interspersed with listric shear zones that are strongly correlated with gold (Figure 177). The developed asymmetric, extensional upper-plate / lower-plate architectures produce up doming in the lower-plate and extensional depositional basins in the upper-plate, both of which are crucial to gold mineralization in the EYC.

[6] Fluid: Extensional rifts in the upper-plate supply a new hydrous fluid reservoir by bringing juvenile sediments down into the upper crust. This additional fluid reservoir increases the ambient fluid volume at appropriate crustal levels and extensional stress regimes drive horizontal and downward fluid flow into adjacent rock units and structures.

[7] Fluid Focus: Lower-plate domal structures facilitate the development of convex architectures to focus and pool fluids and melt by the doming of pre-existing stratigraphy such as komatiites or early low-angle shear zones such as D1 structures (Figure 171; Groves, 2002; Hensen et al., 2007).

[8] Source: Lithospheric extension and high heat flow are possibly fundamental to both the sourcing of gold from the mantle lithosphere by melt and fluid generation and to the transport of these into the upper crust. Mantle partial melting and fluid generation processes are driven by extreme decompression of the mantle lithosphere and elevated thermal gradients during lithospheric thinning (Buck, 1988; Ruppel, 1995). Ascent of mafic granite and syenite magmas as well as dry CO_2- and metal-rich fluids from the mantle lithosphere, is considerably enhanced by formation of mantle penetrating extensional shear zones.

[9] Precipitation Mechanism: The primary precipitation mechanism in the EYC is the mixing of the contrasting fluids; reduced hydrous fluid and dry oxidized CO_2-rich fluid (Neumayr et al., 2007). Many processes following on from lithospheric extension that together bring distant fluids into juxtaposition, allowing mixing, precipitation and mineralization. Specifically, the extensional stress regime drives horizontal flow of hydrous fluids out of reservoirs brought down into the upper crust, and focuses this flow into extensional shear zones (Sheldon et al., 2007). Mantle derived fluids are

focused into the same crustal-scale structures from below and associated with mantle magma ascent conduits also localised where extension was greatest (Figure 146), facilitating mixing of the two fluid types.

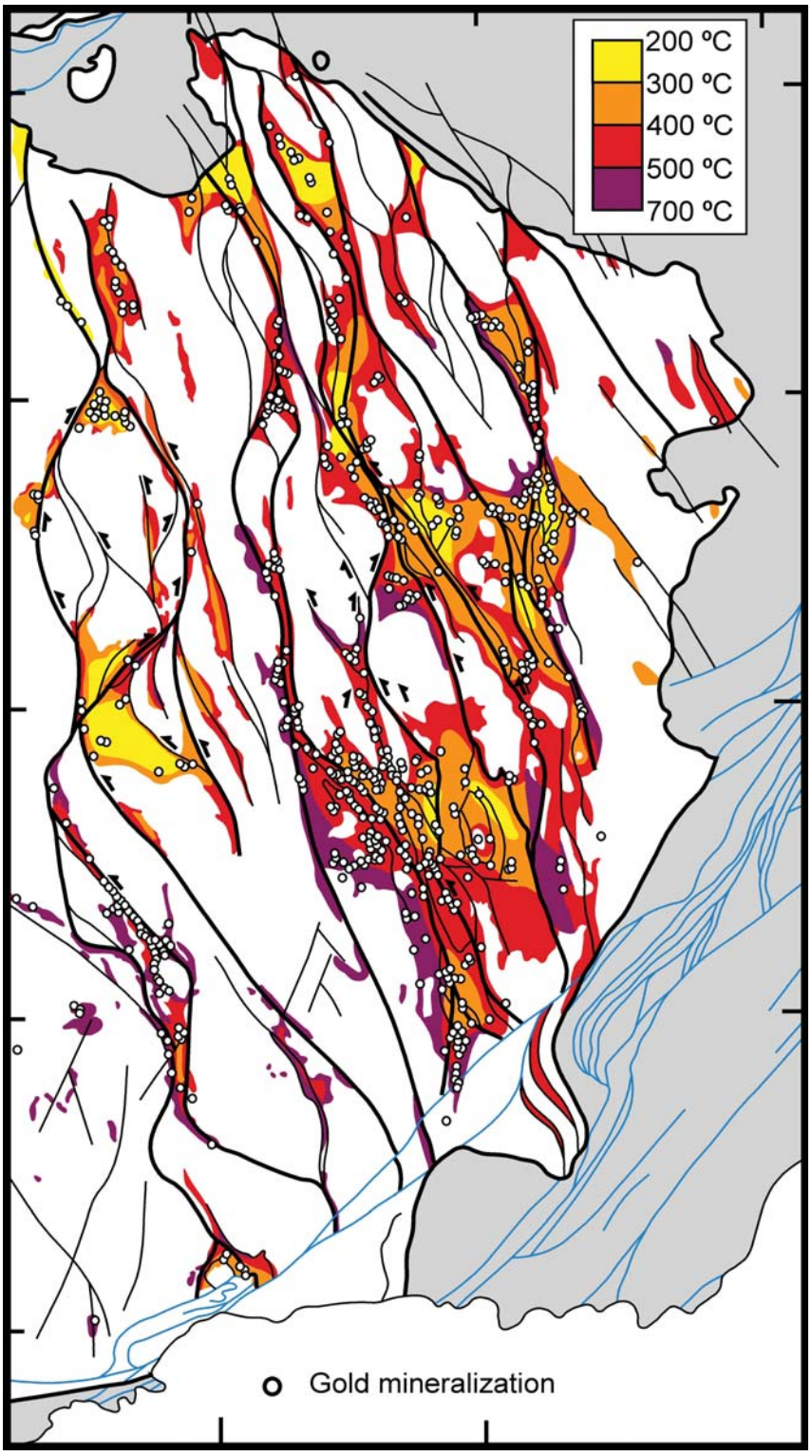

Figure 177: *Gold deposits superimposed on a simplified map of metamorphic temperatures based on assignment of metamorphic facies to assemblages. Gold deposits sourced from Cooper et al. (2007).*

[10] Precipitation Sites: Late orogenic lithospheric extension generated the network of crustal-scale shear zones and faults that gave dynamic fluid pumping and generation of dilational precipitation sites, both during extension (D3b) and during subsequent reactivation events (D4a, D4b, D5). At smaller scales, fluid pathways and dilation sites effecting precipitation are influenced by second-order ad hoc variables such as host rock composition, permeability, rheology and pre-existing structures and geometries.

[11] Remobilization: The possibility for remobilization and later mineralization events, and thus the potential to increase grade and size of deposits, is greatly enhanced by secondary outcomes from lithospheric extension. Firstly, the duration of the thermal anomaly that is crucial to mineralization (M3a-M3b) is extended by the delayed emplacement of significant volumes of Low-Ca granite into shallow crustal levels. Secondly, this protracted 50 Ma thermal anomaly greatly increases the probability for coinciding deformation and reactivation events during this long thermal window, resulting in more structurally controlled mineralization events.

NEOARCHAEAN TECTONIC SETTINGS

Alternative Tectonic Settings

Alternative tectonic settings have been interpreted for different stages in the evolution of the EYC based on the broad metamorphic periods (Figure 164). These cartoons summarize possible scenarios that satisfy the known first-order variables, such as magmatic history, deformation style, structural architecture, metamorphic pressure, temperature and P-T evolutions. These scenarios have been classified as symmetric and asymmetric end-members, representing convective overturn versus conventional plate tectonic settings respectively. Preferred tectonic scenarios are the asymmetric - plate tectonic settings, rather that the symmetric scenarios which require special-case tectonic settings, such as mantle plumes and vertical or diapiric tectonics. Tectonic settings are not limited to the end-members drawn to facilitate discussion (Figure 164); real scenarios could possibly involve **transitions** and **hybridizations** between end-members (Figure 167). For example the hybridized model proposed by Blewett and Czarnota (2005), with plume related processes active in the back arc of a retreating subduction system to the east, generating the volcanic sequences in the early evolution of the EGST (Figure 167).

A compelling reason for conventional plate tectonic settings is that these asymmetric geometries evolve smoothly and progress into distinctly different tectonic settings at different stages in the evolution of the EYC (Figures 167, 169, 173). Similarly smooth transitions are difficult to reconstruct without catastrophic re-organizations at different stages when limiting models to symmetric geometries and vertical tectonics. Furthermore, the final asymmetric architecture of the crust documented by deep seismic imaging (Golbey, 2002), cannot be arrived at by a history involving only symmetric tectonic settings. Few models for Archaean systems have been published that propose transitions from early symmetric up welling scenarios to later asymmetric scenarios in the evolution of a province (Van Kranendonk et al., 2002). Given the current crust is characterized by an asymmetric grain; this observation either brings into doubt early crustal histories dominated by symmetric tectonics, or a lack of imagination traversing between these end-member camps and developing models with transitions from symmetric to asymmetric settings.

Another major problem for symmetric tectonic settings is maintaining the fundamental driver for vertical tectonics and high heat flow by mantle up welling over a protracted period of time, while changing the crustal geological expression. The long (100 Ma) EYC geological history spanning volcanism, granite bloom, crustal shortening, extensional basins, transcurrent shear zones and post-orogenic magmatism, is not consistent with an unchanging fundamental first-order driver. Mantle up welling and plumes have been invoked in the formation of the early mafic and ultramafic volcanic sequence and komatiite extrusives specifically (Rey et al., 2003). Similarly, convective overturn by diapiric vertical tectonics early in the history has been used to explain high-P parageneses (similar to M1) in Palaeoarchaean terranes such as the Pilbara Craton (Collins and Van Kranendonk, 1999; Sandiford et al., 2004; Van Kranendonk et al., 2002, 2004). However, plumes and convective overturn tectonics are not consistent with the granite bloom formed at a later stage (M2), which have

geochemistry requiring subduction and eclogitization of the down-going slab (Champion et al., 2001; Cassidy, 2006; Champion and Cassidy, 2007). Simplistic, purely symmetric tectonic settings cannot be substantiated in the light of documented arc magmatism and subduction related volcanics within EYC volcano-stratigraphy (Brown et al., 2002; Cassidy, et al., 2006; Barley et al., 2002, 2006; Groenewald et al., 2006). Consequently, an early hybrid setting must be invoked (Figure 167), followed by a transition from this period possibly involving vertical compressive stresses to the well-established horizontal tectonics that drove crustal shortening (M2), transpression (D4) and transtension (D5) events later in the EYC evolution (Blewett and Czarnota, 2007c). Furthermore, the duality of high-P/low-G (M1) and high-T/high-G (M2-M3a) thermal regimes in the EYC is one of the hallmarks of plate tectonics (Brown, 2006, 2007a, b, c), and is inconsistent with an ongoing, unchanging vertical tectonic scenario driven by mantle up welling throughout the protracted evolution of the EYC.

Until recently the tectonic paradigm for the Yilgarn Craton was continental collisional orogenesis with accompanying plume, resulting in craton-wide effects such as crustal over-thickening and widespread granite magmatism (Groves and Phillips, 1987; Rey et al., 2003; Van Kranendonk, 2007). Elevated thermal regimes, tight clockwise P-T paths at low pressures and absence of widespread Barrovian metamorphic conditions preclude crustal over-thickening and continent collision orogenesis. Crustal shortening accompanying the granite bloom in the EYC, did not result in significant thickening of the crustal section and is interpreted to have formed during accretionary orogenic processes (Blewett and Czarnota, 2007c; Goscombe et al., 2007). Furthermore, the structural record of the EYC is also incompatible with collisional orogenesis and the heterogeneous and non-pervasive strain distribution, multi-directional transports and stress switches are all more typical of accretionary orogenesis. Continent collision models have also been invoked for the generation of late-orogenic extensional features such as “late basins” by a process of “orogenic collapse” resulting from crustal over-thickening (Van Kranendonk pers. comm. 2007). Apart from the absence of evidence for crustal over-thickening, lithospheric extension can occur within normal thickness crust in a variety of tectonic settings. For example, lower crust delamination and subduction slab roll back both give lithospheric extension, which is further facilitated by the elevated thermal gradients and thermally softened crust primed during the M2 granite bloom (Figure 169).

Switch from Crustal Growth and Accretion to Lithospheric Thinning

Profound thermo-mechanical and mineralization consequences followed the transitional switch from accretion and crustal growth involving subduction, back arc and magmatic arc settings (Figures 165, 166, 167), through a period of accelerating extension (Figure 169) and ultimately thinning of the crustal lithosphere (Figure 173). Extension of the juvenile crust progressed in two stages spanning the M2-M3a period, the second and most extreme of which was most important to gold mineralization. Lithospheric extension was initiated at ~2685 Ma with the formation of growth fault controlled syn-volcanic clastic basins (SVB) and a rapid increase in the volume of High-Ca granitoids (Figure 169). Regional-contact type metamorphism (M2) with moderately high temperature/depth ratio (30-40 ºC/km) was established as a consequence of both the elevated geotherms from lithospheric thinning and advection of heat by volumous granite emplacement into the upper crust. Extension in the crustal established major growth fault structures, some of which penetrated the mantle lithosphere. Crucially these structures were reactivated in later extensional episodes (M3a) and in late-stage transpression and transtension episodes controlling mineralization.

Superimposed on this protracted period of extension and high heat flow was a punctuated shortening event (D2-M2) giving minor crustal thickening, possibly due to arc closure and catastrophic termination of down-going subduction (Blewett and Czarnota, 2007c). This event immediately triggered runaway extension of the crustal lithosphere at ~2670-2665 Ma; coinciding with the termination of all volcanism in the EYC, extreme growth fault reactivation, development of the PVTB’s and increase in the temperature/depth ratio to 40-50 ºC/km (Figure 173). Renewed lithospheric extension at the termination of crustal growth resulted in elevated thermal gradients and mantle derived mafic granite and syenite emplaced into the upper crust (Figure 173). Crucially, these mantle melts indicate sufficient lithospheric thinning to open up conduits for melt and fluids from

the mantle, both of which may have transported gold into the upper crust. Runaway extension was heterogeneously partitioned through the upper crust level that's currently exposed. This is indicated by a network of curviplanar shear zones, newly formed and reactivated growth faults and elongate domains of PVTB's, M3a thermal overprint and mantle derived granitoids (Figure 146).

The key event that initiated runaway lithospheric extension was sudden termination of subduction at the margin of the Yilgarn Craton. This switch may have been caused by a second-order process such as choking of the subduction zone by an oceanic plateau (Blewett and Czarnota, 2007c). Alternative first-order causes could include a sudden global reorganization of tectonic plate trajectories following attainment of a metastable plate configuration. An example of the latter scenario is the sudden plate reconfigurations induced at the culmination of assembly of supercontinents. Tectonic plate reconfigurations followed the culmination of collisional assembly of Gondwana generating stress switches at ~520 Ma (Foster et al., 2009), and culmination of accretionary growth generated subduction slab roll back on the eastern margin at ~440 Ma (Squire and Miller, 2003). If subduction termination and initiation of runaway lithospheric extension in the EYC signifies a global plate reconfiguration event, this should be recorded by similar fundamental switches in Neoarchaean terranes world wide at ~2670-2665 Ma. Stress switches globally at this time may have initiated similar geological responses and processes leading to Au-mineralization like the EYC, with the possibility of a global self-similar mineralization period between 2665 and 2615 Ma.

Further Work Required

The EYCMP has attempted a near comprehensive documentation of metamorphism in the EYC and interpretation of what these outcomes contribute towards geodynamics and mineral exploration. This program established a methodology for the documentation and interpretation of metamorphism on orogenic scales. There are strong arguments for extending this program further, both in generating datasets for the EYC that are currently poorly established (e.g., geochronology, late basins, detailed specific field gradients and crystallization depths of granitoids) and to undertake full programs across the remaining Yilgarn Craton. Further work should aim to generate a comprehensive, integrated, spatial, relational GIS database across the whole Yilgarn Craton, documenting stratigraphic, lithologic, metamorphic, chronologic, fluid, structure, strain, kinematic etc parameters. By delivering a new fundamental dataset across a world-class mineral province on a craton-scale, a completed program will contribute strategic support to the mineral exploration industry. Direct outcomes will be; a temporal series of systematic metamorphic maps across the entire Yilgarn Craton and at different scales of detail; a fully integrated structural-metamorphic-chronologic spatial GIS database across the whole craton; constrained thermo-barometric evolutions in all parts of the craton. These new fundamental datasets will focus mineral exploration efforts and contribute to the genetic links between thermo-barometric evolution of the crust and mineralization processes.

SPECIFIC DATASETS REQUIRED

The EYC program has drawn attention to specific new datasets that are required to solve outstanding geodynamic problems and value-add to mineral exploration in the region. Critical datasets that have been identified as absent or poorly developed, and need to be addressed, are listed below.

[1] The different metamorphic events need to be accurately constrained by direct dating of metamorphic minerals. The recognition of five distinct metamorphic events during the EYC program is an unambiguous driver for robust direct dating of the different metamorphic parageneses. It is preferential that the well-constrained U-Pb series chronometers are applied to peak metamorphic minerals, such as zircon, titanite and monazite. Lu-Hf dating of garnet should still be pursued to document garnet growth in the same samples and possibly constrain duration of thermal anomalies and rates of metamorphism. U-Pb in situ dating of zircons from high-grade M*a* and M1 parageneses should be attempted to constrain geodynamic models during crustal growth phase. U-Pb in situ dating of monazite on metapelite samples should be attempted to resolve the temporal relationship between the clockwise M2 and anticlockwise M3a parageneses. U-Pb dating of monazite can also be

used to date alteration and mineralization parageneses. A widespread U-Pb titanite-dating program is preferred because metamorphic titanite forms across a wide range in metamorphic conditions, potentially representing different metamorphic events. Furthermore, the timing of titanite growth is usually unambiguous in thin section and is a main matrix mineral in common mafic rock types. This methodology may prove to be the most reliable and accurate way of directly dating metamorphic mineral growth. Recent research has solved many earlier problems and a reliable titanite geochronology method is now routinely applied (i.e., Foster et al., 2006).

[2] Compile additional legacy datasets in the EYC that have been recently identified.

[3] All late basins should be sampled in outcrop and from drill core, and determine PT conditions of metamorphism and P-T paths of evolution. A comprehensive database of late basin metamorphic conditions should be established to constrain the extent and variation in M3a metamorphism. Variations in maximum temperatures and depth of burial attained will provide a proxy for the amount of lithospheric extension experienced in different parts of the EYC during M3a.

[4] Aim for greater involvement of the mineral exploration industry so that all pre-existing petrological datasets can be incorporated in the metamorphic database. The proposed collaboration will better document individual alteration systems and their relationship with regional metamorphic patterns and the thermal evolution of the craton.

[5] A weakness in the current dataset (Figure 85) is a paucity of suitable low-temperature (<500 ºC) regional metamorphic rocks that could be sampled more extensively by utilizing legacy drill core. Metamorphic PT conditions can be determined using phase stability constraints, conventional geothermobarometry, illite crystallinity, white mica chemistry, amphibole chemistry and chlorite chemistry.

[6] Another weakness that needs to be addressed is pressure constraints from different generations of granitoids. These data will constrain crystallization depths at all stages in the crustal evolution and across the all parts of the Yilgarn Craton. Methods that can be attempted are igneous hornblende geobarometers and PT calculations from suitable xenoliths, incorporated gneissic screens and from the associated gneissic domains. A large part of the required rock sample set can be drawn from existing GA and GSWA rock samples and lapidary billets. Because magmatic events are typically well dated, this dataset will constrain burial/exhumation rates and be an additional linkage between metamorphic and chronologic datasets. This dataset will be a crucial constraint on the competing vertical versus horizontal tectonic models.

[7] Detailed metamorphic field gradients need to be documented across key major structures, such as the Ida, Ockerburry and Hootanui shear systems. Similarly specific detailed metamorphic field gradients need to be documented across a number of key, well-preserved greenstone belts, such as the Marda, Lake Johnson and Murchison belts. Documenting specific real metamorphic gradients and patterns at this second-order scale is crucial for linking the large-scale metamorphic patterns and metamorphic parageneses into the deformation and mineralization history. A program of specific field gradients will be greatly enhanced by sampling of appropriate material from available drill core.

[8] Where possible detailed structural profiles should be undertaken in conjunction with the detailed metamorphic field gradients. As well as kinematics, geometry, bulk strain and maximum extension direction, structural observations should also constrain the rock flow regime, which has a large bearing on fluid circulation patterns and thus mineralization geometries.

[9] The interpretive EYC maps generated during the EYCMP (Goscombe and Blewett, 2009; Appendix 2) should be updated with new constraints from the EYC, and final versions released. Published interpretive maps should include; peak metamorphic map, alteration map, key assemblage maps, redox-pH and fluid map and bulk strain map.

[10] The metamorphic database and interpretation need to be directly linked and integrated with available structural frameworks, alteration and mineralization systems and other datasets such as

stratigraphy, intrusives and geochronology, to better constrain the geodynamic evolution of the Yilgarn Craton. One way to facilitate direct integration is to document the metamorphic evolution in the mine pits sites described in detail for the Y1 structural program (Blewett and Czarnota, 2005).

[11] Generate synopses of the metamorphic evolution of Neoarchaean crust worldwide, to put the Yilgarn Craton geodynamic evolution and mineralization into a global context.

Acknowledgements

The sponsors are thanked for their ongoing commitment to the ***pmd****CRC* Y4 project. The CEO of ***pmd****CRC* (Bob Haydon) is thanked for his long commitment to the funding of the Module 3 East Yilgarn Craton Metamorphic Project. The director of the GSWA (Dr Tim Griffin) is gratefully acknowledged for facilitating access to legacy thin sections, databases, vehicle, fieldwork support and general ongoing support for this project. GA is thanked for its massive commitment of staff time, XRD and XRF analyses and GIS and other expertise. John Walshe, Martin Van Kranendonk, Steve Wyche, John Miller, Heather Sheldon, Ned Stolz, Kevin Cassidy, Dave Champion, Paul Hanson, David Foster, David Gray, Sandra Romano and Joe Ogierman are thanked for the very helpful discussions and guidance. Richard Chopping and Chris Carson at GA are thanked for reviewing and greatly improving this manuscript. Angus Netting (AM), John Turlet (AM), Ian Pontifex, Liz Webber (GA), Greg Hitchen (CSIRO) and Mike Verrall (CSIRO) are thanked for help with lapidary, XRD and mineral analyses. Terry Brennan (GA) is thanked for help with GIS. Published with permission of the CEO's of the ***pmd****CRC*, GSWA and GA.

References

A

Ahmat, A.L., 1995. Geology of the Kanowna 1:100 000 sheet. *GSWA Explanitory Notes*.

Ahmat, A.L., 1986. Metamorphic patterns in the greenstone belts of the Southern Cross Province, Western Australia. *Geological Survey of Western Australia Professional Papers,* **19**, 1-21.

Alias, G., Sandiford, M., Hand M. and Worley B., 2002. The PT record of synchronous magmatism. Metamorphism and deformation at Petrel Cove, southern Adelaide Fold Belt. *Journal of Metamorphic Geology,* **20**, 351-363.

Allen, C.A., 1987. The nature and origin of the porphyry gold deposits, Western Australia. In: Ho S.E., Groves D.I. (eds), Recent advances in understanding precambrian gold deposits. *University of Western Australia Publication,* **11**, 137-145.

Alsop, G.I. and Holdsworth, R.E., 2006. Sheath folds as discriminators of bulk strain type. *Journal of Structural Geology,* **28**, 1588-1606.

Apted, M.J. and Liou, J.G., 1983. Phase relations among greenschist, epidote-amphibolite and amphibolite in a basaltic system. *American Journal of Science,* **283**, 328-354.

Archibald, N.J. and Bettenay, L.F., 1977. Indirect evidence for tectonic reactivation of a pre-greenstone sialic basement in Western Australia. *Earth and Planetary Science Letters,* **33**, 370-378.

Archibald, N.J., Bettenay, L.F., Binns, R.A., Groves, D.I. and Gunthorpe, R.J., 1978. The evolution of Archaean greenstone terrains, Eastern Goldfields Province, Western Australia. *Precambrian Research,* **6**, 103-131.

Armstrong, T.R., Tracy, R.J. and Hames, W.E., 1992. Contrasting styles of Taconian, Eastern Acadian and Western Acadian metamorphism, central and western New England. *Journal of Metamorphic Geology,* **10**, 415-426.

B

Bagas, L., 1994. Geology of the Cheritons Find 1:100 000 sheet. *GSWA 100K Explanatory Notes*.

Baggott, M.S., Vielreicher, N.M., Groves, D.I., McNaughton, N.J. and Gebre-Mariam, M., 2005. Zircons, dikes, and gold mineralization at Jundee-Nimary: Post ca. 2.66 Ga Archean Lode Gold in the Yandal Belt, Western Australia. *Economic Geology,* **100**, 1389-1405.

Ballevre, M., Pitra, P. and Bohn, M., 2003. Lawsonite growth in the epidote blueschists from the Ile de Groix (Armorican Massif, France): a potential geobarometer. *Journal of Metamorphic Geology,* **21**, 723-735.

Barley, M.E., Krapez, B., Groves, D.I. and Kerrich, R., 1998. The late Archaean bonanza: metallogenic and environmental consequences of the interaction between mantle plumes, lithospheric tectonics and global cyclicity. *Precambrian Research,* **91**, 65-90.

Barley, M.E., Brown, S.J., Krapez, B. and Cas, R.A.F., 2002. Tectono-stratigraphic analysis of the Eastern Yilgarn Craton: an improved geological framework for exploration in Archaean terranes. *Australian Minerals Industry Association Report,* **P437A**.

Barley, M.E., Brown, S.J.A., Cas, R.A.F., Cassidy, K.F., Champion, D.C., Gardoll, S.J. and Krapez, B., 2003. An integrated geological and metallogenic framework for the eastern Yilgarn Craton: Developing geodynamic models of highly mineralised Archaean granite-greenstone terranes. *Australian Minerals Industry Association Report,* **P624**.

Barley, M.E., Brown, S.J.A. and Krapez, B., 2006. Felsic volcanism in the eastern Yilgarn Craton, Western Australia: evolution of a late Archean convergent margin. *Geochim. Cosmochim. Acta,* **70**, A35.

Barnes, S.J. and Hill, R.E.T., 2000. Chapter 9 Metamorphism of komatiite-hosted nickel sulfide deposits. In: *Reviews in Economic Geology,* **11**. Society of Exploration Geologists, Littleton, USA. pp. 310.

Barnicoat, A., 2006. Linking fundamental controls on ore deposition with the exploration process. *Predictive mineral discovery Cooperative Research Centre fact sheet*, 1-4.

Bassias, Y. and Triboulet, C., 1992. Petrology and P-T-t evolution of the Southwest Indian Ridge peridotites. A case study: east of the Melville Fracture zone at 62°E. *Lithos,* **28**, 1 - 19.

Beakhouse, G.P., 2007. Gold, granite and late Archean tectonics: a Superior Province perspective. In: Bierlein, F.P., and Knox-Robinson, C.M., (eds), Proceedings of Geoconferences (WA) Inc. Kalgoorlie '07 Conference. *Geoscience Australia Record,* **2007/14**, 191-196.

Beaumont, C., Jamieson, R.A., Nguyen, M.H. and Lee, B., 2001. Himalayan tectonics explained by extrusion of a low-viscosity crustal channel coupled to focused surface denudation. *Nature,* **414**, 738-742.

Begin, N.J., 1992. Contrasting mineral isograd sequences in metabasites of the Cape Smith Belt, northern Quebec, Canada: three new bathograds for mafic rocks. *Journal of Metamorphic Geology,* **10**, 685-704.

Bennett, J.M., 1989. Comparison of Archaean Pb-Zn(-Au) mineralization at Black Flag and Au mineralization at Lady Bountiful, Mt Pleasant area, Western Australia. B.Sc. honours thesis, University of Western Australia (unpublished).

Beresford, S., Stone, W.E., Cas, R., Lahaye, Y. and Jane, M., 2005. Volcanological controls on the localization of the komatiite-hosted Ni-Cu-(PGE) Coronet Deposit, Kambalda, Western Australia. *Economic Geology* **100**, 1457-1467.

Bevins, R.E. and Merriman, R.J., 1988. Compositional controls on coexisting prehnite-actinolite and prehnite-pumpellyite facies assemblages in the Tal y Fan metabasite intrusion, North Wales: implications for Caledonian metamorphic field gradients. *Journal of Metamorphic Geology* **6**, 17-39.

Beyssac, O., Negro, F., Simoes, M., Chan, Y.C. and Chen, Y.G., 2008. High-pressure metamorphism in Taiwan: from oceanic subduction to arc-collision? *Terra Nova,* **20**, 118-125.

Bhattacharya, A., 1986. Some geobarometers involving cordierite in the FeO-Al2O3-SiO2 (±H2O) system: refinements, thermodynamic calibration, and applicability in granulite facies rocks. *Contributions to Mineralogy and Petrology,* **94**, 387-394.

Bickle, M.J. and Archibald, N.J., 1984. Chloritoid and staurolite stability: implications for metamorphism in the Archaean Yilgarn Block, Western Australia. *Journal of Metamorphic Geology* **2**, 179-203.

Bierlein, F.P., Gray, D.R. and Foster, D.A., 2002. Metallogenic relationships to tectonic evolution – the Lachlan Orogen, Australia. *Earth and Planetary Science Letters,* **202**, 1-13.

Bierlein, F.P., Groves, D.I., Goldfarb, R.J. and Dube, B., 2006. Lithospheric controls on the formation of provinces hosting giant orogenic gold deposits. *Mineralium Deposita,* **40**, 874-887.

Binns, R.A., Gunthorpe, R.J. and Groves, D.I., 1976. Metamorphic patterns and development of greenstone belts in eastern Yilgarn Block, Western Australia. John Wiley and Sons, New York, USA, 303-313.

Bishop, F.C., 1980. The distribution of Fe^{2+} and Mg between coexisting ilmenite and pyroxene with applications to geothermometry. *American Journal of Science,* **280**, 46-77.

Black, L.P., Champion, D.C. and Cassidy, K.F., 2002. Compilation of SHRIMP U-Pb geochronology data, Yilgarn Craton, Western Australia, 1997-2000. *Geoscience Australia Record,* **2002**.

Bleeker, W., 2003. Age, Extent, and rate of sedimentation of an Archean turbidite basin, Slave Craton, Canada. Structure, tectonics and ore mineralization processes, abstracts. *EGRU Contribution,* **64**, 45.

Blewett, R.S., Champion, D.C. Whitaker, A.J., Bell, B., Nicoll, M., Goleby, B.R., Cassidy, K.F. and Groenewald, P.B., 2002a. A new 3D model of the Leonora-Laverton transect: implications for the tectonic evolution of the eastern Yilgarn Craton. *Australian Institute of Geoscientists Bulletin,* **36**, 18-21.

Blewett, R.S., Champion, D.C. Whitaker, A.J., Bell, B., Nicoll, M., Goleby, B.R., Cassidy, K.F. and Groenewald, P.B., 2002b. Three dimensional (3D) model of the Leonora-Laverton transect area: implications for the Eastern Goldfields tectonics and mineralization. In: Geology, geochronology and geophysics of the northeastern Yilgarn Craton, with emphasis on the Leonora-Laverton transect area, Cassidy K.F. (ed). *Geoscience Australia Record,* **2002/18**, 83-100.

Blewett, R.S., Cassidy, K.F., Champion, D.C., Henson, P.A., Goleby, B.R., Jones, L. and Groenewald, P.B., 2004a. The Wangkathaa Orogeny: an example of episodic regional 'D2' in the late Archaean Eastern Goldfields Province, Western Australia. *Precambrian Research,* **130**, 139-159.

Blewett, R.S., Cassidy, K.F., Champion, D.C. and Whitaker, A.J., 2004b. The characterization of granite deformation events in time across the Eastern Goldfields Province, Western Australia, *Geoscience Australia Record,* **2004/10**.

Blewett, R.S. and Czarnota, K., 2005. Tectonostratigraphic architecture and uplift history of the eastern Yilgarn Craton: Terrane structure. ***pmd****CRC* Y1-P763 Module 3 Final Report, pp. 92.

Blewett, R.S. and Czarnota, K., 2007a. A new integrated tectonic framework of the Eastern Goldfields Superterrane. In: Bierlein, F.P., and Knox-Robinson, C.M., (eds), Proceedings of Geoconferences (WA) Inc. Kalgoorlie '07 Conference. *Geoscience Australia Record,* **2007/14**, 27-32.

Blewett, R.S. and Czarnota, K., 2007b. Tectonostratigraphic architecture and uplift history of the Eastern Yilgarn Craton. *Geoscience Australia Record,* **2007/15**.

Blewett, R.S. and Czarnota, K., 2007c. Diversity of structurally controlled gold through time and space of the central eastern goldfields superterrane – a field guide. *GSWA Record,* **2007/19**.

Blichert-Toft, J. and Albarède, F., 1997. The Lu-Hf isotope geochemistry of chondritis and the evolution of the mantle-crust system. *Earth and Planetary Science Letters,* **148**, 243-258

Bloem, E.J.M., Dalstra, H.J., Groves, D.I. and Ridley, J.R., 1994. Metamorphic and structural setting of Archaean amphibolite-hosted gold deposits near Southern Cross, Southern Cross Province, Yilgarn Block, Western Australia. *Ore Geology Reviews,* **9**, 183-208.

Bloem, E.J.M., 1994. Structural controls, alteration history and genesis of Archaean gold deposits near Southern Cross, Yilgarn Block, Western Australia. PhD thesis, University of Western Australia (unpublished).

Bloem, E.J.M., McNaughton, N.J., Groves, D.I. and Ridley, J.R., 1995. *Australian Journal of Earth Sciences,* **42**, 447-451.

Bloem, E.J.M., Dalstra, H.J., Ridley, J.R. and Groves, D.I., 1997. Granitoid diapirism during protracted tectonism in an Archaean granitoid-greenstone belt, Yilgarn Block, Western Australia. *Precambrian Research,* **85**, 147-171.

Blundy, J.D. and Holland, T.J.B., 1990. Calcic amphibole equilibria and a new amphibole-plagioclase geothermometer. *Contributions to Mineralogy and Petrology,* **104**, 208 - 224.

Boger, S.D. and Wilson, C.J.L., 2005. Early Cambrian crustal shortening and a clockwise P-T-t path from the southern Prince Charles Mountains, East Antarctica: implications for the formation of Gondwana. *Journal of Metamorphic Geology,* **23**, 603-624.

Brey, G.P. and Kohler, T., 1990. Gepthermobarometry in four-phase lherzolites II. New thermobarometers, and practical assessment of existing thermobarometers. *Journal of Petrology,* **31**, 1353-1378.

Brown, S.J.A., Barley, M.E., Krapez, B. and Cas, R.A.F., 2002. The late Archaean Melita Complex, Eastern Goldfields, Western Australia: shallow submarine bimodal volcanism in a rifted arc environment. *Journal of Volcanology and Geothermal Research,* **115**, 303-327.

Brown, M. and Solar, G.S., 1999. The mechanism of ascent and emplacement of granite magma during transpression: a syntectonic granite paradigm. *Tectonophysics,* **312**, 1-33.

Brown, M., 2006. Duality of thermal regimes is the distinctive characteristic of plate tectonics since the Neoarchean. *Geology,* **34**, 961-964.

Brown, M., 2007a. Metamorphic conditions in orogenic belts: a record of secular change. *International Geological Review,* **49**, 193-234.

Brown, M., 2007b. Characteristic thermal regimes of plate tectonics and their metamorphic imprint throughout Earth history: when did Earth first adopt a plate tectonics mode behavior? In: Condie K., Pease V. (eds) When did plate tectonics begin? *Geological Society of America Special Publication* (in press).

Brown, M., 2007c. Archean metamorphism and tectonics: latest news and views. *International Association for Gondwana Research Conference Series,* **4**, 23-26.

Brunsmann, A., Franz, G. and Erzinger, J., 2000. Zoisite- and clinozoisite segregations in metabasites (Tauern Window, Austria) as evidence for high-pressure fluid-rock interaction. *Journal of Metamorphic Geology,* **18**, 1-21.

Bucci, L.A., McNaughton, N.J., Fletcher, I.R., Groves, D.I., Kositcin, N., Stein, H.J. and Hagemann, S.G., 2004. Timing and duration of high-temperature gold mineralization and spatially associated granitoid magmatism at Chalice, Yilgarn Craton, Western Australia. *Economic Geology,* **99**, 1123-1144.

Buck, W.R., Martinez, F., Steckler, M.S. and Cochran, J.R., 1988. Thermal consequences of lithospheric extension: pure and simple. *Tectonics,* **7**, 213-234.

Buick, I.S., Hand, M., Williams, I.S., Mawby, J., Miller, J.A. and Nicoll, R.S., 2005. Detrital zircon provenance constraints on the evolution of the Harts Range Metamorphic Complex (central Australia): links to the Centralian Superbasin. *Journal of the Geological Society, London,* **162**, 777-787.

Bunting, J.A., Jackson, M.J. and Chin, R.J., 1978. Throssell 250 K sheet SH51-15. *GSWA Explanatory Notes*.

C

Campbell, I.H., Compston, D.M., Richards, J.P., Johnson, J.P. and Kent, A.J.R., 1998. Review of the application of isotopic studies to the genesis of Cu-Au mineralisation at Olympic Dam and Au mineralization at Porgera, the Tennant Creek district and Yilgarn Craton. *Australian Journal of Earth Sciences,* **45**, 201-218.

Carson, C.J., Powell, R. and Clarke, G.L., 1999. Calculated mineral equilibria for eclogites in CaO-Na2O-FeO-MgO-Al2O3-SiO2-H2O: application to the Pouebo Terrane, Pam Peninsula, New Caledonia. *Journal of Metamorphic Geology,* **17**, 9-24.

Cartwright, I. and Buick, I.S., 1995. Formation of wollastonite-bearing marbles during late regional metamorphic channelled fluid flow in the upper calcsilicate unit of the Reynolds Range Group, Central Australia. *Journal of Metamorphic Geology,* **13**, 397-417.

Cassidy, K.F., Groves, D.I. and McNaughton, N.J., 1998. Late-Archean granitoid-hosted lode-gold deposits, Yilgarn Craton, Western Australia: deposit characteristics, crustal architecture and implications for ore genesis. *Ore Geology Reviews,* **13**, 65-102.

Cassidy, K.F., Champion, D.C., McNaughton, N.J., Fletcher, I.R., Whitaker, A.J., Bastrakova, I.V. and Budd, A.R., 2002. Characterisation and metallogenic significance of Archaean granitoids of the Yilgarn Craton, Western Australia. *Minerals and Energy Research Institute of Western Australia (MERIWA), Report,* **222**, 514p.

Cassidy, K.F. and Champion, D.C., 2004. Crustal evolution of the Yilgarn Craton from Nd isotopes and granite geochronology: implications for metallogeny. In: *SEG 2004, Predictive Mineral Discovery Under Cover*, Muhling J. (ed). *Centre for Global Metallogeny, The University of Western Australia,* **33**, 317-320.

Cassidy, K.F., Champion, D.C., Krapez, B., Barley, M.E., Brown, S.J.A., Blewett, R.S., Groenewald, P.B. and Tyler, I.M., 2006, A revised geological framework for the Yilgarn Craton, Western Australia. *Western Australia Geological Survey Record,* **2006/8**, pp. 8.

Cassidy, K.F., 2006. Geological evolution of the Eastern Yilgarn Craton (EYC), and terrane, domain and fault nomenclature. In: 3D Geological models of the Eastern Yilgarn Craton Y2 Final Report ***pmd****CRC*, Blewett R.S., Hitchman A.P. (eds). *Geoscience Australia Record,* **2006/04**, 1-19.

Cathelineau, M. and Nieva, D., 1985. A chlorite solid solution geothermometer the Los Azufres (Mexico) geothermal system. *Contributions to Mineralogy and Petrology* 91, 235-244.

Cathelineau, M., 1988. Cation site occupancy in chlorites and illites as a funtion of temperature. *Clay Minerals,* **23**, 471-485.

Cesare, B., Meli, S., Nodari, L. and Russo, U., 2005. Fe3+ reduction during biotite melting in graphitic metapelites: another origin of CO2 in granulites. *Contributions to Mineralogy and Petrology,* **149**, 129-140.

Champion, D.C. and Sheraton, J.W., 1997. Geochemistry and Nd isotope systematics of Archaean granites of the Eastern Goldfields, Yilgarn Craton, Australia; implications for crustal growth processes. *Precambrian Research,* **83**, 109-132.

Champion, D.C., Cassidy, K.F. and Budd, A., 2001. Chapter 8. Overview of the Yilgarn magmatism: implications for crustal development. In: Cassidy et al. (eds) Characterization and metallogenic significance of Archaean granitoids of the Yilgarn Craton, Western Australia. *MERIWA Report,* **222**.

Champion, D.C. and Cassidy, K.F., 2002. Granites of the Leonora-Laverton transect area, northeastern Yilgarn Craton. *Geoscience Australia Record,* **2002/18**.

Champion, D.C. and Cassidy, K.F., 2007. An overview of the Yilgarn Craton and its crustal evolution. In: Bierlein F.P., Knox-Robinson C.M. (eds), 2007. Proceedings of Geoconferences (WA) Inc. Kalgoorlie '07 Conference. *Geoscience Australia Record,* **2007/14**, p13-35.

Champion, D.C., Cassidy, K.F. and Smithies, R.H., 2006. Sm-Nd isotopic characteristics of the Pilbara and Yilgarn Cratons, Western Australia: implications for crustal growth in the Archean. *Geochim. Cosmochim. Acta,* **70(1)**, A95.

Chatterjee, N.D., Johannes, W. and Leistner, H., 1984. The system CaO-Al2O3-SiO2-H2O: new phase equilibria data, come calculated phase relations, and their petrological applications. *Contributions to Mineral and Petrology,* **88**, 1-13.

Chen, S.F., 1999. Edjudina 250 K sheet SH51-6. *GSWA Explanatory Notes*.

Chen, S.F., Libby, J.W., Greenfield, J.E., Wyche, S. and Riganti, A., 2001a. Geometry and kinematics of large arcuate structures formed by impingement of rigid granitoids into greenstone belts during progressive shortening. *Geology,* **29**, 283-286.

Chen, S.F., Walter, K.W. and Liu, S., 2001b. Transpression and restraining jogs in the northeastern Yilgarn craton, Western Australia. *Precambrian Research,* **106**, 309-328.

Chen, S.F., Riganti, A., Wyche, S., Greenfield, J.E. and Nelson, D.R., 2003. Lithostratigraphy and tectonic evolution of contrasting greenstone successions in the central Yilgarn Craton, Western Australia. *Precambrian Research,* **127**, 249-266.

Chin, R.J. and Smith, R.A., 1983. Jackson 250 K sheet SH50-12. GSWA Explanatory Notes.

Chin, R.J., Hickman, A.H. and Thom, R., 1984. Hyden 250 K sheet SH50-4. *GSWA Explanatory Notes*.

Clark, M.E., 1980. Localization of gold, Mt Charlotte, Kalgoorlie, Western Australia. B.Sc. Honours thesis, University of Western Australia, pp. 128 (unpublished).

Clark, M.E., Archibald, N.J. and Hodgson, C.J., 1986. The structural and metamorphic setting of the Victory Gold Mine, Kambalda, Western Australia. *Proceedings of Gold '86 Symposium, Toronto*, 243-252.

Clark, M.E., Carmichael, D.M. and Hodgson, C.J., 1988. Metasomatic processes and T-XCO2 conditions of wall-rock alteration, Victory Gold Mine, Kambalda, Western Australia. In: Bicentennial Gold 88. *Geological Society of Australia Extended Abstracts,* **22**, 230-234.

Clark, M.E., Carmichael, D.M., Hodgson, C.J. and Fu, M., 1989. Wall-alteration, Victory gold mine, Kambalda, Western Australia: processes and P-T-XCO2 conditions of metamorphism. In: Keays R.R., Ramsay W.R.H., Groves D.I. (eds), The geology of gold deposits: The perspective in 1988. *Economic Geology Monograph,* **6**, 445-459.

Clarke, G.L., Guiraud, M., Powell, R. and Burg, J.P., 1987. Metamorphism in the Olary Block, South Australia: compression with cooling in a Proterozoic fold belt. *Journal of Metamorphic Geology,* **5**, 291-306.

Clarke, G.L., Powell, R. and Fitzherbert, J.A., 2006. The lawsonite paradox: a comparison of field evidence and mineral equilibria modelling. *Journal of Metamorphic Geology,* **24**, 715-726.

Claoué-Long, J.C., Compston, W. and Cowden, A., 1988. The age of the Kambalda greenstones resolved by ion microprobe - implications for Archaean dating methods. *Earth and Planetary Science Letters,* **89**, 239-259.

Cleverley, J., 2008. Fluid history and sources at Sunrise Dam, Laverton. *Talk on **pmd***CRC webbsite*.

Cohen, L.H., Ito, K. and Kennedy, G.C., 1967. Melting and phase relations in an anhydrous basalt to 40 kilobars. *American Journal of Science,* **265**, 475-518.

Collins, W.J. and Van Kranendonk, M.J., 1999. Model for the development of kyanite during partial convective overturn of Archaean granite-greenstone terranes: the Pilbara Craton, Australia. *Journal of Metamorphic Geology,* **17**, 145-156.

Colopietro, M.R. and Friberg, L.M., 1987. Tourmaline-biotite as a potential geothermometer for metapelites, Black Hills, South Dakota. *Geological Society of America Abstract Program,* **19**, 624.

Compston, W., Williams, I.S., Campbell, I.H. and Gresham, J.J., 1986. Zircon xenocrysts from the Kambalda volcanics: age constraints and direct evidence for older continental crust below the Kambalda-Norseman greenstones. *Earth and Planetary Science Letters,* **76**, 299-311.

Connolly, J.A.D. and Thompson, A.B., 1989. Fluid and enthalpy production during regional metamorphism. *Contributions to Mineralogy and Petrology,* **102**, 347-366.

Connolly, J.A.D. and Petrini, K., 2002. An automated strategy for calculation of phase diagram sections and retrieval of rock properties as a function of physical conditions. *Journal of Metamorphic Geology,* **20**, 697-708.

Cooper, R.W., Abeysinghe, P.B. and Flint, D.J., 2007. Western Australia atlas of mineral deposits and petroleum fields 2007. *GSWA publication*.

Cox, S.F., 1995. Faulting processes at high fluid pressures: an example of fault valve behaviour from the Wattle Gully Fault, Victoria, Australia. *Journal of Geophysical Research,* **100**, 12841-12859.

Cox, S.F. and Ruming, K., 2004. The St Ives mesothermal gold system, Western Australia—a case of golden aftershocks? *Journal of Structural Geology,* **26**, 1109-1125.

Crawford, M.A. and Cox, S.F., 2007. The mechanical and fluid pressure evolution of the Argo shear system during gold mineralization. *Geological Society of Australia Abstracts*, 57.

Currie, K.L., 1971. The reaction 3 cordierite = 2 garnet + 4 sillimanite + 5 quartz as a geologic thermometer in the Opinicon Lake Region, Ontario. *Contributions to Mineralogy and Petrology,* **33**, 215-226.

Czarnota, K., Champion, D.C., Cassidy, K.F., Goscombe, B., Blewett, R.S., Henson, P.A. and Groenewald, P.B., 2008. Geodynamics of the Eastern Goldfields Superterrane. ***pmd****CRC Project Y4 Final Report,* **3**, 10-45.

D

Daczko, N.R., Klepeis, A. and Clarke, G.L., 2001. Evidence of Early Cretaceous collisional-style orogenesis in northern Fiordland, New Zealand and its effects on the evolution of the lower crust. *Journal of Structural Geology,* **23**, 693-713.

Dale, J., Powell, R., White, R.W., Elmer, F.L. and Holland, T.J.B., 2005. A thermodynamic model for Ca-Na clnoamphiboles in Na2O-CaO-FeO-MgO-Al2O3-SiO2-H2O-O for petrological calculations. *Journal of Metamorphic Geology,* **23**, 771-792.

Dalstra, H.J., 1995. Metamorphic and structural evolution of greenstone belts of the Southern Cross-Diemals region of the Yilgarn Block, Western Australia and its relationship to gold mineralization. Masters thesis, University of Western Australia (unpublished).

Dalstra, H.J., Ridley, J.R., Bloem, J.M. and Groves, D.I., 1999. Metamorphic evolution of the central Southern Cross Province, Yilgran Craton, Western Australia. *Australian Journal of Earth Sciences,* **46**, 765-784.

Davis, B.K. and Maidens, E., 2003. Archaean orogen-parallel extension: evidence from the northernEastern Goldfields Province, Yilgarn Craton. *Precambrian Research* 127, 229-248.

Deer, W.A., Howie, R.A. and Zussman, J., 1980. An introduction to the rock forming minerals. Longman. pp. 528

Dewey, J.F., Holdsworth, R.E. and Strachan, R.A., 1998. Transpression and transtension zones. In: Holdsworth R.E., Strachan R.A., Dewey J.F. (eds.). Continental transpressional and transtensional tectonics. *Geological Society of London, Special Publications,* **135**, 1-14.

Diener, J.F.A., Stevens, G., Kisters, A.F.M. and Poujol, M., 2005. Metamorphism and exhumation of the basal parts of the Barberton greenstone belt, South Africa: Constraining the rates of Mesoarchaean tectonism. *Precambrian Research,* **143**, 87-112.

Diener, J.F.A., Powell, R., White, R.W. and Holland, T.J.B., 2007. A new thermodynamic model for clno- and orthoamphiboles in the system Na2O-CaO-FeO-MgO-Al2O3-SiO2-H2O-O. *Journal of Metamorphic Geology,* **25**, 631-656.

Dickin, A.P., 1995. Radiogenic Isotope Geology, Cambridge University Press, 2nd edition

Donohue, C.L. and Essene, E.J., 2005. Granulite-facies conditions preserved in vanadium- and chromium-rich metapelites from the paradise basin, Wind River Range, Wyoming, USA. *Canadian Mineralogist,* **43**, 495-511.

Drummond, B.J., Goleby, B.R. and Swager, C.P., 2000. Crustal signature of Late Archaean tectonic episodes in the Yilgarn craton, Western Australia: evidence from deep seismic sounding. *Tectonophysics,* **329**, 193-221.

Duclaux, G., Rey, P., Guillot, S. and Menot, R.-P., 2007. Orogen-parallel flow during continental convergence: Numerical experiments and Archean field examples. *Geology,* **35**, 715-718.

Dugdale, A.L. and Hagemann, S.G., 2001. The Bronzewing lode-gold deposit, Western Australia: P-T-X evidence for fluid immiscibility caused by cyclic decompression in gold-bearing quartz-veins. *Chemical Geology,* **173**, 59-90.

Dunphy and others, 2003. Compilation of SHRIMP U-Pb geochronological data, Yilgarn Craton, Western Australia, 2001-2002. *Geoscience Australia Record,* **2003/15**, pp. 139.

Duuring, P., 2002. Structural and hydrothermal fluid controls on metallogenesis associated with Archaean granitoids in the Yilgarn Craton, Western Australia: evidence from the Jupiter and Tarmoola gold deposits. PhD thesis, University of Western Australia (unpublished).

Dziggle, A., Knipfer, S., Kisters, A.F.M. and Meyer, F.M., 2006. P-T and structural evolution during exhumation of high-T, medium-P basement rocks in the Barberton Mountain Land, South Africa. *Journal of Metamorphic Geology,* **24**, 535-551.

E

Elias, M., Bunting, J.A. and Wharton, P.H., 1982. Glengarry 250 K sheet SH50-12. *GSWA Explanatory Notes*.

Ellis, D.J. and Green, D.H., 1979. An experimental study of the effect of Ca upon garnet-clinopyroxene Fe-Mg exchange equilibria. *Contributions to Mineralogy and Petrology,* **71**, 13-22.

Elmer, F.L., White, R.W. and Powell, R., 2006. Devolatilization of metabasic rocks during greenschist-amphibolite facies metamorphism. *Journal of Metamorphic Geology,* **24**, 497-513.

El-Shazly, A.K., 1994. Petrology of lawsonite-, pumpellyite- and sodic amphibole-bearing metabasites from north-east Oman. *Journal of Metamorphic Geology,* **12**, 23-48.

Ernst, W.G., 1966. Synthesis and stability relations of ferrotremolite. *American Journal of Science,* **264**, 37-65.

Ernst, W.G., 1976. Petrologic Phase Equilibria. W.H. Freeman, San Francisco.

Evans, K.A., Phillips, G.N. and Powell, R., 2006. Rock-buffering of auriferous fluids in altered rocks associated with the golden Mile-style mineralization, Kalgoorlie Gold Field, Western Australia. *Economic Geology,* **101**, 805-817.

F

Farrell, T.R., 2001. GSWA Duketon 250 K sheet SH51-14. *GSWA Explanatory Notes*.

Farrell, T.R., 2001. GSWA Wiluna 250 K sheet SH51-9. *GSWA Explanatory Notes*.

Ferry, J.M. and Spear, F.S., 1978. Experimental calibration of the partitioning of Fe and Mg between biotite and garnet. *Contributions to Mineralogy and Petrology,* **66**, 113-117.

Ferry, J.M., 1987. Metamorphic hydrology at 13-km depth and 400-550 ºC. *American Mineralogist,* **72**, 39-58.

Findlay, D., 1994. Boudinage control on the emplacement of lodes of the Kalgoorlie goldfield. *Australian Journal of Earth Sciences,* **41**, 105-113.

Findlay, D., 1998. Boudinage on radial fractures: an alternative to magmatic models for the emplacement of nickel ores, Lunnon Shoot, Kambalda, Western Austalia. *Australian Journal of Earth Sciences,* **45**, 943-954.

Fitzsimons, I.C.W. and Harley, S.L., 1994. The influence of retrograde cation exchange on granulite P-T estimates and a convergence technique for the recovery of peak metamorphic conditions. *Journal of Petrology,* **35**, 543-576.

Fletcher, I.R., Dunphy, J.M., Cassidy, K.F. and Champion, D.C., 2001. Compilation of SHRIMP U-Pb geochronological data, Yilgarn Craton, Western Australia, 2000-2001. *Geoscience Australia Record,* **2001/47**, 111p.

Foden, J., Marlina, A.E., Dougherty-Page, J. and Burtt, A., 2006. The timing and duration of the Delamarian Orogeny: correlation with the Ross Orogen and implications for Gondwana Assembly. *The Journal of Geology,* **114**, 189-210.

Foster, D.A., Coyner, S.J., Mueller, P.A., Kamenov, G.D., Gray, D.R. and Goscombe, B.D., 2006. Linking metamorphism, deformation and geochronology of accessory phases: Examples from the Kaoko Belt, Namibia. *Geochimica et Cosmochimica Acta,* **70 (18)**, A182-A182.

Foster, D.A., Goscombe, B.D. and Gray, D.R., 2009. Rapid exhumation of deepcrust in an obliquely convergent orogen: the Kaoko Belt of the Damara Orogen. *Tectonics,* **28**, doi:10.1029/2008TC002317.

Frost, B.R. and Chacko, T., 1989. The granulite uncertainty principle: limitations on thermobarometry in granulites. *Journal of Geology*, **97**, 435-450.

G

Gaidies, F., Abart, R., DeCapitani, C., Schuster, R., Connolly, J.A.D. and Reusser, E., 2006. Characterization of polymetamorphism in the Australpine basement east of the Tauren Window using garnet isopleth thermobarometry. *Journal of Metamorphic Geology,* **24**, 451-476.

Gauthier, L., Hagemann, S.G., Roberts, F. and Pickens, G., 2004. New constraints on the architecture and timing of the giant Golden Mile gold deposit, Kalgoorlie, Western Australia. In Muhling J. et al. (eds), SEG 2004: Predictive mineral discovery under cover. *The University of Western Australia Publication,* **33**, 353-356.

Gauthier, L., Hagemann, S. and Robert, F., 2007. The geological setting of the Golden Mile gold deposit, Kalgoorlie, WA. In: Bierlein F.P., Knox-Robinson C.M. (eds), Proceedings of Geoconferences (WA) Inc. Kalgoorlie '07 Conference. *Geoscience Australia Record,* **2007/14**, 181-185.

Gee, R.D., Baxter, J.L., Wilde, S.A. and Williams, I.R., 1981. Crustal development in the Archaean Yilgarn Block, Western Australia. *Geological Society of Australia, Special Publication,* **7**, 43-56.

Gee, R.D., 1982. Southern Cross 250 K sheet SH50-16. *GSWA Explanatory Notes*.

Ghent, E.D., Robbins, D.B. and Stout, M.Z., 1979. Geothermometry, geobarometry, and fluid compositions of metamorphosed calc-silicates and pelites, Mica Creek, British Columbia. *American Mineralogist*, **64**, 874-885.

Ghent, E.D., Stout, M.Z. and Raeside, R.P., 1983. Plagioclase-clinopyroxene-garnet-quartz equilibria and the geobarometry and geothermometry of garnet amphibolites from Mica Creek, British Columbia. *Canadian Journal of Earth Sciences,* **20**, 699-706.

Ghent, E.D., 1988. Tremolite and H2O activity attending metamorphism of hornblende-plagioclase-garnet assemblages. *Contributions to Mineralogy and Petrology,* **98**, 163-168.

Gibson, C.G., 1907. The geology and mineral resources of Lawlers, Sir Samuel, and Darlot (East Murchison Goldfield), Mount Ida (North Coolgardie Goldfield) and a portion of the Mount Margaret Goldfield. *Geological Survey of Western Australia Bulletin,* **28**.

Giles, D., Betts, P.G., Ailleres, L., Hulscher, B., Hough, M. and Lister, G.S., 2006. Evolution of the Isan Orogeny at the southeastern margin of the Mt Isa Inlier. *Australian Journal of Earth Sciences,* **53**, 91-108.

Goldfarb, R.J., Groves, D.I. and Gardoll, S., 2001. Orogenic gold and geologic time: a global synthesis. *Ore Geology Reviews,* **18**, 1-17.

Goldfarb, R.J., Baker, T., Dube, B., Groves, D.I., Hart, C.J.R. and Gosselin, P., 2005. Distribution, character, and genesis of gold deposits in metamorphic terranes. Society of Economic Geologists, *Economic Geology,* **100th** Anniversary Volume, 407-450.

Golding, L.Y., 1985. The nature of the Golden Mile dolerite south-east of Kalgoorlie, Western Australia. *Australian Journal of Earth Sciences,* **32**, 55-63.

Goleby, B.R., Rattenbury, M.S., Swager, C.P., Drummond, B.J., Williams, P.R., Sheraton, J.E. and Heinrich, C.A., 1993. Archaean crustal structure from seismic reflection profiling, Eastern Goldfields, Western Australia. *Australian Geological Survey Organisation Record,* **1993/15**, pp. 54.

Goleby, B.R., Korsch, R.J., Fomin, T., Bell, B., Nicoll, B.J., Drummond, B.J. and Owen, A.J., 2002a. Preliminary 3-D geological model of the Kalgoorlie region, Yilgarn Craton, Western Australia, based on deep seismic-reflection and potential-field data. *Australian Journal of Earth Sciences,* **49**, 917-933.

Goleby, B.R., Blewett, R.S., Champion, D.C., Korsch, R.J., Bell, B., Groenewald, P.B., Jones, L.E.A., Whitaker, A.J., Cassidy, K.F. and Carlsen, G.M., 2002b. Deep seismic profiling in the NE Yilgarn: insights into its crustal architecture. *Australian Institute of Geoscientists Bulletin,* **36**, 63-66.

Goscombe, B.D. and Trouw, R., 1998. The geometry of folded tectonic shear sense indicators. *Journal of Structural Geology,* **21**, 123-127.

Goscombe, B.D. and Hand, M., 2000. Contrasting P-T paths in the Eastern Himalaya, Nepal: Inverted isograds in a Paired Metamorphic Mountain Belt. *Journal of Petrology,* **41(12)**, 1673-1719.

Goscombe, B. and Hand, M., 2001. Metamorphic model for the Inland Branch of the Damara Orogen: A Paired Metamorphic Mountain Belt (PMMB). *Geological Society of Australia, Specialist Group in Tectonics and Structural Geology, Conference, Ulverstone, Australia. Abstracts,* **64**, 59.

Goscombe, B.D. and Everard, J.L., 2001. Tectonic evolution of Macquarie Island: extensional structures and block rotations in oceanic crust. *Journal of Structural Geology,* **23**, 639-673.

Goscombe, B.D. and Passchier, C., 2003. Asymmetric boudins as shear sense indicators an assessment from field data. *Journal of Structural Geology,* **25(4)**, 575-589.

Goscombe, B.D., Hand, M. and Gray, D., 2003. Structure of the Kaoko Belt, Namibia: Progressive evolution of a classic transpressional orogen. *Journal Structural Geology,* **25**. 1049-1081.

Goscombe, B.D., Hand, M., Gray, D. and Mawby, J., 2003. The metamorphic architecture of a transpressional orogen: the Kaoko Belt, Namibia. *Journal of Petrology,* **44**, 679-711.

Goscombe, B.D., Passchier, C. and Hand, M., 2004a Boudinage classification: end-member boudin types and modified boudin structures. *Journal of Structural Geology,* **26**, 739-763.

Goscombe, B.D., Gray, D. and Hand, M., 2004b. Variation in metamorphic style along the northern margin of the Damara Orogen, Namibia. *Journal of Petrology,* **45**, 1261-1295.

Goscombe, B.D., Gray, D. and Hand, M., 2005a. Extrusional tectonics in the core of a transpressional orogen, the Kaoko Belt, Namibia. *Journal of Petrology,* **46**, 1203-1241.

Goscombe, B., Gray, D. and Hand, M., 2006. Crustal architecture of the Himalayan Metamorphic Front in eastern Nepal. *Gondwana Research,* **10**, 232-255.

Goscombe, B.D. and Gray, D., 2007. The Coastal Terrane of the Kaoko Belt, Namibia: outboard arc-terrane and tectonic significance. *Precambrian Research,* **155**, 139-158.

Goscombe, B., Blewett, R.S, Czarnota K., Maas, R. and Groenewald, B.A., 2007. Broad thermo-barometric evolution of the Eastern Goldfields Superterrane. In: in Bierlein, F.P., and Knox-Robinson, C.M., (eds), 2007. Proceedings of Geoconferences (WA) Inc. Kalgoorlie '07 Conference. *Geoscience Australia Record,* **2007/14**, 33-38.

Goscombe, B. and Gray, D., 2007. Determining crustal architecture using integrated terrane analysis: example from the eastern Nepal Himalayas. *4th International Symposium on Gondwana to Asia, Fukuoka, Japan*.

Goscombe, B.D. and Gray, D., 2008. Structure and strain variation at mid-crustal levels in a transpressional orogen: a review of Kaoko Belt structure and the character of West Gondwana amalgamation. *Gondwana Research Focus Paper,* **13**, 45-85.

Goscombe, B.D. and Gray, D.R., 2009. Metamorphic response in orogens of different obliquity, scale and geometry. *Gondwana Research,* **15**, 151-167.

Goscombe, B.D., Blewett, R.S., Czarnota, K., Groenewald, B.A. and Maas, R., 2009. Metamorphic evolution and integrated terrane analysis of the Eastern Yilgarn Craton: rationale, methods, outcomes and interpretation. *Geoscience Australia Record,* **2009/23**, this record.

Goscombe, B.D. and Blewett, R.S., 2009. Plate 1: East Yilgarn Craton Metamorphism and Strain map. *Geoscience Australia Map Series*.

Gower, C.F. and Boegli, J.C., 1977. Rason 250 K sheet SH51-3. *GSWA Explanatory Notes*.

Grapes, R. and Watanabe, T., 1992. Metamorphism and uplift of Alpine schist in the Franz Josef-Fox Glacier area of the Southern Alps, New Zealand. *Journal of Metamorphic Geology,* **10**, 171-180.

Green, D.H. and Ringwood, A.E., 1972. A comparison of recent experimental data on the gabbro-garnet granulite-eclogite transition. *Journal of Geology,* **80**, 277-288.

Green, D.H. and Ringwood, A.E., 1967. An experimental investigation of the gabbro to eclogite transformation and its petrological applications. *Geochim. Cosmochim. Acta,* **31**, 767-833.

Green, T.H. and Hellman, P.L., 1982. Fe-Mg partitioning between coexisting garnet and phengite at high pressure, and comments ona garnet-phengite geothermometer. *Lithos,* **15**, 252-266.

Griffin, W.L., Belousova, E.A., Shee, S.R., Pearson, N.J. and Reilly, S.Y., 2004. Archaean crustal evolution in the northern Yilgarn Craton. *Precambrian Research,* **131**, 231-282.

Groenewald, P.B., Painter, M.G.M., Roberts, F.I., McCabe, M. and Fox, A., 2000. East Yilgarn geoscience database, 1:100 000 geology Menzies to Norseman – an explanitory note. *GSWA Report,* **78**.

Groenewald, P.B., Doyle, M.G., Brown, S.J.A. and Barnes, S.J., 2006. Stratigraphy and physical volcanology of the Archean Kurnalpi Terrane, Yilgarn Craton – a field guide. *GSWA Record,* **2006/11**.

Groppo, C., Lombardo, B., Rolfo, F. and Pertusati, P., 2007. Clockwise exhumation path of granulitized eclogites from the Ama Drime range (Eastern Himalayas). *Journal of Metamorphic Geology,* **25**, 51-76.

Groves, D.I. and Phillips, G.N., 1987. The genesis and tectonic controls on Archaean gold deposits of the Western Australian Shield: a metamorphic replacement model. *Ore Geology Reviews,* **2**, 287-322.

Groves, D.I., Barley, M.E., Barnicoat, A.C., Cassidy, K.F., Fare, R.J., Hagemann, S.G., Ho, S.E., Hronsky, J.M.A., Mikucki, E.J., Mueller, A.G., McNaughton, N.J., Perring, C.S., Ridley, J.R. and Vearncombe, J.R., 1992. Sub-greenschist- to granulite-hosted Archaean lode-gold deposits of the Yilgarn Craton: a depositional continuum from deep-sourced hydrothermal fluids in crustal-scale plumbing systems. *University of Western Australia Publication,* **22**, 325-337.

Groves, D., 2002. A generic Assessment of orogenic gold provinces: Factors controlling the formation of World-class and giant deposits. Hydrothermal systems, giant ore deposits and a new paradigm for predictive mineral exploration, P511, Yilgarn atlas volume III.

H

Hagemann, S.G. and Ridley, J.R., 1993. Hydrothermal fluids in epi- and katazonal crustal levels in the Archaean: implications for P-T-X-t evolution of lode-gold mineralization. *AGSO Abstracts Record,* **1993/54**, 123-130.

Hagemann, S.G. and Luders, V., 2003. P-T-X conditions of hydrothermal fluids and precipitation mechanism of stibnite-gold mineralization at the Wiluna lode-gold deposits, Western Australia: conventional and infrared microthermometric constraints. *Mineralium Deposita,* **38**, 936-952.

Hall, G.C., 1997. Kalgoorlie exploration model. *Placer Exploration Limited Report,* **WA666/97**.

Hall, C., 2006. The Mount Belches Formation – Black Flag Group, a late basin, or something else? *GSWA Technical Paper*.

Hallberg, J.A., 1985. Geology and mineral deposits of the Leonora–Laverton area, northeastern Yilgarn Block, Western Australia. Hesperian Press, Perth, Western Australia, pp. 140.

Halley, S.W., 2007. Mineral mapping – how it can help us explore in the Yilgarn Craton. In: Bierlein F.P., Knox-Robinson C.M. (eds), Proceedings of Geoconferences (WA) Inc. Kalgoorlie '07 Conference. *Geoscience Australia Record,* **2007/14**, 143-148.

Hamilton, W.B., 2001. Archean tectonics and magmatism: no plate tectonics or plumes. *AGSO Extended Abstracts*, 314-316.

Hammond, R.L. and Nisbet, B.W., 1992. Towards a structural and tectonic framework for the Norseman-Wiluna Greenstone Belt, Western Australia. In: Glover, J.E., and Ho, S.E., (Eds), The Archaean – Terrains, Processes and Metallogeny. Geology Department and University Extension, *The University of Western Australia, Publication,* **22**, 39-50.

Hand, M., Bendall, B.R. and Sandiford, M., 1995. Metamorphic evidence for palaeoproterozoic oblique convergence in the eastern Gawler Craton. *Geological Society of Australia, Abstracts,* **40***, 59.*

Hand, M., Bendall, B.R. and Sandiford, M., 1996. Metamorphic record of strain partitioning during oblique convergence. *Geological Society of Australia Abstracts,* **41**, 178.

Harley, S.L. and Buick, I.S., 1992. Wollastonite-scapolite assemblages as indicators of granulite pressure-temperature-fluid histories: the Rauer Group, East Antarctica. *Journal of Petrology,* **33**, 693-728.

Harris, D.H.M., Williams, P.R., Newton-Smith, J. and Fitzgerald, L.G., 1997. Tectonic fabric development and mineralization of the Duketon greenstone belt, Western Australia. *Australian Journal of Earth Sciences,* **44**, 503-508.

Harris, L.B., Koyi, H.A. and Fossen, H., 2002. Mechanisms for folding of high-grade rocks in extensional tectonic settings. *Earth-Science Reviews,* **59**, 163-210.

Harrison, T.M., Watson, E.B. and Aikman, A.B., 2007. Temperature spectra of zircon crystallization in plutonic rocks. *Geology,* **35**, 635-638.

Hey, M.H., 1954. A new review of the chlorites. *Mineralogy Magazine,* **30**, 277.

Henderson, C.A., 1981. The nature and gebesis of quartz-gold vein systems at the Morning Star deposit, Mount Magnet, Western Australia. B.Sc. Honours thesis, University of Western Australia, pp. 170 (unpublished).

Henson, P.A. and Blewett, R.S., 2006. 3D interpretation of the Eastern Yilgarn: new architectural insights from construction of the 3D map. In: 3D Geological models of the Eastern Yilgarn Craton Y2 Final Report ***pmd****CRC*, Blewett R.S., Hitchman A.P. (eds). *Geoscience Australia Record,* **2006/04**, 207-216.

Henson, P.A., Blewett, R.S., Champion, D.C., Goleby, B.R. and Czarnota, K., 2007. How does the 3D architecture of the Yilgarn control hydrothermal fluid focussing?. In: Bierlein F.P., Knox-Robinson C.M. (eds). Proceedings of Geoconferences (WA) Inc. *Kalgoorlie '07 Conference. Geoscience Australia Record,* **2007/14**, 57-61.

Hill, R.I., Campbell, I.H. and Compston, W., 1989. Age and origin of granitic rocks in the Kalgoorlie-Norseman region of Western Australia: implications for the origin of Archaean crust. *Geochimica et Cosmochimica Acta,* **53**, 1259-1275.

Hill, R.I., Chappell, B.W. and Campbell, I.H., 1992. Late Archaean granites of the southeastern Yilgarn Block, Western Australia: age, geochemistry and origin. *Royal Society Edinburgh, Transactions,* **83**, 211-226.

Hill, R.I. and Campbell, I.H., 1993. Age of granite emplacement in the Norseman region of Western Australia. *Australian Journal of Earth Sciences,* **40**, 559-574.

Ho, S.E., 1984. Alternative host rocks for Archaean gold deposits: nature and genesis of hydrothermal gold deposits, Kanowna, Western Australia. In: Gold mining, metallurgy and geology. Australasian Institute of Mining and Metallurgy, *Geology Abstracts*, pp. 11.

Ho, S.E., 1986. A fluid inclusion study of Archaean gold deposits of the Yilgarn Block, Western Australia. Ph.D. thesis, University of Western Australia (unpublished).

Ho, S.E., 1987. Fluid inclusions: their potential as an exploration tool for Archaean gold deposits. *University of Western Australia Publication,* **11**, 239-263.

Ho, S.E., Groves, D.I. and Bennett, J.M., 1990. Gold deposits of the Archaean Yilgarn block, Western Australia: nature, genesis and explorationj guides. *University of Western Australia Publication,* **20**, pp. 407.

Hobbs, B.E, Means, W.D. and Williams, P.F., 1983. An outline of structural geology. John Wiley, New York, 571 pp.

Hodges, K.V. and Spear, F.S., 1982. Geothermometry, geobarometry and the Al2SiO5 btriple point at Mt. Moosilauke, New Hampshire. *American Mineralogist,* **67**, 1118-1134.

Hodge, J.L., 2007. PhD thesis, University of Western Australia (unpublished).

Hoisch, T.D., 1989. A muscovite-biotite geothermometer. *American Mineralogist,* **74**, 565-572.

Holland, T.J.B. and Powell, R., 1990. An enlarged and updated internally consistent thermodynamic dataset with uncertainties and correlations: the system K_2O-Na_2O-CaO-MgO-MnO-FeO-Fe_2O_3-Al_2O_3-TiO_2-SiO_2-C-H_2-O_2. *Journal of Metamorphic Geology,* **8**, 89-124.

Holland, T.J.B., Baker, J. and Powell, R., 1998. Mixing properties and activity–composition relationships of chlorites in the system MgO–Al2O3–SiO2–H2O. *European Journal of Mineralogy,* **10**, 395–406.

Holland, T.J.B., 1980. The reaction albite = jadeite + quartz determined experimentally in the range 600-1200 ^{O}C. *American Mineralogist* **65**, 129-134.

Holland, T. and Blundy, J., 1994. Non-ideal interactions in calcic amphiboles and their bearing on amphibole-plagioclase thermometry. *Contributions to Mineralogy and Petrology,* **116**, 433 - 447.

Holland, T. and Blundy, J., 1997. Computer program for amphibole-plagioclase geothermobarometry. Available on Holland webbsite.

Hronsky, J.M.A., 1993. The role of physical and chemical processes in the formation of ore-shoots at the Lancefield gold deposit, Western Australia. PhD thesis, University of Western Australia (unpublished).

Hunter, W.M., 1993. Geology of the granite-greenstone terrane of the Kalgoorlie and Yilmia 1:100 000 sheets, Western Australia. *GSWA Report,* **35**.

Huston, D.L., Brauhart, C.W., Drieberg, S.L., Davidson, G.J. and Groves, D.I., 2001. Metal leaching and inorganic sulfate reduction in volcanic-hosted massive sulfide mineral systems: evidence from the paleo-Archean Panorama district, Western Australia. *Geology,* **29**, 687-690.

Hynes, A. and Forrest, R.C., 1988. Empirical garnet-muscovite geothermometry in low-grade metapelites, Selwyn Range (Canadian Rockies). *Journal of Metamorphic Geology,* **6**, 297-309.

I

Indare, A. and Martignole, J., 1985. Biotite-garnet geothermometry in the granulite facies: the influenc of Ti and Al in biotite. *American Mineralogist,* **70**, 272-278.

Ion, J.C., 1982. Wallrock alteration and structural evolution of steeply dipping Golden Mile dolerite hosted lodes of the Perseverance gold mine, Kalgoorlie. B.Sc. Honours thesis, University of Western Australia (unpublished).

Issler, D., McQeen, H. and Beaumont, C., 1989. Thermal and isostatic consequences of simple shear extension of the continental lithosphere. *Earth and Planetary Science Letters,* **91**, 341-358.

Ito, K. and Kennedy, G.C., 1971. An experimental study of the basalt-garnet granulite-eclogite transition. In: Heacock J.G. (ed) The structure and physical properties of the Earth's crust. *American Geophysical Union Geophysics Monograph,* **14**, 303-314.

J

Jamieson, R.A., 1981. Metamorphism during ophiolite emplacement – the petrology of the St Anthony Complex. *Journal of Petrology,* **22**, 397-449.

Jamieson, R.A., Beaumont, C., Nguyen, M.H. and Lee, B., 2002. Interaction of metamorphism, deformation and exhumation in large convergent orogens. *Journal of Metamorphic Geology,* **20**, 1-16.

Jessop, M.J., Law, R.D. and Frassi, C., 2007. The Ridid Grain Net (RGN): An alternative method for estimating mean kinematic vorticity number (Wm). *Journal of Structural Geology,* **29**, 411-421.

Johnson, T.E., Brown, M. and Solar, G.S., 2003. Low-pressure subsolidus and parasolidus phase equilibria in the MnNCKFMASH system: Constraints on conditions of regional metamorphism in western Maine, northern Appalachians. *American Mineralogist,* **88**, 624-638.

Johnson, P.R. and Kattan, F., 2001. Oblique sinistral transpression in the Arabian shield: the timing and kinematics of a Neoproterozoic suture zone. *Precambrian Research,* **107**, 117-138.

Jones, S.A., 2006. Mesoproterozoic Albany-Fraser Orogen-related deformation along the southeastern margin of the Yilgarn Craton. *Australian Journal of Earth Sciences,* **53**, 213-234.

Jones, R.R., Holdsworth, R.E., Hand, M. and Goscombe, B., 2006. Ductile extrusion in continental collision zones: ambiguities in the definition of channel flow and its identification in ancient orogens. In: Law R.D., Searle M.P., Godin L. (eds.) Channel flow, ductile extrusion and exhumation in continental collision zones. *Geological Society, London, Special Publications,* **268**, 201-219.

Jurasky, W., 1989. Petrogenesis and gold mineralization of the Paddington II gold mine, Kalgoorlie, WA. Masters Thesis, Leoben Mining University (unpublished).

K

Kelsey, D.E., White, R.W. and Powell, R., 2003. Orthopyroxene-sillimanite-quartz assemblages: distribution, petrology, quantitative P-T-X constraints and P-T paths. *Journal of Metamorphic Geology,* **21**, 439-453.

Kemp, A.I.S., Shimura, T. and Hawkesworth, C.J., 2007. Linking granulites, sialic magmatism, and crustal growth in arcs: ion microprobe (zircon) U-Pb ages from the Hidaka metamorphic belt, Japan. *Geology,* **35**, 807-810.

Kent, A.J.R. and McDougall, I., 1995. 40Ar-39Ar and U-Pb age constraints on the timing of gold mineralization in the Kalgoorlie gold field, Western Australia. *Economic Geology,* **90**.

Kent, A.J.R. and Hagemann, S.G., 1996. Constraints on the timing of lode-gold mineralization in the Wiluna greenstone belt, Yilgarn Craton, Western Australia. *Australian Journal of Earth Sciences,* **43**, 573-588.

Kent, A.J.R., Cassidy, K.F. and Fanning, C.M., 1996. Archean gold mineralisation synchronous with the final stages of cratonisation, Yilgarn Craton, Western Australia. *Geology,* **24**, 879-882.

Kerrich, R. and Cassidy, K.F., 1994. Temporal relationships of lode gold mineralization to accretion, magmatism, metamorphism and deformation – Archean to present: a review. *Ore Geology Reviews,* **9**, 263-310.

Kim, H.S., 2006. Deformation-induced garnet zoning. *Gondwana Research,* **10**, 379-388.

Kirkwood, D., Milo, M., St-Julien, P. and Therrien, P., 1995. Vertical and fold-axis parallel extension within a slate belt in a transpressive setting, northern Appalachians. *Journal of Structural Geology,* **17**, 329-343.

Knight, J.T., Groves, D.I. and Ridley, J.R., 1993. The Coolgardie Goldfield, Western Australia: district-scale controls on an Archaean gold camp in an amphibolite facies terrane. *Mineral. Deposita,* **28**, 436-456.

Knight, J.T., Ridley, J.R., Groves, D.I. and McCall, C., 1996. Syn-peak metamorphic gold mineralization in the amphibolite-facies, gabbro-hosted Three Mile Hill deposit, Coolgardie Goldfield, Western Australia: a high-temperature analogue of mesothermal gabbro-hosted gold deposits. *Trans. Instn. Min. Metall.,* **105**, B175-B195.

Knight, J.T., Ridley, J.R. and Groves, D.I., 2000. The Archaeanamphibolite facies Coolgardie Goldfield, Yilgarn Craton, Western Australia: Nature, controls, and gold field-scale patterns of hydrothermal wall-rock alteration. *Economic Geology,* **95**, 49-84.

Kohn, M.J. and Spear, F.S., 1990. Two new geobarometers for garnet amphibolites, with applications to southeastern Vermont. *American Mineralogist* **75**, 89-96.

Kohn, M.J. and Spear, F., 2000. Retrograde net transfer reaction insurance for pressure-temperature estimates. *Geology* **28**, 1127-1130.

Koons, P.O., Norris, R.J., Craw, D. and Cooper, A.F., 2003. Influence of exhumation on the structural evolution of transpressional plate boundaries: An example from the Southern Alps, New Zealand. *Geology* **31**, 3-6.

Kosulicova, M. and Stipska, P., 2007. Variations in the transient prograde geothermal gradient from chloritoid-staurolite equilibria: a case study from the Barrovian and Buchan-type domains in the Bohemian Massif. *Journal of Metamorphic Geology* **25**, 19-36.

Krapez, B., Brown, S.J.A., Hand, J., Barley, M.E. and Cas, R.A.F., 2000, Age constraints on recycled crustal and supracrustal sources of Archaean metasedimentary sequences, Eastern Goldfields Province, Western Australia, Evidence from SHRIMP zircon dating. *Tectonophysics,* **322**, 89-133.

Kretz, R., 1983. Symbols for rock-forming minerals. *American Mineralogist,* **68**, 277-279.

L

Lacassin, R. and Mattauer, M., 1985. Kilometre-scale sheath fold at Mattmark and implications for transport direction in the Alps. *Nature,* **315**, 739-742.

Laird, J., 1989. Chlorites: metamorphic petrology. In. Micas. *Mineralogist Society of America Reviews in Mineralogy,* **19**, 405-453.

Lambert, D.D., Foster, J.G., Frick, L.R., Hoatson, D.M. and Purvis, A.C., 1998. Application of the Re-Os isotopic system to the study of Precambrian magmatic sulfide deposits of Western Australia. *Australian Journal of Earth Sciences,* **45**, 265-284.

Langford, R.L. and Farrell, T.R., 1998. Geology of the Duketon 1:100 000 sheet. *GSWA 100K Explanitory Notes*.

Langford, R.L., 2000. Geology of the Wiluna 1:100 000 sheet. *GSWA 100K Explanatory Notes*.

Leake, B.E., 1978. Nomenclature of amphiboles. *Mineral Magazine,* **42**, 533-563.

Libby, J.W., 1992. Reply to discussion: The nature and tectonic significance of the crustal-scale Koolyanobbing shear zone, Yilgarn Craton, Western Australia. *Australian Journal of Earth Sciences,* **39**, 563-565.

Libby, W.G. and DeLaeter, J.R., 1998. Biotite Rb-Sr age evidence for Early Palaeozoic tectonism along the cratonic margin in southwestern Australia. *Australian Journal of Earth Sciences,* **45**, 623-632.

Lin, S., Jiang, D. and Williams, P.F., 1998. Transpression (or transtension) zones of triclinic symmetry: natural example and theoretical modeling. In: Holdsworth, R.E., Strachan, R.A., Dewey, J.F., (eds.), Continental transpressional and transtensional tectonics. *Geological Society of London, Special Publications,* **135**, 41-57.

Liou, J.G., 1971a. Synthesis and stability relations of prehnite, Ca2Al2Si3)10(OH)2. *American Mineralogist,* **56**, 507-531.

Liou, J.G., 1971b. Stilbite-laumonite equilibrium. *Contributions to Mineralogy and Petrology,* **31**, 171-177.

Liou, J.G., 1971c. P-T stabilities of laumontite, wairakite, lawsonite, and related minerals in the system $CaAl_2Si_2O_8$-SiO_2-H_2O. *Journal of Petrology,* **12**, 379-411.

Liou, J.G., Ito, K. and Kuniyoshi, S., 1971. Experimental studies of the phase relations between greenschist and amphibolite in a basaltic system. *Geological Society of America Abstracts,* **3**, 634-635.

Liou, J.G., 1973. Synthesis and stability relations of epidote, $Ca_2Al_2FeSi_3O_{12}(OH)$. *Journal of Petrology,* **14**, 381-413.

Liou, J.G., Kuniyoshi, S. and Ito, K., 1974. Experimental studies of the phase relations between greenschist and amphibolite in a basaltic system. *American Journal of Science,* **274**, 613-632.

Liou, J.G., Kim, H.S. and Maruyama, S., 1983. Prehnite-epidote equilibria and their petrologic applications. *Journal of Petrology,* **24**, 321-342.

Little, T.A., Holcombe, R.J. and Ilg, B.R., 2002. Kinematics of oblique collision and ramping inferred from microstructures and strain in middle crustal rocks, central Southern Alps, New Zealand. *Journal of Structural Geology,* **24**, 219-239.

Liu, S.F., and others, 1998. Geology of the Sir Samuel 1:100 000 sheet. *GSWA 100K Explanatory Notes*.

Lonker, S.W., 1981. The P-T-X relations of the cordierite garnet-sillimanite-quartz equilibrium. *American Journal of Science,* **281**, 1056-1090.

M

Maas, R., Kamenetsky, M.B., Sobolev, A.V., Kamenetsky, V.S. and Sobolev, N.V., 2005. Sr-Nd-Pb isotopic evidence for a mantle origin of alkali chlorides and carbonates in the Udachnaya kimberlite, Siberia. *Geology,* **35**, 549-552

Mandal, N., Dhar, R., Misra, S. and Chakraborty, C., 2007. Use of boudinaged rigid objects as a strain gauge: Insights from analogue and numerical models. *Journal of Structural Geology,* **29**, 759-773.

Marmo, B.A., Clarke, G.L. and Powell, R., 2002. Fractionation of bulk rock composition due to porphyroblast growth: effects on eclogite facies mineral equilibria, Pam Peninsula, New Caledonia. *Journal of Metamorphic Geology,* **20**, 151-165.

Martignole, J. and Sisi, J.C., 1981. Cordierite-garnet-H_2O equilibrium: a geological thermometer, barometer and water fugacity indicator. *Contributions to Mineralogy and Petrology,* **77**, 38-46.

Martinez, F.J., Reche, J., Arboleya, M.L. and Julivert, M., 2004. Retrograde replacement of andalusite by Ca-Na mica in chloritoid-bearing metapelites. PTX modelling of rocks with different Al content in the MnNCKFMASH system. *Journal of Metamorphic Geology,* **22**, 777-792.

Martyn, J.E. and Johnson, G.I., 1986. Geological setting and origin of fuchsite-bearing rocks near Menzies, Western Australia. *Australian Journal of Earth Sciences,* **33**, 1-18.

Mason, D.R., 2004. Thermodynamic modelling of lode-gold deposits in Archaean granitoids: Woodcutters and Lady Bountiful mines, Kalgoorlie region, Western Australia. *Australian Journal of Earth Sciences,* **51**, 431-438.

Massonne, H.-J. and Schreyer, W., 1987. Phengite geobarometry based on the limiting assemblage with K-feldspar, phlogopite, and quartz. *Contributions to Mineralogy and Petrology,* **96**, 212-224.

McCuaig, T.C., Kerrich, R., Groves, D.I. and Archer, N., 1993. The nature and dimensions of regional and local gold-related hydrothermal alteration in tholeiitic metabaslts in the Norseman goldfield: the missing link in a crustal continuum of gold deposits. *Mineral Deposita,* **28**, 420-435.

McCuaig, T.C. and Kerrich, R., 1998. P-T-t-deformation-fluid characteristics of lode gold deposits: evidence from alteration systematics. *Ore Geology Reviews*, **12**, 381-453.

McDonough, W.F., Sun, S., Ringwood, A.E., Jagoutz, E. and Hofmann, A.W., 1991. K, Rb and Cs in the earth and moon and the evolution of the earth's mantle. *Geochim. Cosmochim. Acta, Ross Taylor Symposium volume*.

McGoldrick, P. and Large, R., 1998. Proterozoic stratiform sediment-hosted Zn-Pb-Ag deposits. *AGSO Journal of Australian Geology and Geophysics* 17(4), 189-196.

McIntyre, J.R. and Martyn, J.E., 2001. Early extension in the late Archaean Eastern Goldfields Province, Western Australia. *AGSO Extended Abstracts*, 335-337.

McIntyre, J.R. and Martyn, J.E., 2005. Early extension in the late Archaean northeastern Eastern Goldfields Province, Yilgarn Craton, Western Australia. *Australian Journal of Earth Sciences,* **52**, 975-992.

McNaughton, N.J. and Cassidy, K.F., 1990. A reassessment of the age of the Liberty Granodiorite: implications for a model of synchronous mesothermal gold mineralization within the Norseman-Wiluna Belt, Western Australia. *Australian Journal of Earth Sciences,* **37**, 373-376.

McNaughton, N.J., Cassidy, K.F., Dahl, N., de Laeter, J.R., Golding, S.D., Groves, D.I., Ho, S.E., Mueller, A.G., Perring, C.S., Sang, J.H. and Turner, J.V., 1992. The source of ore components in lode-gold deposits of the Yilgarn Block, Western Australia. *University of Western Australia Publication,* **22**, 351-363.

McNaughton, N.J., Groves, D.I. and Witt, W.K., 1993. The source of lead in Archaean lode gold deposits of the Menzies-Kalgoorlie-Kambalda region, Yilgarn Block, Western Australia. *Mineral Deposita,* **28**, 495-502.

McNaughton, N.J., Mueller, A.G. and Groves, D.I., 2005. The age of the giant Golden Mile deposit, Kalgoorlie, Western Australia: Ion-microprobe zircon and monazite U-Pb geochronology of a synmineralization lamprophyre dike. *Economic Geology,* **100**, 1427-1440.

McQueen, K.G., 1981. Volcanic-associated nickel deposits from around the Widgiemooltha Dome, Western Australia. *Economic Geology,* **76**, 1417-1443.

McQueen, K.G., 1992. The Great Visctoria gold deposit, Marvel Loch, Western Australia: retrograde gold mobilization in a metamorphosed sulphidic iron-formation. *University of Western Australia Publication,* **22**, 365-380.

Mikucki, E.J. and Ridley, J.R., 1993. The hydrothermal fluid of Archaean lode-gold deposits at different metamorphic grades: compositional constraints from ore and wallrock alteration assemblages. *Mineral. Deposita,* **28**, 469-481.

Mikucki, E.J. and Roberts, F.I., 2003. Metamorphic petrography of the Kalgoorlie region eastern goldfields granite-greenstone terrane METPET database. *GSWA Record,* **2003/12**.

Mikucki, J.A., 1997. Contrasting fluid sources and mineralization styles in the Great Eastern lode-gold deposit, Lawlers, Western Australia. PhD thesis, University of Western Australia.

Miller, J. and Rasmussen, B., 2006. Geochronology proposal: Dating of stress switches linked to Au deposition, Wallaby deposit. *Y4 Submission Report*. pp. 2

Miller, J.M., 2005. The structural evolution of the Wallaby gold deposit, Laverton, WA. *Y4 **pmd*****CRC project report*, July 2004 (unpublished).

Moore, A.G., Cas, R.A.F., Beresford, S.W. and Stone, M., 2000. Geology of an Archaean metakomatiite succession. Tramways, Kambalda Ni province, Western Australia: assessing the extent to which volcanic facies architecture and flow emplacement mechanisms can be reconstructed. *Australian Journal of Earth Sciences,* **47**, 659-673.

Morris, P.A., 1994. Geology of the Mulgabbie 1:100 000 sheet. *GSWA 100K Explanatory Notes*.

Morris, P.A. and Witt, W.K., 1997. Geochemistry and tectonic setting of two contrasting Archaean felsic volcanic associations in the Eastern Goldfields, Western Australia. *Precambrian Research,* **83**, 83-107.

Mueller, A.G. and McNaughton, N.J., 2000. U-Pb ages constraining batholith emplacement, contact metamorphism, and the formation of gold and W-Mo skarns in the Southern Cross area, Yilgarn Craton, Western Australia. *Economic Geology,* **95**, 1231-1257.

Mueller, A.G. and Nemchin, A., 2003. A titanite U-Pb age for the 600m-wide pipe of actinolite-epidote skarn in the Wallaby gold deposits, Laverton, Western Australia, and a review of geochronology at Wallably and Granny Smith. *Curtin University Report for Placer Dame Asia Pacific*.

Mueller, A.G., Nemchin, A.A. and Frei, R., 2004. The Nevoria gold skarn deposit, Southern Cross greenstone belt, Western Australia: II, Pressure-temperature-time path and relationship to postorogenic granites. *Economic Geology,* **99**, 453-478.

Münker, C., Weyer, S., Scherer, E. and Mezger, K., 2001. Separation of high field strength elements (Nb, Ta, Zr, Hf) and Lu from rock samples for MC-ICPMS measurements. *Geochemistry, Geophysics, Geosystems,* **2**, 10.1029/2001GC000183

Myers, J.S., 1992. Tectonic evolution of the Yilgarn Craton, Western Australia. *University of Western Australia Publication,* **22**, 265-273.

Myer, J.S., 1997. Preface: Archaean geology of the Eastern Goldfields of Western Australia – regional overview. *Precambrian Research,* **83**, 1-10.

N

Nair, R. and Chacko, T., 2000. Fluid-absent melting of two high grade amphibolites: constraints on the conditions required for orthopyroxene formation. *Geological Association of Canada – Mineralogical Association of Canada, Abstracts*, 24.

Napier, R.W., Guise, P.G. and Rex, D.C., 1998. 40Ar/39Ar constraints on the timing and history of amphibolite facies gold mineralization in the Southern Cross area, Western Australia. *Australian Journal of Earth Sciences,* **45**, 285-296.

Neall, F.B. and Phillips, G.N., 1987. Fluid-wall rock interaction in an Archaean hydrothermal gold deposit: a thermodynamic model for the Hunt Mine, Kambalda. *Economic Geology,* **82**, 1679-1694.

Nelson, D.R., 1995. Compilation of SHRIMP U-Pb zircon geochronology data, 1994. *Geological Survey of Western Australia Record,* **1995/3**, pp. 244.

Nelson, D.R., 1996. Compilation of SHRIMP U-Pb zircon geochronology data, 1995. *Geological Survey of Western Australia Record,* **1996/3**, pp. 168.

Nelson, D.R., 1997. Evolution of the Archaean granite-greenstone terranes of the Eastern Goldfields, Western Australia: SHRIMP U-Pb zircon constraints. *Precambrian Research,* **83**, 57-81.

Nelson, D.R., 1998. Compilation of SHRIMP U-Pb zircon geochronology data, 1997. *Geological Survey of Western Australia Record,* **1998/3**.

Nelson, D.R., 1999. Compilation of SHRIMP U-Pb zircon geochronology data, 1998. *Geological Survey of Western Australia Record,* **1999/3**.

Nelson, D.R., 2000. GSWA Compilation of SHRIMP U-Pb zircon geochronology data, 1999. *Geological Survey of Western Australia Record,* **2000/3**.

Nemchin, A.A., Pidgeon, R.T. and Wilde, S.A., 1994. The age of the granulite facies metamorphism, southwestern Yilgarn Craton, Western Australia. *Precambrian Research,* **68**, 307-321.

Nemchin, A.A. and Pidgeon, R.T., 1999. U-Pb ages on titanite and apatite from the Darling Range granite: implications for late Archaean history of the southwestern Yilgarn Craton. *Precambrian Research,* **96**, 125-139.

Neumayr, P., Walshe, J.L., Petersen, K., Young, C., Roache, A. and Halley, S., 2007. Redox boundaries in gold deposits of the eastern goldfields, Yilgarn, WA – mapping a critical genetic parameter? In: Bierlein F.P., Knox-Robinson C.M. (eds), Proceedings of Geoconferences (WA) Inc. Kalgoorlie '07 Conference. *Geoscience Australia Record,* **2007/14**, 176-180.

Neumayr, P., 2008. Depositional mechanisms in Archaean gold systems. Talk on ***pmd****CRC* webbsite.

Newton, R.C. and Haselton, H.T., 1981. Thermodynamics of the garnet-plagioclase-Al_2O_3-quartz geobarometer. In. Thermodynamics of minerals and melts. Springer-Verlag. pp. 131-147.

Nguyen, P.T., Cox, S., Harris, L.B. and Powell, C.McA., 1998. Fault-valve behaviour in optimally oriented shear zones: an example at the Revenge gold mine, Kambalda, Western Australia. *Journal of Structural Geology,* **20**, 1625-1640.

Nickel, K.G. and Brey, G.P., 1984. Subsolidus orthopyroxene-clinopyroxene systematics in the system CaO-MgO-Al2O3-SiO2 to 60 kbar: a reevaluation of the regular solution model. *Contributions to Mineralogy and Petrology,* **87**, 35-42.

Nicollet, C. and Goncalves, P., 2005. Two contrasted P-T-time paths of coronitic metanorites of the French Massif Central: are reaction textures reliable guides to metamorphic histories? *Journal of Metamorphic Geology,* **23**, 97-105.

Nitsch, K.-H., 1971. Stabilitatsbeziehugen von Prehnit- und pumpellyit-haltiger paragenesen. *Contributions to Mineralogy and Petrology,* **30**, 240-260.

O

Ojala, V.J., 1995. Structural and depositional controls on gold mineralisation at the Granny Smith Mine, Laverton, Western Australia. PhD thesis. University of Western Australia (unpublished).

Ojala, V.J., McNaughton, N.J., Ridley, J.R., Groves, D.I. and Fanning, C.M., 1997. The Archaean Granny Smith gold deposit, Western Australia: age and Pb-isotope tracer studies. *Chronique de la Recherche Miniere,* **529**, 75-89.

Olafsson, M. and Eggler, D.H., 1983. Phase relations of amphibole, amphibole-carbonate, and phlogopite-carbonate peridotite: petrologic constraints on the asthenosphere. *Earth and Planetary Science Letters,* **64**, 305-315.

Oliver, N.H.S., 1996. Review and classification of structural controls on fluid flow during regional metamorphism. *Journal of Metamorphic Geology,* **14**, 477-492.

P

Painter, M.G.M. and Groenewald, P.B., 2001. Geology of the Mount Belches 1:100 000 sheet. *GSWA 100K Explanitory Notes*.

Passchier, C.W., 1987. Stable positions of rigid objects in non-coaxial flow: a study in vorticity analysis. *Journal of Structural Geology,* **9**, 679-690.

Passchier, C.W. and Urai, J.L., 1988. Vorticity and strain analysis using Mohr diagrams. *Journal of Structural Geology,* **10**, 755-763.

Passchier, C.W., 1994. Structural geology across a proposed Archaean terrane biundary in the eastern Yilgarn craton, Western Australia. *Precambrian Research,* **68**, 43-64.

Passchier, C.W. and Trouw, R.A.J., 2005. Microtectonics, 2nd edition. Springer, pp. 366.

Pattison, D.R.M., 2003. Petrogenetic significance of orthopyroxene-free garnet + clinopyroxene + plagioclase ± quartz-bearing metabasites with respect to the amphibolite and granulite facies. *Journal of Metamorphic Geology,* **21**, 21-34.

Perchuk, L.L. and Lavrent'eva, I.V., 1983. Experimental investigation of exchange equilibria in the system cordierite-garnet-biotite. In. Kinematics and equilibrium in mineral reactions (ed. S.K. Saxena), Springer and Verlag, New York.199-239.

Perchuk, L.L. and others, 1985. Precambrian granulites of the Aldan shield, eastern Siberia, USSR. *Journal of Metamorphic Geology,* **3**, 265 - 310.

Perkins, D., Westrum, E.F. and Essene, E.J., 1980. The thermodynamic properties and phase relations of some minerals in the system CaO-Al2O3-SiO2-H2O. *Geochim. et Cosmochim. Acta.,* **44** 61-84.

Phillips, N.G. and Groves, D.I., 1982. Fluid access and fluid-wall rock interaction in the gnesis of the Archaean gold-quartz vein deposit at Hunt Mine, Kambalda, Western Australia. In: Foster R.P. (ed), Gold '82: The geology, geochemistry and genesis of gold deposits, pp. 390-415.

Phillips, N.G. and Groves, D.I., 1983. The nature of Archaean gold-bearing fluids as deduced from gold deposits of Western Australia. *Journal of the Geological Society of Australia,* **30**, 25-39.

Phillip, G.N. and Groves, D.I., 1984. Fluid access and fluid-wall rock interaction in the genesis of the Archaean gold-quartz vein deposit at Hunt Mine, Kambalda, Western Australia. In: Foster R.P. (ed), Gold '82: The geology, geochemistry and genesis of gold deposits, 389-416.

Phillips, G.N., 1985. Archaean gold deposits of Australia. Economic *Geology Research Unit, University of Witwatersrand, Information Circular,* **175**, pp. 41.

Phillips, N.G., 1986. Geology and alteration in the Golden Mile, Kalgoorlie. *Economic Geology,* **81**, 779-808.

Phillips, N.G. and Powell, R., 1993. Link between gold provinces. *Economic Geology,* **88**, 1084-1098.

Phillips, D. and Miller, J.M., 2006. 40Ar/39Ar dating of mica-bearing pyrite from thermally overprinted Archean gold deposits. *Geology,* **34**, 397-400.

Pidgeon, R.T., 1986. The correlation of acid volcanics in the Archaean of Western Australia. *Western Australian Mining and Petroleum Research Institute (now MERIWA) Report,* **27**.

Pidgeon, R.T. and Wilde, S.A., 1990. The distribution of 3.0 Ga and 2.7 Ga volcanic episodes in the Yilgarn Craton of Western Australia. *Precambrian Research,* **48**, 309-325.

Pin, C. and Santos-Zalduegui, J.F., 1997. Sequential separation of light rare-earth elements, thorium and uranium by miniaturized extraction chromatography: application to isotopic analyses of silicate rocks. *Analytica Chimica Acta,* **339**, 79-89

Pitra, P. and De Waal, S.A., 2001. High-temperature, low-pressure metamorphism and development of prograde symplectites, Marble Hall Fragment, Bushveld Complex (South Africa).

Poldervaart A. and Hess, H.H., 1951. Pyroxenes in the crystallization of basaltic magma. *Journal of Geology,* **59**, 472.

Polito, P.A., Bone, Y., Clarke, J.D.A. and Mernagh, T.P., 2001. Compositional zoning of fluid inclusions in the Archaean Junction gold deposit, Western Australia: a process of fluid-wall-rock interaction. *Australian Journal of Earth Sciences,* **48**, 833-855.

Potma, W.A., Schaubs, P.M., Robinson, J.A., Sheldon, H.A., Roberts, P.A., Zhang, Y., Zhao, C., Ord, A. and Hobbs, B.E., 2007. Deformation and fluid flow modelling: exploration case studies from the Eastern Goldfields Superterrane. In: Bierlein F.P., Knox-Robinson C.M. (eds), Proceedings of Geoconferences (WA) Inc. Kalgoorlie '07 Conference. *Geoscience Australia Record,* **2007/14**, 214-217

Powell, R. and Evans, J.A., 1983 A new geobarometer for the assemblage biotite-muscovite-chloritequartz. *Journal of Metamorphic Geology* **1**, 331-336.

Powell, R., Condliffe, D.M. and Condliffe, E., 1984 Calcite-dolomite geothermometry in CaCO3-MgCO3-FeCO3 : an experimental study. *Journal of Metamorphic Geology,* **2**, 33-41.

Powell, R. and Holland, T.J.B., 1988. An internally consistent dataset with uncertainties and correlations: 3. Applications to geobarometry, worked examples and a computer program. *Journal of Metamorphic Geology,* **6**, 173-204.

Powell, R. and Holland, T.J.B., 1990 Calculated mineral equilibria in the pelite system. KFMASH (K20-Fe0-Mg0-Al2O3-SiO2-H20). *American Mineralogist,* **75**, 367-380.

Powell, R. and Holland, T.J.B., 1994. Optimal geothermometry and geobarometry. *American Mineralogist,* **79**, 120-133.

Powell, R., Holland, T.J.B. and Worley, B., 1998. Calculating phase diagrams involving solid solutions via non-linear equations, with examples using THERMOCALC. *Journal of Metamorphic Geology,* **16**, 577-588.

Pownecby, M.I., Wall, J.V. and O'Neill, H.St.C., 1991. An experimental study of the effect of Ca upon garnet-ilmenite Fe-Mn exchange equilibria. *American Mineralogist,* **76**, 1580-1588.

Proyer, A., 2003. Metamorphism of pelites in NKFMASH – a new petrogenetic grid with implications for the preservation of high-pressure mineral assemblages during exhumation. *Journal of Metamorphic Geology,* **21**, 493-509.

Purvis, A.C., 1978. The Southern Cross – Forrestania greenstone belt. PhD thesis, Adelaide University (unpublished).

Purvis, A.C., 1984. Metamorphosed altered komatiites at Mount Martin, Western Australia – Archaean weathering products metamorphosed at the aluminosilicate triple point. *Australian Journal of Earth Science,* **31**, 91-106.

Q

Qiu, Y., Dunphy, J.M., McNaughton, N.J. and Groves, D.I., 1998. Crustal growth and evolution of the southwestern Archaean Yilgarn Craton. *Geological Society of America,* **30**, 395.

Qiu, Y. and Groves, D.I., 1999. Late Archean collision and delamination in the Southwest Yilgarn Craton: the driving force for Archean orogenic lode gold mineralization? *Economic Geology,* **94**, 115-122.

R

Ramsay, J.G., 1967. Folding and fracturing of rocks. Mc Graw and Hill, New York.

Ramsay, J.G. and Graham, R.H., 1970. Strain variation in shear belts. *Canadian Journal of Earth Sciences,* **7**, 786-813.

Reche, J., Martinez, F.J., Arboleya, M.L., Dietsch, C. and Briggs, W.D., 1998. Evolution of a kyanite-bearing belt within a HT-LP orogen: the case of NW Variscan Iberia. *Journal of Metamorphic Geology,* **16**, 379-394.

Ren, S.K. and Heithersay, P.S., 1998. The Kanowna Belle gold deposit and its implications to Archaean gold metallogeny of the Yilgarn Craton. *Proceedings IAGOD symposium,* **9**, 303-318.

Rey, P.F. Philippot, P. and Thebaud, N., 2003. Contribution of mantle plumes, crustal thickening and greenstone blanketing to the 2.75-2.65 Ga global crisis. *Precambrian Research,* **127**, 43-60.

Ridley, J.R., 1992. The thermal causes and effects of volumous, late Archaean monzogranite plutonism. *University of Western Australia publication,* **22**, 275-285.

Ridley, J.R., 1993. Implications of metamorphic patterns to tectonic models of the Eastern Goldfields. *AGSO extended abstracts Record,* **1993/54**, 95-100.

Ridley, J.R., 1993. Implications of metamorphic patterns to tectonic models of the Eastern Goldfields. *Australian Geological Survey Organisation Record,* **54**, 95-100.

Riganti, A., 2002. Geology of the Barlee 1:100 000 sheet. *GSWA 100K Explanatory Notes*.

Ringwood, A.E., 1975. Composition and petrology of the Earth's mantle. McGraw and Hill, New York.

Roberts, I., 2004. Chapter 6 Mineral field of Edjudina. *GSWA Report on Mineral Deposits*.

Rollinson, H.R., 1981. Garnet-pyroxene thermometry and barometry in the Scourie granulites, NW Scotland. *Lithos,* **14**, 225 - 238.

Ross, A.A., Barley, M.E., Brown, S.J.A., McNaughton, N.J., Ridley, J.R. and Fletcher, I.R., 2004. Young porphyries, old zircons: new constraints on the timing of deformation and gold

mineralization in the Eastern Goldfields from SHRIMP U-Pb zircon dating at the Kanowna Belle Gold Mine, Western Australia. *Precambrian Research,* **128**, 105-142.

Ruppel, C., 1995. Extensional processes in continental lithosphere. *Journal of Geophysical Research,* **100-B12**, 24,187-24,215.

S

Salier, B.P., Groves, D.I., McNaughton, N.J. and Fletcher, I.R., 2004. The world-class Wallaby gold deposit, Laverton, Western Australia: An orogenic-style overprint on a magmatic-hydrothermal magnetite-calcite alteration pipe? *Mineralium Deposita,* **39**, 473-494.

Salier, B.P., Groves, D.I., McNaughton, N.J. and Fletcher, I.R., 2005. Geochronological and stable isotope evidence for widespread orogenic gold mineralization from a deep-seated fluid source at ca 2.65 Ga in the Laverton Gold Province, Western Australia. *Economic Geology,* **100**, 1363-1388.

Sandiford, M., 2002. Low thermal Peclet number intraplate orogeny in central Australia. *Earth and Planetary Science Letters,* **201**, 309-320.

Sandiford, M., Hand, M. and McLaren, S., 1998. High geothermal gradient metamorphism during thermal subsidence. *Earth and Planetary Science Letters,* **163**, 149-165.

Sandiford, M., Van Kranendonk, M.J. and Bodorkos, S., 2004. Conductive incubation and the origin of dome-and-keel structure in Archean granite-greenstone terrains: A model based on the eastern Pilbara Craton, Western Australia. *Teconics,* **23**, TC1009.

Scantlebury, G.M., 1983. The characterization and origin of the gold lodes in and around the Brownhill syncline, Golden Mile, Kalgoorlie, Western Australia. B.Sc. Honours thesis, University of Western Australia (unpublished).

Scherer, E., Münker, C. and Mezger, K., 2001. Calibration of the lutetium-hafnium clock. *Science,* **293**, 683-687

Schiffman, P. and Liou, J.G., 1983. Synthesis of Fe-pumpellyite and its stability relations with epidote. *Journal of Metamorphic Geology,* **1**, 91-101.

Schiotte, L. and Campbell, I.H., 1996. Chronology of the Mount Magnet granite-greenstone terrain, Yilgarn Craton, Western Australia: implications for field based predictions of the relative timing of granitoid emplacement. *Precambrian Research,* **78**, 237-260.

Schmid, D.W. and Podladchikov, Y.Y., 2004. Are isolated stable rigid clasts in shear zones equivalent to voids? *Tectonophysics,* **384**, 233-242.

Schmidt, M.W., 1992. Amphibole composition in tonalite as a function of pressure: an experimental calibration of the Al-in-hornblende barometer. *Contributions to Mineralogy and Petrology,* **110**, 304-310.

Scrimgeour, I. and Raith, J.G., 2001. High-grade reworking of Proterozoic granulites during Ordovician intraplate transpression, eastern Arunta Inlier, central Australia. In: Miller, J.A., Holdsworth, R.E., Buick, I.S., Hand, M., (Eds.), Continental reactivation and reworking. *Geological Society Special Publications,* **184**, 261-287.

Sheldon, H.A. and Micklethwaite, S., 2006. Damage and permeability around faults: implications for mineralization. *Geology,* **35**, 903-906.

Sheldon, H.A., Barnicoat, A.C., Zhang, Y. and Ord, A., 2007. Metamorphism in the Eastern Yilgarn Craton: implications for fluid flow and mineralisation. Kalgoorlie'07 Conference, *Geoscience Australia Record,* **2007/14**, 138-142.

Sheldon, H.A., Zhang, Y. and Ord, A., 2008. Archaen gold mineralization in the eastern Yilgarn: Insights from numerical models. ***pmd****CRC Y4 Project Final Report*.

Shackleton, R.M. and Ries, A.C., 1984. The relation between regionally consistant stretching lineations and plate motions. *Journal of Structural Geology,* **6**, 111-117.

Simpson, C. and de Paor, D.G., 1993. Strain and kinematic analysis in general shear zones. *Journal of Structural Geology,* **15**, 1-20.

Skwarnecki, M.S., 1988. Alteration and deformation in a shear zone hosting gold mineralization at Harbour Lights, Leonora, WA. In: Ho S.E., Groves D.I. (eds), Archaean gold mineralization in a normal-motion shear zone at Harbour Lights, Leonora, Western Australia. *University of Western Australia Geology Department Abstracts,* **12**, 111-129.

Skwarnecki, M.S., 1990. The regional setting and genesis of Archaean gold mineralization at Harbour Lights, Leonora, Western Australia. PhD thesis, University of Western Austraila (unpublished).

Smithies, R.H., 1994. Geology of the Roe 1:100 000 sheet. *GSWA 100K Explanitory Notes*.

Smithies, R.H. and Witt, W.K., 1997. Distinct basement terranes identified from granite geochemistry in late Archaean granite-greenstones, Yilgarn Craton, Western Australia. *Precambrian Research,* **83**, 185-201.

Smithies, R.H., 2003. Formation of Earth's early Archaeancontinental crust. *Precambrian Research,* **127**, 89-101.

Sorjonen-Ward, P., Zhang, Y. and Zhao, C., 2002. Numerical modelling of orogenic processes and gold mineralisation in the southeastern part of the Yilgarn Craton, Western Australia. *Australian Journal of Earth Sciences,* **49**, 935-964.

Spray, J.G., 1985. Dynamothermal transition zone between Archaean greenstone and granitoid gneiss at Lake Dundas, Western Australia. *Journal of Structural Geology,* **7**, 187-203.

Spear, F.S., 1981a. Amphibole-plagioclase equilibria: an empirical model for the relation albite + tremolite = edenite + 4 quartz. *Contributions to Mineralogy and Petrology,* **77**, 355-364.

Spear, F.S., 1981b. An experimental study of hornblende stability and compositional variability in amphibolite. *American Journal of Science,* **281**, 697-734.

Spear, F.S. and Rumble, D., 1986. Pressure, temperature, and structural evolution of the Orfordville Belt, West-Central New Hampshire. *Journal of Petrology,* **27(5)**, 1071-1093.

Spear, F.S. and Cheney, J.T., 1989. A petrogenetic grid for pelitic schists in the system SiO2-Al2O3-FeO-MgO-K2O-H2O. *Contributions to Mineralogy and Petrology,* **101**, 149-164.

Spear, F.S., 1993. Metamorphic phase equilibria and pressure-temperature-time paths. *Mineralogical Society of America Monograph, Washington*.

Squire, R.J. and Miller, J.Mc.L., 2003. Synchronous compression and extension in East Gondwana: Tectonic controls on world-class gold deposits at 440 Ma. *Geology,* **31**, 1073-1076.

Squire, R., 2006. Provenance geochronology. *Y4 Project Quarterly Report*. pp. 2.

Squire, R., 2007. Provenance geochronology. *Y4 Project Quarterly Report*. pp. 2.

Squire, R.J., Cas, R.A.F. and Champion, D.C., 2007. The Black Flag Group: a vector to ore at St Ives. In: Bierlein F.P. Knox-Robinson C.M. (eds), 2007, Proceedings of Geoconferences (WA) Inc. Kalgoorlie '07 Conference. *Geoscience Australia Record,* **2007/14**, 13-35.

Stewart, A.J., 1992. Discussion: The nature and tectonic significance of the crustal-scale Koolyanobbing shear zone, Yilgarn Craton, Western Australia. *Australian Journal of Earth Sciences,* **39**, 561-562.

Stewart, A.J., 2001. Laverton sheet SH51-2, 2nd edition. *GSWA 250K Explanitory Notes*.

Stewart, A.J., 2004. Leonora sheet SH51-1. *GSWA 250K Explanitory Notes*.

Stewart, A.J., 2007. Geology, structure and mineral resources of Lake Violet 100K sheet. *GSWA Record,* **2007/21**, 30 pp.

Stipska, P. and Powell, R., 2005. Constraining the P-T path of a MORB-type eclogite using pseudosections, garnet zoning and garnet-clinopyroxene thermobarometry: an example from the Bohemian Massif. *Journal of Metamorphic Geology,* **23**, 725-744.

Stipska, P., Pitra, P. and Powell, R., 2006. Separate or shared metamorphic histories of eclogites and surrounding rocks? An example from the Bohemian Massif. *Journal of Metamorphic Geology,* **24**, 219-240.

Stolz, E.M. and Roache, T.J., 2007. A thoroughly modern gold deposit: integrating multiple technologies at St Ives. In: Bierlein F.P., Knox-Robinson C.M. (eds), Proceedings of Geoconferences (WA) Inc. Kalgoorlie '07 Conference. *Geoscience Australia Record,* **2007/14**, 145-151.

Stone, W.E. and Archibald, N.J., 2004. Structural controls on nickel sulphide ore shoots in Archaean komatiite, Kambalda, WA: the volcanic trough controversy revisited. *Journal of Structural Geology,* **26**, 1173-1194.

Stone, W.E., Beresford, S.W. and Archibald, N.J., 2005. Structural setting and shape analysis of nickel sulfide shoots at the Kambalda Dome, Western Australia: implications for deformation and remobilization. *Economic Geology,* **100**, 1441-1455.

Stowell, H.H. and Crawford, M.L., 2000. Metamorphic history of the Coast Mountains orogen, western British Columbia and southeastern Alaska. *Geological Society of America Special Paper,* **343**, 257-283.

Stowell, H.H. and Stein, E., 2005. The significance of plagioclase dominant coronas on garnet, Weatchee Block, Northern Cascades, Washington, USA. *Canadian Mineralogist,* **43**, 367-385.

Stuwe, K., Sandiford, M. and Powell, R., 1993. Episodic metamorphism and deformation in low-pressure, high-temperature terranes. *Geology,* **21**, 829-832.

Stuwe, K. and Sandiford, M., 1994. Contribution of deviatoric stresses to metamorphic P-T path: an example appropriate to low-P, high-T metamorphism. *Journal Metamorphic Geology,* **12**, 445-454.

Sun, S.S., 1980. Lead isotopic study of young volcanic rocks from mid-ocean ridges, ocean islands and island arcs. *Philosophical Transactions of the Royal Society,* **A297**, 409-445.

Swager, C.P., 1989. Structure of the Kalgoorlie greenstones – regional deformation history and implications for the structural setting of gold deposits within the Golden Mile. *Geological Survey of Western Australia, Professional Papers, Report,* **25**, 59-84.

Swager, C.P., Griffin, T.J., Witt, W.K., Wyche, S., Ahmat, A.L., Hunter, W.M. and McGoldrick, P.J., 1990. Geology of the Archaean Kalgoorlie Terrane – an explanatory note. *Western Australia Geological Survey, Report* **1990/12** reprinted as *Report,* **48**. pp. 26.

Swager, C.P. and Griffins, T.J., 1990. An early thrust duplex in the Kalgoorlie-Kambalda greenstone belt, Eastern Goldfields Province, Western Australia. *Precambrian Research,* **48**, 63-73.

Swager, C.P., Witt, W.K., Griffin, T.J., Ahmat, A.L., Hunter, W.M., McGoldrick, P.J. and Wyche, S., 1992. Late Archaean granite-greenstones of the Kalgoorlie Terrane, Yilgarn Craton, Western Australia, In Glover, J.E., and Ho, S.E., (Eds), The Archaean – Terrains, Processes and Metallogeny. Geology Department and Extension Service, *University of Western Australia Publication,* **22**, 107-122.

Swager, C.P., 1994a. Geology of the Pinjin 1:100 000 sheet. *GSWA 100K Explanetory Notes*.

Swager, C.P., 1994b. Geology of the Kurnalpi 1:100 000 sheet. *GSWA 100K Explanetory Notes*.

Swager, C.P., 1994c. Geology of the Menzies 1:100 000 sheet (and adjacent Ghost Rocks area), *GSWA 100K Explanitory Notes*.

Swager, C.P., 1994. Geology of the Dunnsville 1:100 000 sheet. *GSWA 100K Explanatory Notes*.

Swager, C.P., 1995. Geology of the greenstone terranes in the Kurnalpi-Edjudina region, southeatern Yilgarn Craton. *Western Australia Geological Survey, Report,* **47**, pp. 31.

Swager, C.P., Griffin, T.J., Witt, W.K., Wyche, S., Ahmat, A.L., Hunter, W.M. and McGoldrick, P.J., 1995. Geology of the Archaean Kalgoorlie Terrane – an explanatory note. *Western Australia Geological Survey, Report,* **48** (reprint of *Report,* **1990/12**). pp. 26.

Swager, C.P., 1997. Tectono-stratigraphy of late Archaean greenstone terranes in the southern Eastern Goldfields, Western Australia. *Precambrian Research,* **83**, 11-42.

Swager, C.P. and Nelson, D.R., 1997. Extensional emplacement of a high-grade granite gneiss complex into low-grade greenstones, Eastern Goldfields, Yilgarn Craton, Western Australia. *Precambrian Research,* **83**, 203-219.

Swager, C.P., Goleby, B.R., Drummond, B.J., Rattenbury, M.S. and Williams, P.R., 1997. Crustal structure of granite-greenstone terranes in the Eastern Goldfields, Yilgarn Craton, as revealed by seismic reflection profiling. *Precambrian Research,* **83**, 43-56.

T

Thompson, A.B., 1971. PCO2 in low-grade metamorphism: zeolite, carbonate, clay minerals, prehnite relations in the system CaO-Al2O3-SiO2-CO2-H2O. *Contributions to Mineralogy and Petrology,* **33**, 145-161.

Thompson, A.B., 1976. Mineral reactions in pelitic rocks: 2. calculations of some P-T-X(Fe-Mg) phase relations. *American Journal of Science,* **276**, 425-454.

Thompson, A.B., 1983. Fluid-absent metamorphism. *Journal of the Geophysical Society of London* **140**, 533-548.

Thompson, A.B., Schulmann, K. and Jezek, J., 1997. Thermal evolution and exhumation in obliquely convergent (transpressive) orogens. *Tectonophysics,* **280**, 171-184.

Thompson, R.N., 1982. British Tertiary volcanic province. *Scottish Journal of Geology,* **18**, 49-107.

Thompson, P.H., 1989. Moderate overthickening of thinned sialic crust and the origin of granitic magmatism and regional metamorphism in low-P-high-T terranes. *Geology,* **17**, 520-523.

Thompson, P.H., 2005. Metamorphic constraints on the geological setting, thermal regime, and timingof alteration and gold mineralization in the Yellowknife Greenstone Belt, N.W.T., Canada. In: Gold in the Yellowknife Greenstone Belt, Northwest Territories: Results of the EXTECH III multidisiplinary research project. *Geological Association of Canada, Mineral Deposits Division, Special Paper*.

Tikoff, B. and Greene, D., 1996. Stretching lineations in transpressional shear zones:an example from the Sierrra Nevada Batholith, California. *Journal of Structural Geology,* **19**, 29-39.

Tinkham, D.K., Zuluaga, C.A. and Stowell, H.H. 2001. Metapelite phase equilibria modeling in MnNCKFMASH: The effect of variable Al2O3 and MgO/(MgO+FeO) on mineral stability. *Geological Materials Research,* **3**, 1-42.

Tinkham, D.K. and Ghent, E.D., 2005. Estimating P-T conditions of garnet growth with isochemical phase-diagram sections and the problem of effective bulk-composition. *The Canadian Mineralogist,* **43**, 35-50.

Tirel, C., Brun, J.P. and Sokoutis, D., 2006. Extension of thickened and hot lithospheres: Inferences from laboratory modeling. *Tectonics,* **25**, TC1005.

Triboulet, C., 1992. The (NaCa) amphibole-albite-chlorite-epidote-quartz geothermobarometer in the system S-A-F-M-C-N-H_2O. 1. An empirical calibration. *Journal of Metamorphic Geology,* **10**, 545 - 556.

Tripp, G.I., 2000. Structural geology and gold mineralization of the Ora Banda and Zuleika districts, Eastern Goldfields, Western Australia. Masters Thesis, Curtin University (unpublished).

Tripp, G.I., Cassidy, K.F., Rogers, J., Sircombe, K. and Willson, M., 2007. Stratigraphy and structural geology of the Kalgoorlie greenstones: key criteria for gold exploration. In: Bierlein F.P., Knox-Robinson C.M. (eds), Proceedings of Geoconferences (WA) Inc. Kalgoorlie '07 Conference. *Geoscience Australia Record,* **2007/14**, 203-208.

Tuccillo, M.E., Essene, E.J. and van der Pluijm, B.A., 1990. Growth and retrograde zoning in garnets from high-grade metapelites: Implications for pressure-temperature paths. *Geology,* **18**, 839-842.

V

Valli, F., Guillot, S. and Hattori, K.H., 2004. Source and tectono-metamorphic evolution of mafic and pelitic metasedimentary rocks from the central Quetico metasedimentary belt, Archean Superior Province of Canada. *Precambrian Research,* **132**, 155-177.

Vance, D. and Thirlwall, M.F., 2002. An assessment of mass discrimination in MC-ICPMS using Nd isotopes. *Chemical Geology,* **185**, 227-240

Van Kranendonk, M.J. and Collins, W.J., 1998. Timing and tectonic significance of late Archaean. Sinistral strike-slip deformation in the central Pilbara structural corridor, Pilbara Craton, Western Australia. *Precambrian Research,* **88**, 207-232.

Van Kranendonk, M., Hickman, A.H., Smithies, R.H. and Nelson, D.R., 2002. Geology and tectonic evolution of the Archean North Pilbera terrain, Pilbara Craton, Western Australia. *Economic Geology,* **97**, 695-732.

Van Kranendonk, M.J, Collins, W.J., Hickman, A. and Pawley, M.J., 2004. Critical tests of vertical vs. horizontal tectonic models for the Archaean East Pilbara granite-greenstone terrane, Pilbara Craton, Western Australia. *Precambrian Research,* **131**, 173-211.

Van Kranendonk, M.J., 2007. Litho-structural development of the northern Murchison Domain within the context of Yilgarn Craton evolution. In: in Bierlein, F.P., and Knox-Robinson, C.M., (eds), 2007. Proceedings of Geoconferences (WA) Inc. Kalgoorlie '07 Conference. *Geoscience Australia Record,* **2007/14**, 26-26.

Vervoort, JD, Patchett, PJ, Söderlund, U and Baker, M., 2004. Isotopic composition of Yb and the determination of Lu concentrations and Lu/Hf ratios by isotope dilution using MC-ICPMS. *Geochemistry Geophysics Geosystems,* **5**, Q1102, doi:10.1029/2004GC000721

Vielreicher, N.M., Groves, D.I., Fletcher, I.R., McNaughton, N.J. and Rasmussen, B., 2003. Hydrothermal monazite and xenotime geochronology: a new direction for precise dating of orogenic gold mineralization. *SEG Newsletter,* **53**, 10-16.

W

Walker, I.W. and Blight, D.F., 1983. Barlee 250 K sheet SH51-6. GSWA Explanatory Notes.

Wallis, S.R., 1992. Vorticity analysis in a metachert from the Sanbagawa belt, SW Japan. *Journal of Structural Geology,* **14**, 271-280.

Wallis, S.R., 1995. Vorticity analysis and recognition of ductile extension in the Sanbagawa belt, SW Japan. *Journal of Structural Geology,* **17**, 1077-1093.

Walshe, J.L., Neumayr, P., Cleverley, J., Petersen, K., Andrew, A., Whitford, D., Carr, G.R., Kendrick, M., Young, C. and Halley, S., 2008a. Multiple fluid reservoirs in Eastern Yilgarn gold systems. ***pmd****CRC Y4 Project Final Report*.

Walshe, J.L., Neumayr, P., Cleverley, J., Petersen, K., Andrew, A., Whitford, D., Carr, G.R., Kendrick, M., Young, C. and Halley, S., 2008b. Depositional processes in Eastern Yilgarn gold systems. ***pmd****CRC Y4 Project Final Report*.

Warren, R.G. and Ellis, D.J., 1996. Mantle underplating, granite tectonics, and metamorphic P-T-t paths. *Geology,* **24**, 663-666.

Webb, G., 2001. Allochronous anti-clockwise P-T-t paths across a fold-thrust belt, "patchwork" deformation in the southern Adelaide Fold Belt, South Australia. Honours thesis, University of Adelaide, pp. 62.

Wei, C.J. and Powell, R., 2003. Phase relations in high-pressure metapelites in the system KFMASH (K2O-FeO-MgO-Al2O3-SiO2-H2O) with application to natural rocks. *Contributions to Mineralogy and Petrology,* **145**, 301-315.

Wei, C.J., Powell, R. and Clarke, G.L., 2004. Calculated phase equilibria for low- and medium-pressure metapelites in the KFMASH and KMnFMASH systems. *Journal of Metamorphic Geology,* **22**, 495-508.

Weinberg, R.F., Van Der Borgh, P., Bateman, R.J. and Groves, D.I., 2005. Kinematic history of the Boulder-Lefroy shear zone system and controls on associated gold mineralization, Yilgarn Craton, Western Australia. *Economic Geology,* **100**, 1407-1426.

Wells, P.R.A., 1977. Pyroxene thermometry in simple and complex systems. *Contributions to Mineralogy and Petrology,* **62**, 129-139.

Westaway, J.M. and Wyche, S., 1998. Geology of the Darlot 1:100 000 sheet. *GSWA 100K Explanatory Notes*.

White, S.H., Wijbrans, J.R., Hein, K.A.A., Kloppenburg, A., Beintema, K.A. and Zegers, T.E., 2001. Thermotectonic evolution of the eastern Pilbara granite greenstone terrain: the importance of horizontal tectonics. *AGSO Extended Abstract*.

White, R.W., Powell, R. and Phillips, G.N., 2003. A mineral equilibria study of the hydrothermal alteration in mafic greenschist facies rocks at Kalgoorlie, Western Australia. *Journal of Metamorphic Geology,* **21**, 455-468.

White, R.W., Powell, R. and Holland, T.J.B., 2001. Calculation of partial melting equilibria in the system Na2O-CaO-K2O-FeO-MgO-Al2O3-SiO2-H2O (NCKFMASH). *Journal of Metamorphic Geology,* **19**, 139-153.

Wiedenbeck, M. and Watkins, K.P., 1993. A time scale for granitoid emplacement in the Archaean Murchison Province, Western Australia, by single zircon geochronology. *Precambrian Research,* **61**, 1-26.

Wilkins, C., 1997. Chapter 2.4.1 Regional and contact medtamorphism. In: Greenstone Belts, DeWit M.J., Ashwal L.D. (eds). Clarendon Press, Oxford. pp. 126-163.

Williams, P.R. and Currie, K.L., 1993. Character and regional implications of the sheared Archaean granite-greenstone contact near Leonora, Western Australia. *Precambrian Research,* **62**, 343-367.

Williams, P.R. and Whitaker, A.J., 1993. Gneiss domes and extensional deformation in the highly mineralised Archaean Eastern Goldfields Province, Western Australia. *Ore Geology Reviews,* **8**, 141-162.

Willett, G., Eshuys, E. and Guy, B., 1978. Ultramafic rocks of the Widgiemooltha-Norseman area, Western Australia: petrological diversity, geochemistry and mineralization. *Precambrian Research,* **6**, 133-156.

Witt, W.K., 1991. Regional metamorphic controls on alteration associated with gold mineralisation in the Eastern Goldfields province, Western Australia: Implications for the timing and origin of Archean lode-gold deposits. *Geology,* **19**, 982-985.

Witt, W.K., 1993a. Gold mineralization in the Menzies-Kambalda region, Eastern Goldfields, Western Australia. *GSWA Report,* **39**.

Witt, W.K., 1993b. Lithological and structural controls on gold mineralization in the Archaean Menzies-Kambalda area, Western Australia. *Australian Journal of Earth Sciences,* **40**, 65-86.

Witt, W.K., 1994a. Geology of the Melita 1:100 000 sheet. *GSWA 100K Explanatory Notes*.

Witt, W.K., 1994b. Geology of the Bardoc 1:100 000 sheet. *GSWA 100K Explanatory Notes*.

Witt, W.K. and Davy, R., 1997. Geology and geochemistry of granitoid rocks in the Southwest Eastern Goldfields Province. *GSWA Report,* **49**.

Witt, W.K., Knight, J.T. and Mikucki, E.J., 1997. A synmetamorphic lateral fluid flow model for gold mineralization in the Archean southern Kalgoorlie and Norseman terranes, Western Australia. *Economic Geology,* **92**, 407-437.

Witt, W.K., 1997. Geology and mineralization of the south central Yilgarn Craton, Western Australia – A Field Guide. *GSWA Record,* **1997/8**.

Witt, W.K. and Davy, R., 1997. Geology and geochemistry of Archaean granites in the Kalgoorlie region of the Eastern Goldfields, Western Australia: a syn-collisional tectonic setting? *Precambrian Research,* **83**, 133-183.

Witt, W.K., 1997. Geology of the Ravensthorpe and Cocanarup 1:100 000 sheets. *GSWA 100K Explanatory Notes*.

Witt, W.K., 1998. Geology and mineral resources aof the Ravensthorpe and Cocanarup 1:100 000 sheets. *GSWA Report,* **54**. pp. 152.

Witt, W.K., 2001. A hydrothermal history of the greenstones in the Yilgarn Craton, Western Australia: implications for the exploration for lode-gold mineralization. *AGSO Extended Abstracts*, 406-408.

Woad, G.M., 1981. Nature and genesis of banded iron-formation hosted gold deposits at Water Tank Hill, Mount Magnet, Western Australia. B.Sc. Honours thesis, University of Western Australia, pp. 72 (unpublished).

Wones, D.R., 1989. Significance of the assemblage titanite+magnetite+quartz in granitic rocks. *American Mineralogist,* **74**, 744-749.

Wood, D.A., Joron, J.L., Treuil, M. and Tarney, J., 1979a. Elemental and Sr isotope variations in basic lavas from Iceland and the surrounding ocean floor. *Contributions to Mineralogy and Petrology,* **70**, 319-339.

Wood, D.A., Tarney, J., Varet, J., Saunders, A.D., Bougault, H., Joron, J.L., Treuil, M. and Cann, J.R., 1979b. Geochemistry of basalts drilled in the North Atlantic by IPOD leg 49: implications for mantle heterogeneity. *Earth and Planetary Science Letters,* **42**, 77-97.

Wood, D.A., Tarney, J. and Weaver, B.L., 1981. Trace element variations in Atlantic Ocean basalts and Proterozoic dykes from northwest Scotland: their bearing upon the nature and geochemical evolution of the upper mantle. *Tectonophysics,* **75**, 91-112.

Woodhead, J.D., Hergt, J.M., Davidson, J.P. and Eggins, S.M., 2001. Hafnium isotope evidence for "conservative" element mobility during subduction zone processes. *Earth and Planetary Science Letters,* **192**, 331-346

Wyche, S. and Witt, W.K., 1994. Geology of the Davyhurst 1:100 000 sheet. *GSWA 100K Explanatory Notes*.

Wyche, S., 1998. Kalgoorlie 250 K sheet SH51-9. *GSWA Explanatory Notes*.

Wyche, S., 1999. Geology of the Mulline and Riverina 1:100 000 sheet. *GSWA 100K Explanatory Notes*.

Wyche, S., Chen, S.F., Greenfield, J.E. and Riganti, A., 2001. Geology of the Johnston Range 1:100 000 sheet. *GSWA 100K Explanitory Notes*.

Wyllie, P.J. and Wolf, M.B., 1993. Amphibolite dehydration-melting: sorting out the solidus. In: Prichard H.M., Alabaster T., Harris N.B.W., Neary C.R. (eds), Magmatic processes and plate tectonics. *Geological Society London Special Publication,* **76**, 405-416.

Y

Yang, P. and Indares, A.D., 2005. Mineral zoning, phase relations, and P-T evolution of high-pressure granulites from the Lelukuau Terrane, northeastern Grenville Province, Quebec. *Canadian Mineralogist,* **43**, 443-462.

Yardley, B.W.D. and Valley, J.W., 1997. The petrologic case for a dry lower crust. *Journal of Geophysical Research,* **102**, 12173-12185.

Yardley, B.W.D. and Graham, J.T., 2002. The origins of salinity in metamorphic fluids. *Geofluids,* **2**, 249-256.

Yeats, C.J., Kohler, E.A., McNaughton, N.J., Tkatchyk, L.J., 2001. Geological setting and SHRIMP U-Pb geochronologic evidence for ca. 2680-2660 Ma lode-gold mineralization at Jundee-Nimary in the Yilgarn Craton, Western Australia. *Mineralium Deposita,* **36**, 125-136.

Z

Zeh, A., Holland, T.J.B. and Klemd, R., 2005. Phase relationships in grunerite-garnet-bearing amphiboles in the system CFMASH, with applications to metamorphic rocks from the Central Zone of the Limpopo Belt, South Africa. *Journal of Metamorphic Geology,* **23**, 1-18.

Zhou, T., Phillips, G.N., Denn, S. and Burke, S., 2003. Woodcutters goldfield: gold in an Archaean granite, Kalgoorlie, Western Australia. *Journal of Australian Earth Sciences,* **50**, 553-569.

Tables

Figures

Additional Data on DVD

APPENDICES

FIELD CARDS

FieldCard_DMF(07).pdf	Field criteria for metamorphic facies in mafic and pelites.
FieldCard_FlowRegime(07).pdf	Field criteria for rock flow regime.
FieldCard_QFII(07).pdf	Field criteria for qualitative foliation intensity index.
FieldCard_ShearSense(07).pdf	Field criteria for shear sense determinations.
FieldCard_Strain(07).pdf	Field criteria for semi-quantitative strain determinations.

TALKS

Talk_pmdCRC#1_Goscombe06

Talk_pmdCRC#2_Goscombe06

Talk_pmdCRC#3_Goscombe07

Talk_pmdCRC#4_Goscombe08

Talk_KAL07_Goscombe07

POSTERS

Poster_KAL07_Goscombe07.pdf

Poster_pmdCRC#1_Goscombe08.pdf

Poster_pmdCRC#2_Goscombe08.pdf

Poster_pmdCRC#3_Goscombe08.pdf

Poster_pmdCRC#4_Goscombe08.pdf

Poster_pmdCRC#5_Goscombe08.pdf

ABSTRACTS

Abst_AESC_Czarnota08.pdf

Abst_AESC_Goscombe08.pdf

Abst_KAL07_Goscombe07.pdf

FieldGuide_AESC_Goscombe08.pdf